Geotechnical, Geological and Earthquake Engineering

Rajesh Rupakhety
Símon Ólafsson *Editors*

Earthquake Engineering and Structural Dynamics in Memory of Ragnar Sigbjörnsson

Selected Topics

Springer

Geotechnical, Geological and Earthquake Engineering

Volume 44

More information about this series at http://www.springer.com/series/6011

Rajesh Rupakhety • Símon Ólafsson
Editors

Earthquake Engineering and Structural Dynamics in Memory of Ragnar Sigbjörnsson

Selected Topics

Springer

Editors
Rajesh Rupakhety
Earthquake Engineering Research Center
University of Iceland
Selfoss, Iceland

Símon Ólafsson
Earthquake Engineering Research Center
University of Iceland
Selfoss, Iceland

ISSN 1573-6059 ISSN 1872-4671 (electronic)
Geotechnical, Geological and Earthquake Engineering
ISBN 978-3-319-62098-5 ISBN 978-3-319-62099-2 (eBook)
https://doi.org/10.1007/978-3-319-62099-2

Library of Congress Control Number: 2017958036

Printed on acid-free paper

This Springer imprint is published by Springer Nature
The registered company is Springer International Publishing AG
The registered company address is: Gewerbestrasse 11, 6330 Cham, Switzerland

To Ragnar: our mentor, source of inspiration, and friend.

Preface

This book is a collection of invited papers presented at the International Conference on Earthquake engineering and Structural Dynamics (ICESD) that was held in Reykjavik, Iceland, from 12th–14th June, 2017. The conference was held in honour of late Professor Ragnar Sigbjörnsson. Ragnar received his formal education in structural mechanics, which he applied in solving practical engineering problems and advancing the state-of-the-art in areas such as wind engineering, engineering seismology, earthquake engineering, and offshore engineering. Application of structural dynamics principles in wind and earthquake engineering was his main area of research and teaching. He had a very keen interest and deep understanding of modelling and analysis of random fields, which combined with his knowledge and skills in structural mechanics, established him as a leader in research areas such as structural dynamics and earthquake engineering. Ragnar was also keenly interested in safety science and reliability, and actively studied and pursued research in disaster risk management. Although Ragnar maintained a very diverse and cross-disciplinary research portfolio, his main focus was on (i) earthquake engineering and seismology (ii) dynamics of special structures such as floating bridges, long-span suspension bridges, submerged floating tunnels, and offshore structures, and (iii) earthquake risk evaluation, perception, and management.

This book includes contributions in these three fields. Due to the vast nature of these fields, it is impossible, in a small volume like this, to thoroughly and rigorously address all the issues they deal with. We merely present selected topics within these fields: topics which Ragnar was most interested in and contributed to. Many of the chapters are written by his collaborators, close friends, and colleagues, presenting methods and results that cover and extend beyond the state of the art in structural dynamics and earthquake engineering. Of the 19 chapters presented here, 7 are written by invited Keynote Speakers at the ICESD, who are among the most distinguished scientists and researchers. These chapters showcase, not only the historical perspective of the state-of-the-art, but also the most recent developments and provide a glimpse into the future of research in earthquake engineering and structural dynamics. Other chapters are written by renowned researchers, many of whom were also close collaborators of Ragnar. Some of the chapters are based on the work

initiated and led by Ragnar himself. The book will be useful for both researchers and practising engineers who are interested in the recent advances and future directions in these fields of scientific research and engineering practice.

The book starts with a short biography of Ragnar, entitled, "Ragnar Sigbjörnsson: A Scientist who went from a Tiny Town to World Reknown". The chapter is written by one of Ragnar's daughters, S. Ragnarsdóttir, together with his long-time collaborators S. Ólafsson and Svein Remseth, and his student and apprentice R. Rupakhety. The chapter highlights aspects of Ragnar's life as a scientist and educator, as well as a person and a family man; the latter is perhaps not as well-known to the readers as the former. This is a short description of his fascinating and inspiring journey from a small village of Borgarfjörður Eystri in North Iceland, to become one of the most distinguished scientists not only in Iceland and Norway, but worldwide.

The rest of the chapters are divided into three parts. The first part includes selected topics in earthquake engineering and engineering seismology. It starts with the chapter written by P. Gülkan and M. A. Sözen, presenting a genealogy of performance-based seismic design. This chapter is a must-read for anyone interested in the history of performance-based seismic design (PBSD), its evolution and maturation, as well as uncertainties and challenges in its practical application. The focus is on using structural drift as a central parameter in performance evaluation, which is although a positive influence of PBSD, the authors review and present compelling evidence on the lack of knowledge and tools to accurately estimate seismic drift demands of, for example, reinforced concrete structures. They highlight important considerations for practical use of PBSD, and advise its cautious use with a proper understanding of uncertainties in structural calculation, which may be, to non-specialists, masked by the sense of false confidence offered by advanced structural analysis methods. The second chapter of Part 1, written by Michael N. Fardis, addresses the important issue of structural design to multiple extreme hazards. The chapter describes how the vast knowledge of research and development in seismic design of structures that has accumulated since the 1970s can provide a baseline for structural design for extreme loads such as larger blasts and fire. Ignoring extreme events in structural design is projected as a defeatist stance which is not in lieu with the spirit of modern performance based design. At the same time, the futility to associate probabilities to extreme threats, which are by definition *unknown*, is highlighted and emphasis is placed on consequence-based design method. Design decisions for such extreme events are more rationally based on the expected consequences. Issues such as progressive collapse and unexpected loss of a structural member and its consequences on the global stability of structures are addressed, and are illustrated with experimental and numerical investigations. Based on detailed investigations and thorough analysis of experimental results, the chapter provides guidelines on design features which enhance structural resilience to multiple hazards in contrast to those that are efficient against some hazard but detrimental against others. These guidelines are stipulated in simple terms and serve practical conceptual design of structures resilient to multiple hazards.

Moving on from the philosophy and intricacies of PBSD in Chap. 1 and structural design for extreme loads in Chap. 2, Chap. 3 by A. Ansal et al. addresses a very

important issue in seismic design of structures: the definition of design loads considering local site effects, in particular, the effect of site response in design acceleration spectrum. The chapter addresses the problem of deriving a uniform hazard spectrum (UHS) at the surface of a site based on the UHS at the bedrock. The chapter introduces a simplified procedure to derive a response spectrum at surface based on UHS at the bedrock and probabilistic treatment of uncertainties in site amplification through site response analysis using multiple hazard-compatible ground motions and Monte Carlo simulation of soil layer thickness and shear wave velocities. Modelling of damping in nonlinear time history analysis of structures is addressed in Chap. 4 by A. J. Carr and A. M. Puthanpurayil. Modelling damping at global level, by using models such as mass and/or stiffness proportional models has been found to be unrealistic in many studies. In lieu of stiffness and inertial properties, formulation of damping properties at element level, and subsequent assembly of global damping matrix is desirable, and consistent within the general framework of finite element analysis. This chapter presents the formulation of damping matrix at element level, both for discretized elements and continuum models, and illustrates the advantages of this approach against the conventional damping models based on global structural mass and stiffness matrices.

Challenges in modelling the seismic response of reinforced concrete (RC) walls, which are very effective in carrying lateral forces due to wind and earthquakes, is discussed in Chap. 5 by T. Isakovic and M. Fischinger. This chapter underlines the limitation in modelling inelastic response of structures referred to as a difficult obstacle in successful implementation of PBD, as discussed in Chap. 1 by P. Gülkan and M. A. Sözen. Isakovic and Fishinger present the basic features of a macro element capable of modelling flexural-axial-shear interaction in RC walls. They also present experimental results that demonstrate the efficacy of the proposed macro element to model complex axial-flexural-shear interactions and capture global response of the experimentally tested walls. In Chap. 6, I. Takewaki et al. address one of the most pressing contemporary issues in earthquake engineering: modelling of near-fault ground motions and their effects on structures. They use double- and triple-impulse excitations to represent near-fault ground motions and derive approximate closed-form solutions for response of elastoplastic system subjected to such motions. The approximate solutions are shown to be close to that obtained from inelastic analysis of recorded near-fault ground motions. Closed-form solutions of these kind are very valuable to study a large number of structures, to conduct reliability analysis, as well as in parametric analysis to understand the effects of different ground motion and structural parameters in seismic reliability of structures. Effect of near-fault ground motions on seismically isolated liquid storage tanks is addressed in Chap. 7 by S. Öncü-Davas et al. This chapter investigates the effectiveness of simple analytical models of near-fault ground motion in predicting the seismic response of base-isolated liquid storage tanks. Their results indicate that not all analytical models match the response induced by actual near-fault ground motion equally well. The success of the analytical models was found to be dependent on the response quantity being investigated: bearing displacement, isolation system shear

force, and fluid-tank shear forces were found to be represented more accurately than sloshing displacements.

Wave height and total energy of landslide-generated tsunamis is addressed by J. Eliasson in Chap. 8. Submarine landslides triggered by even small earthquakes can cause large tsunamis. Eliasson uses translatory wave theory, which was originally proposed by him, to estimate the initial wave height and the associated wave energy. Equations to estimate these parameters are given and a general outline to use the results in estimating their exceedance statistics, which essentially constitute a probabilistic tsunami hazard curve, is presented.

Estimation of surface strain rate tensor field from GPS network, and the subsequent interpretation of seismicity of Iceland is presented in Chap. 9 by R. Sigbjörnsson et al. Based on GPS measurements from the base stations of the National Land Survey of Iceland, the methodology of estimating strain rate tensor and vorticity tensor is demonstrated. The results, based on data assembled between 1993 and 2004, indicate a velocity field governed by rigid plate motion of the North American Plate and the Eurasia Plate. Significant strain rates exist in the rift between the two plates. The largest shear strain is in the South Iceland Seismic Zone, where the epicentral areas of the two ~Mw6.5 earthquakes in June 2000 conform to the regions of largest strain rates. Stochastic modelling of strong ground motion due to earthquakes in South Iceland Seismic Zone (SISZ) is presented in Chap. 10 by Ólafsson et al. Ground motion records from the recent earthquakes were found to have a source spectra which fit well with the point source model of Brune. Source parameters of the four largest earthquakes in Iceland for which accelerometric records are available are estimated and used to construct theoretical models of peak ground motion parameters. Such models are based on source spectra of point source, with incorporation of attenuation in the near- and far-field, and provide closed-form solutions for root-mean-square (rms) acceleration, which can be converted to peak acceleration through peak factors that depend on duration of shaking. The resulting model is shown to fit the recorded data better than purely empirical Ground Motion Prediction Equations (GMPEs), and can also be used to simulate artificial ground motion models, stochastically equivalent to the data they are calibrated from.

Seismic vulnerability of Icelandic residential buildings is presented in Chap. 11 by B. Bessason and R. Rupakhety. Based on damage data collected during recent earthquakes, the chapter provides a review of the types of damages sustained by buildings and their corresponding frequencies. Fragility and vulnerability curves for different building typologies, and their application in scenario risk estimation are presented. Buildings in South Iceland are found to be very resilient to earthquakes of magnitude 6.5 or lower, even in the near-source area where ground acceleration as high as 80% of acceleration due to gravity has been recorded. Most of the damage was of non-structural type, which indicates that despite the good structural performance, considerable risk of injury/casualty exists due to movement of household objects. This risk was somewhat mitigated due to the fortunate timing of the earthquakes in June 2000 and May 2008. Measures to improve seismic safety in South Iceland should focus on prevention of hazardous movement of building contents,

which is more easily accomplished than improving structural performance, but perhaps, overlooked due to complacency and lack of safety culture.

Damage to non-structural elements and the subsequent loss of function and cost of repair are a growing concern in earthquake engineering research. Infill walls constitute a major concern in this regard. Damage and failure are not only costly, but may also cause serious injuries to the occupants. M. Vailati et al. present in Chap. 12, a novel technology of earthquake resilient and energy-efficient infill panels using hollow concrete or clay blocks that are dry-juxtaposed, rather than joint with mortar layers. The joints consist of recycled-plastic elements forming a preferential sliding plane to accommodate horizontal displacements imposed by ground shaking. Experimental and analytical results presented in the chapter show that the proposed infill panels are not only structurally more resilient than traditional mortar-joined brick walls, they are also more energy efficient.

The second part of the book contains three chapters written by Ragnar's colleagues and collaborators at Norwegian University of Science and Technology (NTNU). These chapters are related to structural dynamics, design, and monitoring of special bridges; namely long-span suspension bridges, floating bridges, and marine bridges. These chapters are based mostly on research carried out at NTNU to find innovative solutions to make the E39 Highway in Norway ferry-free under the Coastal Highway Route E39 Project, in collaboration with the Norwegian Public Roads Administration (NRPA). The highway needs to cross many deep and wide fjords where conventional bridges are not feasible, and more challenging modern solutions are being sought. The first chapter in this section, Chap. 13 by A. Fenerci and O. Øiseth, is about the Hardanger Bridge, which Ragnar studied as a young engineer during his early career at NTNU. The bridge is the longest suspension bridge in Norway with a main span of 1310 meters. The chapter presents full-scale measurements and analysis of wind-induced vibrations of the bridge, which lies in a complex terrain. The results indicate that mean wind speed and vertical turbulence intensity are the two most important wind parameters influencing dynamic response of the bridge. Lateral response is controlled by the along-wind turbulence while cross-wind turbulence was found to produce torsional vibrations. The results show that variability in wind field in complex terrain can result in large scatter in dynamic response. Modelling of such effects is essential in reliable design and is being actively pursued at NTNU.

In Chap. 14, K. A. Kvåle et al. present methods of simulation and monitoring of a floating bridge dynamics. The bridge discussed in this chapter is the Bergsøysund Bridge, a 931 m long arch-shaped pontoon bridge. The chapter presents the theoretical framework of dynamic modelling of floating bridges considering fluid-structure interaction, modelling of random water waves, as well as time- and frequency-domain solution strategies of the governing equations of motion. Results of dynamic simulation of the Bergsøysund Bridge using the finite element method are presented, and compared with results of operational modal analysis carried out from an extensive structural monitoring system installed on the bridge. Stochastic dynamic second-order response analysis of marine bridges is presented in Chap. 15 by B. J. Leira. This chapter presents the formulation of basic equations of motion of

second-order wave-induced loading on floating and submerged bridges, and demonstrates a simplified procedure to estimate second-order loading. The simplified procedures for a submerged tunnel bridge with surface pontoons are compared with more refined methods, namely, the numerical panel model. A case study of the 3700 m long Sognefjord Bridge is presented, and the results from simplified analysis methods were found to be in good agreement with those obtained from refined models.

The last part of the book is related to selected topics in seismic risk assessment, risk communication/perception, and management. This part consists of four chapters. The first chapter of this part, Chap. 16 by C. S. Oliveira et al. discusses new tools and methods for the analysis of generalized impacts of earthquakes. The chapter is based on research carried out in the last decade by the Group of Seicmic Risk of Instituto Superior Técnico (IST), Lisbon, Portugal. The chapter focuses on indicators of earthquake impact. Of particular interest is the newly developed idea of Disruption Index (DI) which is a holistic measure of earthquake impact, that incorporates the physical damages to different elements of an infrastructure, the loss of function due to such damages, and the complex interactions and interdependencies between these elements including the cascading effects of loss of functionality of an element due to damage in another element. The chapter also provides a framework for incorporating the impact indicators with performance indicators such as risk reduction worth and risk achievement work to mitigate risk. Chap. 17 by G. Musacchio et al. presents the main findings of the UPStrat-MAFA (Urban Disaster Prevention Strategies using Macrosiesmic and Fault sources) project, that incorporated a multi-disciplinary approach to disaster prevention encompassing strategies based on the analysis of level of risk and information. Ragnar was one of the key persons in the project, and was very enthusiastic about it. Uses of macroseismic information and its probabilistic treatment for hazard analysis are presented. A holistic approach to risk assessment, through the DI (see Chap. 16) was one of the most important contributions of the project, and some of its applications are detailed in this chapter. The project strongly emphasized prevention strategies based on education and communication of risk, and developed video games for children, and audio-visual products for the general public. A summary of these achievements and products is presented in this chapter.

Chapter 18 by R. Sigbjörnsson et al., is the penultimate chapter of this book, and is related to gender-dependence on the perception of earthquake effects and residential safety. The chapter presents statistical analysis of response to a questionnaire survey campaign carried out in the epicentral area of the two ~Mw 6.4 earthquakes in South Iceland. The questions addressed in this chapter are the actions taken by people inside their houses during earthquakes. The results indicate that a significant proportion of the respondents (~15%) could not move during the earthquakes. While majority of male did not seek shelter, most of the female respondents sought shelter. The results also showed that female take more time than male to recover from the negative experience of earthquakes. It was also observed that the female respondents were biased towards higher intensities (macroseismic,

Modified Mercalli Intesnity), while the male respondents were biased towards lower intensities.

In the final chapter in this book, Chap. 19, S. Platt discusses and analyses the factors affecting the speed and quality of post disaster recovery and resilience. The chapter provides an insight about post-disaster resilience and recovery from a comparison of ten recent earthquake disasters. The analysis indicates that speed of recovery is, at least for the disaster studied in this chapter, not strongly dependent on exogenous factors of size of impact, population demographics and economics factors. Both speed and quality of recovery are shown to be strongly related to the post-disaster management and decision making. The chapter provides key issues to be considered by governments and decision makers in hazard prone countries to "build back better" after a disaster. Despite growing knowledge, research and development in seismic resilient construction, earthquakes are a serious threat to our society. While some countries are better prepared to mitigate and manage disasters, others are very poorly prepared. In the latter case, post-disaster recovery becomes a very complicated process with several national and international actors. Lack of local leadership and a clear and rational vision for recovery and reconstruction makes disasters more disastrous. It is our belief that earthquake engineers have a prominent role to play, not only in designing and constructing resilient infrastructure, but also in shaping the reconstruction plan, as they are well equipped with the knowledge to learn what went wrong during a disaster, and how it can be fixed. Involvement of earthquake engineers in academic research as well as practical participation in disaster mitigation planning and post-disaster reconstruction decision-making will be vital for our future earthquake resilient societies.

We wish to extend our gratitude to all the authors of the included chapters for their contributions to this book. We are thankful to Professor Atilla Ansal, who proposed the idea of the ICESD, and provided us continuous support and encouragement in preparing this book. Special thanks are due to Petra van Steenbergen, Springer executive editor of Earth Sciences, Geography and Environment, for her support in preparing this book. We are grateful to the international scientific committee of the ICESD and other colleagues for reviewing the chapters presented in this book, and for providing valuable comments and suggestions for improvement.

Selfoss, Iceland

Rajesh Rupakhety
Símon Ólafsson

Contents

Ragnar Sigbjörnsson: A Scientist Who Went from a Tiny Town to World Renown

Ragnar Sigbjörnsson was born on May 7, 1944, in Borgarfjörður Eystri, a small village in the northeast of Iceland. This village remained very dear to him. His parents were Sigbjörn Jakob Guðmundsson (1904–1970), a carpenter and an organist, and Jónanna Steinsdóttir (1906–1979), a housewife. Ragnar was one of three brothers: Bjarni, the eldest (1938–1981); Ragnar, the middle child; and Guðmundur Ingi, the youngest (1947) (Fig. 1).

Fig. 1 *left* Ragnar with his maternal grandmother Guðrún **right top**: Ragnar's parents Jónanna and Sigbjörn **right bottom** The three brothers (from left) Guðmundur Ingi, Bjarni and Ragnar

Ragnar's family home in Borgarfjörður Eystri was named Ásgarður. There, he grew up in a big family with his parents, brothers, both grandmothers, and two maternal uncles. From a young age, he was greatly influenced by Jóhannes S. Kjarval (1885–1972) who was, and still is, one of Iceland's most beloved artists. Kjarval grew up in Geitavík, also in Borgarfjörður Eystri, and went there every summer to stay at his summer cabin. Ragnar often followed him around, watching him paint in nature. On one occasion, Kjarval gave him a piece of string in the colours of the national flag. Ragnar treasured this string and tied a knot on both ends so it would not unravel. Many years later, when Ragnar was at university, he met Kjarval again. Kjarval asked him if he still had the string. Ragnar had to tell him, with great sadness, that it had gone missing. Ragnar, who picked up a few tricks from Kjarval, was himself a good painter and even sold paintings during his school years. This experience shaped him and gave him a great love of and appreciation for art.

As a child, Ragnar already had the strong urge to ask questions, get answers and challenge things. He was always experimenting, for example, on how high a box kite or various types of balsa-wood aeroplanes could fly and asking what needed to be changed or improved so that they did better. He built all kinds of models, not to have on the shelf, but on which to experiment.

At the age of 13, he went to a boarding school called Alþýðuskólinn á Eiðum. It was not very common that children from his remote village would seek further education since the town lacked an overland connection during winter until 1965. However, Ragnar's desire and urge to know more drove him to pursue his education. To attend school, he had to make a two-day's journey. He had to walk or ski, sometimes in heavy snow or blizzards, for a day until he reached the farm, Unaós, where he stayed overnight and continued onward with a vehicle. Ragnar's diligence, endurance, and perseverance definitely came from this early hardship in seeking an education. These are traits that he carried throughout his life—always working as hard as he could, driven by desire to know more, and possessing a strong will and determination.

Ragnar moved to Akureyri, at the age of 16 to attend secondary school at Menntaskólinn á Akureyri (MA), where he met his future wife Bjarnveig Höskuldsdóttir (1946). Music was second nature to Ragnar, as he was brought up in a very musical family. He played classical guitar. During his years in Eiðar and Akureyri, he played in a few groups. During his life, the guitar was never far away from him. He loved playing either to relax or to be at the centre of a party, singing and strumming. Ragnar graduated from MA in June 1965. At that time, he and Bjarnveig moved to Reykjavík (Fig. 2).

During his MA and university years, Ragnar worked for the Icelandic Road Administration, building structures, for example, roads and bridges, during summer vacations. Ragnar was always thankful for the opportunity to work for the Icelandic Road Administration. He said many times that this made it possible for him to pursue his education at MA and the University of Iceland. He also worked for the National Land Survey of Iceland. While working there, he met Jón í Möðrudal (1880–1971) who taught him to sight-read music in the church in Möðrudalur. Jón once told Ragnar's parents that he had never taught such a quick-learning teenager.

Fig. 2 *left*: Ragnar on graduation day from MA *middle*: Ragnar was fond of music and played guitar from an early age *right*: Ragnar and Bjarnveig on their wedding day

In July 1964, Ragnar and his younger brother were building bridges across rivers in Njarðvík. Usually, everyone went home for the weekend, but, as the brothers lived in Reykjavík, it was not possible for them. Therefore, the brothers decided to climb the magnificent mountain of Dyrfjöll (Door Mountains, 1136 m, shown in Fig. 3). It was a warm, sunny day on that side (Fljótdalshérað). When they came up through the pass and looked over Borgarfjörður Eystri, they could only see the highest peaks of Staðarfjall and Svartfell due to heavy fog rolling in below. Jökuldalur (Glacier Valley), named after the small glacier situated below, is on this side of Dyrfjöll. The brothers decided to go down through the pass and jump onto the glacier. They followed the glacier until they found the glacial river that they knew would take them home. When they came down, the fog had lifted and they arranged for someone to drive them back to Njarðvík. Not many had done this before them, and it was considered quite a dangerous achievement at that time.

In the autumn of 1965, Ragnar began his engineering studies at the University of Iceland. In February 1966, their first daughter, Anna Birna, was born. Ragnar and Bjarnveig got married on September 30, 1967, and he finished his studies at the University of Iceland in June 1968.

After finishing his first engineering degree in Iceland, Ragnar and his young family headed to Denmark, where he earned his master's degree from the Technical University of Denmark (DTU) in 1971 and a PhD from the same university in 1974. Following his studies in Denmark, he was hired as a research engineer at SINTEF, the research foundation of the Norwegian Institute of Technology (NTH), which is now called the Norwegian University of Science and Technology (NTNU).

Ragnar had a solid mathematical background, which was important when it came to stochastic modelling of environmental loads, such as wind, sea waves, and earthquakes, and their associated effects on structures. His exceptional skill in applying knowledge to practical problems soon made him a prominent researcher at

Fig. 3 The Dyrfjöll (Door Mountains, 1136 m) in Borgarfjörður Eystri (photo credit: Hafþór Snjólfur Helgason)

SINTEF in the development of safe offshore structures for the oil and gas industry and long suspension bridges in cooperation with the Norwegian Public Road Administration. Ragnar worked at NTH/SINTEF until 1979. During this time, he and his family lived in Heimdal, Trondheim. Two more daughters were born in Norway, Sólveig (October 1977) and Bryndís (July 1979) (Fig. 4).

The family returned to Iceland in the autumn of 1979, when Ragnar initially took a research position and later a professorship at the University of Iceland. The family settled down in the beautiful town of Mosfellsbær, where they built a home designed by Ragnar.

Although Ragnar lived in Iceland for the remainder of his life, he continued to have strong contact and collaboration with his colleagues in Norway. In 1979, Ragnar and Ivar Langen published a textbook on the dynamic analysis of structures (*Dynamisk Analyse av. konstruksjoner*, in Norwegian). Ragnar had very close and productive collaboration with his colleagues and friends Erik Hjorth-Hansen, Svein Remseth, and Bernt Leira, among others, at NTNU, as well as at the Norwegian Public Roads Administration (NPRA). Ragnar held a professorship at NTNU until his death and had been supervising MSc and PhD students at NTNU for a long period. He was an excellent supervisor and was very much appreciated by the students and his colleagues.

A major effort made by Ragnar, when he went to NTNU in 2009, was the planning of a research program for fjord crossings along the highway route E39 on the western coast of Norway. The seven or eight major fjords require bridges to span between 2000 and 5000 meters. Ragnar's knowledge and experience from planning offshore struc-

Fig. 4 Ragnar with his wife and daughters in 2003

tures and various types of bridges, such as submerged floating tunnels, floating bridges, and suspension bridges, was of vital importance in defining the research required for the new bridges requiring extreme spans. The research program was planned for several PhD students and postdoctoral researchers, along with additional research by senior personnel acting as supervisors. At present, between 15 and 20 temporary positions at NTNU are financed by this research program. The project comprises the theoretical development of methods of analysis and numerical models of load processes based on meta-ocean data and integrated analysis of interactions between the bridge structure and the fluid, air, and soil environments. These are complex problems, and there is a definite need to compare numerical simulations with measurements. Ragnar played a vital role in the planning of the instrumentation on two bridges with relevance to the E39 project, the Hardanger Bridge and the Bergsøysundet Bridge (see Chaps. 12 and 14 for more details). Ragnar had, as a young researcher, worked on the analysis and design of Hardanger Bridge and was very excited when one of his first, major engineering projects was built and opened to traffic. The instrumentation program planned by Ragnar has already provided, and continues to do so, very valuable data that have proved important for the validation of load and interaction modelling.

When Ragnar came to the University of Iceland in 1979, he soon became a leader in engineering research. He was the director of the Engineering Research Institute during its starting phase of 1983–1990. Ragnar also headed the Applied Mechanics Laboratory, a small research group that focussed on research in structural mechanics. Gradually, he focussed his research on earthquakes and their effects on structures. Ragnar established the Icelandic Strong Motion Network in 1986. The Icelandic Strong Motion Network has recorded many significant earthquakes in Iceland, and it

is the most important source of strong ground-motion data in Iceland. The Icelandic Strong Motion Network has tremendous value for seismic-hazard assessment in Iceland. In 2000, he founded the Earthquake Engineering Research Centre of the University of Iceland. He was its director until he retired in 2014 and the head of its Board of Directors until his passing. Ragnar contributed to the establishment of seismic design provisions of the most noteworthy, contemporary civil engineering works. He was very successful in applying the results of his research to solving practical problems and was consulted by various industries in Iceland regarding the safe design of their structures, most notably power plants near seismically hazardous areas in the south Iceland lowlands, as well as in northern Iceland. The advances in strong-motion monitoring, structural monitoring, seismic-hazard assessment, and structural design that he initiated are very important for Iceland, with the majority of its 330,000 inhabitants living close to seismically active areas.

While very active and productive in academic research and practical consulting, Ragnar was equally passionate about his teaching at the University of Iceland. He played an important role in shaping the current curricula of the civil engineering degree at both the BS and the MS levels. He was very ambitious as a teacher and designed, coordinated, and taught advanced courses, such as continuum mechanics, computational mechanics, stochastic mechanics, structural dynamics, earthquake engineering, risk analysis, etc. Many of these courses are still very relevant to the curriculum and are being taught following his vision and objectives. Ragnar spent a lot of time preparing lecture notes, slides, and other educational materials for his students. He continuously worked to provide his students with the most up-to-date information, not only on the classical theories that he taught, but also on their practical implications and developments at the forefront of research (Fig. 5).

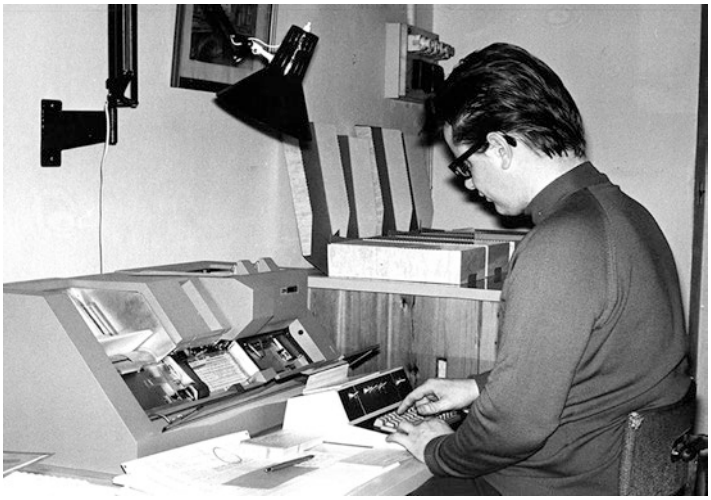

Fig. 5 Ragnar programming on a punching machine during his early career at University of Iceland

Fig. 6 Ragnar with his friend and colleague Prof. Athol J. Carr during his visiting professorship at the University of Canterbury

Ragnar was very active internationally and had numerous contacts worldwide. One of his most notable research collaborations was with the late Professor Nicholas Ambraseys at Imperial College London, where Ragnar was a visiting professor during 2001–2003. A review of an earthquake catalogue for Iceland was among the many works they completed. In 2006, he was a visiting professor at the University of Canterbury in New Zealand with Professor Athol Carr, a time he greatly enjoyed and fondly remembered. He participated in many international scientific conferences. In 2014, he attended the Second European Conference on Earthquake Engineering and Seismology (2ECEES) in Istanbul, Turkey. Ragnar was very satisfied with the conference and enjoyed his time in Istanbul by visiting its magnificent monuments, which brought back memories from earlier visits (Figs. 6 and 7).

Ragnar was very enthusiastic about the last international project he worked on, the EU project UPStrat-MAFA (Urban Disaster Prevention Strategies using MAcroseismic and FAult sources). He played a valuable role in this project, which produced many innovative methods and products for the prevention of urban disasters due to earthquakes and volcanoes. He worked very closely with his friends and collaborators, Carlos Sousa Oliveira and Gaetano Zonno, during this project. Ragnar played a very important role in producing the special issue of the prestigious journal of the Bulletin of Earthquake Engineering, presenting the research results of the UPStrat-MAFA project. He was a co-editor of this issue as well.

Fig. 7 *Left*: Ragnar and his colleagues with their spouses (*from left to right*, Bjarnveig, Ragnar, Carlos Sousa Oliveira, Isabel Oliveira, Gaetano Zonno, and Cecilia Zonno) during the gala dinner of the 2ECEES; *Right*: Ragnar and Bjarnveig enjoying their time in Istanbul during the 2ECEES

Fig. 8 *Left*: Ragnar on the deck of MSC Orchestra during the IZIIS-50 conference; he was very fond of offshore structures, bridges and wind turbines (in the background). *Right:* Ragnar delivering his last international conference lecture onboard MSC Orchestra during the IZIIS-50 conference

Ragnar's appetite for engaging in scientific work, initiating scientific dialogue, and disseminating research results was perhaps best exemplified by his strong will, despite his degrading health, to participate in his last international conference: The IZIIS International Conference on Earthquake Engineering and Engineering Seismology, which was held on the cruise ship MSC Orchestra travelling in the Baltic Sea May 12–16, 2015. He was very passionate about this conference and delivered a lecture on offshore-earthquake engineering (Fig. 8).

Ragnar was very fond of travelling and learning about various different cultures. He appreciated the natural beauty and sociocultural heritage of the places he visited. In 2012, he and Bjarnveig travelled to Nepal to attend the wedding of his student and apprentice Rajesh Rupakhety. Ragnar enjoyed the trip very much and often mentioned that he felt like he had been there before. He was touched by the landscape and mountains of the country and captured a magnificent photograph of the Machhapuchhre Mountain from the balcony of his hotel room in Pokhara early in

Fig. 9 Ragnar and Bjarnveig in traditional Nepalese dress, ready to attend the wedding ceremony of his student and apprentice

the morning, before the clouds started covering the mountain top. For many years to follow, Ragnar talked about his experience of waking up and seeing this magnificent mountain standing right in front of him (Fig. 9).

Ragnar's fondness for bridges is perhaps best exemplified by an adventure that took place in Nepal. After a long and tiring trip to Pokhara, Ragnar, Bjarnveig, Rajesh, and Puja (Rajesh's wife) made a late stop in Abu Khaireni for lunch on their way back to Kathmandu. Despite being tired, Ragnar spotted a suspension bridge over the Marsyangdi River. As soon as he spotted it, walking across the bridge and understanding its dynamic characteristics became his priority. Lunch could wait (Fig. 10).

Apart from music, Ragnar was very interested in poetry and knew an enormous number of poems. He enjoyed reading poems and found it to be relaxing for the soul. One of his last and most consuming projects was to publish the book *Gengin Spor* in cooperation with his younger brother Guðmundur Ingi. This book is a tribute to their maternal uncle, Bjarni Steinsson (1902–1963), and contains poems by Bjarni that Ragnar's mother collected over the years. Ragnar visited his birthplace of Borgarfjörður Eystri in June 2014, where a special ceremony was held to celebrate the release of *Gengin Spor* (Fig. 11).

Fig. 10 *Main photo*: The Abu Khairini Suspension Bridge over the Marsynagdi River in Gorkha, Nepal **inset**: Ragnar with Rajesh following him, crossing the bridge and investigating its vibrational characteristics

Fig. 11 Ragnar in his hometown Borgarfjörður Eystri, on his way to celebrate the release of *Gengin Spor*

Fig. 12 Ragnar receiving the Knight's Cross of the Order of the Falcon from the then president of Iceland, Olafur Ragnar Grimsson

All those who knew Ragnar were aware that he was very skilled and passionate about his work. Ragnar was open to new ideas and was not afraid to venture into new research territory. He was aware of the human element of engineering, and his interdisciplinary work set an example for others to follow. Ragnar was a popular teacher. As a mentor, he had tremendous influence on numerous engineers and researchers, both in Iceland and abroad. Ragnar was among the most active and productive researchers at the University of Iceland, and he received numerous awards for his work. In 2003, the president of Iceland awarded Ragnar the Knight's Cross of the Order of the Falcon for his work in the fields of science and education. Ragnar was a Rotarian and had received the highest award in Rotary, the Paul Harris Award, for his outstanding contribution (Fig. 12). He was also a Freemason. He found these societies to be both rewarding and immensely enjoyable.

Ragnar passed away on July 15, 2015, after a short battle with cancer. Ragnar was a very influential teacher and researcher at the University of Iceland in applied mechanics, earthquake engineering, and engineering seismology. He was also a family man who loved his wife, daughters, and their families. He enjoyed hosting banquets and trying new things in the kitchen. If a celebration contained a four- to five-course meal, it was perfect. His elegance and accuracy shone through when he was setting a table for a celebration; it was always exquisite. He worked until the day he died; he never gave up, and he taught people around him to never give up. The evening before he passed away, he was still working hard to finalize a research article and a special volume of the UPStrat-MAFA project that was published in the Bulletin of Earthquake Engineering.

Ragnar leaves behind a large legacy, and his work has led to great progress in engineering education and in earthquake research. His contributions have opened numerous doors for engineers and researchers to come. Memories of him, filled with love, inspiration, motivation, sympathy, and elegance, will be cherished by many for the rest of their lives.

Reykjavík, Iceland — Solveig Ragnarsdóttir
Selfoss, Iceland — Rajesh Rupakhety
Reykjavík, Iceland — Símon Ólafsson
Trondheim, Norway — Svein Remseth

Part I
Earthquake Engineering and Engineering Seismology

Chapter 1
Genealogy of Performance-Based Seismic Design: Is the Present a Re-crafted Version of the Past?

P. Gülkan and Mete A. Sözen

Abstract Structural engineering for earthquake resistance is undergoing a major revision in its approach toward the fulfillment of seismic safety and utilitarian serviceability in design. Rather than sticking to the established precepts of prescriptive design rules, design has turned toward the achievement of specific results through procedures that are tailored for different buildings and uses. These procedures represent notable research contributions, but they are complicated conceptually for implementation in structural engineering practice, and nonlinear building response estimates, frequently assumed to be performance, can vary within broad limits even for simple applications.

In this text we relate the history of code developments. We focus on the two main requirements of earthquake-resistant design of building structures: (1) Life Safety and (2) Protection of the Investment and relate the two demands to current concepts of Performance-Based Building Design. While we provide a personalized vision for the way in which the PBSD framework developed and matured during the last half century, a thorough historiography is not within the scope of the text. We nominate drift to serve as the prime metric for performance judgment.

Keywords Performance-based seismic design • Base shear • Drift ratio

P. Gülkan (✉)
Program of Civil Engineering, Middle East Technical University-Northern Cyprus Campus, Güzelyurt, Mersin 10, Turkey
e-mail: polatgulkan@gmail.com

M.A. Sözen
School of Civil Engineering, Purdue University, W. Lafayette, IN 47906, USA

R. Rupakhety, S. Ólafsson (eds.), *Earthquake Engineering and Structural Dynamics in Memory of Ragnar Sigbjörnsson*, Geotechnical, Geological and Earthquake Engineering 44, https://doi.org/10.1007/978-3-319-62099-2_1

1.1 An Unofficial History of Building Codes

Performance based structural design has been with us for much longer than is recognized. A good example is the design and construction of the cathedral at Beauvais, France. The construction of the cathedral was initiated in 1225 with the desire of "reaching heights taller than all existing cathedrals." In 1284, as the vaulting reached 48 m, supporting walls collapsed during construction. Another effort was made to go higher, but it also was terminated by another collapse. It was then decided not to go any higher because satisfactory performance was clearly elusive. The tools of the building trade that existed then did not meet the challenge of the objective.

Following the repair of the cracks in St. Peter's dome in Rome in the eighteenth century using a procedure related to what is currently called virtual work, structural design has been (as Cross called it) a craft, or something between science and art, that is based on experience. This important linchpin is sometimes sacrificed to the false exactness provided by computerized, nonlinear analysis of approximate models of the structure.

It was the extreme damage from the Messina earthquake of 1908 that inspired the Italian engineering community to develop a scientific base for the design of earthquake resistant building structures. Knowing better, but realizing that the engineering community of early twentieth century would be more comfortable with force related design, they based their design procedure on mythic/imaginary lateral forces of which demands could be readily combined with requirements of gravity forces. The approach was endorsed by the Japanese engineering community and then readily accepted by the international earthquake engineering community because it permitted prescriptive provisions to be drafted for codes. It took around a century to realize that drift, and not force, was the primary driver for the earthquake performance of most buildings. Drift controlled the force, not vice versa (Sozen 1981). Recognition of drift as a design criterion put the emphasis on performance that could be seen and measured. In principle, this works for existing buildings as well as in the design stage of new buildings.

A historic survey of prescriptive requirements on how to build for better seismic performance shows that these landmarks were always reached after cataclysmic experiences. These early regulations, such as were passed after the 1509 Istanbul Earthquake, 1755 Lisbon Earthquake, or the 1880 Luzon (Manila) Earthquakes, were limited to descriptions of allowable building materials and building heights. They predated the extensive use of reinforced concrete and steel. Unreinforced masonry was an allowable material in these early regulations, and no quantitative method was provided for calculating either demands or capacities. Thus they are primitive seismic codes in today's light, regulating some features of construction but not employing the quantitative methods civil engineers would later develop. That notwithstanding, these efforts are impressive for making such early attempts to improve the building stock's earthquake resistance.

The major earthquake that shook Istanbul in the summer of 1509 led to the banning of stone masonry construction in the city, because most deaths had occurred

when such buildings collapsed. This decision paved the way for the emergence of another form of disaster that plagued the city for the next four centuries: fires consumed not only timber construction but also much of the cultural heritage. Following the 1755 earthquake in Lisbon, which destroyed the city center area known as Baixa, the Marquis of Pombal gathered a group of builders to determine the best manner of earthquake-resistant construction to use for rebuilding. The type of construction selected became known as the Pombalino wall. In its complete form, it is also referred to as "gaiola" or "cage" construction. Most, if not all, of the buildings reconstructed in the reconfigured planned Baixa area were constructed with Pombalino walls, and sometimes (but not always) with complete "gaiola" timber frames, Tobriner (1984b), Langenbach (2003).

The practice of developing, approving, and enforcing building codes varies considerably among nations. Several countries have adopted model codes, including earthquake regulations, on a national basis, such as Japan, New Zealand, and Italy. In such countries, building codes are developed by government agencies or quasi-governmental standards organizations and then made to apply across the country by the central government. Until 2000, the USA had three major model codes and associated seismic regulations, and even after their integration into the International Building Code, the process of adopting and enforcing the regulations, sometimes with substantial variations, is left to state and local governments. Similarly, in India each municipality and urban development authority has its own building code, which is mandatory for all construction within its jurisdiction. In Europe, the Eurocode is a pan-European building code that has all but superseded the older national building codes. Each country must now develop its own national country annex to localize the contents of the Eurocode. The seismic component of the Eurocode is only one part of that model code. While the consistency of the regulations across European national boundaries provides a better technical basis for its seismic and other provisions, the more important motive for such a code of European scope is economic. The Euro economic block can compete more effectively against the nations outside it if its design, construction, and building material industries are guided by consistent provisions.

A model building code is a convenient resource that can be adopted by the appropriate jurisdiction as its legal requirement. This makes the cost of maintaining and updating a code more economical and also provides more design and construction consistency from one city to the next than would be the case if each developed its own code. That multiplicity of codes in a country was the rule throughout the nineteenth century and in many cases, has only gradually trended toward nationally uniform provisions in the twentieth century. Two important interests that have pushed for uniformity are the construction and building material industries, which can operate more efficiently if they have one set of rules, and the insurance industry, which desires up-to-date code provisions that can be easily evaluated for rate-setting purposes.

Tobriner (1984a) provides a historical survey of the development of building codes, noting that they originated primarily in the form of requirements for fire-resistant construction in the increasingly more congested urban settlements, and

then only much later in most countries had seismic regulations been added to them. The first systematic national building standard was the London Building Act of 1844. Among the provisions, builders were required to give the district surveyor 2 days' notice before building, and they contained regulations regarding the thickness of walls, height of rooms, the materials used in repairs, the dividing of existing buildings. The placing and design of chimneys, fireplaces, and drains were to be enforced, and streets had to be built to minimum requirements.

The City of Baltimore passed its first building code in 1859. The Great Baltimore Fire occurred in February, 1904. Subsequent changes were made that matched the contemporary fire-resistant regulations of some other large cities in the United States. In Paris, under the reconstruction of much of the city by Baron Haussmann during the Second Empire (1852–1870), great blocks of apartments were erected, and the height of buildings was limited by law to six stories. Though height limits were instituted for city planning reasons, they later sometimes became part of seismic codes in determining allowable structural systems for various heights.

1.2 Codes: Prescriptive and Performance-Based

Building code requirements are usually a combination of prescriptive requirements that spell out exactly how something is to be done, on the one hand, and performance requirements that just outline what the required level of performance is and leave it up to the designer how this is achieved, on the other. An example of the former would be a rule-of-thumb for spacing of anchor bolts in house construction. An example of the latter would be to have the engineer calculate interstory drift and then design concrete cladding to accommodate the specific distortion of the building. In recent years, there has been a move among many building codes towards more performance requirements and less prescriptive requirements. Performance-based code requirements still require tight definitions so that adequate performance can be evaluated by the building regulatory agency. The fire protection field has developed performance-based design approaches for many years, in which testing or other data can be used to provide alternate means of fire protection instead of following the prescriptive requirements of a code.

In recent years, several countries beginning with Australia, have moved to much shorter, objective-based building codes. Rather than prescribing specific details, objective-based codes list a series of objectives all buildings must meet while leaving open how these objectives will be met. When applying for a building permit the designers must demonstrate how they will meet each objective. This makes it necessary for approving authorities to employ correspondingly qualified personnel so that a productive synergy can be created between innovative designs and traditional safety concerns. It also requires a high degree of professionalism, because it gives the architect and engineer more leeway, as compared to more prescriptive requirements, and also requires a higher level of building code enforcement review. Seismic isolation, inclusion of damping devices, response history analyses, and

displacement-based design are some of the innovative approaches currently in use in some places where this higher level of design and review capacity is present. Each of these represents challenges in analysis and design that require an intimate knowledge of the underlying mechanics-based mathematical theory and its limitations. As such, they are best performed by professionals with considerable experience because there are alternative approaches that require deep insight on the part of the engineer. These are individuals who know what they don't know.

Seismic codes begin with the goal of providing safety, and many stop there in most respects, but some include requirements for protecting the functionality of essential buildings, such as fire stations, hospitals, and emergency communications and data processing centers. This is discussed in the separate chapter on Essential Facilities and is only mentioned in passing here. Some of the most stringent regulations of this type were passed in California after the 1971 San Fernando Earthquake, when the Hospital Seismic Safety Act of 1972 was passed. The Veterans Administration adopted its own regulations after that earthquake, regulations that seek to not provide not only safe hospitals but also more functional ones placing an emphasis on drift. Some voluntary above-code (performance-based design) approaches lead an owner to invest in the cost of higher seismic protection to achieve less property damage in earthquakes, but the most common seismic design criteria that go beyond the goal of providing safety are related to protecting essential functions.

1.3 Performance-Based Building Design

It would be naïve to attempt to compose a timeline with appropriate citations for the way performance-based seismic design has evolved during the last 25 years. It also would be futile to assume that such a compendium would fail to offend a good many people who would likely feel to have been omitted or at least slighted. This is a criticism we are prepared to accept. A useful, if slightly dated, compilation devoted to performance-based seismic engineering has been assembled (Bertero and Bertero 2004).

Such has been the interest shown by the world's earthquake structural engineering community in the reformatted approach to the required performance to sizing structural systems for seismic effects on the basis of basic capacity design concepts that the sheer number of publications would be an overwhelming task for anyone to list. In contradiction of the title for this paper, it is also not easy to pin parentage on any single individual for having begotten the groundbreaking, seminal concept for performance or displacement-based design at any stage of the advance of the trade. There was no Biot, for example, to figure out the concept of the response spectrum as a design tool, work out its details, and place it in front of engineers for their use. Its growth was the usual pattern for scientific progress and technical development: a cross-fertilization of experience, concepts, and laboratory tests culminating in convergence, after having occasionally followed false leads, on the true path toward predefined performance. Seemingly random ideas become crystallized into unified

methodology when they receive the acceptance of their peers. A history of performance-based seismic design is also strongly dependent on the geographic setting: differing visions exist in Europe, the USA, and elsewhere as to how it arrived at its current station (Priestley 2000).

Two contrasting visions have contributed to the birth of performance in reinforced concrete buildings. The 1960 earthquake in Agadir, a resort town in Morocco, wreaked shocking damage on buildings that had been designed to no seismic provisions (Clough 1962). In the interest of countering the undesirable impression that reinforced concrete buildings might be unsuitable in seismic regions, PCA had Blume et al. (1961) produce a book where the importance of deformability for acceptable performance was stressed. Much of the development during the last 30 years that has occurred in the USA has received the support of FEMA, a federal agency charged, along with other duties, with the management of risk from natural hazards. The driving need has been an issue of significant concern to earthquake hazard mitigation specialists in the expected poor seismic performance of older, seismically vulnerable concrete buildings, commonly referred to as non-ductile concrete buildings (ATC 2013). These buildings, which include older construction dating from the early 1900s, were predominantly constructed prior to 1980, after which U. S. seismic codes for concrete buildings were considered to have been improved. While not all non-ductile concrete buildings are hazardous, many have weak, brittle, or incomplete lateral force-resisting systems. These buildings may have gravity-load support systems that cannot accommodate potential lateral deformations or drifts if subjected to strong earthquake ground motions. The position expressed by FEMA (ATC 2012) was that "Performance-Based Seismic Design (PBSD) is a concept that permits the design and construction of buildings with a realistic and reliable understanding of the risk of life, occupancy, and economic loss that may occur as a result of future earthquakes. It is based on an assessment of a building's design to determine the probability of experiencing different types of losses, considering the range of potential earthquakes that may affect the structure. The first step involves the selection of a desired performance level by a building owner or regulator. Then an input ground motion, scenario event, or earthquake hazard level is selected for which this performance is to be achieved. A designer then conducts a performance assessment, which is intended to determine if the selected performance level is met, or exceeded, at the selected hazard level. In the PBSD process, the building design is then adjusted until the performance assessment indicates a risk of loss that is deemed acceptable by the building owner or regulator."

Those are fine words, but each of these tasks involves considerable uncertainty. Two hundred years of mathematical theory and a 100 years or more of research and development in reinforced concrete structural systems notwithstanding, our analytical ability to extract a tomographic understanding of how structures will respond to dynamic earthquake effects is still limited. A repudiation of Wilson's dictum[1] does not appear to be imminent because materials have properties that can only be esti-

[1] Wilson (2000) observes that structural engineering must contend with many poorly known or estimated parameters in its pursuit of creating structures that serve communities in some way.

mated, forces are not accurately known, and structures can only be analyzed approximately. That is a rephrased version of the 25-century old Aristotelian counsel: "It is the mark of an educated mind to rest satisfied with the degree that the nature of the subject admits, and not to seek exactness where only an approximation is possible." The randomness and prior unknown nature of earthquake ground motions emphasize that exact references to return periods in the manner of performing rocket science probably have little credibility.

1.4 Considerations

Engineers need to work with imperfect knowledge much of the time. More often than not, the demands on and the capabilities of a particular structure are not known with the accuracy required by exact analysis. This is primarily why experience drives design, and that is why processes for proportioning, whether they are made into law in codes or whether they reside in text books, comprise an intricate and complex mix of methods. These methods may be categorized in three types:

1. *Methods that explain as well as predict*. An example is the flexural theory of reinforced concrete. If we ignore the flaws at the edges of its domain of application, such as conditions at a plastic hinge or for a very lightly reinforced section, the flexural theory may be considered a well-understood topic that can be used to predict the response of a range of sections with confidence, the range having been defined in the field and in the laboratory. Whether the section is rectangular or circular, its strength can be determined using the same fundamental concepts.
2. *Methods that predict but do not explain*. Examples are proportioning methods used for shear or bond strength in reinforced concrete. They are used with the implicit hope that they can be used to predict capacity but, even in the best instance, their first principles are derived from observation and their results have been calibrated through observations. As such, they do not lend themselves to projection outside of the range of parameters considered in their development. For example, determining the strength of a girder with a circular section from theory calibrated by data from girders with rectangular sections is not a straightforward procedure and requires knowledge over and above that contained within the method.
3. *Methods that neither predict nor explain*. Many of the minima and maxima specified in codes fall in this category. The required minimum amount of shrinkage and temperature reinforcement does not follow from any sort of first principle other than the common sense of having some reinforcement to counteract the probable effects of volume changes.

Most practicing engineers know instinctively in what manner these three types are to be used in design. Above all, they do understand that methods of Type 2 are one-way streets. One uses the method to arrive at proportions that are likely to pro-

vide safety and serviceability for the assumed demands. But it would be folly, for example, to use a crack-width expression that may be used to predict a characteristic crack width from a given reinforcement stress to determine reinforcement stress from a crack-width measurement. Minima/maxima included in Type 3 are not methods at all, although they may play a critical role in protecting engineers from themselves.

In the realm of proportioning for earthquake resistance, another layer of gauze, the equivalent static lateral force, is introduced. For proportioning to resist gravity loads, the demand may be exaggerated but it does represent the action. The force to be resisted exists with or without the structure. For earthquake effects, the assumed lateral force is a chimera. It cannot exist unless there is a structure in a state of deformation. Its magnitude depends, among other things, on the strength of the structure. Nevertheless, the tradition to this day in proportioning of earthquake resistant structures has been to initiate the proportioning exercise with a specified base shear. That pivotal beginning tends to lump all three types of methods used in design in the category of those that neither predict nor explain. The approach is pragmatic. It allowed proportioning for earthquake resistance of low- and even moderate-rise buildings without the need to understand structural dynamics at the beginning of the twentieth century. Its remaining in use in the twenty-first century is questionable. Despite the false start with virtual forces, existing methods are able to produce satisfactory structures because there is much experience subtly built into them and because, fortunately, strength is not a critical factor for earthquake resistance of most structures.

Given earthquake intensity, the response of the structure can be sensed from three indices listed below in order of importance:

1. *The ratio of lateral drift capability to height*. The drift-ratio capacity is a measure of the toughness of a structure. It is controlled by a myriad of methods involving all three categories listed above. The object is to avoid brittle failure. Contrary to early understanding, drift capability can be determined explicitly only for monotonically increasing displacement. If displacement reversals into the nonlinear range of response are involved, determination of limiting drift ought to be demoted to Type 2 in the categories listed above.
2. *The ratio of stiffness to mass*. This index value is best expressed in terms of the period for the first translational mode. For regular buildings, it is, without question, the most important index value indicating the suitability of the structure. Because the period is determined either using an expression based on tradition or calculated from a model that is only an approximation of the actual building, one does not expect the period to be actually that of the building. However, the second option is intelligible and can be improved to determine the period of the building quite closely, especially if the s sub-grade is firm and the nonstructural elements are either light or well defined in the model.
3. *The ratio of weight to strength*. The common index value is the ratio of the building weight to the base shear strength. It is appropriate to remember that the base shear strength, even if it is determined from a lengthy limit analysis to establish the minimum or from a so-called push-over routine, refers to an arbitrarily

selected story-force distribution and is not a general strength attribute of the structure. It is also relevant to note that, unless the engineer is especially creative and adventurous so as to maximize the tributary floor area per frame, even modest structures of low to medium height posses a base-shear strength coefficient verging on 10% or more. Daring the arbitrariness of the story-force distribution, the base shear strength coefficient is based on limit analysis, an intelligible procedure for determining the minimum base shear. The method may be classified as Type 1. But the base shear strength of the structure so calculated is not in the same category as the design base shear.

With the above discussion as a background, we enter the realm of Performance Based Design. We do not attempt a definition knowing that it is still in an embryonic state, but we do recognize its two liberating aspects: (1) The basic criteria for the structure will be determined by amicable concordance of a board of stakeholders including, but not limited to, the developer, the insurance carrier, the mortgage carrier (if any), the building authority(ies), the architect, the contractor, and the engineer; and (2) the choice of the framing and sizing will depend on a knowledge-based prediction of building response. The question of concern in this paper is the prediction of building response.

Although addressing an evaluation rather than a design task, the report prepared for the Building Seismic Safety Council by the Applied Technology Council Project 33 (1997a, b) is a comprehensive document that may have all the attributes, general and specific, of the building code of the near future. To capture all aspects of this document in a paper is out of the question. Its flavor is captured by the first ten actions listed in its Table 1.1 (pp. 2–3). The engineer of record, in concert with the owners, insurers, the local building authority, and other stakeholders is to undertake the following tasks:

1. Select Rehabilitation Objective
2. Select Performance Level
3. Select Shaking Hazard
4. Evaluate Other Seismic Hazards [such as geotechnical problems]
5. Obtain As-Built Information Including Historical Status
6. Select Rehabilitation Method
7. Select Analysis Procedure
8. Create Mathematical Model
9. Perform Force and Deformation Evaluation
10. Apply Component Acceptance Criteria

It is evident that the procedure could be applied in design simply by replacing the word “rehabilitation” by the word design and skipping Step 5. In the following, the focus will be on Steps 9 and 10.

The Commentary to FEMA 273 (ATC 1997a, b) provides a lucid picture of what is to be done (Fig. 1.1). Under increasing lateral deformation, the member or structural system goes through several states identified by level of damage. Initially, the

Table 1.1 Timeline for use of static equivalent lateral forces to calculate drift

Year	Source	Period, T	Base shear coeff., C	Base shear, V	Story-force distribution	Amplifier for soil	Cracked section?	Drift limits
1951	Anderson et al. (1951)	$\frac{0.05H}{\sqrt{b}}$	0.015/T	CW	Option A	No	No	No
1959	Blume et al. (1961)	N/10	$\frac{0.05}{\sqrt[a]{T}}$	0.67CW	Option B	No	No	No
1967	SC, SEAOC, (1967)	N/10	$\frac{0.05}{\sqrt[a]{T}}$	0.67CW	Option B	No	No	No
1972	VA 1972	0.08 N	$1.25A_{max}/T$	0.25CW	Option B	Yes	Yes	Note D1
1974	SC, SEAOC, (1974)	N/10	$1/15\sqrt{T} < 0.12$	0.67CSW	Option C	Yes	No	Note D2
1978	ATC (1978)	$0.025h^{0.75}$	$1.2A_vST^{0.67}$	0.14CW	Option C	Yes	No	Note D3
1994	IBC (1994)	$0.03h^{0.75}$	$1.5S/4T^{0.67}$	CW/12	Option C	Yes	No	Note D4
1997	IBC (1997)	$0.03h^{0.75}$	C_v/T	CW/8	Option C	Yes	Yes	Note D5

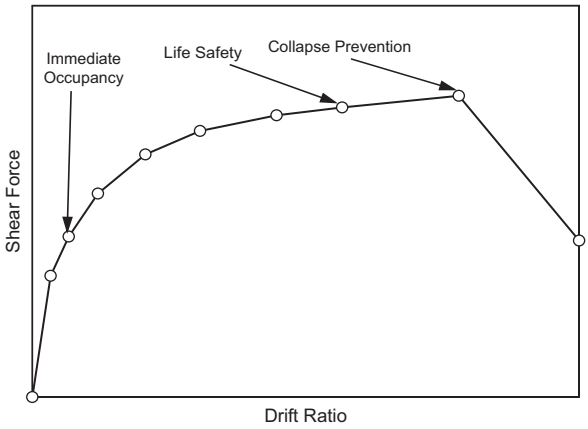

Fig. 1.1 The conceptual pushover curve tool

system responds linearly. Its response is above reproach. Within this range, response can be determined using Type 1 methods.

A certain amount of nonlinearity is tolerated (not defined quantitatively in Fig. 1.1) as indicated by "Immediate Occupancy." At this stage, "…the structure retains a significant portion of its original stiffness and most if not all of its strength." "Significant," perhaps the most insignificant adjective in engineering writing, is not quantified.

At "Collapse Prevention," the building has experienced "extreme damage" and "if laterally deformed beyond this point, the structure can experience instability and collapse." From that, it is understood the building should be stable as long as "Collapse Prevention" is not released, despite the qualifier "extreme" for the damage.

At the life-safety level, "substantial damage has occurred to the structure and it may have lost a significant amount of its original stiffness." Juxtaposing this definition against the definition of "Immediate Occupancy," it may be inferred that the fraction of the original stiffness lost at that stage may be equal to the fraction of the original stiffness remaining at this stage. But that does not help quantify either portion. The only quantitative reference is to the relationship between the useful drift limit and the actual drift limit. It is suggested that if the limiting drift is known, it should be reduced by one fourth to define the useful limit.

The hard and important truth in the softly composed Commentary is that the governing criterion for safety is identified as drift and not strength. It is the engineering equivalent of a revolution. The lines of Section C2.5.1 of the Commentary to FEMA-273 make light, indirectly, of the traditional requirements for a nominal base shear force or equivalent static lateral design forces. The concept has now become so deeply ingrained in the performance-based seismic design lexicon that all later versions of FEMA, Eurocode, and other national codes contain it, albeit expressed in different phrases. No unanimity exists yet for the quantification of these stages or their metrics.

1.5 Review of Drift Demand in U.S. Building Codes

Before attempting a policy for drift determination, it is instructive to make a brief survey of experience with drift, recognizing that engineering confidence depends, to a large extent, on experience.

Both the perceived impact and the anticipated magnitude of drift have changed with time since the 1930s, the time of the first movements in the U.S.A. toward the assembly of professional canons for earthquake-resistant design. Some of the highlights that pertain to drift in the development of model codes for earthquake-resistant design are recorded below.

In organizing the available experience and science on earthquake resistant design, the initial focus of the profession was exclusively on strength. We refer to two publications that capture the perspectives in the U.S.A. of the period from 1930 to 1960: Anderson et al. (1951) and Binder and Wheeler (1960). In the professional consciousness, drift was, besides being negligibly small, a concern related to preserving the investment and possibly to reducing the likelihood of pounding. But it did not impact safety. The attitude was made abundantly clear in the book by Blume et al. (1961), a text that arguably broke much new ground in many respects, that contained the statement, well in keeping with the spirit of the times, "… *lateral displacement is seldom critical in a multi-story reinforced concrete building*" [p. 200] despite the far-seeing suggestion made earlier in the book in reference to ascertaining the likelihood of pounding: "*A less rigorous appearing rule, but one which may in fact be both more accurate and more rational, is to compute the required separation as the sum of deflections computed for each building separately on the basis of an increment in deflection for each story equal to the yield point deflection of that story, arbitrarily increasing the yield deflections of the two lowest stories by multiplying them by a factor of 2*." Despite sensitivity to the contradiction of using a static analysis for a dynamic effect, professional documents have continued to use, exclusively or as an option, static equivalent lateral forces to calculate drift, although this process has taken different turns and magnitudes as summarized in Table 1.1. More recent code versions of the information in Table 1.1 are not easy to summarize in tabular form.

Notation and annotations for Table 1.1

T: Period
H, h: Total height
W: Total weight
N: Number of stories
A_v: Coefficient reflecting response in the range of nearly constant velocity response
C_v: Coefficient reflecting response in the range of nearly constant velocity response and varying with site characteristics
S: Coefficient reflecting site characteristics

Notes on Requirements for Drift Control for Table:

D1
The VA Code (VA 1972) used different factors for force and drift. For example, while the force reduction factor was ¼ for "ductile moment resisting" frames with light and flexible walls, the amplifier for the calculate drift using the reduced force was set at 3. In addition, the VA Code required that the stiffness of reinforced concrete frames be based on "cracked sections." The drift-ratio limit was set at 0.8%. The limit was reduced to 0.26% for frames encasing brittle glass windows.

D2
In 1974, the limiting story-drift ratio was set at 0.5%. In addition, the lateral force was amplified by 1/K, where K = 0.67 for properly detailed frames.

D3
Similarly to what was done in the VA Code, the ATC-3 Model Code recommended a force-reduction factor of 7 for shear in reinforced concrete frames and an amplification factor of 6 for deflection. It is interesting to note that these factors were set at 8 and 5.5 for steel frames.

D4
Calculated story drift ratio (for the reduced force) for a ductile frame shall not exceed 0.33% if the period is less than 0.7 s and 0.25% otherwise.

D5
Story drift ratio to be determined for the reduced force but then amplified by 70% of the force-reduction factor and to be limited by 2.5% for frames with calculated periods less than 0.7 s and by 2% for frames with higher periods.

Option A

$$F_x = V\frac{w_x h_x}{\Sigma(wh)}$$

F_x = lateral force at level x
w_x = weight at level x
h_x = height of level x above base
V = design base shear

Option B

$$F_x = \frac{(V - F_t)w_x h_x}{\sum_{i=1}^{n} w_i h_i}$$

$$F_t = 0.004V\left(\frac{h_n}{D_s}\right)^2 \text{ if } \left(\frac{h_n}{D_s}\right) > 3, \text{otherwise } F_t = 0.$$

F_i, F_x = lateral force at level i, x
w_i, w_x = lateral force at level i, x
h_n, h_i, w_x = height to level n, i, x
V = design base shear

Option C

$$F_x = \frac{(V - F_t) w_x h_x}{\sum_{i=1}^{n} w_i h_i}$$

$$F_t = 0.07TV < 0.25V \qquad \text{and } F_t = 0 \text{ if } T \leq 0.7 \text{ s}$$

F_i, F_x = lateral force at level i, x
w_i, w_x = lateral force at level i, x
h_n, h_i, w_x = height to level n, i, x
V = design base shear

Table 1.1 contains different expressions for the base shear that has shown changes in relation to the coefficient representing the earthquake action but it provides a narrow perspective of professional opinion in the USA with respect to drift. It is compiled in reference to a specific structure, one that may be considered to be a seven-story frame with an infinite number of spans so that its response can be understood in terms of a tree as shown in Fig. 1.2. The structure is assumed to have the appropriate details to qualify as a special moment-resisting frame. Its calculated period is a little less than 0.7 s. All requirements included in Table 1.1 refer to a frame of seven stories with a calculated period barely less than 0.7 s.

The report by Anderson et al. (1951) implied that the drift should be calculated by using the lateral forces selected for design but provided no guidance as to what to do with the results. The decision was left to "engineering judgment," a sign that may be taken as the precursor of Performance Based Design. The 1959 issue of the Blue Book (SEAOC 1959) introduced the sensitivity of the design shear force to the type of framing. For the selected frame, the coefficient was 0.67. The nominal period for a frame was set at O.l N, where N is the number of stories. Distribution of the lateral forces over the height of the building was made linearly proportional to mass and height, the "linear distribution."

In 1972, the code developed by the Veterans Administration (VA 1972) was a landlord's code and set high standards in new directions. The design base shear coefficient was increased. It was made a function of the specific site. By itself, that is not so significant, because it can be reduced in the next step that involves the reduction of the design force. However, the Veterans Administration Code also prescribed a modest "response reduction factor" of 4 for ductile frames and an amplifier of 3 for the deflection obtained using the design shear. In addition, the designer was asked to use cracked sections in determining the stiffness of the structural elements of reinforced concrete. The drift requirement was increased substantially.

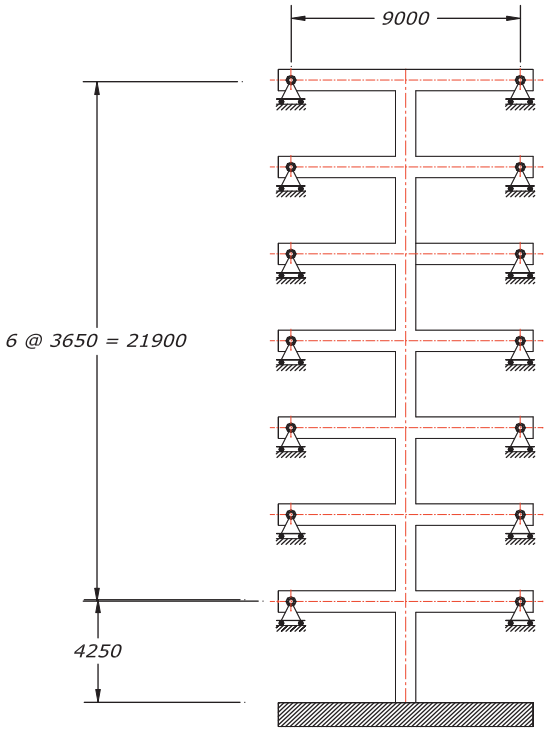

Fig. 1.2 Tree-like frame

In 1974, the Blue Book definition of the base shear coefficient (SEAOC 1974) was changed, as was the distribution of lateral forces over the height of the building. If the calculated period was 0.7 s or less, the distribution conformed to that for the "linear mode shape."

Report ATC-3 (1978) of the Applied Technology Council, a product of a group of engineers dealing with earthquake resistance, introduced a different approach to period determination. Unless it was determined by dynamic analysis, the period was to be determined as a function of the total height of the frame. The definition of the base shear coefficient was based on two different approaches. For low periods, it was set as a constant in recognition of the "nearly constant acceleration response" range identified by Newmark (Blume et al. 1961). For higher periods shown in Table 1.1, it was set as an inverse function of the period (the "nearly constant velocity response range"). For reinforced concrete frames, the "response reduction factor" was set at 7. The amplifier for drift was set at 6. That general concept continues today, with R and C_d values defined for many elaborately defined framing systems.

The 1994 edition of the Uniform Building Code, based on the allowable stress concept, (ICBO 1994) used the ATC-3 definition for the period with a different constant and raised the "response reduction factor" for frames to a generous 12, a constant that in later issues was reduced by a factor of 2/3 when the capacity design approach was adopted.

After the Northridge 1994 and Kobe 1995 events, the Uniform Building Code (ICBO 1997) was modified as recorded in Table 1.1. The critical change in the draft requirement was that the designer was asked to assume cracked sections to determine stiffness but was not told how to determine the cracked section stiffness.

From the narrow perspective of a specific seven-story frame, the events over the years are summarized in Fig. 1.3, showing the changes in maximum story-drift ratios (the tree structure for which the story drift was calculated was assigned the following properties: elastic modulus, E = 30,000 MPa, moment of inertia 0.067 m^4 columns and 0.043 m^4 girders, mass 50 t/joint). The calculated drift in 1959 was indeed small enough to provide a foundation for the general opinion that it was not an important issue. The drift ratio determined by the method included in the Veterans Administration Code of 1972 (VA 1972) changed the scene. While the calculated story-drift ratio for the specific frame considered was 3%, the allowable drift set by the VA was 0.8% if there were no brittle elements involved. If brittle elements were involved, the permissible drift was reduced to approximately 0.25%. Drift drove the design. It is also seen in Fig. 1.3 that the drifts calculated according to the 1994 and 1997 versions of UBC were of comparable magnitude, but in both cases, they were admissible. The last bar shown in Fig. 1.3 represents an estimate of the maximum story-drift ratio for the assumed frame based on the method by LePage (1997) which provides a frame of reference for the drift such a frame might experience if subjected to strong ground motion.

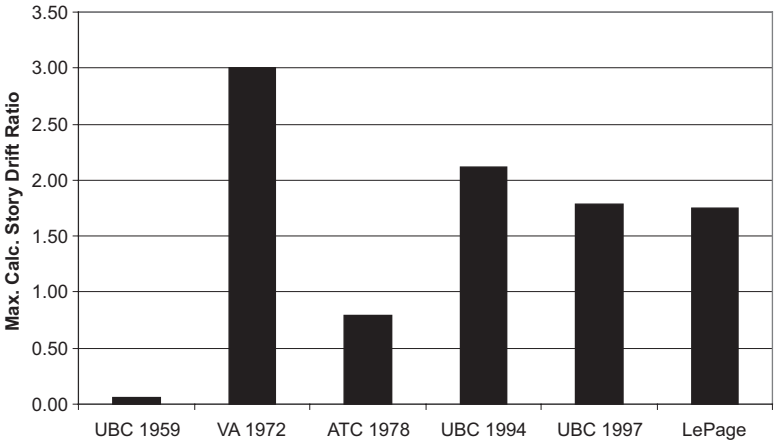

Fig. 1.3 Drift ratios in percent among different codes

1.6 Drift Determination

A main issue in the process of determining drift is whether it should be related to static equivalent forces. It has been well established that the drift of a low- to moderate-rise building is dominated primarily by Mode l in a given plane. This is certainly acceptable if the building is reasonably uniform in the distribution of mass, stiffness, and story height before it is subjected to strong ground motion. To handle this problem simply and specifically (the generalization of nonlinear drift being approximately equal to linear drift is not specific enough to be used in design as the linear drift response may vary by 100% depending on the assumed damping factor), LePage (1997) devised a very simple procedure.

In the nearly constant acceleration and nearly constant velocity ranges as identified by Newmark (Blume et al. 1961), LePage (1997) proposed that the drift range representing a reasonable upper bound to what would be expected in a strong earthquake for a reinforced concrete building with nonlinear response would be expressed by Eq. (1.1).

$$S_{da} = KT\sqrt{2} \tag{1.1}$$

K = a constant with the dimension length/time determined from displacement spectra (damping factor = 2%) suitable for the site. For stiff soil, the constant was proposed as 250 mm/s for ground motions indexed by an effective peak ground acceleration of 0.5 g.
T = calculated period (uncracked section) in s.

LePage specified that the period, T, in this equation be the period calculated for the un-cracked reinforced concrete structure amplified by $\sqrt{2}$. It is important to note that this was not in expectation of a cracked section that would reduce stiffness to one half of uncracked section. It was used because it had been found convenient for organizing the data in an earlier study by Shimazaki and Sozen (1984), who had also defined the spectral displacement response by determining the envelope to specific displacement response spectra calculated using a damping factor of 2% for a collection of ground motions assumed to represent motions from comparable site conditions. Shimazaki normalized the response spectra in deference to the energy spectrum, on the premise that the drift increase caused by nonlinear response would be less if the energy response did not increase or if it increased at a low rate with increase in period. Using the basic concept by Shimazaki and LePage of normalizing the spectrum in relation to velocity, the LePage spectrum was restated in terms of the peak ground velocity.

$$S_{dv} = \frac{V_g}{\sqrt{2}}T \tag{1.2}$$

S_{dv} = spectral displacement

V_g = peak ground velocity
T = calculated first mode period

In a study of the effects of the ground motions measured in Anatolia during the two earthquakes of 1999, Öztürk (2003) noted that, for structural systems with low base-shear strengths, the drift response tended to exceed the limit set by LePage as given in Eq. (1.3).

$$S_{de} = \frac{V_g^2}{G_\pi c_y}(1+T) \tag{1.3}$$

S_{de} = spectral displacement
V_g = peak ground velocity
c_y = base shear strength coefficient
G = acceleration of gravity
T = calculated period used as a dimensionless coefficient

Combining Eqs. (1.2) and (1.3):

$$S_d = \max\left(S_{dv}, S_{de}\right) \tag{1.4}$$

The results of Eq. (1.4) are shown in Figs. 1.4 and 1.5 for base shear strength coefficients of 0.15 and 0.2. Even if it is presumptuous to suggest that Eq. (1.4) should be used to determine drift response in proportioning, it is plausible to assume that it would be a good vehicle for summarizing the uncertainties in determining drift. Simple and straightforward as it is, Eq. (1.4) still requires knowledge about the building properties (T) and the intensity and character of the ground motion (at least the peak ground acceleration or its relationship to the peak ground velocity) even if

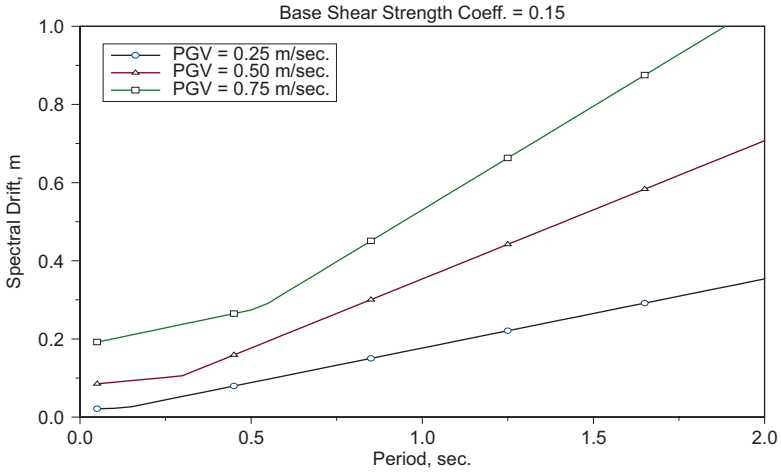

Fig. 1.4 Performance of Eq. (1.4) for $C_v = 0.15$

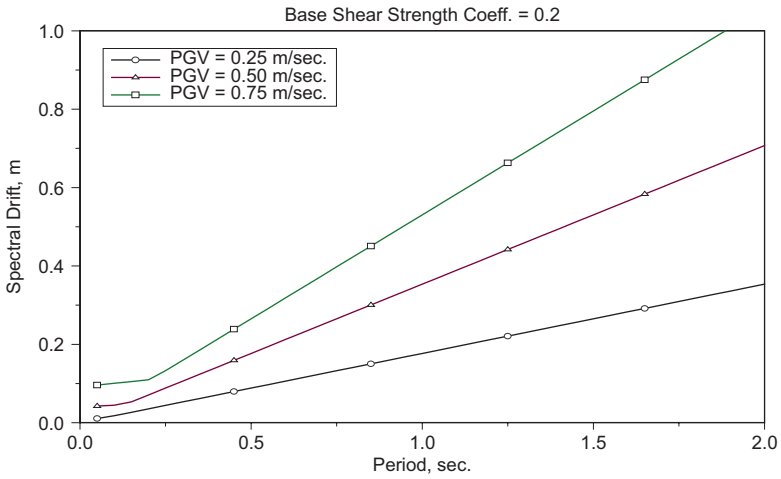

Fig. 1.5 Performance of Eq. (1.4) for $C_v = 0.2$

we ignore the variations that may be introduced by the subgrade. In addition, there are uncertainties involved in translating the spectral value to story drift.

1.7 Drift Limit

Given a drift-demand prediction with a defined level of confidence, one needs a range of drift magnitudes to correspond to the various states of damage. Of course, the first requirement is the limiting drift capability, the limit of drift that the element in question can sustain without collapse. Initially, this limit referred to what the reinforced concrete member could sustain under monotonically increasing displacement. Despite the fog surrounding the nonlinear displacement component of the shear-displacement relationship under monotonically increasing displacement, it was possible to obtain by theory a safe lower bound to drift capability. This limit would be generous especially if the axial load was moderate vis-a-vis the cross section, and there was sufficient transverse reinforcement, never mind the definitions of "moderate" and "sufficient." However, laboratory testing (not more rigorous field experience) introduced another hurdle. Subjected to reversals of displacement into the range of nonlinear response, reinforced concrete elements tended to lose strength and stiffness at a lower drift limit than that under monotonic loading. The issue has been investigated by a host of researchers using different loading histories, specimens, and/or analytical constructs. Two investigators have produced pragmatic expressions for determining the drift capability of reinforced concrete columns with rectilinear reinforcement. Pujol (2002) has drawn on experimental data from 15 reports (Ang 1985, Arakawa 1987, 1988, 1989, Bett 1985, Imai and Yamamoto 1986, Kanda et al. 1988, Nagasaka 1982, Ohue et al. 1985, Petrovski and Ristic

1984, Saatcioglu and Özcebe 1989, Soesinawati et al. 1986, Umehara and Jirsa 1982, Xiao and Martirossyan 1998 and Zahn et al. 1986) to derive a simple expression for the drift-limiting drift ratio:

$$DR_p = \frac{\rho_w \cdot f_{wy}}{v_{\max}} \cdot \frac{a}{d} \leq 4 \text{ and } a/d \tag{1.5}$$

DR_p = limiting drift ratio
ρ_w = ratio of cross-sectional area of hoops at spacing s
f_{wy} = yield stress of transverse reinforcement
v_{max} = ratio of the maximum value of the shear force to the cross-sectional area of reinforced concrete member defined as the product bd, where b is the width of the section and d is the effective depth
a = span length from maximum moment at face of joint to point of no moment
d = effective depth of the section

Because of the nature of its derivation, the use of Eq. (1.5) is properly limited to the ranges of the variables covered in the experimental studies:

Compressive strength (cylinder) of the concrete:	20 to 85 MPa
Longitudinal reinforcement ratio:	0.5% to 5%
Unit force at yield of transverse reinf., $\rho_w f_{wy}$:	0 to 8 MPa
Ratio of axial load to the product Ag*f'c	0 to 0.2
Shear span ratio, a	1.3 to 5
Ratio of max. Unit shear stress to sq. root of f_c' $\left(v\sqrt{f_c''}\right)$ in SI:	0.17 to 0.8

Equation (1.5) was expressed as a "reasonable lower bound" to the data in the spirit of other strength expressions used in building codes. The limit referred to the drift at which the element lost 20% of its strength under cyclic loading. It is understood that it can be used directly as a limit to the rift capability of a column with an axial load not exceeding 20% of that obtained as the product of Ag*fc (gross area times the compressive cylinder strength of concrete). There is no parameter in the expression reflecting the effect of the axial load.

Another expression that is easy to use to determine limiting drift of reinforced concrete sections with rectilinear hoops is offered by Eberhard and Berry (2003). Analyzing data from 62 tests of reinforced concrete specimens having rectangular sections with and without axial load, Eberhard and Berry proposed the following expression for the mean limiting drift:

$$DR_e = \frac{13}{400}\left(1 + 50\frac{\rho_s f_{wy}}{f_c'}\frac{d_b}{D}\right)\left(1 - \frac{P}{A_g f_c'}\right)\left(1 + \frac{L}{10D}\right) \tag{1.6}$$

DR_e = limiting drift ratio in percent
ρ_s = volumetric ratio of transverse reinforcement to confined core
f_{wy} = yield stress for transverse reinforcement
d_b = diameter of longitudinal reinforcing bar
D = depth of section
P = axial load
A_g = gross area of section
f_c = cylinder strength of concrete
L = clear height or span

The event defining the drift limit was identified as the buckling of the longitudinal reinforcement. It is important to note that the expression includes explicitly terms defining the diameter of the longitudinal reinforcing bars and the axial load as well as the slenderness of the element. The supporting data are listed in web sites http://ce.washington.edu/-peera l and https://nisee.berkeley.edu/elibrary/. The coefficient of variation was 0.26 with the mean at 1.0.

Equations (1.5) and (1.6) refer to different limiting phenomena. Equation (1.5) sets the drift limit corresponding to a 20% reduction in strength. Equation (1.6) refers to buckling of the longitudinal bars leading, presumably, to a perceptible strength reduction. Still, their impact is the same. They define the limiting drift capability. Neither expression is qualified by the threat of another phenomenon reducing the specified drift capability. In both cases it is assumed that the transverse reinforcement is sufficient to develop the nominal shear strength of the element corresponding to the development of flexural capacity. With that information, it becomes of interest to compare the limiting drifts determined by Eqs. (1.5) and (1.6). Because the two equations contain different parameters, it is not possible to compare their results without making specific assumptions about some of the parameters.

We assume the following: (a) concrete compressive strength is set at 27.5 MPa, (b) yield stress of the transverse reinforcement is 415 MPa, (c) the ratio $P/(A_g f'_c)$ is 0.2. In the case of Eq. (1.5), the maximum shear is set at 4 MPa or approximately 15% of the compressive strength. To evaluate Eq. (1.6), the volumetric ratio of the transverse reinforcement ratio is approximated as twice the ratio ρ_w.

Equation (1.5) is designed for direct implementation. Eq. (1.6) refers to the mean. It would be prudent to modify Eq. (1.6) depending on the confidence level desired. The modification would depend on the judgment of the stakeholders. One cannot guess at what a group of stakeholders with different concerns would choose, but for the sake of the comparison it may be plausible to reduce the mean by not less than two and not more than three standard deviations.

The variation of the calculated limiting drift capability with the transverse reinforcement ratio for two different column slenderness values is shown in Figs. 1.6 and 1.7 (slenderness is taken to be the ratio of clear height to depth). It is reassuring to see that, in the range considered, a cautious implementation of Eq. (1.6) would be considered to give the same results, in the range of the expected accuracy, as Eq. (1.5). On the other hand, it is disturbing to find that the drift ratio limit from Eq.

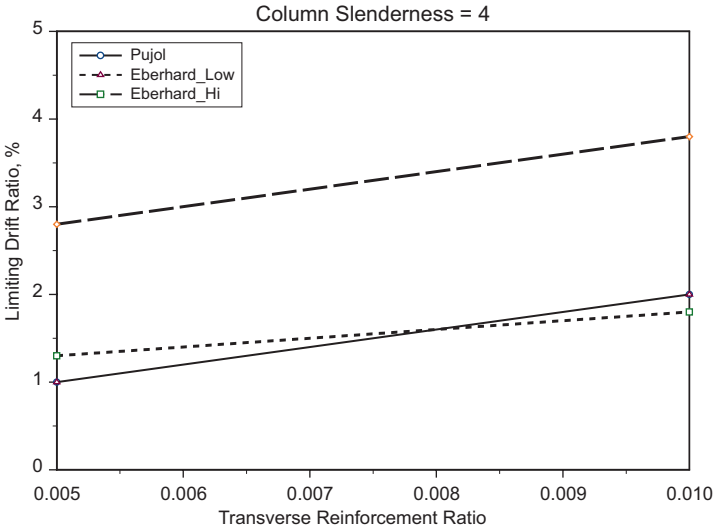

Fig. 1.6 Limiting drifts: $\lambda = 4$

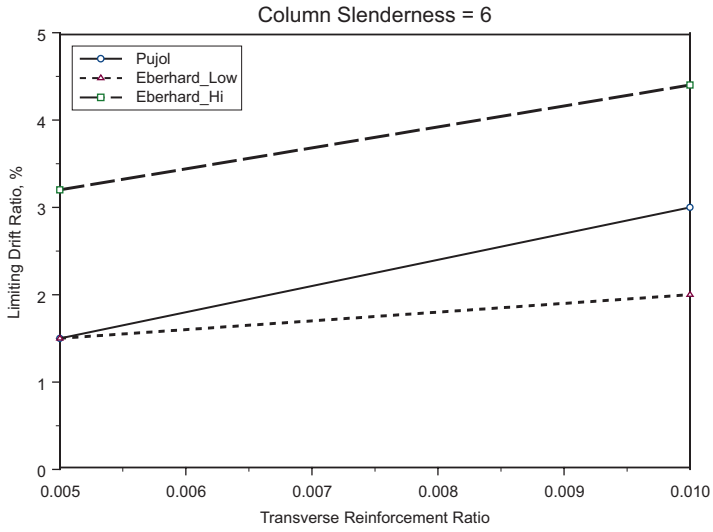

Fig. 1.7 Limiting drifts: $\lambda = 6$

(1.5) and Eq. (1.6) as modified is as low as 2%. This does not leave much range for negotiation considering that the drift ratio at yield may be as high as 1%.

1.8 Concluding Remarks

As discussed, the drift demand is based on a chain of estimates: peak ground acceleration, peak ground velocity, nonlinear displacement response, and the response of the building (modal shapes and their combinations). Each set of assumptions involves uncertainty and it would be difficult to claim that, even in the best of circumstances, the probable error in the final result would be less than 100%. Typically, each of these guesses is made with a built-in factor of safety, and if that is indeed the case, it might be plausible to deal with the drift demand so obtained as the upper-bound estimate.

The brief discussion of the expressions for drift-ratio limit by Pujol (Eq. (1.5)) and Eberhard and Berry (Eq. (1.6)) suggests that two expressions lead to comparable results if the results of Eq. (1.6) are reduced by three standard deviations. For a column with sufficient web reinforcement such that the entire shear, corresponding to flexural strength, may be assigned to the web reinforcement and with a slenderness ratio of four, the limiting drift ratio is 2%. This result, of itself, is not disturbing, but considering that the drift ratio at yield could be approximately 1%, it does not leave much room for negotiation. It might have been that the experts who were referring to the waypoints on the shear-drift relationship of a column failing in flexure (Fig. 1.1) might have been thinking of behavior under monotonic loading.

It is not unreasonable to proportion the columns for a limiting drift ratio of 2%. If the response limit exceeds 2% and if the nonstructural components are attached directly to the frame, the building is likely to be very nearly a total loss. However, it is unlikely that there will not be a tendency by a member of the board of stakeholders to ask for relief. Could the limiting drift be increased to 4% to save on framing costs? The answer is yes. Relief can be provided by softening artificially the implicit set of criteria that lead to a limiting drift ratio of 2%.

Consider Eq. (1.5). Strictly, the concerns leading to it are opaque to the engineer. But should the engineer so desire, the Pujol paper (1999) is within reach. Why should the engineer's actions be controlled by the safety concepts of the researchers developing Eq. (1.5)? A peremptory study of the paper would reveal that, even if the format of Eq. (1.5) is not changed, a mean rather than a lower bound can be crafted to permit a drift ratio of 5% for the case considered. And may the question, "will the structure sustain multiple excursions to large displacements leading to strength decay in every design-level earthquake" not be asked? After all, the reduction of drift capacity because of displacement reversals was a laboratory, and not a field, event where the range of variability is likely to be much broader, as shown in Fig. 1.8 of an exercise to calculate the collected results of a round-robin competitive exercise to predict the results of drift for a solitary column (Fajfar 2014). With individually calculated estimates ranging between extremes separated by as much as a factor

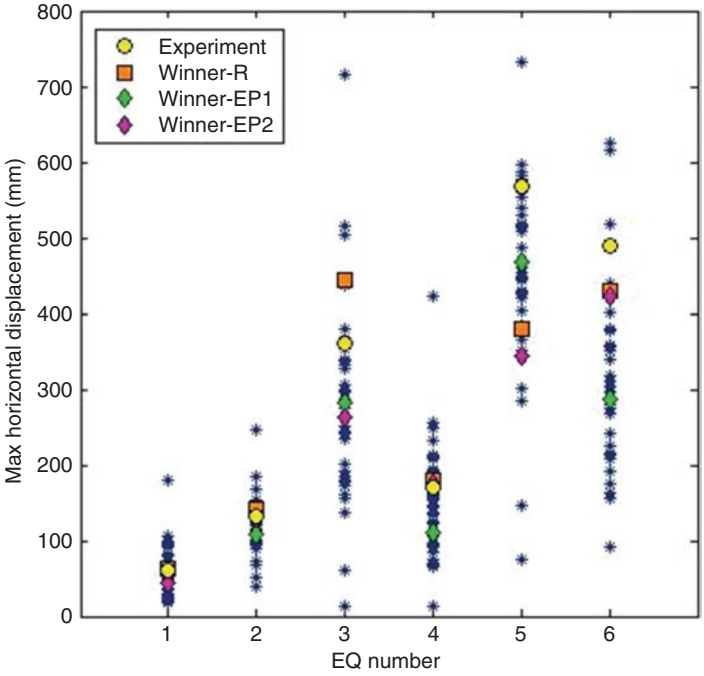

Fig. 1.8 Calculated displacements for a column specimen subjected to simulated earthquakes in the laboratory (Fajfar 2014)

of seven, the results do not instill much confidence in the calculation tools of our trade. A similar, sobering observation was made for the prediction of tests conducted for the CAMUS program at Saclay (Labbé and Altinyollar 2011). Despite heavy betting on the imputed correctness of refined nonlinear tools to tell engineers what real structures are likely to do during physical earthquake motions, there is as yet only the indication that additional research is needed (Bayhan and Gülkan 2011). The possibly apocryphal reply by a Chinese statesman to the question of what influence the French revolution had on world history (that it was too early to say) might find resonance with the state of the performance-based design developments currently underway.

There are other options. If Eq. (1.6) is used directly, the drift ratio permitted would be 8%. If the paying stakeholders find out that by using a higher limiting drift ratio the cost of the building will be reduced legally, what is their reaction likely to be, especially if they happen to have made their fortunes by taking risks? Can the engineer stem the tide?

In Plato's Republic, the interactions within the board of stakeholders could possibly lead to a result that will serve society well. In another republic, it may open the doors to intolerable risk. As long as the state of the art on the behavior of reinforced concrete buildings does not change for the better dramatically, the actors in Performance Based Design ought to be limited to cautious specialists. Opening the

doors of decision completely to nonprofessionals may lead to embarrassment of professionals. We haven't yet had enough public discourse to find our limitations and to calibrate our theory accordingly. The encouraging concert between computed and observed results paraded in some publications may be little more than Procrustean exercises.

Table 9.5 (b) of the Building Code requirements for Structural Concrete (ACI-318-02) is titled Maximum Permissible Computed Deflections. Why is the word "Computed" in the title? Is it because the profession that would be enriched by the title Maximum Permissible Deflections would not be the engineering profession?

Performance Based Design provides a rare opportunity to elevate the quality of thinking in the engineering community. It has already made a strong positive influence by placing the concern for drift control at center stage, but if it is to be released for general use soon, it is best released with reference to computed rather than to implied actual drift ratios.

References

Anderson AW et al (1951) Lateral forces of earthquake and wind. In: Proceedings of American Society of Civil Engineers, vol. 77, April

Ang BG, Priestley MJN, Paulay T (1985) Seismic shear strength of circular bridge piers. Research report No. 85–5, Department of Civil Engineering, University of Canterbury, Christchurch, New Zealand, July, 408 p

Applied Technology Council (1997a) NEHRP guidelines for the seismic rehabilitation of buildings (FEMA 273, ATC 33 Project), October, Washington DC

Applied Technology Council (1997b) NEHRP commentary on the guidelines for the seismic rehabilitation of buildings (FEMA 273, ATC 33 Project), October, Washington DC

Applied Technology Council (2012) Seismic performance assessment of buildings, vol. 1 – Methodology, FEMA P-58-1, September

Applied Technology Council (2013) Evaluation of the methodology to select and prioritize collapse indicators in older concrete buildings, ATC-78-1, April

Arakawa T, He M, Arai Y, Mizoguchi M (1987) Ultimate shear strength of spirally-confined concrete columns. Trans Jpn Concr Inst 9:305–312

Arakawa T, He M, Arai Y, Mizoguchi M (1988) Shear resisting behavior of reinforced concrete columns with spiral hoops. Trans Jpn Concr Inst 10:155–162

Arakawa T, Arai Y, Mizoguchi M, Yoshida M (1989) Shear resisting behavior of short reinforced concrete columns under biaxial bending-shear. Trans Jpn Concr Inst 11:317–324

ATC (1978) Tentative provisions for the development of seismic regulations for buildings (ATC 3–06). Applied Technology Council, Redwood City

Bayhan B, Gülkan P (2011) Buildings subjected to recurring earthquakes: a tale of three cities. Earthquake Spectra 27(3):635–659

Bertero R, Bertero VV (2004) Performance-based seismic engineering: development and application of a comprehensive conceptual approach to the design of buildings. In: Bozorgnia Y, Bertero VV (eds) From engineering seismology to performance-based engineering. CRC Press, Boca Raton

Bett BJ, Klingner RE, Jirsa JO (1985) Behavior of strengthened and repaired reinforced columns under cyclic deformations. PMFSEL report no. 85–3, Department of Civil Engineering, University of Texas at Austin, Texas, December, 75 pp

Binder RW, Wheeler WT (1960) Building code provisions for Aseismic design. In: Proceedings of the second world conference on earthquake engineering, Tokyo, pp 1843–1857
Blume JA, Newmark NM, Corning LH (1961) Design of multistory reinforced concrete buildings for earthquake motions. Portland Cement Association, Skokie
Clough RW (1962) The Agadir, Morocco Earthquake, February 29, 1960, American Iron and Steel Institute
Eberhard MO, Berry MP (2003) A simple performance model for bar buckling. In: Proceedings of PEER conference on performance based design, Hakone, Japan
Fajfar P (2014) Private communication
Imai H, Yamamoto Y (1986) A study on causes of earthquake damage of Izumi high school due to Miyagi-ken-Oki earthquake in 1978. Trans Jpn Concr Inst 8:405–418
International Conference of Building Officials (ICBO) (1994) Uniform building code, vol 2, 5360 S. Workman Mill Rd., Whittier, CA
International Conference of Building Officials (ICBO) (1997) Uniform building code, vol. 2, 5360 S. Workman Mill Rd., Whittier
Kanda M, Shirai N, Adachi H, Sato T (1988) Analytical study on Elasto-plastic hysteretic behaviors of reinforced concrete members. Trans Jpn Concr Inst 10:257–264
Labbé P, Altınyollar A (2011) Conclusions of an IAEA–JRC research project on the safety significance of near-field seismic motions. Nucl Eng Des 241:1842–1856
Langenbach R (2003) Cross-walls instead of shear-walls: a proposed research project for the retrofit of vulnerable reinforced concrete buildings in earthquake areas based on the traditional "hımış" construction. In: Proceedings of the fifth [Turkish] national conference on earthquake engineering, Istanbul. Available on www.conservationtech.com
LePage A (1997) A method for drift control in earthquake-resistant design of reinforced concrete building structures. Thesis submitted to the Graduate College of the University of Illinois, Urbana, IL, June
Nagasaka T (1982) Effectiveness of steel fiber as web reinforcement in reinforced concrete columns. Trans Jpn Concr Institute 4:493–500
Ohue M, Morimoto H, Fujii S, Morita S (1985) The behavior of R.C. Short columns failing in splitting bond shear under dynamic lateral loading. Trans Jpn Concr Inst 7:293–300
Öztürk BO (2003) Seismic drift response of building structures in seismically active and near fault regions. Thesis submitted to Purdue University for the degree of Doctor of Philosophy
Petrovski J, Ristic D (1984) Reversed cyclic loading test of bridge column models. Report IZIIS 84–164, Institute of Earthquake Engineering and Engineering Seismology, September, 62 pp
Priestley MJN (2000) Performance based seismic design. In: Proceedings of the 12th world conference on earthquake engineering, Auckland, New Zealand
Pujol S (2002) Drift capacity of reinforced concrete columns subjected to displacement reversals. Thesis submitted to Purdue University for the degree of Doctor of Philosophy
Pujol S, Ramirez JA, Sozen MA (1999) Drift Capacity of reinforced concrete columns subjected to cyclic shear reversals. In: Krishnan K (ed) ACI special publication SP-187. ACI, Farmington Hills, Michigan, pp 255–274
Saatcioglu M, Özcebe G (1989) Response of reinforced concrete columns to simulated seismic loading. ACI Struct J, January–February, pp 3-12
Seismology Committee, Structural Engineers Association of California (SAEOC) (1959) Recommended lateral force requirements and commentary, 171 2nd Street, San Francisco, CA
SEAOC (1967) Recommended lateral force requirements, seismology committee, structural engineers Association of California, July
Seismology Committee, Structural Engineers Association of California (SAEOC) (1974) Recommended lateral force requirements and commentary, 171 2nd Street, San Francisco, CA
Shimazaki K, Sozen MA (1984) Seismic drift of reinforced concrete structures. Technical report, Hazama-Gumi, Tokyo, pp 145–165

Soesianawati MT, Park R, Priestley MJN (1986) Limited ductility design of reinforced concrete columns. Report 86–10, Department of Civil Engeering, University of Canterbury, Christchurch, New Zealand, March, 208 pp

Sozen MA (1981) Review of earthquake response of RC buildings with a view to drift control. In: Ergünay O, Erdik M (eds) State-of-the-art in earthquake engineering. Kelaynak Press, Ankara

Tobriner S (1984a) The history of building codes to the 1920s. In: Proceedings, SEAOC annual convention, structural engineers association of California, Sacramento, CA

Tobriner S (1984b) A history of reinforced masonry construction designed to resist earthquakes: 1755–1907. Earthq Spect 1(1), November

Umehara H, Jirsa JO (1982) Shear strength and deterioration of short reinforced concrete columns under cyclic deformations. PMFSEL report no. 82–3, Department of Civil Engineering, University of Texas at Austin, Austin, Texas, July, 256 pp

Veterans Administration (VA) Office of Construction (1972) Report of the earthquake and wind forces committee, earthquake resistant design requirements for VA hospital facilities, Washington, DC

Wilson EL (2000) Three-dimensional static and dynamic analysis of structures. Computers and Structures Inc., Berkeley

Xiao Y, Martirossyan A (1998) Seismic performance of high strength concrete columns. J Struct Eng Am Soc Civil Eng (ASCE) 124(3, March):241–251

Zahn FA, Park R, Priestley MJN (1986) Design of reinforced concrete bridge columns for strength and ductility. Report 86-7, Department of Civil Engineering, University of Canterbury, Christchurch, New Zealand, March, 380 pp

Chapter 2
Synergies and Conflicts Between Seismic Design and Design for Other Extreme Actions

M.N. Fardis

Abstract Fire, blast, impact, earthquake beyond design and other extreme events are neglected in structural design but account for a good part of the actual rate of failures. In view of the uncertainty about such events, structures should be designed to be resilient to their foreseeable consequences. The paper presents an overview and sample results of an investigation of critical components, subassemblies thereof and whole concrete structures under simulated blast or impact, loss of columns due to extreme events, or under exposure to fire or earthquake loading. Design measures which promote resilience to earthquake, such as base isolation, footing uplift and dry joints, are evaluated for blast or progressive collapse. The role of masonry infills against progressive collapse is discussed. On the basis of the outcomes, design features which enhance resilience to multiple hazards are elaborated and contrasted to those which are efficient against one type of hazard but adverse for others.

Keywords Structural design • Reliability • Seismic design • Seismic resilience

2.1 Introduction: Extreme Loadings on Structures

> *I will never get to know the unknown since, by definition, it is unknown. However, I can always guess how it might affect me and should base my decisions around that... The probabilities of very rare events are not computable; the effect of an event on us is much easier to ascertain. We can have a clear idea of the consequence of an event, even if we do not know how likely it is to occur. I don't know the odds of an earthquake, but I can imagine how San Francisco might be affected by one. The idea that, in order to make a decision, you need to focus on the consequences (which you can know) rather than the probability (which you can't know) is the central idea of uncertainty*. – The Black Swan (Taleb 2008)

For buildings and civil engineering structures, the Black Swan (Taleb 2008) is an unforeseen extreme threat – natural or human-made. The disaster is sometimes

M.N. Fardis (✉)
University of Patras, Patras, Greece
e-mail: fardis@upatras.gr

R. Rupakhety, S. Ólafsson (eds.), *Earthquake Engineering and Structural Dynamics in Memory of Ragnar Sigbjörnsson*, Geotechnical, Geological and Earthquake Engineering 44, https://doi.org/10.1007/978-3-319-62099-2_2

major. Society, feeling the repercussions, often holds poor engineering as the culprit. However, deficiencies in scientific and technical (S/T) knowledge are more to blame than the designers of failed structures. In fact, structural engineering is not in a position yet to design against extreme events. With the exception of earthquakes, this discipline and its R&D are focused on normal loadings (i.e., due to gravity or environmental actions characterized by well-defined statistical regularity). Based on rigorous descriptions of such loadings as random processes, it has developed reliability schemes of various levels of accuracy or approximation to design civil infrastructures for a target probability of failure in their design service life (JCSS 2001; CEN 2002a; fib 2012). However, one of the forefathers of that design approach recognised early on (Ditlevesen 1980, 1983):

> "*the often appearing orders of magnitude of positive difference between observed failure rate and calculated theoretical failure probability …*" at least "*… for certain types of structures, such as big dams, large bridges and high rise buildings…*"

and attributed it to *"gross errors"*. Another pioneer of reliability-based structural design notes (Ellingwood et al. 2007):

> *Studies in many countries have shown that the risk of structural failure due to such effects as fire, vehicular impact, explosions and other abnormal events in some instances may be comparable to the risks associated with hazards that traditionally have been addressed in structural design.*

The discrepancy between what is accounted for and what is not has been recognized by major codes, which group error together with blast, impact, fire, etc., as exceptional ("*accidental*") situations against which structures should be "*robust*" (JCSS 2001; CEN 2002a, b; fib 2012).

Alongside intentional, human-made threats, the complexity and density of the built environment is growing and its vulnerability to extreme events increases because of:

- the computerization of structural design,
- the reduction of safety margins due to advancements in scientific and technical knowledge,
- less continuity of connections for efficient prefabricated construction or dismantlement for reuse/recycling (for sustainable use of resources),
- wider spacing of vertical supports for better functionality and versatility in occupancy,
- slimmer structures thanks to high strength materials,
- open spaces in modern buildings, connected horizontally and/or vertically and allowing a fire to propagate through the full extent of the building.

All the above lead to structures that are more vulnerable to hazards outside their design envelope. Progress in engineering to avert or mitigate disasters due to extreme threats has not kept pace. Of course, it is a truism to say that technology cannot control nature and that there is only so much it can do to prevent human-made threats.

Structural design must strive to limit loss of functionality due to an extreme event by maximizing robustness. However, structural engineering is ill-prepared for a new paradigm of design against extreme threats. Modern codes (CEN 2002a, 2006; fib 2012) have indeed introduced ultimate limit state (ULS) design of new structures against accidental actions. Given that there is no meaningful probabilistic description of these types of exceptional loadings, the level of accidental actions against which the structure should be designed at the ULS is meant to be postulated by the owners of the facility; it is also up to them to specify against which accidental actions the structure should be designed. However, feedback from the industry's first attempts to explicitly design against certain accidental actions using the EN-Eurocodes points to gaps in knowledge that should be filled in for this experiment to bear fruit.

R&D in support of design against blast, impact or fire is in its infancy compared to what earthquake engineering R&D has achieved and how these advancements have been put into practice. So, earthquake engineering provides the baseline for design against extreme loads, underpinned by:

- the vast amount of knowledge and R&D results accumulated since the 1970s on design against extreme dynamic loadings on the basis of deformation capacity and ductility,
- the major achievements in performance-based earthquake engineering, which far surpass those of other engineering disciplines in performance-based design.

Moreover, there are commonalities between the various types of extreme threats and the design/retrofit/recovery approaches for resilience to them, which are worth considering.

In lieu of a futile effort to associate probabilities with extreme threats, or the defeatist stance of preparing communities to face the social and economic consequences of structural failures due to such threats, R&D project PRESCIENT, recently concluded at the University of Patras, focused on the structural consequences of such threats, in an effort to find ways to limit them. It promoted a holistic paradigm for the design of new concrete structures for resilience to postulated extreme threats, emphasizing robustness and limitation of damage.

2.2 State-of-the-Art in Design of Concrete Structures for Resilience

2.2.1 Design for Resilience to Earthquakes

R&D in support of structural design against various natural or man-made hazards which threaten buildings or other civil infrastructures has reached a satisfactory level only against earthquakes. Despite this progress, modern-day seismic design (i.e., of the past 40 years) allows earthquake-resistant structures to undergo

significant inelastic deformations under extreme ground motions but expects them to escape collapse thanks to energy dissipation and ductility. Energy dissipation is normally hysteretic and, like ductility, implies significant structural damage and, in turn, significant direct costs. Structural earthquake engineering has always focused on the magnitude of the peak displacement of the response, which is taken to determine failure or not in a black-and-white fashion. Damage (the shades of grey) is not considered worthy of much attention; if it is too serious, the member (or even the structure) is presumed to be replaced or remodeled in a way that masks the damage; if it is light, it will just be repaired.

The past 30 years have seen impressive advancements in the development and application of devices for seismic isolation and/or supplemental damping as a very effective – yet costly – means to shield the superstructure from damage. Especially if these devices self-center to zero residual displacement, they are the ultimate seismic resilient system. However, owing to the intrinsically different natures of blast and seismic loading, questions arise about the performance of seismically isolated structures under blast loading.

A structure can also be protected from seismic damage and residual deformations if it rocks as a whole with respect to the ground or if its components rock in a stable manner with respect to each other as rigid bodies, possibly with supplemental energy dissipation, to reduce the displacement response. Resilient systems of such jointed construction were proposed and successfully tested in the mid ‘80s to mid ‘90s (Ishizuka et al. 1984; Nakaki et al. 1999; Priestley et al. 1999). They comprise:

- frames of precast concrete beams connected dry to prefabricated columns by means of concentric, unbonded post-tensioning strands running through the beam-column joints seamlessly; and/or
- prefabricated concrete walls connected dry to the foundation by using vertical, concentric unbonded tendons.

A dry-jointed frame accommodates horizontal seismic motions through rotations of the beam ends with respect to the face of the column and rotation of the column base in a pocket within the foundation; a wall accommodates the seismic motion via rotation of its base section with respect to the foundation. The modeling, design, technology and details of the system have matured by now to near perfection, allowing application during the first decade of the century to buildings in high seismic areas: San Domingo (Stanton et al. 2003), San Francisco – the 39-story Paramount building (Englekirk 2002) and Christchurch, NZ – where a building constructed with this system came through the Feb. 2011 catastrophic earthquake unscathed (Pampanin et al. 2011).

2.2.2 *Design Against Progressive Collapse Due to Blast or Impact*

R&D on events that may lead to progressive collapse started with the internal gas explosion that fell a good part of all 22 stories of the precast concrete Ronan Point tower in London in 1968. The first building code provisions against progressive collapse – in the UK, as early as 1968 – were fully prescriptive. Interest spread in the US after two suspended steel platforms (skywalks) collapsed at the Kansas City Hyatt Regency Hotel in 1981 under live load, and after L'Ambiance Plaza, a 16-story building in Bridgeport, Conn., collapsed in 1987 upon erection of post-tensioned flat slabs on steel columns. Research efforts intensified in the US following the wave of intentional events around the world: the 1983–84 blasts that destroyed the US Embassy buildings, the US Marine headquarters and the French military barracks in Beirut (the total death toll was 374); the 1993 and 1995 bomb blasts in the parking garage of Tower 1 at the World Trade Centre (WTC) in New York and at the A.P.Murrah building in Oklahoma City (the total death toll was 174); the 1996 bombing of one of the Khobar Towers in Dhahran, Saudi Arabia (a success story in that the collapse was limited to the 8-story façade made of precast-concrete wall panels); the 1998 explosions at the US embassies in Nairobi and Dar es Salaam (the total death toll was 224); the aircraft crash-cum-fire in the WTC Towers 1 and 2 and the US Pentagon on 9/11/2001 (the total death toll rose to 2933); the 2002–04 bomb attacks on the US Consulate in Karachi, a nightclub in Bali, the Marriott hotel in Jakarta, four housing compounds in Riyadh, the UN headquarters in Baghdad and the Hilton hotel in Taba, Egypt (total death toll: 333), etc. Most of the over 4000 casualties from these events were due not to the direct effects of blast, but to the ensuing structural collapse or fire.

Under pressure from these intentional events, the US took the lead in R&D against progressive collapse due to blast. R&D roadmaps were drawn, based primarily on a five-year, non-military R&D program on progressive collapse and design and retrofitting against it (Multihazard Mitigation Council 2003). The second half of the decade saw a stream of public R&D results, analytical and experimental (Sasani et al. 2006; Yi et al. 2008; Sasani and Sagiroglu 2008; Su et al. 2009; Lew et al. 2011; Fujikura et al. 2008; Fujikura and Bruneau 2011; Hayes et al. 2005; Razaqpur et al. 2007), which, along with classified R&D, produced valuable application documents (Ellingwood et al. 2007; US Department of Defense 2009; Dusenberry 2010; US Department of Homeland Security 2011; GSA 2013). They also influenced the European standard on accidental loadings (CEN 2006), which covers essentially only internal (gas) explosions and vehicular impact.

Besides the traditional prescriptive approach to new buildings (i.e., of using continuous steel ties all over each floor and along the vertical elements to arrest progressive collapse should a vertical support be lost), two approaches have been promoted:

(a) to designate certain elements, which are vital for the stability of the whole, as key elements and design them to resist prescribed threats, or
(b) to assume that a key element (one at a time) is lost and verify that the rest of the system can sustain its loss, no matter the threat.

In option (a), the large inelastic deformations and internal forces induced in key elements by the impulsive loading should be estimated (e.g., on the basis of Smith and Hetherington 1994; Mays and Smith 1995; Ngo et al. 2007) and checked against the corresponding capacities. Option (b) normally requires a large-displacement, material-nonlinear dynamic analysis, with instant removal of incapacitated key elements (see Kwasniewski 2010; Brunesi et al. 2015; Fascetti et al. 2015). The analysis may instead be static and – under certain, ill-justified conditions – even linear, with the gravity loads on all floors above and all bays around such an element multiplied by empirical dynamic load factors accounting for inelastic deformation.

2.2.3 Structural Design for Resilience to Fire

In recent years, Europe has seen major fire disasters in quite a few important tunnels and concrete buildings, causing dozens of casualties and huge direct and indirect losses. Despite the frequency of major fires in Europe and around the world, R&D activity in structural fire design has not yet succeeded in overcoming the large gaps in knowledge and the shortcomings in our current approach to structural fire safety. This is even more so for concrete structures, as they are considered more fire-resistant and, hence, have received less attention than steel, timber or composite construction. Structural fire design, currently entering European engineering practice through the gradual application of the EN-Eurocodes (Høj 2005; Lennon et al. 2007), focuses solely on the safety of occupants and fire fighters during a specified duration of uncontrolled fire; minimization of damage to facilitate repair and re-use is not addressed. Besides, it is based primarily on prescriptive, semi-empirical approaches which focus on member strength against gravity loads and have been derived mainly from standard tests of isolated elements in small furnaces. It is presumed that the system's fire resistance is the minimum resistance among all its individual components, with little attention being paid to deformations and displacements, to interactions among the components of the system, or to damage due to fire that does not lead to collapse (Bailey 2009; Kruppa et al. 2001).

To shed light into areas of limited knowledge, landmark fire tests were carried out at BRE-Cardington on full sized, multi-story, multi-bay buildings (Lennon 2003; Usmani 2000; Bailey et al. 1999; Matthews et al. 2005; Bailey 2002). The test on a 7-story, steel-framed, composite-floor building, in particular, gave a wealth of data and new knowledge and prompted the development of fundamental models for the mechanical behavior of isolated horizontal composite components for various boundary conditions (Bailey and Moore 2000; Usmani et al. 2001; Usmani 2000). Less data was obtained from the tested 7-story, flat-slab-frame RC building, as all

its instrumentation was lost 18 min after ignition. Despite this loss, the residual damage, deformations and resistance of the building showed where the previous approach to structural fire design had been adequate or too conservative. For concrete buildings, however, there is still need for fundamental models of the thermal-mechanical response of single one- or two-way horizontal elements with various restraint conditions at the boundaries to enhance our understanding of their structural behavior under fire and carry out parametric studies.

The state-of-the-art in structural fire design, its limitations and the R&D needs have been the subject of key joint actions in Europe (European Commission 2007; Gambarova et al. 2005; Dimova et al. 2007; fib 2007, 2008) and the US (Beitel and Iwankiw 2002; National Institute of Standards and Technology 2003). Their conclusions are in tune with the views of top experts in fire design of concrete structures (Kodur 2003; Høj 2005; Taerwe et al. 2005; Kodur and Raut 2008; Mostafaei et al. 2009; Ghoreishi et al. 2009; Kodur et al. 2011) as follows: The current trend toward performance-based structural fire design is not supported yet by advanced computational tools or rational simulation and design procedures. There are hardly any models that go well beyond isolated members with highly idealized boundary conditions and that are able to capture interactions with the rest of the structural system during the course of fire. As a consequence of the current limitations of numerical modeling and fire testing, there is a serious dearth of parametric analyses of the global response of structures under realistic fire scenarios, let alone fire assessment procedures, although they are vital for performance-based structural fire safety and design.

2.3 Cyclic Tests of Dry-Jointed Precast Frame on Fixed or Rocking Footings

A structure consisting of rigid components with flexible, nonlinear elastic connections is expected to sustain earthquakes with little damage, epitomizing seismic resilience. To allow rigid-body rocking of the vertical members in earthquakes, their base is rotationally unrestrained in a pocket in the foundation. Walls have the rotation of their base weakly restrained by the concentric, unbonded tendon running up the wall; so they have a clear shear deficiency in the very critical dry joint at their base. In view of these weaknesses, a variant of the dry-jointed rocking system has been built and tested. In this variant, the blast-vulnerable dry-joint at the base of the vertical elements is replaced by a robust, monolithic connection to an isolated footing, which is not connected to neighboring ones through tie beams, so that it may uplift and rock on the ground. This concept was implemented in a two-story, two-bay, nearly full-scale frame (Stathas et al. 2017c). The frame was subjected to a specified history of top displacement cycles under an inverted triangular distribution of story forces. At each step, the force applied to the intermediate level was one-half of the force required at the top level in order to achieve the top displacement specified for that step.

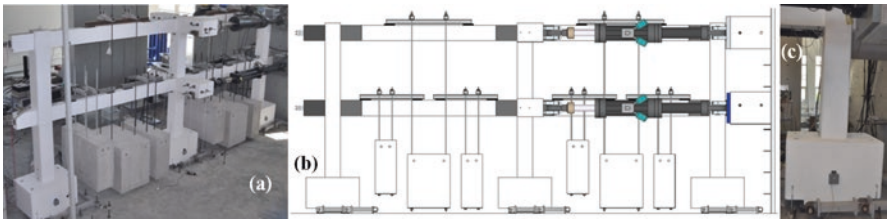

Fig. 2.1 Precast, dry-jointed frame with actuators and added masses mounted (**a**, **b**); (**c**) uplifting and rocking of footing supported on device which allows rotation but blocks horizontal movement

The 2.14 m-long central part of each beam was precast, with its top and bottom bars protruding from the precast beam's end sections and lap-spliced with the top and bottom bars of the cast-in-situ 0.5 m-long end segments shown in dark color in Fig. 2.1b. The top and bottom bars of the cast-in-situ beam segments crossed the column unbonded, inside plastic ducts. With this detailing, the column-beam interface was kept closed under serviceability gravity loads thanks to post-tensioning by two cables running the full length of the beam, unbonded and concentric. During an earthquake, alternating moments with opposite signs across the column cause the dry joints at the beam-column interfaces to open and then close by virtue of the prestressing force. Thanks to the unbonded length of the beam bars within the column, fixed-end rotations at those interfaces are expected to allow the interstory drift to develop without plastic hinging (and hence damage) at the beam ends (Ishizuka et al. 1984; Nakaki et al. 1999; Priestley et al. 1999). The ties in one half of the beam's cast-in-situ end regions closest to the column were very dense, to enhance the compression strength of the top and bottom edge of the section against the high contact stresses produced when the dry joint is open at the opposite edge of the section.

The base of the two-story tall, precast columns was fixed with non-shrink mortar in a pocket of the footing. In the rocking version of the frame, supporting pivots at quarter points of the base allowed uplift of the footings but prevented horizontal movement (see Fig. 2.1b, c). With the pivots fixed at the quarter points, uplift occurred exactly at the uplift moment given by Crémer et al. (2002). However, in this setup, the moment at the base of the footing does not increase any further after the onset of uplift. By contrast, the moment acting on the underside of a footing supported on a soil-like continuum can asymptotically increase to twice the uplift moment. The artificial cap imposed on the moment at the base of the footing, combined with the relatively large footing depth, increased the moment at the top of the ground story columns for a given column shear. This increase caused yielding at the top of the rocking columns (Fig. 2.3b); this is something not expected in a real-life, dry-jointed rocking frame.

Weights totaling 200 kN were suspended from the two stories and produced normalized axial force values at the base of the columns around 0.05 (see Fig. 2.1a, b).

The rocking frame was subjected to two full displacement cycles (Fig. 2.2a). Its footings were then tied to the laboratory floor. The fixed-base frame was subjected to a sequence of top displacement cycles bracketing the whole range from before yielding to beyond ultimate displacement, conventionally identified with a 20% drop of lateral force resistance relative to the peak value (Fig. 2.2b, c). The fixed-base frame developed its peak resistance at about the maximum displacement imposed on the rocking frame; that resistance was more than twice the peak force experienced by the rocking frame. Had the rocking frame been subjected to larger displacements, it would have reacted with larger forces, albeit not much larger. The peak forces would have been even higher (but not much higher) if the pivot had been allowed to shift from the quarter point to the edge of the footing. The fact of the matter is that the rocking frame develops much lower forces than the fixed-base one under the same top drift, because its columns experience most of the top drift as rigid body rotation, in lieu of chord rotations at the base (Fig. 2.4a, b). So, its

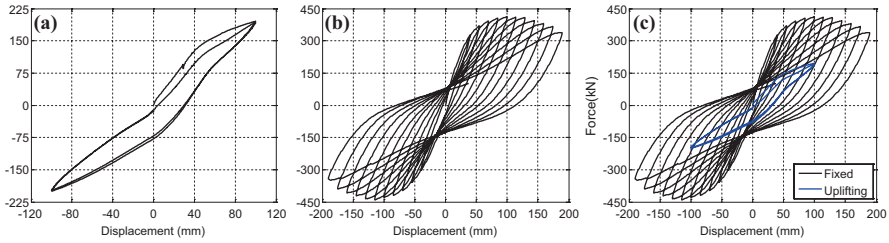

Fig. 2.2 Base shear v. top displacement: (**a**) rocking frame; (**b**) fixed-base frame; (**c**) the two tests compared

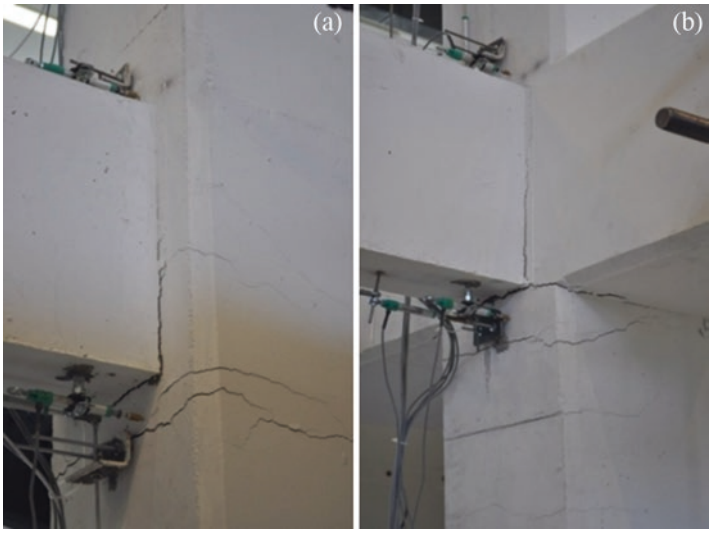

Fig. 2.3 Opening of dry-joints (**a**) and plastic hinging of column tops (**b**) at the ground story of the rocking frame

columns suffer much less damage. By contrast, the rotations over the end regions of 1st story beams account for most of the top drift ratio of the frame; they were nearly fully accommodated by the opening and closing of the dry joints (Fig. 2.3a).

Unlike the rocking frame, the fixed-base one developed plastic hinges at the base of all three columns. Their rotations accounted for a good part of the overall displacement at roof level (Figs. 2.5a, b and 2.6a, b). The accompanying rotations at beam ends took place partly at the dry joint at the column face and partly at the interface of the precast part with the cast-in-situ 0.5 m-long segment (Fig. 2.5c, d). There was a very large strength contrast across that interface: 35.1 MPa 150 mm-cylinder strength in the precast beams vs. 71.9 MPa 50 mm-cube strength in the cast-in-situ plug between the precast beam and the column. That contrast, together with the very sparse ties near the end of the precast beam, led to the formation of plastic hinges at every interface between these two types of beam segments in the frame (Fig. 2.4b). Once they formed, these hinges outcompeted the dry joints in hosting the overall deformation of the beams. Fig. 2.6c–f shows that the magnitude of the rotation near each beam end stabilizes, while the overall deformation of the beam increases to match the rotation at the base of the column (Fig. 2.6a, b). The growing difference between these two rotations takes place around the interface of the precast beams with the cast-in-situ end segments. It is worth noting that the amplitude of the rotations at the dry joints as well as all beam flexural deformations

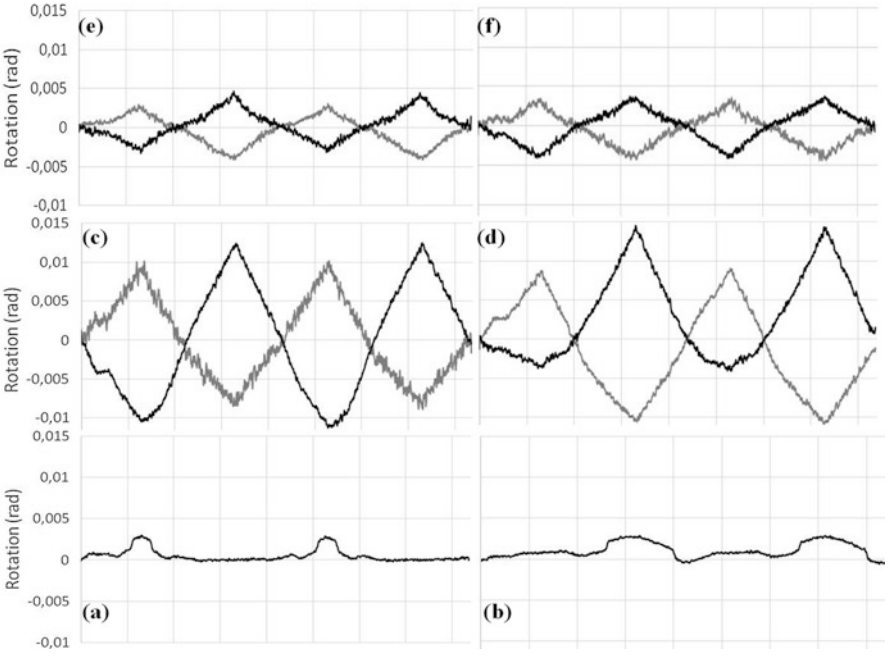

Fig. 2.4 Rocking frame: (**a**), (**b**) chord rotations at the base of the outer columns; (**c**), (**d**) rotation of section 225 mm from the end of the 1st story beam with respect to the column face; (**e**), (**f**) ibid., 2nd story beams; (**a**), (**c**), (**e**): left-hand half of frame; (**b**), (**d**), (**f**): right-hand half

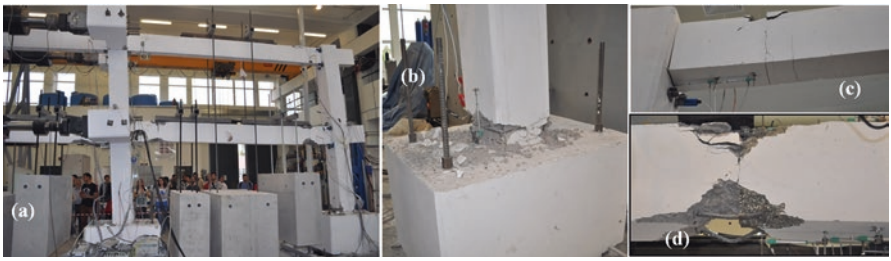

Fig. 2.5 Fixed-base dry-jointed frame: (**a**) maximum overall deformation; (**b**) typical damage, column base; (**c**) opening of dry joint at column face and of interface of precast segment with cast-in-situ concrete at top story beam; (**d**) typical damage around interface of precast and cast-in-situ parts of ground story beam

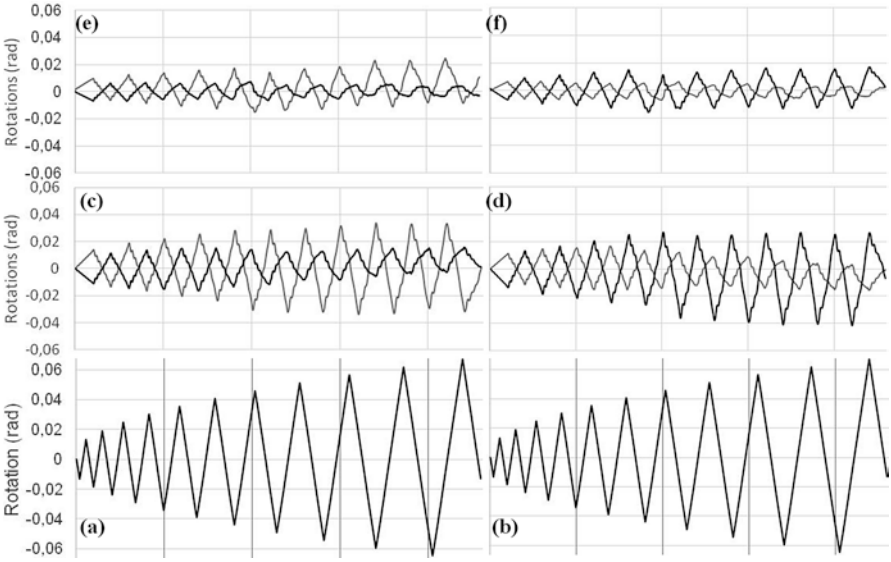

Fig. 2.6 Fixed-base frame: (**a**), (**b**) chord rotations at the base of the outer columns; (**c**), (**d**) rotation of section 225 mm from the end of the 1st story beam with respect to the column face; (**e**), (**f**) ibid., 2nd story beams; (**a**), (**c**), (**e**): left-hand half of frame; (**b**), (**d**), (**f**): right-hand half

occurring outside the plastic hinges around the cast-in-situ precast interfaces reach their peak values when the frame attains its peak resistance. After that point, the amplitude of these deformations drops, whereas that of flexural deformations in the vicinity of the interfaces increases at an ever faster pace until the frame fails.

To conclude, even after considering the much more challenging displacement demands imposed on the fixed-base frame, the rocking one performed much better and was almost free of damage. The plastic hinging observed at the top of the ground story columns would not have taken place if the footings had been sitting on top of a realistic soil deposit and if they had been free to rotate about their toe, in

lieu of their quarter points, in plan. Therefore, the rocking, dry-jointed frame on footings which are free to rotate, unconstrained by tie-beams, etc., is a resilient system. However, its robustness to impact or blast is questionable. Moreover, the flexibility of the rocking system is at the expense of robustness to progressive collapse if a column is lost. Note, though, that catenary action in the continuous, unbonded tendon, which can stretch over its full length and has considerable strength reserves, can markedly increase the load bearing capacity of the beam. These questions are addressed in later sections of this paper.

2.4 Building with Conventional Seismic Design or Base Isolation Under Blast

Blast scenarios were simulated on the prototype building shown in Fig. 2.7. The building was designed to the Eurocodes for a cylinder concrete strength of 20 MPa, reinforcement yield stress of 500 MPa, floor loads due to finishings of 1 kN/m^2, weight of exterior wall of 1.25 kN/m per floor, live load of 2 kN/m^2 (0.6 kN/m^2 quasi-permanent load, acting all the time), design peak ground acceleration (PGA) on rock of 0.2 g, a Soil C Type 1 spectrum (i.e., with corner period of 0.6 s between the acceleration- and the velocity-controlled regions and a soil factor of 1.15 multiplying the spectrum on rock) and Ductility Class Medium (DC M). Thanks to the large cross-sectional sizes (0.6 m square columns, 0.6 m deep by 0.3 m wide beams, 0.21 m thick slab), the minimum reinforcement for DC M suffices almost everywhere.

The lowest three periods of the building calculated using the secant-to-yield-point stiffness of the members from Biskinis and Fardis (2010a) and Part 3 of Eurocode 8 are:

- 1.62 s, 0.52 s and 0.29 s in the long and
- 2.03 s, 0.64 s and 0.35 s in the short direction in plan.

The first mode in each direction accounts for 81 to 82% of the total mass, the second one for another 10 to 11%.

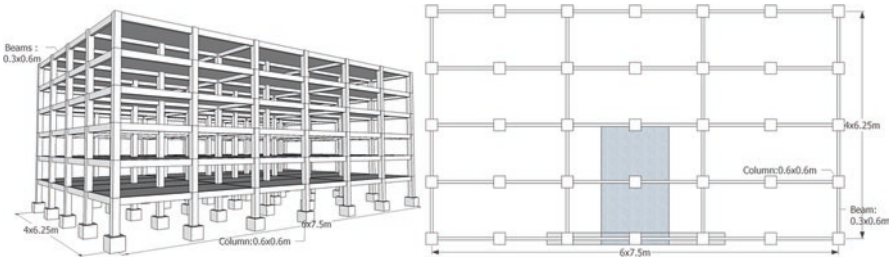

Fig. 2.7 Schematic and framing plan of building analysed for earthquake and blast; slab and outer frame subassemblies tested and modelled under conditions simulating loss of a central outer column are highlighted

A base-isolated version was also designed, with a double foundation system sandwiching a 0.6 m diameter lead rubber bearing (LRB) under each column. For 100 mm of elastomer, the stiffness of each LRB unit is 2800 kN/m. The minimum reinforcement prescribed by Eurocode 2 for buildings not designed for earthquake suffices in the superstructure.

Each design option was subjected to nonlinear dynamic analyses for 14 pairs of ground motions with a PGA of 0.23 g; each pair came from modulating a historic bidirectional record to fit the Eurocode 8 spectrum. Performance was assessed via the mean over the 14 flexural damage ratios in individual members. This ratio is defined as the peak during the response of the ratio of the chord rotation demand at the member end to the corresponding limit in (CEN 2005) for significant damage, i.e., 75% of the ultimate capacity per Biskinis and Fardis (2010b). The damage ratio pattern of the conventional design is shown in Fig. 2.8. It ranges from 0.5 to 0.6 at the base of interior columns and in the beams of stories 2 to 4. In the base-isolated building, it ranges from 0.25 to 0.5 at the base of interior columns, but is less than 0.25 elsewhere.

Two blast scenarios were postulated:

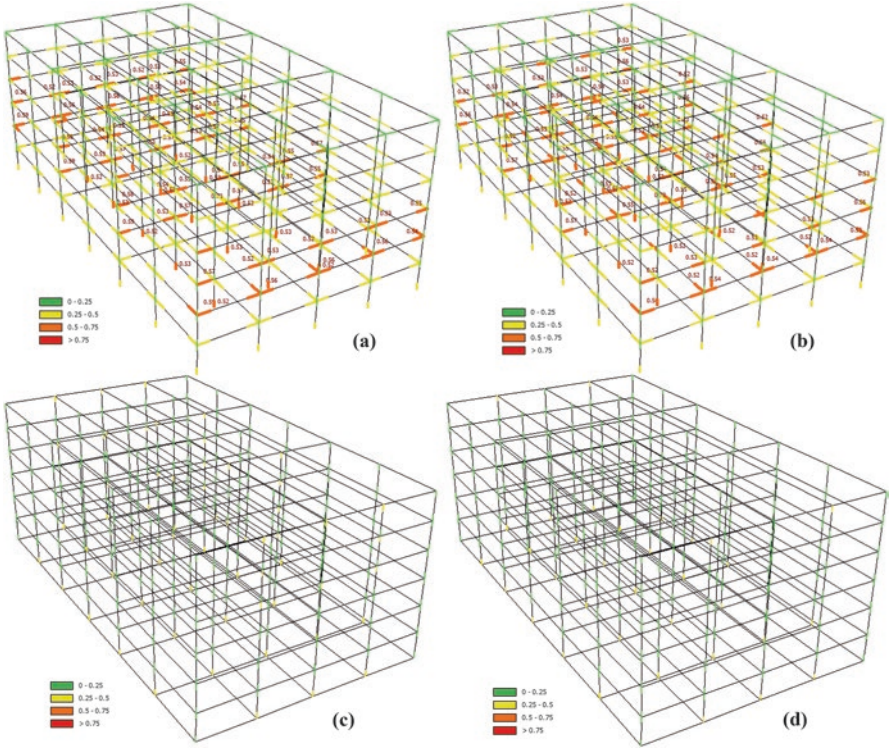

Fig. 2.8 Flexural damage ratio under design earthquake of (**a**), (**b**) conventionally designed building (**c**), (**d**) base-isolated building ((**b**), (**d**): ground motions rotated by 90-deg with respect to (**a**), (**c**))

- 25 MN blast scenario: peak force of 12.5 MN at the top and mid-height of target column.
- 9 MN blast scenario: peak force of 4.5 MN at the top and mid-height of target column.

The two scenarios were applied to the following columns:

- the central one on the long side, which is engaged in one-way frame action (only along the perimeter);
- an intermediate column on the long side of the perimeter, which is engaged in two-way frame action;
- a corner column, hit parallel to the long or to the short side of the perimeter.

When the central column was targeted, dynamic loading was applied not only to that column, but also at mid-height of the adjacent columns. The peak force of that loading was 5 MN in the 25 MN blast scenario and 1.75 mN in the 9 MN blast. The peak force of each dynamic loading was applied instantly, dropping off by 90% in 0.1 s and to zero in 0.2 s. Such a loading excites modes with periods around 0.4 s.

Figures 2.9 and 2.10 depict the predicted inelastic behavior in the six blast scenarios simulated for the building with the conventional seismic design and the base-isolated building, respectively. In all of them, the targeted column(s) fail in flexure and in shear, albeit marginally in the 9 MN blast. The blast excites local vibration around the directly hit elements; the global response plays a secondary role. In fact, the major difference in the response of the base-isolated building from the one with conventional design is that the global features of its vibration are more pronounced. As a result, it experiences more widespread damage to other elements in the vicinity of the targeted column(s) and beyond. By contrast, damage to the building with the conventional seismic design is more localized around the directly affected column(s).

The 25 MN blast fails in flexure the base of the column above and the ends of the beams, which are connected to the targeted column in the direction of the blast loading. Under the 9 MN blast, these elements yield but do not fail. A 25 MN blast attack on the central column of the long side, which is accompanied with blast loading on the two outer columns to the left and right, causes all columns to yield at the base of the ground story in the conventionally designed building or at the 2nd story in the base-isolated one. Sporadic column yielding occurs at the base of the 2nd story in the former and at that of the ground story in the latter. All other 25 MN blast loadings act on the building with an eccentricity in plan, which induces certain torsional response around the vertical and concentrates column and beam yielding to one side of the building, spreading it, though, to the upper stories. The 9 MN blast does not cause yielding of elements other than those in the close vicinity of the targeted column.

The time-histories of the displacement at mid-height of the targeted column in Fig. 2.11 show a single, large amplitude half-cycle followed by a large permanent

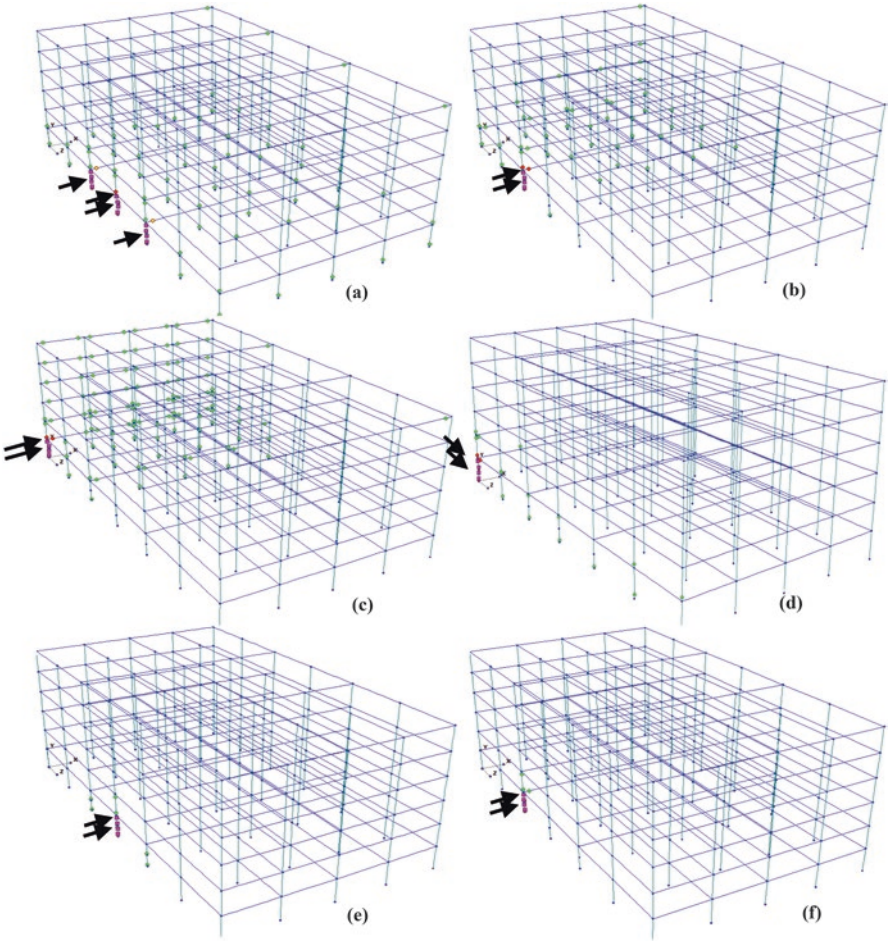

Fig. 2.9 Damage prediction in conventional seismic design (**a**)–(**d**) 25 MN blast; (**e**), (**f**) 9 MN blast; (**a**), (**e**) central column on long outer side targeted; (**b**), (**f**) intermediate outer column targeted; (**c**) corner column targeted along short side in plan; (**d**) ibid., along long side in plan. *Green circle*: flexural yielding; *yellow circle*: serious flexural damage, but not failure; *red circle*: flexural failure; *purple square*: shear failure

drift. The displacements anywhere else in the structure exhibit a similar half-cycle of much smaller amplitude, followed neither by vibration nor by permanent drift. The relative magnitude of the displacements in the various scenarios reflects the relative severity of the overall damage inflicted on the building by the blast.

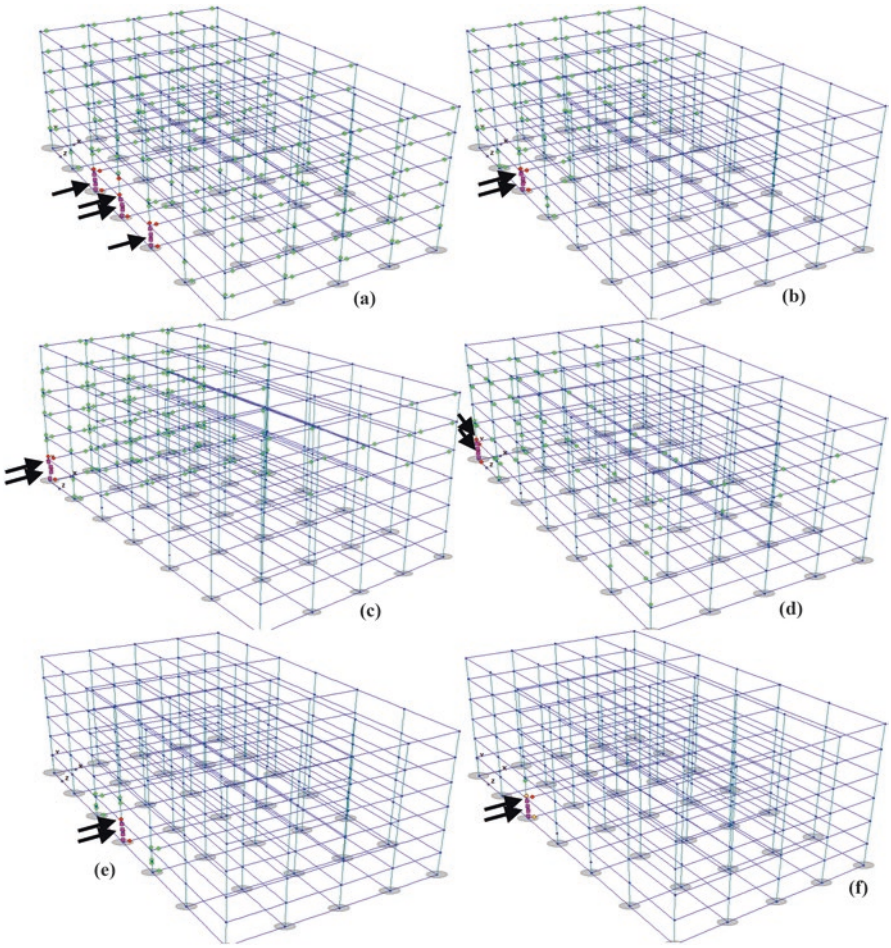

Fig. 2.10 Damage prediction in base-isolated building (**a**)–(**d**) 25 MN blast; (**e**), (**f**) 9 MN blast; (**a**), (**e**) central column on long outer side targeted; (**b**), (**f**) intermediate outer column targeted; (**c**) corner column targeted along short side in plan; (**d**) ibid., along long side in plan. *Symbols* as in Fig. 2.9

2.5 Progressive Collapse Potential After Loss of One Column Due to Blast

The conclusion of the nonlinear dynamic analysis carried out for postulated blast loading was that any outer column of the prototype building in Fig. 2.7 is condemned if directly hit by the blast. However, damage to adjacent frame members or

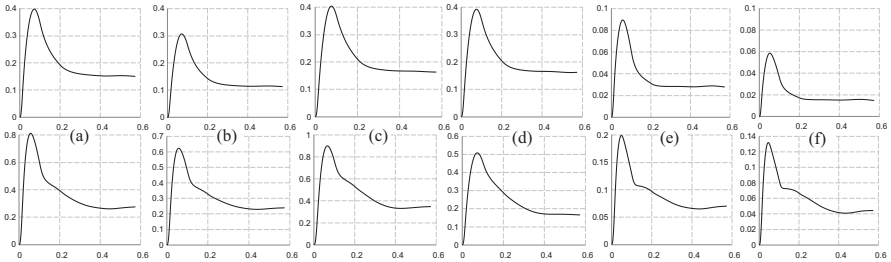

Fig. 2.11 Displacement history (m vs. s), mid-height of targeted column (**a**)–(**d**) 25 MN blast; (**e**), (**f**) 9 MN blast; (**a**), (**e**) central column on long outer side targeted; (**b**), (**f**) intermediate outer column targeted; (**c**) corner column targeted along short side in plan; (**d**) ibid., along long side in plan. *Top row*: conventional seismic design; *bottom row*: base-isolated building

other elements of the building is not predicted to be large enough to compromise their gravity load bearing capacity.

To investigate the consequences of the loss of one outer column, the quasi-permanent gravity loads that acted on floor slabs adjacent to the targeted, and presumably lost, column were multiplied at all floors by a factor gradually increasing from 1.0 to 2.0, the value of 2.0 being the dynamic amplification of the static load effects when static loads on these slabs are applied instantaneously as a step function owing to abrupt loss of a column. The quasi-permanent gravity loads acting on all other slabs in the building had their nominal values. Nonlinear static analyses of the 3D frame structure with the ground story column removed was carried out for these loadings with the amplification factor on the loads of the floor slabs adjacent to the failed column increasing from 1.0 to 2.0 at all floors. Out-of-plane bending of slabs was neglected.

Figure 2.12 depicts the distribution of plastic hinges and beam failures at an amplification factor of 2.0 under the three column loss scenarios. If the central column on a long side in plan is lost (Fig. 2.12a), the first beam to yield or fail does so when the amplification factor equals 1.14 or 1.37, respectively. All beams connected to columns above the lost ground story column fail in flexure at both ends when the amplification factor reaches 1.49. If the column lost, unlike the central one, is engaged in two-way frame action because of being connected to beams at right angles to the perimeter (Fig. 2.12b), yielding or ultimate failure of one of these beams takes place for the first time when the amplification factor exceeds 1.18 or 1.88, respectively. The beams which are connected to the columns above the failed one and are at right angles to the perimeter fail at all stories when the amplification factor on the gravity loads of the slabs adjoining the failed column reaches the value of 1.94. If the missing column is a corner one (Fig. 2.12c), the first beam to yield does so at an amplification factor of just 1.08, but no beam fails afterwards, even when the amplification factor reaches 2.0. So, removal of the central column on a long side in plan (Fig. 2.12a), which is in one-way frame action, is more likely to produce progressive collapse. As such a column is not connected to a beam at right angles to the perimeter, the two beams framing into this column along the perimeter

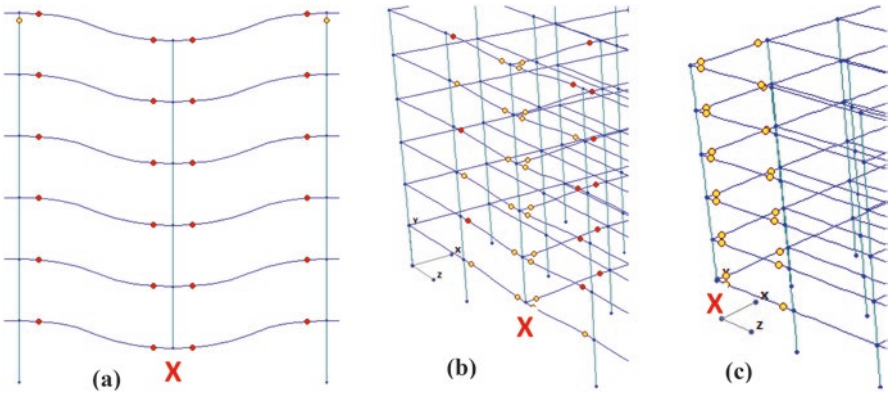

Fig. 2.12 Damage predicted by nonlinear static analysis for assumed dynamic amplification (by 100%) of gravity loads contributing to the axial load of a presumed failed column (X) which is: (**a**) in one-way frame action; (**b**) two-way frame action; (**c**) at a corner in plan. *Yellow circle*: yielding; *red circle*: flexural failure

have to take all the tributary load of the failed column and may exceed their ultimate plastic-hinge-rotation capacity; they could collapse alongside the outer span of the one-way slabs they support.

More representative of the response of the structure when a ground-story column instantly loses its gravity load capacity is a nonlinear dynamic analysis, with the gravity loads coming from the floor panels adjacent to the failed column applied instantaneously. Such an analysis predicts the vertical vibrations of the beam-column joint at the top of the failed column depicted in Fig. 2.13. If the column that collapses abruptly is the central one on the long side of the perimeter and is engaged only in one-way frame action, it was computed that the beam it supports deflects by about 75 mm over a span of 15 m, after going through a maximum deflection of 125 mm. The corresponding values for an intermediate column on the perimeter in two-way frame action were 65 mm and about 90 mm; those for a corner column were 40 mm and 60 mm. This vertical vibration did not induce any further damage to any element. Elements unloaded and reloaded elastically during their free vibration. These findings show that the simulation by pushdown analysis, with gravity loads in the tributary area of the column multiplied by a dynamic amplification of 2.0, is overly conservative.

Note that, in the very common case of buildings having floors with the same geometry and similar gravity loads, loss of a lower-story column deactivates the still intact columns above it and puts the beams and slabs of all stories under the same loss-of-support condition as in the story of the failed column. Only when there are differences between floors do the columns connecting them redistribute loads from the more heavily loaded floor(s) to the less loaded one(s) and/or from the floor(s) with the more flexible beam(s) to the one(s) with the stiffer beam(s). The question is, then, whether a beam can still support the distributed floor loads in its new tributary area without the support it lost.

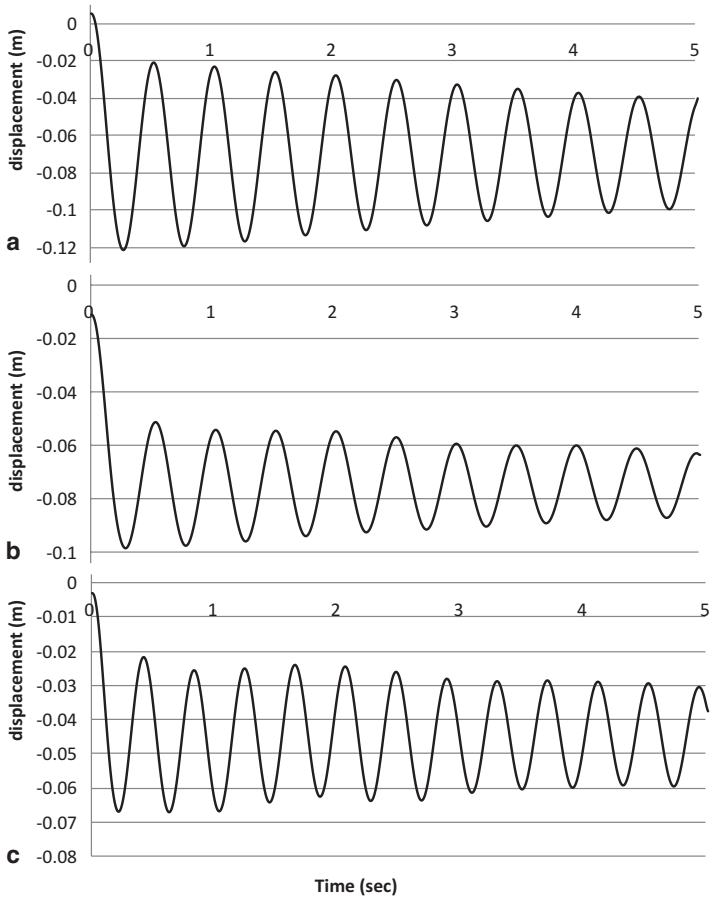

Fig. 2.13 Free vertical vibration of the top of a ground-story column of the 6-story regular building right after instant column collapse due to blast, from nonlinear dynamic analysis for instantaneous application of the gravity loads on the floor panels adjacent to a failed column: (**a**) at the centre of a perimeter frame with one-way frame action; (**b**) at an intermediate position with two-way frame action; (**c**) at a corner where two perimeter frames meet

To answer this question, the parts of the prototype building in Fig. 2.7 which are directly affected by the loss of the central outer column, shown as shaded in Fig. 2.7, were tested under conditions simulating a column loss (Stathas et al. 2017a, b). More specifically, the two spans supported by the lost column were tested alongside one shear-span-long part of the columns and beams framing into the end joints of these beams with appropriate boundary conditions. Monotonically increasing distributed vertical loads were applied, representing the reaction force from the one-way floor slab supported on the beam, as well as the weight of the beam and of the

exterior wall in one story. The large increase in deflection of the beam after loss of its central support reduces the reaction force delivered to it from the one-way slab it supports. This reduction should be accommodated by a redistribution of forces in the slab. In order to quantify these phenomena and estimate whether a new stable configuration of the slab-beam subassembly is feasible after loss of a central outer column, we need the nonlinear relationships between the deflection of the beam at the location of the missing column (which is the same as that of the slab at its subsiding exterior support) along with (a) the net vertical load applied on the beam and (b) the reacting force at the exterior support of the one-way slab. The frame subassembly tests answer part (a) of the question. To answer part (b), a testing campaign was carried out on slab specimens representing the corresponding shaded area in Fig. 2.7. The main outcome of the slab tests was the dependence of the reacting force at the exterior support on the vertical deflection there. In extremis, under deflections at which the beam cannot even carry its own weight, the slabs it supports should be able to survive without it and carry the weight of the beam and of any walls resting on it.

The tests on one-way slab specimens simulating loss of support of the perimeter beam due to failure of an exterior column followed detailed analyses of a slab surrounded by beams and columns which are intact (except for the column lost to blast). These analyses have shown that, thanks to the in-plane stiffness of the slab and the unyielding supports along its three sides, the perimeter beam does not move at right angles to its axis when a column under it is removed. Hence, the edge of the slab supported on this beam may be considered as fixed horizontally, while it moves vertically owing to the deflection of the perimeter beam. Further detailed analyses of a continuous beam with more than three equal spans have shown that the magnitude of the force to be applied at an outer support in order to have a given vertical displacement is not markedly affected by the assumption that the continuous beam is restrained against rotation over its second internal support. So, the behavior of the slab when the perimeter beam loses one of its supporting columns could be studied experimentally on a two-span slab specimen, with one outer support fixed when the opposite one moves only vertically. Following this reasoning, two one-way slab specimens were tested as in Fig. 2.14. At the central support the slab was connected to a beam that was free to rotate about its axis and to translate in the long direction of the slab. At one outer support, all degrees-of-freedom were fully fixed. At the other, the slab was connected to a 0.4 m-wide beam that was free to rotate about its axis and could only move vertically, i.e., the slab was horizontally restrained there in its long direction. The two slab specimens differed in their top reinforcement. One had top reinforcement only over the supports by the beams, while the other had continuous top reinforcement throughout the specimen length, increased over the first interior support. In both slabs, the bottom reinforcement was continuous across the supports. A uniform distributed load supplemented the self-weight. Vertical displacement of the outer support produced, in the first slab specimen, a wide crack at the section where the top bars over the central support ended. In the other slab, yielding and plastic hinging took place at the two sections across the central sup-

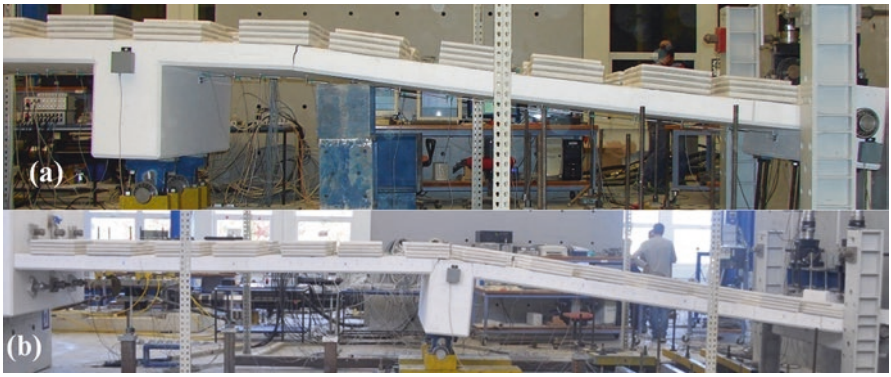

Fig. 2.14 Slab tests and failure mode: (**a**) discontinuous top reinforcement; (**b**) continuous top reinforcement

porting beam. From then on, both specimens sustained the continuously increasing vertical displacement of the outer support by tensile membrane action.

The frame subassemblies tested comprised two, full beam spans of a perimeter frame on either side of a column presumed to be lost to blast (Fig. 2.15). The length of the columns above and below, and the extension of the beams into the adjacent bays, were also included, up to their points of inflection, as determined by an elastic analysis for gravity loads of the full frame with the ground story column removed. Every extremity of these members representing a point of inflection was built as a hinge, allowing rotation in the plane of the frame but preventing displacement. In one test, the beams were monolithic with the columns. In the other, columns and beams were precast with the same geometry and reinforcement. Longitudinal bars protruding from each end of the precast beams were lap-spliced with those of 0.5 m-long cast-in-situ end segments, which crossed the column inside plastic ducts, neutralizing the bond in the joint with the columns. The 0.5 m-wide gap between the end of a precast beam and a precast column was filled with cast-in-situ non-shrink concrete. The dry connection between a column and the cast-in-situ beam end was kept closed under normal gravity loads by post-tensioning with two cables which ran concentric and unbonded all along the beam. To enhance the strength of the compressive zone of the cast-in-situ segments in view of the high contact stresses that develop at its edge when the dry connection opens, especially under seismic loading, tie spacing was reduced to 50 mm in the one-half of the length of the cast-in-situ beam segments close to the column. Six concentrated loads were applied on the beam's top surface, increasing in unison.

The monolithic specimen developed flexural plastic hinges at the inner faces of the two side columns and at both sides of the central stub emulating the central column. Failure was due to rupture of the bottom bars at mid-span, at a vertical force about 20% less than the peak resistance and a deflection of more than twice the value at peak resistance. In the other test, the concentric prestress increased by 30% the vertical load capacity compared to the monolithic specimen. The dry joints

Fig. 2.15 Frame subassemblies after test: (**a**) monolithic; (**b**) precast, with dry-joints and concentric pre-stressing of the beam

opened, preventing plastic hinging at beam ends. Failure over the one half of the beam end regions, which had ties at 90 mm centers, was due to shear. The critical shear crack started at the section where the top flange ended, 0.5 m from the column, and ended at the section separating the end region with ties at 50 mm centers from the one with ties at 90 mm centers. In the test with the precast beam, the column sections above and below the connection with the beam cracked and yielded.

The results of the beam tests were combined with those of the slabs to establish the margin of bearing capacity of the perimeter beam, above what is needed to support the weight of the beam and the beam's tributary loads from the slab. This margin is due to the flexural capacity of the beam as enhanced by arching and catenary actions and to the tensile membrane mechanism in the slab. It is available to bear the weight of exterior walls and any other part of the building envelope supported by the beam. Figure 2.16 depicts the magnitude of this margin in terms of the beam deflection at the location of the missing column. The conclusion drawn from these figures is that the perimeter beam can survive loss of the most critical outer column, even when it supports, in addition to its tributary floor loads, a façade as heavy as 23.5 kN/m for the precast, prestressed beam design, no matter whether the slab has continuous top reinforcement or not. Such a peak resistance is attained at a deflection of 200 mm. Continuous top reinforcement in the slab increases the peak resistance of the monolithic design from 12 kN/m to 17.5 kN/m at the expense of larger deflections (370 instead of 200 mm). The precast, prestressed beam design can bear

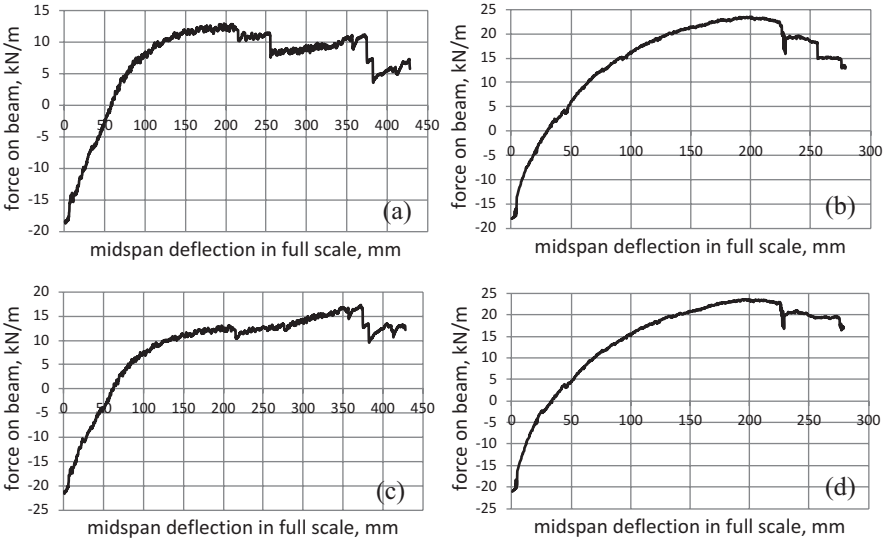

Fig. 2.16 Force capacity of perimeter beam in full-scale building of Fig. 2.7, over what it needs to support the dead loads from the slab and the beam, as a function of the beam deflection upon loss of a supporting column: (**a**), (**b**) slab top reinforcement only over supports; (**c**), (**d**) top reinforcement continuous all over the slab; (**a**), (**c**) monolithic frame; (**b**), (**d**) precast frame with dry joints and concentric, unbonded tendons

a common façade weighing 1 to 1.5 kN/m with a deflection of 30 to 40 mm over a 15 m span, i.e., within the usual serviceability limits. The monolithic design may deflect by 60 to 70 mm under such a façade.

2.6 Masonry Infills Preventing Collapse of Upper Stories Due to Column Loss Below

There are many examples where the upper stories of buildings survived loss of one or more critical ground story columns in an earthquake because they bridged the gap left at the location of a failed interior column, or they cantilevered outside the line circumscribing the still intact columns after losing one corner column (Fig. 2.17b) or a corner column and nearby ones (Fig. 2.17a). In such cases, the upper stories work as deep beams, with the uppermost and the lowermost floors (including the beams) playing the role of tension and compression flanges, and the masonry infills the role of webs connecting these flanges. Floors and infills play the same roles in cases where the loss of ground vertical members is caused by an explosion or impact. In the example shown in Fig. 2.17c, the explosion took place within the outer bay of the building's framing system. The neighboring building braced laterally the part of the damaged building left to cantilever over that bay.

Fig. 2.17 Examples of upper floors working as cantilevering deep-beams with the infills in the role of the web, after loss of support due to (**a**), (**b**) the Kalamata, GR, 1986 earthquake; (**c**) gas explosion (Netanya, IL)

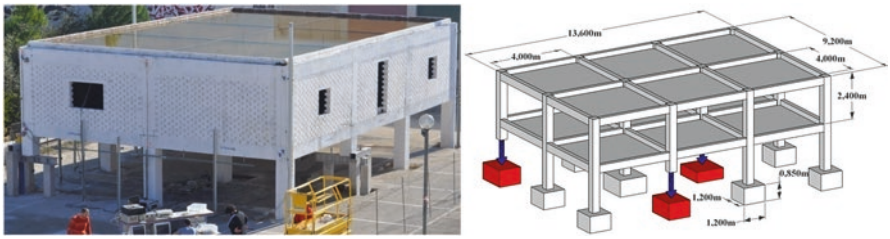

Fig. 2.18 Two-story infilled RC frame building, for instant loss-of-column tests

Beam action across its full depth, thanks to the infills, was essential for this part to profit from the bracing action.

To study in detail a mechanism of the type demonstrated in Fig. 2.17, the two-story RC frame test building of Fig. 2.18 had its upper story infilled all along the perimeter. The inverted web of the beams alongside the perimeter infill wall of the second story and a parapet at roof level allowed flooding the floors with water to a depth sufficient to simulate the weight of floor finishings and the quasi-permanent fraction of live loads (30% of the nominal live load per CEN (2002a), as well as the effect of the 0.6:1 scale on density.

All columns were 0.4 × 0.4. Beams were 0.4 m-deep and 0.25 m-wide and had two, 12 mm-dia. bars at the top and bottom, continuous over all supports. Two more 12 mm-dia. bars were added to the top flange up to a distance of 1.4 m from the face of the column. Slabs were 0.14 m thick, with two-way top and bottom reinforcement of 8 mm-dia. on 200 mm centers.

The mean cylinder concrete strength was 32.7 MPa at the ground story and 30.8 MPa at the story above.

Infill walls were 125 mm thick, with a compressive strength of 8.1 MPa in the vertical direction and 7.9 in the horizontal. The elastic modulus was 4.24 GPa in both directions; 45-deg compression tests gave a shear modulus of 2.9 GPa and a shear strength of 1.08 MPa.

One interior column, an intermediate one on the long side of the perimeter, and a corner column were seated on special devices allowing instant removal of the support and release of the column's axial load. There was a window-type opening in one of the two infill panels which were in contact with the corner column and one door and another window in the two infill panels adjoining the intermediate perimeter column. As the building had infills only along the perimeter and the interior column supported by far the largest axial force among the three columns removed, its removal had the most marked impact on the rest of the building. However, even that impact was minor; there was no visible cracking of the infills or the concrete, let alone yielding of the reinforcement. The floor had a maximum dynamic deflection of 8 mm at 0.1 sec after the removal of the column and a permanent, albeit elastic, one of 6.5 mm (see brown line in Fig. 2.19). A nonlinear dynamic analysis (blue line in Fig. 2.19) captures fairly well the measured response.

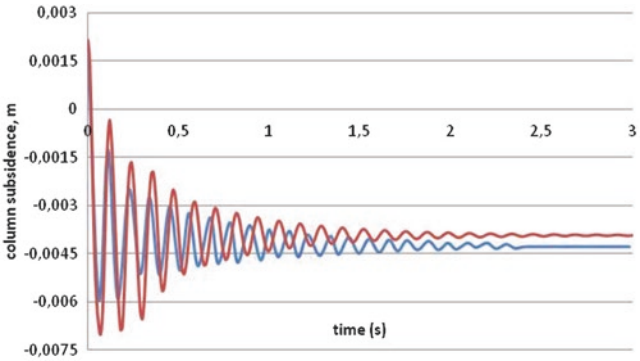

Fig. 2.19 Floor deflection due to instant removal of the central column

Fig. 2.20 Building without infills above the intermediate perimeter column removed in the final test phase

In a final phase, the water level increased to a weight equivalent of one more story. The intermediate outer column was then instantly removed, after knocking down the infills of the entire side above (Fig. 2.20). Cracks appeared in the parapets and the concrete, but closed after the loading due to the water was removed. The maximum deflection at the perimeter reached 9 mm, to stabilize soon afterwards at 8 mm

2.7 Structural Effects of Fire Exposure on Concrete Members

The temperature history at every point inside the mass of a reinforced concrete member can be computed by solving numerically the differential equation of the heat transfer problem, namely through finite differences. An explicit scheme, such as the central difference formula, can be adopted, provided that a very fine discretization in space and time is used. The thermal conductivity and the specific heat of concrete are given in CEN (2004b) as a function of the local temperature. The emissivity coefficients of concrete and of the air are also given in the same source. Gas temperature histories are given in CEN (2002b) for a standard fire scenario, an external fire or a hydrocarbon fire. They may also be obtained from a computational fluid dynamic (CFD) solution of the fire problem for the applicable fire load and compartment geometry. Once the temperature history is obtained at every point inside the mass of a reinforced concrete member, the corresponding thermal strain is computed per CEN (2004b) and used as initial strain in the temperature-dependent, stress-strain laws of steel or concrete, given also in CEN (2004b).

The concentric axial load capacity of a column computed in this way (defined as the maximum axial force that the column can bear under uniform strain conditions throughout the section) is depicted in Fig. 2.21 as a function of the column size and the duration of the fire. The capacity reduction increases as the column cross-sectional size decreases, whereas the ratio and the cover of vertical steel bars play a very secondary role. Note that the axial force capacity on the vertical axis is computed for the mean material strengths, not their design values. Note also that the seismic design rule of limiting the axial load of the column in the combination of gravity loads with the design seismic action leads to values of the acting axial force well below the curves in Fig. 2.21, even for the smallest of column sizes. So, fire does not seem to pose a major threat to the axial load capacity of columns. At any rate, a large, nearly square, column section seems to safeguard best the gravity load capacity of the column under fire conditions.

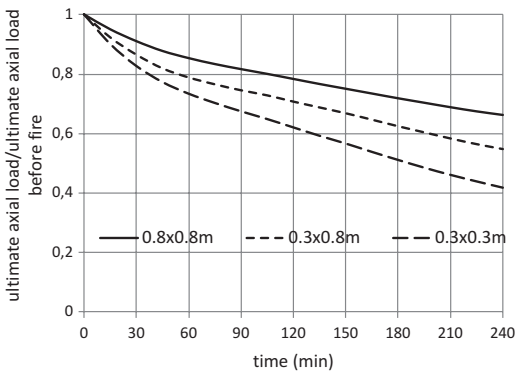

Fig. 2.21 Reduction of concentric axial force capacity of columns of various sizes due to exposure to standard fire (mechanical ratio of vertical bars: 0.15; 25 mm cover of 8 mm ties; 20 mm dia. vertical bars)

If unrestrained, a concrete slab whose underside is exposed to a uniform heat flux due to fire will assume a spherical shape owing to the temperature differential across its thickness and will expand uniformly in all directions owing to the mean increase in temperature over the thickness. So, if it is freely supported along a circular ring, it will deform at zero net axial force and moment. For any other type of support, internal forces and moments will develop along its line of support, such that the curvilinear vertical projection of the line of support on the spherical surface is made to coincide with the line of support itself. This is easier in a two-way square slab because the square line of support differs the least from its vertical projection on the spherical surface. By contrast, the more the ratio of the two sides in plan differs from 1.0, the more distant the rectangular line of support from its curvilinear vertical projection on the spherical surface is and the larger the internal and boundary forces needed to make these lines coincide are. If the two-way slab is thought of as a system of one-way strips along the short and the long dimension in plan, indexed here by x and y, respectively, the deviation is largest along the longer sides, i.e., the ones indexed by y. So, the boundary forces necessary to achieve compatibility of deflections may be thought of as the outcome of a load q acting downwards on the shorter strips, i.e., those indexed by x, and upwards on the longer ones. This is equivalent to an increase, Δq, of the portion, q_x, of the vertical distributed load, q, borne by the x-strips and an equal and opposite reduction, $-\Delta q$, of the portion, q_y, that goes to the y-direction strip. The shorter the x-direction side of the slab compared to the y-direction one, the larger Δq is. As a matter of fact, Δq is often larger than q_y. Then, the y-direction is uplifted by the load $q_y - \Delta q < 0$, whereas the x-direction is pushed very much down by the load $q_x + \Delta q$ and may yield or even fail in flexure by sagging moments – especially so, as the yield stress of the bottom bars at mid-span is seriously reduced by the elevated temperature of these bars. So, slabs with an aspect ratio in plan much larger than 1.0 are quite vulnerable under fire conditions.

The slabs surrounding the one exposed to fire restrain its lateral expansion by developing compressive in-plane forces and applying them on the latter slab. This confinement action is enhanced by the lateral stiffness of the vertical elements connecting the floor on fire to the ones above and below. The larger the stiffness of these elements, the higher the constraint is. This mechanism has a positive effect on the flexural capacity of the slab, as in-plane compression normally increases its moment resistance. A collateral negative effect is the second-order moments produced in the slab, which are equal to the in-plane axial compression times the large deflections of the span exposed to fire. They reduce hogging moments, but increase the predominant sagging ones. These effects take place in both horizontal directions in plan and can be expressed analytically in a way allowing their analytical prediction, be it iteratively, as the in-plane rigidity of both the slab that is exposed to fire and the ones surrounding and confining it is a function of their axial compression.

Alongside the state of in-plane forces in the slab exposed to fire and the ones around it, an analytical estimation of the transverse load Δq transferred from direction y to direction x is feasible. It is based on the compatibility of out-of-plane deflections in directions x and y at the center of every single slab in the floor – the

one exposed to fire and all others. It is iterative, owing to the strongly nonlinear and coupled moment-curvature and axial force-mean strain relationship of the slab sections, especially in the span which is exposed to fire, as well as to the second-order moments produced by the slab deflections and the in-plane forces according to the above paragraph.

The above were applied to a floor system with the design parameters of the building in Fig. 2.7, consisting of four, 6.25 m spans in direction x (as in the short direction in plan of the building in Fig. 2.7) and four, 7.5 m ones in direction y (i.e., as though the building in Fig. 2.7 had beams in the short direction in plan along all column lines and the longer side in plan were 4 × 7.5 = 30 m long instead of 6 × 7.5 = 45 m). The design of the slab for the ultimate limit state under factored gravity loads per CEN (2004a) gave bottom reinforcement of corner, exterior and interior panels equal to 293, 215, 181 and 156 mm^2/m, respectively, in the short direction in plan, or 204, 183, 117 and 124 mm^2/min in the long direction. Continuous, two-way reinforcement providing 377 mm^2/m was placed at the bottom – a significant surplus over the required areas. The required top reinforcement in corner, exterior and interior panels is 455, 365, 355 and 316 mm^2/m, respectively, in the short direction in plan, or 370, 372, 229 and 251 mm^2/m in the long direction. Continuous, two-way reinforcement of 251 mm^2/m was placed all over the top surface, increased to 503 mm^2/m over all supports in the short direction of the slabs or to 402 mm^2/m in the long direction – again well in excess of the required amounts. This is considered as the base case. Another one, called enhanced reinforcement, has continuous, two-way reinforcement of 503 mm^2/m all over the bottom surface.

A 6.25 m-by-7.5 m interior slab with the base case reinforcement fails after 15 and before 30 min of exposure to the standard fire per (CEN 2002b) if the 4 × 4 slab system is supported on a 5 × 5 system of 0.8 × 0.8 m columns of a usual story height (Fig. 2.22). A perimeter slab of the same system fails even before 15 min of exposure. The interior slab can survive exposure to standard fire for almost 45 min if the column size increases to 1.3 × 1.3 m (Fig. 2.23). However, neither the interior nor a perimeter slab survive for 30 min when just the enhanced reinforcement is placed all over the bottom surface (Figs. 2.24 and 2.25) without increasing the size of the columns, but an exterior one does, if the columns increase in size (Fig. 2.27). As evidenced by a comparison of Figs. 2.23 and 2.26, which refer to interior slabs with different reinforcement but the same supporting frame, a mere increase in bottom reinforcement is not effective in extending the safe life of the slab during a fire. The yield stress of the bottom bars is so much reduced by their exposure to the high temperatures of the slab underside that the quasi-permanent load on the slab cannot be accommodated by a mere redistribution of moments from the span to the supports. Much more effective in increasing the sagging moment resistance of the slab is the in-plane compression which gradually builds up thanks to the restraint of the lateral thermal expansion of the slab by the surrounding cool slabs and the lateral stiffness of columns. However, this in-plane compression is a mixed blessing. It is the second-order moments it produces acting on the large thermal deflection of the slab that ultimately bring down the exposed-to-fire slab.

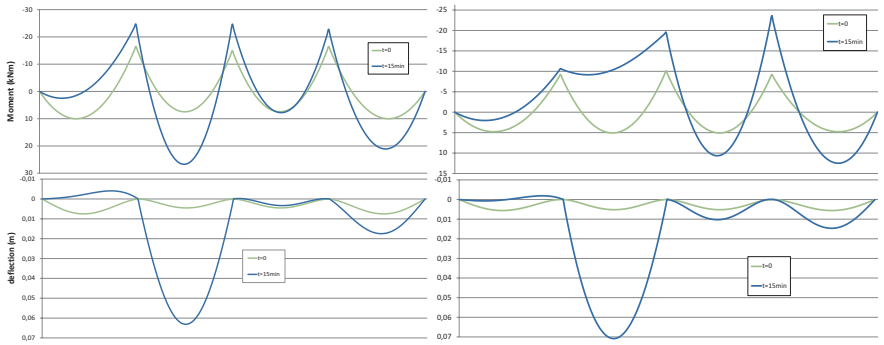

Fig. 2.22 Moment (*top*) and deflection (*bottom*) diagrams along mid-width of a single interior slab panel exposed to 15 min of standard fire; 1 m-wide strip of the slab: (*left*) parallel to the short side of the slab panel; (*right*) parallel to the long side; 4 × 4 slab system with base case reinforcement over 0.8 × 0.8 m columns

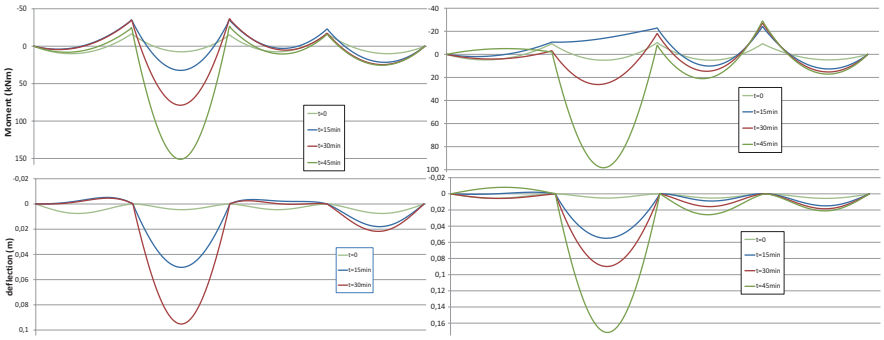

Fig. 2.23 Moment (*top*) and deflection (*bottom*) diagrams along mid-width of a single interior slab panel exposed to standard fire for 30 to 45 min; 1 m-wide strip of the slab: (*left*) parallel to the short side of the slab panel (deflections at 45 min are not shown, as they are well outside the vertical scale); (*right*) parallel to the long side; 4 × 4 slab system with base case reinforcement over 1.3 × 1.3 m columns

To investigate the effect of the slab's aspect ratio on its response to fire, the long side was increased from 7.5 to 11.25 m (i.e., as if there were four equal spans in the long direction of the building shown in Fig. 2.7). The slab aspect ratio then increased from 7.5/6.25 = 1.2 to 11.25/6.25 = 1.8. The bottom reinforcement required in corner, exterior or interior panels changed to 410, 374, 200 and 198 mm^2/m, respectively, in the short direction in plan and to 115, 141, 59 and 77 mm^2/m in the long direction. Two-way, continuous reinforcement of 503 mm^2/m was placed at the bottom, i.e., as in the enhanced case of the slabs with aspect ratio of 1.2, well above the required amount. The top reinforcement required at the corner, exterior and interior slab panels is 593, 550, 510 and 500 mm^2/m, respectively, in the short direction in plan, or 241, 285, 127 and 154 mm^2/m in the long direction. The two-way reinforce-

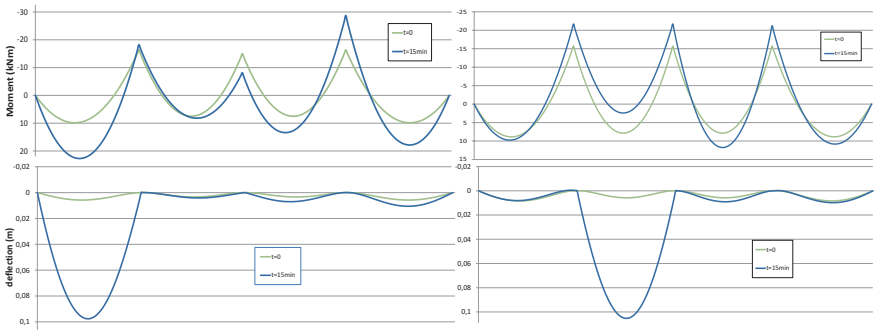

Fig. 2.24 Moment (*top*) and deflection (*bottom*) diagrams along mid-width of a single exterior slab panel exposed to standard fire for 15 min; 1 m-wide strip of the slab: (*left*) parallel to the short side of the slab panel; (*right*) parallel to the long side; 4 × 4 slab system with enhanced reinforcement over 0.8 × 0.8 m columns

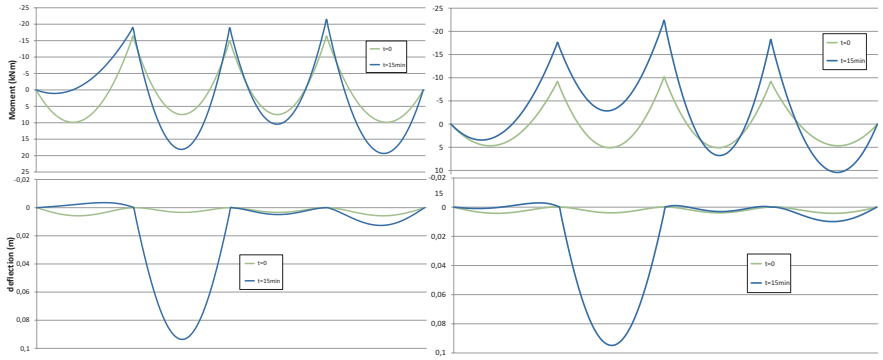

Fig. 2.25 Moment (*top*) and deflection (*bottom*) diagrams along mid-width of interior slab panel exposed to standard fire for 15 min; 1 m-wide strip of the slab: (*left*) parallel to the short side of the slab panel; (*right*) parallel to the long side; 4 × 4 slab system with enhanced reinforcement over 0.8 × 0.8 m columns

ment of 251 mm^2/m was maintained all over the top surface, but increased to 628 mm^2/m over all the supports in the short direction of the slabs. With the new layout and reinforcement, the interior and perimeter slab panels of a floor on 0.8 × 0.8 m columns could not survive the standard fire not even for 15 min. If the column size increases to 1.3 × 1.3 m, these slab panels survive for over 15 min but fail before reaching 30 min of exposure to the standard fire (Figs. 2.28 and 2.29).

Witness, in Fig. 2.28, the inverted (concave downwards) shape of the bending moment diagram in the secondary direction, i.e., for strips of the slab parallel to the long sides in plan, 15 min after the onset of fire exposure; it shows that these strips are borne by those parallel to the short sides, instead of contributing themselves to the capacity of the two-way slab to bear the gravity loads. The moment diagrams in Figs. 2.22, 2.23 and 2.29 show a similar tendency of the secondary direction to

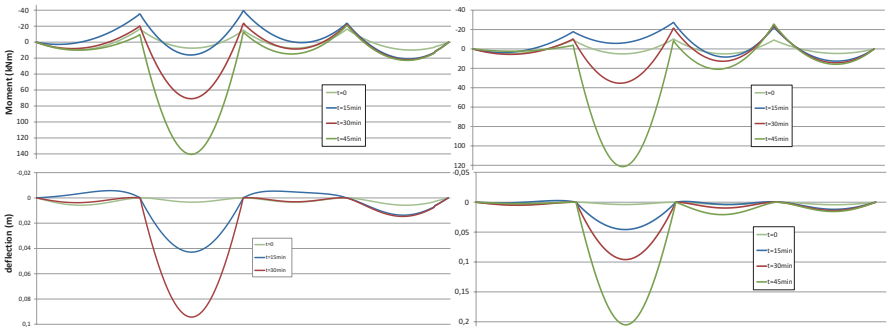

Fig. 2.26 Moment (*top*) and deflection (*bottom*) diagrams along mid-width of a single interior slab panel exposed to standard fire for 30 to 45 min; 1 m-wide strip of the slab: (*left*) parallel to the short side of the slab panel (deflections at 45 min are not shown, as they are well outside the vertical scale); (*right*) parallel to the long side; 4 × 4 slab system with enhanced reinforcement over 1.3 × 1.3 m columns

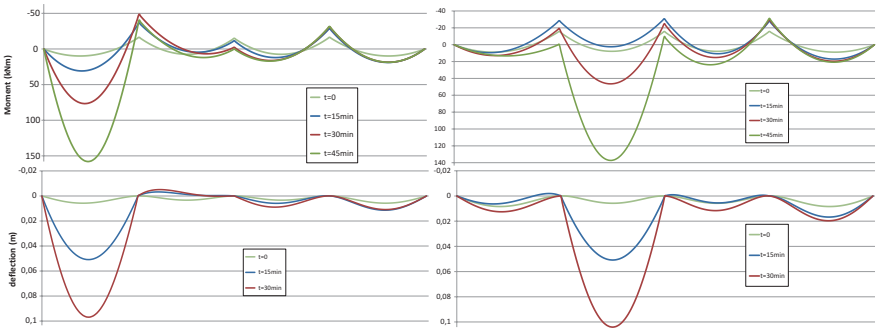

Fig. 2.27 Moment (*top*) and deflection (*bottom*) diagrams along mid-width of a single exterior slab panel exposed to standard fire for 30 to 45 min; 1 m-wide strip of the slab: (*left*) parallel to the short side of the slab panel (deflections at 45 min are not shown, as they are well outside the vertical scale); (*right*) parallel to the long side; 4 × 4 slab system with enhanced reinforcement over 1.3 × 1.3 m columns

offload its share of the gravity load on the primary direction of the slab (i.e., from the strips parallel to the long sides to those parallel to the short sides in plan) at 15 min of fire exposure. The redistribution of gravity loads from the secondary to the primary direction of the two-way slabs reduces the deflection of the former due to gravity loads and increases that of the latter in order to offset the larger thermal deflection of the strips parallel to the long side ones (recall that the curvature of the slab due to the fire is the same in both horizontal directions and tends to produce much larger deflection along the long sides of the slab in plan than along the short ones).

There is a very large discrepancy in the mid-span deflections between the two directions of the slab that is exposed to fire in Figs. 2.23, 2.26, 2.28 and 2.29 at the

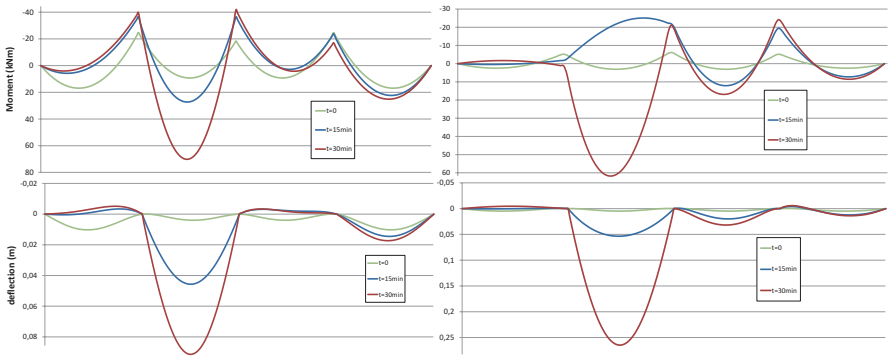

Fig. 2.28 Moment (*top*) and deflection (*bottom*) diagrams along mid-width of a single interior slab panel with dimensions 6.25 m-by-11.25 m exposed to standard fire for 30 min; 1 m-wide strip of the slab: (*left*) parallel to short side of slab panel; (*right*) parallel to long side; 4 × 4 slab system over 1.3 × 1.3 m columns

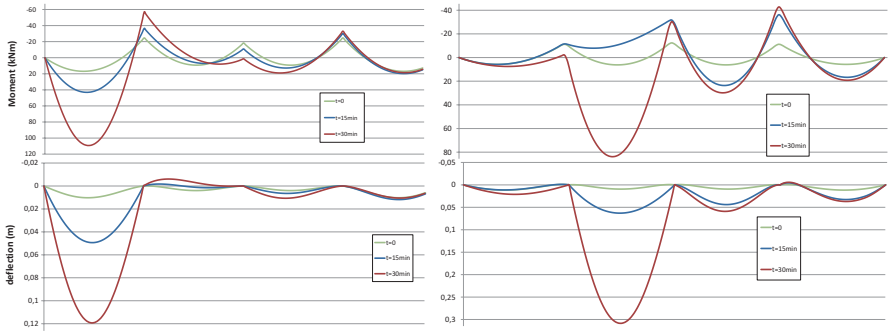

Fig. 2.29 Moment (*top*) and deflection (*bottom*) diagrams along mid-width of a single exterior slab panel with dimensions 6.25 m-by-11.25 m exposed to standard fire for 30 min; 1 m-wide strip of the slab: (*left*) parallel to short side of slab panel; (*right*) parallel to long side; 4 × 4 slab system over 1.3 × 1.3 m columns

last instant for which deflections are plotted in those figures. The reason is that at that instant the slab has already failed in sagging bending in one of the two directions. A smaller discrepancy between the two directions appears at the last time-instant in Figs. 2.22, 2.24 and 2.26. It is indicative of impending failure.

The conclusion of the slab analyses for fire is that the slab cannot resist for long the combined effects of fire and gravity loads by virtue of its reinforcement alone; the bottom bars lose most of their strength soon after the onset of fire exposure. Increasing the concrete cover or the cross-sectional area of bottom reinforcement is not cost-effective against failure due to fire. By contrast, increasing the lateral stiffness (and hence the size) of vertical members, in combination with a (nearly) square layout of the slabs in plan, is more effective.

2.8 Factors in Design of Concrete Structures for Multiple Extreme Hazards

To achieve a single-concept, holistic design, not a juxtaposition of multiple ones for different hazards, we should know which structural features enhance resilience to all hazards and which ones help for some but not for others. There is no single recipe for all structures, but principles can be established and nearly optimal solutions can be sought, profiting from synergies and conciliating conflicting demands across hazards.

Some structural features enhance resistance and resilience to one hazard but are detrimental when another type of threat is considered:

1. Static indeterminacy, continuity of load paths and connections, strength and deformation capacity of connections or members: They are good for robustness and resistance to any hazard, averting partial or local collapse. However, in case local or partial collapse does occur, a structure which is horizontally broken up from the outset into structurally independent units or compartments will be spared progressive, total collapse.
2. Mass: Large mass is favorable in case of blast, impact or fire, but is adverse for seismic performance.
3. Building frames with beams which are weaker than the columns, hence normally shallow: They are good for global ductility and the prevention of a soft-story mechanism in case of earthquake. However, to sustain loss of a supporting column, a beam must be strong; to utilize arch action in such conditions, it must be deep.
4. Concrete structures with dry joints (i.e., non-monolithic connections kept together by means of unbonded pre-stressing tendons), lending themselves to dismantlement and reuse: They can rock in a stable way and are seismically resilient. However, they may be more vulnerable to fire and possibly to blast or impact, too.
5. Seismic isolation: It is the ultimate means to achieve resilience to the horizontal component of the earthquake, as it minimizes residual global displacements and structural damage. However, it allows superstructures with members of smaller size and less reinforcement – and indeed without detailing for ductility (notably bottom bars in beams which run through beam-column joints discontinuously, widely spaced ties throughout a column's height, floor slabs which are not required to act as horizontally rigid diaphragms and hence do not have two-way reinforcement at both top and bottom). Such superstructures are vulnerable to blast or impact and fire.

By contrast, some structural features enable resistance to many (or even to all) hazards:

1. Large lateral stiffness: It is effective in case of earthquake as it reduces seismic deformation demands. It may also be effective in blast or impact conditions for

the same reason, and because it is normally associated with increased force resistance. It is also good under fire conditions because it restrains thermal expansion of the part of floor slabs which is exposed to fire, inducing significant in-plane compression and increasing, therefore, the slab's flexural capacity. In this way it helps the slab to keep sustaining the gravity loads, despite the detrimental effect of fire temperatures on the strength of slab materials (notably on the strength of bottom bars).

2. Large-size columns: They increase the lateral stiffness with all the positive consequences listed above. Moreover, they are less vulnerable to hazards producing large local demands on structural members, such as blast or impact. They can also sustain most of their axial force capacity under prolonged fire, thanks to the still-cool inner core, despite the loss of a sizeable concrete skin and the severe strength reduction in the vertical bars and the confining perimeter tie.
3. Closely-spaced stirrups all along a column's height and not just in the plastic hinge zones at column ends: They increase the shear resistance all along the column and prevent failure under loadings which produce large, local shear demands, such as blast or impact. They also prevent shear failure under seismic loadings in columns which are captive owing to contact with infill walls over part of their height.
4. Beam bottom bars which do not stop before the supports but run continuously through them over several spans: They increase markedly the ability of the beam to bridge over columns which are completely shattered by explosion or impact. They also increase the moment resistance of the beam at the supports in sagging bending during an earthquake, as well as the deformation capacity and the ductility of the beam in hogging bending at the supports.
5. Two-way frame action: It enhances bi-directional lateral force resistance against horizontal earthquake components from any direction. It also helps the 3D frame survive loss of one or more columns to blast or impact by mobilizing the beams in both horizontal directions (e.g., if a perimeter two-way column is lost, the beam along the perimeter works with one intermediate support less and one intermediate span about twice as long as before, while the beam at right angles to the perimeter works as the cantilevering outer span of a continuous beam in the orthogonal direction).
6. Two-way floor slabs, almost square in plan: They go together with two-way frame action and all the positive side effects listed under 5 above. They have about the same reinforcement in both horizontal directions, which is optimum for diaphragm action in earthquakes. They also experience less redistribution of vertical load between the two horizontal directions because the deflections of a slab exposed to fire that is nearly square in plan are close to the stress-free deflections of a circular slab, which is free to deform into the spherical shape induced by the fire. By contrast, this spherical shape is quite incompatible with the support conditions of a long, one-way slab, which then experiences a severe force and moment redistribution for which its reinforcement is not designed.

7. Two-way reinforcement throughout a slab's top surface: No matter whether it is one- or two-way, a floor slab normally does not require top reinforcement away from its supports. Such reinforcement is essential, though, for the tensile membrane action and the redistribution of moments which accompany the loss of a perimeter or interior beam under the slab. Moreover, although a floor slab can be very effective as a diaphragm in an earthquake even with two-way reinforcement only at the bottom surface, it is better to have such reinforcement shared by both surfaces of the slab. Finally, as the bottom reinforcement of a slab exposed to fire is eventually doomed, it is good to have some reinforcement at the unexposed top surface, which is mobilized in catenary action against gravity loads when the sagging moment capacity of the slab is lost alongside the bottom reinforcement.
8. Bottom bars in slabs which do not stop at the supporting beams but run seamlessly through them over several spans: They increase markedly the ability of the slab to bridge over interior beams that sink owing to loss of a supporting interior column due to blast or impact. They also allow effective tensile membrane action to develop in a slab which loses a supporting perimeter or interior beam. They also escape loss of anchorage over an intermediate zone of the slab soffit which is exposed to fire and may also experience spalling of the cover.
9. Masonry infills of building frames: If they have a plan- and height-wise uniform layout, non-load-bearing masonry infills (with or without openings) have a very beneficial effect on the seismic performance of the building by increasing its lateral stiffness (and hence reducing the deformation demands on the structural frame) and enhancing its global lateral force resistance and energy dissipation (Panagiotakos and Fardis 1996; Fardis and Panagiotakos 1997; Fardis et al. 1999). Moreover, masonry infills in full contact with the surrounding frame members connect adjacent floors in shear and allow the stories above a failed column to bridge the gap by acting as a deep multi-layer sandwich beam. The floors (top, bottom and intermediate ones) work as membrane elements contributing to flexural resistance; the infills in-between serve as the shear core. This mechanism has saved numerous multistory concrete buildings after complete loss of a corner column or of several internal or perimeter ones in earthquakes (see Figs. 2.17a, b). It can do the same in case of loss of one or more columns due to blast or impact, preventing progressive collapse (Fig. 2.17c).

These considerations are summarized in two tables: Table 2.1 for conceptual design and Table 2.2 for detailing.

Table 2.1 Conceptual design of concrete buildings for robustness to multiple hazards

Feature in conceptual design (ranked from the most favorable for robustness to the most unfavorable)	Earthquake	Progressive collapse due to blast or impact	Fire
Large columns	Very favorable	Very favorable	Very favorable
High lateral stiffness, especially on the perimeter	Favorable	Very favorable	Favorable
Thick, monolithic slabs throughout floor plan	(Favorable)	Very favorable	Very favorable
Masonry infills	Very favorable	Very favorable	Neutral
Uniform column sizes	Favorable	Favorable	Favorable
Square columns	(Favorable)	(Favorable)	Very favorable
Two-way frame action of every column	(Favorable)	Favorable	(Favorable)
Two-way floor slabs, square in plan	Favorable	Neutral	Very favorable
Continuity of load paths, static indeterminacy	Very favorable	Neutral	Favorable
Large mass	Very unfavorable	Favorable	Favorable
Large beams	Very unfavorable	Very favorable	Favorable
Seismic isolation	Very favorable	Unfavorable	Neutral
Precast post-tensioned members with dry joints	Favorable	Neutral	Unfavorable

Table 2.2 Detailing of concrete buildings for robustness to multiple hazards

Detailing	Earthquake	Progressive collapse due to blast or impact	Fire
Closely-spaced ties over full column height	Very favorable	Very favorable	Favorable
Beam bars continuous across interior joints	Very favorable	Very favorable	Favorable
Slab bars continuous across interior supports	Favorable	Very favorable	Favorable
Two-way slab reinforcement	Favorable	Favorable	Very favorable
Top reinforcement over entire slab surface	Favorable	Very favorable	Favorable
Concrete cover of reinforcement	Neutral	Neutral	(Favorable)

Acknowledgment The research leading to these results received funding from the General Secretariat for Research and Technology, grant ERC-12 of the Operational Program "Education and lifelong learning", co-funded by the European Union (European Social Fund) and national resources.

References

Bailey CG (2002) Holistic behavior of concrete buildings in fire. ICE Struct Build 152(3):199–212
Bailey CG (2009) Science and technology developments in structural fire engineering. Struct Eng Inter 19(2):155–164
Bailey CG, Moore DB (2000) The structural behavior of steel frames with composite floor slabs subject to fire. Struct Eng 78(11) Part 1: Theory: 19–27; Part 2: Design: 28–33
Bailey CG, Lennon T, Moore DB (1999) The behavior of full-scale steel framed buildings subjected to compartment fires. Struct Eng 77(8):15–21
Beitel J, Iwankiw N (2002) Analysis of needs and existing capabilities for full-scale fire resistance testing. NIST GCR 02-843, Building & Fire Research Laboratory, National Institute of Standards and Technology, Gaithersburg, p 86
Biskinis D, Fardis MN (2010a) Deformations at flexural yielding of members with continuous or lap-spliced bars. Struct Concr 11(3):127–138
Biskinis D, Fardis MN (2010b) Flexure-controlled ultimate deformations of members with continuous or lap-spliced bars. Struct Concrete 11(2):93–108
Brunesi E, Nascimbene R, Parisi F, Augenti N (2015) Progressive collapse fragility of reinforced concrete framed structures through incremental dynamic analysis. Eng Struct 104:65–79
CEN (2002a) European standard EN 1990:2002 Eurocode: basis of structural design. Comite Europeen de Normalisation, Brussels
CEN (2002b) European standard EN 1991-1-2:2002 Eurocode 1: actions on structures – Part 1–2: General actions –actions on structures exposed to fire. Comite Europeen de Normalisation, Brusells
CEN (2004a) European standard EN 1992-1-1:2004 Eurocode 2: design of concrete structures – Part 1–1: General rules and rules for buildings. Comite Europeen de Normalisation, Brussels
CEN (2004b) European standard EN 1992-1-2:2004 Eurocode 2: design of concrete structures – Part 1–2: General rules – stuctural fire design. Comite Europeen de Normalisation, Brussels
CEN (2005) European standard EN 1998-3:2005 Eurocode 8: design of structures for earthquake resistance – Part 3: Assessment and retrofitting of buildings. Comite Europeen de Normalisation, Brusells
CEN (2006) European standard EN 1991-1-7:2006 Eurocode 1: actions on structures – Part 1–7: General actions – accidental actions. Comite Europeen de Normalisation, Brussels
Crémer C, Pecker A, Davenne L (2002) Modelling of nonlinear dynamic behavior of a shallow strip foundation with macro-element. J Earthq Eng 6(2):175–212
Dimova S, Pinto A, Oztas A, Geradin M, Altinyollar A (2007) Identification of needs for improved fire protection by use of the Eurocodes EUR 22859 European Commission. Joint Research Centre, Ispra
Ditlevesen O (1980) Formal failure probability and observed failure rate. In: Proceeding 11th IABSE congress, Vienna
Ditlevesen O (1983) Fundamental postulate in structural safety. ASCE J Eng Mechs 109(4):1096–1102
Dusenberry DO (ed.) (2010) Handbook for blast-resistant design of buildings. Wiley, p 484
Ellingwood BR, Smilowitz R, Dusenberry DO, Duthinh D, Lew HS, Carino NJ (2007) Best practices for reducing the potential for progressive collapse in buildings. NlSTlR 7133, National Institute of Standards and Technology, Gaithersburg, MD

Englekirk RE (2002) Design-construction of the Paramount – a 39-story precast pre-stressed concrete apartment building. PCI J 47(4):56–71
European Commission, Joint Research Centre (Ispra) (2007) Seminar and working meeting on Eurocodes – approach and recent advances in fire design: minutes and presentations
Fardis MN, Panagiotakos TB (1997) Seismic design and response of bare and infilled reinforced concrete buildings Part II: Infilled structures. J Earthq Eng 1(3):473–503
Fardis MN, Bousias SN, Franchioni G, Panagiotakos TB (1999) Seismic response and design of RC structures with plan-eccentric masonry infills. Earthq Eng Struct Dyn 28:173–191
Fascetti A, Kunnath S, Nisticò N (2015) Robustness evaluation of RC frame buildings to progressive collapse. Eng Struct 86:242–249
fib (2007) Fire design of concrete structures – materials, structures and modelling. Bulletin 38. Federation Internationale du Beton, Lausanne
fib (2008) Fire design of concrete structures – structural behavior and assessment. Bulletin 46. Federation Internationale du Beton, Lausanne
fib (2012) Model Code 2010 – final draft. Bulletins 65 & 66. Federation Internationale du Beton, Lausanne
Fujikura S, Bruneau M (2011) Experimental investigation of seismically resistant bridge piers under blast loading. ASCE J Bridge Eng 16(1):63–71
Fujikura S, Bruneau M, Lopez-Garcia D (2008) Experimental investigation of multihazard resistant bridge piers having concrete-filled steel tube under blast loading. ASCE J Bridge Eng 13(6):586–594
Gambarova PG, Felicetti R, Meda A, Riva P (2005) Proceedings workshop "fire design of concrete structures. What now? What next?" Politecnico di Milano. Starrylink Editrice. Brescia:340p
Ghoreishi M et al (2009) Estimating the response of structural systems to fire exposure: state-of-the-art review. In: 11th Internatinal conference fire & materials San Francisco: 475–483
GSA (2013) Alternate path analysis and design guidelines for progressive collapse resistance. General Services Administration
Hayes J, Stanley C, Woodson SC, Pekelnicky RG, Poland CD, Corley WG, Sozen MA (2005) Can strengthening for earthquake improve blast and progressive collapse resistance? ASCE J Struct Eng 131(8):1157–1177
Høj N (2005) Keep concrete attractive – fire design of concrete structures. In: Proceeding of fib symposium Budapest: 1097–1105
Ishizuka T, Hawkins NM, Stanton JF (1984) Experimental study of the seismic resistance of a concrete exterior column beam sub-assemblage containing un-bonded post-tensioning tendons. Civil Engineering Department, University of Washington, Seattle, WA
JCSS (2001) Probabilistic model code Joint Committee on structural safety, Technical University of Denmark
Kodur V (2003) Fire resistance research needs for high performing materials. NRCC-45405. Institute for research in construction. National Research Council of Canada
Kodur V, Raut NK (2008) Fire resistance of reinforced concrete columns – state-of-the-art and research needs *ACI SP-255*. American Concrete Institute, Farmington Hills, pp 95–121
Kodur V, Garlock M, Iwankiw N (2011) Structures in fire: state-of-the-art, research and training needs fire technology. doi:10.1007/s10694-011-0247-4
Kruppa J et al (2001) Rational fire safety engineering approach to fire resistance in buildings. CIB Report, Publishing 269
Kwasniewski L (2010) Nonlinear dynamic simulations of progressive collapse for a multistory building. Eng Struct 32:1223–1235
Lennon T (2003) Whole building behavior – results from a series of large scale tests. In: Proceedings of CIB-CTBUH International conference on Tall Buildings, Kuala Lumpur
Lennon T, Moore DB, Wang YC, Bailey CG (2007) Designers' guide to EN1991-1-2, EN1992-1-2, EN1993-1-2 and EN1994-1-2. T.Telford Publishers, London
Lew HS, Bao Y, Sadek F, Main JA, Pujol S, Sozen MA (2011) An experimental and computational study of reinforced concrete assemblies under a column removal scenario, Techn. Note 1720, National Institute of Standards and Technology, Gaithersburg

Matthews SL, Ganisious TDG, Rupasingle R, Waleed N, Lennon T (2005) Full-scale structural and fire performance tests upon the Cardington European concrete building. In: Proceedings of fib symposium, Budapest: 1106–1111

Mays GC, Smith PD (eds.) (1995) Blast effects on buildings. T.Telford Publications, London, 121p

Mostafaei H, Sultan M, Bénichou N (2009) Recent developments on structural fire performance engineering: a state-of-the-art report. IRC-275, Institute for Research in Construction, National Research Council of Canada, 34p

Multihazard Mitigation Council (2003) Prevention of progressive collapse: report on the July 2002 national workshop and recommendations for future efforts. National Institute of Building Sciences, Washington, DC

Nakaki SD, Stanton JF, Sritharan S (1999) An overview of the PRESSS 5-story precast test building. PCI J 44(2):28–39

National Institute of Standards & Technology (2003) Workshop for development of a national R&D roadmap for structural fire safety design and retrofit of structures: NlSTlR 7133, Gaithersburg, 183p

Ngo T, Mendis P, Gupta A, Ramsay J (2007) Blast loading and blast effects on structures – an overview. *eJ Struct Eng* Special Issue: Loading on structures: 76–91

Pampanin S, Kam WY, Haverland G, Gardiner S (2011) Seismic performance of a post-tensioned precast concrete building (PRESSS technology) during the 22nd Feb 2011 Christchurch earthquake. In: Proceedings of New Zealand Concrete Industry conference, Rotorua, NZ

Panagiotakos TB, Fardis MN (1996) Seismic response of infilled RC frame structures. In: 11th world conference on Earthquake Engineering, Acapulco, paper P–4 (225)

Priestley MJN, Sritharan S, Conley J, Pampanin S (1999) Preliminary results from the PRESSS five story test building. PCI J 46(6):42–67

Razaqpur G, Tolba A, Contestabile E (2007) Blast loading response of reinforced concrete panels reinforced with externally bonded GFRP laminates. Compos Part B 38(5–6):535–546

Sasani M, Bazan M, Sagiroglu S (2006) Experimental and analytical progressive collapse evaluation of an actual reinforced concrete structure. ACI Struct J 104(6):731–739

Sasani M, Sagiroglu S (2008) Progressive collapse of reinforced concrete structures: a multihazard perspective. ACI Struct J 105(1):98–103

Smith PD, Hetherington JG (1994) Blast and ballistic loading of structures. Butterworth Heinemann, Oxford, p 320

Stanton J, Pizano Thomen V, Pizano Battle V (2003) Design of the Cala building using PRESSS technology. In: Proceedings of fib symposium: concrete structures in seismic regions, Athens

Stathas N, Bousias SN, Palios X, Strepelias E, Fardis MN (2017a) Tests and simple model of RC frame subassemblies for postulated loss of column. *J Struct Eng*, ASCE. doi:10.1061/(ASCE)ST.1943-541X.0001951

Stathas N, Bousias SN, Palios X, Strepelias E, Fardis MN (2017b) Continuous one-way RC slabs with sinking outer support: tests and simple model *J Struct Eng, ASCE*. doi:10.1061/(ASCE)ST.1943-541X.0001887

Stathas N, Palios X, Strepelias E, Fardis MN, Bousias SN, Sarkis A (2017c) Dry-jointed precast concrete frame on rocking or fixed footings under cyclic lateral loading. Bull Earthq Eng 15. doi:10.1007/s10518-017-0151-5

Su Y, Tian Y, Song X (2009) Progressive collapse resistance of axially-restrained frame beams. ACI Struct J 106(5):600–609

Taerwe L et al (2005) Real scale fire test on an industrial hall: temperature evolution and assessment after fire. In: Proceedings of fib symposium, Budapest: 1112–1117

Taleb NN (2008) The black swan: the impact of the highly improbable. Penguin Books Ltd, London, 444p

US Department of Defense (2009) Unified facilities criteria: design of buildings to resist progressive collapse (ufc 4–023-03). Washington, DC, p 176

US Department of Homeland Security (2011) Preventing structures from collapsing. Report BIPS 05, buildings & infrastructure protection series. Science & Technology Directorate, Washington, DC, 180p

Usmani AS (2000) Application of fundamental structural mechanics principles in assessing the Cardington fire tests. In: Proceedings of first international workshop on structures in fire, Copenhagen

Usmani AS, Rotter JM, Lamont S, Sanad AM, Gillie M (2001) Fundamental principles of structural behavior under thermal effects. Fire Safe J 36:721–744

Yi W-J, He Q-F, Xiao Y, Kunnath SK (2008) Experimental study on progressive collapse-resistant behavior of reinforced concrete frame structures. ACI Struct J 105(4):433–439

Chapter 3
A Simplified Approach for Site-Specific Design Spectrum

A. Ansal, G. Tönük, and A. Kurtuluş

Abstract The design acceleration spectrum requires site investigations and site-response analyses in accordance with the local seismic hazard. The variability in earthquake source and path effects may be considered using a large number of acceleration records compatible with the earthquake hazard. An important step is the selection and scaling of input acceleration records. Likewise, a large number of soil profiles need to be considered to account for the variability of site conditions. One option is to use Monte Carlo simulations with respect to layer thickness and shear wave velocity profiles to account for the variability of the site factors. The local seismic hazard analysis yields a uniform hazard acceleration spectrum on the bedrock outcrop. Site-specific response analyses also need to produce a uniform hazard acceleration spectrum on the ground surface. A simplified approach is proposed to define acceleration design spectrum on the ground surface that may be considered a uniform hazard spectrum.

Keywords Site response • Input motion scaling • Uniform hazard spectrum

A. Ansal (✉)
Özyegin University, Istanbul, Turkey
e-mail: atilla.ansal@ozyegin.edu.tr

G. Tönük
MEF University, Istanbul, Turkey
e-mail: gokce.tonuk@mef.edu.tr

A. Kurtuluş
Özyegin University, Istanbul, Turkey
e-mail: asli.kurtulus@ozyegin.edu.tr

R. Rupakhety, S. Ólafsson (eds.), *Earthquake Engineering and Structural Dynamics in Memory of Ragnar Sigbjörnsson*, Geotechnical, Geological and Earthquake Engineering 44, https://doi.org/10.1007/978-3-319-62099-2_3

3.1 Introduction

The design acceleration spectrum on the ground surface would require detailed site characterization and site response analyses utilizing all available information and data concerning geotechnical and geological site conditions with respect to the findings of local seismic hazard assessment. The earthquake excitations affecting structures may vary significantly due to the properties of soil and rock layers encountered in the soil profile. These differences may lead to variations in the amplitude, duration, and frequency content of the acceleration time histories. An important step in site specific response analysis is the selection and scaling of hazard compatible input acceleration records. Relatively large numbers of acceleration records compatible with the site-dependent earthquake hazard in terms of fault mechanism, magnitude and distance range recorded on stiff site conditions need to be used as input for site response analysis to account for the variability in earthquake source and path effects. Likewise, the observed variability of site conditions may be taken into account by conducting site response analyses for a large number of soil profiles to assess design acceleration spectra with respect to different performance levels. The goal of a site-specific hazard analysis is to develop a uniform hazard design acceleration spectrum on the ground surface.

The simpler option for defining, a site-specific design acceleration spectrum on the ground surface is to use contemporary ground motion prediction equations formulated in terms of site and source parameters (Abrahamson et al. 2014; Boore et al. 2014; Campbell and Bozorgnia 2014). However, all of these formulations ignore all site-specific information and yield only a generic assessment of the earthquake characteristics on the ground surface (Bazzurro and Cornell 2004a, b). The second option is to use empirical formulations, such as amplification factors suggested by Borcherdt (1994) based on equivalent average shear wave velocity, V_{s30}. It was observed, based on recorded ground motion data (Ansal et al. 2014, 2015) and based on parametric studies (Baturay and Stewart 2003; Haase et al. 2011), that use of average shear wave velocity (V_{s30}) would not yield realistic spectral accelerations on the ground surface, specifically in the case of relatively soft or loose medium deep and deep soil deposits. In addition, these procedures are deterministic procedures that would lead to surface ground motion levels with unknown exceedance rates that may be non-uniform, non-conservative, and inconsistent across frequency (Bazzurro and Cornell 2004a, b).

The use of ground motion prediction equations and amplification functions to estimate site specific ground motion has been studied by many researchers. One of the main issues investigated was the effect of neglecting soil nonlinearity. It was observed by Tsai (2000) that the hazard curve may be severely distorted if the soil condition of a nonlinear site is treated inadequately, and calculated results would likely overestimate the seismic hazard in high frequencies. The ground-motion relation obtained empirically by regression analysis and linear amplification factors applied to bedrock motions are not sufficient to model the characteristics of a nonlinear soil response. In addition, Stewart and Seyhan (2013) summarized that the

V_{s30} approach was based on the strong motion records obtained during the 1989 Loma Prieta earthquake was based on limited data concerning relatively weak motion amplification with nonlinear effects from numerical simulations (Dobry et al. 2000). Thus, it may not be reliable to use V_{S30} for calculating site amplification for all site and earthquake levels (Huang et al. 2010).

As summarized by Cramer (2003, 2006), the state of practice in calculating a site-specific ground motion has been to calculate probabilistic bedrock ground motion and then multiply it by a deterministic site-amplification factor. Due to uncertainty in estimating site amplification, the state of the practice is to use the median site- amplification factor, and the resulting ground motion is a hybrid answer that is no longer truly probabilistic. To overcome this problem, one must calculate the effects of uncertainty on the estimate of a site-amplification factor and use the resulting site-amplification distribution in a probabilistic methodology as suggested by McGuire et al. (2001) that site amplification distributions be used to modify bedrock ground-motion attenuation relations into site-specific relations prior to the calculation of seismic hazard.

In this respect, Lee and Anderson (2000) developed a methodology to calculate probabilistic bedrock ground motions and site amplifications separately and then probabilistically combine the results. While Toro and Silva (2001) have proposed an approach by constructing a site-specific ground-motion attenuation relation for each period of interest using a source-path-site random vibration theory (RVT) model that includes site amplification.

3.2 Selection and Scaling of Input Acceleration Records

There are uncertainties concerning the selection of input time histories as well as the representative soil profiles in conducting site-specific response analysis. The selection and scaling of input acceleration time histories is the major controlling factor in site response analysis (Ansal et al. 2015; Tönük and Ansal 2010; Tönük et al. 2013; Kottke and Rathje 2008; Haase et al. 2011). In this process, one of the primary concerns is to select acceleration time histories recorded under similar tectonic conditions within the range of the expected magnitude (M_w) that may take place within the range of the estimated fault distance. The approach adopted in the proposed scheme is to utilize the findings from the deaggregation analysis to select the probable fault type, magnitude, and distance ranges in the selection of acceleration time histories recorded on stiff soil conditions with an average shear wave velocity of $V_{s30} \geq 760$ m/s.

The adopted scaling procedure needs to have three goals: (a) to obtain the best fits by an optimization algorithm with respect to target uniform hazard acceleration spectrum determined based on local hazard assessment on the rock outcrop, (b) to control the fit of the scaled acceleration spectrum if it is matching the target acceleration spectrum within the considered period range, (c) to decrease the scatter in the acceleration spectra after scaling.

The uniform hazard acceleration spectrum on the rock outcrop is determined by a probabilistic assessment of all possible earthquake source zones in the investigated area. Thus, it is based on a series of acceleration time histories. From this perspective, it may be considered as incorrect to select and scale a single recorded acceleration time history to match the uniform hazard acceleration spectrum which happens to be the result of series of acceleration time histories. However, engineering structures are designed based on this uniform hazard acceleration spectrum to be on the safe side for all possible earthquake occurrences with the exception of the near fault effects. Similarly, when the site response is calculated based on a series of acceleration time histories obtained under local hazard compatible conditions, the purpose is to account for possible acceleration time histories that may be generated by all possible faults in the region.

Bazzurro and Cornell (2004a, b) observed, based on a statistical study, that the additional knowledge of magnitude and fault distance (M and R), which implicitly define the average response spectrum shape, do not appreciably improve the estimation of the site amplification function. However, the site amplification function can be considered, to a certain extent, as independent of input acceleration time histories. Therefore, the effect of M and R may be insignificant. If the intention is to determine the absolute values of the design acceleration spectrum on the ground surface rather than the amplification function, M and R values, as well as the fault type, have a significant effect on the calculated design acceleration spectrum on the ground surface (Durukal et al. 2006).

Bommer and Acevedo (2004) and Bommer et al. (2000) recommended using real acceleration records for engineering analyses. Kottke and Rathje (2008) and Rathje et al. (2010) developed a procedure for the selection and scaling of the suitable acceleration records. The authors also investigated the effects of selection and scaling of earthquake records for site response analyses (Ansal et al. 2015, 2012; Ansal and Tönük 2007; Tönük and Ansal 2010; Tönük et al. 2014) and observed that the scaling approach adopted may have a significant effect on the outcome of the site-response analysis.

The most widespread option is to scale selected input acceleration records with respect to peak ground accelerations (PGA) estimated by the probabilistic earthquake hazard analysis. The alternative proposed in this study, termed spectrum scaling, is based on scaling each selected acceleration record separately to obtain the best fit to the target uniform hazard acceleration spectrum by an optimization routine using peak acceleration as the scaling factor without modifying the frequency content. This approach allows the selection of records with smaller scaling factors as well as those with better fits that can be expressed numerically based on the sum of the squares of the differences between the spectral accelerations of the target uniform hazard spectrum and scaled acceleration spectrum. Thus, it would be possible to select a set of hazard-compatible input acceleration time histories that would fit a target uniform hazard spectrum on the rock outcrop with significantly limited scatter.

A parametric study is conducted for an actual case where the seismic hazard was observed to vary in the magnitude range of M_w = 6.5–7.5 and PGA range of 0.15–0.25 g. The general comparison of the two approaches for the selected 22 input

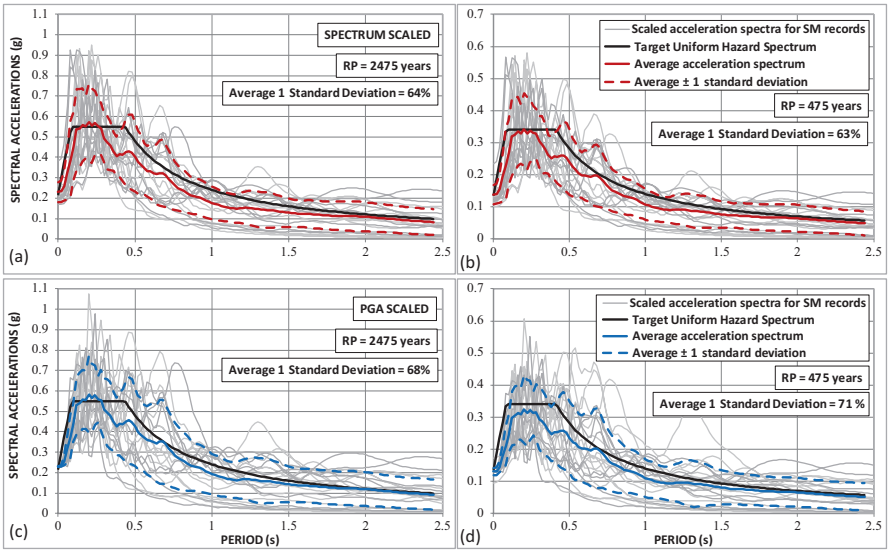

Fig. 3.1 Comparison of PGA and spectrum scaled input acceleration records

acceleration time histories (Peer 2014) is shown in Fig. 3.1. The difference between PGA and spectrum scaling is not very significant. However, the scatter of the acceleration spectra for input acceleration records is reduced in the case of spectrum scaling and it is important to decrease the scatter in the input level since it will directly affect the scatter on the ground surface during the site-response analysis.

The average 1 standard deviation over the period range of 0-4 s for a 475-year return period, in the case PGA, scaling is 71%, while in the case of spectrum scaling, is 63% of the median. For a 2475-year return period, in the case PGA scaling, the average is 68%, while in the case of spectrum scaling, the average is 64% of the median, showing the decrease in the scatter in the case of spectrum scaling.

3.3 Site Response Analysis for Site-Specific Design Spectrum

Considering the possible differences in soil profiles within relatively short distances and observations in previous earthquakes (Hartzell et al. 1997), an approach needs to be adopted based on a detailed site-response analysis for the assessment of site-specific design earthquake acceleration spectra. It was also observed by Baturay and Stewart (2003) that ground response analysis is needed for spectral acceleration predictions for soft sites. However, not much difference was observed for stiff soil sites.

Detailed site investigations were conducted for a specific construction site in Turkey with relatively thick, medium stiff soil layers based on seven, existing soil borings. The variations of shear wave velocities with depth were determined from

SPT blow counts using the empirical relationship proposed by Iyisan (1996) and from shear wave velocity measurements by the in-hole PS logging method.

The slightly modified version of the site response analysis code, Shake91 (Idriss and Sun 1992), accounting for the frequency effect as suggested by Sugito et al. (1994), was used to evaluate the effects of local soil stratification and to calculate acceleration response spectra on the ground surface (Ansal et al. 2009, 2015). A site-response analysis was conducted for the case composed of 7, existing shear wave velocity profiles using 22 input acceleration time histories (Peer 2014) yielding 154 site-response analyses for each return period of 475 and 2475 years to account for the variability in site conditions and input acceleration records.

One simplified approach to develop a uniform hazard spectrum on the ground surface is to perform a probabilistic assessment of the results from a site-response analysis conducted for available soil profiles using the selected set of input motions. The frequency distribution for the calculated PGA on the ground surface is assumed to be a normal distribution with a specific median and standard deviation based on 154 calculated PGAs. At the second stage, PGAs corresponding to a 10% and 2% exceedance probability are determined corresponding to the same probability levels in the uniform hazard spectra. In the case of a 475-year return period, the difference between the PGA based on probabilistic interpretation (Fig. 3.2b) and by median+1 standard deviation (Fig. 3.2a) is nearly the same. However, in the case of a 2475-year return period, the difference between PGAs from probabilistic interpretation (Fig. 3.2d) and by median+1 standard deviation (Fig. 3.2c) is more significant. Therefore, in the case of a 475-year return period, it may be justified to adopt a

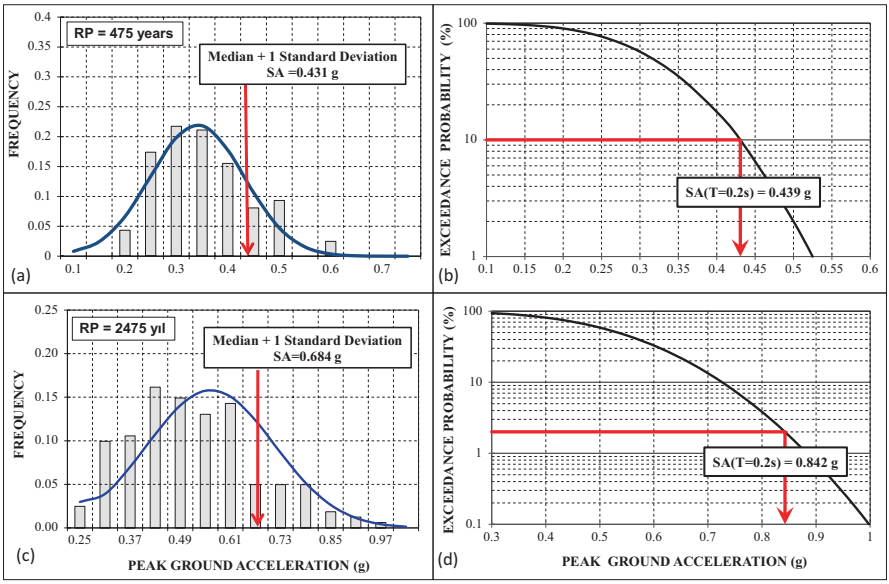

Fig. 3.2 Comparison of PGA calculated based on probabilistic evaluation with respect to exceedance levels of 10% and 2% and as the sum of median+1 standard deviation

median+1 standard deviation PGA, as the design PGA since the results are very similar to the probabilistic interpretation. However, in the case of a 2475-year return period, the difference between the PGA based on probabilistic interpretation and median+1 standard deviation is significantly different. Thus the design PGA may be adopted corresponding to 2% exceedance by probabilistic approach.

The acceleration spectra corresponding to 10% (RP = 475 years) and 2% (RP = 2475 years) are calculated by again assuming a normal distribution for each period level based on 154 calculated acceleration response spectra as shown in Fig. 3.3. The spectral accelerations calculated for a 10% exceedance probability based on a probabilistic approach (Fig. 3.3a) are similar or slightly above those calculated based on median+1 standard deviation. However, in the case of RP = 2475 years, the a probabilistic spectrum corresponding to the 2% exceedance (Fig. 3.3b) is higher, and thus more conservative compared to spectrum calculated based on median+1 standard deviation. In the case of 475-year return period, it may be justified to adopt the median+1 standard deviation spectrum as the design spectrum since the results are very similar to the probabilistic approach. However, in the case of 2475-year return period, the difference between the probabilistic interpretation and the median+1 standard deviation spectrum is significant.

In the case of RP = 475 years, the average of the difference ratio (the ratio of the difference between spectral accelerations calculated based on a 10% exceedance probability and by median+1 standard deviation to median acceleration) within the period range of 0-4 s is calculated as 21%. While for RP = 2475 years, the average of this ratio is calculated as 58%, indicating the importance of the difference between the two approaches. Thus, it would be preferable to adopt the probabilistic acceleration spectrum corresponding to a 2% exceedance probability as the design spectrum.

For developing a uniform hazard acceleration spectrum on the ground surface, two issues need to be taken into consideration. The first issue is the probability of the uniform hazard acceleration spectrum on the engineering bedrock outcrop. The second issue is the probability of the uniform hazard acceleration spectrum on the ground surface. In a more comprehensive probabilistic assessment, the contribution of all probability levels was taken into account based on the concept of total

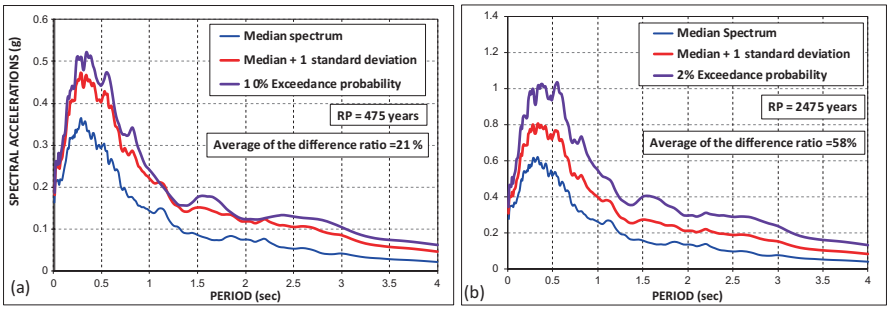

Fig. 3.3 Acceleration spectra on the ground surface for RP = 475 and 2475 years

probability originally suggested by Jalayer and Cornell (2003). Ansal et al. (2011) adopted the approach suggested by Jalayer and Cornell (2003) and conducted a total probability analysis as shown in Fig. 3.4. The uniform hazard spectrum for RP = 2475 years and 475 years, calculated based on the total probability analysis, yielded very similar acceleration spectra to the proposed simplified approach, where the design acceleration spectrum is assumed to correspond to the median+1 standard deviation for both RP = 475 and 2475 year. Average difference ratios are calculated as the ratio of the absolute difference between the spectral accelerations calculated by the total probability approach and based on median+1 standard deviation to the median spectral acceleration for the period range of 0-4 s. For both RP = 475 and 2475 years hazard levels, there appears to be considerable differences in the spectral acceleration in the mid period range of 0.5-2.5 s. In the case of acceleration spectrum based on probabilistic interpretation, the average difference ratio for RP = 475 years decreases to 120% from 152% and for RP = 2475 years, decreases to 80% from 141%. These results indicate that the acceleration spectra obtained by probabilistic interpretation for RP = 475 and 2475 years are closer to the acceleration spectra obtained by total probability theory and, thus, may be used to determine the design acceleration spectrum.

The second issue controlling the outcome of site response analyses is the variability of site conditions with respect to shear wave velocity and thickness assigned to each soil layer and, thus, the depth of engineering bedrock. The Monte Carlo simulation scheme has been adopted to study the effect of variability of the assigned shear wave velocities for each soil layer in a case study again composed of 7 soil borings. Slightly different to what was reported by Rathje et al. (2010), the effect of variability is studied by generating Monte Carlo simulations (MCS) for the 7 soil profiles, assuming the assigned shear wave velocities are average values and the range of possible variation is ±40% of this value. 1000 soil profiles were generated for each 7 soil borings.

A total of 154,000 site response analyses for 1000 Monte Carlo simulations for the 7 borings and for 22 acceleration records were conducted, and as an example, the distribution of PGA is plotted for 475- and 2475-year return periods. The main

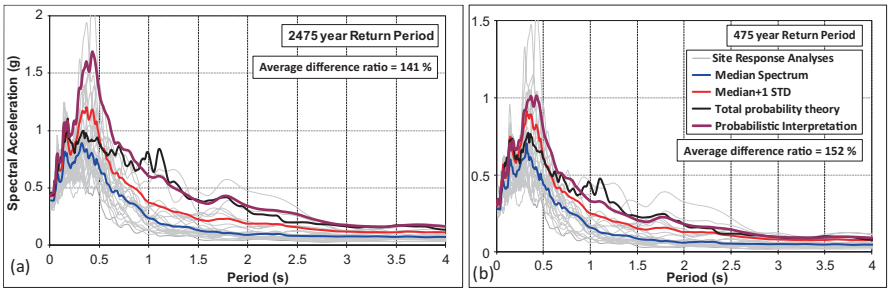

Fig. 3.4 Acceleration spectra for RP = 475 and 2475 years based on total probability analysis in comparison with acceleration spectra obtained by probabilistic interpretation and as median+1 standard deviation

purpose is to compare the calculated PGA by probabilistic interpretation fitting the distribution with a normal distribution function and calculating the corresponding to 10% and 2% exceedance levels (Fig. 3.5b, d). and by the sum of median+1 standard deviation (Fig. 3.5b, d). The two PGAs calculated based on both approaches for RP = 475 years are very similar, justifying the use of both values for design spectra. However, in the case of RP = 2475 years, the difference between the probabilistic interpretation (PGA = 0.756 g) and median+1 standard deviation (PGA = 0.686 g) is significant. Therefore, to be on the conservative side, it may be preferable to adopt the PGA corresponding to 2% exceedance (PGA = 0.756 g) as the design PGA acceleration for RP = 2475 years.

The hazard acceleration spectrum for RP = 475 years calculated based on probabilistic interpretation for a 10% exceedance level and median+1 standard deviation spectral accelerations is shown in Fig. 3.6a. For these cases, the difference ratio is defined as the ratio of the absolute difference of the spectral accelerations calculated based on the probabilistic interpretation and as median+1 standard deviation to the median spectral accelerations. The average of these difference ratios for the period range of 0-4 s is 5% for RP = 475 years; while for RP = 2475 years, it is 19%.

The differences between the acceleration spectra obtained with and without Monte Carlo simulations can also be compared with respect to the average difference ratio calculated for the period range of 0-4 s as given in Figs. 3.6b, d. This time, the difference ratio is defined as the ratio of the absolute difference between the average spectral accelerations calculated with and without Monte Carlo simulations to the median spectral accelerations calculated for the Monte Carlo simulations. The average of these difference ratios for the period range of 0-4 s is 37% for RP = 475 years; while for RP = 2475 years, it is 124%.

In the case of RP = 2475 year, the difference between the spectra obtained by median+1 standard deviation and based on the probabilistic interpretation are significantly different, as also observed in Fig. 3.5. The differences between the acceleration spectra obtained with and without Monte Carlo simulations is negligible for RP = 475 years, as shown in Fig. 3.6d. The spectrum calculated based on actual soil profiles yielded more conservative results, thus the initial proposal to adopt median+1 standard deviation appears applicable in defining approximately the uniform hazard acceleration design spectra on the ground surface for both RP = 475 and 2475 years.

At the second stage, the Monte Carlo simulation model has been adopted to study the effect of the variability of the soil stratification with respect to layer thickness that also controls the depth of engineering bedrock for each soil layer in the case study composed of seven soil borings.

In this second case, a total of 15,400 site response analyses for 100 Monte Carlo simulations for the 7 borings and for 22 acceleration records were conducted and acceleration spectrum corresponding to median+1 standard deviation and a 10% exceedance probability (475-year return period) acceleration spectra were calculated, as shown in Fig. 3.7a. The difference between the two acceleration spectra is negligible. In the comparison of the acceleration spectra obtained with and without Monte Carlo simulations, the difference is again negligible and the small difference

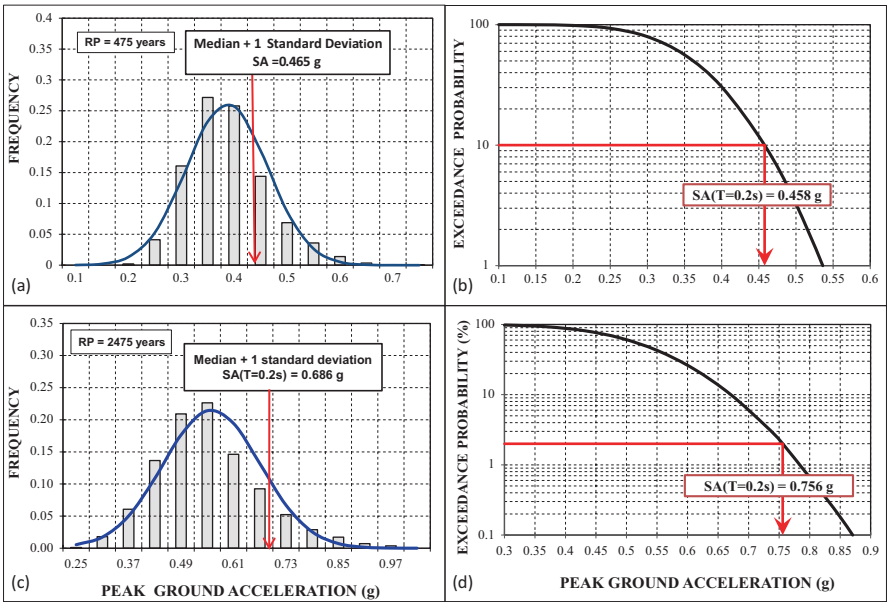

Fig. 3.5 Comparison of PGA calculated based probabilistic evaluation with respect to exceedance levels of 10% and 2% and as the sum of median+1 standard deviation

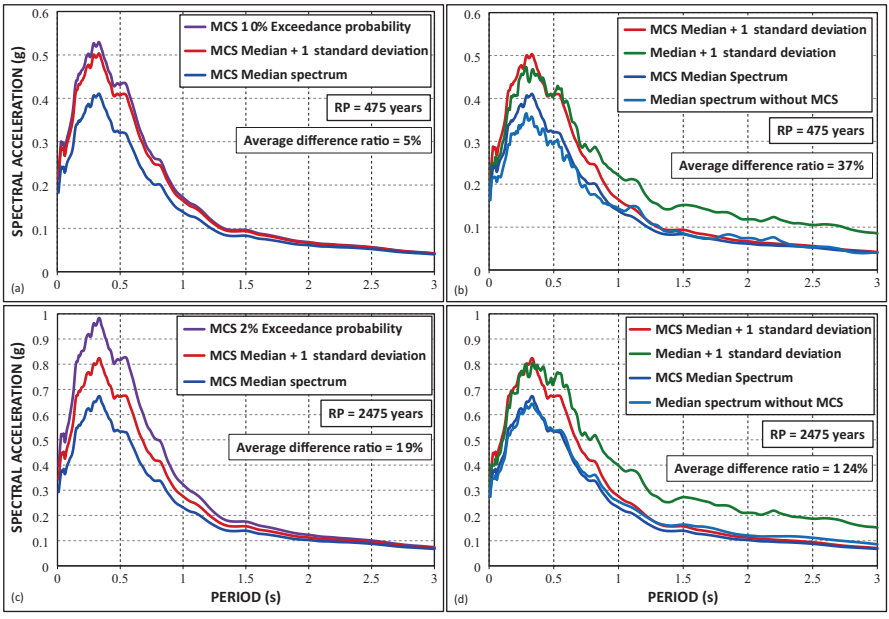

Fig. 3.6 Acceleration spectra with and without MCS for RP = 475 and 2475 year with respect to shear wave velocity variations

is only visible for the period range of less than 1 s (Fig. 3.7b). Thus, the initial proposal to adopt median+1 standard deviation appears to be applicable in defining the uniform hazard acceleration design spectra on the ground surface also for the case of the possible variability that may exist with respect to soil stratification.

In the case of RP = 2475 years or a 2% exceedance probability, as observed in Fig. 3.7c, the difference between the spectra corresponding to the 2% exceedance and median+1 standard deviation is significant. As also observed in Fig. 3.6, the spectra calculated for the 2% exceedance for all periods have higher spectral accelerations in comparison to those calculated as median+1 standard deviation. One possible reason for such an outcome is the higher acceleration levels of the input acceleration time histories leading to larger scatter in the statistical distribution of the calculated acceleration spectrum for the 2475-year return period.

The site response analyses conducted on the existing 7 soil profiles without MCS yielded similar, and slightly higher, spectral accelerations. At this stage, it is possible to assume that site response analyses conducted only on the existing limited amount of soil profiles may be assumed to be sufficient to yield the uniform acceleration hazard spectra on the ground surface for RP = 2475 and 475 years.

It is interesting to observe that for the case of RP = 475 years, the variability introduced by Monte Carlo simulations for each the existing soil profile determined based on borings and in-situ shear wave velocity measurements did not lead to significant variations. Thus, for the case of RP = 475-year return period, it would be

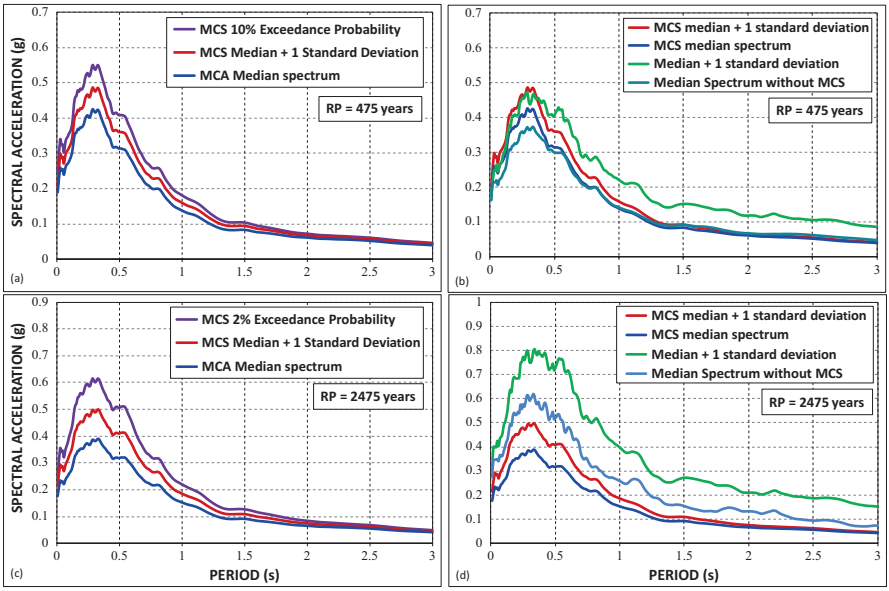

Fig. 3.7 Median, median+1 standard deviation, for RP = 475 and 2475 year acceleration spectra with and without MCS with respect to layer thickness

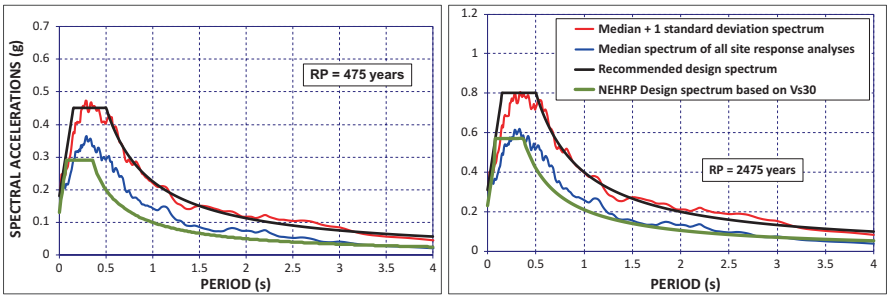

Fig. 3.8 Comparison of acceleration design spectra for RP = 475 and 2475 years calculated by site response analysis and NEHRP procedure based on V_{s30}

reasonable to assume that both procedures presented to obtain the uniform hazard acceleration design spectrum are realistic and acceptable.

In the case of RP = 2475 years, the results, as shown in Fig. 3.5c, d, indicate larger scatter. However, the variability introduced by the Monte Carlo simulations with respect to shear wave velocities, as well as with respect to layer thickness, was not very significant and generally above the median+1 standard deviation spectrum calculated based only on the existing limited number of real soil profiles. Therefore, it appears justified to adopt the median+1 standard deviation spectrum as the uniform hazard acceleration design spectrum for RP = 2475 years.

If the simpler approach is adopted by using V_{s30} to estimate the design spectra on the ground surface based on the NEHRP procedure, the calculated acceleration spectra are much lower in comparison to those calculated by site response analyses as shown in Fig. 3.8. In the selection of the design acceleration spectrum for the 2475-year return period, median+1 standard deviation spectrum was adopted, since probabilistic interpretation yielded relatively high spectral accelerations. Such large differences with respect to NEHRP methodology is likely due to the thickness of the soil deposits that were approximately between 60 and 110 m for the selected 7 soil profiles, indicating the limitations of the NEHRP methodology that may not always yield reliable results.

3.4 Conclusions

A simplified procedure is developed to determine acceleration design spectra on the ground surface for two, mostly adopted return periods. The procedure is not a fully probabilistic procedure that would yield uniform hazard acceleration spectra on the ground surface. The case study composed of 7 soil profiles was utilized in a parametric study to demonstrate the applicability of the proposed approach. The proposed approach is based on performing multiple numbers of site response analysis using the selected and properly scaled hazard compatible acceleration records. The design acceleration spectra calculated based on these limited number of soil profiles are compared with the site response results obtained from a large number of soil profiles

obtained by Monte Carlo simulations with respect to shear wave velocity and layer thickness in the soil profiles. The results calculated for a 475-year return period are not affected by the introduced variability with respect to layer thickness and shear wave velocity. Thus, it appears possible to define a semiempirical, uniform design hazard acceleration spectrum for RP = 475 years based on a sufficient number of soil profiles using a sufficient number of hazard compatible acceleration time histories based on a simple probabilistic interpretation. In the case of a 2475-year return period, the results from a large number of site response analyses indicate scatter. However, the results based on a limited number of soil profiles using a number of acceleration records yielded design acceleration spectra slightly higher than the probable design spectrum calculated based on a large number of site response analyses conducted on a large number of simulated soil profiles generated by Monte Carlo simulations. However, the uniform hazard design acceleration spectrum may be calculated based on simplified probabilistic interpretation to be on the conservative side.

References

Abrahamson NA, Silva WJ, Kamai R (2014) Summary of the ASK14 ground motion relation for active crustal regions. Earthq Spectra 30:1025–1055

Ansal A, Tönük G. (2007) Source and site effects for microzonation. In: Pitilakis K (ed) Earthquake geotechnical engineering, Ch. 4. Springer, pp 73–92

Ansal A, Kurtuluş A, Tönük G (2009) Earthquake damage scenario software for Urban areas. In: Papadrakakis M, Charmpis DC, Lagaros ND, Tsompanakis (eds) Computational structural dynamics and earthquake engineering, Structures and Infrastructures Series, Ch.2. Springer, pp 377–391

Ansal A, Tönük G, Kurtuluş A. (2011) Site specific earthquake characteristics for performance based design. In: Proceedings of the 5th international conference on geotechnical earthquake engineering, Santiago, Chile

Ansal A, Tönük G, Kurtuluş A, Çetiner B (2012) Effect of spectra scaling on site specific design earthquake characteristics based on 1D site response analysis. In: Proceedings of 15WCEE, Lisbon, Portugal

Ansal A, Kurtuluş A, Tönük G (2014) Site response from Istanbul vertical arrays and strong motion network. In: Proceedings of 10th U.S. national conference on earthquake engineering, frontiers m of earthquake engineering, Anchorage, Alaska, 21–25 July 2014

Ansal A, Tönük G, Kurtuluş A (2015) A methodology for site specific design earthquake. In: SECED 2015 conference: earthquake risk and engineering towards a resilient world, Cambridge UK, July 2015

Baturay M, Stewart P (2003) Uncertainty and bias in ground motion estimates from ground response analyses. Bull Seismol Soc Am 93(5):2025–2042

Bazzurro P, Cornell AC (2004a) Nonlinear soil-site effects in probabilistic seismic-hazard analysis. Bull Seismol Soc Am 94(6):2110–2123

Bazzurro P, Cornell CA (2004b) Ground-motion amplification in nonlinear soil sites with uncertain properties. Bull Seismol Soc Am 94(6):2090–2109

Bommer JJ, Acevedo AB (2004) The use real earthquake accelerograms as input to dynamic analysis. J Earthq Eng 8(1):43–91

Bommer JJ, Scott SG, Sarma SK (2000) Hazard-consistent earthquake scenarios. Soil Dyn Earthq Eng 19:219–231

Boore DM, Stewart JP, Seyhan E, Atkinson GA (2014) NGA-West2 equations for predicting PGA, PGV, and 5% damped PSA for shallow crustal earthquakes. Earthq Spectra 30:1057–1085

Borcherdt RD (1994) Estimates of site dependent response spectra for design (methodology and justification). Earthq Spectra 10(4):617–654

Campbell KW, Bozorgnia Y (2014) NGA-West2 ground motion model for the average horizontal components of PGA, PGV, and 5% damped linear acceleration response spectra. Earthq Spectra 30:1087–1115

Cramer CH (2003) Site specific seismic hazard analysis that is completely probabilistic. Bull Seismol Soc Am 93(4):1841–1846

Cramer CH (2006) Quantifying the uncertainty in site amplification modeling and its effects on site-specific seismic hazard estimation in the upper Mississippi embayment and adjacent areas. Bull Seismol Soc Am 96(6):2008–2020

Dobry R, Borcherdt RD, Crouse CB, Idriss IM, Joyner WB, Martin GR, Power MS, Rinne EE, Seed RB (2000) New site coefficients and site classification system used in recent building seismic code provisions (1994/1997 NEHRP and 1997 UBC). Earthq Spectra 16:41–68

Durukal E, Ansal A, Tonuk G (2006) Effect of ground motion scaling and uncertainties in site characterisation on site response analyses. In: Proceedings of eighth U.S. national conference on earthquake engineering, San Francisco, CA

Haase JS, Choi YS, Bowling T, Nowack RL (2011) Probabilistic seismic-hazard assessment including site effects. Bull Seismol Soc Am 101(3):1039–1054

Hartzell S, Cranswick E, Frankel A, Carver D, Meremonte M (1997) Variability of site response in the Los Angeles urban area for Evansville, Indiana, and the surrounding region. Bull Seismol Soc Am 87:1377–1400

Huang YN, Whittaker AS, Luco N (2010) NEHRP site amplification factors and the NGA relationships. Earthq Spectra 26:583–593

Idriss IM, Sun JI (1992) Shake91, A computer program for conducting equivalent linear seismic response analysis of horizontally layered soil deposits. University of California, Berkeley

Iyisan R (1996) Correlations between shear wave velocity and in-situ penetration test results. Tech J Turkish Chamber Civil Eng 7(2):1187–1199. (in Turkish)

Jalayer F & Cornell, A. (2003) A technical framework for probability-based demand and capacity factor design (DCFD) seismic formats, PEER report, Pacific Earthquake Engineering Center, College of Engineering, University of California, Berkeley

Kottke AR, Rathje EM (2008) A semi-automated procedure for selecting and scaling recorded earthquake motions for dynamic analysis. Earthq Spectra 24(4):911–932

Lee Y, Anderson JG (2000) Potential for improving ground-motion relations in Southern California by incorporating various site parameters. Bull Seismol Soc Am 90(6B):S170–S186

McGuire RK, Silva WJ, Constantino C (2001) Technical basis for revision of regulatory guidance on design ground motions: hazard and risk-consistent ground motion spectra guidelines, NUREG/CR-6728, prepared for U.S. Nuclear Regulatory Com., Office of Nuclear Regulatory Research, Division of Engineering Technology

PEER. Pacific Earthquake Engineering Research Center, Strong Motion Database, http://peer.berkeley.edu/ 2014.

Rathje EM, Kottke AR, Trent WL (2010) Influence of input motion and site property variabilities on seismic site response analysis. J Geotech Geoenviron 136:607–619

Stewart PJ, Seyhan E (2013) Semi-empirical nonlinear site amplification and its application in NEHRP site factors. PEER report 2013/13, Pacific Earthquake Engineering Research Center, College of Engineering, University of California, Berkeley

Sugito M, Aida ve T. Masuda N (1994) Frequency dependent equilinearized technique for seismic response analysis of multi-layered ground. In: Proceedings of JSCE, J Geotech Eng, 493:49–58

Tönük G, Ansal A (2010) Selection and scaling of ground motion records for site response analysis. In: 14th European conference of earthquake engineering, Ohrid, paper no. 1386

Tönük G, Ansal A, Kurtuluş A, Çetiner B (2014) Site specific response analysis for performance based design earthquake characteristics. Bull Earthq Eng 12(3):1091–1105

Toro GR, Silva WJ (2001) Scenario earthquakes for Saint Louis, MO, and Memphis, TN, and seismic hazard maps for the central United States region including the effect of site conditions, Final technical report to the USGS. Risk Engineering, Inc., Boulder

Tsai CCP (2000) Probabilistic seismic hazard analysis considering nonlinear site effect. Bull Seismol Soc Am 90(1):66–72

Chapter 4
Inherent Damping in Nonlinear Time-History Analyses: A Recommended Modelling Approach

Athol J. Carr and Arun M. Puthanpurayil

Abstract In a nonlinear dynamic analysis, the most popular way of representing the inherent damping exhibited by the structure is by adopting the classical Rayleigh damping model. Although a large number of studies have identified issues with this model, it remains the most popular choice in the currently available non-linear time-history analysis software. A new paradigm for modelling damping was proposed by the authors in Puthanpurayil AM, Lavan O, Carr AJ, Dhakal RP (Bull Earthq Eng 14:2405–2434, 2016) and is summarised in this chapter. This new model provides for the damping effects at an elemental level. The chapter outlines the performance of the elemental damping models in comparison to the classical global damping models by conducting Incremental Dynamic Analyses (IDA) on a four-storey RC frame designed to Eurocodes. The IDA study presented in the chapter illustrates the fact that the elemental damping models give a more reliable estimate for the structural responses in comparison to all other models.

Keywords Damping • Nonlinear time-history analysis • Incremental dynamic analysis • Seismic response

A.J. Carr (✉)
University of Canterbury, Christchurch, New Zealand

Carr Research Ltd., Christchurch, New Zealand
e-mail: athol.carr@canterbury.ac.nz

A.M. Puthanpurayil
Beca Ltd., Wellington, New Zealand

University of Canterbury, Christchurch, New Zealand
e-mail: ama299@uclive.ac.nz

R. Rupakhety, S. Ólafsson (eds.), *Earthquake Engineering and Structural Dynamics in Memory of Ragnar Sigbjörnsson*, Geotechnical, Geological and Earthquake Engineering 44, https://doi.org/10.1007/978-3-319-62099-2_4

4.1 Introduction

The damping models used in the non-linear time-history analyses are trying to mimic the observed decay phenomenon that is usually referred to as the damping in the structure. In an inelastic dynamic analysis, the majority of the energy dissipation in the system is reflected in the member hysteresis. However, the analysis still needs to reflect the dissipation in the components of the structure in which energy dissipation or non-linearity is not modelled, e.g., cracking of infill walls, gravity columns, movement of partitions, etc. The overall mechanisms that contribute to this *unmodelled dissipation* are complex and need to be explicitly defined by an appropriate damping matrix. All the currently employed damping models are an approximation to the decay phenomenon until the physical mechanism that causes the decay of the structural vibration is described.

The damping models currently used assume that the damping is viscous. Rayleigh (1877) believed that the decay phenomenon was due to friction effects, Love (1906) thought that it was caused by structural non-linearity, i.e., hysteresis. Rayleigh stated that he used a viscous damping model solely for mathematical convenience. Engineers have, since then, continued to use the viscous damping model without considering the implications.

Experimental evidence indicates that the decay is not viscous. The levels of viscous damping observed appear to be amplitude dependant as the decay is not bounded by a simple exponential envelope, i.e., the damping ratios are not constant with time. If the damping is not viscous, then we never have a linearly elastic structure, and modelling should reflect this.

The present chapter consolidates the elemental damping models proposed by the authors and presents an investigation to identify the most appropriate damping model for nonlinear dynamic analysis. An indication of the most suitable damping model for nonlinear dynamic analysis according to the authors is also presented.

4.2 Rayleigh Damping – Is It Appropriate for a Nonlinear Dynamic Analysis?

At present, the most popular model used to represent the damping phenomenon in a non-linear time-history analysis is the Rayleigh damping model. This has been traditionally used as:

1. the model is highly computationally efficient since it uses the already computed mass and stiffness matrices;
2. it is easy to fit into the computationally efficient modal analysis framework.

While the above points are no longer important due to the advances in the currently available computational resources, the Rayleigh damping model continues to be used.

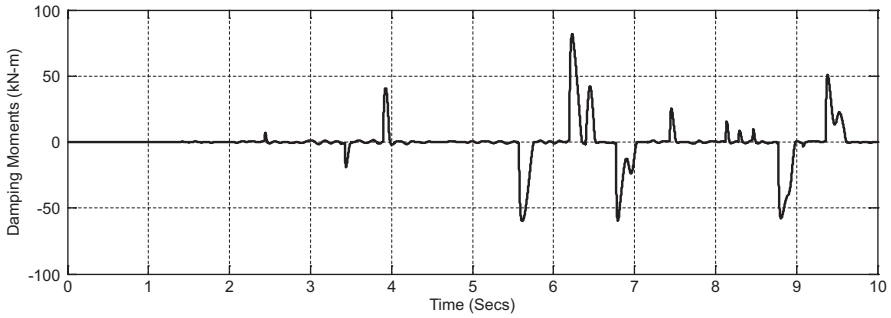

Fig. 4.1 Damping moment plot for the four-storey frame for the first storey middle node (Adopted from Carr et al. 2017)

The adoption of the Rayleigh damping model has no physical or mathematical justification. The Rayleigh damping model exhibits very high damping associated with the near rigid-body modes and exhibits linearly increasing damping as the modal frequency increases. Neither effect matches observed structural damping characteristics.

Crisp (1980) describes the unrealistic increases in the relative contribution of the damping actions based on a large number of analyses of multi-storey frame structures. Figure 4.1, adopted from Carr et al. (2017), illustrates the appearance of unrealistic damping actions in the nonlinear dynamic analysis of a four-storey frame. The yielding moment of the girder meeting the joint is 100kN-m, only slightly larger than the maximum damping moment at the joint. Studies have shown that these damping moments affect the observed adjacent member moments and the overall structural displacement response.

Significant research has been undertaken to investigate the issues of using the Rayleigh damping model in nonlinear dynamic analyses. These works have been described in Crisp (1980), Shing and Mahin (1987), Leger and Dassault (1992), Bernal (1994), Hall (2006), Charney (2008), Zarein and Medina (2010), Jehel et al. (2014), Chopra and McKenna (2016), Puthanpurayil et al. (2016) and Carr et al. (2017). The majority of these works identify the presence of unrealistic damping actions (forces and moments) as one of the main impediments in the adaptation of the Rayleigh damping model into the nonlinear domain. Suggestions of different ways to remedy the unrealistic damping actions by modification of the basic model have been proposed. Except for Crisp (1980), Chopra and McKenna (2016), Puthanpurayil et al. (2016) and Carr et al. (2017), the authors suggest different adaptive modifications of the basic Rayleigh damping model to correct the unrealistic damping actions. The authors understand that few of these adaptive modifications have been adopted in commercial software.

Sharpe (1974) and Carr (1982) both used the tangent stiffness matrix to overcome the unrealistic damping actions associated with large, inelastic deformations when using the Rayleigh damping model. This model maintains damping proportionality in the inelastic structure. The Rayleigh parameters need adjustment as the

natural frequencies in the structure change to maintain a damping level similar to that associated with the initial, linear elastic structure.

The Wilson and Penzien (1972) formulation model has the requirement of computing all of the modes of free vibration and results in a fully-populated damping matrix. This method has been used in commercially available software since 1980 and results were first presented by Crisp (1980) and Carr (1982, 2016). The model has computational penalties. However, these penalties are not significant reasons not to use this model for non-linear time-history analyses. PERFORM-3D (CSI 2011) and Chopra and McKenna (2016) introduced a reduced Wilson-Penzien damping formulation which only includes a lesser number of modes in comparison to the complete number of modes of the classical Wilson-Penzien modal damping formulation. The number of modes required in a relatively complex structure to represent the *unmodelled* dissipation is a question which needs further research.

4.3 A Different Approach to Modelling Inherent Damping

The classical approach to modelling damping was to define the damping matrix at the system level. The most popular approach is to use the Rayleigh viscous damping, where the damping force is proportional to the instantaneous velocity. As per Rayleigh damping, the damping matrix is as follows Chopra (1995, 2012),

$$\mathbf{C} = \alpha \mathbf{M} + \beta \mathbf{K} \tag{4.1}$$

where $\mathbf{M}$ is the mass matrix, $\mathbf{K}$ is the stiffness matrices and α, β are the damping coefficients based on a preconceived damping ratio. Though the model is an approximation, it performs relatively well in linear elastic dynamic analyses (in earthquake engineering, the higher modes of the structure are not significantly excited and rigid body modes are precluded).

As already stated, in his book, Rayleigh (1877) identifies the real cause of dissipation as friction and modelling the damping phenomenon as viscous is a pure mathematical convenience. Further, based on Lord Kelvin's experiments on torsional oscillation of wires, he observed that the damping might be hysteretic in nature as it might depend on the previous state of the body (Love 1906). Similar observations were made by Adhikari (2000).

From these observations, the damping phenomenon, in reality, is spatio-temporally nonlocal in nature and trying to predict the response only using the instantaneous velocities as the relevant *state variables* is not a true reflection of reality. The function of the causal mathematical model representing damping is to indirectly reflect the dissipation phenomenon. If the observations made by Lord Kelvin and Adhikari are taken into account, the use of Rayleigh damping, even in linear dynamics, becomes debatable as the mathematical function is not mimicking the reality. As the effect of damping is less in linear elastic dynamics, its use in this situation may be justified (Wilson and Clough 1962).

Puthanpurayil et al. (2016) proposed a new, innovative way of formulating dissipation phenomenon by defining the damping model at an element level and assembling the elemental damping in a manner similar to assembling the stiffness or mass matrices to obtain the global damping matrix. The damping matrix formulated at element level is devoid of the inherent issues present in the current damping modelling approaches.

4.3.1 Why Elemental Level Modelling of Damping?

From a realistic physical point of view, the *unmodelled dissipation* phenomenon emanates from the elements within the structure. All the gravity and nonstructural components contributing to this phenomenon are either attached directly or indirectly to the elements contributing to the hysteretic response. Damping occurs when these attached primary members deform thereby causing cracks, friction and failure in the nonstructural components along with the damping of the elastic portion of the inelastic members. It is imperative, and physically justified, that an ideal damping model should be defined at the element level. Different portions of a structure may indicate different amounts of damping. This cannot be replicated in a global damping model.

4.4 Overview of the Elemental Damping Models

This section briefly describes the elemental damping models presented in this chapter. The elemental damping models are broadly classified based on the way the damping matrix is formed as follows:

- Discrete elemental damping models
- Continuum elemental damping models

In the discrete elemental damping models, the damping matrix is introduced at the element level after a semidiscretisation procedure is undertaken. In the continuum models, the damping is introduced at the continuum level and on semidiscretisation, produces the elemental damping matrix. The elemental damping matrix thus obtained is then assembled similarly to mass and stiffness matrices. These models can be further classified based on the way the coefficients are computed and the mass formulation. In this approach, the element mass matrix may be either the element consistent mass matrix or a diagonalized version of it. The member deformation modes are required in order to compute the element damping matrices (e.g., beams require the flexural modes and frequencies).

4.4.1 Discrete Elemental Damping Models (Puthanpurayil et al. 2016)

Two elemental models which are the elemental counterparts of the global models are described in this section. These are the:

1. Elemental Rayleigh damping (elemental adaptation of the classical Rayleigh damping)
2. Elemental Wilson-Penzien model (elemental adaptation of the classical Wilson-Penzien model).

A very brief theoretical overview of the elemental models is given. Additional information regarding the implementation of these models may be found in Puthanpurayil et al. (2016).

- *Elemental Rayleigh damping model*

The main motivation behind the formulation of the elemental Rayleigh damping model is from the simplicity and familiarity of the Rayleigh damping model normally applied at system global level in classical structural dynamics (Puthanpurayil et al. 2016). The elemental Rayleigh damping is a direct adaptation of the Global Rayleigh damping at the element level. The form of the element damping matrix is given as (Puthanpurayil et al. 2016),

$$\mathbf{C}_e = \alpha_{eRD}\mathbf{M}_e + \beta_{eRD}\mathbf{K}_e \tag{4.2}$$

where α_{eRD} and β_{eRD} are the elemental damping coefficients. The main difference between the elemental Rayleigh damping and the classical Rayleigh damping (which is predominantly implemented at a global level) exists in the computation of these damping coefficients. In the elemental Rayleigh damping, the coefficients are computed as,

$$\left.\begin{aligned} \alpha_{eRD} &= 2\xi_{eR1}\frac{\omega_e^i\omega_e^j}{\omega_e^i+\omega_e^j} \\ \beta_{eRD} &= 2\xi_{eR2}\frac{1}{\omega_e^i+\omega_e^j} \end{aligned}\right\} \tag{4.3}$$

where ω_e^i and ω_e^j are the ith and the jth elemental frequencies. ξ_{eR1} and ξ_{eR2} are elemental damping ratios which need to be parameterised as outlined in Puthanpurayil et al. (2016).

- *Elemental Wilson-Penzien model*

For easier reference, a very brief overview of the mathematical background of the elemental Wilson-Penzien model, as adapted from Puthanpurayil et al. (2016) is presented. Let $\boldsymbol{\Phi}_e$ represent the full $N_e \times N_e$ elemental modal matrix and ω_e^2

represent the $N_e \times N_e$ diagonal frequency matrix. By classical modal analysis, the elemental displacements $\mathbf{d}_e(t)$ can be expressed as,

$$\mathbf{d}_e(t) = \Phi_e \mathbf{q}_e(t) \tag{4.4}$$

where $\mathbf{q}_e(t)$ is the generalized coordinate. In the derivation of the global Wilson-Penzien model, the damping matrix assumes the same orthogonality property as the mass and stiffness matrices (Wilson and Penzien 1972). At the elemental level, the same assumption is valid by pre-multiplying the equation of motion by Φ_e^T and using Eq. (4.4),

$$\mathbf{M}_{di}\ddot{\mathbf{q}}_e(t) + \mathbf{C}_{di}\dot{\mathbf{q}}_e(t) + \mathbf{K}_{di}\mathbf{q}_e(t) = \mathbf{F}_e(t) \tag{4.5}$$

where, $\mathbf{M}_{di}$, $\mathbf{C}_{di}$ and $\mathbf{K}_{di}$ represent the diagonalized mass, damping and stiffness matrices. The respective individual terms in these matrices are given as follows,

$$\begin{aligned} M_{di}^i &= \left(\varphi_e^i\right)^T \mathbf{M}_e \left(\varphi_e^i\right) \\ C_{di}^i &= \left(\varphi_e^i\right)^T \mathbf{C}_e \left(\varphi_e^i\right) \quad i = 1, 2 \ldots\ldots N_e \\ K_{di}^i &= \left(\varphi_e^i\right)^T \mathbf{K}_e \left(\varphi_e^i\right) \end{aligned} \tag{4.6}$$

An elemental level constant denoted as ξ_{eWP}^i corresponding to the ith elemental mode is introduced, and the elemental modal damping coefficient, C_{di}^i can be then written as,

$$C_{di}^i = 2M_{di}^i \xi_{eWP}^i \omega_e^i \tag{4.7}$$

From Eq. (4.6) we get,

$$\mathbf{C}_e = \left(\Phi_e^{-1}\right)^T \mathbf{C}_{di} \left(\Phi_e^{-1}\right) \tag{4.8}$$

and from Eq. (4.6),

$$\left(\Phi_e^{-1}\right)^T = \mathbf{M}_e \Phi_e \mathbf{M}_{di}^{-1} \tag{4.9}$$

$$\left(\Phi_e^{-1}\right) = \mathbf{M}_{di}^{-1} \Phi_e^T \mathbf{M}_e \tag{4.10}$$

Substituting Eq. (4.7), (4.9) and (4.10) in Eq. (4.8), we get,

$$\mathbf{C}_e = \Theta_e \Psi_e \Theta_e^T \tag{4.11}$$

where Θ_e is the mass normalized elemental mode shape matrix. Ψ_e is a diagonal matrix with diagonal elements given by,

$$\psi_e^i = \frac{2\xi_{eWP}^i \omega_e^i}{M_{di}^i} \tag{4.12}$$

In the present study, for application convenience, ξ_{eWP} (the elemental Wilson-Penzien damping ratio) is assumed to be constant for all elements and *assumed to be same as the global damping ratio (the damping ratio used for the global Wilson-Penzien model)*. For further details on this refer Puthanpurayil et al. (2016).

4.4.2 Continuum Damping Models

In the continuum damping models, the damping term is introduced at the continuum level. Two damping forces are introduced to represent the internal damping action and the external damping action (mainly attributed to air resistance in a physical sense). The external term can be very important if the structure is immersed in a fluid where there will be drag forces applied on the structure. The Euler Bernoulli beam continuum, enhanced with the damping term, is given as,

$$\rho A(x)\frac{\partial^2 w(x,t)}{\partial t^2} + F_{\text{int}}(x,t) + F_{ext}(x,t) + \frac{\partial^2}{\partial x^2}\left(EI(x)\frac{\partial^2 w(x,t)}{\partial x^2}\right) = f(x,t) \tag{4.13}$$

where, $F_{\text{int}}(x, t)$ is the internal damping force caused by internal resistance and $F_{\text{ext}}(x, t)$ is the external damping force. x refers to the spatial ordinate and t refers to the time ordinate. To simplify the presentation, the initial conditions are assumed to be zero and the boundary conditions are not explicitly listed as the semidiscretization is applicable to a variety of boundary conditions.$\rho, A(x), E$ & $I(x)$ refer to material density, geometric area, modulus of elasticity and second moment of area of the beam continuum. $f(x, t)$ is the externally applied load; $w(x, t)$ is the transverse displacement.

The external damping force is assumed as,

$$F_{ext}(x,t) = \gamma_{air}\frac{\partial w(x,t)}{\partial t} \tag{4.14}$$

γ_{air} is the external air damping coefficient.

Kelvin-Voigt, time hysteresis damping, Russell's damping and extended Sorrentino models are differentiated by the way $F_{\text{int}}(x, t)$ is defined. These are

discussed in Sects. 4.4.2.1 and 4.4.2.2. Banks and Inman (1991) and Friswell et al. (2007) provide more details regarding these models.

4.4.2.1 Spatially Local Continuum Damping Models

In the local continuum model, the damping force at a point is the function of the response at the same point.

- *Kelvin-Voigt damping*

In Kelvin-Voigt damping the $F_{\text{int}}(x,t)$ is given as,

$$F_{\text{int}}(x,t) = \frac{\partial^2}{\partial x^2}\left(c_s I(x)\frac{\partial^3 w(x,t)}{\partial t \partial x^2}\right) \tag{4.15}$$

where c_s refers to the damping coefficient which converts strain rate into stress. The elemental Kelvin-Voigt damping matrix is obtained by semidiscretization of Eq. (4.13) incorporating Eqs. (4.14) and (4.15). The authors note that, on semidiscretization, the damping matrix obtained is proportional to the element stiffness matrix. This model could be viewed as a continuum version of the classical global Rayleigh damping model.

- *Time hysteresis damping*

The time hysteresis damping force is given as,

$$F_{\text{int}}(x,t) = EI(x)\int_0^t g(t-\tau)\frac{\partial}{\partial \tau}\left(\frac{\partial^4 w(x,\tau)}{\partial x^4}\right)d\tau \tag{4.16}$$

$g(t-\tau)$ is the causal damping kernel function which is adopted as,

$$g(t) = \mu e^{-\mu t} \tag{4.17}$$

where, μ is a relaxation parameter. Adhikari (2000) provides more details regarding this model.

Incorporation of Eq. (4.16) in the equation of motion results in an integro-differential equation and cannot be solved using the classical methods of time integration. Efficient techniques exist for linear dynamics, but very few methods can be used to solve the equation of motion in nonlinear dynamics. One of the methods that is capable of solving this is the AAR method developed by the authors (Puthanpurayil et al. 2014). The AAR method is a method based on modified total equilibrium Newmark framework which solves the integro-differential equation of motion very efficiently in nonlinear dynamics.

4.4.2.2 Nonlocal Continuum Damping Models

A spatially nonlocal model and a spatio-temporally nonlocal model are described in this section. Spatially nonlocal damping models are models in which the damping force at a point is a function of the responses at all points in the domain. In the spatio-temporally nonlocal damping models, the damping force at a point is a function of responses at all points in the spatial domain along with response history. The damping model described by Russell (1991) falls under the category of spatially nonlocal model and the extended Sorrentio (Friswell et al. (2007)) model falls under the category of spatio-temporally nonlocal model.

- *Russell's damping model*

Russell (1991) pioneered the development of nonlocal damping models by the development of a spatial hysteresis model. In the spatial hysteresis model, the internal damping term is described as a torque acting on a beam at a point x due to the differential rotation of the beam at points ξ near x.

$$F_{\text{int}}\left(x,\xi,t\right) = -2\frac{\partial}{\partial x}\left\{\int_0^L h\left(x,\xi\right)\left[\frac{\partial^2 w\left(x,t\right)}{\partial x \partial t} - \frac{\partial^2 w\left(\xi,t\right)}{\partial x \partial t}\right] d\xi\right\} \tag{4.18}$$

In effect, the Russell's model is a spatially nonlocal, but a temporally local, model. Therefore, it can be considered as a viscous model with spatially nonlocal terms. For more details on this see Banks and Inman (1991).

- *Extended Sorrentino damping model (ESM)*

ESM is a very generic model as it is a spatio-temporally nonlocal model. In the case of ESM,

$$F_{\text{int}}\left(x,t\right) = \frac{\partial^2}{\partial x^2}\left(\int_0^L \int_{-\infty}^t C_{\text{int}}\left(x,\xi,t-\tau\right)\frac{\partial^3 w\left(\xi,\tau\right)}{\partial \xi^2 \partial \tau} d\tau d\xi\right) \tag{4.19}$$

$C_{\text{int}}\left(x,\xi,t-\tau\right)$ is a spatio-temporal kernel function. Refer to Friswell et al. (2007) for additional details.

For all of these elemental damping models, the function parameters to match the observed decay phenomenon of the structure in free-vibration must be selected by the analyst or in subsequent research. This is no different to analysts trying to match the two parameters of the Rayleigh damping to approximate the *right* amount of damping observed in the real structure. The ability to choose different causal damping kernel functions has the advantage that these models would be able to model hysteretic or friction damping without introducing the difficulties with the conventional attempts to model these types of damping.

4.5 Numerical Study

This section investigates the performance of the elemental damping models in comparison to the global, classical damping models. First, a single ground motion study is presented, and then, an incremental dynamic analysis study is presented.

4.5.1 Single Ground Motion Study

This section presents the single ground motion study performed using the four-storey frame described in Puthanpurayil et al. (2016). The main aim of this section is to highlight the issues associated with the inherent damping modelling in a bit more detail. Figure 4.2 illustrates the roof displacement and Fig. 4.3 illustrates the damping moments.

It can be clearly seen from these plots that there is an effect of the damping moments on the overall response. The global Rayleigh model with initial stiffness exhibits the highest damping moments. Damping moments are spurious forces exhibited by the damping models at the onset of nonlinearity (Puthanpurayil et al. 2016). Though a preliminary indication of the performance of different damping models are illustrated in this section, in order to get a better understanding of the models, an IDA study is presented in the next section.

4.5.2 Incremental Dynamic Analysis Study

This section consolidates the IDA results from Puthanpurayil et al. (2016) and Carr et al. (2017) along with responses of the continuum damping models. The frame description is given in Puthanpurayil et al. (2016), but is presented here briefly again

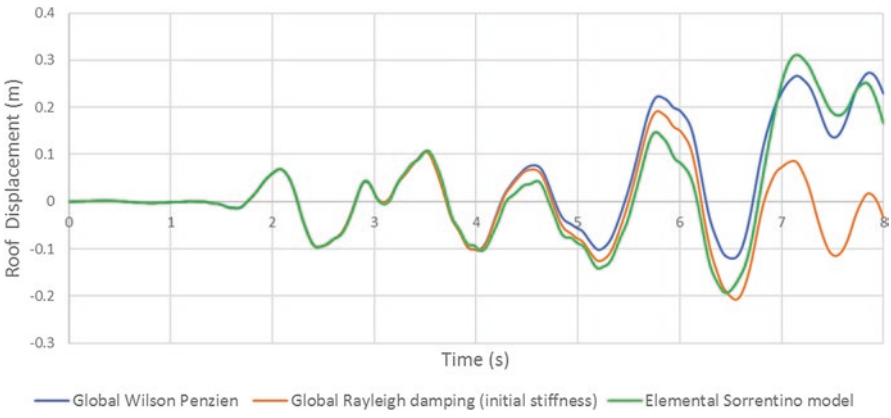

Fig. 4.2 Roof displacement of the four-storey frame

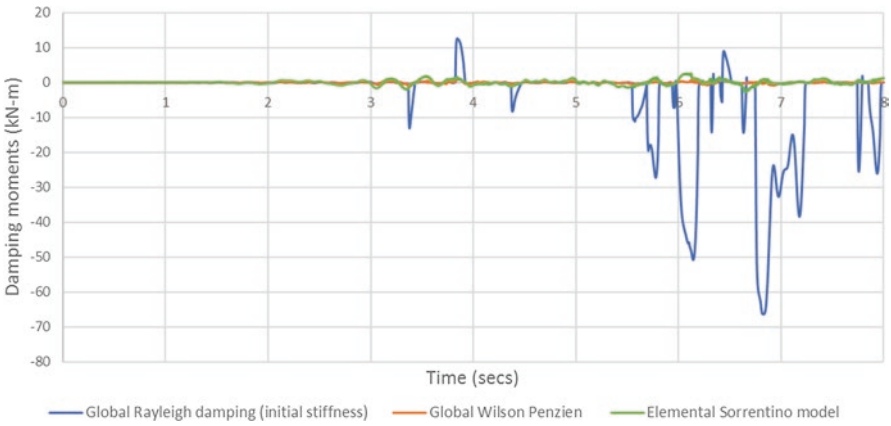

Fig. 4.3 Damping moment plot for first-storey node

for completeness. A four-storey RC frame described in Arede (1997), designed in accordance with Eurocode 8 (EC8) and Eurocode 2(EC2), is used for the study. The frame is designed for ductility class high, assuming a PGA of 0.3 g. Appendix A presents the geometric and material properties of the frame.

All existing elemental and global damping models are compared in this section. The following abbreviations are used to identify different damping models included in the plots hereafter:

- Initial stiffness based global Rayleigh damping (ISRD)
- Tangent stiffness based global Rayleigh damping with constant coefficients (TSRD),
- Global Wilson-Penzien (GWP)
- Elemental Rayleigh damping with updated proportionality coefficients (ELRD)
- Elemental Wilson-Penzien model implemented as a constant damping matrix (EWP)
- Elemental Wilson-Penzien model implemented as a tangent matrix (UEWP)
- Elemental Kelvin Voigt (ELKV)
- Elemental Time hysteresis (ELTH)
- Elemental Russell model (ELR)
- Elemental extended Sorrentino model (EESM).

In all the plots, the global models are presented with continuous lines and elemental models are presented with dashed lines.

4.5.3 *Elemental Damping vs. Global Damping*

As stated above, the elemental damping matrix computation can be done using either the consistent mass or using the diagonal mass. As similar results are obtained either in the consistent mass or diagonal mass formulation, only the consistent mass formulation results are presented in this section. No additional penalty in the form of higher computational demand occurs, even if the consistent mass formulation is used, as only small matrices are used for the elemental damping matrix computation. In real structures, every degree of freedom is associated with mass. Hence, the authors believe that the consistent mass formulation is more robust in terms of its mathematical closeness to the physical reality. For more details on the effects of the mass formulation, refer to Puthanpurayil et al. (2016).

The mass matrix used for the damping matrix computation adopts the classical, consistent mass formulation for the Euler Bernoulli beams. As the purpose of the IDA study was to illustrate qualitatively the effect of the damping models on the performance assessment of the structure, a set of seven, artificial, far-field ground motions scaled to five intensity measures (represented by the peak ground acceleration PGA) were used. The intensity measures to which the ground motions were scaled are 0.3 g, 0.4 g, 0.5 g, 0.6 g and 0.7 g. The global models also adopt the consistent mass formulation for the damping matrix computation instead of the normal lumped mass formulation for consistency.

Figure 4.4 illustrates the mean IDA curves for location-independent peak interstorey drift ratio as the engineering demand parameter (EDP). All the elemental damping models give higher drifts when compared to those of the global damping models. Figure 4.5 illustrates the peak damping moments for all the models. The ISRD model gives the highest damping moment, which is a higher moment than the yield moment of the frame. All the elemental damping models produce relatively small damping moments.

Although it is very difficult to get a direct correlation between the damping moments and their effect on the structural peak responses, it is shown that the lesser the damping moment, the larger the structural response. Damping is an observed phenomenon and unless physical science comes up with an exact model for the real physics of damping, all the models are mathematical approximations. From a structural perspective, a conservative approximation (from a safety point of view) would be better than an unconservative approximation. The elemental models tend to predict more conservative responses, and, as a result, the authors believe that they produce more realistic responses with less untoward side effects.

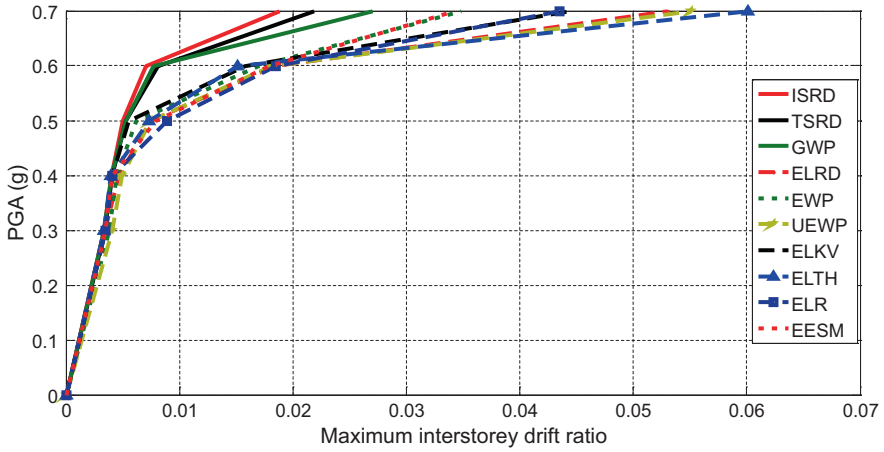

Fig. 4.4 IDA results for the interstorey drift ratio

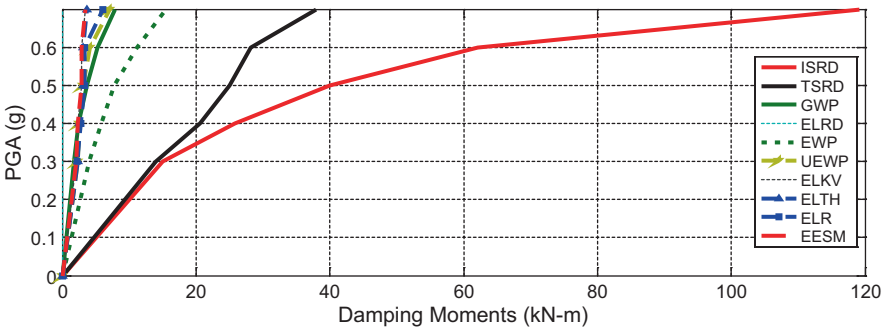

Fig. 4.5 IDA results for peak damping moment

4.5.4 Which Might be a Better Model?

The authors believe that updated elemental Wilson-Penzien model indicates a more realistic option than the current, commonly adopted Rayleigh models. The updated elemental Wilson-Penzien model exhibits low damping actions and shows responses that are very similar to those of the more complicated continuum damping models. Figure 4.2 clearly illustrates that the updated Wilson-Penzien damping model shows results similar to the elemental time- hysteresis model. The elemental Rayleigh damping may also be a modelling option; however, explicit parametrisation is required at every element level, increasing the challenges in using it.

4.6 Conclusions

A summary of the performance of the elemental damping models in comparison to global damping models is presented. The IDA results presented show that the elemental damping models perform much better than the global damping models. The elemental damping models may have significant computational advantages in that the structure damping matrix itself may be dispensed with, and the damping actions can be directly computed at the element level. Based on the results presented, a preferred elemental damping model for generic use in nonlinear time-history analysis is reccomended. More research needs to be done to confirm this initial insight of the preferred model.

Acknowledgements The authors gratefully acknowledge the funding provided by Earthquake Commission (EQC) in the form of a postgraduate research scholarship. The authors also acknowledge the motivation and useful insights given by Associate Professor Oren Lavan of Israel Technion and Professor Rajesh Dhakal of University of Canterbury.

Details of the Four-Storey Frame

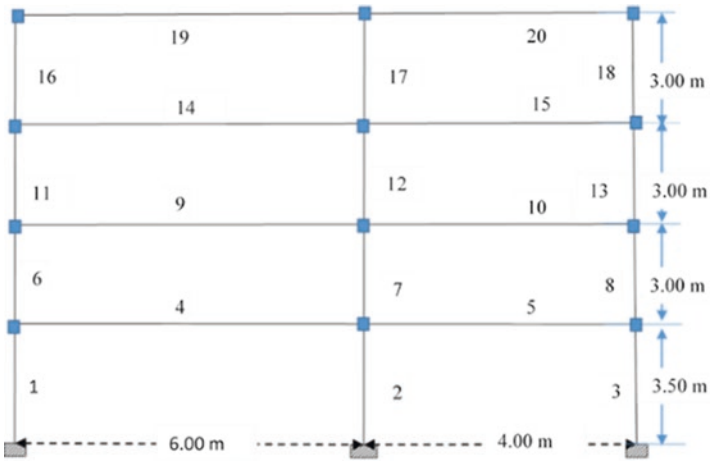

Material Property

Dynamic Young's modulus = $3.5\times10^{10}\ N/m^2$

Geometric Properties

Member number	Width (mm)	Depth (mm)
1,6,11,16,17,12,7,2,3,8,13,18	450	450
4,5,9,10,14,15,19,20	300	450

Nodal Mass

Floor level	Mass per node (kg)
1st floor	29,800
2nd -4th floor	29,500

References

Adhikari S (2000) Damping models for structural vibration. Dissertation, University of Cambridge

Arede AJ (1997) Seismic assessment of reinforced concrete frame structures with a new flexibility based element. Dissertation, Universidade Do Porto

Banks HT, Inman DJ (1991) On damping mechanisms in beams. Trans ASME, J Appl Mech 58:716–723

Bernal D (1994) Viscous damping in inelastic structural response. ASCE J Struct Eng 120(4):1240–1254

Carr AJ (1982) Ruaumoko manual. Report, University of Canterbury, Christchurch

Carr AJ (2016) Ruaumoko users guide, vol 5. Carr Research Ltd, Christchurch

Carr AJ, Puthanpurayil AM, Lavan O, Dhakal RP (2017) Damping models for inelastic time history analysis: a proposed modelling approach. 16th world conference in earthquake engineering, Santiago, Chile, January 2017

Charney FA (2008) Unintended consequences of modeling damping in structures. J Struct Eng 134(4):581–592

Chopra AK (1995) Dynamics of structures-theory and applications to earthquake engineering. Prentice Hall inc., Boston

Chopra AK (2012) Dynamics of structures: theory and application to earthquake engineering. Prentice Hall inc., Boston

Chopra AK, McKenna F. (2016) Modeling viscous damping in nonlinear response history analysis of buildings for earthquake excitation. Earthquake Engineering and Structural Dynamics

Crisp DJ (1980) Damping models for inelastic structures. ME Report, Department of Civil Engineering, University of Canterbury, Christchurch. New Zealand, February 1980

CSI (2011) User guide PERFORM-3D, computers and structures Inc. Berkeley California, USA

Friswell MI, Sondipon A, Lei Y (2007) Non-local finite element analysis of damped beams. Int J Solids Struct 44:7564–7576

Hall JF (2006) Problems encountered from the use (or misuse) of Rayleigh damping. Earthq Eng Struct Dyn 35:525–545

Jehel P, Leger P, Ibrahimbegovic A (2014) Initial versus tangent stiffness-based Rayleigh damping in inelastic time history analysis. Earthq Struct Dyn 43:467–484

Leger P, Dussault S (1992) Seismic-energy dissipation in MDOF structures. ASCE Jo Struct Eng 118(6):1251–1267

Love AEH (1906) A treatise on the mathematical theory of elasticity. Cambridge University press, Cambridge

Puthanpurayil AM, Carr AJ, Dhakal RP (2014) A generic time domain implementation scheme for non-classical convolution damping models. Eng Struct 71:88–98

Puthanpurayil AM, Lavan O, Carr AJ, Dhakal RP (2016) Elemental damping formulation: an alternative modelling of inherent damping in nonlinear dynamic analysis. Bull Earthq Eng 14:2405–2434

Rayleigh L (1877 (Re-issued 1945)) Theory of sound, Second ed. Dover Publication, New York

Russell DL (1991) On mathematical models for the elastic beam with frequency proportional damping. Control and Estimation in Distributed Parameter Systems, SIAM, 125–169

Sharpe RD (1974) The seismic response of inelastic structures. Ph.D Dissertation, Department of Civil Engineering, University of Canterbury

Shing PB, Mahin SA (1987) Elimination of spurious higher-mode response in pseudodynamic tests. Earthq Struct Dyn 15:425–445

Wilson EL, Clough R (1962) Dynamic response by step by step matrix analysis. In: Symposium on the use of computers in civil engineering, Lisbon

Wilson EL, Penzien J (1972) Evaluation of orthogonal damping matrices. Int J Numer Methods Eng 4:5–10

Zareian F, Medina RA (2010) A practical method for proper modeling of structural damping in inelastic plane structural systems. Comput Struct 88:45–53

Chapter 5
Challenges in Modelling the Seismic Response of RC Walls

T. Isakovic and M. Fischinger

Abstract Recent earthquakes have clearly demonstrated that many key mechanisms of the seismic response of RC structural walls are still not adequately understood. To improve the knowledge about RC walls, adequate numerical models are needed. A robust macro MVLEM-FD-SFI element has been developed at the University of Ljubljana. It can be efficiently used to model very complex axial-flexural-shear interactions which are typical of the seismic response of many RC walls. The element was evaluated by several experiments that were selected for case studies within the International Wall Institute. The element MVLEM-FD-SFI can capture different aspects of the global response very well, e.g., it can describe the buckling of the longitudinal bars as well as the significant degradation of different shear mechanisms.

Keywords RC shear walls • Seismic response • Axial-shear-flexural interaction • Macro models • Experiments

5.1 Introduction

The majority of modern standards for the seismic design of structures include requirements that are aimed to protect structures against brittle types of damage and failure. However, in many cases, a large scatter of the results can be obtained complying with the requirements of these standards. This is particularly true for those fundamental steps in the design which are related to the shear response and buckling of the longitudinal reinforcement.

The engineering and research community has recognized a substantial lack of knowledge relating to the estimation of the shear response, even in the case of monotonic types of loading. For example, in Bentz et al. (2006) it is stated, "[e]ven

T. Isakovic (✉) • M. Fischinger
Faculty of Civil and Geodetic Engineering, University of Ljubljana, Ljubljana, Slovenia
e-mail: tatjana.isakovic@fgg.uni-lj.si

R. Rupakhety, S. Ólafsson (eds.), *Earthquake Engineering and Structural Dynamics in Memory of Ragnar Sigbjörnsson*, Geotechnical, Geological and Earthquake Engineering 44, https://doi.org/10.1007/978-3-319-62099-2_5

though the behaviour of reinforced concrete in shear has been studied for more than 100 years, the problem of determining the shear strength of reinforced concrete beams remains open to discussion. Thus, the shear strengths predicted by different current design codes (ACI 2005, AASHTO 2004, CEN 2004, CSA 2004, JSCE 1986) for a particular beam section can vary by factors of more than 2. In contrast, the flexural strengths predicted by these same codes are unlikely to vary by more than 10%." In some cases, the differences can be even more drastic. For example, within the competition (Vecchio and Collins 1986), which included 43 leading researchers from 13 different countries, the ratio of the maximum to minimum predicted value of the shear strength for one of the specimens was as large as six to one.

Although substantial progress has been recently achieved with the development of the simplified compression field theory (Bentz et al. 2006), there are still a lot of issues that are not adequately resolved, particularly concerning the seismic (cyclic) response of RC structures, where in many cases, complex axial-flexural-shear interaction has been observed.

The seismic response is particularly complex in buildings containing RC structural walls. Consequently, even the basic mechanisms of the response are not adequately clarified and should be studied in more detail. In order to achieve this goal, an international Virtual Wall Institute (Wallace 2016) was initiated in 2014 by Prof. John Wallace from UCLA. Different universities all over the world (USA, Europe, Japan, New Zealand, South America) and leading world researchers in the field have been cooperating in order to make progress in the seismic analysis and design of RC structural walls, which are amongst the most-used building systems in the world. Broad experimental and analytical studies have been performed in order to clarify different aspects of different RC wall systems all over the world.

The University of Ljubljana has been primarily involved in the evaluations of available numerical models. The recently developed, robust force-displacement based engineering macro multiple-vertical-line element model – MVLEM-FD, which is capable of describing very complex axial-flexural-shear interaction (MVLEM-FD-SFI), is described in Sect. 5.2. In order to provide a wide range for its use and to enable the analysis of various types of buildings (including dual frame-wall systems) the element was included into a local version of the OpenSees program (OpenSees 2011, 2016).

The MVLEM model has been verified by many experimental studies of different types of RC walls (including several blind-simulations of large shake table tests organized by Japanese, American and French institutions). Recently, it has been tested within the research schedule of the Wall Institute. The results of this research are presented in this paper. The basic features of the walls, which were selected in case studies, are overviewed in Sect. 5.3.1. The main properties of the basic MVLEM-FD and its extended version MVLEM-FD-SFI are presented in Sect. 5.3.2. MVLEM-FD-SFI is evaluated in Sect. 5.3.3.

5.2 Main Features of the MVLEM-FD Element

The multiple-vertical-line element model MVLEM was originally proposed by Japanese researchers (Kabeyasawa et al. 1983) and later elaborated on by many other researchers (e.g. Vulcano et al. 1989). While most of them have used a stress-strain version of the element, the research group at the University of Ljubljana (UL) has developed a forced-displacement (FD) based version – MVLEM-FD. In order to provide a wide range of use and to enable the analysis of various types of buildings (including dual frame-wall systems), the element was included into the OpenSees program (2011).

5.2.1 Basic MVLEM-FD, Which Is Capable of Describing Axial-Flexural Interaction

The element model follows the basic idea proposed by Japanese researchers. In this element, several vertical springs are connected by rigid beams at the top and the bottom nodes of the element (Fig. 5.1). These springs simulate axial and flexural behaviours of wall segments using relatively simple force-displacement hysteretic rules (Fig. 5.2a).

In the basic version of the model, the shear response is uncoupled from the axial and flexural response. To define the shear response, a horizontal spring is added at the centre of gravity of the cross-section of the wall (see the horizontal spring in Fig. 5.1). The shear response is defined with hysteretic rules, presented in Fig. 5.2b. A special *ShearSlip* material was incorporated into the OpenSees program to be able to describe this response. Note however, that various materials incorporated into the OpenSees program can be used to define the characteristics of horizontal and vertical springs, depending on the specific features of the analysed wall.

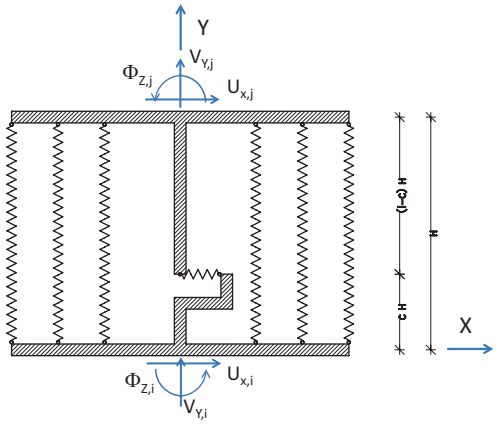

Fig. 5.1 Multiple-vertical-line-element model (MVLEM-FD)

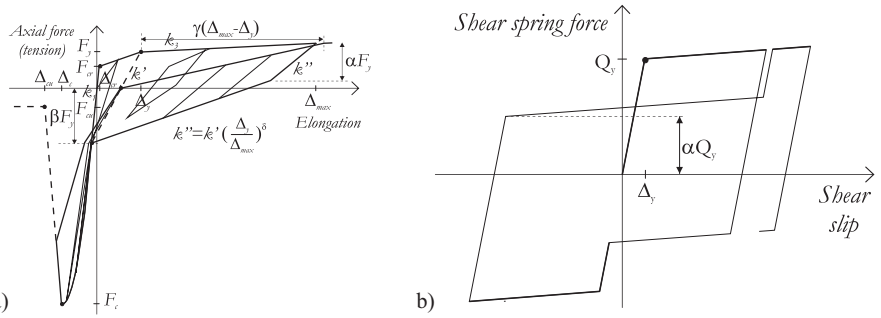

Fig. 5.2 Hysteretic rules controlling the springs in the MVLEM-FD: (**a**) Vertical springs, (**b**) Horizontal springs

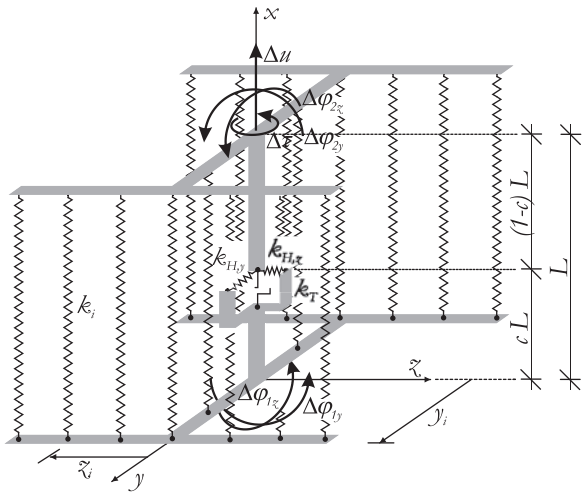

Fig. 5.3 3D multiple-vertical-line-element model (MVLEM-FD-3D)

Most of the available versions of MVLEM proposed by other researchers are 2-D elements. In 2005, the research group at the University of Ljubljana developed, for the first time, a 3D version of this element MVLEM-FD-3D (Fig. 5.3).

The models, presented above, were successfully used in several benchmark studies (CAMUS 3; NEES, San Diego wall – best prediction; E-defense – best prediction). They are appropriate for the predominantly flexural response of walls. If the response is considerably affected by shear, the new version of the element MVLEM-FD-SFI, which is capable of taking into account complex, axial-flexural-shear interactions, is recommended. This new model is described in more detail in Sect. 5.2.2.

5.2.2 *MVLEM-FD-SFI, Which Is Capable of Describing Axial-Shear-Flexural Interaction*

To account for the axial force - bending moment - shear force (N-M-V) interaction, the MVLEM-FD was modified in 2011 (Rejec 2011) and incorporated into the OpenSees program (OpenSees 2011). The modified element is illustrated in Fig. 5.4 (only the 2D element is shown for clearer illustration). In contrast to the basic MVLEM-FD, where only one shear spring is available, in the MVLEM-FD-SFI, each vertical spring is linked to a corresponding shear spring, as had already been proposed by Wallace (Orakcal et al. 2006).

The shear behaviour and the resistance, modelled by the horizontal springs, depend on the mechanisms that transfer shear force over the cracks (Fig. 5.5). The mechanisms consist of: (a) dowel effect of vertical bars, (b) axial resistance of horizontal/shear bars, and (c) interlock of aggregate particles in the crack. The capacity of the latter is highly dependent on the crack's width.

Therefore, each spring is composed of three components (Fig. 5.6): HSA to account for aggregate interlock, HSD to account for the dowel action, and HSS to account for the axial resistance of the shear reinforcement. The current characteristics of each component depend on the deformations/displacements at the effective

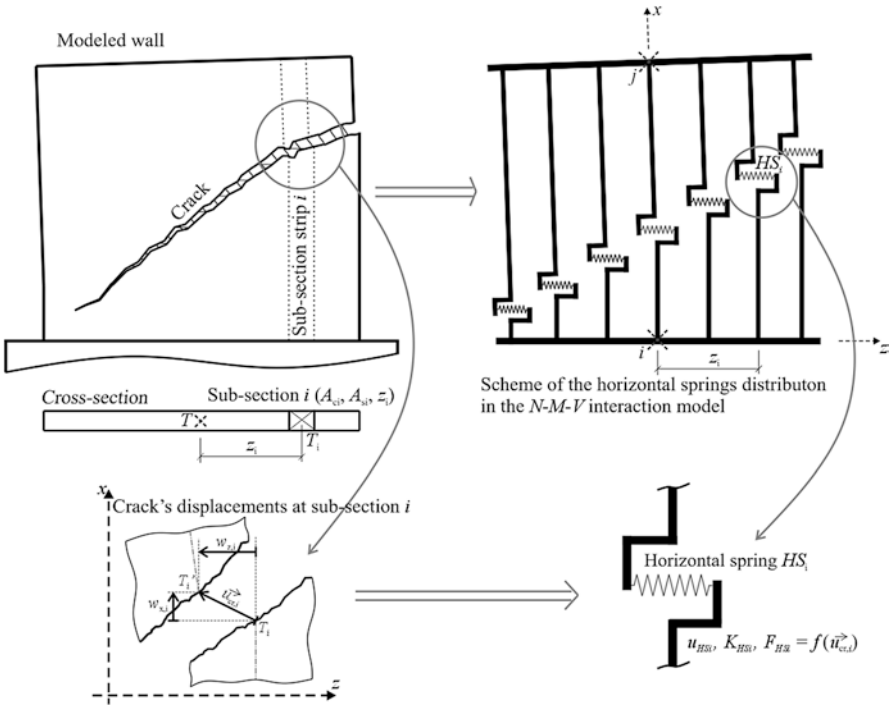

Fig. 5.4 Model accounting for inelastic shear and shear-flexural interaction in structural walls (the vertical springs are not shown)

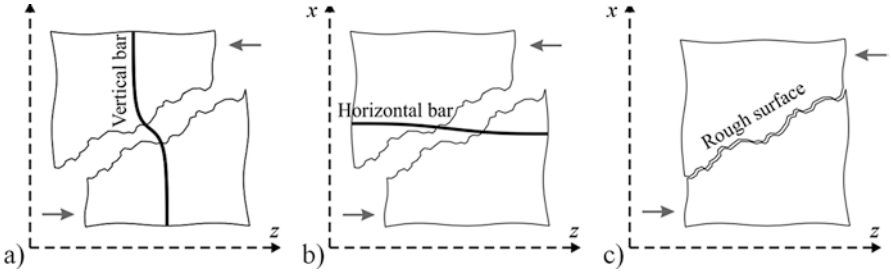

Fig. 5.5 Mechanisms of shear force transfer over a crack: (**a**) dowel effect of vertical reinforcement; (**b**) axial resistance of horizontal/shear reinforcement and (**c**) interlock of aggregate in the crack

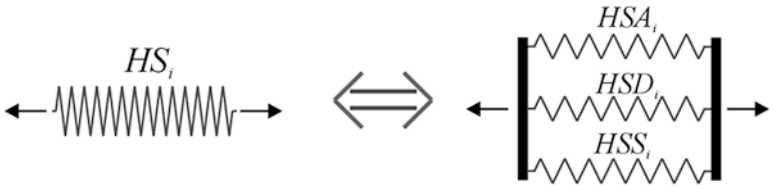

Fig. 5.6 Each horizontal spring is composed of 3 components to account for aggregate interlock (*HSA*), dowel (*HSD*), and shear/horizontal reinforcement (*HSS*) mechanisms

cracks of the element. The displacements are linked to the current displacements of the nodes of the element.

The constitutive relations for the individual springs are based on the semi-empirical relations found in the literature (a detailed description is given in Rejec 2011). Aggregate interlock is modelled by the Lai-Vecchio model (Vecchio and Lai 2004) and dowel action by the expressions proposed by Dulacska (1972) and Vintzeleou and Tassios (1987). The force-displacement relation for HSS springs is based on the bar-slip model proposed by Elwood and Moehle (2003).

For modelling the HSA mechanism, a special *ShearSlip* material was incorporated into OpenSees. However, this is not an exclusive option. An alternative is the hysteretic model, which is typically used for modelling the other two mechanisms (HSD and HSS) contributing to the shear response.

5.3 Experimental Verification of the MVLEM-FD-SFI

5.3.1 A Brief Description of the Experimentally Tested Walls Used to Verify the MVLEM-FD-SFI

The basic MVLEM-FD model was successfully applied in different blindsimulations of large scale shake table tests of RC walls, where the response was predominantly flexural. Initially, the MVLEM-FD-SFI was tested using the results of a large-scale

Table 5.1 Basic features of the selected specimens

Label of the test	Aspect ratio	Level of the axial load	Level of the shear demand	Type of failure	Reference
WSH6	2.02	0.11 $A_g f_c$	3.6 $\sqrt{f_c}$	CB	(Dazio et al. 2009)
RW2	3.00	0.09 $A_g f_c$	2.7 $\sqrt{f_c}$	CB	(Thomsen and Wallace 1995)
S6	1.26	0.05 $A_g f_c$	6.4 $\sqrt{f_c}$	CB, SS	(Vallenas et al. 1979)
R2	2.54	0.00 $A_g f_c$	2.7 $\sqrt{f_c}$	BR	(Oesterle et al. 1975)
RW-A15-P10-S78	1.50	0.10 $A_g f_c$	7.8 $\sqrt{f_c}$	DC, CB, SS	(Tran and Wallace 2012)

Legend: A_g – area of the wall, f_c compression strength of concrete, CB – compression/buckling failure, BR – bar buckling followed by the rupture of the longitudinal bars, DC - significant shear-flexural interaction and diagonal compression failure, SS – shear sliding

shaking table test of RC walls where the predominately shear failure was observed (Fischinger et al. 2017). Since the results of these validations can be found in the literature, and due to space limitations, the results of these simulations are not presented in this paper. Instead, the recent study, which was included into the research schedule of the Wall Institute, is described. Most of the analysed specimens used to test the capabilities of currently available numerical models for RC walls were selected to span the range of important wall characteristics, such as wall aspect ratio (shear span ratio), axial load, shear demand and failure mode.

All specimens were rectangular walls, which were subjected to in-plane flexure, shear and axial loading. The aspect ratio (the ratio of the wall height and the wall width) ranged from 1.5 to 3.0. The shear demand/capacity ratio was less than 1.0, including 3 walls with predominantly flexural behaviour and 2 specimens with a shear-flexural interaction response. Failure modes included tension and compression controlled responses (e.g., bar fracture or concrete crushing and bar buckling, 4 specimens), as well as diagonal compression failure (1 specimen). Axial load ranged from 0% to 10% of the axial wall capacity. The basic features of the selected specimens are reported in Table 5.1. In the last column of the Table 5.1, the references where the complete data about the tests can be found, are provided.

All these walls, with the exception of RW2, were modelled using the MVLEM-FD-SFI model. The wall RW2 was modelled using the basic version of MVLEM-FD. The important N-M-V interaction was observed only in specimens S6 and RW-A15-P10-S78. The second wall is presented in more detail in Fig. 5.7, since it is employed to spotlight the basic features of the MVLEM-FD-SFI model. Modelling of the analysed walls using the MVLEM-FD-SFI element is presented in Sect. 5.3.2. The comparison of selected experimental and numerical data is described in Sect. 5.3.3.

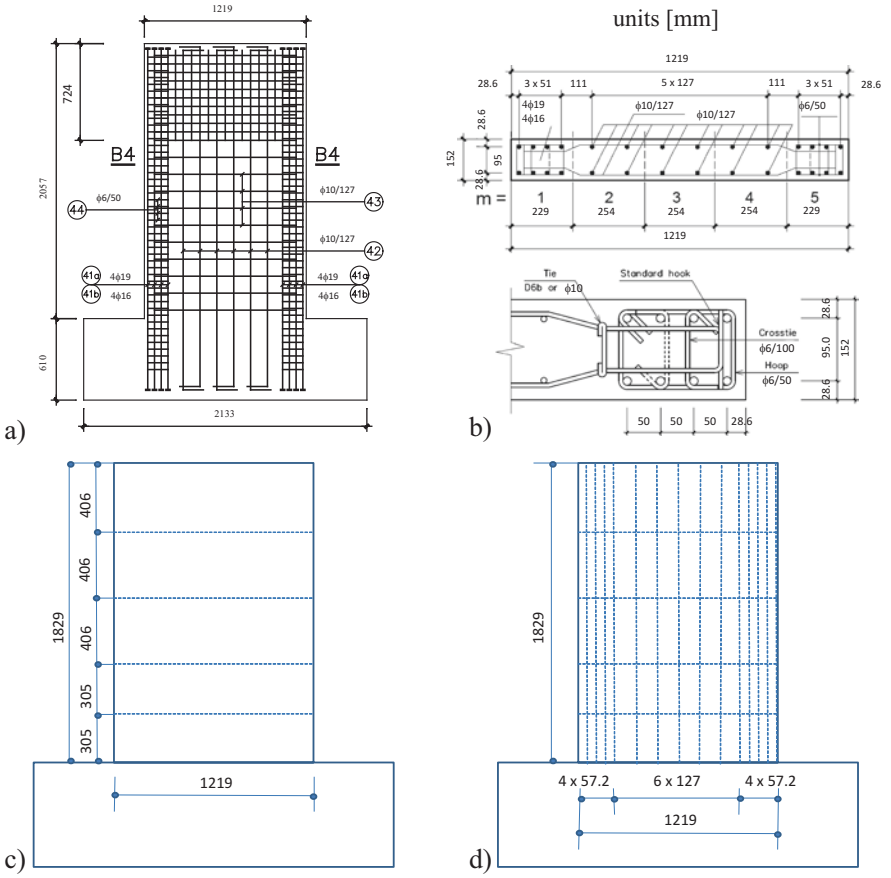

Fig. 5.7 The specimen RW-A15-P10-S78: (**a**) reinforcement layout, (**b**) cross-section and reinforcement details, (**c**) discretization into MVL elements, (**d**) discretization of elements to segments, used to define vertical springs

5.3.2 Modelling of Walls Using MVLEM-FD-SFI

5.3.2.1 Mesh Information

In general, at the bottom of a wall, shorter elements should be provided in order to be able to model the flexural response properly (the abrupt variations of curvatures along the plastic hinge length). The length of subsequent elements is, then, typically increased.

However, in specimen RW-A15-P10-S78, the mesh of elements was defined considering the locations of the devices which were used to measure the displacements in order to allow the consistent comparison of experimental and analytical results.

The wall was modelled with five elements (see Fig. 5.7c). The length was 30.5 cm and 40.6 cm of two bottom and three top elements, respectively.

The elements were divided into a certain number of vertical springs, which were connected by rigid beams at the top and the bottom nodes of the elements (see Fig. 5.1). In wall RW-A15-P10-S78, all elements included 14 vertical springs.

The properties of vertical springs were defined based on the corresponding segments of the wall cross section (see Fig. 5.7d). In general, the cross section of all analysed walls was divided into segments based on the location, number and properties of the longitudinal bars.

The segments in the boundary regions were shorter than other segments in order to define the strength of the wall more precisely. The segments in these regions typically included two to four bars. For example, in wall RW-A15-P10-S78 the boundary regions were divided into four segments (see Fig. 5.7d and b). In each segment, a pair of longitudinal bars was located in its centre.

In general, the length of the segments in the inner parts of tested walls was two to three times larger than that in the boundary regions. It was defined based on the distances between the longitudinal bars. Two to four bars were included in these segments, depending on the geometry of the wall. For example, the inner part of the wall RW-A15-P10-S78 between boundary regions was divided into six segments of equal length (see Fig. 5.7d). Each segment included two longitudinal bars located in its centre.

5.3.2.2 Properties and Modelling of Vertical Springs

In all walls with a considerable amount of reinforcement in boundary regions, the boundary segments were modelled combining two materials (*parallel* material as defined in OpenSees). Material *VertSpringType2* was used to model the concrete part of the segment. The properties of confined concrete were taken into account according to the model proposed by Paulay and Priestley (1992). The Menegotto and Pinto (1973) or the hysteretic model (OpenSees 2016) was used to model longitudinal bars.

The inner segments were modelled taking into account only the *VertSpringType2* material combining the properties of the unconfined concrete and properties of the longitudinal bars.

5.3.2.3 Properties and Modelling of Shear Springs

In the analysis of specimens RW-A15-P10-S78 and S6, all mechanisms which influence the shear response (HSA, HSD, HSS) were modelled by means of the *Hysteretic* model (see the manual of the OpenSees program system). The constitutive relations for the individual springs were defined according to the semiempirical models proposed in the literature (see Sect. 5.2.1). The properties of the *Hysteretic* model were selected based on the typical shapes of hysteretic loops, reported in the literature.

Typical hysteretic loops corresponding to different shear mechanisms are presented in Sect. 5.3.3.2, for the example of the specimen RW-A15-P10-S78.

5.3.2.4 Load Application

Prior to the cyclic analysis of the specimens, a vertical force was applied at the top of the walls. Subsequently, the cyclic analysis was performed by imposing the displacements at the top of the wall in accordance with the reported test schedules. For example, in specimen RW-A15-P10-S78, the reverse cyclic lateral drifts were applied under displacement control. The first drift level to be applied was 0.1%, followed by 0.25%. Then, the drift level was increased up to 1% in 0.25% increments. After that, the drift was increased in 0.5% increments up to 3%. The loading protocol is presented in Fig. 5.8a.

In all analysed walls, the corresponding horizontal load pattern consisted of one horizontal force at the top of the wall. The exception was specimen S6, which represented the bottom three stories of the seven-story wall. Consequently, the load pattern was more complex. It consisted of three horizontal forces applied at the top of each story and the bending moment applied at the top of the tested specimen. These forces were expressed in proportion to the total lateral force, corresponding to the applied displacement at the top of the wall. The load pattern and the loading protocol of wall S6 is presented in Fig. 5.8b and c, respectively.

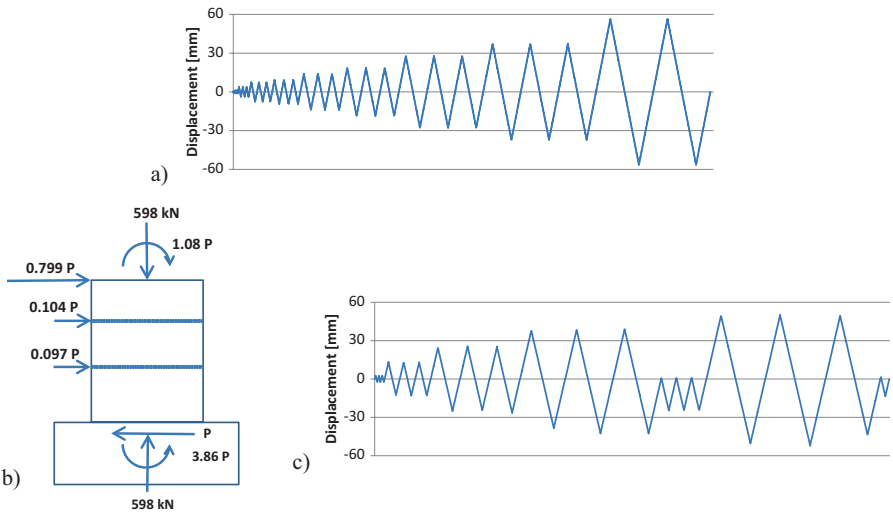

Fig. 5.8: (**a**) Displacements imposed at the top of the wall RW-A15-P10-S78, (**b**) Load pattern of the specimen S6 (horizontal forces and the moment are expressed in proportion to the total shear force at the bottom of the wall), (**c**) Horizontal displacements applied at the top of the wall S6

5.3.3 *Comparison of Analytical and Experimental Results*

5.3.3.1 Global Response Parameters

The MVLEM-FD-SFI was tested evaluating different aspects of the response. In Fig. 5.9 experimentally measured and analytically defined lateral load versus top displacement relationships for specimens RW-A15-P10-S78 and S6 are presented. Taking into account the complexity of the response, which was considerably affected by the N-M-V interaction, the analytical estimation of the global response was quite good.

In general, the strength, as well as the stiffness, of both walls were evaluated with good accuracy throughout both tests. The only exception was the initial stiffness,

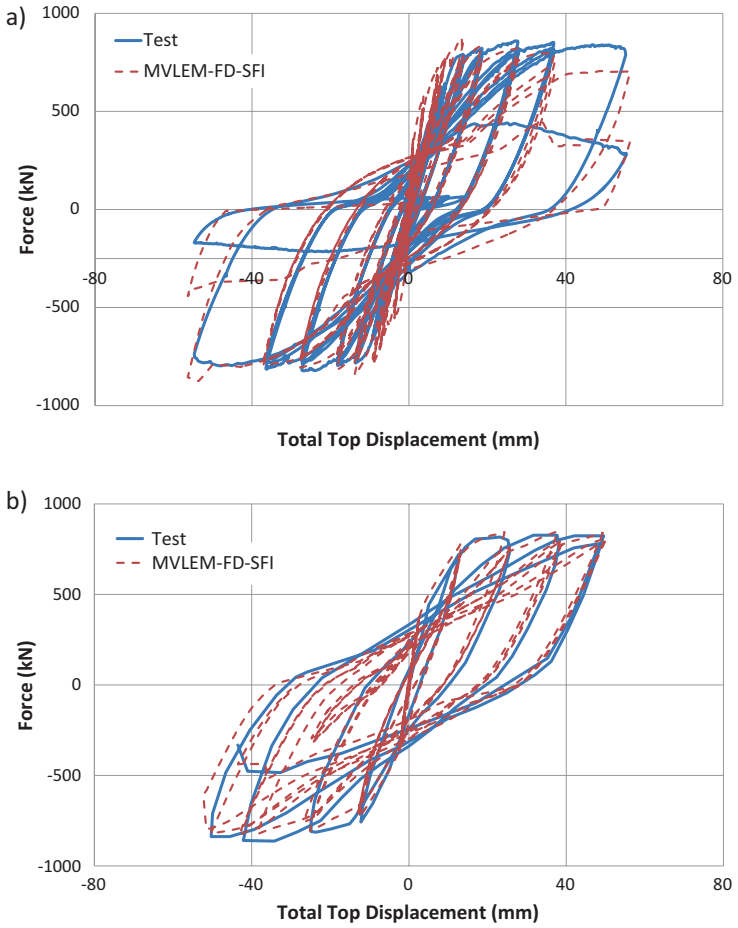

Fig. 5.9 Lateral load – top displacement relationships: (**a**) specimen RW-A15-P10-S78, (**b**) specimen S6

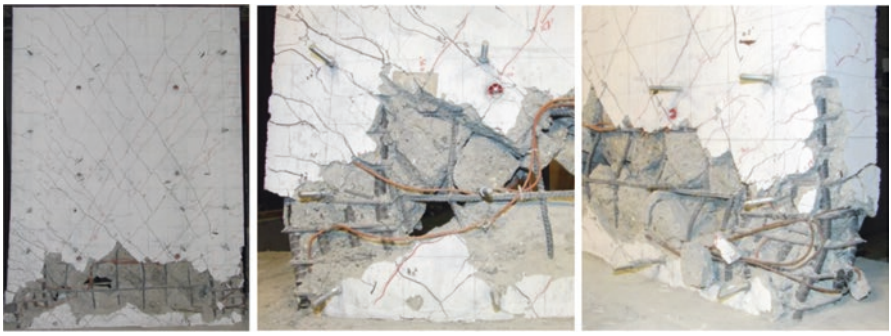

Fig. 5.10 Damage of the specimen RW-A15-P10-S78 after the test (Tran and Wallace 2012)

which was overestimated. This confirmed the previous observations of the authors (e.g. Fischinger et al. 2017), who found that the initial stiffness in the majority of the experiments is typically reduced compared to the stiffness corresponding to the gross cross-sectional properties of the specimens.

During the final cycles of the tests, global buckling of the longitudinal bars in the boundary regions of both walls was observed. The central part of the specimen RW-A15-P10-S78 between boundary regions failed due to shear sliding (see Fig. 5.10). Buckling of the boundary longitudinal bars and sliding of the central part of the wall considerably reduced the shear strength of the wall (see Figs. 5.9a and 5.11a). The analysis revealed that the shear strength was degraded mainly due to the considerable deterioration of the dowel mechanism (see next subsection).

The MVLEM-FD-SFI model estimated the shear, as well as the flexural, response quite well in all cycles of the test. This is evident from Fig. 5.11a and b, where the relationship between the shear force and top shear and top flexural displacements are presented, respectively. The top shear displacements were calculated by summing the shear displacements of single elements that were used to model the wall (note that the programme code includes an option to report the shear displacements in each element). The flexural displacements were obtained by subtracting the shear displacements from the total displacements.

The element also captured well the horizontal displacements at different heights of the wall. The comparison of measured and calculated displacements along wall RW-A15-P10-S78 corresponding to the 0.75%, 1.5% and 3% drift are presented in Fig. 5.12.

The shear, as well as the flexural displacement, profiles coincided with the measurements quite well (Fig. 5.13). The shear and flexural displacements were calculated in the same manner as explained before in the case of the top shear and flexural displacements.

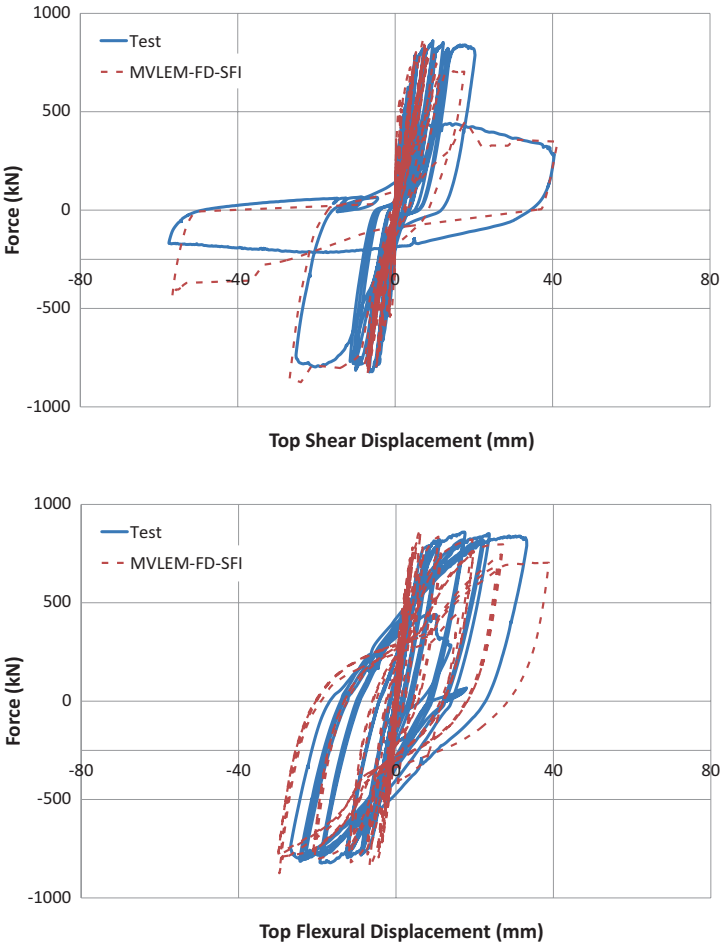

Fig. 5.11 (**a**) Shear and (**b**) Flexural response of specimen RW-A15-P10-S78

5.3.3.2 Components of the Shear Resistance Mechanism

At the beginning, the shear response of the wall was predominantly influenced by the aggregate interlock spring (HSA). The properties of this spring considerably influenced the initial stiffness of the wall, as well as the cracking force. An example of the HSA force-displacement response is presented in Fig. 5.14a. It corresponds to the shear spring linked to the outer vertical segment of the wall RW-A15-P10-S78.

When the HSA mechanism was deteriorated, the shear response was predominantly influenced by the dowel (HSD) and horizontal reinforcement (HSS) mechanisms. In walls similar to RW-A15-P10-S78 and S6, which include a relatively large amount of longitudinal reinforcement (particularly in the boundary regions), the

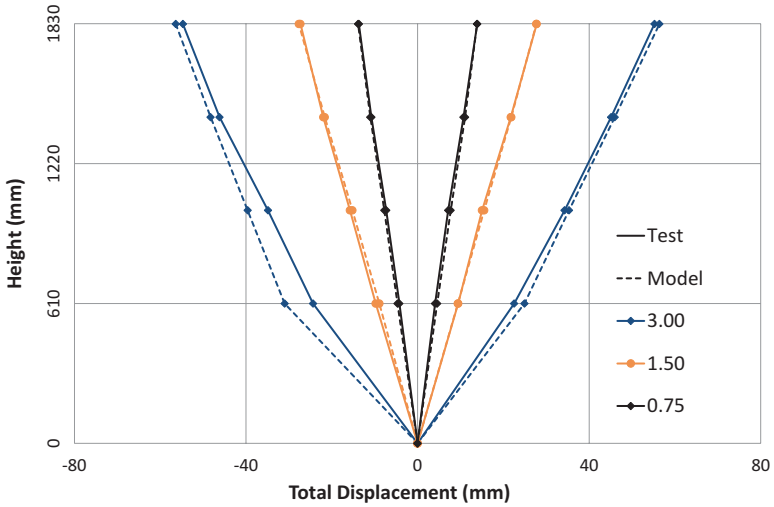

Fig. 5.12 Total horizontal displacements at different heights of the wall RW-A15-P10-S78

shear response after cracking is predominantly influenced by the HSD mechanism. The influence of the shear reinforcement and the HSS mechanism are less important in such structures. This is evident from Fig. 5.14, where the HSD and HSS force-displacement responses of the shear spring linked to the outer vertical segment of the wall RW-A15-P10-S78 are presented. The maximum force contributed by HSD was more than 15 times larger than that corresponding to the HSS mechanism. Consequently, the shear strength of the wall RW-A15-P10-S78 was considerably reduced when the HSD mechanism deteriorated. In general, the role of the HSD mechanism is less important in lightly reinforced walls.

5.4 Conclusions

Recent earthquakes have clearly demonstrated that many key mechanisms of the seismic response of RC structural walls are still not adequately understood. The NSF SAVI Wall Institute has been organized in order to study different aspects of their response. The University of Ljubljana has been primarily involved in analytical studies of different types of walls, using its own, recently developed MVLEM-FD-SFI element. The basic features of this element are presented in this paper. The element has been evaluated by the range of experiments selected within the Wall Institute as case studies. It has been found that the proposed element can describe complex, axial-flexural-shear interactions and can capture all important mechanisms of the global response reasonably well. This is one of the few models than can describe the significant deterioration of the strength of RC walls due to the buckling of the longitudinal bars and associated significant degradation of different types of shear mechanism.

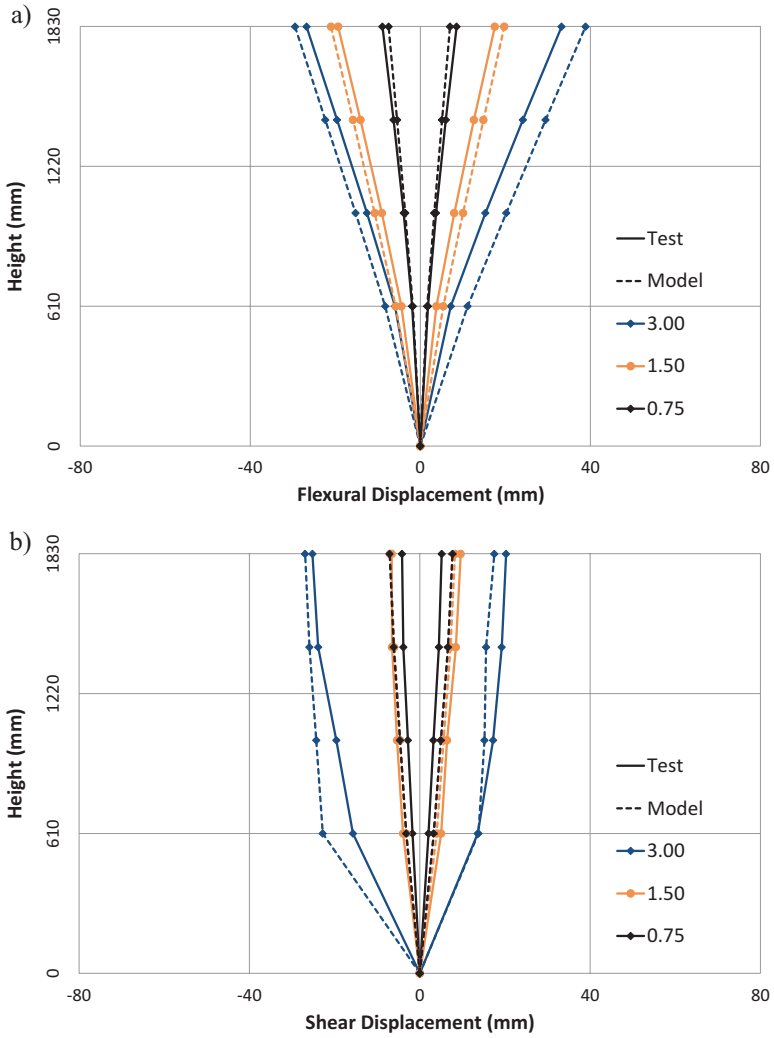

Fig. 5.13 (**a**) Flexural and (**b**) Shear horizontal displacements along the wall RW-A15-P10-S78

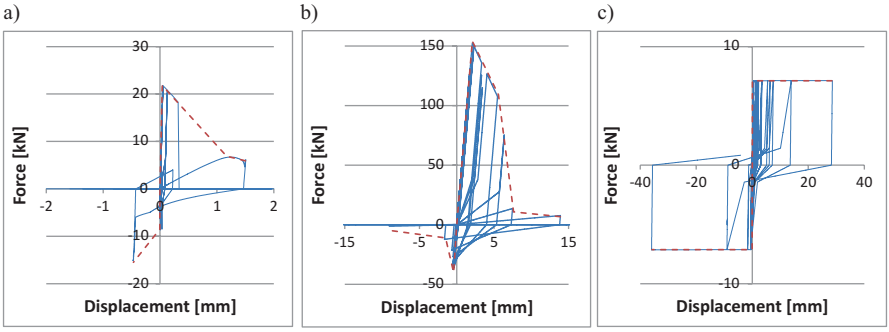

Fig. 5.14 Different shear mechanisms corresponding to the outer shear spring of specimen RW-A15-P10-S78: (**a**) HSA, (**b**) HSD, and (**c**) HSS

Acknowledgements The MVLEM-FD-SFI element was developed as part of the PhD dissertation work of Klemen Rejec, which was funded by the Slovenian National Research Agency.

References

AASHTO (2004) AASHTO LRFD, Bridge design specifications and commentary, 3rd edn. American Association of State Highway Transportation Officials, Washington, DC, 1264 pp

ACI (2005) ACI Committee 318, Building Code Requirements for Structural Concrete (ACI 318–05) and Commentary (318R-05), American Concrete Institute, Farmington Hills, Mich., 2005, 430 pp

Bentz EC, Vecchio FJ, Collins MP (2006) Simplified modified compression field theory for calculating shear strength of reinforced concrete elements. ACI Struct J 103(6):614–624

CEN (2004) EN 1992–1-1:2004 Eurocode 2. Design of concrete structures. Part 1: general rules and rules for buildings, 230 pp

CSA (2004) CSA Committee A23.3, Design of Concrete Structures (CSA A23.3–04). Canadian Standards Association, Mississauga, p 214

Dazio A, Beyer K, Bachmann H (2009) Quasi-static cyclic tests and plastic hinge analysis of RC structural walls. Eng Struct 31:1556–1571

Dulacska H (1972) Dowel action of reinforcement crossing cracks in concrete. ACI Struct J 69(12):754–757

Elwood KJ, Moehle JP (2003) Shake table tests and analytical studies on the gravity load collapse of reinforced concrete frames, PEER Report 2003/01. University of California, Berkeley

Fischinger M, Kante P, Isakovic T (2017) Shake-table response of a coupled RC wall with thin T-shaped piers. Accepted for publication in ASCE Structural Journal

JSCE (1986) JSCE, Specification for design and construction of concrete structures: design, JSCE Standard, Part 1. Japan Society of Civil Engineers, Tokyo

Kabeyasawa T, Shiohara H, Otani S, Aoyama H (1983) Analysis of the full-scale seven-story reinforced concrete test structure. J Fac Eng, University of Tokyo, 431–478

Menegotto M, Pinto PE (1973) Method of analysis of cyclically loaded RC plane frames including changes in geometry and non-elastic behavior of elements under normal force and bending. Preliminary Report IABSE, Vol 13

Oesterle RG, Fiorato AE, Johal LS, Carpenter JE, Russell HG, Corley WG (1975) Earthquake resistant structural walls – tests of isolated walls. Report NSF Grant No. GI-43880, PCA R/D Ser. 1571, Portland Cement Association, Illinois, USA

OpenSees (2011) Open system for earthquake engineering simulation, version 1.6.0, compiled at University of Ljubljana, Faculty of Civil and Geodetic Engineering

OpenSees (2016) Open system for earthquake engineering simulation, User Command-Language Manual, ver 2.5.0. http://opensees.berkeley.edu/wiki/index.php/Command_Manual. Last access Nov 2016

Orakcal K, Massone LM, Wallace JW (2006) Analytical modeling of reinforced concrete walls for predicting flexural and coupled shear-flexural Responses, PEER Report 2006/07. University of California, Berkeley

Paulay T, Priestley MJN (1992) Seismic design of reinforced concrete and masonry buildings. A Wiley Interscience Publication, John Wiley & Sons, New York

Rejec K (2011) Inelastic shear behaviour of RC structural walls under seismic conditions. Dissertation, University of Ljubljana

Thomsen JH, Wallace JW (1995) Displacement-Based Design of RC Structural Walls: An Experimental Investigation of Walls with Rectangular and T-shaped Cross-sections, Report No. CU/CEE-95/06, Department of Civil Engineering, Clarkson University, Potsdam, New York, USA

Tran TA, Wallace JW (2012) Experimental study of nonlinear flexural and shear deformations of reinforced concrete structural walls. In: Proceedings of the 15th world conference on earthquake engineering, Lisbon, Portugal. 3913

Vallenas JM, Bertero VV, Popov EP (1979) Hysteretic behavior of reinforced concrete structural walls, Report No. UCB/EERC-79/29, EERI, College of Engineering, UC Berkeley, Berkeley, USA

Vecchio FJ, Collins MP (1986) The modified compression-field theory for reinforced concrete elements subjected to shear. ACI J 83-22:219–231

Vecchio FJ, Lai D (2004) Crack shear-slip in reinforced concrete elements. J Adv Concr Technol 2(3):289–300

Vintzeleou EN, Tassios TP (1987) Behavior of dowels under cyclic deformations. ACI J 84(1):18–30

Vulcano A, Bertero VV, Caloti V (1989) Analytical modeling of R/C structural walls. In: Proceedings of the 9th WCEE, Tokyo-Kyoto, Maruzen, 6, 41–46

Wallace JW (2016) NSF SAVI Wall Institute - Virtual International Institute for Performance Assessment of Structural Wall Systems. http://apedneault4.wixsite.com/wall-institute. Last access Nov 2016

Chapter 6
Critical Response of Elastic-Plastic Structures to Near-Fault Ground Motions and Its Application to Base-Isolated Building Structures

Izuru Takewaki, Ryo Taniguchi, and Kotaro Kojima

Abstract The earthquake response of an elastic-plastic structure to near-fault ground motions can be well represented by the response to a double impulse or a triple impulse with the equivalent magnitude. This is based on the fact that the main part of most near-fault ground motions consists of a few-cycle, nearly sinusoidal waves, transformable into a double impulse or a triple impulse, and such waves govern the maximum response. It is shown that, when a double impulse or a triple impulse is adopted as an input, the earthquake response is composed of a free vibration component only. This enables the closed-form expression of the critical elastic-plastic response maximizing the response with respect to the impulse timing. In order to demonstrate the practical applicability of the proposed theory, a base-isolated building is employed, and an approximate and simple expression of the maximum plastic deformation at the isolation story is derived.

Keywords Critical response • Elastic-plastic response • Near-fault ground motion • Base-isolated building

6.1 Introduction

According to the development of earthquake ground motion recording techniques, various properties of ground motions have been disclosed. For example, the characteristics and effects of near-fault ground motions have been investigated extensively (Bertero et al. 1978, Singh 1984, Hall et al. 1995, Iwan 1997, Sasani and Bertero

I. Takewaki (✉) • R. Taniguchi • K. Kojima
Department of Architecture and Architectural Engineering, Kyoto University, Kyoto 615-8540, Japan
e-mail: takewaki@archi.kyoto-u.ac.jp; fm-rtaniguchi@archi.kyoto-u.ac.jp; fm-kojima@archi.kyoto-u.ac.jp

R. Rupakhety, S. Ólafsson (eds.), *Earthquake Engineering and Structural Dynamics in Memory of Ragnar Sigbjörnsson*, Geotechnical, Geological and Earthquake Engineering 44, https://doi.org/10.1007/978-3-319-62099-2_6

2000, Mavroeidis et al. 2004, Makris and Black 2004, Alavi and Krawinkler 2004, Kalkan and Kunnath 2006, Rupakhety and Sigbjörnsson 2011, Vassiliou et al. 2013, Vafaei and Eskandari 2015, Khaloo et al. 2015). Fling step and forward directivity are widely recognized, special keywords to characterize such near-fault ground motions (Mavroeidis and Papageorgiou 2003, Bray and Rodriguez-Marek 2004, Makris and Black 2004, Kalkan and Kunnath 2006, Mukhopadhyay and Gupta 2013a, b, Hayden et al. 2014, Yang and Zhou 2014). Especially after the Northridge earthquake in 1994, Hyogoken-Nanbu (Kobe) earthquake in 1995 and Chi-Chi (Taiwan) earthquake in 1999, a strong interest has been taken by many earthquake structural engineers.

The fling-step and forward-directivity inputs have been characterized by two or three wavelets. For this class of ground motions, much useful research has been conducted. Mavroeidis and Papageorgiou (2003) investigated the characteristics of this class of ground motion in detail and proposed some simple models. Makris and Black (2004) examined the effects of two or three wavelets on structural inelastic responses. Kalkan and Kunnath (2006) introduced two or three simple sinusoidal wavelets based on the research of Sasani and Bertero (2000) and investigated the influence of near-fault ground motions on tall buildings. Takewaki et al. (2012) employed a sinusoidal wave for pulse-type waves.

Most of the previous works on near-fault ground motions deal with the elastic response, except Makris and Black (2004), Kalkan and Kunnath (2006), Mylonakis and Voyagaki (2006), Moustafa et al. (2010), Vassiliou et al. (2013), Khaloo et al. (2015), because the number of parameters (e.g. duration and amplitude of pulse, ratio of pulse frequency to structure natural frequency, change of equivalent natural frequency for the increased input level) to be considered on this topic is high and the computation of the elastic-plastic responses is quite complicated.

Kojima and Takewaki (2015a, b) recently introduced double or triple impulses as representatives of near-fault ground motions and derived some closed-form solutions of the critical response of SDOF (single-degree-of-freedom) elastic-plastic structures under such double or triple impulses. The amplitude of the double impulse was modulated so that its maximum Fourier amplitude coincides with that of the corresponding one-cycle sinusoidal input (Kojima and Takewaki 2015a). It was shown that, since only the free vibration appears under such double impulse input, the energy balance approach plays a simple and key role in the derivation of the closed-form solution of a complicated elastic-plastic response. The extension of the theory for the fling-step, near-fault ground motion to the forward-directivity, near-fault ground motion was made by Kojima and Takewaki (2015b). Furthermore, Kojima and Takewaki (2015c) extended their approach to long-duration ground motions. This approach is based on an innovative concept of transformation of input and unchanged treatment of an elastic-plastic structure itself as compared to the conventional, equivalent linearization method for elastic-plastic structures and has overcome a difficulty encountered for elastic-perfectly plastic structures since 1960 (Caughey 1960, Iwan 1961).

In the earthquake-resistant design of structures, resonance is a key phenomenon, and it has been investigated extensively. While the resonant frequency maximizing

the response must be computed for a specified input level by changing the excitation frequency in a parametric manner for the sinusoidal input (Caughey 1960, Iwan 1961), no iteration is needed in the method for the double impulse (Kojima and Takewaki 2015a, b, c). This is because the resonant equivalent frequency can be derived directly without the repetitive procedure. In the double impulse, the analysis can be done without the concept of input frequency (timing of impulses) before the second impulse. The resonance can be proved by using the energy balance and the timing of the second impulse can be characterized as the time with zero restoring force. The maximum elastic-plastic response after an impulse can be obtained by equating the initial kinetic energy computed by the initial velocity to the sum of hysteretic and elastic strain energies. It should be pointed out that not only the critical response (Drenick 1970, Takewaki 2007) but also the critical resonant frequency can be obtained automatically for the increasing input level of the double impulse.

The double impulse is introduced here as a substitute of the fling-step, near-fault ground motion and a critical elastic-plastic response of a two-degree-of-freedom (2DOF) building structure model under the critical double impulse is evaluated. The input of impulse is expressed by the instantaneous change of velocities of the structural masses. As pointed out before, since only the free vibration appears under such double impulse, the energy balance approach plays an important role in the derivation of the solution of a complicated elastic-plastic critical response, as in Kojima and Takewaki (2015a, b, c). It has been shown that the critical timing of the double impulse is characterized by the timing of the second impulse at the zero story shear force in the first story (Taniguchi et al. 2016). This criticality is also characterized by the maximization of the sum of the momenta of all masses. This timing certainly guarantees the maximum energy input by the second impulse which causes the maximum plastic deformation after the second impulse. Because the response of 2DOF elastic-plastic building structures is quite complicated due to the phase difference between two masses compared to SDOF models for which a closed-form critical response can be derived, the upper bound of the critical response has been introduced in the reference (Taniguchi et al. 2016) by using the convex model (Ben-Haim and Elishakoff 1990, Ben-Haim et al. 1996). The accuracy of the derived upper bound has been discussed in comparison with the actual response analysis result to the double impulse. The validity and accuracy of the proposed theory for the double impulse have also been investigated through comparison with the response analysis result to the corresponding one-cycle sinusoidal input as a representative of the fling-step, near-fault ground motion. In this paper, the extension of the proposed theory for 2DOF models into base-isolated buildings is made through the simplification of the model into SDOF models.

Figure 6.1 shows the Rinaldi Station fault-normal component during the Northridge earthquake in 1994 and the modeling of the main part into a one-cycle sine wave (Kalkan and Kunnath 2006, Khaloo et al. 2015). The one-cycle sine wave will be further transformed into a double impulse, as explained in the following section.

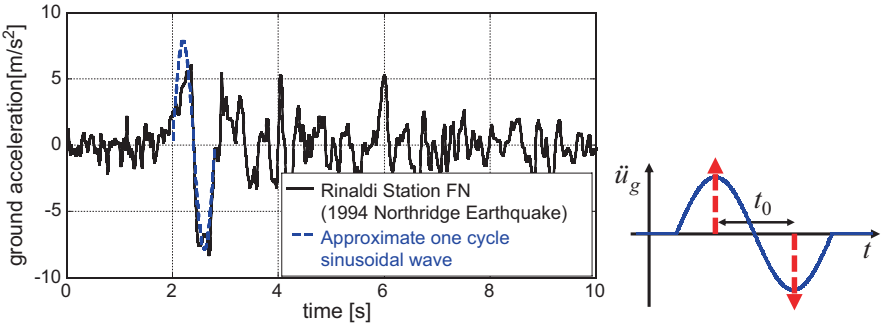

Fig. 6.1 Rinaldi Station fault-normal component during the Northridge earthquake in 1994 and modeling of main part into a one-cycle sine wave and double impulse

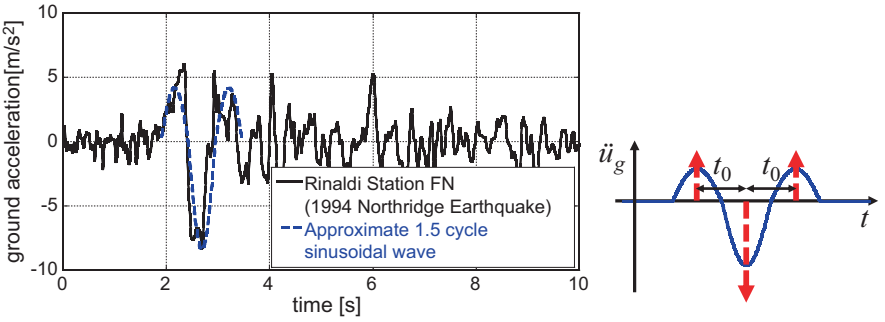

Fig. 6.2 Rinaldi Station fault-normal component during the Northridge earthquake in 1994 and modeling of main part into a one and a half-cycle sine wave and triple impulse

Figure 6.2 presents the same Rinaldi Station fault-normal component during the Northridge earthquake in 1994 and the modeling of the main part into a one and a half-cycle sine wave (Kalkan and Kunnath 2006, Khaloo et al. 2015). The one and a half-cycle sine acceleration wave implies the one-cycle sine velocity wave and will be further transformed into a triple impulse explained later.

6.2 Double Impulse Input

Near-fault ground motions exhibit some peculiar characteristics which are related to the fault directivity, the Doppler effect, the velocity of fault rupture, etc. The fault-parallel component is called the fling-step input and can be represented by a one-cycle sinusoidal wave. On the other hand, the fault-normal component is called the forward-directivity input and can be expressed by a series of three sinusoidal wavelets (Kojima and Takewaki 2015a) (see Fig. 6.3). It has further been pointed out (Makris and Black 2004) that a one-cycle sinusoidal wave can also express the

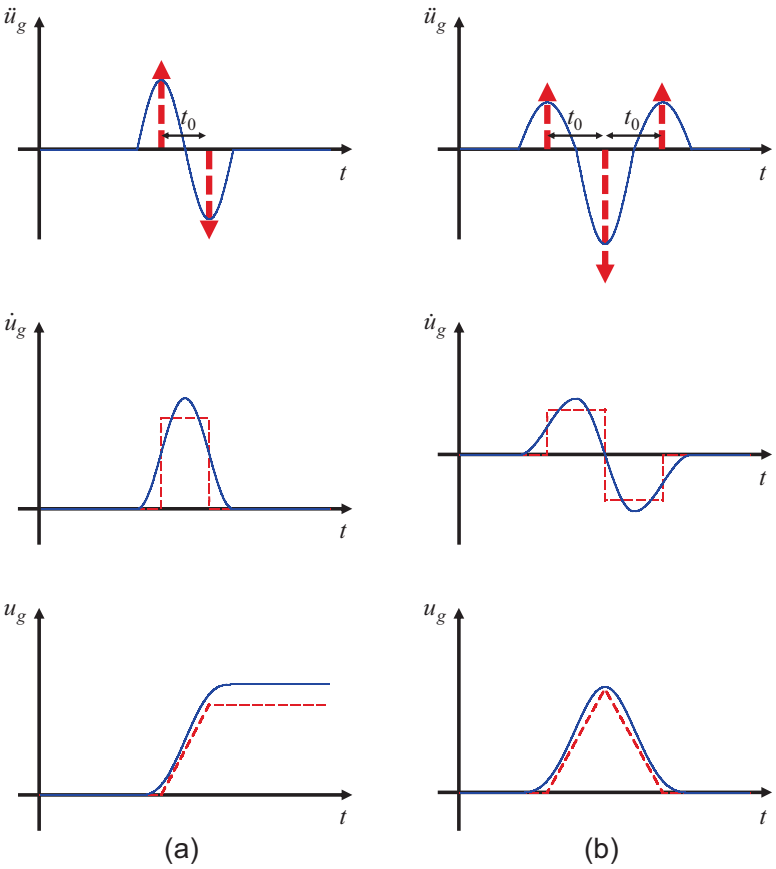

Fig. 6.3 Two simple wavelets and their transformation into double and triple impulses: (**a**) Fling-step input and double impulse, (**b**) Forward-directivity input and triple impulse (Kojima and Takewaki 2015a)

forward-directivity input in some cases. This section is aimed at simplifying the typical near-fault ground motions by a double impulse (Kojima and Takewaki 2015a).

Consider a double impulse ground acceleration $\ddot{u}_g(t)$, as shown in Fig. 6.3a, expressed by

$$\ddot{u}_g(t) = V\delta(t) - V\delta(t - t_0) \tag{6.1}$$

where V is the given velocity and t_0 is the time interval between two impulses. It should be remarked that the area under the acceleration pulse (V in Eq. 6.1) is defined by Bertero (Anderson and Bertero 1987) as incremental ground velocity in order to distinguish between the net increment of the ground velocity and the peak

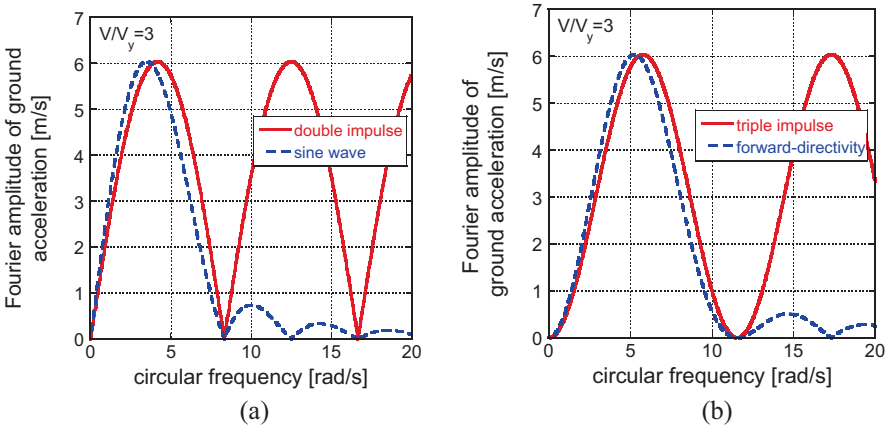

Fig. 6.4 Adjustment of input level of double or triple impulse to the corresponding one-cycle or one and a half-cycle sine wave based on Fourier amplitude equivalence: (**a**) Double impulse, (**b**) Triple impulse (Kojima and Takewaki 2015a, b)

ground velocity. The time derivative is denoted by an overdot. The comparison with the corresponding one-cycle sinusoidal wave as a representative main part of the near-fault ground motion is plotted in Fig. 6.1a (Mavroeidis and Papageorgiou 2003, Makris and Black 2004, Kalkan and Kunnath 2006, Kojima and Takewaki 2015a). The corresponding velocity and displacement of such double impulse and sinusoidal wave are also plotted in Fig. 6.3a. As pointed out earlier, the double impulse is a good approximation of the corresponding sinusoidal wave even in the form of velocity and displacement on the condition that the correspondence of the maximum Fourier amplitude is guaranteed. Figure 6.4 shows the adjustment of the input level of the double or triple impulse to the corresponding one-cycle or one and a half-cycle sine wave based on Fourier amplitude equivalence ((a) double impulse, (b) triple impulse). It may be interesting to note that, since the Fourier amplitude is related to the velocity of ground motions (or velocity response spectrum), this correspondence is meaningful. The Fourier transform of $\ddot{u}_g(t)$ of the double impulse input can be expressed as

$$\begin{aligned}\ddot{U}_g(\omega) &= \int_{-\infty}^{\infty}\left\{V\delta(t)-V\delta(t-t_0)\right\}e^{-\mathrm{i}\omega t}dt \\ &= \int_{-\infty}^{\infty}\left\{V\delta(t)e^{-\mathrm{i}\omega t}-V\delta(t-t_0)e^{-\mathrm{i}\omega t_0}e^{-\mathrm{i}\omega(t-t_0)}\right\}dt \\ &= V\left(1-e^{-\mathrm{i}\omega t_0}\right)\end{aligned} \tag{6.2}$$

Consider an elastic-perfectly plastic SDOF model. Let V_y denote the product of the natural circular frequency ω_1 and the yield deformation d_y of the SDOF model. This quantity indicates the input velocity giving just the yield deformation after the

first impulse. The closed-form expression of the maximum deformation $u_{\max}^{(1)}$ after the first impulse and $u_{\max}^{(2)}$ after the second impulse can be derived as follows (Kojima and Takewaki 2015a, Kanno and Takewaki 2016).

$$u_{\max}^{(1)} = \begin{cases} \dfrac{d_y}{V_y} V & \left(0 < V < V_y\right) \\ \dfrac{1}{2}\dfrac{d_y}{V_y^2} V^2 + \dfrac{1}{2} d_y & \left(V \geq V_y\right) \end{cases} \tag{6.3}$$

$$u_{\max}^{(2)} = \begin{cases} 2\dfrac{d_y}{V_y} V & \left(0 < V < \dfrac{1}{2} V_y\right) \\ 2\dfrac{d_y}{V_y^2} V^2 + \dfrac{1}{2} d_y & \left(\dfrac{1}{2} V_y \leq V < V_y\right) \\ \dfrac{d_y}{V_y} V + \dfrac{3}{2} d_y & \left(V \geq V_y\right) \end{cases} \tag{6.4}$$

The maximum deformation defined by $u^c = \max\left\{u_{\max}^{(1)} \quad u_{\max}^{(2)}\right\}$ can then be expressed as

$$u^c = \begin{cases} 2\dfrac{d_y}{V_y} V & \left(0 < V < \dfrac{1}{2} V_y\right) \\ 2\dfrac{d_y}{V_y^2} V^2 + \dfrac{1}{2} d_y & \left(\dfrac{1}{2} V_y \leq V < V_y\right) \\ \dfrac{d_y}{V_y} V + \dfrac{3}{2} d_y & \left(V_y \leq V < \left(\sqrt{3}+1\right) V_y\right) \\ \dfrac{1}{2}\dfrac{d_y}{V_y^2} V^2 + \dfrac{1}{2} d_y & \left(V \geq \left(\sqrt{3}+1\right) V_y\right) \end{cases} \tag{6.5}$$

In this model, the plastic deformation after the second impulse (larger than that after the first impulse) can also be derived as follows (Kojima and Takewaki 2015a). This will be used later.

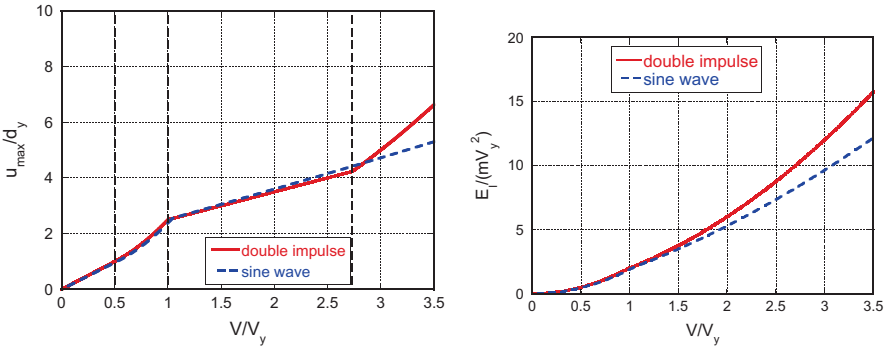

Fig. 6.5 Comparison of double impulse and the corresponding one-cycle sine wave: (**a**) Ductility, (**b**) Earthquake input energy (Kojima and Takewaki 2015a)

$$\frac{d_p^{(2)}}{d_y}\begin{cases} 0 & \left(0 < V < \frac{1}{2}V_y\right) \\ 2\frac{V^2}{V_y^2} - \frac{1}{2} & \left(\frac{1}{2}V_y \le V < V_y\right) \\ \frac{1}{2}\frac{V^2}{V_y^2} + \frac{V}{V_y} & \left(V \ge V_y\right) \end{cases} \tag{6.6}$$

Figure 6.5a presents the correspondence of the maximum deformation responses to the double impulse and the corresponding sinusoidal input adjusted in Fig. 6.4a. On the other hand, Fig. 6.5b shows the comparison of earthquake input energies to both inputs. It can be observed that relatively good correspondence can be observed up to the input level $V/V_y = 3$ in the deformation. In order to guarantee good correspondence in the wide range, the level of the corresponding sinusoidal input is amplified. Figure 6.6 presents the correspondence of the maximum deformation responses to the double impulse and the corresponding amplified sinusoidal inputs (amplification 1.0–1.2 from the level specified in Fig. 6.4a). It can be observed that the amplification factor 1.15 or 1.2 is the best.

Figure 6.7 illustrates the maximum deformation for two recorded ground motions (Rinaldi Station component during the 1994 Northridge earthquake and Kobe University NS component during the 1995 Hyogoken-Nanbu earthquake) and the proposed one by the critical double impulse. Since the recorded ground motion is fixed, the initial velocity V is fixed and V_y (product of the natural circular frequency ω_1 and the yield deformation d_y) is changed here. Because ω_1 is closely related to the resonance condition, d_y is changed principally. This procedure is similar to the well-known elastic-plastic response spectrum developed between 1960–1970 in which the strength is changed for a constant natural period, i.e., stiffness. The solid line is

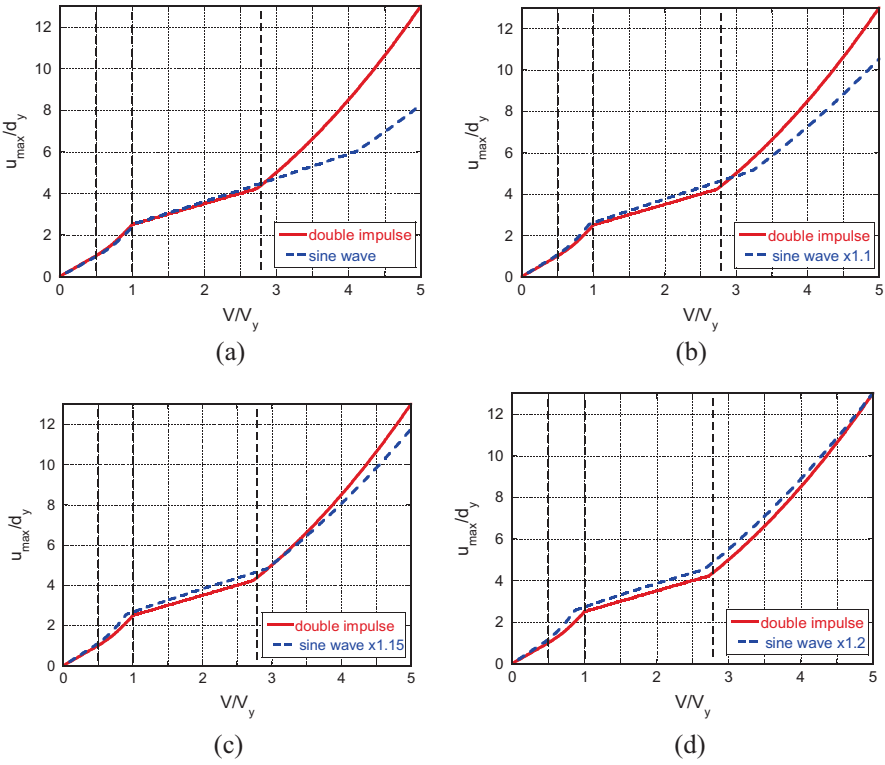

Fig. 6.6 Correspondence of maximum deformation responses to double impulse and amplified sinusoidal inputs (amplification factor α): (**a**) α=1.0, (**b**) α=1.1, (**c**) α=1.15, (d) α=1.2

obtained by changing V_y for the specified V using the method for the double impulse and the dotted line is drawn by conducting an elastic-plastic time-history response analysis on each model with a varied V_y under the recorded ground motion. It can be observed that the result by the proposed method is a fairly good approximate of the recorded pulse-type ground motions.

6.3 Triple Impulse Input

As pointed out in the previous paper (Kojima and Takewaki 2015b), it is well accepted that the fling-step input (fault-parallel) of the near-fault ground motion can be represented by a one-cycle sinusoidal wave and the forward-directivity input (fault-normal) of the near-fault ground motion can be expressed by three wavelets of sinusoidal input (see Fig. 6.3). The previous paper and this paper intend to simplify these typical, near-fault ground motions by double impulse or triple impulse (Kojima and Takewaki 2015b). This is because the double impulse and triple

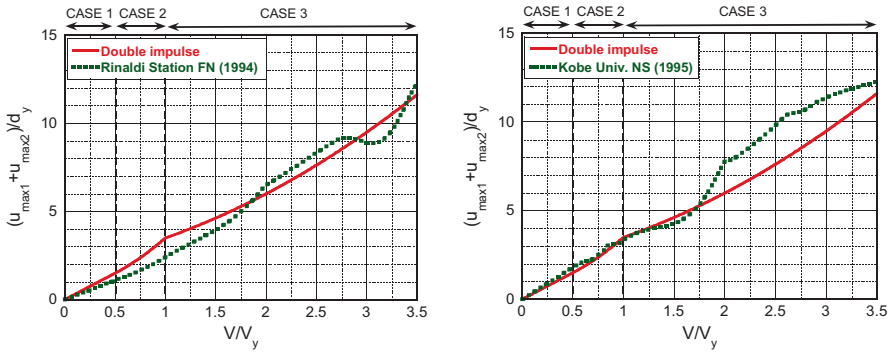

Fig. 6.7 Maximum amplitude of deformation for the recorded ground motions and the proposed one: (**a**) Rinaldi Station fault-normal component, (**b**) Kobe University NS component (Kojima and Takewaki 2016a)

impulse have a simple characteristic and a straightforward expression of response can be expected even for elastic-plastic responses based on a simple energy approach to free vibrations. Furthermore, the double impulse and triple impulse enable us to describe directly the critical timing of impulses (resonant frequency) which is not possible for the sinusoidal and other inputs without a repetitive procedure.

Consider a ground motion acceleration $\ddot{u}_g(t)$ as a triple impulse, as shown in Fig. 6.3b, expressed by

$$\ddot{u}_g(t) = 0.5V\delta(t) - V\delta(t-t_0) + 0.5V\delta(t-2t_0) \tag{6.7}$$

where $0.5V$ is the given initial velocity and t_0 is the time interval among three impulses. The comparison with the corresponding three wavelets of sinusoidal waves as a representative of the forward-directivity input of the near-fault ground motion (Mavroeidis and Papageorgiou 2003, Kalkan and Kunnath 2006) is also plotted in Fig. 6.2. The corresponding velocity and displacement of such a triple impulse and three wavelets of sinusoidal waves are plotted in Fig. 6.3b. The Fourier transform of $\ddot{u}_g(t)$ of the triple impulse input can be derived as

$$\begin{aligned}
\ddot{U}_g(\omega) &= \int_{-\infty}^{\infty} \left\{0.5V\delta(t) - V\delta(t-t_0) + 0.5V\delta(t-2t_0)\right\} e^{-i\omega t} dt \\
&= \int_{-\infty}^{\infty} \left\{0.5V\delta(t)e^{-i\omega t} - V\delta(t-t_0)e^{-i\omega t_0}e^{-i\omega(t-t_0)}\right. \\
&\left. +0.5V\delta(t-2t_0)e^{-i\omega 2t_0}e^{-i\omega(t-2t_0)}\right\} dt \\
&= V\left(0.5 - e^{-i\omega t_0} + 0.5e^{-i\omega 2t_0}\right)
\end{aligned} \tag{6.8}$$

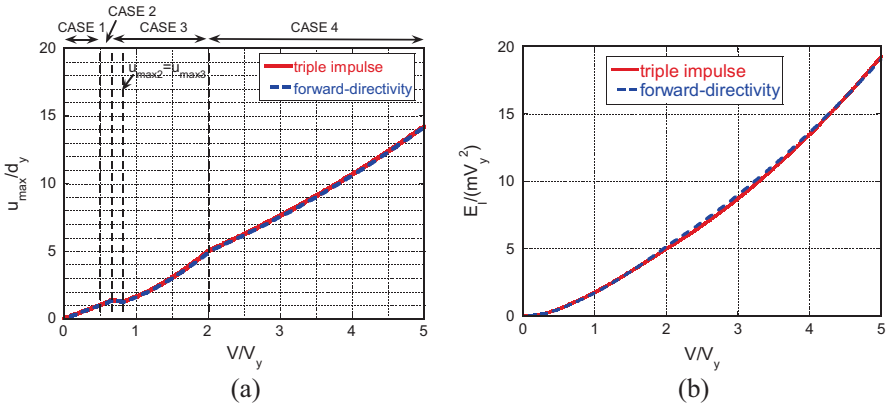

Fig. 6.8 Comparison of triple impulse and the corresponding three wavelets of sinusoidal waves: (**a**) Ductility, (**b**) Earthquake input energy

The closed-form expression of the maximum deformation to the triple impulse can be found in the reference (Kojima and Takewaki 2015b). A somewhat complicated discussion should be made on the effect of the timing of the third impulse on the maximum response because the critical response may be determined for the second impulse.

Figure 6.8a shows the comparison of the deformation ductility under the triple impulse and the corresponding three wavelets of sinusoidal waves (designated as forward-directivity), and Fig. 6.8b presents the comparison of the earthquake input energy under the same input (Kojima and Takewaki 2015b). It can be observed that the response of the triple impulse is a good substitute for that of the forward-directivity input. In order to demonstrate the comparison of time histories under the triple impulse and the forward-directivity input, the comparison for the input level $V/V_y = 3$ is shown in Fig. 6.9 (deformation ductility in Fig. 6.9a and restoring force in Fig. 6.9b). It can be found that a good correspondence exits even in the time histories. Figure 6.10 illustrates the comparison of the restoring force-deformation relation for the input level $V/V_y = 3$.

6.4 2DOF Model

In the case of 2DOF models, the derivation of the critical response to the double impulse becomes very difficult. This is because two masses do not respond in the same phase (see Fig. 6.11). In spite of this difficulty, Taniguchi et al. (2016) showed that the critical timing can be derived as the time when the restoring force in the first story becomes zero (see Fig. 6.12). This property is very important and characterizes the critical excitation of the double impulse to the 2DOF model. Although the critical timing has been made clear, the derivation of the critical response still seems

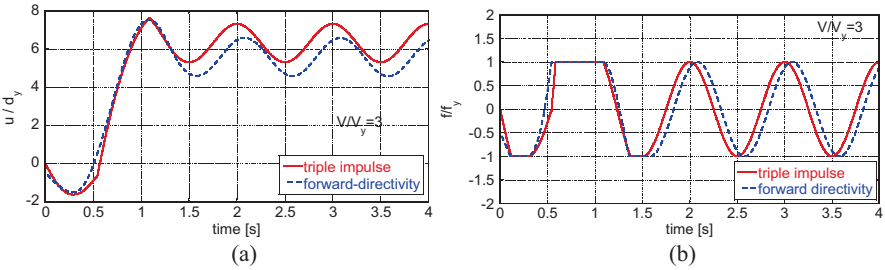

Fig. 6.9 Comparison of response time history under a triple impulse with that under the corresponding three wavelets of sinusoidal waves: (**a**) Normalized deformation, (**b**) Normalized restoring force

Fig. 6.10 Comparison of restoring-force characteristic under a triple impulse with that under the corresponding three wavelets of sinusoidal waves

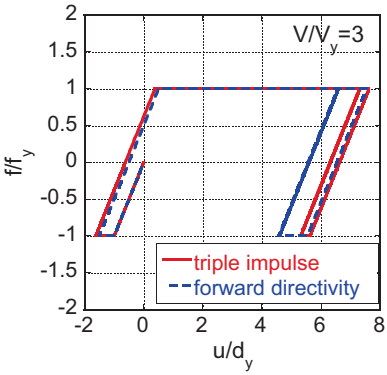

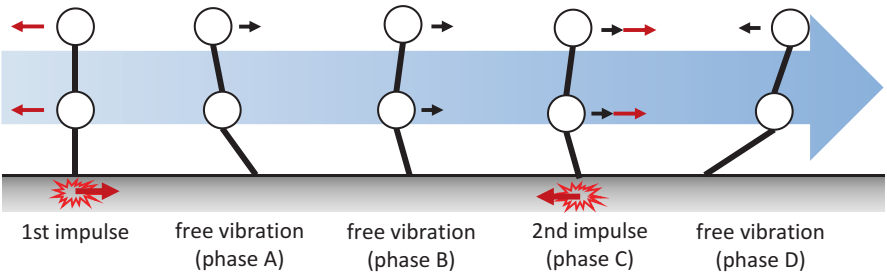

Fig. 6.11 Response process of 2DOF model under a double impulse

difficult. On the other hand, Taniguchi et al. (2016) proposed an upper bound on the critical response by using the convex model (Ben-Haim and Elishakoff 1990, Ben-Haim et al. 1996).

Figure 6.13 illustrates the critical plastic deformation after the second impulse in the first story and their upper and lower bounds (Taniguchi et al. 2016) in which the response of the SDOF system under double impulse and the response of the 2DOF system under the corresponding one-cycle sinusoidal wave are also plotted. The

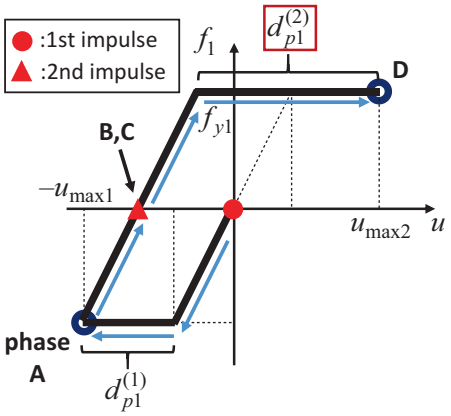

Fig. 6.12 Response process and critical second impulse timing of 2DOF model under a double impulse in restoring-force characteristic

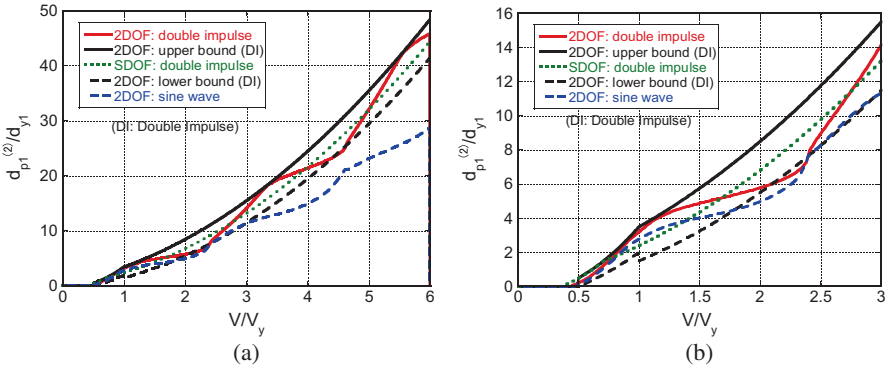

Fig. 6.13 Critical plastic deformation after the second impulse in the first story and their upper and lower bounds together with the upper bound of SDOF system and the response under the corresponding one-cycle sinusoidal wave: (**a**) Comparison up to $V/V_y = 6$, (**b**) Magnified

SDOF system is constructed by using the mass (sum of both masses), the stiffness (the first story stiffness) and the yield deformation (the first-story yield deformation). The definition of V_y in the 2DOF model is different from that for the SDOF model. The detail is shown in the reference (Taniguchi et al. 2016). It can be seen that the actual critical plastic deformation after the second impulse in the first story corresponds fairly well with the response under the corresponding one-cycle sinusoidal wave up to about $V/V_y = 3$. Furthermore, the upper and lower bounds can be bound the actual critical plastic deformation (although the lower bound is approximate due to the uncertain assumption).

Figure 6.14 presents the comparison of the proposed upper bound response with the response to the recorded ground motion (Rinaldi Station FN 1994). In this

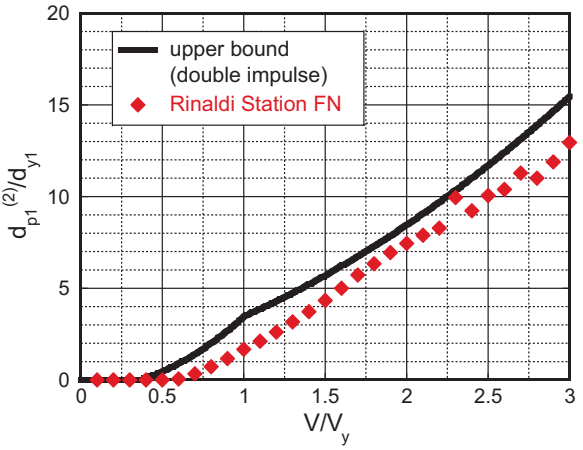

Fig. 6.14 Maximum plastic deformation in the first story of 2DOF model under Rinaldi Station FN component (V_y is varied) and upper bound of plastic deformation in the first story after the second impulse under the corresponding double impulse transformed from Rinaldi Station FN component

figure, the yield deformation has been changed principally. It can be observed that the upper bound derived by Taniguchi et al. (2016) is a tight upper bound except in a smaller range of V/V_y.

6.5 Transformation of 2DOF Model into SDOF Models: Application to Base-Isolated Building

Consider a base-isolated building structure as shown in Fig. 6.15. It is assumed here that the isolators are natural rubbers and hysteretic dampers are used for damping systems. Then, the restoring-force characteristic in the base-isolation story can be modeled by an elastic-perfectly plastic model. This means the negligence of the second slope compared to the initial stiffness. If desired, the positive second slope can be considered. However, the expression of the response may be slightly complicated. Let m_1 and m_2 denote the isolation-story mass and the super-structure mass and let k_1 and k_1 denote the isolation-story stiffness and the super-structure stiffness.

It is often the case that base-isolated building structures are modeled into a simplified model. A 2DOF model is a good, simplified model. However, further simplification into an SDOF model is desirable because a closed-form solution (Kojima and Takewaki 2015a) can be used for the SDOF model under the double impulse.

Consider two SDOF models, i.e. SDOF (a) model and SDOF (b) model under the double impulse. The SDOF (a) model is a model with series springs and ignored base-isolation story mass, and the SDOF (b) model is a model with a rigid super-structure (see Fig. 6.15). Let m_e, k_e and d_{ye} denote the equivalent mass, equivalent stiffness and equivalent yield deformation of the equivalent SDOF model, respectively. For the SDOF (a) model, those equivalent quantities can be expressed as follows.

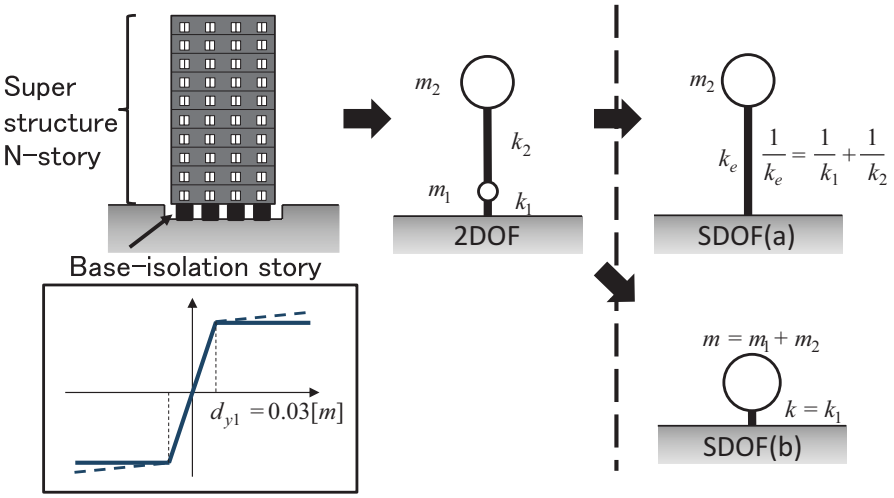

Fig. 6.15 Modeling of base-isolated building into a SDOF model with series springs and ignored base-isolation story mass and SDOF model with a rigid superstructure

$$\begin{aligned} m_e &= m_2 \\ 1/k_e &= 1/k_1 + 1/k_2 \\ f_y &= k_1 d_{y1} = k_e d_{ye} \end{aligned} \tag{6.9}$$

On the other hand, for the SDOF (b) model, those equivalent quantities can be expressed as follows.

$$\begin{aligned} m_e &= m_1 + m_2 \\ k_e &= k_1 \\ d_{ye} &= d_{y1} \end{aligned} \tag{6.10}$$

For numerical simulations, consider a base-isolated N-story shear building model. The fundamental, natural period of the superstructure with a fixed base is given by $0.1 \times N[\mathrm{S}]$. The stiffness, k_2, is obtained from this condition. The yield displacement is given by $d_{y2} = 0.02 \times N[M]$. The floor mass per story is assumed to be $200 \times 10^3[KG]$. Then $m_2 = 200 \times 10^3 \times N[KG]$.

The yield displacement of the base-isolation story is $d_{y1} = 0.03\ [M]$. The fundamental, natural period of the base-isolated building with a rigid superstructure is given by 1.0[s] (the stiffness is the sum of the isolators and steel dampers). The stiffness, k_1, is obtained by this condition. The mass of the base-isolation story is $m_1 = 600 \times 10^3[KG]$.

Figure 6.16 shows the comparison of the critical plastic deformation in the base-isolation story after the second impulse among the 2DOF model (time-history response analysis), the SDOF (a) model (series spring model and ignored base-

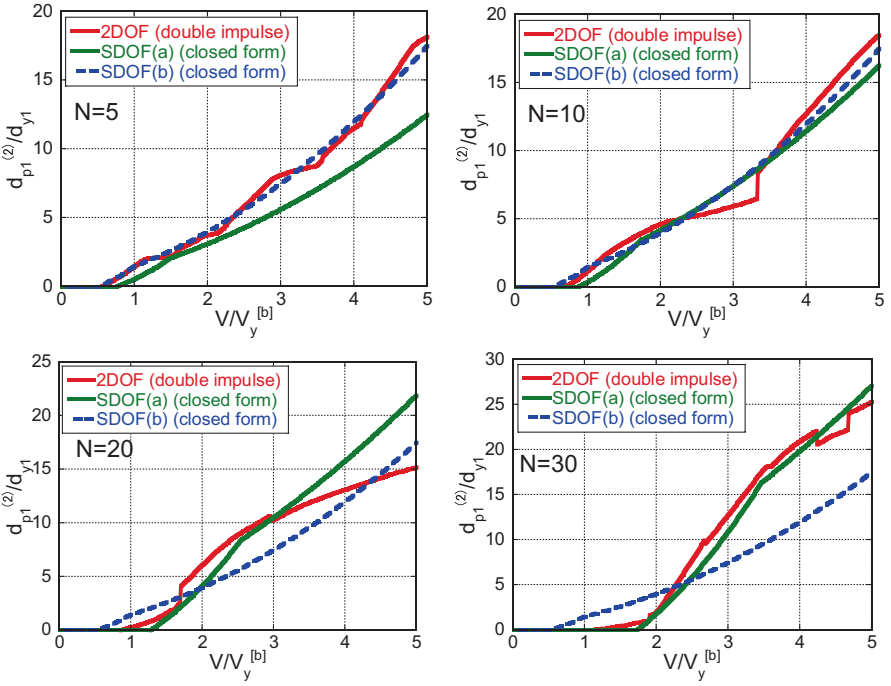

Fig. 6.16 Plastic deformation in a base-isolation story in 5, 10, 20 and 30-story base-isolated buildings after the second impulse under double impulse with respect to input level (2DOF model, SDOF model: (**a**) with series springs and SDOF model, (**b**) with rigid superstructure)

isolation story mass) and the SODF (b) model (rigid super-structure model). The critical plastic deformation of the SDOF model after the second impulse was shown in Eq. (6.6). It can be observed that, while the SDOF (b) model with a rigid superstructure is a better model for a low-rise building model ($N = 5$, 10), the SDOF (a) model with series springs and ignored base-isolation story mass is a better model for a high-rise building model ($N = 30$). It can also be observed that, for $N = 20$, the SDOF (a) model can simulate the response of the 2DOF model in the lower input level up to $V/V_y = 3$, and the response of the SODF (b) model is closer to the actual response in the range of $V/V_y = 4 - 5$.

6.6 Conclusions

It has been shown that good, approximate, elastic-plastic responses of SDOF models to near-fault ground motions can be derived by using the responses to the corresponding double and triple impulses with the equivalent magnitude. The original energy approach played an important role in the derivation of such good approximate responses in closed form. The maximum plastic deformation of a 2DOF model

under the double impulse can be evaluated using the upper bound theory because a complicated problem of phase lag between both masses exists. Furthermore, it has been shown that the maximum plastic deformation of a base-isolated building structure with an elastic-plastic force-deformation characteristic in the base-isolation story can be evaluated by either a simplified SDOF model with a rigid superstructure or a simplified model with series springs. The accuracy of the SDOF models depends on the number of stories of the superstructures. It has been observed that, while the SDOF (b) model with rigid super-structure is a better model for a low-rise building model ($N = 5$, 10), the SDOF (a) model with series springs and ignored base-isolation story mass is a better model for a high-rise building model ($N = 30$). The concept explained here can be applied to the rocking vibration of rigid blocks (Dimitrakopoulos and DeJong 2012, Makris and Kampas 2016, Nabeshima et al. 2016) and the dynamic stability problems of structures (Kojima and Takewaki 2016b, c).

Acknowledgements Part of the present work is supported by the Grant-in-Aid for Scientific Research (KAKENHI) of Japan Society for the Promotion of Science (No.15H04079). This support is greatly appreciated.

References

Alavi B, Krawinkler H (2004) Behaviour of moment resisting frame structures subjected to near-fault ground motions. Earthq Eng Struct Dyn 33(6):687–706

Anderson JC, Bertero VV (1987) Uncertainties in establishing design earthquakes. J Struct Eng ASCE 113(8):1709–1723

Ben-Haim Y, Elishakoff I (1990) Convex models of uncertainty in applied mechanics. Elsevier, Amsterdam

Ben-Haim Y, Chen G, Soong TT (1996) Maximum structural response using convex models. J Eng Mech ASCE 122(4):325–333

Bertero VV, Mahin SA, Herrera RA (1978) Aseismic design implications of near-fault San Fernando earthquake records. Earthq Eng Struct Dyn 6(1):31–42

Bray JD, Rodriguez-Marek A (2004) Characterization of forward-directivity ground motions in the near-fault region. Soil Dyn Earthq Eng 24(11):815–828

Caughey TK (1960) Sinusoidal excitation of a system with bilinear hysteresis. J Appl Mech 27(4):640–643

Dimitrakopoulos EG, DeJong MJ (2012) Revisiting the rocking block: closed-form solutions and similarity laws. Proc R Soc A 468:2294–2318

Drenick RF (1970) Model-free design of aseismic structures. J Eng Mech Div ASCE 96(EM4):483–493

Hall JF, Heaton TH, Halling MW, Wald DJ (1995) Near-source ground motion and its effects on flexible buildings. Earthquake Spectra 11(4):569–605

Hayden CP, Bray JD, Abrahamson NA (2014) Selection of near-fault pulse motions. J Geotech Geoenviron Eng ASCE 140(7)

Iwan WD (1961) The dynamic response of bilinear hysteretic systems, Ph.D. Thesis, California Institute of Technology

Iwan WD (1997) Drift spectrum: measure of demand for earthquake ground motions. J Struct Eng ASCE 123(4):397–404

Kalkan E, Kunnath SK (2006) Effects of fling step and forward directivity on seismic response of buildings. Earthquake Spectra 22(2):367–390

Kanno Y, Takewaki I (2016) Robustness analysis of elastoplastic structure subjected to double impulse. J Sound Vib 383:309–323

Khaloo AR, Khosravil H, Hamidi Jamnani H (2015) Nonlinear interstory drift contours for idealized forward directivity pulses using "Modified Fish-Bone" models. Adv Struct Eng 18(5):603–627

Kojima K, Takewaki I (2015a) Critical earthquake response of elastic-plastic structures under near-fault ground motions (Part 1: Fling-step input). Frontiers in Built Environment (Specialty Section: Earthquake Engineering), Volume 1, Article 12

Kojima K, Takewaki I (2015b) Critical earthquake response of elastic-plastic structures under near-fault ground motions (Part 2: Forward-directivity input). Frontiers in Built Environment (Specialty Section: Earthquake Engineering), Volume 1, Article 13

Kojima K, Takewaki I (2015c) Critical input and response of elastic-plastic structures under long-duration earthquake ground motions. Frontiers in Built Environment (Specialty Section: Earthquake Engineering), Volume 1, Article 15

Kojima K, Takewaki I (2016a) Closed-form critical earthquake response of elastic-plastic structures on compliant ground under near-fault ground motions. Frontiers in Built Environment (Specialty Section: Earthquake Engineering), Volume 2, Article 1

Kojima K, Takewaki I (2016b) Closed-form dynamic stability criterion for elastic-plastic structures under near-fault ground motions. Frontiers in Built Environment (Specialty Section: Earthquake Engineering), Volume 2, Article 6

Kojima K, Takewaki I (2016c) A simple evaluation method of seismic resistance of residential house under two consecutive severe ground motions with intensity 7. Frontiers in Built Environment (Specialty Section: Earthquake Engineering), Volume 2, Article 15

Makris N, Black CJ (2004) Dimensional analysis of rigid-plastic and elastoplastic structures under pulse-type excitations. J Eng Mech ASCE 130:1006–1018

Makris N, Kampas G (2016) Size versus slenderness: two competing parameters in the seismic stability of free-standing rocking columns. Bull Seismol Soc Am 106(1) published online

Mavroeidis GP, Papageorgiou AS (2003) A mathematical representation of near-fault ground motions. Bull Seismol Soc Am 93(3):1099–1131

Mavroeidis GP, Dong G, Papageorgiou AS (2004) Near-fault ground motions, and the response of elastic and inelastic single-degree-freedom (SDOF) systems. Earthq Eng Struct Dyn 33:1023–1049

Moustafa A, Ueno K, Takewaki I (2010) Critical earthquake loads for SDOF inelastic structures considering evolution of seismic waves. Earthq Struct 1(2):147–162

Mukhopadhyay S, Gupta VK (2013a) Directivity pulses in near-fault ground motions—I: identification, extraction and modeling. Soil Dyn Earthq Eng 50:1–15

Mukhopadhyay S, Gupta VK (2013b) Directivity pulses in near-fault ground motions—II: estimation of pulse parameters. Soil Dyn Earthq Eng 50:38–52

Mylonakis G, Voyagaki E (2006) Yielding oscillator subjected to simple pulse waveforms: numerical analysis & closed-form solutions. Earthq Eng Struct Dyn 35:1949–1974

Nabeshima K, Taniguchi R, Kojima K, Takewaki I (2016) Closed-form overturning limit of rigid block under critical near-fault ground motions. Frontiers in Built Environment (Specialty Section: Earthquake Engineering), Volume 2, Article 9

Rupakhety R, Sigbjörnsson R (2011) Can simple pulses adequately represent near-fault ground motions? J Earthq Eng 15:1260–1272

Sasani M, Bertero VV (2000) Importance of severe pulse-type ground motions in performance-based engineering: historical and critical review. In: Proceedings of the twelfth world conference on earthquake engineering, Auckland, New Zealand

Singh JP (1984) Characteristics of near-field strong ground motion and their importance in building design. In: Proceedings of the Applied Technology Council (ATC), Seminar on earthquake ground motion and building damage potential, San Francisco, March 27, ATC 10–1, pp 23–42

Takewaki I (2007) Critical excitation methods in earthquake engineering. Elsevier, Amsterdam, Second edition in 2013, Oxford

Takewaki I, Moustafa A, Fujita K (2012) Improving the earthquake resilience of buildings: the worst case approach. Springer, London

Taniguchi R, Kojima K, Takewaki I (2016) Critical response of 2DOF elastic-plastic building structures under double impulse as substitute of near-fault ground motion. Frontiers in Built Environment (Specialty Section: Earthquake Engineering), Volume 2, Article 2

Vafaei D, Eskandari R (2015) Seismic response of mega buckling-restrained braces subjected to fling-step and forward-directivity near-fault ground motions. Struct Design Tall Spec Build 24:672–686

Vassiliou MF, Tsiavos A, Stojadinovic B (2013) Dynamics of inelastic base-isolated structures subjected to analytical pulse ground motions. Earthq Eng Struct Dyn 42:2043–2060

Yang D, Zhou J (2014) A stochastic model and synthesis for near-fault impulsive ground motions. Earthq Eng Struct Dyn 44:243–264

Chapter 7
Comparison of Ground Motion Pulse Models for the Seismic Response of Seismically Isolated Liquid Storage Tanks

S. Öncü-Davas, H. Gazi, E. Güler, and Cenk Alhan

Abstract Liquid storage tanks constitute an important portion of the critical infrastructure whose failure in case of an earthquake would lead to significant economic losses. Seismic base isolation is an emerging technology for assuring seismic safety of these critical structures. It reduces the effective seismic forces by shifting the fundamental period of the structural system out of the resonance range via use of laterally flexible isolation system elements. Despite the success of these structures under frequently occurring typical far-fault earthquakes, their behavior under near-fault earthquakes are being questioned recently. Near-fault earthquake records may contain long-period velocity pulses with high amplitudes, which may be close to or even coincident with the periods of isolation systems and/or the period of the sloshing fluid inside the tanks. This may result in unacceptably large isolation system and/or sloshing fluid displacements which would threaten the safety of the isolation system and the tank superstructure. Thus, both engineers and researchers turn to numerical investigations of the behavior of seismically isolated liquid storage tanks under near-fault earthquakes. However, there is a scarcity of the number of recorded near-fault ground motions as of today, and thus, artificially developed near-fault earthquakes, which are also known as pulse models, are being used as an alternative to recorded near-fault earthquakes in evaluating the near-fault behavior of these structures. There is no question that the reliability of the results obtained from such investigations which make use of pulse models would be strongly dependent on how realistic these models are. Therefore, it is deemed necessary to assess the capability of popular, current pulse models in representing the effects of near-fault ground motions on the responses of seismically isolated liquid storage tanks. For this purpose, we compare the structural response parameters, including isolator and sloshing displacements and isolation system and fluid-tank shear forces of a prototype, seismically isolated liquid storage tank under recorded near-fault earthquakes, and their approximate counterpart synthetic pulse models.

S. Öncü-Davas • H. Gazi • E. Güler • C. Alhan (✉)
Civil Engineering Department, İstanbul University, İstanbul, Turkey
e-mail: cenkalhan@istanbul.edu.tr

R. Rupakhety, S. Ólafsson (eds.), *Earthquake Engineering and Structural Dynamics in Memory of Ragnar Sigbjörnsson*, Geotechnical, Geological and Earthquake Engineering 44, https://doi.org/10.1007/978-3-319-62099-2_7

Keywords Liquid storage tanks • Seismic base isolation • Near-fault earthquakes • Synthetic ground motion pulse models

7.1 Introduction

Liquid storage tanks may be used to store chemicals, petroleum products, and toxic and flammable fluids, besides water in water-distribution systems (Jaiswal et al. 2007; IITK-GSDMA 2007; Shrimali and Jangid 2004). These structures are strategically and vitally important for many industries (Saha et al. 2013), and damage to these structural systems may cause significant economic losses. Therefore, it is a crucial issue to protect these structures from the detrimental effects of earthquakes, which may be achieved by seismic isolation.

As of today, it is widely accepted by the modern structural design society that seismic isolation, based on the idea of lengthening the fundamental period of the structural systems by means of laterally flexible isolation systems, is a successful, alternative earthquake resistant design method (Martelli et al. 2014). It successfully protects structures from the harmful effects of far-fault earthquakes with high-frequency contents, but unfortunately, it may amplify the structural response parameters when subjected to near-fault earthquakes (Makris 1997) that contain large velocity and/or displacement pulses with long periods. Of particular interest is the potentially large isolation system displacements that may cause tearing and/or buckling problems in the isolators and thus threaten the safety and the integrity of the entire structural system.

A large number of research studies is devoted to investigating the behaviors of seismically isolated buildings under near-fault earthquakes. Mazza and Vulcano (2009), Providakis (2009), Sehhati et al. (2011), Alhan and Öncü-Davas (2016), and Alhan et al. (2016a) are among the recent examples of these studies. On the other hand, investigating the dynamic behavior of other types of structural systems, such as base-isolated liquid storage tanks, is becoming more and more appealing in recent years. Unlike buildings, the dynamic behavior of liquid storage tanks includes the sloshing of the fluid inside and tank-fluid interaction besides the dynamic response of the tank itself. When seismically isolated, the dynamic behavior becomes even more complex. Just like with buildings, near-fault earthquakes pose a significant threat to seismically isolated liquid storage tanks. Resonant-like behavior, causing amplifications in the isolation system and the tank superstructure responses, may occur if the periods of pulses of near-fault ground motions are close to the isolation periods of seismically isolated liquid storage tanks (Alhan et al. 2016b). Shrimali and Jangid (2004), Panchal and Jangid (2008), Abalı and Uçkan (2010), Shekari et al. (2010), Fallahian et al. (2013), Alhan and Gazi (2015), and Gazi et al. (2015a) are among the recent examples of research studies investigating the dynamic behaviors of base-isolated liquid storage tanks under near-fault ground motions.

Since the researchers concentrate on investigating the behaviors of seismically isolated structures in recent years as summarized above, ground motion records with near-fault characteristics are in high demand. In the face of scarcity of recorded near-fault ground motions, synthetic ground motion pulse models are used in lieu of these records (e.g. Alhan and Öncü-Davas 2016; Alhan et al. (2016a, b), Dicleli and Buddaram 2007). In particular, such synthetic ground motion pulse models are appealing in parametric investigations as they may be generated with various required pulse periods and amplitudes.

There are several analytical pulse models, which are generated by various researchers (Hall et al. 1995; Makris 1997; Makris and Chang 2000; Alavi and Krawinkler 2001; Agrawal and He 2002; Menun and Fu 2002; Mavroeidis and Papageorgiou 2003; He and Agrawal 2008) in the literature to simulate pulse-like ground motions. Among these researchers, Hall et al. (1995) classified ground displacement pulses in near-fault ground motions into two main groups and denoted the pulses with a forward-only displacement and the pulses with a forward and backward displacement as A and B, respectively. Half-cycle, forward velocity pulses and full-cycle, forward-backward velocity pulses are modeled by Makris (1997) as Type-A and as Type-B pulses, respectively. A ground motion pulse, exhibiting n main pulses in its displacement history is denoted a Type C_n pulse and modeled by Makris and Chang (2000). The velocity pulses in near-fault ground motions with a forward rupture directivity effect are modeled by Agrawal and He (2002) using decaying sinusoids. Among these pulse models, the ones presented by Hall et al. (1995), Makris (1997), Alavi and Krawinkler (2001), Makris and Chang (2000), and Menun and Fu (2002) have piecewise-functions and are valid for specific time intervals. However, the pulse models presented by Mavroeidis and Papageorgiou (2003), Agrawal and He (2002), and He and Agrawal (2008) have single functions and were verified using a large number of recorded ground motions (Dicleli and Buddaram 2007).

Thanks to their simple mathematical expression, Agrawal and He (2002) and Makris (1997) Type-A and Type-B pulse models are specifically convenient for use in parametric investigations. Although Wang et al. (2002), Gazi et al. (2015b), and Öncü-Davas et al. (2015) revealed that the pulse model presented by Agrawal and He (2002) can be efficiently used in lieu of the recorded near-fault ground motions to investigate the effects of those ground motions on structural response parameters of seismically isolated *buildings*, its efficiency in case of seismically isolated *liquid storage tanks* is yet to be investigated.

To the best of authors' knowledge, there is no study that compares the response parameters of seismically isolated liquid storage tanks under historical near-fault ground motion records to the response parameters obtained under counterpart synthetic pulse models representing these records. Therefore, in order to investigate the capability of Makris (1997) and Agrawal and He (2002) pulse models in representing the effects of pulse-like near-fault ground motions on the responses of seismically isolated liquid storage tanks, the comparison of the structural response parameters of a prototype, seismically isolated liquid storage tank under historical earthquakes and their approximate counterpart synthetic pulse models is presented

in this study. Bearing displacement, sloshing displacement, isolation system shear force, and fluid-tank shear force are considered as the structural response parameters. Nonlinear time history analyses for the isolated tanks, mounted on the nonlinear isolation systems considered in this study are conducted in 3D–BASIS-ME (Tsopelas et al. 1994).

7.2 Structural Model

The benchmark, base-isolated liquid storage tank used in this study is obtained from Gazi et al. (2015a), who used the tank superstructure and overall geometry presented by Tsopelas et al. (1994) but introduced their own elastomeric isolation system properties. The circular storage tank filled with water, shown in Fig. 7.1, consists of a steel wall and a concave-down steel roof. It is mounted on a concrete base which is supported on an isolation system consisting of rubber based isolators exhibiting hysteretic energy dissipation and nonlinear material behavior. The radius of the tank is R = 60 ft (18.29 m), while the total height of the tank is 42 ft (12.80 m).

The height of the water is equal to H = 40 ft (12.19 m), while the thickness of both the steel wall and the concave-down steel roof is h = 1 in (2.54 cm). In addition, the thickness and the radius of the rigid concrete basemat are 1.5 ft (45.72 cm) and 61 ft (18.59 m), respectively. As for the weight of the steel tank, including the walls, the roof, and the weight of the concrete basemat, they are equal to 1123.8 kips (4998.9 kN) and 2629.8 kips (11697.9 kN), respectively, while the water inside the

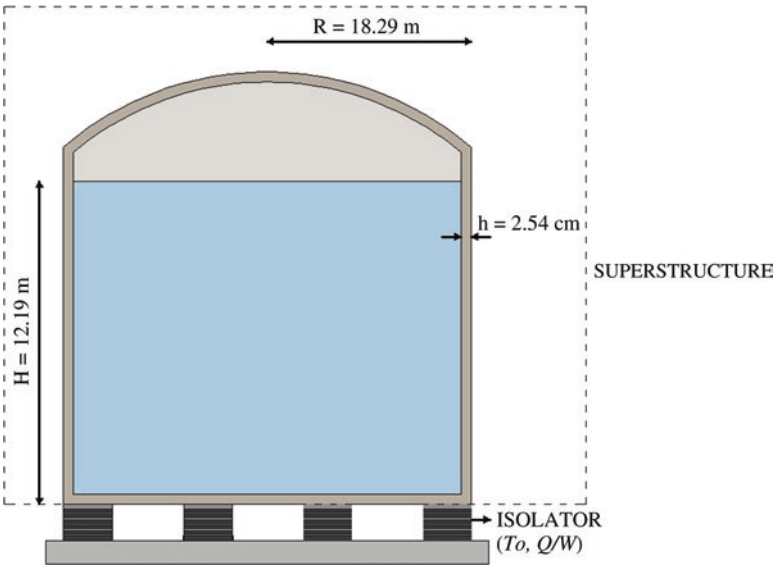

Fig. 7.1 Liquid storage tank with base isolation (geometric dimensions from Tsopelas et al. 1994)

tank weighs 28387.4 kips (126273.4 kN). Thus, the total weight above the isolation system equals 32141 kips (142970.3 kN).

Nonlinear time history analyses of this base-isolated liquid storage tank are conducted in 3D–BASIS-ME, which is an academic software developed by Tsopelas et al. (1994) that can efficiently be used to model and conduct dynamic analyses of seismically isolated liquid storage tanks. The subject program follows the mechanical analog provided by Haroun and Housner (1981) to model the base-isolated liquid storage tanks. While the readers are referred to Haroun and Housner (1981) for theoretical details, in brief, Haroun and Housner's analog takes into account the deformability of the tank wall along with sloshing of the fluid and models the fundamental sloshing mode and the fundamental tank-fluid vibration mode as single-degree-of-freedom systems. For modeling base-isolated liquid storage tanks, Tsopelas et al. (1994) suggested that these single-degree-of-freedom systems can be modeled to be supported on a common rigid basemat that is placed on an isolation system. In addition, the convective fluid would be attached to the concrete basemat rigidly. For this benchmark model, the weights of the sloshing fluid mode, the tank-fluid vibration mode, and the rigid-convective fluid mode, including the weight of the concrete basemat, are 16317 kips (72581.6 kN), 12000 kips (53378.7 kN), and 3824 kips (17009.999 kN), respectively, while the critical damping ratios for the abovementioned first two modes are assumed to be %0.5 and %2, respectively.

There are 52 identical elastomeric isolators placed in a double-symmetric way underneath the rigid concrete base mat. Typical center-to-center distance between these isolators is equal to 17 ft (5.18 m). The rigid-body-mode isolation period (T_0) of the liquid storage tank in question is taken as 4 s, while yield displacement (D_y) is assumed as 1.5 cm. The characteristic strength ratio (Q/W) of the isolation system is taken as 5%, excluding the sloshing mode weight of 72581.6 kN. The isolation period, yield displacement, and characteristic strength ratio are among the typical practical range of commonly used isolation system properties. Using a bi-linear force-deformation relationship (Naeim and Kelly 1999), the related post-yield stiffness (K_2) and pre-yield (K_1) stiffness values for the isolation system would be equal to 17704.10 kN/m and 252552.1 kN/m, respectively.

7.3 Synthetically Developed Pulse Models

As mentioned in the introduction, many researchers are focused on investigating various aspects of the responses of seismically isolated structures subjected to near-fault earthquakes. But, the number of recorded historical earthquakes including near-fault effects can be insufficient to perform comprehensive parametric studies. In order to meet this need, various synthetic pulse models are proposed in the literature, which simulate the near-fault pulse by considering systematically varied parameters. Two of these models (Makris 1997; Agrawal and He 2002) are used in various research studies owing to their analytical simplicity:

(A) Makris (1997) developed cycloidal Type-A and Type-B pulse models that represent the pulse-like ground motions with forward and forward-backward velocity pulses, respectively. The ground acceleration, velocity, and displacement expressions of Type-A are given by

$$\ddot{u}_A(t) = \omega_p \alpha \sin(\omega_p t) \quad 0 \le t \le T_p \tag{7.1}$$

$$\dot{u}_A(t) = \alpha - \alpha \cos(\omega_p t) \quad 0 \le t \le T_p \tag{7.2}$$

$$u_A(t) = \alpha t - (\alpha / \omega_p)\sin(\omega_p t) \quad 0 \le t \le T_p \tag{7.3}$$

Similar analytical expressions for Type-B are given as:

$$\ddot{u}_B(t) = \omega_p (2\alpha)\sin(\omega_p t + \pi/2) \quad 0 \le t \le T_p \tag{7.4}$$

$$\dot{u}_B(t) = -(2\alpha)\cos(\omega_p t + \pi/2) \quad 0 \le t \le T_p \tag{7.5}$$

$$u_B(t) = (2\alpha/\omega_p) - (2\alpha/\omega_p)\sin(\omega_p t + \pi/2) \quad 0 \le t \le T_p \tag{7.6}$$

Here, ω_p is the circular frequency of the sinusoid; $\alpha = \upsilon_p/2$ is the half of the amplitude of the pulse velocity and the pulse period (T_p) is calculated as $T_p = 2\pi/\omega_p$.

(B) The other popular pulse model (Agrawal and He 2002) presents the closed-form approximations for representing forward rupture directivity effects of pulse-like ground motions. The displacement and the velocity functions are given as follows:

$$u(t) = \left[se^{\beta t}\left[\beta \sin(\varphi t) - \varphi \cos(\varphi t) \right] + s\varphi \right] / \omega_p^2 \tag{7.7}$$

$$\dot{u}(t) = se^{\beta t} \sin(\varphi t) \tag{7.8}$$

Then, the ground acceleration function is obtained by differentiating Eq. (7.8):

$$\ddot{u}(t) = se^{\beta t}\left[\beta \sin(\varphi t) + \varphi \cos(\varphi t) \right], \quad \beta = -\zeta_p \omega_p, \varphi = \omega_p \sqrt{1-\zeta_p^2} \tag{7.9}$$

where the initial amplitude of the pulse is (s); the pulse decaying factor is (ζ_p), and the circular frequency of sinusoid is (ω_p).

7.4 Recorded Near-Fault Ground Motions

Two representative, recorded near-fault earthquakes with long-period and large-amplitude velocity pulses are simulated in this study. The time-histories of the RRS228 component of the 1994 Northridge Earthquake, which is recorded at the Rinaldi Receiving Station, and N90 component of the 1992 Landers Earthquake at Lucerne Valley Station are obtained from the PEER Strong Ground Motion Database (2005) and COSMOS Virtual Data Center (2013), respectively. The peak ground acceleration (PGA) and velocity (PGV) of the RRS228 record are 0.838 g and 166.1 cm/s, respectively, and the PGA and PGV of the N90 record are 0.731 g and 145.45 cm/s, respectively.

For evaluating the capability of the Makris (1997) and Agrawal and He (2002) pulse models in representing the historical, near-fault ground motions on the response of the seismically isolated liquid storage tank, the synthetically developed counterparts of RRS228 and N90 components are created by these pulse models. The synthetic pulse model parameters used for modeling the RRS228 component are taken from Makris and Chang (2000) and Agrawal and He (2002), whereas the parameters of the N90 component are obtained from Makris (1997) and Agrawal and He (2002). These parameters are reported in a graphical format in Fig. 7.2.

The compliance between the velocity time-histories of the recorded ground motions and their synthetic pulse counterparts, which are generated by making use of Eqs. (7.2), (7.5), and (7.8), are illustrated in Fig. 7.3. As seen in Fig. 7.3, the general trend of the velocity time-histories of generated records capture the real records well.

For a quantitative comparison, the peak values and the root-mean-square (RMS) values of the velocity time-histories for all cases are tabulated in Table 7.1. It is clear

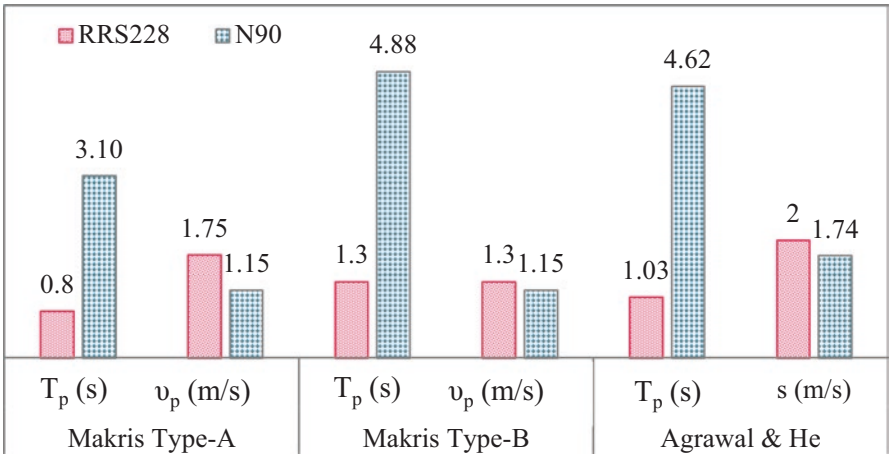

Fig. 7.2 Ground motion parameters for the pulse models (parameters are obtained from Makris (1997); Makris and Chang (2000); and Agrawal and He (2002))

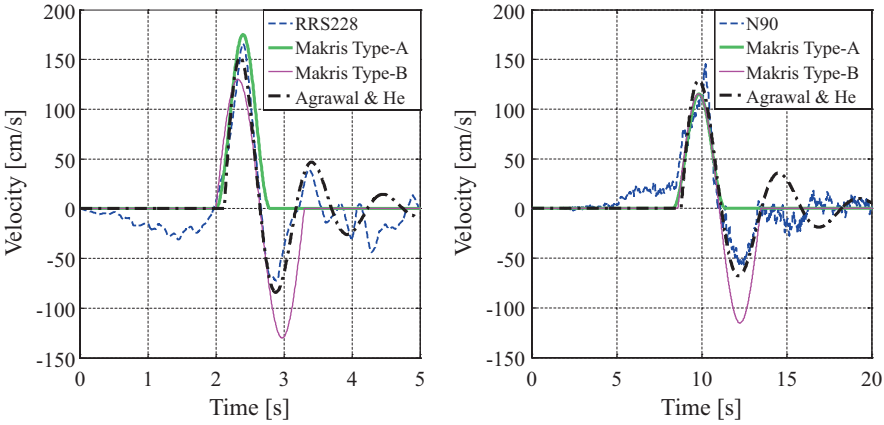

Fig. 7.3 Velocity time histories: RRS228 record and N90 record

Table 7.1 Peak and RMS values of the velocity time-histories

	RRS228		N90	
Earthquake component	Peak (cm/s)	RMS (cm/s)	Peak (cm/s)	RMS (cm/s)
Original record	166.05	26.94	145.45	40.96
Makris type-A	175.00	24.79	115.30	36.40
Makris type-B	130.00	27.11	115.30	39.16
Agrawal & He	151.66	24.03	128.91	41.21

that, for all models, both the peak and the RMS values of the pulse models are close to the corresponding values obtained from the real, historical records. However, the focus of this study is rather on determining the capability of the Makris (1997) and Agrawal and He (2002) pulse models in representing *the effects* of the subject RRS228 and N90 motions *on the seismic responses* of the benchmark, seismically isolated liquid storage tank, which is discussed in the next section.

7.5 Results

In order to evaluate the capability of the Makris (1997) and Agrawal and He (2002) pulse models in representing the effects of historical, near-fault ground motions on the responses of a prototype, seismically isolated liquid storage tank, nonlinear time history analyses of the benchmark model are carried out under both the recorded ground motions (RRS228 and N90) and their synthetically generated counterparts via 3DBASIS-ME (Tsopelas et al. 1994).

First of all, in order to provide a visual comparison of the seismic responses obtained under the real historical records and the synthetic ground motion pulse models, the time-history plots of base displacement (BD), sloshing displacement

(SD), isolation system shear force (ISSF), and fluid-tank interaction shear force (F-TSF) are given in Fig. 7.4 under N90 (a-d) and RRS228 (e-h), respectively. Although all pulse models seem to capture the response histories in a global sense, it can be observed that under both the RRS228 and N90 record, the best fit seems to be provided by the Agrawal and He (2002) model, followed by the Makris (1997) Type B particularly in case of N90. In case of RRS228, there is a non-matching reversal pulse observed in base displacement and isolation system shear force in the case of the Makris (1997) Type-B for RRS228 record. The worst match, particularly in terms of sloshing displacement, is obtained by the Makris (1997) Type-A pulse model. Please note that the Makris (1997) Type A pulse model was not as successful as the other models in terms of capturing the velocity time history of the actual ground motion records (see Fig. 7.3).

Although there still exists a general compliance between the time histories corresponding to the synthetic pulse models and the actual recorded ground motions, none of these time histories fits each other exactly. Synthetic pulses may seem to lack in capturing the structural responses caused by the actual ground motions due to their lack of high frequencies (Rupakhety and Sigbjörnsson 2011), as seen in Fig. 7.4h.

In order to compare peak and root-mean-square (RMS) seismic response values, calculated peak and RMS values are provided in a comparative fashion in Fig. 7.5. Peak seismic responses obtained under historical, near-fault earthquake records (N90 and RRS228) and their synthetically generated counterpart ground motions are given in Fig. 7.5a, b, whereas RMS seismic responses are presented in Fig. 7.5c, d. It is clearly observed from these figures that both the peak and RMS responses obtained under the synthetic pulse models are within the ballpark values obtained under actual historical records. However, in order to specifically determine which pulse model works the best and which response can be captured well in detail, i.e., for quantifying the level of consistence between the real record and their synthetically generated counterparts in terms of the seismic responses, the error ratios of peak and RMS values are calculated via the following equation:

$$\mathrm{er} = \mathrm{r}_{\mathrm{generated}} \,/\, \mathrm{r}_{\mathrm{real}} \tag{7.10}$$

where er is the error ratio; $\mathrm{r}_{\mathrm{generated}}$ is the value of the structural response obtained under the synthetic ground motion, and $\mathrm{r}_{\mathrm{real}}$ is the value of the structural response for the real, historical earthquake record. A value of er = 1.0 represents the condition where the subject seismic response obtained under the real, historical near-fault earthquake record is captured perfectly by the synthetic ground motion pulse model. If er < 1.0 or er > 1.0, it would mean that the seismic analysis that made use of the synthetic ground motion pulse model had underestimated or overestimated the seismic response to be obtained under the real, near-fault earthquake record, respectively.

The error ratios calculated for both the peak and the RMS values of the responses are presented in Fig. 7.6. A first observation is that although the success of the pulse models in representing the actual, near-fault earthquake records in terms of the

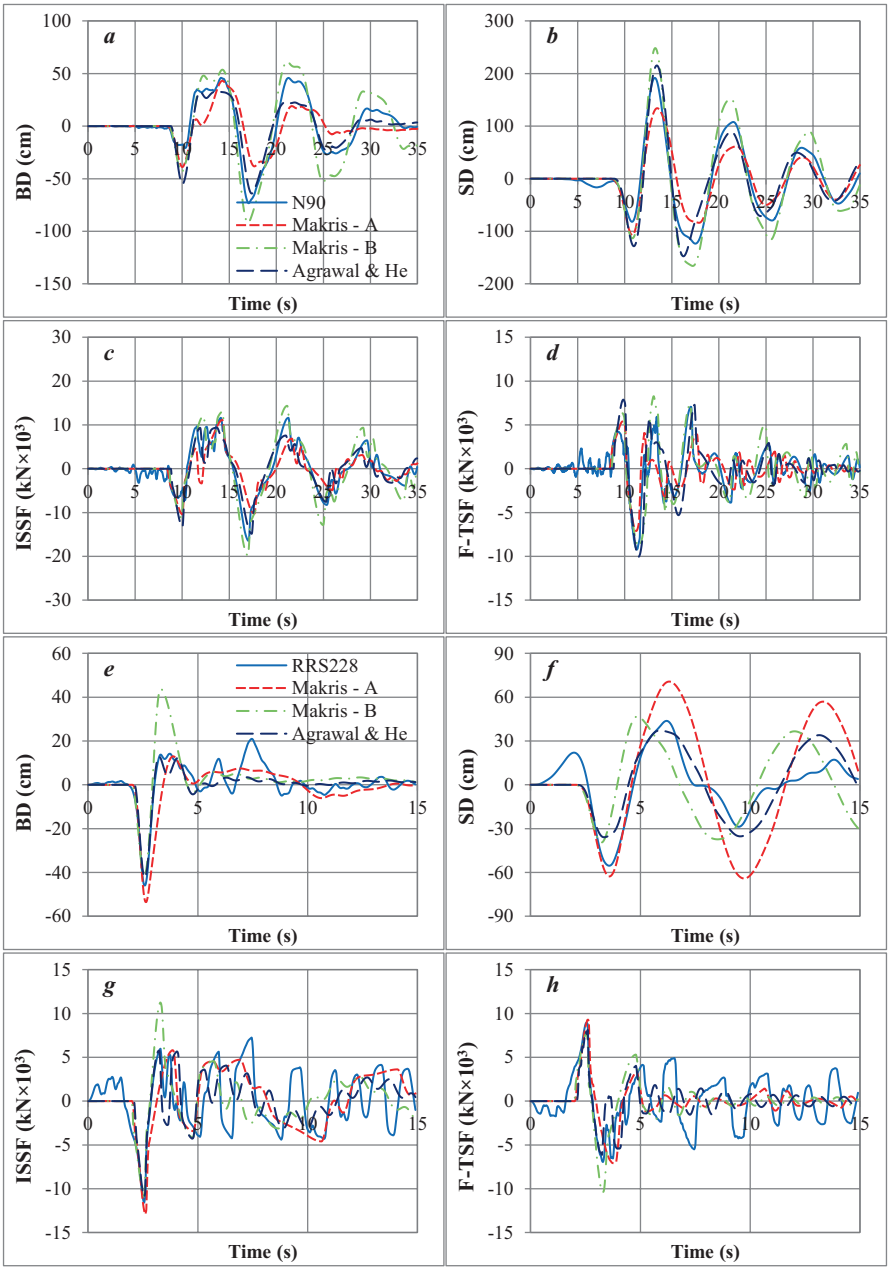

Fig. 7.4 Time histories of base displacement [BD] (**a** and **e**), sloshing displacement [SD] (**b** and **f**), isolation system shear force [ISSF] (**c** and **g**), and fluid-tank shear force [F-TSF] responses (**d** and **h**) under N90 and RRS228 earthquake records

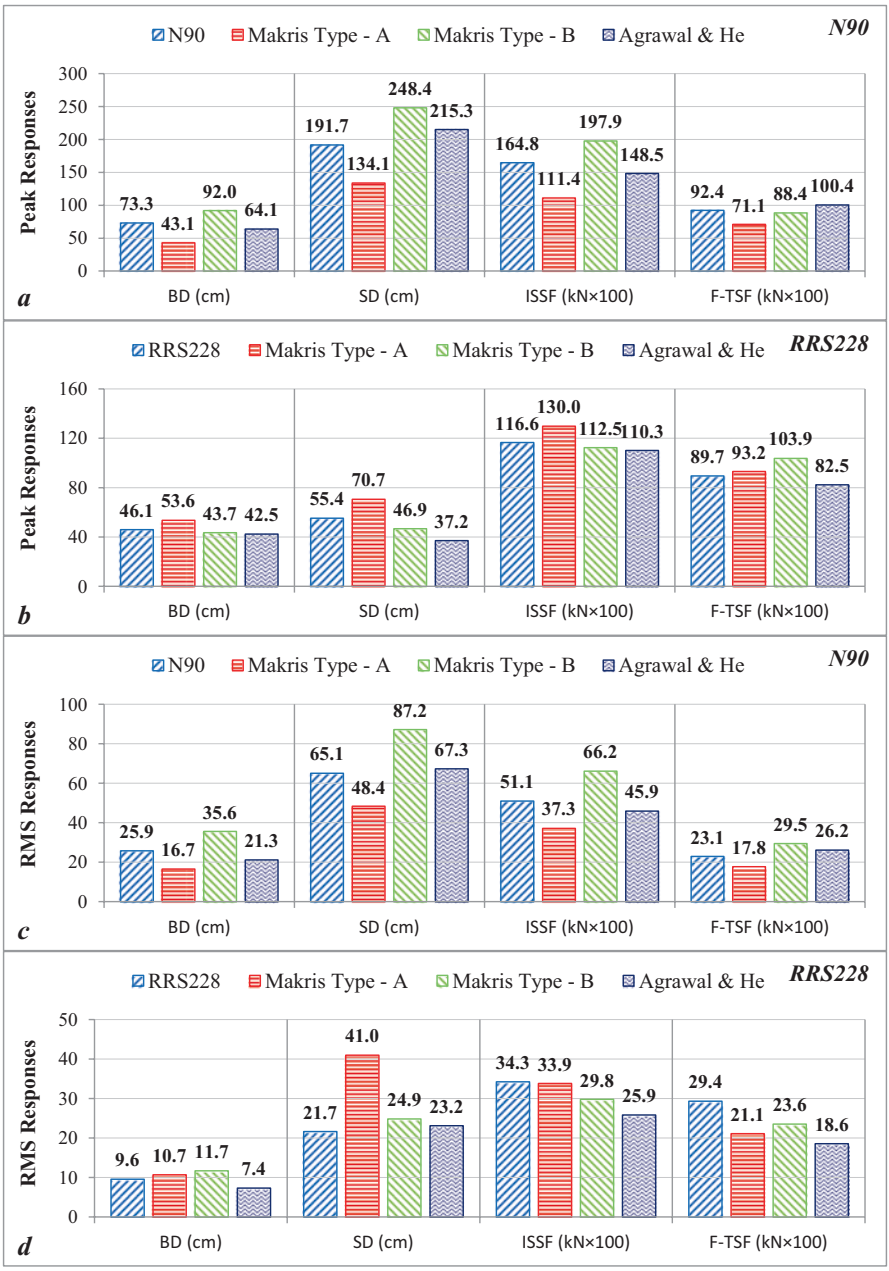

Fig. 7.5 Peak (**a** and **b**) and root-mean-square (**c** and **d**) responses of base displacement [BD], sloshing displacement [SD], isolation system shear force [ISSF] and fluid-tank shear force [F-TSF] responses under N90 and RRS228 earthquake records

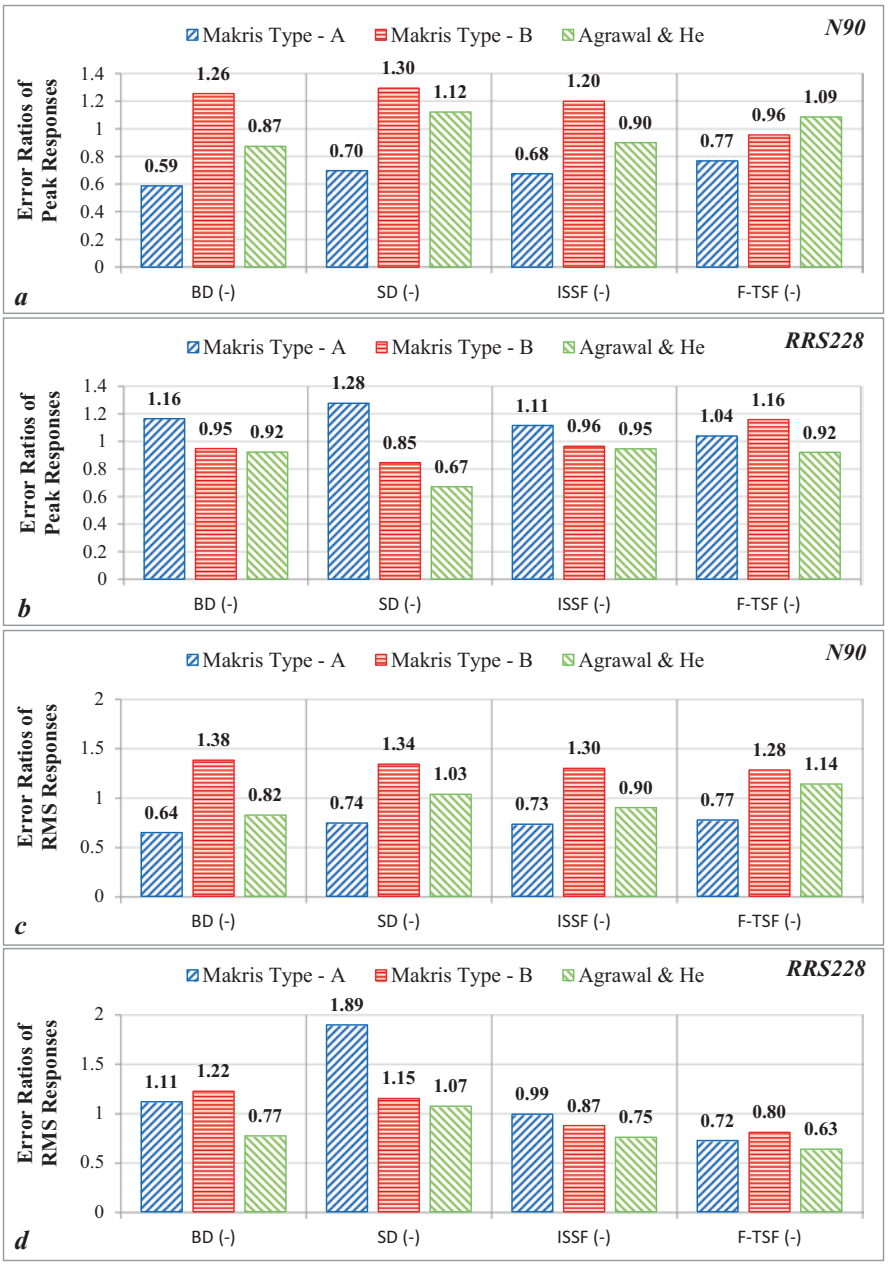

Fig. 7.6 Error ratios of peak (**a** and **b**) and root-mean-square (**c** and **d**) responses of base displacement [BD], sloshing displacement [SD], isolation system shear force [ISSF] and fluid-tank shear force [F-TSF] responses under N90 and RRS228 earthquake records

resulting seismic responses varies depending on the type of the response parameter, in general, the Agrawal and He (2002) pulse model followed by Makris (1997) Type B provides better fits compared to the Makris (1997) Type A pulse model. The error ratios in peak values for the Agrawal and He (2002) pulse models are within the range of 0.87 to 1.12 (max 13% difference) except for the sloshing displacement response error ratio, which is 0.67 in the case of RRS228. The error ratios in peak values for the Makris (1997) Type B pulse models are within the range of 0.85 to 1.30 (15% underestimation to 30% overestimation). Note that the maximum error ratios (0.85 and 1.30) are again in the sloshing displacement response. Furthermore, although the error ratios in terms of RMS values deviate from 1.0 more compared to the error ratios in terms of peak values, in general, the tendencies in error ratios of the RMS values as observed from Figs. 7.6c, d, are in parallel with the tendencies observed in error ratios of the peak responses.

7.6 Conclusions

Near-fault earthquake records may contain long-period velocity pulses with high amplitudes which may be close to, or even coincident with, the periods of isolation systems and/or the period of the sloshing fluid inside the seismically isolated liquid storage tank. This may cause unacceptably large isolation system and/or sloshing fluid displacements that would threaten the safety of the isolation system and the tank superstructure. Thus, recently, both engineers and researchers have focused on investigating the behavior of seismically isolated liquid storage tanks under near-fault earthquakes. However, there is a scarcity of the number of recorded near-fault ground motions as of today, and thus, artificially developed near-fault earthquakes, which are also known as pulse models, are being used as an alternative. In order to investigate the capability of the Makris (1997) Type-A and Type-B and Agrawal and He (2002) pulse models in representing the effects of pulse-like, near-fault ground motions on the responses of seismically isolated liquid storage tanks, the comparison of bearing displacement, sloshing displacement, isolation system shear force, and fluid-tank shear force responses of a prototype, seismically isolated liquid storage tank under historical earthquakes and their approximate counterpart synthetic pulse models is presented in this study.

It is concluded that the success of the investigated pulse models in representing the actual, historical, near-fault ground motions in terms of the seismic responses of seismically isolated liquid storage tanks vary with respect to the characteristics of the historical earthquake record and the type of the seismic response. Regardless, it can be said that, in particular, the Agrawal and He (2002) and Makris (1997) Type-B pulse models are very successful in terms of capturing the overall bearing displacement, isolation system shear force, and fluid-tank shear force response behaviors. Although their success is slightly lower when it comes to sloshing displacements, it can still be read as acceptable considering that a very simple pulse, which can be defined as a closed-form analytical formulation, is successful in representing a real

earthquake record with a frequency content similar to the records considered in this study. However, the investigation should be enhanced by use of more, recorded, near-fault earthquakes containing various frequencies in order to make a more general conclusion on the success of such pulse models in representing the effects of near-fault ground motions on the responses of seismically isolated liquid storage tanks.

References

Abalı E, Uçkan E (2010) Parametric analysis of liquid storage tanks base isolated by curved surface sliding bearings. Soil Dyn Earthq Eng 30:21–31

Agrawal AK, He WL (2002) A closed form approximation of near fault ground motion pulses for flexible structures. In: 15th ASCE proceeding of engineering mechanics conference, June 3, New York

Alavi B, Krawinkler H (2001) Effect of near-fault ground motions on the response to frame structures (Report no: 138), The John A. Blume earthquake engineering center, Stanford University, Stanford

Alhan C, Gazi H (2015) Influence of isolation system characteristic strength on the earthquake behavior of base-isolated liquid storage tanks. In: 2nd International conference on computational and experimental science and engineering (ICCESEN-2015), Oct. 14–19, pp.233–233, Antalya, Turkey

Alhan C, Öncü-Davas S (2016) Performance limits of seismically isolated buildings under near-field earthquakes. Eng Struct 116:83–94

Alhan C, Gazi H, Kurtuluş H (2016a) Significance of stiffening of high damping rubber bearings on the response of base-isolated buildings under near-fault earthquakes. Mech Syst Signal Process 79:297–313

Alhan C, Güler E, Gazi H (2016b) Behavior of base-isolated liquid storage tanks under synthetic near-fault earthquake pulses. In: 5th International symposium on life-cycle civil engineering (IALCCE'16), Oct. 16–19, pp 2415–2419, Delft, Holland

COSMOS (2013) Strong-Motion Virtual Data Center. http://db.cosmos-eq.org/. 3 January 2013

Dicleli M, Buddaram S (2007) Equivalent linear analysis of seismic-isolated bridges subjected to near fault ground motions with forward rupture directivity effect. Eng Struct 29:21–32

Fallahian M, Mellati A, Tehrani MH, Khoshnoudian F, Tarverdi M (2013) Parametric analysis of liquid storage tanks base isolated by double concave friction pendulum system. In: International conference on advances in structural civil and environmental engineering (SCEE 2013), Kuala Lumpur, Malaysia

Gazi H, Kazezyilmaz-Alhan CM, Alhan C (2015a) Behavior of seismically isolated liquid storage tanks equipped with nonlinear viscous dampers in seismic environment. In: 10th Pacific Conference on Earthquake Engineering (PCEE 2015), Nov. 6–8, pp USB-Online, Sydney, Avustralia

Gazi H, Öncü-Davas S, Alhan C (2015b) Comparison of ground motion pulse models for the drift response of seismically isolated buildings. In: Urban Planning and Civil Engineering, Sisiopiku V.P., Ramadan O. E., Eds., Athens Institute for Education and Research, pp 321–332

Hall JF, Heaton TH, Halling MW, Wald DJ (1995) Near-source ground motion and its effects on flexible buildings. Earthq Spectra 11:569–605

Haroun MA, Housner GW (1981) Seismic design of liquid storage tanks. J Tech Counc ASCE 107(1981):191–207

He WL, Agrawal AK (2008) An analytical model of ground motion pulses for the design and assessment of smart protective systems. ASCE J Struct Eng 134(7):1177–1188

Indian Institute of Technology Kanpur (2007) IITK-GSDMA guidelines for seismic design of liquid storage tanks. Natl Inf Cent Earthq Eng, Kanpur

Jaiswal OR, Rai DC, Jain SK (2007) Review of seismic codes on liquid-containing tanks. Earthquake Spectra 23(1):239–260

Makris N (1997) Rigidity, plasticity, viscosity: can electrorheological dampers protect base isolated structures from near source ground motions? Earthq Eng Struct Dyn 26:571–591

Makris N, Chang S (2000) Effect of viscous, viscoplastic and friction damping on the response of seismic isolated structures. Earthq Eng Struct Dyn 29:85–107

Martelli A, Clemente P, De Stefano A, Forni M, Salvatori A (2014) Recent development and application of seismic isolation and energy dissipation and conditions for their correct use. In: Ansal A (ed) Perspectives on European engineering and seismology, Book series: geotechnical, geological and earthquake engineering, vol 1. Springer, Cham, pp 449–488

Mavroeidis GP, Papageorgiou AS (2003) A mathematical representation of near-fault ground motions. Bull Seismol Soc Am 93(3):1099–1131

Mazza F, Vulcano A (2009) Nonlinear response of RC framed buildings with isolation and supplemental damping at the base subjected to near-fault earthquakes. J Earthq Eng 13:690–715

Menun C, Fu Q (2002) An analytical model for near -fault ground motions and the response of SDOF systems. In: 7th U.S. national conference on civil engineering (7NCEE), July 21–25, Boston, USA

Naeim F, Kelly JM (1999) Design of seismic isolated structures: from theory to practice, mechanical characteristics and modeling of isolators. Wiley, New York, pp 93–121

Öncü-Davas S, Gazi H, Alhan C (2015) Comparison of ground motion pulse models for the acceleration response of seismically isolated buildings. In: Khatip JM (ed) Architecture anthology I: architectural construction, materials and building technologies. Athens Institute for Education and Research, Athens, pp 229–240

Panchal VR, Jangid RS (2008) Variable friction pendulum system for seismic isolation of liquid storage tanks. Nucl Eng Des 238:1304–1315

PEER (2005) Pacific earthquake engineering resource center: NGA database. University of California, Berkeley. http://peer.berkeley.edu/nga/. 3 January 2013

Providakis CP (2009) Effect of supplemental damping on LRB and FPS seismic isolators under near-fault ground motion. Soil Dyn Earthq Eng 29:80–90

Rupakhety R, Sigbjörnsson R (2011) Can simple pulses adequately represent near-fault ground motions? J Earthq Eng 15:1260–1272

Saha SK, Sepahvand K, Matsagar VA, Jain AK, Marburg S (2013) Stochastic analysis of base-isolated liquid storage tanks with uncertain isolator parameters under random excitation. Eng Struct 57:465–474

Sehhati R, Rodriguez-Marek A, Elgawady M, Cofer WF (2011) Efeect of near-fault ground motions and equivalent pulses on multi-story structures. Eng Struct 33:767–779

Shekari MR, Khaji N, Ahmadi MT (2010) On the seismic behavior of cylindrical base-isolated liquid storage tanks excited by long-period ground motions. Soil Dyn Earthq Eng 30:968–980

Shrimali MK, Jangid RS (2004) Seismic analysis of base-isolated liquid storage tanks. J Sound Vib 275:59–75

Tsopelas PC, Constantinou MC, Reinhorn AM (1994) 3D-BASIS-ME: computer program for nonlinear dynamic analysis of seismically isolated single and multiple structures and liquid storage tanks. In: Technical report NCEER-94-0010, State University of New York at Buffalo. National Center for Earthquake Engineering Research, New York

Wang Y, McFarland DM, Vakakis AF, Bergman LA (2002) Efficacy of a nonlinear base isolation system subjected to near-field earthquake motions. In: International conference on advances and new challenges in earthquake engineering research, Harbin, People's Republic of China (PRC)

Chapter 8
Initial Wave Height and Total Energy of Landslide-Generated Tsunamis from Translatory Wave Theory

Jonas Elíasson

Abstract The conventional opinion of scientists is that tsunamis are usually caused by earthquakes, but the discovery of the huge submarine landslides on the continental shelf of the North Atlantic Ocean has changed this view considerably. Most tsunamis are triggered by earthquakes, but if it starts a landslide, the tsunami can become enormous, even though the earthquake is small. The energy balance in such tsunamis was studied for the first time using the translatory wave theory by Eliasson and Sigbjörnsson. The theory was originally proposed by Eliasson. The mechanical wave energy generated in tsunamis of such origin is estimated for landslides on mountain slopes and submarine landslides. The initial tsunami wave height is estimated and compared to the results of the block slide estimation method. The energy transmission of the water wave can be translatory or by a solitary group of oscillatory waves where the length of the group varies according to water depth. In a case study, the Tohoku tsunami and earthquake in 2011 in Japan is found to be caused by a coseismic slip and a landslide in combination. A discussion of applying the theory to find a hazard curve for a tsunami wave from different sources at a given location is discussed.

Keywords Tsunami waves • Landslide • Initial energy

J. Elíasson (✉)
Earthquake Engineering Research Centre, School of Engineering and Natural Sciences, University of Iceland and Disaster Prevention Research Institute, Kyoto University, Kyoto, Japan
e-mail: jonaseliassonhi@gmail.com

R. Rupakhety, S. Ólafsson (eds.), *Earthquake Engineering and Structural Dynamics in Memory of Ragnar Sigbjörnsson*, Geotechnical, Geological and Earthquake Engineering 44, https://doi.org/10.1007/978-3-319-62099-2_8

8.1 Introduction

When an earthquake triggers a tsunami, the tsunami can become enormous even though the earthquake is small. Some years ago, it was discovered that huge submarine landslides on the continental shelf of the North Atlantic Ocean have caused large tsunamis. In Bryant (2014) Table 7.1, 11 submarine landslides with slide volumes 20–20.000 km^3 are listed. Submarine landslides of that magnitude run as translatory waves.

The energy balance in such tsunamis was studied for the first time using the translatory wave theory by Eliasson and Sigbjörnsson (2013). Translatory waves have been known for a long time (Stoker 1957) without the theory being widely used, but the theory for translatory wave tsunamis was originally proposed by Eliasson (2008).

Translatory flood waves can be produced by successive flow augmentations in rivers from rain bursts when successive waves, each caused by a flow increase, merge into one flood wave that travels down the river channel at high speed. The destructive power of such floods may be enormous (Eliasson et al. 2007).

The numerical treatment of such waves using the numerical solutions of the St. Venant's equations is well known (see e. g. Julien 2002), but the name translatory wave is usually not mentioned. Analytical solutions are possible for stationary flows using a constant velocity wave progressing down an inclined plane or in a funnel as in Eliasson et al. (2007), where it is also demonstrated that numerical solutions of the St. Venant's equations can produce exactly that kind of flow.

In the onset of a landslide, the debris will accelerate from zero velocity up to terminal velocity rather quickly and move from there as a flow controlled by the slope and the internal friction in the slide. This is exactly what a translatory wave does, so this solution to the St. Venant's equations is the chosen tool to investigate the energy balance in landslide flows. This was done in Eliasson and Sigbjörnsson (2013) (see Fig. 8.1 in the paper) and here this result is applied to tsunamis.

Prediction of tsunamis is very important in disaster prevention, and a large warning system is maintained all over the world. Numerical simulations of tsunami waves are an invaluable part of the warning system (Kerridge 2005; Ward and Asphaug 2003; Tinti et al. 1999), but the uncertainty about initial wave heights (Day 2003), and total wave energy generation is a problem.

There are also several snags in the numerical modeling of tsunamis. Ordinary storm waves create steep wave crests that break in the shore line, but tsunamis are more like a bore or a moving hydraulic jump, as seen in Fig. 8.1. A lot of energy is lost in the jump, but how this affects the final inundation height is unclear as the bore keeps moving inland with water behind it that has not lost any energy. Then there is the role of the wave dispersion and reflection (Dutykh and Dias 2009), it is sometimes present and sometimes not depending on the bathymetry.

In short, mathematics and numerical schemes are well developed in tsunami modeling, but there are pitfalls that can be difficult to avoid. Still, the initial conditions in the source area are the biggest uncertainty. It has, therefore, been concluded

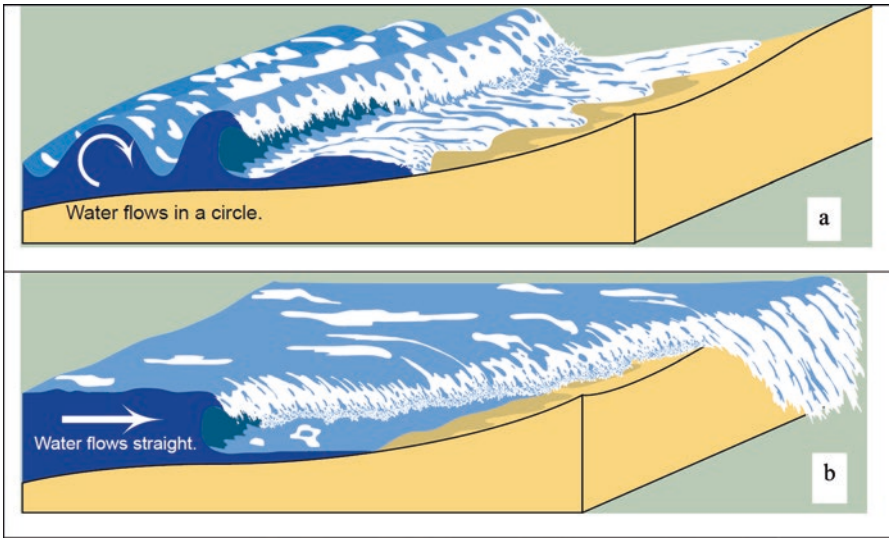

Fig. 8.1 Difference between storm waves (**a**) and tsunamis (**b**)

that verification and validation are necessary for each case, even for models that have been through this process before (Synolakis et al. 2008).

8.2 Lanslide Tsunamis

8.2.1 General Properties of Submarine Translatory Wave Slides

The following formula describes the front of a translatory wave in an inclining channel (Eliasson and Sigbjörnsson 2013).

$$\frac{y}{y_0} + \ln\left(1 - \frac{y}{y_0}\right) = I_0 \frac{x - Vt}{y_0}; \quad x - Vt \le 0 \tag{8.1}$$

The following notation is used:

y landslide thickness (also called depth)
y_0 landslide normal depth (uniform flow)
V wave velocity of the landslide
x streamwise coordinate
t time
g acceleration of gravity
I_0 channel slope

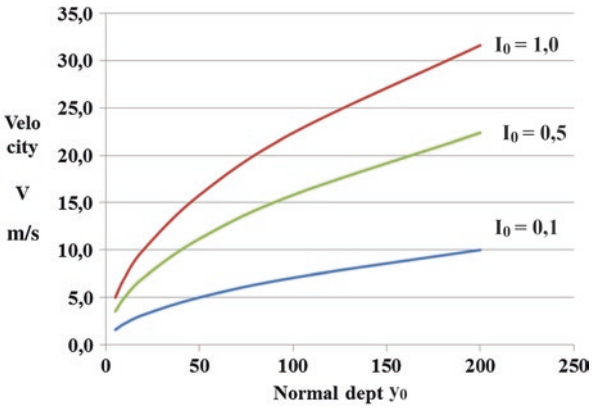

Fig. 8.2 Velocity V of a submarine translatory wave for three slopes I0

The form, represented in Eq. 8.1 is an approaching wave that passes the origin at time zero, x = t = 0 = > y = 0, arriving at any point x, at the time t = x/V. A plot of the function is shown in Fig. 8.1 in Eliasson et al. (2007). As time progresses, y approaches the normal depth y_0 value, there the water velocity is:

$$V = C_T \sqrt{g' y_0 I_0} \tag{8.2}$$

C_T is the total flow resistance coefficient, and g' is the reduced acceleration of gravity. Estimates of C_T are given in Eliasson and Sigbjörnsson (2013). When the normal depth, y_0, is large, the V becomes very large (see Fig. 8.2). The normal depth, y_0, can be calculated from Eq. 8.2 if V is known and vice versa. The maximum debris flow is q = V y_0. It may be shown that after the wave passes any point, the depth of the debris flow, y, approaches the normal depth, y_0, very quickly and when the bottom slope I_0 changes, y_0 and V adapt quickly to the new environment (Eliasson et al. 2007). Theoretically, the wave stops when I_0 becomes zero. In practice, this happens earlier. During the flow, a lot of water gets mixed into the debris flow. This water flows out again when the velocity goes down. This means that the higher internal friction, C_T in Eq. 8.2, gets larger and the slide stops long before it reaches flat bottom, $I_0 = 0$, just as avalanches on dry land. Exactly when this happens cannot be determined, analytically nor numerically.

Compared with translatory waves on land, they run in exactly the same manner, we just have to replace g' with g. Application of St. Venants equations to simulate a flood wave travelling over dry land simulates a submarine translatory wave perfectly, and such flood waves create a tsunami when they flow out in the sea (Eliasson 2008).

Analytical expressions describe the front of the translatory wave. The back side is not a stable wave but a backwater recession. When all this is put together, the translatory wave looks like the schematic diagram shown Fig. 8.3.

The slide creates a disturbance on the surface that progresses with velocity, C, in the direction of the slide. The slide itself has the moving translatory wave in front

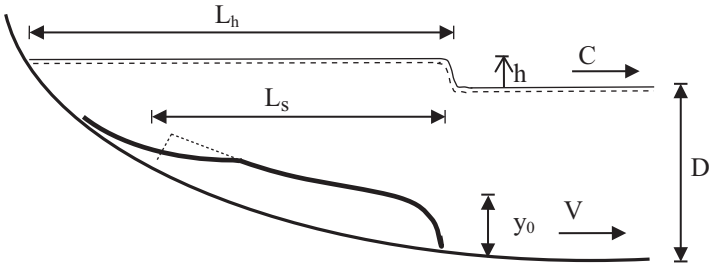

Fig. 8.3 Schematic picture of a submarine landslide with normal depth y_0 progressing with velocity V

but the recession part, or the tail, behind the wave. This tail starts where the scar left by the wave ends, so the point where it meets the wave profile (see Eq. 8.1) moves towards the wave head. The tail will thus eat up the wave if it does not stop before that happens. The broken line behind the wave marks how long back we have to stretch the wave form to have an equal amount of debris inside the dotted line as is in the tail.

Let us suppose that Fig. 8.3 shows the situation when the wave stops. The effective length of the wave, L_s, will not increase any further, but the V has still the theoretical value given by Eq. 8.2.

In this situation, we consider three cases when estimating the total energy and wave height, h. To do so, we assume $y_0 << D$, water velocities V to be small ($V << C$) and potential energy dominating.

Case 1

$V > C = \sqrt{gD}$, V is the theoretical value of V, Eq.8.2.

Case 2

$V < C = \sqrt{gD}$, V is the theoretical value of V, Eq.8.2

Case 3

Sudden increase in the depth D immediately in front of the wave.

(8.3)

8.2.2 Expressions for Energy and Wave Height

The mechanical wave energy generated in the three cases is estimated. The different types are landslides down mountain slopes, submarine landslides or plates moving vertically and horizontally. The initial tsunami wave height is estimated and compared to results from other estimation methods. The energy transmitted to the water by the movement of the landslide is estimated from the moving mass and the total wave energy estimated from the amount of mechanical energy in the slide using the assumption that turbulent energy transmitted to the water cannot be regenerated as

mechanical wave energy. The wave energy transmission away from the source area can be translatory or by a solitary group of oscillatory waves, where the length of the group varies according to water depth. The wave transmission and shoaling can be estimated in numerical models, but the run up height and attenuation are very difficult to control in numerical calculation because of difficulties in modeling the breaking of water waves and the amount of energy dissipated in this process (Svendsen 2006). The emphasis will, therefore, be on wave energy generation in the source area.

8.2.2.1 Case 1

In this case, the surface disturbance, or the water wave, cannot run away from the translatory wave, i. e., the submarine landslide that causes it. The two wave fronts will, therefore, be at the same place, or the same coordinate x, at any time. This is the situation shown in Fig. 8.3.

The water volume above the still water level will, therefore, simply be equal to the displacing volume or the total volume of the slide. In estimating the energy, we have to distinguish between two schemes in both cases, a slide that originates from land (a) or a slide that originates at the sea bottom (b).

8.2.2.2 Case 1a

The slide has a certain width, B. The displaced water volume will be equal to the total volume of the slide, W_T

$$W_{T1a} = B\int_0^{Lh} y\,d\xi \approx By_0 Lh;\ \xi = Vt - x \tag{8.4}$$

In reality, $W_T < y_0 L_h$ so $W_T = y_0 L_h$ is on the safe side, but the approximation will be acceptable as the front of the translatory wave is very steep. This can be deducted from Eq. 8.1, and Fig. 8.6 in Eliasson et al. (2007) and shows this property of the translatory wave very well.

The slide will hit the water with a great splash and run on the bottom until it stops. As the Case 1 water wave cannot outrun the slide, the water will be lifted the distance y_0 from the bottom, and this will be the resulting height of the water wave when the slide suddenly stops. This added potential energy will be the energy of the water wave. In that situation, the energy added to the water will be:

$$E_{W1a} = \tfrac{1}{2} y_0 \rho g W_{T1a} = \tfrac{1}{2} \rho g y_0^{\,2} B\ L_h \tag{8.5}$$

The wave will progress in the x direction with the shallow water velocity $C = \sqrt{gD}$. In a numerical model, the initial condition for the tsunami wave height h will be zero everywhere except in the source area where $h = y_0$ in a square of size $B\ L_h$.

8.2.2.3 Case 1b

The slide will leave a scar in the seabed of size $L_s B$. A part of the slide, κL_s will be outside the scar and leave a hole in the scar area of $\kappa L_s B$. We assume $0 < \kappa \leq 1$.

$$W_{T1b} = B \int_0^{\kappa Ls} y d\xi \approx \kappa B y_0 L_s;\ \xi = Vt - x \tag{8.6}$$

Assuming the hole in the scar to be of volume W_{T1b} we will find:

$$E_{W1b} = \tfrac{1}{2} y_0 \rho g W_{T1b} 2 = \rho g y_0^{\,2} B L_s \tag{8.7}$$

8.2.2.4 Case 2

In this case, the water wave will run away from the translatory wave. The water wave front will therefore be at a coordinate x_w when the slide stops. In this case, the wave on Fig. 8.3 would be ahead of the front of the slide, because when the slide passes the point where V = C, or the depth $D = V^2/g$, the surface wave will run faster than the slide from that point.

In estimating the energy, we still have to distinguish between the two schemes (a) and (b) as before.

8.2.2.5 Case 2a

The position of this point on the slope, x_v, has to be identified using Eq. 8.2. With Cm denoting the average shallow water wave velocity in $x_w - x_v$, we will have:

$$L_{ha} = x_v + \left(x_w - x_v\right) C_m / V \tag{8.8}$$

The slide has a certain width, B. The displaced water volume will be equal to the total volume of the slide, W_T,

$$W_{T1a} = B \int_0^{xw} y d\xi \approx B y_0 xw; \xi = Vt - x; \xi = 0 \text{ in } x = x_w \tag{8.9}$$

but the wave height will be slightly less than before.

$$h_{2a} = y_0 x_w / L_{ha} \tag{8.10}$$

The energy of the water wave becomes:

$$E_{W2a} = ½\ h_{2a}{}^2 \rho g B\ L_{ha} \tag{8.11}$$

In a numerical model, the initial condition for the tsunami wave height, h, will be zero everywhere, except in the source area, where we will have $h = h_{2a}$ in a square of size $B\ L_h$.

8.2.2.6 Case 2b

If the slide starts where $C < V$, we will have:

$$L_{hb} = L_s + \left(x_w - x_v\right) C_m / V \tag{8.12}$$

However, it is possible that the slide starts at a point where $C > V$. This will be discussed in the next section.

The slide will leave a scar in the seabed of size $L_s B$. A part of the slide, κL_s long, will be outside the scar and leave a hole in the scar of area $\kappa L_s B$. At = 0 there will be a through in the water table approximately corresponding to this hole. It is not shown in Fig. 8.4.

$$W_{T2b} = B \int_0^{\kappa Ls} y d\xi \approx \kappa B y_0 Ls; \xi = Vt - x; \xi = 0 \text{ in } x = x_w \tag{8.13}$$

To find h_{2b}, the wave height as in Eq. 8.10, we have to use the relation:

$$h_{2b} L_{hb} = W_{T2b} \tag{8.14}$$

The hole is y_0 deep, but the wave is h_{2b} high, so the energy of the water wave becomes:

$$E_{W2a} = ½\left(y_0{}^2 \kappa L_s + h_{2b}{}^2 L_{hb}\right) \rho\ gB \tag{8.15}$$

8.2.2.7 Case 3

A translatory wave with the velocity given by Eq. 8.2 will, in theory, continue to flow until the bottom slope, I_0, is zero, but will stop before that, as already stated. The water wave will, therefore, run into deeper water with the higher wave velocity of C_2, and that affects the wave height. When I_0 fades out to a flat bottom, there is no problem in the numerical model. In the rare occasions when there is a sudden increase in the ocean depth, it may provide better results to find the height, h_2, of the initial wave in the deeper water.

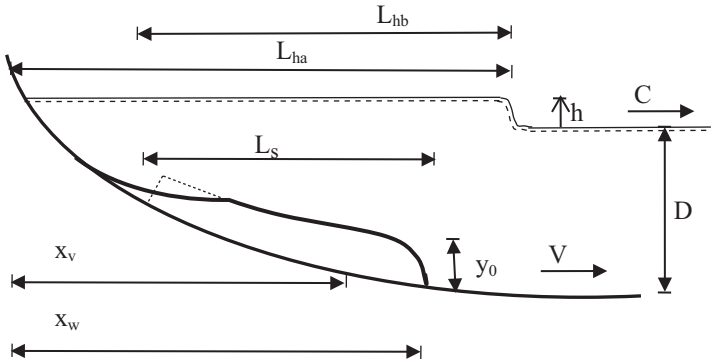

Fig. 8.4 Schematic picture showing how a *Case 2* submarine landslide is different from the slide shown in Fig. 8.3

$$h_2 = h_1 \left(C_1 / C_2 \right)^{1/2} = h_1 \left(D_1 / D_2 \right)^{1/4} \tag{8.16}$$

Here, index 1 refers to shallower and 2 to deeper water. Equation 8.16 assumes continuous energy flow and the translatory wave motion to be preserved. However, the translatory wave may be transformed into a group of oscillatory waves. The details of this transformation are not clear.

Similarily, it is not quite clear what will happen in the case when the slide starts at a depth where C > V. In this case, the point marked with x_v in Fig. 8.4 does not exist, but if the run time of the slide can be estimated, the water wave height can easily be found.

8.3 Discussion and Comparison

The translatory wave theory is a simple and effective way to derive initial conditions for use in numerical tsunami models. Its results may be compared with other models.

One of the most interesting is the well-known block slide model. There, we have a single block sliding down a plane with inclination, α, and internal friction, φ°. As the frictional force in the block slide model is constant, but increases with the velocity squared in the translatory wave model, the terminal velocity of the block will be many times that of the translatory wave (Eliasson and Sigbjörnsson 2013). In most cases, the length of a landslide will be greater than the length of a corresponding block, but the block wave will be higher if the total volume is the same.

A large block sliding a long way at high velocity underwater is a bit unrealistic. To divide the slide into many blocks, or a train of blocks, is a good remedy against this drawback (Tinti et al. 1997), but the model still suffers from the fact that the friction is constant at all velocities. Block slide models may be good for a small

sliding distance and low velocities, then the blocks have a chance to stay in one piece. But at high velocities, the blocks must break up into rubble. Then we have a translatory wave slide, so the terminal velocity will, in most cases, be closer to that model.

8.4 Case Study: Tōhoku Tsunami, Japan

The most famous tsunami event of recent years took place off the Pacific coast of Tohoku, Japan, on Friday 11 March 2011 at 05:46 UTC. It was caused by a Mw 9.0 undersea megathrust earthquake with the epicenter approximately 70 km east of the Oshika Peninsula of Tohoku and the hypocenter at an underwater depth of approximately 30 km (see Fig. 8.5). The earthquake event and the devastation caused by the tsunami are very well documented (see for e.g. Wikipedia 2016, and associated references).

From the data obtained in the exploratory drilling at the site shown in Fig. 8.5, it was concluded (JAMSTEC 2013) that the tsunami was caused by the huge mass movement shown in Fig. 8.6.

The details of the bottom deformation are estimated in Fuji et al. (2011) and pictured in their Fig. 3b. The contours shown there look like a slide scar 150 km long with L_s and B about 110 km and y_0 about 8 m, using the symbols in Fig. 8.4.

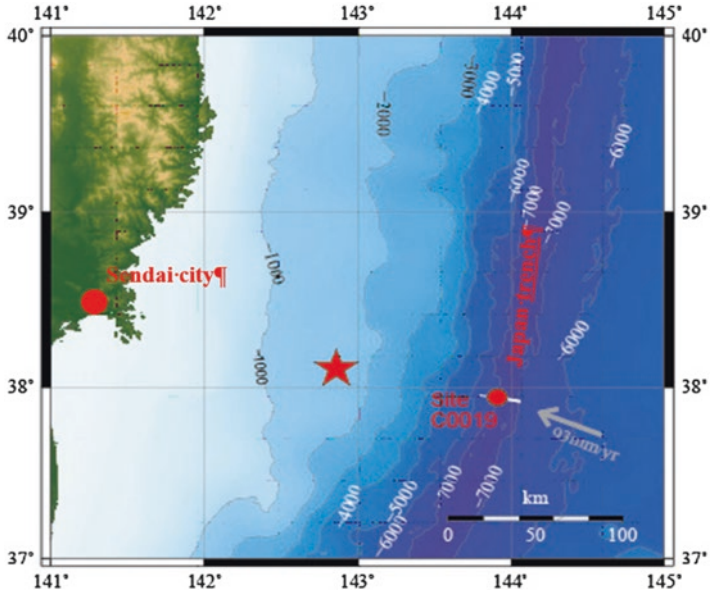

Fig. 8.5 Location chart of the tsunami site with the epicenter (red star), a drilled exploration well (site C00 19; see also Japan Agency for Marine-Earth Science and Technology (JAMSTEC 2013)

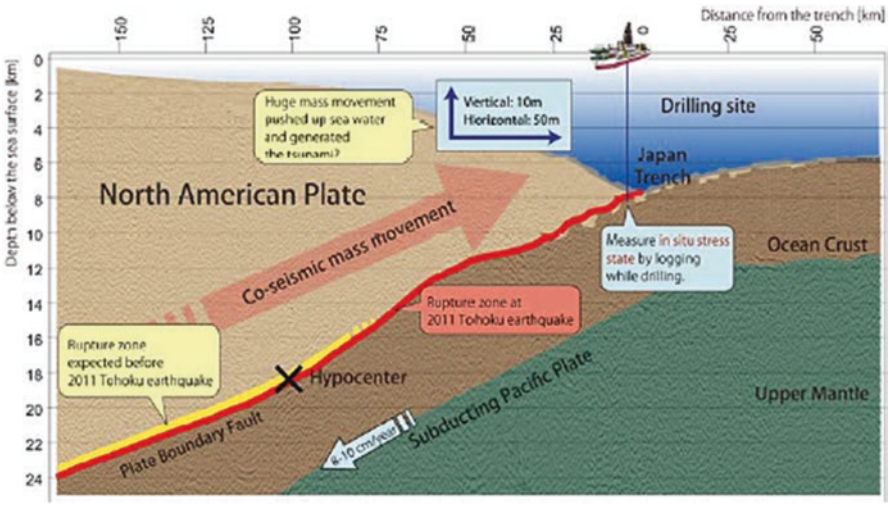

Fig. 8.6 The co-seismic mass movement and the subsequent mass movement at the ocean bottom (from JAMSTEC 2013)

This would be a Case 2b slide, stopping 25–75 km from the trench (Fig. 8.6) where the average slope is about 4/50 or $I_0 = 9\%$. It is interesting to note that layers of fine sediments on such a slope can easily liquefy, slide down the slope and cause a bottom deformation similar to the one pictured in Fuji et al. (2011).

No evidence has been found to support this suggested slide event, but the information on the bottom deformation given in Fuji et al. (2011) is considered reliable and it is supported by a co-seismic slip model (see GIS 2011.

The suggested slide would have characteristics that can be calculated using the equations for the Case 2b slide, with the note on the deep water slides given in the Case 3 section because the slide occurs at great depth with the high velocity of tsunami waves, so Eq. 8.12 does not apply. Instead, the run time of the slide has to be estimated to obtain the L_{bh}.

If the slide is due to liquefaction, the movement will start at the onset of the strong motion and stop with it. According to graphs in Fuji et al. (2011), this time is about t = 30 sec.

Using the velocity V = 2 m/s, we get a horizontal flow path of 60 m. This corresponds fairly well to Fig. 8.7, giving 56 m as the maximum horizontal deformation. We also get L_{bh} = 250*30 = 7500 m = 7.5 km. As the flow path is short, the $\kappa \sim 0$. Now we get

$$L_{bh} = Ls + 7.5 = 110 + 7.5 = 117.5\,\text{km}$$

Next, we need the slide volume. Figure 8.6 shows the coseimic movement as a thick brown arrow inclining 9% upwards. The liquefied mass is sliding 9% downwards, so the resulting displacement is fairly horizontal. The uplift caused by the

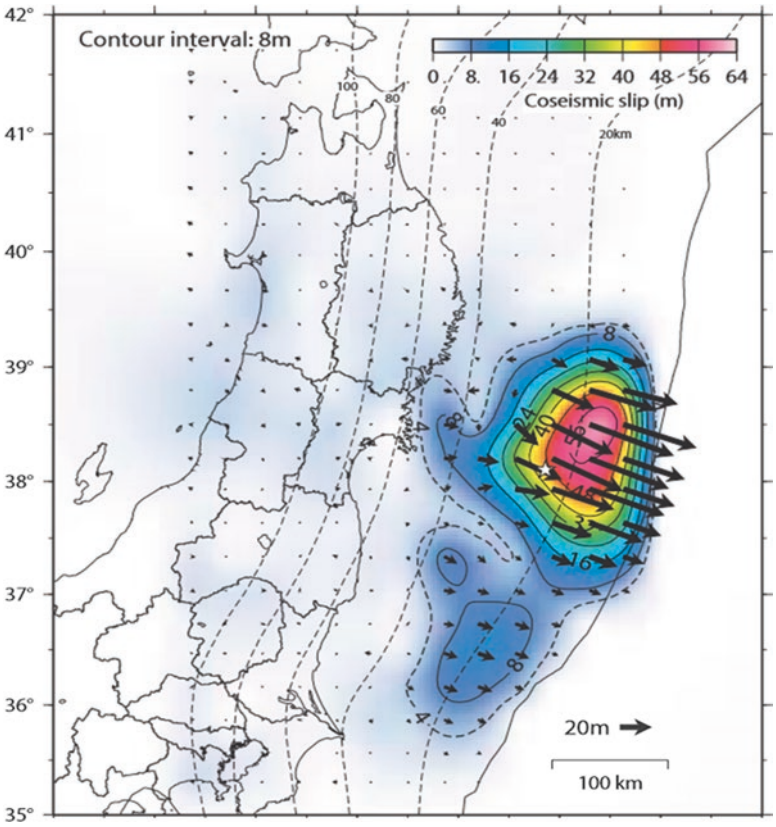

Fig. 8.7 The 2011 off the Pacific coast of Tohoku Earthquake: Coseismic Slip Distribution Model

coseismic movement means that there will be just a small hole in the scar area. This means a modification of Eqs. 8.12, 8.13, 8.14, and 8.15 to the following

$$W_{T2b} = By_0L_s = 1^*110000^*8^*110000 = 9.6810^{10}\,m^3.$$

$$h_{2b} = W_{T2b}/\left(L_{hb}B\right) = 8^*110/117.5 = 7.5\,m$$

$$E_{W2a} = \tfrac{1}{2}h_{2b}{}^2L_{hb}\rho\ gB = \tfrac{1}{2}\ 7.5^{2*}117500^*1025^*9.81^*110000 = 3.6\ 10^{15}\,Nm$$

The simulation from NOAA (2011) shows the spread of the translatory tsunami very well. Comparing this with a ring wave spreading in an effective 90° conical channel gives a resulting average wave height of 2–3 feet in a distance of 900 km from the source. According to C = 250 m/s, this should occur after 1 h. This checks fairly well against Fig. 8.8.

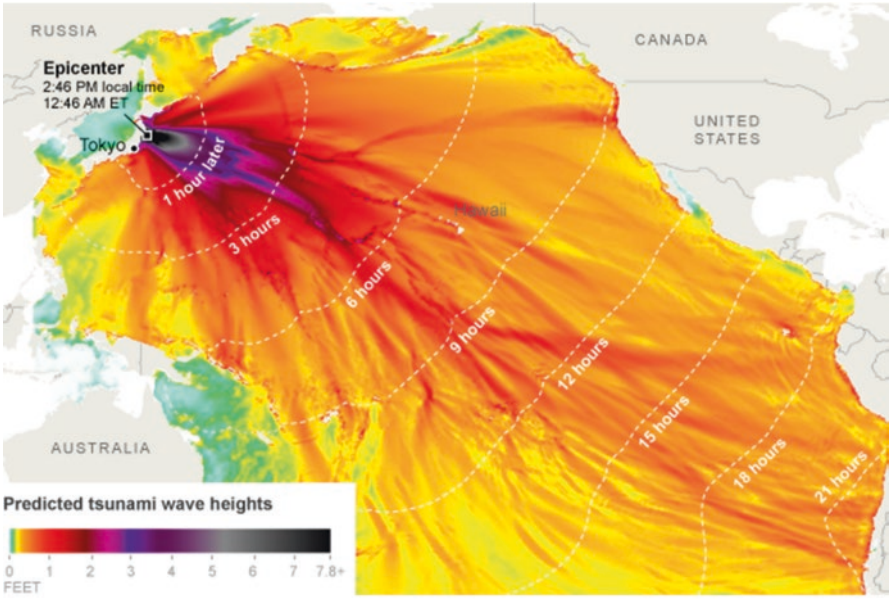

Fig. 8.8 Spreading of the Tohoku tsunami in the Pacific Ocean March 11th 2011 (NOAA Center for Tsunami Research, Pacific Marine Environmental Laboratory; NOAA (2011) (Printed in the NY Times)

It is found that the coseismic movement documented by Japanese scientists is also accompanied by a landslide that explains the bottom deformations that caused the very strong Tohoku tsunami in the Pacific Ocean, simulated numerically by Japanese and USA scientists (GIS 2011, NOAA 2011). This suggests that the co-seismic slip of the earthquake triggers a sliding of the surface sediments. In combination, they cause the bottom deformation. Finally, it can be concluded that the co-seismic slip and the landslide are both responsible for the Tohoku tsunami in March 2011, not the co-seismic slip alone.

This result can be checked against the simulation results published in NOAA (2011).

8.5 Applications of the Translatory Wave Theory

Using translatory wave theory to estimate the expressions for energy and wave height in the source area (Sect. 8.2.2) opens up the possibility of estimating the exceedance statistics for the tsunami wave height in a given location.

To find tsunami wave heights in a given point, the potential source areas have to be known, and the transfer functions for the wave energy and height have to be

known, too. Approximate analytical methods can give good results as a first approximation, as is demonstrated in the case study presented above.

In Eliasson and Sigbjörnsson (2013), hazard curves for a reference point in south Iceland are presented. The tsunami wave heights are estimated in the reference point; the frequency of the event at the source is estimated, and after the transfer functions have been applied, the hazard curves are found by numerical integration.

This process involves the following steps:

1. Identification of the seismic event and its interval of recurrence.
2. Estimation of the translatory wave. There does not have to be one; the deformation may not have a linear dimension large enough to create a rubble slide, then so the deformation can be estimated from the seismic moment. This is done in Eliasson and Sigbjörnsson (2013) applying Okal and Synolakis theory (Okal and Synolakis 2003).
3. The source values for the energy and wave height in the source area have to be estimated, both the average value and the coefficient of variation (standard deviation/mean value).
4. Numerical integration of all the different probabilities of occurrence into one hazard curve for the reference point.

The effect of the coefficient of variation on the hazard curve is quiet surprising. The estimation of its value is very difficult. Usually there are not enough observations of serious tsunami events in order to establish a reliable value for this coefficient. However, to leave it out corresponds to estimating its value to be zero, and that is totally unsatisfactory. In Fig. 8.4 in Eliasson and Sigbjörnsson (2013) the effect of three different values, common in geophysical data, is demonstrated and the difference is quite striking.

Such analyses are very important in order to identify the sources that cause the largest tsunami threats. To take an example, there are 8 identified tsunami sources in the North Atlantic Ocean, 6 of these contribute significantly to the previously described hazard curve in the danger zone. This is the zone above 2 m, meaning that the tsunami has to be 2 m or higher to pose any significant threat alone, i.e., without being accompanied by a flood of different origin.

8.6 Conclusions

The translatory theory can explain generation of tsunamis that are otherwise difficult to explain. It is particularly handy to explain the initial surface disturbance that is the onset of the tsunami and the associated wave energy. This is because both the landslide and the tsunami wave behave like translatory waves. Later, the tsunami wave can develop into an oscillatory wave in deep water.

The translatory wave is a pseudo-stationary flow process but different from stationary flows in classical hydraulics as the surface moves in a fixed frame but does not stand still. This implies that equations of ordinary hydraulics do not work on

translatory waves. On the other hand, numerical simulations using the full St. -Venant equation system show the same results for the incoming wave as obtained by translatory wave theory.

This theory leads to simple formulas that give the initial wave height and wave energy in the source area of the tsunami. Distinction has to be made between two cases: Case 1, slides originating from land and Case 2, slides formed on the bottom. Each case must be divided in two schemes: (a) if the surface disturbance is in the same phase as the front of the slide or (b) if the surface wave outruns the slide. Every time the results are simple formulas for the initial wave height and energy. When the path of the tsunami runs over deep water immediately following the source area, it may be convenient to use the same transported energy defined in Case 3. This is a translatory wave in the deep water with the same energy transport as the source area wave, but with higher speed of propagation and lower wave height.

Analyses like these can be extended to form a part of a procedure that gives, as a result, a hazard curve for the probability of occurrence of tsunamis of certain height at a given location. Further research on this problem is considered important.

References

Bryant E (2014) Tsunami the underrated hazard, 3rd edition. Springer International Publishing, DOI 10.1007/978-3-319-06133-7

Day S (2003) Tsunami Hasard in the Atlantic Ocean. Benfield Hazard Research Center

Dutykh D, Dias F (2009) Energy of tsunami waves generated by bottom motion. In: Proceedings of the Royal Society of London A: mathematical, physical and engineering sciences, Vol. 465, No. 2103, pp. 725–744

Elíasson J (2008) A glacial burst tsunami near Vestmannaeyjar, Iceland. J Coast Res:13–20

Eliasson J, Sigbjörnsson R (2013) Assessing the risk of landslide-generated Tsunamis, using translatory wave theory. International Journal of Earthquake Engineering and Hazard Mitigation (IREHM), 1(1), pp. 61–71. http://www.praiseworthyprize.org/jsm/index.php?journal=irehm&page=article&op=view&path%5B%5D=13599

Eliasson J, Kjaran SP, Holm SL, Gudmundsson MT, Larsen G (2007) Large hazardous floods as translatory waves. Environ Model Softw 22(10):1392–1399

Fujii Y, Satake K, Sakai SI, Shinohara M, Kanazawa T (2011) Tsunami source of the 2011 off the Pacific coast of Tohoku Earthquake. Earth Planets Space 63(7):815

GIS (2011) Land and sea areas of crustal movement and slip distribution model of the Tohoku-Pacific Ocean Earthquake: Coseismic Slip Distribution Model; Geographical Survey Institute, Japan. http://www.gsi.go.jp/cais/topic110520-index-e.html

JAMSTEC (2013) Causal mechanisms of large slip during the Tohoku Earthquake of 2011 revealed through hydraulic analysis of faultdrilling samples from the deepsea scientific drilling vessel Chikyu, Press release (Oct 8th 2013), Japan Agency for Marine-Earth Science and Technology. http://www.jamstec.go.jp/e/about/press_release/20131008/

Julien PY (2002) River mechanics. Cambridge University Press, Cambridge

Kerridge D (2005) The threat posed by tsunami to the UK. Department for Environment, Food and Rural Affairs. Flood Management Division, London

NOAA (2011). https://www.youtube.com/watch?v=Lo5uH1UJF4A&feature=youtu.be

Okal EO, Synolakis CE (2003) A theoretical comparison of tsunamis from dislocations and landslides. Pure Appl Geophys 160(10–11):2177–2188

Stoker JJ (1957) Water waves. Intersciense Publishers, New York
Svendsen IA (2006) Introduction to nearshore hydrodynamics. World Scientific Publishing, Hackensack
Synolakis CE, Bernard EN, Titov VV, Kânoğlu U, González FI (2008) Validation and verification of tsunami numerical models. Pure Appl Geophys 165(11–12):2197–2228
Tinti S, Bortolucci E, Vannini C (1997) A block-based theoretical model suited to gravitational sliding. Nat Hazards 16(1):1–28
Tinti S, Bortolucci E, Armigliato A (1999) Numerical simulation of the landslide-induced tsunami of 1988 on Vulcano Island, Italy. Bull Volcanol 61(1): 121–137
Ward SN, Asphaug E (2003) Asteroid impact tsunami of 2880 March 16. Geophys J Int 153(3): F6–F10
Wikipedia (2016) 2011 Tōhoku earthquake and tsunami. https://en.wikipedia.org/wiki/2011_T%C5%8Dhoku_earthquake_and_tsunami

Chapter 9
Surface Strain Rate Tensor Field for Iceland Based on a GPS Network

Ragnar Sigbjörnsson, J. Snæbjörnsson, G. Valsson, Th. Sigurdsson, and Rajesh Rupakhety

Abstract The theme of this paper is the transformation of velocities from a GPS network into a surface strain rate field that illustrates recent and underlying movements within the tectonic system of Iceland. The surface strain rates presented are derived using GPS measurements at the base stations of the National Land Survey of Iceland reference network. The GPS observations are discussed, and the derived average velocity field for an 11-year period, from 1993 to 2004, is presented. The measurements at the westernmost and the easternmost points, which are located on the oldest parts of the country, i.e., the North America plate and the Eurasia plate, respectively, show the rigid movement of the two crustal plates. The average northwards velocity of the two plates is 25 mm/year, and the differential movement is 22 mm/year in the direction 281° from north. The definitions of strain rate tensor and vorticity tensor are outlined and applied in a numerical analysis to derive tensor strain rates from the GPS data. The strain rate tensor field is displayed on maps showing normal and shear strain rate fields, along with principal and dilatation rate fields, as well as the vorticity field. The derived tensor fields are discussed and interpreted in relation to the present-day view on the tectonism of Iceland and recent tectonic activity. The results indicate that most of the significant strain is concentrated on a tongue zone that goes from the North American plate into a slit in the Eurasian plate. The results clearly show the strained volcanic zone of Iceland and the rigid zones with zero strain on either side of it.

R. Sigbjörnsson • R. Rupakhety
Earthquake Engineering Research Centre, University of Iceland,
Austurvegur 2a, IS-800 Selfoss, Iceland

J. Snæbjörnsson (✉)
School of Science and Engineering, Reykjavik University,
Menntavegi 1, IS-101 Reykjavik, Iceland
e-mail: jonasthor@ru.is

G. Valsson • Th. Sigurdsson
The National Land Survey of Iceland, Stillholt 16-18, IS-300 Akranes, Iceland

R. Rupakhety, S. Ólafsson (eds.), *Earthquake Engineering and Structural Dynamics in Memory of Ragnar Sigbjörnsson*, Geotechnical, Geological and Earthquake Engineering 44, https://doi.org/10.1007/978-3-319-62099-2_9

Keywords Mid-Atlantic ridge • Strain rate tensor • Crustal strain • Seismicity of Iceland

9.1 Introduction

The objective of this study is to map crustal strain rates in Iceland as inferred from surface observations applying the global positioning system (GPS). GPS observations and the derived average velocity field for the period 1993 to 2004 are presented. The definition of strain rate and the results of a numerical analysis are outlined.

The present analysis of the surface strain field is the first comprehensive mapping covering the central part of the whole country. However, GPS results for smaller areas have been published (see, for instance, Camitz et al. 1995; Alex et al. 1999; LaFemina et al. 2005; Geirsson et al. 2006; Perlt and Heinert 2006). Furthermore, studies on strain precursors and strain induced by the South Iceland earthquakes in June 2000 have been presented in Lindman (2001) and Árnadóttir et al. (2001).

The techniques applied herein to obtain crustal strain rates in geodetic networks are applied widely in geologically active areas of the world (see for instance, Fujii and Nakane 1979; Savage et al. 1991; Lisowski et al. 1991; Murray and Lisowski 2000; Árnadóttir et al. 1999; Badawy 2005; Williams et al. 2006). Especially worth mentioning, is the study by Kahle et al. (2000) on GPS-derived strain rate fields and seismic hazard. Nishimura and Hashimoto (2006) also present an interesting study of a complex plate system based on a GPS network covering most of southern Japan. Their data clearly shows that a short-term, local variation is sometimes larger than the total trend over the 6-year observation period. Becker et al. (2005) present a similar study for southern California, where they also present stress estimates. Pollitz and Vergnolle (2006) put forward a relationship between long-term fault slip rates and instantaneous velocities imposed by the bounding Pacific and Juan de Fuca (JdF) plates on the North American plate and report a time varying strain. They suggest a model where cumulative displacement caused by co-seismic slips on a fault is followed by a visco-elastic deformation. Most of the observations mentioned above are, however, from areas with predominant crustal compression in large plate segments.

Iceland is a part of the rift zone, the Mid-Atlantic Ridge, shown on Fig. 9.1, which separates the North American and the Eurasian plates. The ridge comes ashore at the Reykjanes Peninsula in the southwest, and the rift zone goes through the country along the seismic and volcanic zones of Iceland as it continues to the northeast. It is well known that volcanism, earthquakes and geothermal activity are, to a certain degree, related in Iceland (Bergerat et al. 1998). It is an open question whether they are all caused by crustal plate motion and subsequent strain. Nevertheless, there is a clear relationship between crustal plate tectonics and volcanism. Thordarson and Larsen (2007) give an excellent overview of the Icelandic

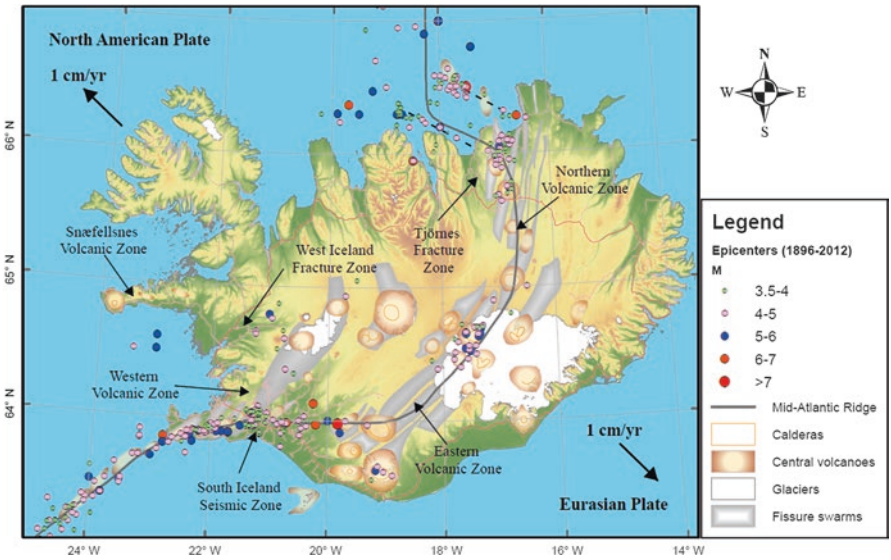

Fig. 9.1 Main tectonic structures and earthquake epicentres: The *grey areas* indicate volcanic zones; *solid lines* indicate rift zones offshore, representing parts of the Mid-Atlantic Ridge; the rift zones on land are located at the Eastern, Western and Northern Volcanic Zones; *dashed lines* indicate offshore fracture zones and seismic lineation; The main seismic and volcanic zones are pointed out; *circles* denote epicentres of earthquakes larger than moment magnitude 3.5 between 1896 and 2012. Earthquake epicentres and size are mainly based on Stucchi et al. (2013) with some adjustments based on Ambraseys and Sigbjörnsson (2000) as explained in D'Amico et al. (2016)

volcano zones. It may be a matter of opinion whether the Western Volcanic Zone and the Mid Iceland Belt belong to active plate boundaries, but the Eastern Volcanic Zone certainly does and has supplied 87% of the total 87 million m^3 that Iceland's volcanoes have emitted in the last 1100 years (Thordarson and Larsen 2007). Gudmundsson (2000) also shows that volcanic systems are formed as the plates are pulled apart and illustrates how dike injection along the plate boundaries can either trigger or suppress earthquakes. The difference in strain between triggering and suppressing zones can be seen in the following study of the kinematics resulting from the fact that the western and the eastern ends of the geodetic network show rigid motion with almost zero average strain over an 11-year period.

9.2 GPS Data and Kinematics

The National Land Survey of Iceland has carried out and coordinated two GPS campaigns in Iceland (Valsson et al. 2007) covering the whole country. In the first campaign in 1993, a network of 119 base stations was established (Magnusson et al. 1997). The GPS observations were repeated in 2004, using the same network

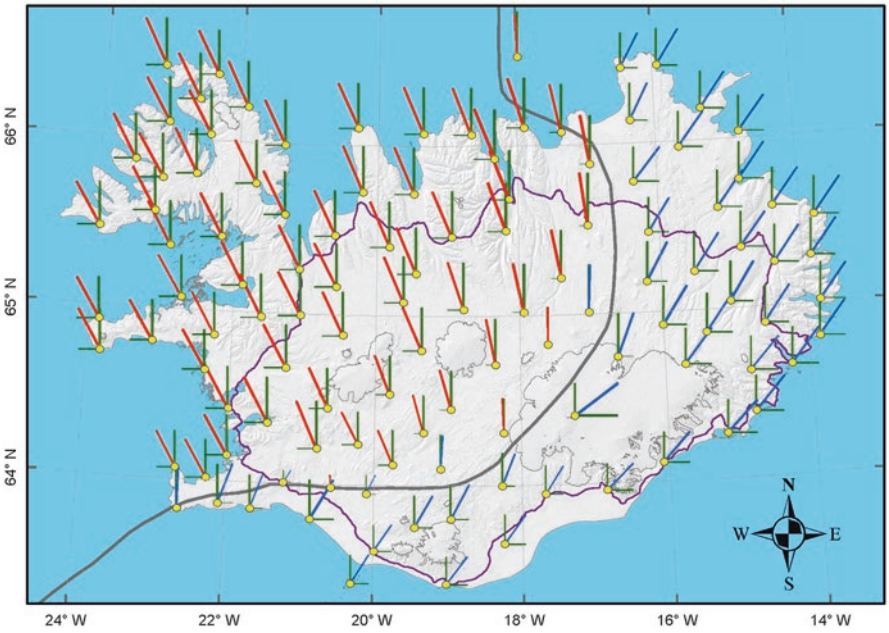

Fig. 9.2 Average horizontal velocities derived from GPS measurement campaigns in 1993 and 2004 carried out by the National Land Survey of Iceland (Valsson et al. 2007). The north-south, east-west and resultant velocity vectors are shown with lines originating from *yellow circles*, which represent the GPS stations. The *grey* trace representing the plate boundaries across Iceland is not based on the velocities, but is rather a simplified representation based on the geological structure shown in Fig. 9.1

(Valsson et al. 2007), resulting in the velocity field presented in Fig. 9.2. The velocities are represented by vectors given by the coloured lines. The length of the coloured lines defines the magnitude of the velocity vector and the sense of the motion, and the yellow circles indicate the location of the GPS stations.

The results indicate northward motion of the whole country, with a maximum average (11-year) displacement of approximately 27 cm, which is equivalent to maximum average velocity of 25 mm/year. In addition, it is seen that the western part of the country is moving westward (indicated by the red lines in Fig. 9.2), while the eastern part is clearly moving eastward (indicated by the blue lines in Fig. 9.2). This depicts the distinguishing features of the currently accepted view on tectonism in Iceland (see for instance, Bergerat et al. 1998), characterized by the ridge between the North American and Eurasian Plates in Iceland (see Fig. 9.1). This ridge is marked by the Northern Volcanic Zone, with the rift axis extending northward from Vatnajokull Glacier, and by the Eastern Volcanic Zone south of Vatnajokull Glacier. It then crosses the South Iceland Lowland and passes along the Reykjanes Peninsula towards southwest, i.e., the North-Atlantic ridge.

The basic seismotectonics of Iceland can be visualised from the earthquake epicentres displayed in Fig. 9.1. Looking at Figs. 9.1 and 9.2, we sense the association

between the geologically active regions and the crustal surface velocities. The rift zone in the form of volcanic zones and seismic transfer zones in the south and the north takes a complicated form, but the main kinematic feature is that the area belonging to the North American plate is being drawn away from the Eurasian plate by the differential velocity of these two, rigid plates.

The rigid plate motion is computed as an average of 11 GPS points in the west and the east, respectively. The standard deviation of their velocities is only around 3%, so these two parts can be considered to be moving as rigid plates. The differential motion of the two areas studied indicates that the North American plate has moved away from the Eurasian plate by 24.2 cm, or with a velocity of 2.2 cm/year, in the direction 281° from north on the average. This is very close to the drift during last 10 million years of the Icelandic hot spot relative to the North American plate as presented by Thordarson and Larsen (2007).

An indication of how well the kinematics displayed by the evaluated velocity field compares to modern interpretations of Icelandic volcanism can be seen by the intense crustal deformation of the Husavik-Flatey Fault (Gudmundsson (2007), where the plates are pulled apart. The South Iceland Seismic Zone (SISZ), on the other hand, is dominated by strike-slip seismic events, and the separation of the velocity field forms a line that is parallel to the 64° latitude, where most major earthquakes in the SISZ have occurred (Ambraseys et al. 2002, 2004).

It should be pointed out, however, that a slight drift of the differential velocity vector of the rigid plate zones can change the local kinematics dramatically, regardless of whether the change occurs in the eastern or western zone (Murray et al. 1995). A directional shift in the differential velocity vector will either increase stress buildup in the SISZ or in the Tjörnes Fracture Zone (TFZ, see Fig. 9.1), depending on whether the shift is in a counter clockwise or clockwise direction. According to Thordarson and Larsen (2007), a shift of 40° in the counter clockwise direction did happen between 10 and 20 million years ago. Tesauro et al. (2005) report continuous GPS observations from many central European networks, but the velocities are an order of magnitude lower than those estimated here. Serpelloni et al. (2005) report results from 11 years of continuous and discontinuous GPS observations where the velocities are of the same order of magnitude as here, but their velocities show remarkably little fluctuation throughout the period (1992–2003). The model of Pollitz and Vergnolle (2006) predicts systematic variation of velocities with time, but the model assumes that the variations are triggered by co-seismic events. In contrast to this, some of the data published by Nishimura and Hashimoto (2006) show significant time variation in the velocity trends.

The velocity of 2.2 cm/year is 15% higher than the prediction of the Nuvel −1 plate motion models, but the direction of 281°N is fairly close to the predicted one (see, e.g., Sigmundsson 2006 and/or http://ofgs.ori.u-tokyo.ac.jp/~okino/platecalc_new.html). Other plate motion models give velocity and direction numbers far off the observed values. However, herein, the focus is on the crustal strain rates as observed on the surface, so rigid plate tectonics will not be discussed further.

9.3 Analysis of Strain Rate

The average velocity field shown in Fig. 9.2 is a useful quantity for studying background tectonic motion, as discussed in Sect. 9.2. Other processes, such as regional or local deformations, are more clearly visualised using the strain rate field derived from the relative velocities. From a civil engineering point of view, it is primarily the strain rate field that is of concern. As long as the velocity field, as well as the derived acceleration, is sufficiently small, inertial forces can be neglected. Furthermore, when the velocity field is uniform in space, no strain or vorticity (spin) that may harm structural systems is induced.

To facilitate the following discussion, a simplified presentation of tensor strain rates is provided. Assuming that the velocity vectors of neighbouring points, P_o and P, are given as $\mathbf{u}^o$ and $\mathbf{u}$, respectively, the velocities can be related using a Taylor series expansion around P_o. Hence, $\mathbf{u} = \{u_i\} = \{u_1, u_2, u_3\}$ can be expressed to the first order as follows (Spain 2003):

$$u_i = u_i^o + u_{i,j} dx_j \tag{9.1}$$

Here, the Einstein summation convention is applied, where the comma denotes the partial derivative. The relative motion of the points is readily obtained as:

$$dx_i = u_i - u_i^o = u_{i,j} dx_j \tag{9.2}$$

The tensor, $u_{i,j}$, is the *velocity gradient tensor*. In the general case, we have $u_{i,j} \neq u_{j,i}$ which implies that this tensor is not symmetric. It is, however, possible to construct the velocity gradient tensor as a sum of a symmetric and antisymmetric part (see, for instance, Akivis and Goldberg 2003). That is:

$$u_{i,j} = e_{ij} + \omega_{ij} \tag{9.3}$$

where

$$e_{ij} = \frac{1}{2}\left(u_{i,j} + u_{j,i}\right)$$

$$\omega_{ij} = \frac{1}{2}\left(u_{i,j} - u_{j,i}\right) \tag{9.4}$$

The tensor denoted e_{ij} is a measure of the deformation and is called the *rate of strain tensor.* The ω_{ij} tensor is, on the other hand, a measure of rigid body rotation and is referred to as the rotational velocity tensor or *vorticity tensor*. Hence, the velocity field, Eq. (9.1), can now be expressed as follows:

Table 9.1 Example of computed strain rates

Point No.	Normal strain		Shear	Principal strain		Principal direction (° from North)	Dilatation (μstrain per year)
	e_{11} (μstrain per year)	e_{22} (μstrain per year)	e_{12} (μstrain per year)	e_{I} (μstrain per year)	e_{II} (μstrain per year)		
A	0.1933	0.0351	−0.1199	0.2578	−0.0294	−28.29	0.2284
B	0.0360	−0.0024	−0.0133	0.0402	−0.0066	−17.36	0.0336

$$u_i = u_i^o + \omega_{ij} dx_j + e_{ij} dx_j \tag{9.5}$$

The first two terms on the right-hand side refer to rigid-body motion, i.e., translation and rotation, respectively, while the last term describes the rate of strain due to the relative velocity of the points.

The outlined theory, formally derived using Cartesian tensors for simplification, is valid for small displacements and velocities. In the general case, for large distances, it is required to apply curvilinear coordinates to approximate the surface of the geoid. For smaller distances and velocities, the general equations for strain rate reduce to the above-given equation for e_{ij}.

An additional insight into the surface strain rate field can be gained through computation of principal strain rates and principal directions. These are readily obtained as eigenvalues and eigenvectors of the strain rate tensor. The results are as follows for the principal strain rates:

$$\left.\begin{matrix} e_I \\ e_{II} \end{matrix}\right\} = \frac{e_1 + e_2}{2} \pm \sqrt{\left(\frac{e_1 - e_2}{2}\right)^2 + e_{12}^2} \tag{9.6a}$$

while the principal direction is given by:

$$\vartheta_P = \frac{1}{2} \tan^{-1}\left(\frac{2e_{12}}{e_1 - e_2}\right) \tag{9.6b}$$

Here, the index 1 and 2 refer, respectively, to the longitude and latitude (see also the notation used in Table 9.1).

9.4 Numerical Results

9.4.1 Interpolation of Velocity Field

The strain rates are computed numerically from the velocities derived from the GPS observations, using a triangulation network covering the central part of the island as indicated in Fig. 9.3. The Westfjords (NW part of the country, see Figs. 9.1 and 9.2)

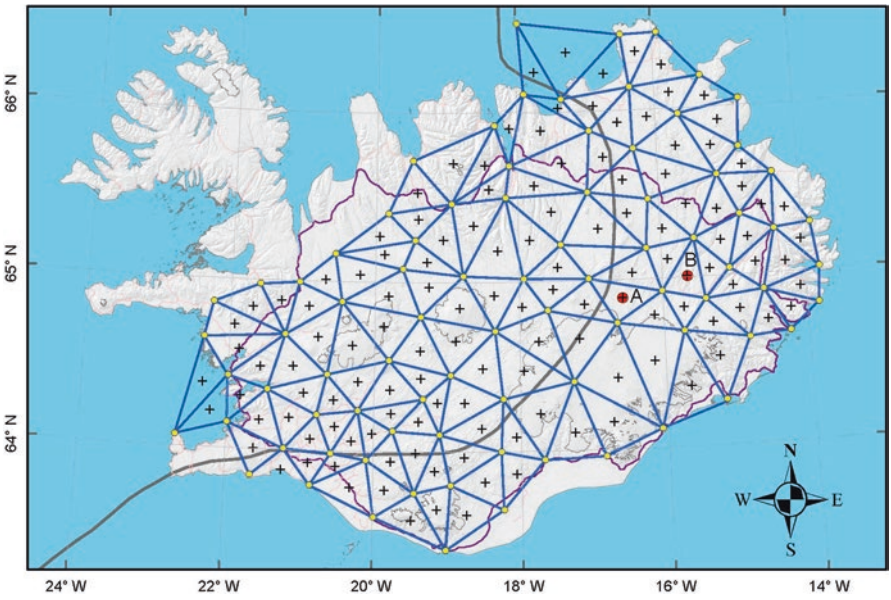

Fig. 9.3 Triangulation used in numerical computations of the strain rate tensor field, the centroids of the *triangles* are indicated, and two points, A and B, marked with the *red circles* are selected as reference points for investigation of principal strains and directions in the following sections

are not included as the strain rate there is close to zero anyway, but that boundary zone provides increased accuracy and numerical stability. For each triangle, a linear velocity interpolation field is assumed as a first approximation, i.e.:

$$u_i\left(x_j\right) = a_i + b_{ij}x_j \tag{9.7}$$

The unknown parameters, a_i and b_{ij}, are estimated by introducing the velocities at the corner points of the triangles, i.e., the reference stations. Then the strain rate tensor and the vorticity tensor are readily obtained using Eq. (9.4) or its curvilinear representation in the general case.

Applying this procedure, the components of the strain rate tensor are obtained. The resulting values, which are constant within each triangle for the applied approximation (Eq. (9.7)), are plotted at the centroid of each triangle. Simplified interpolation and smoothing of the results, based on Delaunay triangulation, yield the colour maps displayed in Fig. 9.4 with the scale given by the colour bar to indicate the intensity of the strain rate component. The smoothing is not carried out to the full extent of the boundary defined by the triangulation net (see Fig. 9.3) to minimise possible boundary effects.

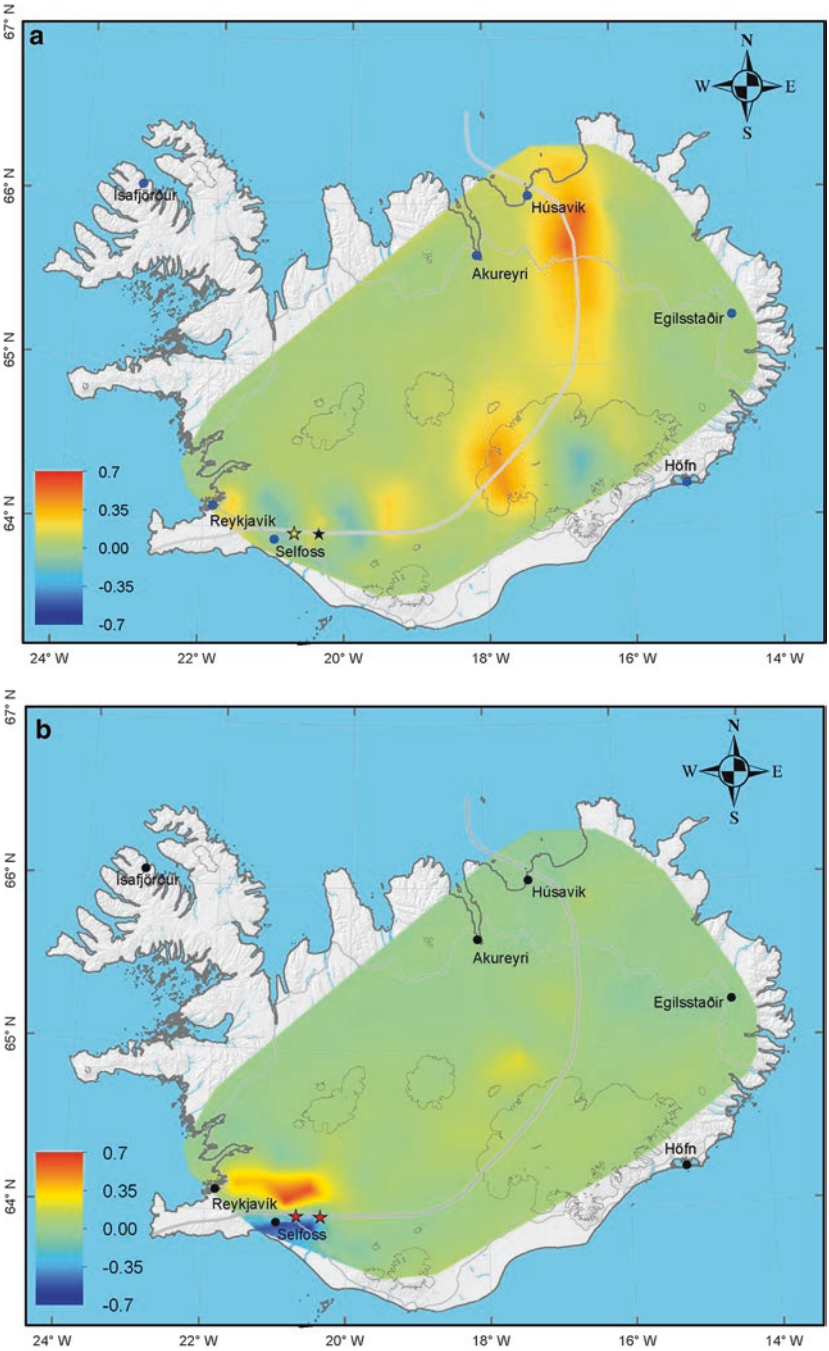

Fig. 9.4 The strain rate tensor field: (**a**) Normal strain rate east-west component. (**b**) Normal strain rate north-south component. (**c**) Shear strain rate (in an east-north coordinate system)

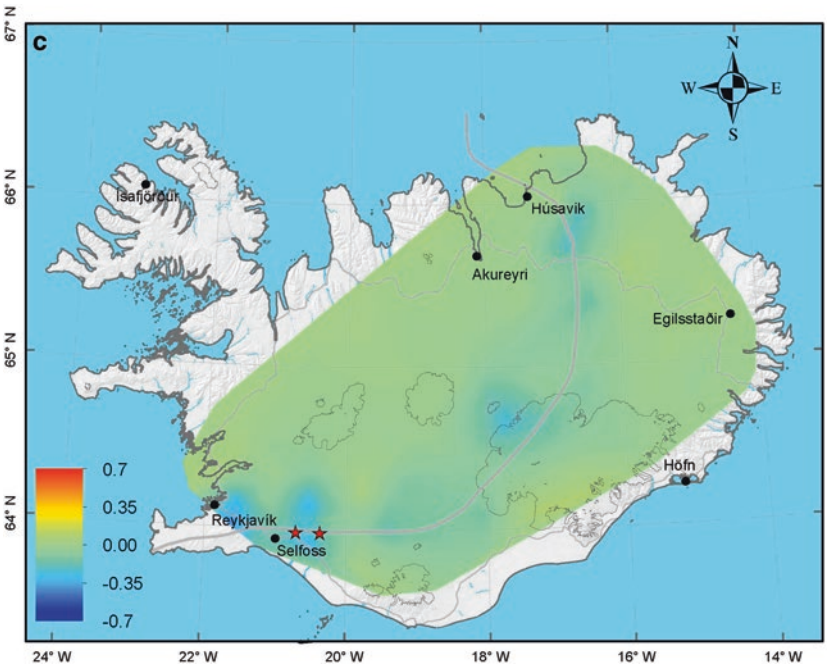

Fig. 9.4 (continued)

9.4.2 Maps of Strain Rate Components

The basic components of the strain rate tensor field are shown in Fig. 9.4a, b and c in spherical coordinates derived using the radius of curvature at the study area. The corresponding principal strain rate components are plotted in Fig. 9.5, along with the dilatation rate (volumetric strain rate) and vorticity tensor field.

Figure 9.4a shows the east-west normal strain rate. The largest positive strain rate is observed in the Northern Volcanic Zone (NVZ), 0.5 μstrain/year (on average during the recording period). This is in the north-eastern part of the triangulation net where the TFZ comes ashore (see Fig. 9.1). Another area with positive strain (red) is seen in the Eastern Volcanic Zone (EVZ), west of Vatnajokull Glacier, while the area to its east, where a volcanic eruption occurred in 1996, shows a negative strain rate (blue). This demonstrates that volcanoes can easily create their own strain field within their local vicinity (LaFemina et al. 2005). The data resolution is somewhat blurred around central Vatnajokull Glacier, as only one GPS point is located there. West of the EVZ, there is an east-west linear area along the SISZ with alternating values of positive and negative, east-west normal strain.

The north-south strain rates (Fig. 9.4b) are generally small, as they should be when the rigid plate motion on both sides is almost the same. The north-south normal strain is largest in the SISZ, where it is seen to be positive north of the 64° lati-

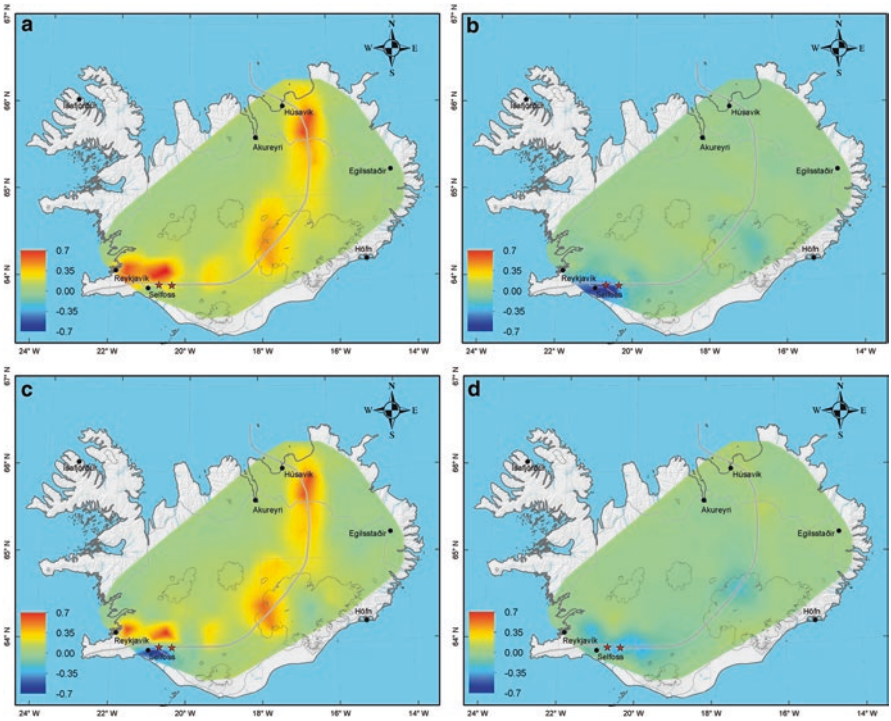

Fig. 9.5 The principal strain rate tensor and vorticity field. (**a**) First principal strain rate. (**b**) Second principal strain rate. (**c**) Dilatation rate. (**d**) Vorticity tensor

tude and negative south of the same latitude. The highest strain rates in this area are ±0.7 μstrain/year (on average during the recording period). Also, in this case, the strain rates conform to the overall kinematics of the area.

The shear strain rates shown in Fig. 9.4 are predominantly small, except in the SISZ and the NVZ, which conforms to the above-inferred kinematics of the motion. The same can be said about the dilation and vorticity fields pictured in Fig. 9.5c and d, where the only significant vorticity is generated on the rift zone marking the plate boundary.

Figure 9.6 shows the dilation rate plotted together with earthquake epicentres, which clearly illustrates the direct association between tectonic activity and crustal strain, discussed partly in Sect. 9.2.

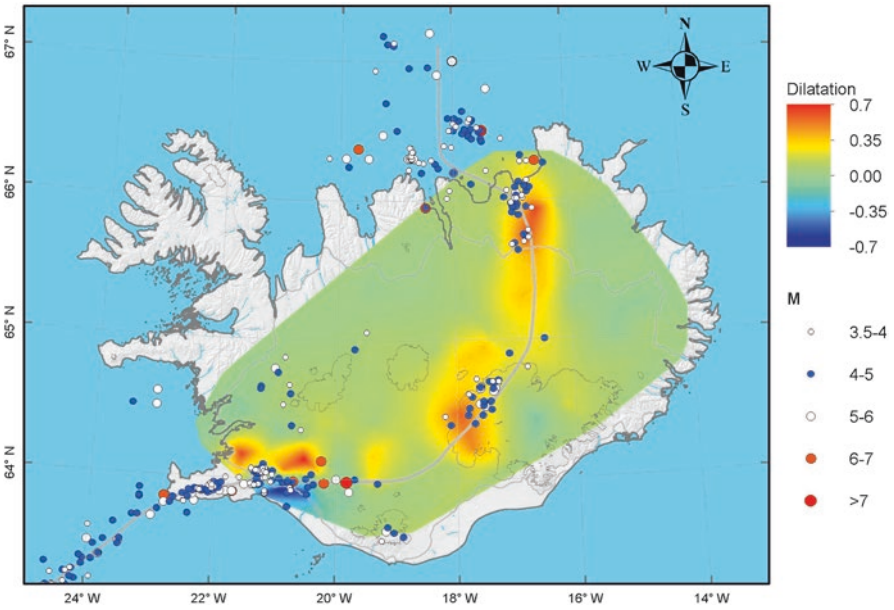

Fig. 9.6 The dilatation rate plotted along with earthquake epicentres. The circles denote earthquake epicentres with a magnitude larger than 3.5 between 1896 and 2012

9.4.3 Principal Strain Rates and Directions

It is of interest to investigate the principal strains (see Fig. 9.5) more closely and compute their principal directions. As pointed out above, however, this primarily has meaning for areas where the compatibility equations are fulfilled, in other words, in areas outside the plate boundary zone. As a study site, we have chosen two points, Point A and Point B, roughly 60 km apart in the area north of Vatnajökull Glacier (see Fig. 9.3). Point B is identified as being outside the rift zone, while Point A is on the outskirts of the zone of volcanic activity north of the Mt. Kverkfjöll Volcano, close to the rift axis. The strain rate components for these two points are shown in Table 9.1. For Point B, which is considered representative of the rigid behaviour of the area, we see from Fig. 9.7 that the principal direction of strain tends towards east-south-east, which is broadly in agreement with the general orientation of faults in the area. The principal direction is also evident from Fig. 9.2.

It is seen in Fig. 9.5 and Table 9.1 that the east-west strain rate at Point B (see Fig. 9.5b) is positive, while the north-south strain rate (see Fig. 9.5c) is negative. Considering the magnitude of the strain rate in each direction, this likely indicates that the area is primarily under east-west *tension,* and that the north-south *compression* is simply due to the Poisson effect, corresponding to a Poisson ratio equal to roughly 0.16, which seems a reasonable value for the crust at the surface. Moving westward, approaching the volcanic zone, the Poisson ratio decreases, suggesting

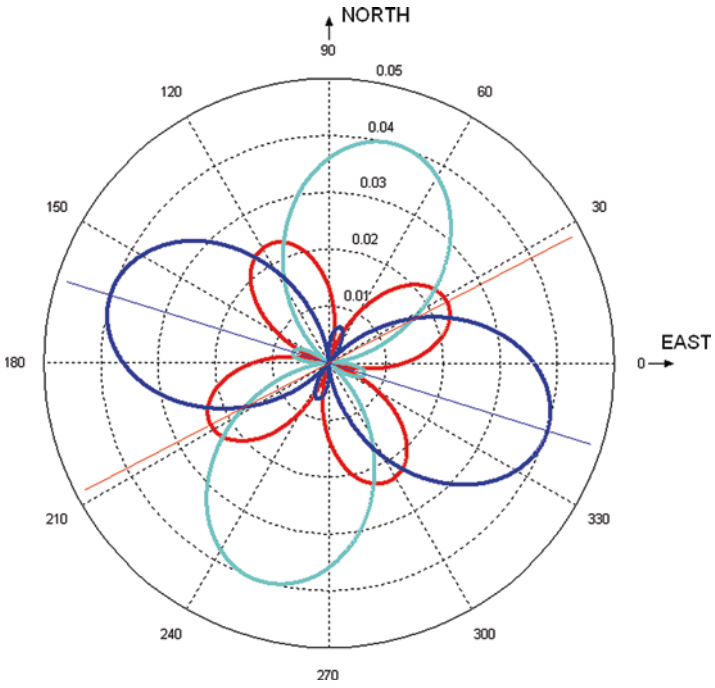

Fig. 9.7 Example of polar representation of strain rate components at Point B (see Table 9.1). The strain rate, e_1 (east-west), is denoted by the *blue curve*; e_2 (north-south) is given by the *cyan curve* and e_{12} by the *red curve*. The principal direction is shown by the *blue line* (−17.4°) and the direction of the maximum shear strain rate by the *red line* (27.6°)

increasing fracturing at the surface (the Poisson ratio is equal to 0.1 at Point A). The shear strain rate is found to be negative (see Fig. 9.4c), which indicates that the area toward the north is moving towards the west; in other words, the shear motion might be interpreted as being left lateral. The strain rate values at Point B are generally low. However, looking westward (see Fig. 9.5b), it is seen that the tensional strain rate increases, exceeding 0.1 μstrain/year when passing the 16°W longitude. A similar pattern emerges looking at the shear strain rates (see Fig. 9.4c), except that the values are now all negative, supporting the above-mentioned left lateral movement. Roughly the same pattern is seen in Fig. 9.5c, which displays a dilatation rate characteristic of the east-west tension.

These analyses indicate that the induced strain rates at Point B are rather small, at least compared with the high activity in the rift zone towards west, i.e., Point A. This is, however, not the case when we look at the displacement rate (see Fig. 9.2). Considerable horizontal movements are expected at Point B during the next 50 years. These movements are, however, largely uniform, resulting in the low strain rates discussed above. The vorticity tensor depicted in Fig. 9.6d supports this. The computed vorticity for the study site is only −0.0101 μ/year. This is a small value, especially in view of the oscillation of the sign of the vorticity between plus

and minus for the triangles in the neighbourhood of the study site. However, we see that the vorticity increases slightly toward the west before it turns negative (see Fig. 9.6d). This happens only within the rift zone. Therefore, the low vorticity supports the apparent uniform velocity field seen in Fig. 9.2 at Point B.

This discussion has been confined to the area east of the Northern Volcanic Zone. However, the same, more or less, applies to the area west of the rift zone. Similar results can be obtained, for instance, in the area north of Hofsjökull Glacier.

In the Eastern Volcanic Zone, the first principal strain rate component tends to be positive. This indicates rift and supports the information already inferred from Fig. 9.5b. In the South Iceland Lowland (SISZ), the motion is dominated by shear, especially in the western part. It can be seen in Figs. 9.4, 9.5 and 9.6 that the highest strain rates conform to the epicentral area of the south Iceland earthquakes in June 2000 (about 20.5°W meridian, see Fig. 9.1). In this area, the shear rate is negative, which is also the case for the vorticity. The discontinuity point in the strain field around the 21°W meridian may also be noted.

9.5 Discussion

Outside the boundaries of the rift zone separating the North-American and the Eurasian plates, which are the main areas of deformations and rupture, the strain rates tend to be small. The vorticity field also indicates that the blocks outside the boundary zone behave as rigid solids in translational motion, at least on a time scale of 11 years.

The present magnitude and direction of the differential velocities vector between the two rigid plate zones indicate that the rift across the plate boundaries occurs without compression being created from this velocity or strain field, except for the compressive strain created by the shear strain in the SISZ zone, which can be related to strike-slip movement from east to west. Small changes in the direction of the differential velocity vector, in the future, may change this situation.

For the two blocks outside the rift zone, the compatibility equations for the strain rate tensor components are fulfilled, which is not necessarily the case within the rift or boundary zone between the two plates, where even the computed Poisson ratio may fall outside the physically admissible range. From a theoretical point of view, this implies that the blocks are behaving like elastic solids, while the rift boundary zones are broken down in elements divided by faults and fractures.

An improved understanding and linkage between a kinematic model of the tectonic system and the strain rate calculations may have important engineering applications. Although the GPS velocities mostly reflect past occurrences, future mapping of strain buildup may help to indicate where the next earthquakes are likely to occur. Crustal strain causes elongation or contraction of distances on the surface, and this can be of importance for design of structures. Large structures, subjected to the strain e_I at point A in Table 9.1, may suffer additional loading due to differential base movements, whereas similar structures at point B would not be exposed to

such loading. The actual load on the structure would, among other things, depend upon how the earth's crust redistributes the deformation locally. This issue calls for further research.

9.6 Conclusion

The results of the GPS campaigns performed in 1993 and 2004 for the ground-based reference stations in the National Land Survey of Iceland network indicate a velocity field governed by rigid plate motion of the North American plate and the Eurasian plate comparable to the Nuvel – 1 models.

Looking at seismic data (Figs. 9.1 and 9.6), inferences may be drawn that the boundary between the North American and Eurasian plates in Iceland follows the volcanic and seismic transfer zones. The differential velocity vector of the two plates has an average magnitude of 2.2 cm/year and direction 281° from north.

Significant strain rates are generated in the rift/boundary zone between the two plates. The largest shear strain is in the South Iceland Seismic Zone, which roughly follows the orientation of the differential velocity vector. Two strong earthquakes (~M6.5) occurred within this zone in 2000 and the areas of the highest strain rates conform to the epicentral areas. In the north and the east volcanic zones, the first principle strain is positive (tension) in the E-W direction. Outside the main seismic and volcanic zones, crustal strains are rather small, indicating rigid body motion.

Acknowledgements The present work was supported by Landsvirkjun (the National Power Company of Iceland) and the University of Iceland Research Fund.

References

Akivis MA, Goldberg VV (2003) Tensor calculus with applications. World Scientific Publishing Company, Singapore, 380 pages

Alex R, Einarsson P, Heinert M, Niemeier W, Ritter B, Sigmundsson F, Willgalis S (1999) GPS-mefikampagne 1995 zur bestimmung von Deformationen der Erdkruste in Südwest-Island. Zeitschrift für Vermessungswesen 124(12):377–388

Ambraseys N, Sigbjörnsson R (2000) Re-appraisal of the seismicity of Iceland. Polytechnica – Engineering seismology, Earthquake Engineering Research Centre, University of Iceland, Selfoss, ISBN 9797-989-91-4X: 196 pages

Ambraseys NN, Smit P, Sigbjörnsson R, Suhadolc P, Margaris B (2002) Internet-site for European strong-motion data. European Commission, Research-Directorate General, Environment and Climate Programme, Brussels. URL: http://www.ised.hi.is Date visited: 30 April 2006

Ambraseys N, Douglas J, Sigbjörnsson R, Berge-Thierry C, Suhadolc P, Costa G, Smit P (2004) European strong-motion database, vol 2. Imperial College of Science, Technology and Medicine, London

Árnadóttir T, Thomley S, Pollitz FF, Darby DJ (1999) Spatial and temporal strain rate variations at the northern Hikurangi margin, New Zealand. J Geophys Res 104(B3):4931–4944

Árnadóttir T, Hreinsdóttir S, Gudmundsson G, Einarsson P, Heinert M, Volksen C (2001) Crustal deformation measured by GPS in the South Iceland Seismic Zone due to two large earthquakes in June 2000. Geophys Res Lett 28:4031–4033

Badawy A (2005) Present-day seismicity, stress field and crustal deformations of Egypt. J Seismol 9:267–276

Becker TW, Hardebeck JL, Anderson G (2005) Constraints on fault slip rates of the southern California plate boundary from GPS velocity and stress inversions. Geophys J Int 160(2):634–650

Bergerat F, Gudmundsson A, Angelier J, Rognvaldsson ST (1998) Seismotectonics of the central part of the South Iceland Seismic Zone. Tectonophysics 298(4):319–335

Camitz J, Sigmundsson F, Foulger G, Jahn C-H, Völksen C, Einarsson P (1995) Plate boundary deformation and continuing deflation of the Askja volcano, North Iceland, determined with GPS, 1987–1993. J Bull Volcanol 57(2)

D'Amico C, Albarello D, Sigbjörnsson R, Rupakhety R (2016) Seismic hazard assessment for Iceland in terms of macroseismic intensity using a site approach. Bull Earthq Eng 14(7):1945–1955

Fujii Y, Nakane K (1979) Anomalous crustal strain prior to the 1923 Kanto, Japan earthquake as deduced from analysis of old triangulation data. In: Wyss M (ed) Contributions to current research in geophysics 8: Earthquake prediction and seismicity patterns. Birkhauser Verlag, ISBN 3-7643-1122-3

Geirsson H, Árnadóttir T, Völksen C, Jiang W, Sturkell E, Villemin T, Einarsson P, Sigmundsson F, Stefánsson R (2006) Current plate movements across the Mid-Atlantic Ridge determined from 5 years of continuous GPS measurements in Iceland. J Geophys Res 111:B09407. doi:10.1029/2005JB003717

Gudmundsson A (2000) Dynamics of volcanic systems in Iceland: example of tectonism and volcanism at Juxtaposed hot spot and Mid-Ocean Ridge Systems. Annu Rev Earth Planet Sci 28:107–140

Gudmundsson A (2007) Infrastructure and evolution of ocean-ridge discontinuities in Iceland. J Geodyn 43:6–29

Kahle H-G, Cocard M, Peter Y, Geiger A, Reilinger R, Barka A, Veis G (2000) GPS-derived strain rate field within the boundary zones of the Eurasian, African, and Arabian plates. J Geophys Res 105(B10):23353–13370

LaFemina PC, Dixon TH, Malservisi R et al (2005) Geodetic GPS measurements in South Iceland: strain accumulation and partitioning in a propagating ridge system. J Geophys Res Solid Earth 110(B11.) Art. No. B11405

Lindman M (2001) Strain precursors for the June 2000 earthquakes, South Iceland, Luleå University of Technology, 302 CIV, ISSN 1402-1617, 98 pages

Lisowski M, Savage JC, Prescott WH (1991) The velocity field along the San Andreas fault in central and southern California. J Geophys Res 96(B5):8369–8389

Magnusson I Th, Thorbergsson G, Björnsson J Th (1997) GPS-mælingar í grunnstöðvaneti 1993 og ný viðmiðun ISN93 við landmælingar á Íslandi. National Land Survey of Iceland (www.lmi.is)

Murray MH, Lisowski M (2000) Strain accumulation along the Cascadia subduction zone. Geophys Res Lett 27(22):3631–3634

Murray F, Einarsson P, Bilham R, Sturkell E (1995) Rift-transform kinematics in South Iceland: deformation from Global Positioning system measurements, 1986 to 1992. J Geophys Res 100(B4):6235–6248

Nishimura S, Hashimoto M (2006) A model with rigid rotations and slip deficits for the GPS-derived velocity field in southwest Japan. Tectonophysics 421(3–4):187–207

Perlt J, Heinert M (2006) Kinematic model of the South Icelandic tectonic system. Geophys J Int 164:168–175

Pollitz FF, Vergnolle M (2006) Mechanical deformation model of the western United States instantaneous strain-rate field. Geophys J Int 167(1):421–444

Savage JC, Lisowski M, Prescott WH (1991) Strain accumulation in Western Washington. J Geophys Res 96(B9):14493–14507

Serpelloni E, Anzidei M, Baldi P et al (2005) Crustal velocity and strain-rate fields in Italy and surrounding regions: new results from the analysis of permanent and non-permanent GPS networks. Geophys J Int 161(3):861–880

Sigmundsson F (2006) Iceland geodynamics: crustal deformation and divergent plate tectonics. Springer, Berlin

Spain B (2003) Tensor calculus. Dover Publications

Stucchi M, Rovida A, Capera AG, Alexandre P, Camelbeeck T, Demircioglu MB, Gasperini P, Kouskouna V, Musson RM, Radulian M, Sesetyan K (2013) The SHARE European earthquake catalogue (SHEEC) 1000–1899. J Seismol 17(2):523–544

Tesauro M, Hollenstein C, Egli R et al (2005) Continuous GPS and broad-scale deformation across the Rhine Graben and the Alps. Int J Earth Sci 94(4):525–537

Thordarson T, Larsen G (2007) Volcanism in Iceland in historical time: volcano types, eruption styles and eruptive history. J Geodyn 43:118–152

Valsson G, Sigurdsson Th, Völksen C, Rennen M (2007) ISNET 2004 – Nidurstödur úr endurmælingum Grunnstödvanets Íslands, National Land Survey of Iceland (www.lmi.is)

Williams TB, Kelsey HM, Freymueller JT (2006) GPS-derived strain in northwestern California: termination of the San Andreas fault system and convergence of the Sierra Nevada-Great Valley block contribute to southern Cascadia forearc contraction. Tectonophysics 413(3–4):171–184

Chapter 10
Determination of Parameters for Stochastic Strong Motion Models Representing Earthquakes in the South Iceland Seismic Zone

Símon Ólafsson, Ragnar Sigbjörnsson, and Rajesh Rupakhety

Abstract The parameters for a point source model are estimated using strong ground motion recorded in the largest earthquakes in south Iceland since a strong motion network established (from 1986 to 2008). The model is found to provide a good fit to the ground motion records. Parameters were estimated for the earthquakes of 17th June 2000 M_w 6.5, 21st June 2000 M_w 6.4, 29 May 2008 M_w 6.3 and 25 May 1987 M_w 5.8. Great variability in parameters was observed. A mean kappa, $\kappa = 0.04$ s, was observed. The stress drop for the three larger events had an estimated average value of 80×10^5 Pa and an average dislocation of 90 cm. Closed form relations for root-mean-squared (rms) acceleration are presented for the ground motion in the near and far field. A peak factor is then applied to rms acceleration in order to obtain peak ground acceleration. The model can be applied instead of empirical ground motion prediction equations to estimate ground motion and potential seismic hazard in Iceland. Its estimated parameters can be used in the framework of stochastic modelling to simulate artificial ground acceleration for the dynamic analysis of structures.

Keywords Brune's source model • Kappa • Stress drop • Icelandic strong motion network • Attenuation

S. Ólafsson (✉) • R. Sigbjörnsson • R. Rupakhety
Earthquake Engineering Research Centre, University of Iceland, Selfoss, Iceland
e-mail: simon@hi.is; rajesh@hi.is

R. Rupakhety, S. Ólafsson (eds.), *Earthquake Engineering and Structural Dynamics in Memory of Ragnar Sigbjörnsson*, Geotechnical, Geological and Earthquake Engineering 44, https://doi.org/10.1007/978-3-319-62099-2_10

10.1 Introduction

The stochastic method is widely used for simulation of ground motions for engineering purposes. This method is frequently used to produce artificial records in areas where there are few or no recordings of strong motion available (for an overview see Boore 2003). The method, in its basic form, is based on a point source approximation defined in the frequency domain, which can then be regarded as a filter with white noise input. The method is based on the work of Aki (1967), Brune (1970), Hank and McGuire (1981), Boore (1983), Atkinson and Boore (1995) and others. Several programs are available on the internet to implement the stochastic ground motion simulation algorithm. SMSIM is one of them and is based on a point source model (see Boore 1983, 1996). The programs FINSIM and EXSIM take into account the geometry of the fault, which is divided into subfaults, each of which is modelled as a point source (Beresnev and Atkinson 1998).

The stochastic method was first applied to Icelandic earthquakes by Ólafsson and Sigbjörnsson (1999) using Brune's point source model extended with an exponential term accounting for anelastic attenuation. The root-mean-squared acceleration of the ground motion was expressed in closed form, and then, a peak factor was applied to estimate peak ground acceleration. In Ólafsson et al. (1998), the estimation of source parameters for the Vatnafjöll earthquake (25 May 1987, M_w 5.8) is described. In Ólafsson (1999), source parameters were obtained from all the available strong motion data from Iceland at that time. These data were recorded by the Icelandic Strong Motion Network (IceSMN) (see Sigbjörnsson et al. 2014) and are available freely on the internet (see Ambraseys et al. 2004). The source parameters estimated from these data were the corner frequency, seismic moment, stress drop and kappa. An assumption of a frequency independent quality factor (Q) was made as all the records were at a distance of less than a 100 km from the fault. Due to the lack of data at that time, it was proposed to use the point source model as a ground prediction model instead of applying empirical ground motion prediction models calibrated from data recorded in other parts of the world.

In this article, we present the results of applying the extended Brune's model (Brune 1970) to the most relevant events in the recent years, the June 17th 2000 M_w 6.5, June 21st 2000 M_w 6.4 and May 29th 2008 M_w 6.3 events (Sigbjörnsson and Olafsson 2004; Sigbjörnsson et al. 2009; Pedersen et al. 2003). We estimate model parameters by calibrating the models to recorded strong motion data from these earthquakes and also present ground motion prediction models based on these parameters, which are compared with purely empirical attenuation equations available in the literature. All these events occurred in the South Iceland Seismic Zone, which is an approximately 80 km long and 30 km wide transform zone that extends from Hellisheiði in the west to Mt. Hekla in the east. Most earthquakes in the SISZ have a right lateral strike-slip mechanism. They occur on parallel N-S trending faults with near vertical fault planes, and their hypocenter is shallow, with some earthquakes rupturing to the surface while some are with buried faults. The epicenters of the earthquakes considered in this study are shown in Fig. 10.1.

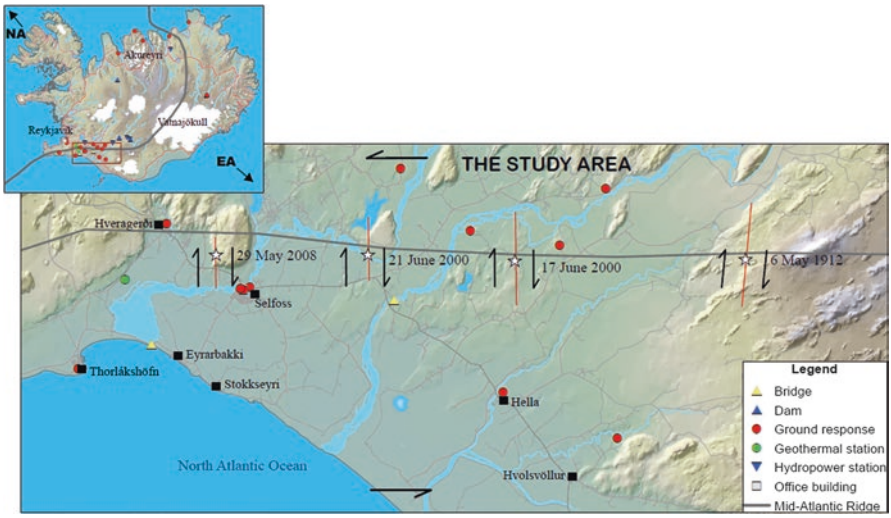

Fig. 10.1 The south Iceland lowland and the SISZ. Approximate fault traces of the four largest earthquakes that have been recorded by the IceSMN are indicated with the *red lines*, with stars indicating epicenters. The accelerograph stations of the IceSMN are indicated by symbols described in the legend

10.2 Ground Motion Model

The parameters of the source model are calibrated from the S-wave portion of the accelerograms that contains most of the energy at epicentral distances less than 100 km. Then parameters, kappa, κ, ω_c (corner frequency) and M_0 (seismic moment), are estimated by fitting Fourier amplitude spectra obtained from the S-wave window of the acceleration records to the Brune's model that has been extended with an exponential term to account for high-frequency decay. The far-field model of Brune is defined as follows, in Eq. 10.1, as a displacement amplitude spectrum:

$$\left|D(\omega)\right| = \frac{2C_P R_{\theta\phi} M_0}{4\pi\beta^3 \rho R} \frac{1}{\left(1+\left(\omega/\omega_c\right)^2\right)} \exp\left(-\frac{1}{2}\kappa\omega\right) \tag{10.1}$$

Here, $C_p = 0.707$ is the factor that accounts for the partition of the energy between the components; $R_{\theta\phi}$ is the S-wave radiation pattern (average is 0.55); β is the shear wave velocity, and ρ is the density of the crust. Anderson and Hough (1984) found that it was possible to describe strong-motion acceleration with a frequency independent Q in shallow crust and a spectral decay parameter of $\kappa = R/Q\beta$. Here, ω_c is the corner frequency (angular), and $f_c = \omega_c/2\pi$ is measured in hertz.

The radius of the dislocation, r, is related to the corner frequency as:

$$r = 2.34 \cdot \beta / \omega_c \tag{10.2}$$

The stress drop, $\Delta\sigma$, is given by:

$$\Delta\sigma = \frac{(7/16)M_0}{r^3} \tag{10.3}$$

The average displacement of the fault is

$$u = \frac{M_0}{\mu A} \tag{10.4}$$

where A is the area of the fault and μ is rigidity given as $\mu = \rho\beta^2$. The high frequency attenuation is controlled by the parameter κ, which is assumed to be distance independent (see Anderson and Hough 1984) and a frequency independent Q that changes linearly with distance from the source. The distance term in Eq. 10.1, is represented by R and is a function of the hypocentral distance, D.

In order to model the ground motion in the near field, it may be necessary to apply a geometric attenuation term with exponent $n = 2$, unlike 1 used in Eq. 10.1, for the far field. The following expressions are suggested for the geometrical spreading function (Ólafsson and Sigbjörnsson 1999):

$$R = \begin{cases} D_2^{1-n} D^n & D_1 < D \le D_2 \\ D & D_2 < D \le D_3 \end{cases} \tag{10.5}$$

where $1 < n \le 2$. Here, d is the epicentral distance, and h is a depth parameter. The parameters, D_1, D_2 and D_3, are used to set the limits for the different zones of the spreading function. The parameter, n, is usually in the range of 1 to 2 but this study assumes that $n = 2$ for $D < D_2$ and that $n = 1$ for D greater than D_2 and less than D_3 (taken here as 100 km).

10.3 Estimation of Parameters

Olafsson (1999) presents source parameters based on Brune's extended model calibrated from all Icelandic data available at that time. The estimation of the source parameters for the Vatnafjöll earthquake is described in Olafsson et al. (1998). The same method is used here to calibrate the parameters of the June 2000 and May 2008 earthquakes. A brief description of the method follows.

After selecting the S-wave window from the strong-motion records and computing the acceleration spectra, the values for Q were obtained by fitting a regression line to the spectra from 2 to 25 Hz. The amplitude spectra, $A(\omega) = \omega^2 D(\omega)$, are dominated by the exponential term at high frequencies. Having determined Q, κ is obtained as $\kappa = R/Q\beta$. For the estimation of the corner frequency and the seismic moment, the Fourier displacement spectra obtained from the strong-motion records

are fitted to Eq. 10.1 using non-linear optimization. Usually, the displacement spectra, $D(\omega)$, is obtained by dividing the acceleration spectra, $A(\omega)$, with ω^2, $D(\omega) = A(\omega)/\omega^2$. Before the optimization is performed, the exponential term is removed by dividing by $e^{-\omega R/2Q\beta}$ to obtain the spectra at the source. To estimate the source spectra, geometric attenuation needs to be considered as well. The attenuation term in Eq. 10.1, $R \sim D^n$ with $n = 1$, does not apply at all distance ranges from the source. For the largest Icelandic earthquakes, we have found that, close to the fault, $n = 2$. We do not have enough data to determine n for distances larger than 100 km, where typically $n = 0.5$ to account for surface waves.

An alternative method for determining the source parameters, seismic moment and corner frequency is to use the spectral moment method (see Andrew 1986). This method is also applied here, in addition to the non-linear optimization, and found, in many cases, to give estimates with lower standard deviations.

10.3.1 Results of Estimates of the Parameters κ, ω_c and M_0

The following values were used for all earthquakes: S-wave velocity and density, $\beta = 3.5$ km/s and $\rho = 2.8$ g/cm^3. For earthquakes in California, Anderson and Hough (1984) found that average kappa is $\kappa = 0.045$ s. It can be said that $\kappa = \kappa_0$ is approximately valid for distances less than 100 km. For the south Iceland earthquakes, the average value of kappa was 0.042 s. The results were similar for all the earthquakes, except for the 21 June 2000 event for which $\kappa = 0.034$ s. We observed that for distances less than 100 km, κ was independent of distance.

After κ is obtained from the records, the parameters, ω_c and M_0, are estimated by fitting the Brune displacement spectrum (Eq. 10.1) applying the two methods described above. The standard deviation of the parameters, which was large, was examined for both methods. The result with the lowest standard deviation was chosen to select the final value of the estimated parameters. As an example, a record from a horizontal component of ground acceleration obtained at the Thorlakshofn station during the June 17th 2000 earthquake is shown in Fig. 10.2a. The S-wave portion of the record is indicated by two vertical lines and shown in red. The second peak that can be observed later in the record is due to a dynamically triggered event that occurred in Hengill volcano which is located 40 km west of the main fault (see Antonioli et al. 2006). In Fig. 10.2b, the theoretical spectrum with the estimated parameters is compared to the spectrum computed from the S-wave window.

The Vatnafjöll earthquake of 25 May 1987 was estimated to have a seismic moment of $M_0 = 5.3 \times 10^{31}$ N-m (M_w 5.8 with the Hanks-Kanamori equation), a fault radius of $r = 3.6$ km, stress drop of 48×10^5 Pa and dislocation of $u = 33$ cm. These results are similar to those reported in Ólafsson et al. (1998).

The two earthquakes in 2000, on the 17th and 21st of June, were similar in size. The former earthquake, on June 17th, had a seismic moment of $M_0 = 53 \times 10^{31}$ N-m (M_w6.5), with a fault radius of $r = 6.6$ km, and the June 21st earthquake had a seismic moment of $M_0 = 41 \times 10^{31}$ N-m (M_w 6.4) and a fault radius of $r = 6.0$. The stress

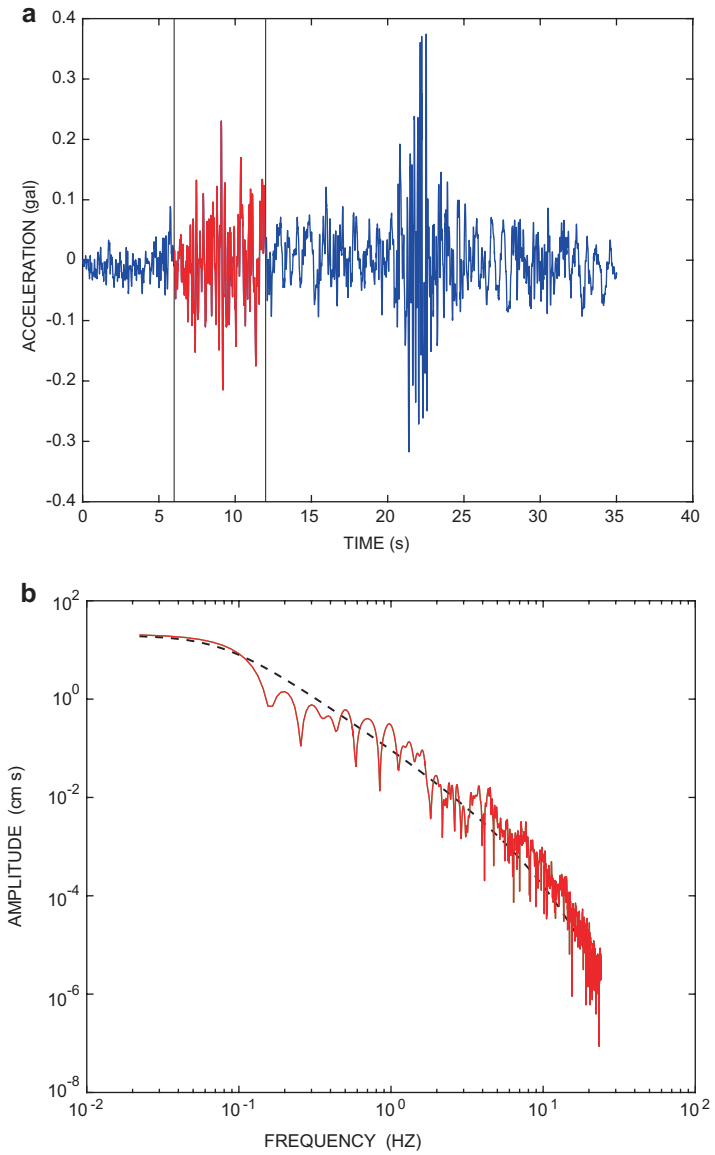

Fig. 10.2 (**a**) A ground acceleration record from the Thorlakshofn station from the 17 June 2000 earthquake. The selected S-wave window is indicated by *vertical lines*. (**b**) Brune's point source model, Eq. 10.1, represented by the *black dashed line*, fitted to the displacements amplitude spectrum (*red line*) computed from the S-wave window shown in (**a**)

drop was similar for the two events, $\Delta\sigma = 80 \times 10^5$ Pa. The dislocation was estimated as 89 cm and 78 cm for the former and latter events, respectively.

The earthquake on 29 May 2008 was considered a single event, although rupture occurred on two faults, due to how close in time they occurred. For this event, $M_0 = 30 \times 10^{31}$ N-m (M_w 6.3) and a fault radius of $r = 5.4$ km were estimated. The stress drop was similar as the two 2000 events ($\Delta\sigma = 80 \times 10^5$ Pa), and dislocation was estimated as $u = 94$ cm.

The fault planes for the three events on 17.06.2000, 21.06.2000 and 29.05.2008 were estimated to be of similar area, ≈ 100 km^2. The fault plane area of the M_w 5.8 Vatnafjöll earthquake was estimated to be 30 km^2.

10.4 Relating PGA with Model Parameters

Using the Parseval theorem and carrying out the integration, a relation can be derived for root-mean-squared acceleration, a_{rms}, as a function of parameters of the Brune model. Carrying out symbolic integration, we end up with a function in closed form which has a term containing sine integrals, $\Psi(\kappa\omega_c)$ (see Ólafsson and Sigbjörnsson 1999; Ólafsson 1999; Ólafsson and Rupakhety 2017). The term, $\Psi(\kappa\omega_c)$, can be approximated by an exponential function.

10.4.1 Far-Field, a_{rms}, Equation

The root-mean-squared acceleration, a_{rms}, for the far-field spectrum can be written as follows:

$$a_{\text{rms}} = \frac{0.57 \cdot \Delta\sigma^{2/3} \exp\left(-0.75\left(\kappa\omega_c\right)^{0.87}\right) M_o^{1/3}}{\beta\rho\sqrt{\kappa T_d} R} \tag{10.6}$$

10.4.2 Near-Field, a_{rms}, Equations

Based on the Brune near-field source model, the a_{rms} ground motion model can be represented by the following equation:

$$a_{\text{rms}} = \frac{2}{\sqrt{\pi}} \frac{C_p \Delta\sigma}{\rho\beta\sqrt{\kappa_0}} \sqrt{\frac{\exp\left(-1.1\left(\kappa_0\omega_c\right)^{0.92}\right)}{T_0}} \tag{10.7}$$

Here, T_0 is the source duration defined as follows (see Beresnev 2002):

$$T_0 = \frac{0.6}{f_c} \tag{10.8}$$

The near-field spectral decay parameter is represented by κ_0, and taken to be 0.042 s for south Iceland. Here, $\kappa = \kappa_0$ holds as it is assumed that the parameter, κ, does not change with distance within a distance of 100 km from the fault.

10.4.3 Duration Model

Duration is a necessary parameter in the ground motion models that are described in this paper. The functional form used to approximate duration is

$$T_d = c_1 \frac{r}{\beta} + c_2 d^{c_3} \tag{10.9}$$

where c_1, c_2 and c_3 are magnitude dependent parameters. The duration used is 90% of the cumulative energy duration and can be approximated by a function such as in Eq. 10.9. Based on duration data obtained from the strong ground motion recorded in the 17 June 2000 south Iceland and the 25 May 1987 Vatnafjöll earthquake of 1987, the parameters, c_1, c_2, c_3, were estimated (see Ólafsson and Rupakhety 2017). With $(r/\beta) = 1.9$ s and $(r/\beta) = 1.4$ s for the M_w 6.5 and M_w 5.8 earthquakes (assuming $\beta = 3.5$ km/s), the following equations can be obtained:

$$T_d = \begin{cases} 1.5\dfrac{r}{\beta} + 0.10 d^{0.20} & for \quad M_w 6.5 \\ 2.0\dfrac{r}{\beta} + 0.05 d^{0.17} & for \quad M_w 5.8 \end{cases} \tag{10.10}$$

In Fig. 10.3a, we present duration as a function of epicentral distance for M_w 6.5 and 5.8 earthquakes, as described by Eq. 10.10. The green dots represent the duration of the S-wave window used in the estimation of source parameters and the blue triangles represent the duration corresponding to 90% of cumulative energy obtained from the ground motion records of the 17 June 2000 M_w 6.5 event. In Fig. 10.3b, we have present rms-acceleration, a_{rms}, calculated using Eq. 10.6 for each recorded ground motion versus. a_{rms} obtained directly from the record for all the four earthquakes considered in this study. Good agreement is found between measured and estimated values.

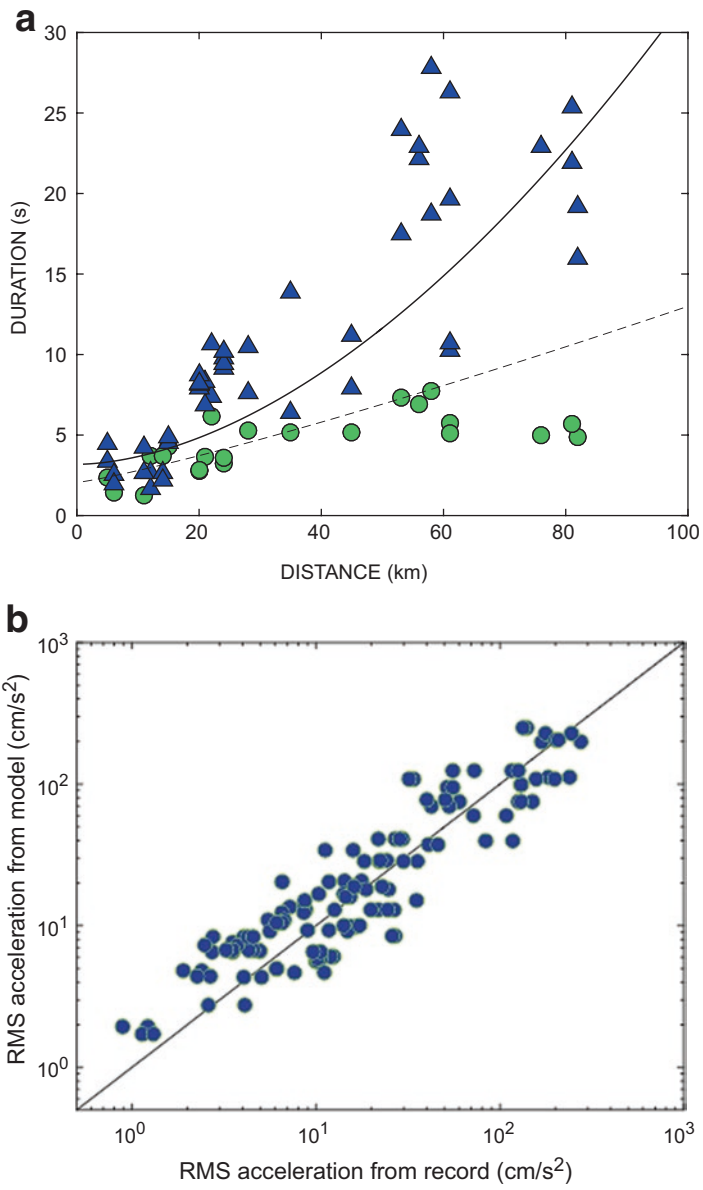

Fig. 10.3 (**a**) Duration with respect to epicentral distance for the earthquake on 21 June 2000. *Blue triangles* represent duration computed based on 90% cumulative energy. The *green dots* represent the duration of the S-wave window. The *solid line* is obtained from the model of Eq. 10.9. (**b**) comparison between recorded rms acceleration and the corresponding values estimated from the proposed model (Eq. 10.6). The datapoints are obtained from all records obtained in the four largest earthquakes recorded by the IceSMN

10.4.4 Determination of PGA

Applying the theory of locally stationary Gaussian random processes, the relationship between *PGA* can be related to a_{rms} with a peak factor given by:

$$p = \sqrt{2\ln\left(\frac{2.8T_d}{T_0}\right)} \quad for \quad T_d \geq 1.36T_0 \tag{10.11}$$

where $a_{\max}$ is the expected value of PGA. Here, T_0 represents the predominant period of the strong motion phase. Vanmarcke and Lai (1980) determined the peak factor $p = a_{\max}/a_{\text{rms}}$ for several Californian strong motion records and obtained a median value of $p = 2.74$.

For the four earthquakes considered in this study, the mean peak factor calculated with Eq. 10.11 was $p = 2.9$, with an average predominant period of 6 Hz. The mean peak factor computed as factor $p = a_{\max}/a_{\text{rms}}$ was, however, 3.3, with a standard deviation of 0.7.

10.5 Simulation with the Stochastic Method

Applying the stochastic method (see Boore 2003 for an overview), the Brune model can be applied to simulate ground motion records using the estimated parameters. Considering the model (Eq. 10.1), with the parameters estimated from recorded ground motion, to be a filter with white noise input, ground motion time series can be simulated as the response of the filter. Ground motion simulated in this manner is stochastically equivalent to the spectrum used in simulation.

The method used here for the simulation is to discretise the Brune model and obtain a discrete time series filter (see Ólafsson and Sigbjörnsson 2011). Using this approach, a record simulated with the point source model of Eq. 10.1 is presented in Fig. 10.4a. In Fig. 10.4b, the acceleration spectrum of the simulated record (blue) is compared with the theoretical spectra (red) obtained from Eq. 10.1.

10.6 Ground Motion Prediction Model

In this section, it is demonstrated how Brune's points source model with the estimated parameters can be applied to obtain attenuation curves (ground motion prediction equations). Such equations can be used instead of purely empirical GMPEs whose functional form and model parameters are not directly related to the source and path parameters.

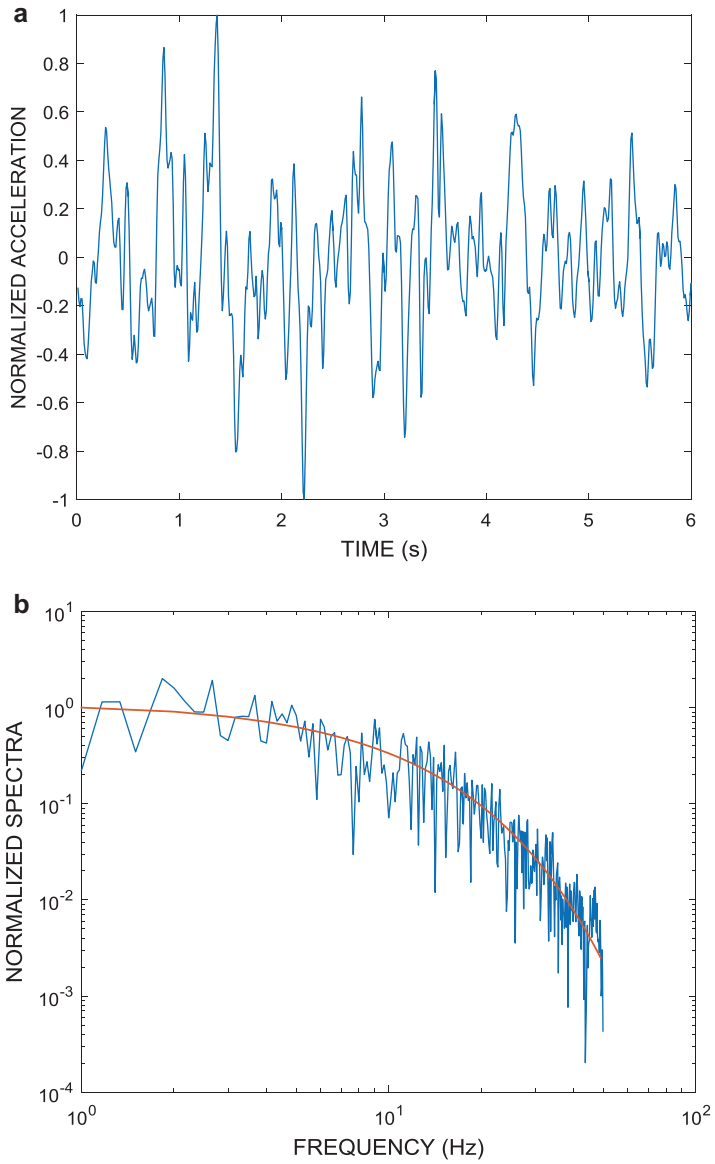

Fig. 10.4 (**a**) Simulated ground motion record for the station at Thorlakshofn (M_w 6.5, and epicentral distance 52 km). (**b**) Spectrum computed from the simulated record in (**a**) (*in blue*) compared to the theoretical spectra (in *red*) given by Eq. 10.1

As an example, the results for the modelling of the earthquake at Hestfjall on 21 June 2000 M_w 6.4 are presented. The far-field source model of Eq. 10.7 is applied with R ~ D^n with $n = 1$ for all distances less than 100 km. The model (here called O&R 2017 model) is shown in Fig. 10.1 for the estimated stress drop,

$\Delta\sigma = 83 \times 10^5$ Pa (black line and triangles) and $\Delta\sigma = 50 \times 10^5$ Pa (dot-dash). The GMPEs of Ambraseys et al. 2005 (dotted) and Akkar et al. 2014 (dash) are also shown.

It can be seen from Fig. 10.1 that the Akkar et al. (2014) model gives values of PGA close to the fault that are in better agreement with recorded data. The Ambraseys et al. (2005) model, which is similar to the point source model with a stress drop of $\Delta\sigma = 50$ bar, gives values that are too low. This trend has also been observed from some of the GMPEs in the literature based on data from other regions. This can be expected if the models are developed based on earthquakes with a stress drop that is, on average, lower than $80–100 \times 10^5$ Pa.

In general, the Akkar et al. (2014) model gives a good approximation to the PGA close to the fault of the four earthquakes from south Iceland. There is also a good correspondence between recorded PGA values and that predicted by the ground motion model based on the theoretical spectrum of Eq. 10.1, when a stress drop of 83 bar is used. It can, however, be observed from Fig. 10.5a and b that the Akkar et al. (2014) model does not follow the slope of the attenuation function particularly well and, for example, predicts too high values farther away from the fault.

In Fig. 10.5b, the attenuation curve based on theoretical point source model (black line) follows more closely the slope of the attenuation of recorded data and also captures the steeper rate of attenuation close to the fault using a geometrical spreading function that is proportional to D^2 in the near-fault region; we approximate $D_2 = 30$ km for a M_w 6.5 earthquake and $D_2 = 20$ km for $M_w = 5.8$. The magnitude dependent duration function can also be adjusted to account for the regionally dependent rate of attenuation.

10.6.1 Near-Field Model and PGA

Using the near-field equation of Eq. 10.7 (plus Eqs. 10.8 and 10.11) and parameters in Sect. 10.3.1, the corresponding PGA = 0.53 g for a M_w 6.5 earthquake within ~6.5 km from the source, which agrees reasonably well with recorded data, as is also evident from Fig. 10.5b. For an M_w 6.4 earthquake, the same equation gives a PGA of 0.41 g.

To get an idea of the PGA values we can expect in the near-field for an M_w 7 earthquake, which could occur on the eastern part of the SISZ, we use information about surface displacements that were observed by Bjarnason et al. (1993). They estimated that the length of the fault was 20 km and the maximum slip was 3 m. If the fault is assumed to break to the surface, we can expect that the depth of the fault is about 15 km. This gives a fault with an area of 300 km^2. A circular fault with this area would have a radius of 9.8 km. Using the Hanks Kanamori relation, we obtain a seismic moment of $M_0 = 3.1 \times 10^{33}$ N-m. Assuming a density of 2.8 g/cm^3 and an S-wave velocity of 3.5 km/s, then Eqs. 10.3 and 10.4 give a stress drop of 145×10^5 Pa and a dislocation of 3 m. Using the near-fault model of Eq. 10.10, we get a PGA of 0.78 g, assuming the peak factor is 3. These results agree reasonably well with the

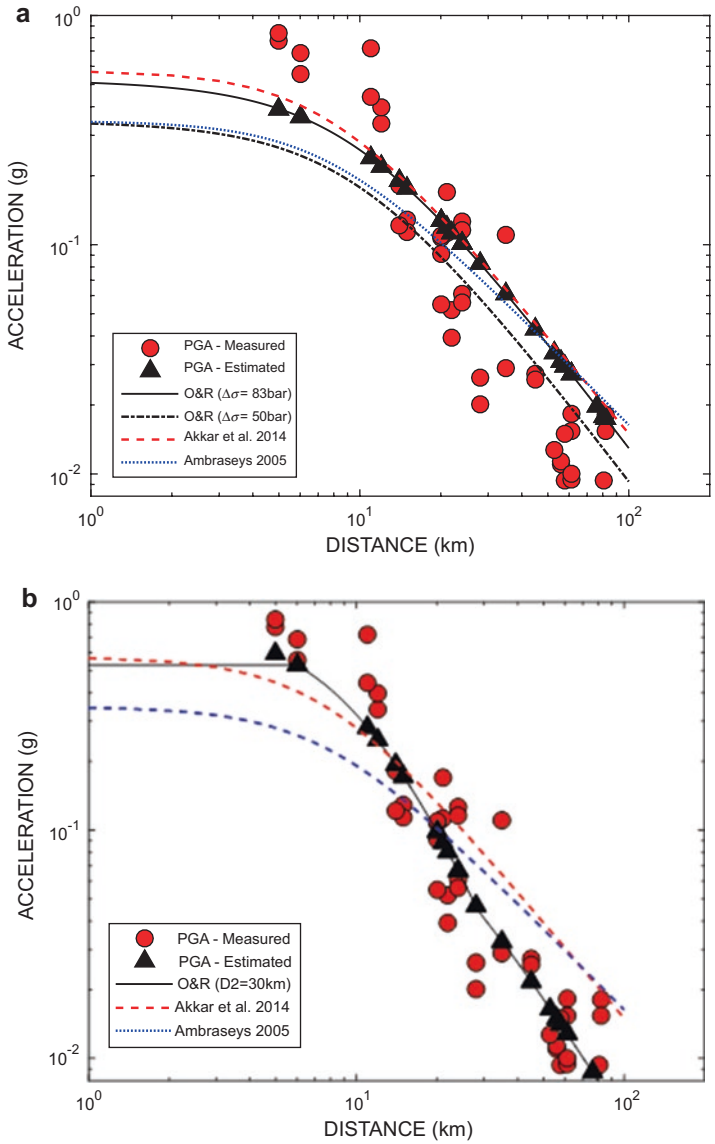

Fig. 10.5 (**a**) Point source model of Eq. 10.7, ($R = D$ for all $D < 100$ km) applied to recorded horizontal PGA from the 21st June 2000 (M_w 6.4) earthquake shown here for stress drop, $\Delta\sigma = 83 \times 10^5$ Pa (*black line* and *triangles*) and $\Delta\sigma = 50 \times 10^5$ Pa (*dot-dash*). Also shown are the models of Akkar et al. (2014) and Ambraseys et al. (2005) for M_w 6.4. (**b**) Same as in (**a**), but the geometric attenuation of the theoretical model is modified as $R \sim D^2$ for all $D < 30$ km)

mean of the PGA values we have measured close to the source. The GMPE of Akkar et al. (2014) gives similar results.

10.7 Conclusions

We present the source parameters for the largest earthquakes that have occurred in south Iceland in the recent years. The ground motion is well represented by the Brune point source model. The June 2000 earthquakes and the May 2008 earthquake had similar stress drops of 80×10^5 Pa. The 1987 Vatnafjöll earthquakes had a stress drop of 48×10^5 Pa. In general, we notice an increase in stress drop with earthquake size. Using the estimated parameters, M_0, ω_c, and κ, and a duration function, the model can be used for simulation of strong motion records which are stochastically equivalent to the data which is used to calibrate the theoretical spectral model. The model can also be applied instead of an empirical GMPE. This approach is advantageous in areas where recorded data is limited to calibrate a purely empirical GMPE. In addition, since the model is based on physical parameters, unlike empirical GMPEs whose functional form and model parameters are mostly empirically calibrated, it might be more reliable in estimating ground motion scenarios not covered by recorded data. It is found that the model based on the theoretical spectra follows the attenuation pattern of recorded data closely when corrections for faster attenuation in the near fault are incorporated. The resulting model was found to be close to the Akkar et al. (2014) model close to the fault, but followed the recorded data better at distances greater than about 20 km from the fault. Based on this model, the expected PGA in the near source of an earthquake of size M_w 7 (similar to the 1912 Earthquake) is estimated to be 0.78 g.

Acknowledgements The research presented herein was supported by the National Power Company and the University of Iceland Research Fund.

References

Aki K (1967) Scaling law of seismic spectrum. J Geophys Res 72:1217–1231

Akkar S, Sandıkkaya MA, Bommer JJ (2014) Empirical ground-motion models for point-and extended-source crustal earthquake scenarios in Europe and the Middle East. Bull Earthq Eng 12(1):359–387

Ambraseys N, Smit P, Douglas J, Margaris B, Sigbjörnsson R, Olafsson S, Costa G (2004) Internet site for European strong-motion data. Boll Geofis Teor Appl 45(3):113–129

Ambraseys NN, Douglas J, Sarma SK, Smit PM (2005) Equations for the estimation of strong ground motions from shallow crustal earthquakes using data from Europe and the Middle East: horizontal peak ground acceleration and spectral acceleration. Bull Earthq Eng 3(1):1–53

Anderson JG, Hough SE (1984) A model for the shape of the Fourier amplitude spectrum of acceleration at high frequencies. Bull Seismol Soc Am 74(5):1969–1993

Andrews DJ (1986) Objective determination of source parameters and similarity of earthquakes of different sizes. In: Das S, Boatwright J, Sholz CH (eds) Earthquake source mechanics, Maurice Ewing Series 6. American Geophysical Union, Washington, DC, pp 259–267

Antonioli A, Belardinelli ME, Bizzarri A, Vogfjord KS (2006) Evidence of instantaneous dynamic triggering during the seismic sequence of year 2000 in south Iceland. J Geophys Res Solid Earth 111(B3)

Atkinson GM, Boore DM (1995) Ground-motion relations for eastern North America. Bull Seismol Soc Am 85(1):17–30

Beresnev IA (2002) Source parameters observable from the corner frequency of earthquake spectra. Bull Seismol Soc Am 92(5):2047–2048

Beresnev IA, Atkinson GM (1998) FINSIM-a FORTRAN program for simulating stochastic acceleration time histories from finite faults. Seismol Res Lett 69(1):27–32

Bjarnason IT, Cowie P, Anders MH, Seeber L, Scholz CH (1993) The 1912 Iceland earthquake rupture: growth and development of a nascent transform system. Bull Seismol Soc Am 83:416–435

Boore JM (1983) Stochastic simulation of high-frequency ground motions based on seismological models of the radiated spectra. Bull Seismol Soc Am 73:1865–1894

Boore DM (1996) SMSIM: Fortran programs for simulating ground motions from earthquakes: Version 1.0. US Department of the Interior, US Geological Survey

Boore DM (2003) Simulation of ground motion using the stochastic method. Pure Appl Geophys 160(3–4):635–676

Brune JN (1970) Tectonic stress and the spectra of seismic shear waves from earthquakes. J Geophys Res 75(26):4997–5009

Hanks TC, McGuire RK (1981) The character of high-frequency strong ground motion. Bull Seismol Soc Am 71:2071–2095

Ólafsson S (1999) Estimation of earthquake-induced response. Department of Structural Engineering, Norwegian University of Science and Technology

Ólafsson S, Rupakhety R (2017) Source parameters from acceleration records for earthquakes during the period 1987–2008 in South Iceland. In: 16th world conference on earthquake engineering, 16WCEE 2017, Santiago Chile, January 9th to 13th 2017, Paper No. 4572

Ólafsson S, Sigbjörnsson R (1999) A theoretical attenuation model for earthquake-induced ground motion. J Earthq Eng 3(03):287–315

Ólafsson S, Sigbjörnsson R (2011) Digital filters for simulati.on of seismic ground motion and structural response. J Earthq Eng 15(8):1212–1237

Ólafsson S, Sigbjörnsson R, Einarsson P (1998) Estimation of source parameters and Q from acceleration recorded in the Vatnafjöll Earthquake in South Iceland. Bull Seismol Soc Am 88(2):556–563

Pedersen R, Jónsson S, Árnadóttir T, Sigmundsson F, Feigl KL (2003) Fault slip distribution of two June 2000 M w 6.5 earthquakes in South Iceland estimated from joint inversion of InSAR and GPS measurements. Earth Planet Sci Lett 213(3):487–502

Sigbjörnsson R, Ólafsson S (2004) On the South Iceland earthquakes in June 2000: strong-motion effects and damage. Boll Geofis Teor Appl 45(3):131–152

Sigbjörnsson R, Snæbjörnsson JT, Higgins SM, Halldórsson B, Ólafsson S (2009) A note on the M6.3 earthquake in Iceland on 29 May 2008 at 15:45 UTC. Bull Earthq Eng 7(1):113–126

Sigbjörnsson R, Ólafsson S, Rupakhety R, Halldorsson B, Acharya P, Snæbjörnsson JT (2014) Strong-motion monitoring and accelerometric recordings in Iceland. In: Proceedings of the 2nd European conference on earthquake and engineering seismology (2ECEES). Istanbul, Turkey

Vanmarcke EH, Lai SP (1980) Strong motion duration and rms amplitude of earthquake records. Bull Seismol Soc Am 70:1293–1307

Chapter 11
Seismic Vulnerability of Icelandic Residential Buildings

Bjarni Bessason and Rajesh Rupakhety

Abstract The seismicity in Iceland is related to the Mid-Atlantic plate boundary which crosses the country from north to south. Since 1700, there have been 25 earthquakes of magnitude six or greater in the two major seismic zones in Iceland. For many of the historical earthquakes (older than 100 years), detailed written descriptions are available that describe the damage from farm to farm. For the most recent earthquakes, like the two south Iceland earthquakes of June 2000 and the south Iceland earthquake of May 2008, comprehensive building-by-building loss data exist. The loss data in these cases are split into a number of subcategories of structural and non structural damage. The building stock in south Iceland has changed significantly from 1700 to the present. For ages, vulnerable turf and stone houses dominated, but in the twentieth century, concrete buildings and timber buildings took over. Seismic codes were implemented in 1976 and have gradually improved the seismic capacity of present building stock. In this book chapter, an overview of the seismic performance of old and new Icelandic buildings is given. Observed and reported damage caused by three earthquake sequences and a single event are discussed; first, the damage caused by two earthquakes in August 1784 in south Iceland; then, by the 1896 earthquake sequence in south Iceland; then, the damage after a single event in 1934 in north Iceland; and finally, the loss data from the 2000 and 2008 earthquakes in south Iceland. The main focus is on the last three events for which most of the data exist.

Keywords Loss data • Fragility curves • Risk maps • Vulnerability curves • Non-structural damage • Low-rise buildings

B. Bessason (✉)
Faculty of Civil and Environmental Engineering, University of Iceland, Reykjavík, Iceland
e-mail: bb@hi.is

R. Rupakhety
Earthquake Engineering Research Centre, University of Iceland, Selfoss, Iceland
e-mail: rajesh@hi.is

R. Rupakhety, S. Ólafsson (eds.), *Earthquake Engineering and Structural Dynamics in Memory of Ragnar Sigbjörnsson*, Geotechnical, Geological and Earthquake Engineering 44, https://doi.org/10.1007/978-3-319-62099-2_11

11.1 Introduction

Knowledge of seismic vulnerability of buildings is a fundamental issue when evaluating earthquake risk, in loss prediction, in disaster planning, in preparation of mitigation and retrofit programs, and in development of building codes. Fault mechanism and wave propagation, as well as the vulnerability of buildings, are known to be region and country specific. The main reason is different tectonic settings and geology, together with differences in structural forms, building materials, and traditions. Whenever possible, it is important to carry out site-specific, post-earthquake damage studies in order to learn from destructive earthquakes and construct reliable seismic vulnerability relationships for different building typologies.

The seismicity in Iceland is related to the Mid-Atlantic plate boundary which crosses the country from north to south (Einarson 1991). Within Iceland, the boundary shifts eastwards in the south and back westwards in the north through two, complex fracture zones. The one in the south is called the South Iceland Seismic Zone and is in the middle of the largest agricultural region in the country. The other in the north is called the Tjörnes Fracture Zone (Fig. 11.1). The largest earthquakes in the country have occurred within these zones, mostly associated with a strike-slip motion at shallow depths (5–10 km). In the South Iceland Seismic Zone, the earthquakes tend to occur in sequences, typically every hundred years. One such sequence occurred in 1784 when two earthquakes (Ms7.1 and Ms6.7) hit on 14 August and 16 August with approximately 20 km distance between the two epicentres. A detailed farm-by-farm description of the damage from these two events exists (Halldórsson et al. 2013). Another sequence began in 1896, when five earthquakes of magnitude greater than six struck the area within 2 weeks (Thoroddsen 1899, Sigbjörnsson and Rupakhety 2014). A single event of size 7 occurred in 1912, which many scientists consider to be the last earthquake of the sequence that started in 1896.

A new sequence started in 2000 in the South Iceland Seismic Zone when two earthquakes of magnitude M_w6.5 struck on the 17th and 21st of June. They were followed by the third event, an M_w6.3 earthquake, on 29 May, 2008, called the Ölfus earthquake (Fig. 11.1).

These earthquakes caused a lot of damage, but no buildings collapsed, and fortunately, there was no loss of life, and nobody was seriously injured (Bessason et al. 2012, 2014; Bessason and Bjarnason 2016).

In Iceland, all buildings are registered in an official database which contains detailed information, such as date of construction, number of floors, floor area, main building material, geographical location, type of use, and replacement value. Natural catastrophe insurance of buildings is mandatory and is administered by the Iceland Catastrophe Insurance (ICI). Therefore, after catastrophic events like large earthquakes, the repair cost for every damaged building is estimated by trained assessors in order to settle the individual insurance claims. Since 1990, an array of strong motion acceleration meters has been operated in Iceland. These accelerometers have recorded detailed ground acceleration during strong earthquakes at many locations in Iceland. In particular, the June 2000 earthquakes and the May 2008 earth-

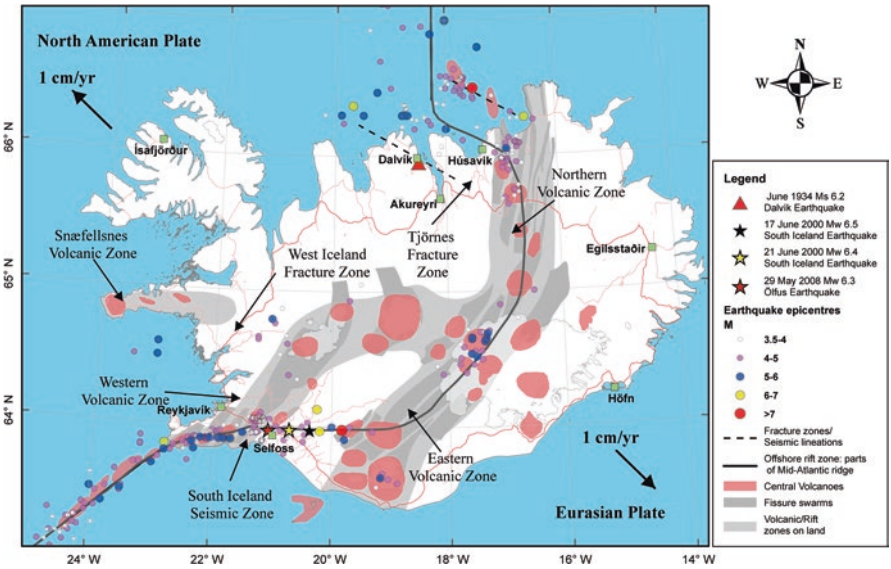

Fig. 11.1 The South Iceland Seismic Zone (*SISZ*) and the Tjörnes Fracture Zone (*TFZ*). Locations of epicentres of the three south Iceland earthquakes of June 2000 and May 2008 are shown with the stars; and that of the 1934 Dalvík earthquake is indicated with the *red triangle*; the *circles* represent epicentres of earthquakes larger than magnitude 3.5 between 1896 and 2012 (based on data from The Icelandic Meteorological Office, the Icelandic Institute of Natural History and National Land Survey of Iceland)

quake were very well recorded by the Icelandic Strong Motion Network (ICESMN, Sigbjörnsson et al. 2014). Strong ground motion data from Iceland have been used to develop ground motion prediction equations (GMPEs) (Ólafsson and Sigbjörnsson 2002; Rupakhety and Sigbjörnsson 2009). The data are available at the Internetsite for European Strong-Motion Data (ISESD) (Ambraseys et al. 2002).

The building stock in Iceland has changed significantly from 1700 to the present. For ages, vulnerable turf and stone houses dominated, but in the twentieth century, concrete and timber buildings took over. Seismic codes were implemented in 1976 and have gradually improved the seismic capacity of the present building stock. The main aim of this contribution is to give an overview of the seismic performance of old and new Icelandic buildings based on both historical damage data as well as loss data from recent earthquakes.

11.2 Damage in Historical Earthquakes

11.2.1 The August 1784 South Iceland Earthquakes

On the 14th and 16th of August, 1784, two destructive earthquakes occurred in south Iceland (Fig. 11.1). Three people were killed and there was a lot of structural damage. The magnitude of these earthquake has been estimated (not measured) as 7.1 (M_s) and 6.7 (M_s) (Halldórsson et al. 2013). Based on faults and fissures as well as observed damage, the epicentres have also been roughly estimated (Fig. 11.2). Since most of the faults and fissures are in a north-south direction, the estimated longitude of these epicentres is more accurate than the latitude. The bishop at Skálholt Cathedral in south Iceland requested priests in the area to register damage at all farms in their parish and deliver a written report to him. Because of this work, a detailed damage description exists for every farm in the area. From the above information, a damage map has been created (Fig. 11.2) (Halldórsson et al. 2013).

At many farms in the epicentral area, all buildings collapsed, including residential buildings and different types of animal housing and food barns, etc. At this time, most of the buildings were single-story turf and stone with thick walls and heavy

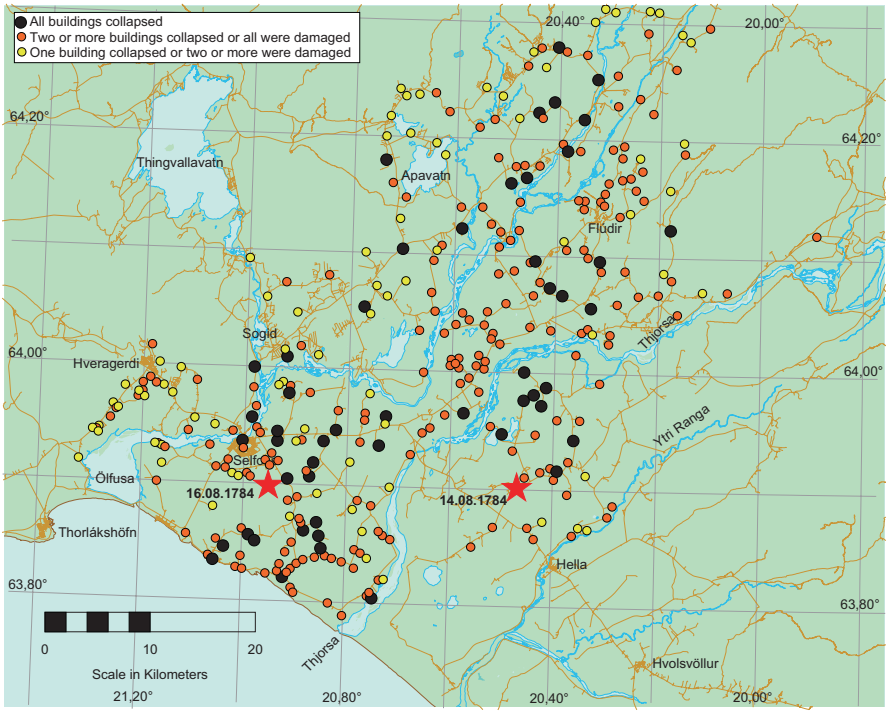

Fig. 11.2 Observed damage after the two south Iceland earthquakes of August 1784 (based on data from the National Land Survey of Iceland and Halldórsson et al. 2013)

turf roofs. Binding between the stones and the turf was very limited and the structures were very vulnerable to lateral shaking (Fig. 11.3). Use of timber was limited mainly to roof rafters. Only a few buildings at that time had a timber frame structure.

Fig. 11.3 Turf and stone houses: (**a**) from Húsavík around 1900 (Photo: Icelandic and Faroese Photographs of Frederick W. W. Howell, Cornell University Library), (**b**) from Skógar Museum in south Iceland

11.2.2 The 1896 South Iceland Earthquake Sequence

In 1896, six, destructive earthquakes occurred in the SISZ. Thoroddsen (see, for example, Thoroddsen 1899) provides a detailed description of damage caused by these earthquakes. Macroseismic effects, magnitude, and a summary of damage patterns caused by these earthquakes are also given in Sigbjörnsson and Rupakhety (2014). The first event of the sequence occurred on the 26th of August, almost at midnight, without any warning or clear precursor. This earthquake was felt over the whole southern part of Iceland, and its effects were the most destructive in the Rangárvellir, Land, Holt, and Gnúpverjahreppur areas. In Land, for example, 28 out of 35 farms were completely damaged. The next earthquake struck the following morning and caused buildings partially damaged by the earthquake the day before to completely collapse. On the 5th of September, two strong earthquakes occurred, the first one had epicentre close to Selfoss and the second one about 20 km east of Selfoss. The effects of these two earthquakes were the strongest in Skeid, Holt, and Flói. It severely damaged an 80-m long suspension bridge over the Ölfusá River by Selfoss, and two people died in a collapsed house in Selfoss. On the night of the 6th of September, another strong earthquake occurred north-west of Selfoss and caused 24 farms in Ölfus to collapse. The sixth, and the last, destructive earthquake of the sequence occurred on the 10th of September, but was followed by many smaller aftershocks. A more detailed description of the damage distribution caused by this sequence of earthquakes can be found in Sigbjörnsson and Rupakhety (2014).

11.2.3 The Dalvík Earthquake in 1934

In June 1934, a destructive earthquake of size 6.2 Ms occurred 2–3 km from the village of Dalvík in North Iceland (Fig. 11.1). A lot of structural damage was reported in Dalvík and its surroundings (Halldórsson et al. 2013; Thráinsson 1992). Almost all houses in this area were damaged, and more than half of them had serious damage (could not be used). A local builder was asked by Icelandic authorities to give an overview of the damage (Guðmundsson 1951). His findings are shown in Table 11.1.

Six out of 17 turf/stone buildings and six out of 33 concrete buildings had collapsed or had suffered total damage, whilst no timber building had such damage.

Table 11.1 Observed damage at Dalvík after the 1934 earthquake

Building material/type	Number of buildings	Damage state			
		Minor/no damage	Light	Severe	Total damage
Turf and stone	17	2	8	1	6
Concrete	33	7	4	16	6
Timber	27	13	10	4	0
Total	77	22	22	21	12

Furthermore, 43 of 77 (56%) buildings had severe or total damage. If only concrete and timber buildings are considered, the same proportion is obtained (34/60). Finally, it must be underlined that concrete houses at this time had very limited reinforcement and most likely poor concrete strength as well. At this time, it was common to use course gravel and stone boulders in the concrete mixture to stretch it out. Many concrete structures experienced large open cracks after the earthquake (Fig. 11.4).

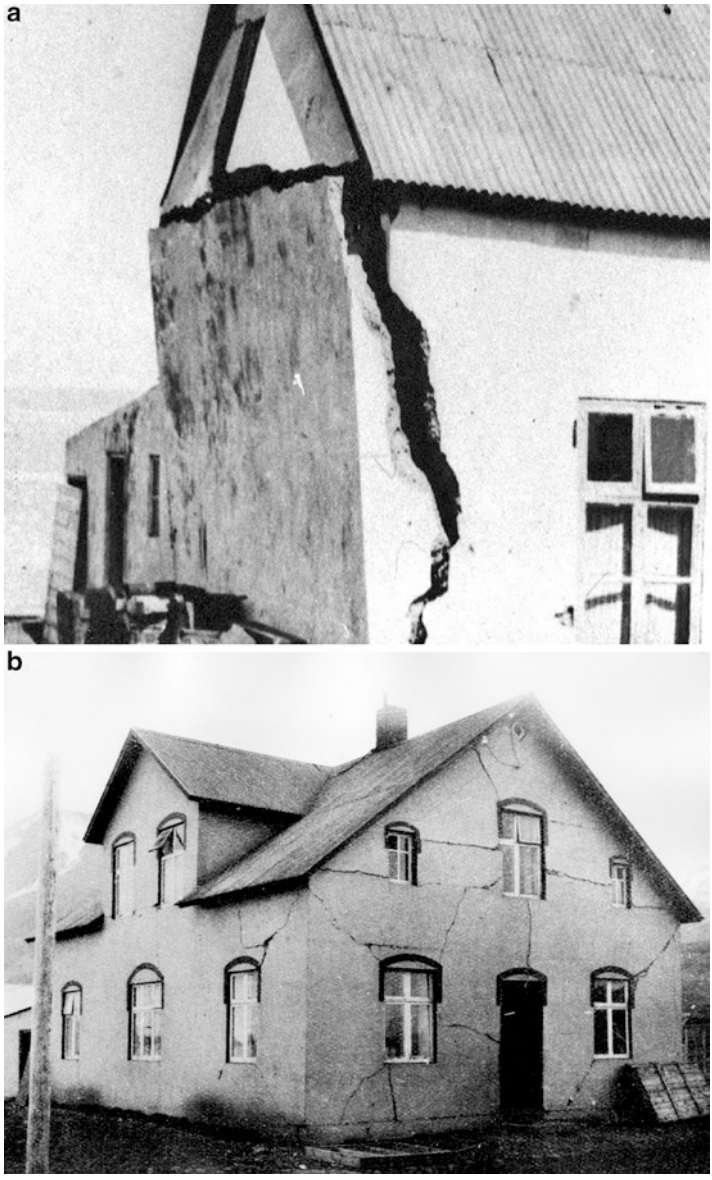

Fig. 11.4 Damaged concrete buildings at Dalvík after the Ms6.2 earthquake in June 1934 (Photos: (**a**) Svarfdælinga Provincial Archives, (**b**) National Museum and RUV)

11.3 Background Material and Loss Data from Recent Earthquakes

11.3.1 The South Iceland Earthquakes of June 2000 and May 2008

On the 17th of June and again on the 21st of June 2000 two M_w6.5 earthquakes occurred in the SISZ. Both events were right-lateral, strike-slip earthquakes with a fault striking in the north–south direction. The approximated focal depths were 6.3 km and 5.7 km, respectively. The highest recorded PGA was 0.64 g at a distance of 5.7 km from the fault in the first one and 0.84 g at a distance of 3.1 km from the fault in the second one (Thórarinsson et al. 2002). They were followed by the third one, an earthquake on May 29th, 2008, called the Ölfus earthquake (Fig. 11.5). Like the June 2000 earthquakes, it was also a shallow, right-lateral, strike-slip earthquake, with a fault striking in the north–south direction, and the highest recorded peak ground acceleration (PGA) was 0.88 g (Halldórsson and Sigbjörnsson 2009).

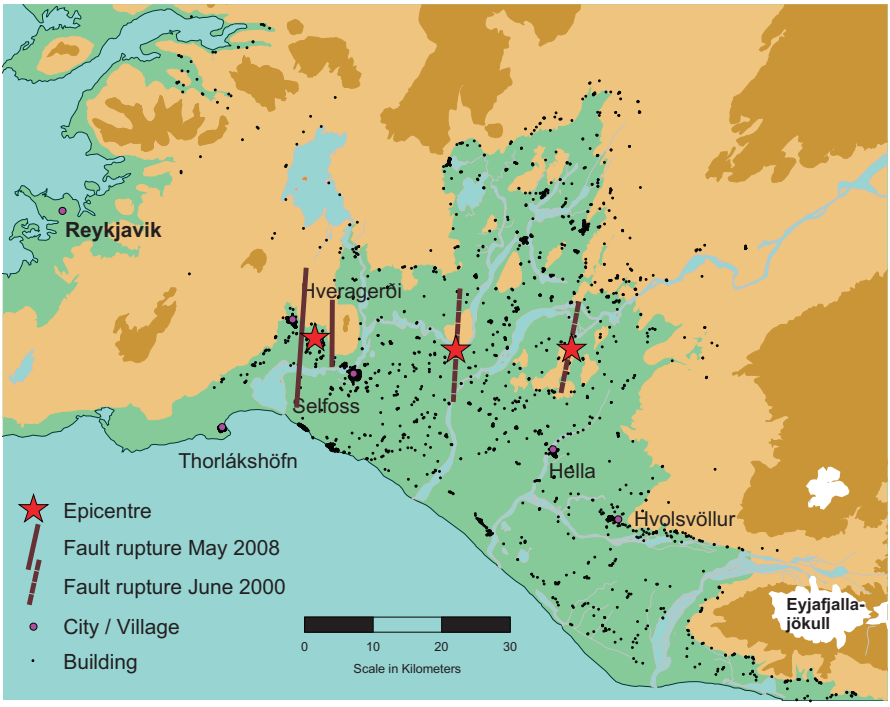

Fig. 11.5 A map of south Iceland showing the epicentre and the faults of the south Iceland earthquakes of June 2000 and May 2008, as well as the location of buildings in the area. The *green area* in the middle frames the south Iceland lowland (based on data from the National Land Survey of Iceland and Registers Iceland)

11.3.2 Building Typology Classes

The SISZ crosses the south Iceland lowland, which is the largest agricultural region in the country, with many farms, a number of small villages, service centres, and modern infrastructure (Fig. 11.1). The population was 15,000 in January 2000 and 18,600 in January 2008 (www.hagstofa.is). The majority of the buildings were built after 1940 (Fig. 11.6). Those built before 1940 are mostly timber houses. Between 1940 and 1960 it was common to build concrete buildings, as well as special buildings of hollow pumice blocks. The pumice block buildings can be classified as masonry or brick buildings and have some similarities with southern European-type masonry buildings. Between 1960 and 1980, concrete buildings dominated, whilst since 1980 timber frame structures have been more common (Fig. 11.6). The majority of the structures are in-situ-cast or in-situ-built buildings, although prefabricated houses do exist. The lateral, load-bearing system is dominated by structural walls. Seismic codes were implemented in Iceland in 1976, and since then, nearly all concrete buildings have reinforcement in all structural supporting systems. Eurocode 8 was implemented in 2002. Minimum reinforcement requirements in structural walls prescribed in these codes may have governed the design for seismic resistance in stiff, low-rise buildings in the region. In the timber houses, the exterior and interior load-bearing walls are made of timber work with plywood cladding sheets and exterior wooden siding. In newer houses, the timber construction is more solid, forming

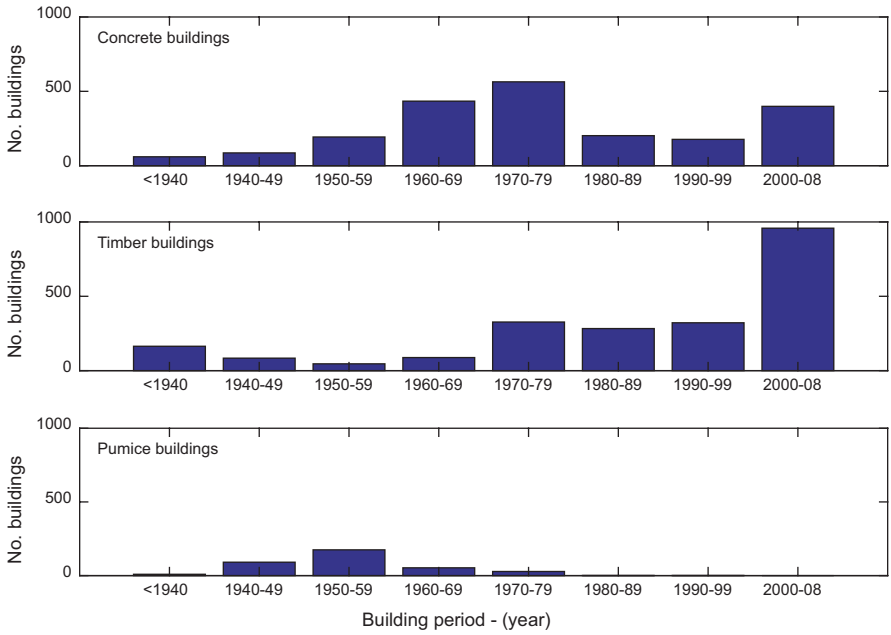

Fig. 11.6 Age distribution of buildings in the south Iceland lowland (Bessason et al. 2014)

strong shear walls. The prescribed wind loads are very high in Iceland, among the highest in Europe. According to the Eurocodes (EN 1990–1-4) and the associated National documents, the fundamental value of the basic wind velocity is $v_{b,0} = 36$ m/s. Timber houses in Iceland, designed to withstand such strong winds, are therefore well suited to withstand earthquake forces.

The majority of the buildings are low-rise, single-family dwellings, and town houses, with one to two stories being dominant. A few buildings can be classified as multi-family apartment blocks, and of those, none is taller than five stories. In Fig. 11.7, some examples of residential buildings in the town of Selfoss in south Iceland are shown.

In recent studies of loss data from the south Iceland earthquakes in 2000 and 2008 the year 1980, (around when seismic codes were implemented in Iceland), has

Fig. 11.7 Examples of buildings in the town of Selfoss in south Iceland: (**a**) single-story timber building; (**b**) two-story RC building; (**c**) two-story RC apartment block; (**d**) three-story RC apartment blocks (Google maps – Street viewer)

Table 11.2 Main building typologies of low-rise residential buildings in the south Iceland lowland

Typology	Description	Proportion (%)
RC Pre-1980	Reinforce concrete buildings built **before 1980**	38
RC Post-1980	Reinforce concrete buildings built **after 1980**	14
Timber Pre-1980	Timber buildings built **before 1980**	16
Timber Post-1980	Timber buildings built **after 1980**	23
Pumice	Brick buildings made of hollow pumice blocks mainly built before 1980	9

been used as the cutting point to distinguish between older and newer buildings (Bessason et al. 2012, 2014; Bessason and Bjarnason 2016). Table 11.2 shows the definition of building typologies used in these studies as well as the proportion of how the dwellings in the south Iceland lowland are divided into these typologies. The listed proportions are not exact since they were not the same at 2000 and 2008.

11.3.3 Loss Data

Natural catastrophe insurance of buildings is mandatory in Iceland and is administered by the Iceland Catastrophe Insurance (ICI) fund. Therefore, after catastrophic events like large earthquakes, the repair and replacement cost for every damaged building is estimated by trained assessors in order to settle the individual insurance claims.

After the earthquakes in June 2000, the loss assessment work started right after the second event, and in 2008, it also started only a few days later. The assessment work was carried out by assessors with a technical background who worked in pairs. The main steps of the procedure were as follows:

1. A property owner reported damage to his local insurance company, which then informed ICI.
2. Assessors familiarized themselves with technical drawings and other related information about the damaged properties.
3. Assessors performed inspections of the property where all building damage was documented, marked on drawings, and photographed.
4. Assessors prepared a damage assessment report. The report included a description of the damage and a cost estimate for the repairs.

After the June 2000 events, the assessed damage was divided into five subcategories of structural and non-structural damage (Table 11.3). The damage data after the 2008 earthquake was classified in more detail, or in ten subcategories, and then further divided into 4 to 8 headings (Table 11.4). In total, the damage was broken down into 62 headings. The details of the damage data after the 2008 earthquake were used to map the main statistics of the damage in Bessason et al. (2014). The ten subcategories used in damage mapping after the 2008 earthquakes can be

Table 11.3 Subcategories of damage used in the survey after the 2000 earthquakes

Category	No.	Subcategory
Structural damage	1	Excavation, foundations and bottom slab
	2	Interior and exterior supporting structure (walls, columns, beams, roofs)
Non-structural damage	3	Interior finishing work (partition walls, mortar, suspended ceilings, cladding)
	4	Interior fixtures, paintwork, flooring, wall tiles, windows, doors, etc.
	5	Plumbing (cold water, hot water and sewer pipes), radiators, electrical installations

Table 11.4 Subcategories of damage used in the survey after the 2008 earthquake

Category	No.	Subcategory
Structural damage	1	Excavation, fill and earthwork
	2	Foundations and bottom slab
	3	Exterior supporting structure (walls, columns, beams, stairways)
	4	Roof structure
	5	Interior supporting structure (walls, columns, beams, slabs, stairways)
Non-structural damage	6	Interior finishing work (partition walls, mortar, ceiling cladding)
	7	Interior fixtures, incl. Kitchen and bathrooms, doors, flooring, wall tiles, etc.
	8	Windows, glass, exterior doors, wall cladding etc.
	9	Paintwork outdoors and indoors, including crack filling and surface treatment
	10	Plumbing (cold water, hot water and sewer pipes), radiators, electrical installations

combined and reduced to the same and identical subclasses as were used after the 2000 events in order to make a comparison. The loss data from the 2000 and 2008 earthquakes are complete in the sense that both databases include both damaged and undamaged buildings, which are rare to find in loss data sets (Pitilakis et al. 2014).

11.3.4 Intensity Measure

When evaluating fragility or vulnerability curves, an intensity measure (IM) must be used to link the loss to the strength of the ground motion. The majority of the affected buildings were low-rise, shear wall buildings. For such systems, the natural period is low and this justifies the use of peak ground acceleration (PGA) as a suitable IM. PGA (m/s^2) at a damaged property site was estimated by using a ground motion prediction equation (GMPE) developed by Rupakhety and Sigbjörnsson (2009):

$$\log_{10}\left(PGA\right) = -1.038 + 0.387 \cdot \mathrm{M_w} - 1.159 \cdot \log_{10}\left(\sqrt{\mathrm{H}^2 + 2.6^2}\right) + 0.123 \cdot S + 0.287 \cdot P \tag{11.1}$$

where H (km) is the shortest horizontal distance from the site to the surface of the fault trace; S is a site factor which takes the value 0 for rock sites and 1 for stiff soil sites; and P is an error/scatter term which follows a standard normal distribution, i.e., P∈N(0,1). Most of the strong motion data used to calibrate the parameters in Eq. (11.1) were taken from recent, large-magnitude Icelandic earthquakes, but they were also augmented by records from continental Europe and the Middle East. Both the horizontal components were used from each station. The main characteristic of the GMPE given by Eq. (11.1) is that it predicts a relatively high PGA in the near fault area, whilst the attenuation with distance is more than generally found in other GMPE (see for instance Ambraseys et al. 1996).

11.3.5 Elimination of Accumulated Effect in the June 2000 Earthquakes

The two June 2000 earthquakes in south Iceland struck with a 4 day interval and their, causative faults are approximately 20 km apart. Many buildings were, therefore, subjected to strong ground motion from the two events and can be expected to have accumulated damage from both of them. Computed PGA contours from both events using Eq. (11.1) was used to create a scenario hazard map from both events (Fig. 11.8). The maximum PGA at each location, i.e., PGA = *max*($\mathrm{PGA_{17June2000}}$, $\mathrm{PGA_{21June2000}}$), was used to determinate the contours. All buildings located between the two faults have been excluded in order to eliminate the accumulated earthquake effect. The observed loss can then be approximately assumed to be from two independent events. That is, all buildings located east of the 17 June earthquake fault are considered to have been affected only by that event, and all buildings located west of the 21 June earthquake fault are considered to have been only affected by that event (Bessason and Bjarnason 2016).

11.4 Damage Observations from Recent Earthquakes

11.4.1 Presentation of the Damage Data

There are a number of ways to develop vulnerability models and present the observed damage from the south Iceland earthquakes of June 2000 and May 2008. Here, the focus will be on presenting fragility curves, risk maps, and vulnerability

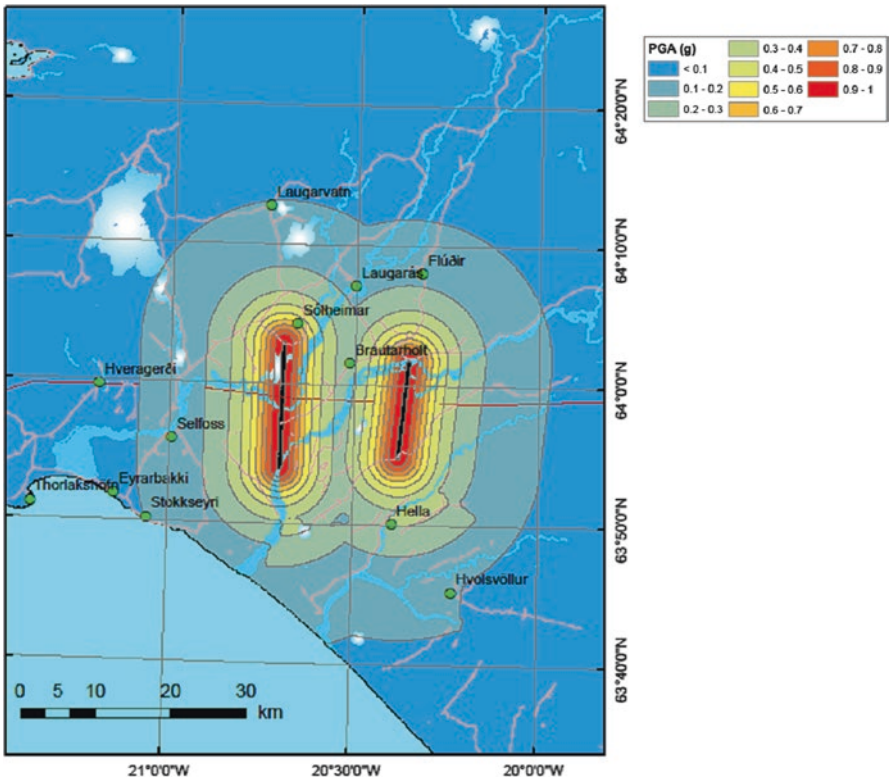

Fig. 11.8 A scenario hazard map for the two south Iceland earthquakes of June 2000 (the approximate locations of the causative faults of the 17 and 21 June earthquakes are indicated by the *black lines* to the east and west, respectively)

curves, as well as showing some statistics of the relative proportion of structural and non-structural damage.

Fragility curves provide the probability of exceeding a specified damage state for a given ground motion intensity. They are important in disaster management and risk reduction planning since they can be used to predict an overview of expected damage in a specified region. For instance, the expected proportion of collapsed buildings, expected proportion of severely damaged buildings, etc. can be estimated by using a hazard scenario, exposure data, and fragility curves. This information may then be used to predict the number of fatalities and injuries.

Vulnerability curves, on the other hand, provide the mean loss for a given building typology and given ground motion intensity. They are, therefore, useful for predicting expected losses, which can be of value for public authorities, government, and insurance companies. Vulnerability curves can be estimated directly from loss data (Rossetto et al. 2014), or they can be estimated indirectly from fragility curves. Indirect methods are commonly used to determine vulnerability curves when the

damage description is only qualitative, such as, no damage, minor damage, moderate damage, severe damage, etc.

Since the estimated repair cost is available for every affected dwelling after the June 2000 and May 2008 earthquakes, it is possible to compute the damage factor (DF) for every dwelling:

$$DF = \frac{\text{Estimated repair cost}}{\text{Replacement value}} \tag{11.2}$$

Here, the replacement value is obtained from the official inventory register. The DF is in the range of 0 to 1 (0–100%) where 0 means no damage and 1 means total loss.

11.4.2 Fragility Curves

The first step in evaluating fragility curves is to define damage states. Since the damage factor is known for every dwelling, it can be used for this purpose. Dolce et al. (2006) used the DF to define the damage states shown in Table 11.5, and they were then used in Bessason and Bjarnason (2016) to compute fragility curves from the Icelandic loss data.

A lognormal distribution (LN) was used as the functional form of the curves. The methodology presented by Shinozuka et al. (2000) was applied to estimate the two LN parameters with combined loss data from all three south Iceland earthquakes.

For each building typology (Table 11.2) and each damage state (Table 11.5), a two parameter lognormal distribution was fitted to the data by using a maximum likelihood method. The likelihood function was given as in Shinozuka et al. (2000):

$$L = \prod_{i=1}^{N} \left[G\left(a_i\right) \right]^{y_i} \left[1 - G\left(a_i\right) \right]^{1-y_i} \tag{11.3}$$

where G is the fragility curve for a specific damage state; a_i is the predicted PGA for building i based on Eq. (11.1); y_i represents a realization of a Bernoulli random variable Y which has the value 1 if the damage state in question is exceeded, and 0

Table 11.5 Definition of damage states for fragility curves (Dolce et al. 2006)

Damage state	Range of damage factor (%)	Description of damage
DS0	0	No damage
DS1	>0–5	Slight
DS2	>5–20	Moderate
DS3	>20–50	Substantial to heavy
DS4	>50	Very heavy to total

otherwise; and N is the number of affected buildings of each typology. Based on the lognormal assumption, G is given as:

$$G(a) = \Phi\left(\frac{\ln\left(\frac{a}{\mu}\right)}{\zeta}\right) \tag{11.4}$$

where Φ is the standardized normal distribution function, and μ and ζ are the median and dispersion parameters of the lognormal distribution. In order to estimate these parameters, a standard algorithm (built-in function in Matlab®) was used to find the minimum of −ln(L) where L is given by Eq. 11.3, and, at the same time, it was checked that the derivatives of the −ln(L) with respect to μ and ζ were zero:

$$\frac{d(-\ln L)}{d\mu} = 0 \quad \text{and} \quad \frac{d(-\ln L)}{d\zeta} = 0 \tag{11.5}$$

The parameters of the lognormal distribution, LN(α,β), are related to μ and ζ as α = ln(μ) and β = ζ. Furthermore, the mean value, m, and standard deviation, σ, of a lognormally distributed random variable can be computed from α and β by well-known formulas. The results for the five building typologies are shown in Fig. 11.9. More details and numerical values of the estimated parameters and comparison of how the data fit the curves can be found in Besssason and Bjarnason (2016).

It must be mentioned that the loss data from 2008 have the most weight at high ground accelerations, while at lower shaking, the two June 2000 earthquakes contribute more. Overall, the probability of exceeding DS1, DS2, and DS3 is less for post-1980 concrete and timber buildings than for pre-1980 concrete and timber buildings, which is not surprising. Furthermore, the pumice buildings are more vulnerable (DS2 and DS3) than the other building typologies. Finally, it can be mentioned that the probability of exceeding DS2 and DS3 is low or less than 0.1 for pre-1980 and post-1980 RC and timber buildings, while it is higher for the pumice buildings.

11.4.3 Risk Maps

By combining a hazard scenarios in terms of PGA for the two south Iceland earthquakes of June 2000 (Fig. 11.8) and the fragility curves defined by the LN model (Fig. 11.9), it is possible to compute scenario risk maps for these two events and all five building classes. Such risk maps are shown in Fig. 11.10 for pre-1980 RC buildings and in Fig. 11.11 for Post-1980 RC buildings. The maps for pre-1980 RC buildings show that, in Selfoss, the probability of exceeding DS0 (No damage) was in the range 0.10–0.20 (Fig. 11.10a), while the probability of exceeding DS1 was less than

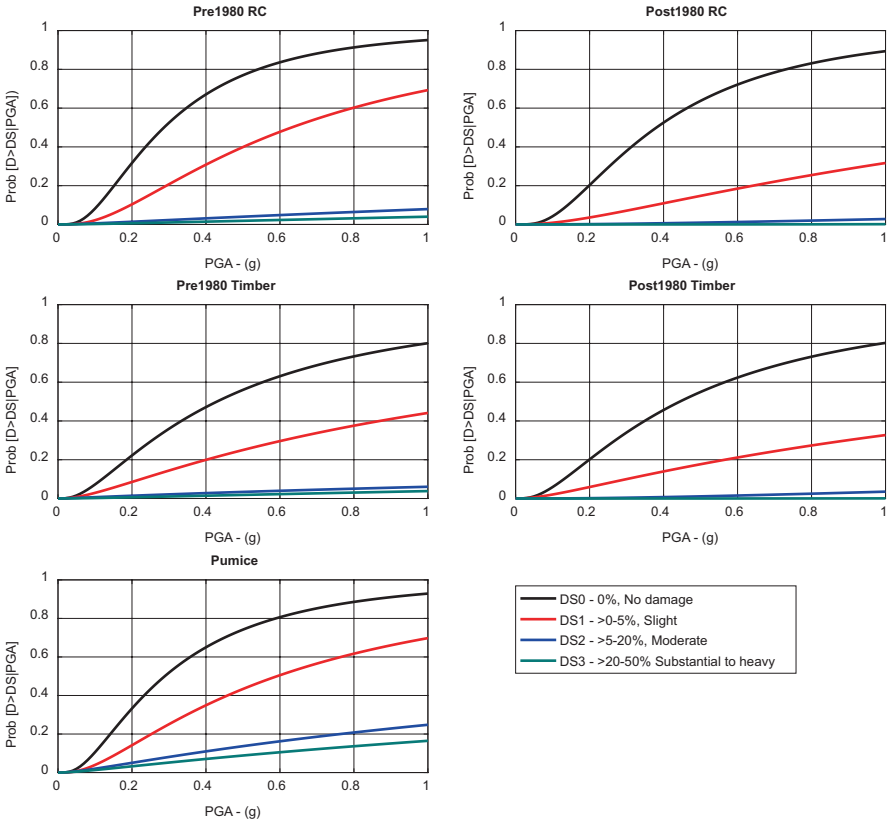

Fig. 11.9 Fragility curves for pre-1980 RC buildings, post-1980 RC buildings, pre-1980 timber, post-1980 timber and pumice buildings (Bessason and Bjarnason 2016)

0.05 (Fig. 11.10b). The map in Fig. 11.11 shows that the newer RC building (Post-1980) performed better than the older ones. The probability of exceeding DS2 was less than 0.10 everywhere in the affected area, except for the pumice buildings (Fig. 11.8). One limitation of the presented results is that the effect of damage accumulation between the two events, which would be most significant in the area between the two faults, is not adequately modelled in the fragility curves. Since strong earthquakes in SISZ tend to occur in sequences, the effect of accumulated damage is important and needs further investigation so that it can be properly included in future fragility curves.

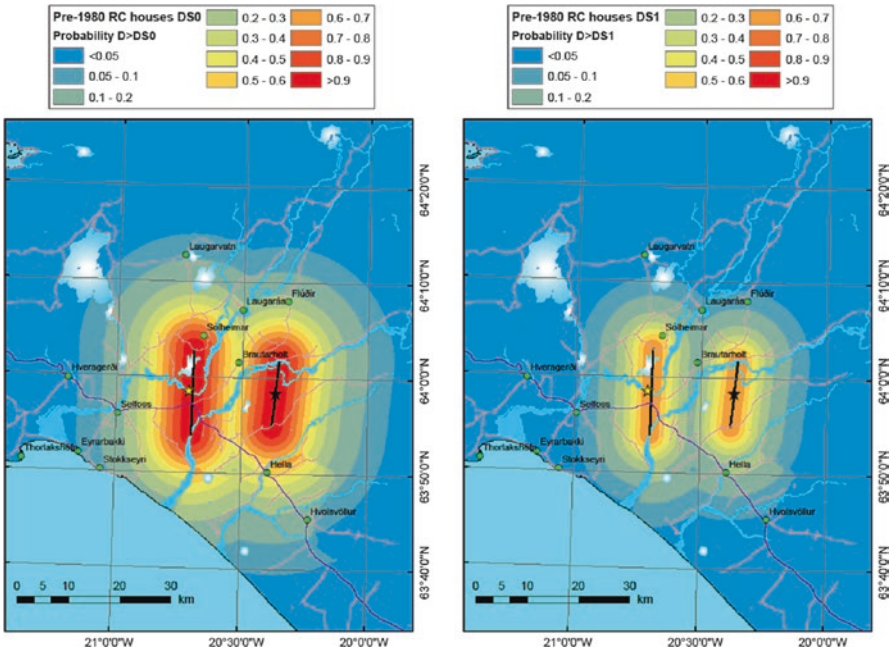

Fig. 11.10 Scenario risk map for reinforced concrete buildings built before 1980 (pre1980), (**a**) probability that damage state will exceed DS0, (**b**) probability that damage state will exceed DS1

11.4.4 Vulnerability Curves

Vulnerability curves can be computed using different methodologies. In Bessason et al. (2012), a statistical vulnerability model was fitted to the loss data from the May 2008 south Iceland earthquake. For each of the five building typologies (Table 11.5), the loss data were split into four groups reflecting four different intensity levels. The lowest level was defined by computed PGA at the building site in the range of 0.05–0.09 g, the next level for PGA in the range of 0.09–0.18 g, then 0.18–0.34 g, and the fourth level for PGA 0.34–0.60 g. For each bin and each building typology, a four-parameter model was computed: one parameter representing the ratio of undamaged buildings (DF = 0) to the total number of buildings; one parameter representing the ratio of total damaged buildings (DF = 1) to the total number of buildings; and then two parameters of a lognormal probability distribution fitted to damaged buildings (0 < DF < 1). For prediction of loss, it is necessary to rely on the mean value for each of the above acceleration bins. Other, more sophisticated, statistical methods can be used, for instance by applying generalised linear models (GLM), generalised additive models (GAM), and Gaussian Kernel models (GKS). These models are described in the GEM empirical vulnerability assessment guidelines (Rossetto et al. 2014). They were used by Maqsodd et al. (2016) on Australian data. Here, the vulnerability curves were estimated indirectly

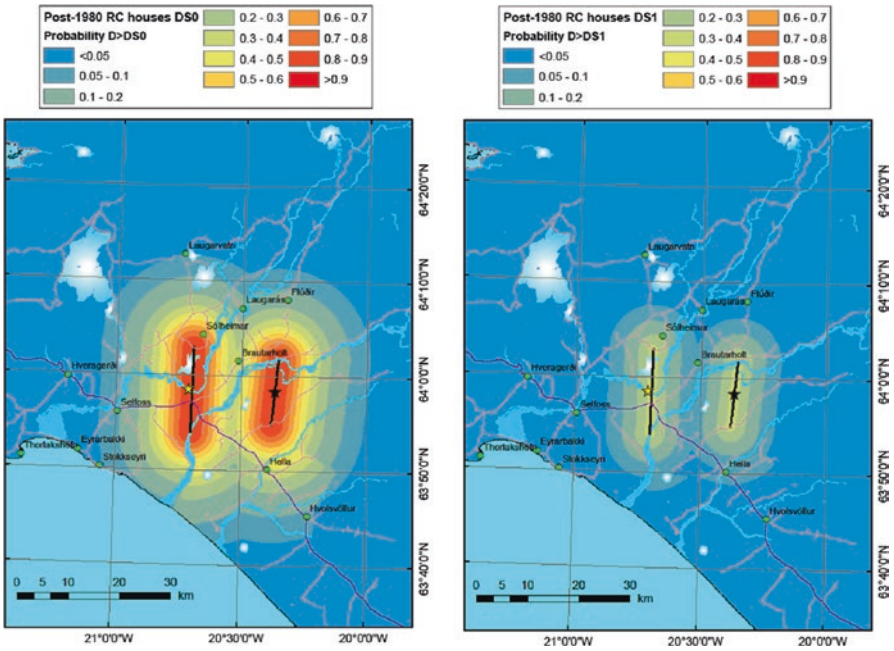

Fig. 11.11 Scenario risk map for reinforced concrete buildings built after 1980 (post-1980), (**a**) probability that damage state will exceed DS0, (**b**) probability that damage state will exceed DS1

from the fragility curves shown in Fig. 11.9 by using median values for each damage state, i.e., $DS0_{med} = 0$, $DS1_{med} = 0.025$, $DS2_{med} = 0.125$, $DS3_{med} = 0.35$, and $DS4_{med} = 0.75$:

$$V(PGA) = (G_{DS0} - G_{DS1}) \cdot DS1_{med} + (G_{DS1} - G_{DS2}) \cdot DS2_{med} + (G_{DS2} - G_{DS3}) \cdot DS3_{med} + (G_{DS3}) \cdot DS4_{med}$$

where G_{DS0} is the fragility curve for damage state DS0, G_{DS1} is the fragility curve for DS1, etc. (Fig. 11.12). At a PGA of 0.5 g, the estimated loss for a pre-1980 building is, as an example, around 3%, while for a pumice building, it is approximately 13%. It must be underlined that those curves are approximations and no error estimates or confidence intervals are given. In general, the vulnerability curves for pumice buildings showed the highest values whilst the vulnerability curves for both post-1980 RC and post-1980 timber lay lowest on the graph, i.e., for buildings built after the implementation of seismic codes in Iceland.

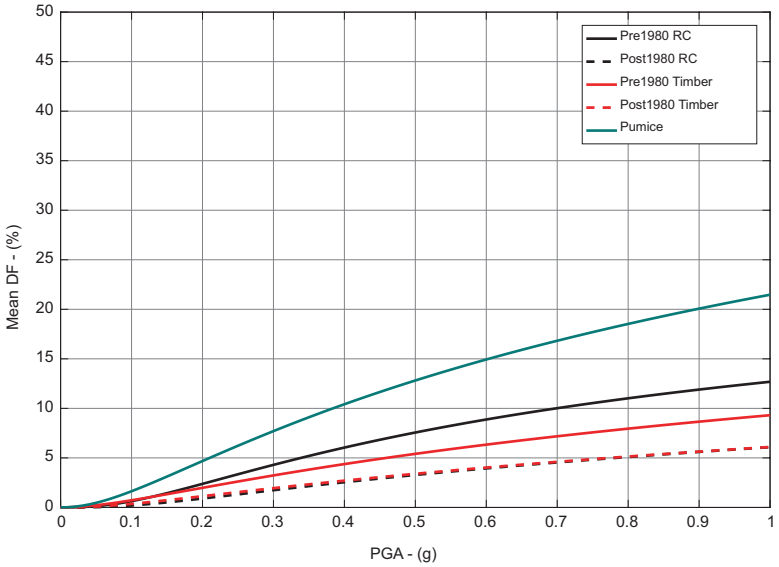

Fig. 11.12 Vulnerability curves for pre-1980 RC, post-1980 RC, pre-1980 timber, post-1980 timber and pumice buildings

11.4.5 Structural and Non-structural Damage

Fragility curves or vulnerability models for non-structural seismic loss alone have not yet been developed to our knowledge. However, studies of the loss data from the three south Iceland earthquakes have shown that most of the losses are related to non-structural damage (Bessason et al. 2014; Bessason and Bjarnason 2016). In those studies, the loss data were divided into five subclasses of structural and non-structural damage (Table 11.3). The observed loss for each damaged building was split proportionally between the subcategories, such that the total sum was 100%. From these data, the average proportion of each subclass of damage in each building typology could be estimated. The relative distribution of different damage subclasses is shown in Fig. 11.13. The results presented here are averaged over all houses, independent of ground motion intensity. Damage subclass 4, which is represented by the fourth bars in the histograms of Fig. 11.13, was the largest for all typologies. This shows that non-structural damage of interior fixtures, paintwork, flooring, wall tiles, windows, and doors contributed most to the overall damage of all building types. The second, most dominant damage type was subclass 2. It was related to damage of interior and exterior supporting structures (walls, columns, beams, roofs). The results indicate that damage in new concrete and timber buildings was mostly non-structural (sum of bars 3, 4 and 5). Relatively, more structural damage was observed during the June 2000 earthquakes than the May 2008 earthquake, which may be partly explained by better performance of buildings which were repaired and/or retrofitted after the June 2000 earthquakes, but also may be

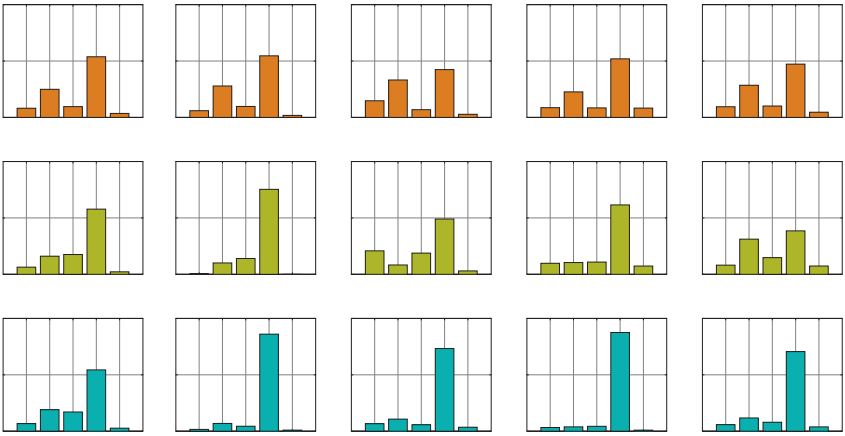

Fig. 11.13 Classification of damage data in five subcategories (Table 11.3) for five building typology classes (Table 11.2). (**a**) 17 June 2000 Mw6.5 earthquake, (**b**) 21 June 2000 Mw6.5 earthquake, (**c**) 29 May 2008 Mw6.3 earthquake (Bessason and Bjarnason 2016)

due to the larger intensity ground motion and the longer duration as these two earthquakes were of larger magnitude than the 2008 event. More details of the May 2008 loss data can be found in Bessason et al. (2014), which showed that most of the losses of the residential buildings were related to flooring and indoor paintwork.

11.5 Summary and Conclusions

Seismic hazard in Iceland is moderate to high. Destructive earthquakes in the magnitude range of six to seven have occurred frequently in the two main seismic zones in Iceland, i.e., the South Iceland Seismic Zone and the Tjörnes Fracture Zone. Twenty-five earthquakes of magnitude six or greater have struck in these two zones since 1700. Historical descriptions of damage are available for most of these events and, in many cases, are quite detailed. For more recent earthquakes, comprehensive loss data exist based on insurance claims. This chapter summarises earlier observations and studies of seismic performance of Icelandic buildings and is meant to give an overview of how the vulnerability these buildings have changed over time and to present suitable models for estimation of seismic risk to residential buildings in future earthquakes.

- In destructive earthquakes occurring before 1900, most of the residential houses, as well as animal shelters, in the epicentral area collapsed. The buildings at that time were made of turf and stone with limited binding material and were seismically very vulnerable.

- Towards the middle of the twentieth century, building tradition in Iceland started to change, with timber and concrete houses replacing old turf and stone houses. These newer houses, especially those where timber was not used for structural framing but mainly for roof rafters, and concrete were mostly unreinforced and believed to be of poor quality and were vulnerable to ground shaking. For example, the 1934 Dalvík Earthquake caused severe damage and collapse of many buildings in the village of Dalvík, which was ~2–3 km from the earthquake epicentre.
- The performance of the current residential building stock in south Iceland is very good. The three recent earthquakes, two Mw6.5 in June 2000 and a Mw6.3 in May 2008 which occurred in the largest agricultural region in south Iceland lowland, caused quite low overall damage to residential buildings. Not a single building collapsed in the region. In Hveragerði, where recorded peak ground acceleration during the May 2008 earthquake was close to 85% of acceleration of gravity, overall damage to residential buildings was around 5% of their insured value (see Rupakhety et al. 2016). This level of ground shaking is almost twice the current 475 year mean return period PGA in the SISZ. This shows that the new buildings in SISZ possess significant overstrength and ductility. Timber frame and reinforced concrete buildings performed exceptionally well during these earthquakes, and serious structural damage was sustained mostly by old, unreinforced concrete or pumice block houses. Buildings in Iceland are designed for very severe wind loads, and the resulting structural system seems inherently effective for seismic resistance as well. The buildings are low rise and mostly of regular planar configuration, which also improves their seismic performance. Newer buildings built after the implementation of seismic codes in 1976 performed far better than older building typologies.
- Based on damage data collected from recent earthquakes, the probability of exceeding damage state DS2 (5–20% loss), even in the epicentral area, is expected to be less than 0.10 for both timber and concrete buildings. Hollow block pumice buildings (brick buildings) mainly built before 1980 are more vulnerable, however, and can be expected to suffer severe damage under strong shaking. There are only a few pumice buildings in SISZ, and these are no longer built.
- Losses suffered by all types of buildings during these three recent earthquakes were mainly due to non-structural damage. During the latest earthquake, non-structural damage accounted for more than 75% of all losses in buildings built after 1980. The most frequent type of damage was related to interior fixtures, paintwork, flooring, wall tiles, windows, and doors.

The main findings from recent earthquakes in south Iceland are quite encouraging and indicate that low-rise residential buildings in seismic zones in Iceland behave satisfactorily in earthquakes of magnitude 6.5 or less. However, larger earthquakes can be expected in Iceland, and the extrapolation of fragility functions and vulnerability relationships based on loss data from lower magnitudes to higher are not reliable. It should also be emphasized that the buildings in the study area are low

rise and very regular. Taller and more slender structures in the area might be at higher seismic risk, mainly in the near-fault area. Building typology in Reykjavik, the most populated place in Iceland, is quite different to that in the south Iceland lowland. There are many tall buildings in Reykjavik. Given the lack of loss data from such buildings, estimation of seismic risk for buildings in Reykjavik might need to rely on a combination of empirical data and analytical models of building vulnerability. Financial losses due to recent earthquakes have been relatively low for the intense shaking many buildings experienced, and no human casualty or serious injury was caused. However, in spite of the low probability of structural damage and collapse and the resulting injury/casualty, the risk of serious injury or death due to falling of heavy household contents should not be neglected, especially if a strong earthquake strikes when most of the people are indoors and not alert, for example sleeping during the night. Methods to improve seismic safety in south Iceland should focus on prevention of hazardous movement of building contents. Apart from financial losses and injury/death of people, even minor, non-structural damage can cause distress and disrupt the daily lives of people living in a seismically active area like the SISZ. Such effects can be reduced by implementing simple protective measures to reduce seismic risk due to building contents and non-structural elements.

Acknowledgements The authors acknowledge financial support from the University of Iceland Research Fund. A part of the work presented here was undertaken for the EU project KnowRISK, which is co-financed by the European Commission's Humanitarian Aid and Civil Protection Grant Agreement ECHO/SUB/2015/718655/PREV28.

References

Ambraseys N, Simpson KA, Bommer JJ (1996) Prediction of horizontal response spectra in Europe. Earthq Eng & Struct Eng 25(4):371–400

Ambraseys N, Smit P, Sigbjörnsson R, Suhadolc P, Margaris B (2002) Internet-Site for European Strong-Motion Data (ISESD). European Commission, Research-Directorate General, Environment and Climate Programme

Bessason B, Bjarnason JÖ (2016) Seismic vulnerability of low-rise residential buildings based on damage data from three earthquakes (Mw6.5, 6.5 and 6.3). Eng Struct 111:64–79

Bessason B, Bjarnason JÖ, Guðmundsson A, Sólnes J, Steedman S (2012) Probabilistic damage curves for low-rise buildings based on field data. Earthquake Spectra 28(4):1353–1378

Bessason B, Bjarnason JÖ, Guðmundsson A, Sólnes J, Steedman S (2014) Analysis of damage data of low-rise building subjected to a shallow Mw6.3 earthquake. Soil Dyn Earthq Eng 66:89–101

Dolce M, Kappos A, Masi A, Penelis G, Vona M (2006) Vulnerability assessment and earthquake damage scenarios of the building stock of Potenza (Southern Italy) using Italian and Greek methodologies. Eng Struct 28:357–351

Einarsson P (1991) Earthquakes and present-day tectonics in Iceland. Tectonophysics 189(1–4):261–279

Guðmundsson G (ed) (1951) Öldin okkar – Minnisverð tíðindi 1931–1950. Forlagið Iðunn, Reykjavík. (in Icelandic)

Halldórsson B, Sigbjörnsson R (2009) The Mw6.3 Ölfus earthquake at 15:45 UTC on 29 May 2008 in South Iceland: ICEARRAY strong-motion recordings. Soil Dyn Earthq Eng 29:1073–1083

Halldórsson P, Björnsson S, Brandsdóttir B, Sólnes J, Stefánsson R, Bessason B (2013) Jarðskjálftar á Íslandi. In: Sólnes J, Sigmundsson F, Bessason B (eds) Natural hazard in Iceland – volcanic eruptions and earthquakes. Háskólaútgáfan and Viðlagatrygging Íslands, Reykjavik. (in Icelandic)

Icelandic Property Registers. http://www.skra.is/english/property-register/

Maqsood T, Edwards M, Ioannou I, Kosmidis I, Rossetto T, Corby N (2016) Seismic vulnerability function for Australian buildings by using GEM empirical vulnerability assessment guidelines. Nat Hazards 80(3):1625–1650

Ólafsson S, Sigbjörnsson R (2002) Attenuation of strong-motion in the South Iceland earthquakes of June 2000, proceedings of the 12th European conference earthquake engineering, CD-ROM:Paper 412. Elsevier, London

Pitilakis K, Crowley H, Kaynia AM (2014) Introduction. In: Pitilakis K, Crowley H, Kaynia AM (eds) SYNER-G*:* typology definition and fragility curves for physical elements at seismic risk. Springer, New York

Rossetto T, Ioannou I, Grant DN, Maqsood T (2014) Guidelines for empirical vulnerability assessment, GEM Technical Report 2014–08, 140 pp. GEM Foundation, Pavia, Italy. doi:10.13117/GEM.VULN-MOD.TR2014.11

Rupakhety R, Sigbjörnsson R (2009) Ground-motion prediction equations (GMPEs) for inelastic response and structural behavior factors. Bull Earthq Eng 7(3):637–659

Rupakhety R, Ólafsson S, Sigbjörnsson R (2016) Damage to residential buildings in Hveragerði during the 2008 Ölfus Earthquake: simulated and surveyed results. Bull Earthq Eng 14(7):1945–1955

Shinozuka M, Feng MQ, Lee J, Naganuma T (2000) Statistical analysis of fragility curves. J Eng Mech 126:1224–1231

Sigbjörnsson R, Rupakhety R (2014) A saga of the 1896 South Iceland earthquake sequence: magnitudes, macroseismic effects and damage. Bull Earthq Eng 12:171–184

Sigbjörnsson R, Ólafsson S, Rupakhety R, Halldórsson B, Acharya P, Snæbjörnsson JTh (2014) Strong-motion monitoring and accelerometric recordings in Iceland. In: Proceedings of the 2nd European conference earthquake engineering & seismology, Istanbul

Thórarinsson Ó, Bessason B, Snæbjörnsson J, Ólafsson S, Baldvinsson GI, Sigbjörnsson R (2002) The South Iceland Earthquakes in 2000: strong motion measurements. In: Proceedings of the 12th European conference earthquake engineering, CD-ROM:Paper 321. Elsevier, London

Thoroddsen T (1899) Jordskjaelvene i efteraaret 1896. Dansk Geogr Tidskr 14:93–113. (in Danish)

Thráinsson H (1992) Damage assessment for two Icelandic earthquakes. In: Proceedings of the 10th world conference earthquake engineering. A.A. Balkema, Rotterdam

Chapter 12
Earthquake-Safe and Energy-Efficient Infill Panels for Modern Buildings

Marco Vailati, Giorgio Monti, and Giorgia Di Gangi

Abstract The recent earthquakes that occurred in Central Italy, in L'Aquila in 2009 and in Amatrice in 2016, have shown, once again, how infill panels and partitions, widely used as non-structural elements in reinforced concrete frames, are significantly vulnerable when subjected to seismic actions. Moreover, they highly affect the structural behavior and seismic response of typical, multi-story buildings, strongly influencing their repair costs due to the inevitable damage they usually undergo during seismic events. Therefore, they should be designed to withstand earthquakes forces, both in-plane and out-of-plane, so to ensure the safety of the occupants. In addition to seismic performance, infill panels play the primary role of providing comfort to occupants through adequate thermal and acoustic insulation. In this paper, an innovative solution of earthquake-safe and eco-friendly infill panels is presented, which are, at the same time, thermally and acoustically efficient, thus avoiding waste of energy and respecting the environment. The proposed innovative technology is tested with different surface finishes, boundary conditions and temperatures. A comparison of the proposed technology with respect to conventional infill typologies is provided, highlighting pros and cons.

Keywords Infill walls • Mortar-free infills • Structural and thermal properties of infills

12.1 Introduction

The system proposed in this work is based on hollow blocks (either in concrete or clay) that are dry-juxtaposed, rather than joined with mortar layers, by means of recycled-plastic joints, conceived to become a preferential sliding plane to

M. Vailati (✉) • G. Monti • G. Di Gangi
Department of Structural and Geotechnical Engineering, Sapienza University of Rome, Rome, Italy
e-mail: marco.vailati@uniroma1.it; giorgio.monti@uniroma1.it; giorgia.digangi@uniroma1.it

R. Rupakhety, S. Ólafsson (eds.), *Earthquake Engineering and Structural Dynamics in Memory of Ragnar Sigbjörnsson*, Geotechnical, Geological and Earthquake Engineering 44, https://doi.org/10.1007/978-3-319-62099-2_12

accommodate the horizontal displacements imposed by earthquakes, thus preventing breaking of the blocks. The joint is made by a horizontal plane with size of 300 × 258 mm and thickness of about 2 mm on which thermoformed hollow teeth are extruded outwards, so to be inserted in the block holes (Vailati et al. 2014). Vertical plastic strips are also foreseen to prevent out-of-plane collapse.

Three types of external infill panels have been studied and subjected to laboratory tests: (1) with a rough surface, (2) with a surface finish, (3) with a surface finish and an improved constraint condition. All infills have been tested under distributed load, by using a particular system of airbags that simulates the inertia forces due to groundshaking. The tests have been conducted at the laboratory of the Faculty of Engineering of the University of Porto, Portugal.

12.2 Modern Approach to Building Design

The modern way to design buildings takes into account different aspects that could be summarized with the watchword *integrated design*.

Designers operate within a framework that encompasses both energy and structural aspects, looking for green buildings that are also safe against earthquakes, while trying to fulfill the basic aesthetic requirements.

As a matter of fact, modern technical codes are, nowadays, considering the construction as a combination of structural elements, non-structural elements and equipment. Non-structural elements are internal and external partitions which must be designed in a way to reduce damage and prevent falling on the occupants during an earthquake.

Integrated design approach and *integrated team process* are, in fact, the two main components of the whole building design approach. Regarding the first point, some targets have to be balanced, like accessibility, aesthetics, historic preservation, sustainability, flexibility, etc. As for the latter, an interactive approach during the design process is required, involving all the stakeholders and considering all phases of the project. Only by implementing this approach, can a high-performance building be achieved.

12.3 Green Philosophy and Structural Safety

The need to design high-performance and green buildings – and save as much energy as possible – has changed the conception of construction practice towards *sustainability* (Kibert 2013). These common purposes now involve almost 60 national green building councils that establish performance goals for their countries.

Thus, the modern whole building design approach has to take into account these aspects through the implementation of the most advanced technologies and strate-

gies currently available. Buildings can be defined as sustainable also considering the materials selection; the *closed* loop is a process that envisages the use, reuse and recycling process of materials rather than their disposal.

While the concept of green buildings is currently largely widespread, it is important to highlight that, to achieve high-performance building requirements, the structural performance during earthquakes should be of major concern.

An effective and full integration among thermal-acoustic efficiency and earthquake safety could lead to innovative solutions, from both the architectural and the structural standpoints. Ultimately, structural and non-structural elements adopted in the building process should pursue the following targets:

- insulation and, consequently, less energy dispersion, providing an internal thermo-hygrometric comfort;
- equipment integration;
- safe performance during earthquakes.

12.4 Mortar-Free Technology

The innovative technology proposed here has been developed considering the common observation during past earthquakes that non-structural elements are vulnerable and play an important role in the overall damage and, in some cases, interact with the structural systems to cause additional damage. At least until 1980, the role of non-structural elements, such as the infill panels, were neglected. The trend was to analyze the structure as a bare frame, determining its response and subsequently applying deformations to the non-structural elements without considering their interactions with the frame itself. This misconception led to an unavoidable miscalculation of the seismic response of the structural system, which is significant when the infill panels are heavy brick or masonry walls which provide extra stiffness and inertia to the overall structure (Vailati and Monti 2016).

The Eurocodes include certain requirements in design of such panels, considering the collapse limit state for both in-plane and out-of-plane behavior, and only for the in-plane behavior in the damage limit state. In the draft of the Italian New Technical Code, the construction is now considered as a combination of structural elements, non-structural elements and equipment. Non-structural elements are finally being addressed in seismic design codes. In FEMA 356, modelling methods for infill walls are outlined.

The objective of the proposed technology is to reduce the stiffness of the infill panels, thereby reducing their unwanted interaction with structural elements, and also to enhance their deformation capacity to reduce damages: cracking during in-plane deformation and total or partial overturning during out-of-plane deformation (Vailati and Monti 2014).

12.5 External Infills: Components, Stratigraphy, Assembly

The innovative system of infill panels is assembled by using recycled plastic joints in place of mortar layers, to join juxtaposed hollow clay blocks. Each joint is made of a planar surface with protruding teeth that fit into the holes of the blocks. Based on the location of the joint (at the panel base, along the panel height, or at its top), the teeth are placed on one or both surfaces (Fig. 12.1). They allow relative displacements to take place between blocks so that each joint becomes a preferential sliding plane; the displacements are distributed along the wall height almost linearly, thus reducing the in-plane stiffness. Out-of-plane collapse is prevented by the use of vertical strips that form a strengthening net.

The controlled industrial process of plastic joints ensures the stability of the physical-mechanical properties of each piece (with a size of 300 × 258 mm), with a thickness of about 2 mm. Moreover, uniaxial tensile tests on material samples have shown that their elastic modulus, E, is around 400 MPa.

Considering thermo-hygrometric performances, different stratigraphies are proposed, using different kinds of insulation materials to facilitate the adaptability of the solution according to the needs. The external infills are made with a double facing of clay blocks with an insulation layer placed between them. The components are assembled starting from the floor, proceeding upwards with subsequent layers. Single joints with teeth only on the top surface are used on the first layer. The assembly continues until the topmost row using the double joints (with teeth on both surfaces) and is completed with vertical strips (Figs. 12.2 and 12.3). The last row in contact with concrete frame uses the single joint.

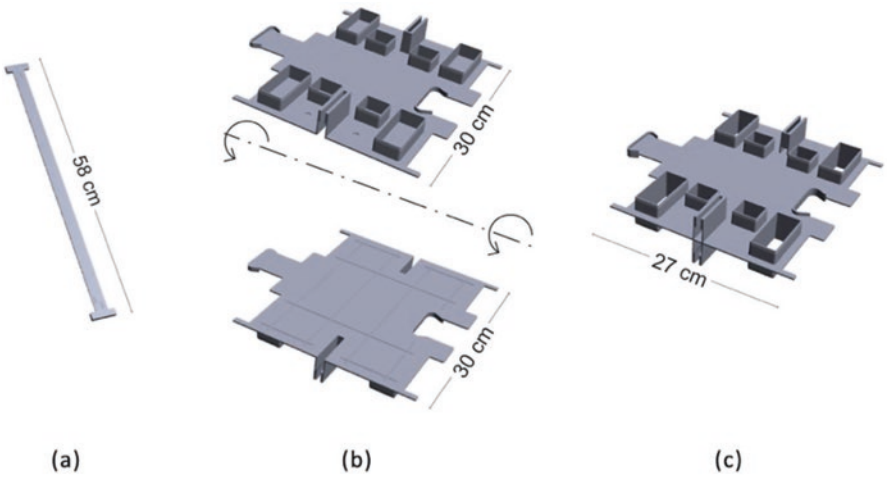

Fig. 12.1 Recycled-plastic components: (**a**) vertical strip, (**b**) single joints, (**c**) double joint

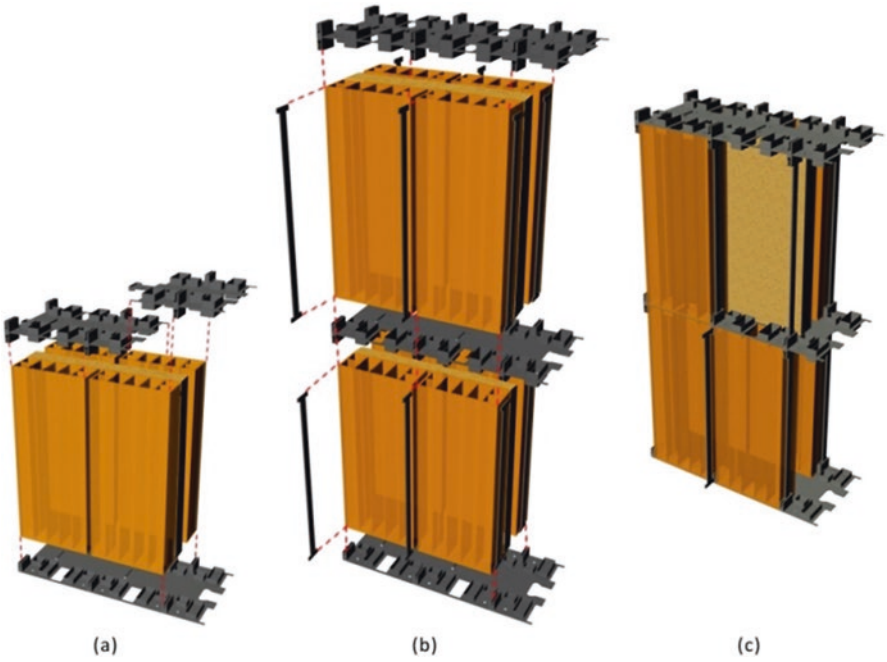

Fig. 12.2 Assembly of components and stratigraphy: (**a**) first row, (**b**) second and subsequent layers, (**c**) completed assembly

12.6 Structural Behavior Testing

These tests represent the first part of a larger campaign aimed at studying the influence of the in-plane deformation on the out-of-plane resistance and at quantifying the energy dissipation in both mechanisms. The results of three, full-scale walls tested under different boundary conditions and surface finishes are presented here. The tests were carried out at the laboratory of the Faculty of Engineering of the University of Porto, Portugal. Figure 12.4 shows the configuration of the concrete frame/wall system, indicating the different boundary conditions along the interface between the infill panel and the concrete frame.

Figure 12.5 shows the configuration of the testing equipment, the points of load application and response measurement. The arrangement of airbags used to apply the distributed load intended to model inertial effects during earthquakes is shown in Fig. 12.6.

Table 12.1 summarizes the main parameters of the tests performed. In figures from 8 to 10, the specimens before testing are shown (Figs. 12.7, 12.8, and 12.9).

The fixing system with wooden boards has been adopted in the last test specimen to evaluating the effect of the improvement of the frame connections. In fact, it was noticed that, at the end of the second test, the absence of an effective transfer mecha-

Fig. 12.3 Phases of assembly of first dry infill panel (from *top-left* to *bottom-right* picture)

nism of the tangential forces caused a sliding of the wall, thus decreasing its out-of-plane resistance.

12.6.1 Experimental Results

The specimens were submitted to cyclic loads. After the initial phase where the load was made to decrease and increase to reduce the unavoidable gaps between the system components, the pressure of the airbags was increased until the conventional maximum displacement of 60 mm was attained at control point 8 (see Fig. 12.5). At this point, three or four alternate load cycles from 60 to 0 millimeters, with a constant velocity of 0.1 mm/sec, were applied until the end of the test. The force-displacement curve of the first test is shown in Fig. 12.10.

It can be noticed that, from the second cycle, the out-of plane force-displacement curve stabilizes after the second cycle, and the subsequent cycles after this overlap. This means that, after the first cycle, the gaps reduce to almost zero and the system permits the dissipation of energy due to deformation of the plastic strips and the friction between the components. This effect is a phenomenon quite peculiar to this

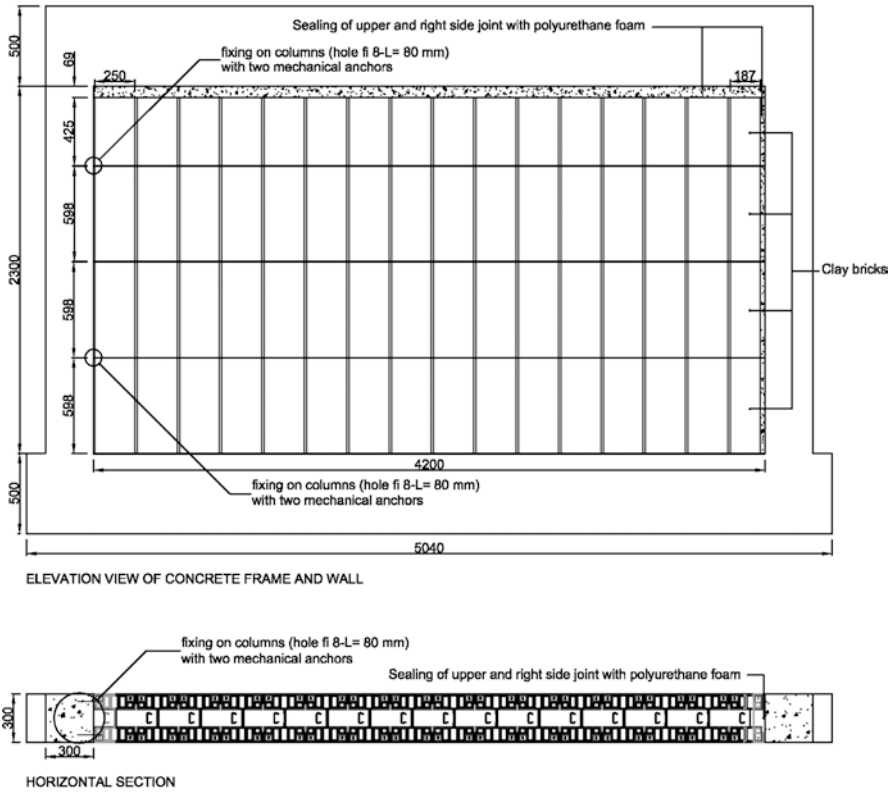

Fig. 12.4 Out of plane testing configuration of the infills

technology. In fact, in traditional infill panels, with their high in-plane and out-of-plane stiffness, does not allow sufficient displacements to dissipate energy.

Figure 12.11 clearly shows the effect of the different boundary conditions. On the right side of the infill, the polyurethane foam resists the rotation of the wall, as seen from the opening of the mid joint, which is considerably larger on the left side than on the right side. The blocks still appear undamaged while the plastic parts had been deformed. It should be noted that only the horizontal mid joint has opened, implying a linear displacement pattern between the mid-height and the top/bottom of the wall.

Figure 12.12 shows the deformation of the infill corresponding to maximum displacement reached during the tests. The kinematic behavior of the wall is similar to that observed during application of the 30 mm displacement. Blocks and recycled plastic joints and strips do not appear damaged, and they are still working well without any critical issues.

As shown in Fig. 12.10 at point 3, the residual displacement is nearly 15 mm. It should be noted that the residual displacement is not due to the plastic strips but due to sliding of teeth inside the blocks, holes (Fig. 12.13).

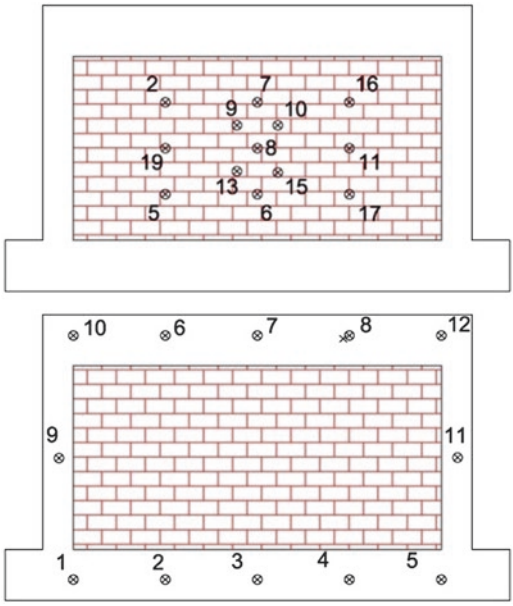

Fig. 12.5 Position of displacement control points (*above*) and of load cells (*below*)

Fig. 12.6 The airbags used to apply the load; *left and right*: lateral views; *center*: rear view

The force-displacement curve of the second test is shown in Fig. 12.14.

The stiffness increase due to surface finish changed the kinematics of the structural system. In this case, for low force values, the wall behavior resembled that of a rigid block; the arch behavior observed in the first test did not develop in this case. As a confirmation of this hypothesis, one should note that, along the bottom of the

Table 12.1 Scheme of the test set-up and monitoring equipment

Test set-up	**Monitoring system**
Wall height: 240 cm	13 strain gauges
Wall width: 420 cm	12 load cells
Thickness: 30 cm	
Horizontal joints: 5	
Weight of infill panel: 1.1 kN/m^2	
Surface finish:	
Specimen 1: rough surface	
Specimen 2: plaster with retaining plastic mesh	
Specimen 3: as in 2, with different base connection	

Fig. 12.7 First test specimen with rough surface

infill, plaster detached from the concrete beam. Figure 12.15 shows this particular behavior of the second test with surface finish.

When the displacement of the control point is increased to 10 mm (Fig. 12.16), only a minor increase in plaster detachment was noticed. Surface cracking had not initiated and the global behavior was still rigid. When the displacement was increased to 30 mm (Fig. 12.17), the rigid behavior continued but with significant plaster detachment that extended to the left end of the wall where its connection with the frame is less effective. As a counterbalance of a shift, it exhibits a significant decrease of the overall force, as shown at point 3 of Fig. 12.14.

The displacement of the control point was further increased to 40 and 50 mm, without any noticeable change in the wall kinematics. Figures 12.18 and 12.19 do not provide further information about the behavior of the wall; plaster detachment increased and the out-of-plane sliding of the wall prevented any other resisting

Fig. 12.8 Second test specimen with surface finish made by plaster and retaining plastic mesh

Fig. 12.9 Third test specimen with surface finish made by plaster and retaining plastic mesh. The smaller pictures show the connection system along the edges

mechanism to develop overall higher stiffness. It should be noticed that at each load step analyzed previously, due to load reversal, a momentary and sharp decrease of the stiffness occurs, which is due to the reduction of friction force. After contact is restored, friction force grows again and the stiffness becomes almost the same as before. As regards the characteristic point 6 in Fig. 12.14, it should be noticed that the residual displacement is greater than the first test. This is because the high out-of-plane stiffness has produced a permanent displacement without drawing the elasticity of the structural system.

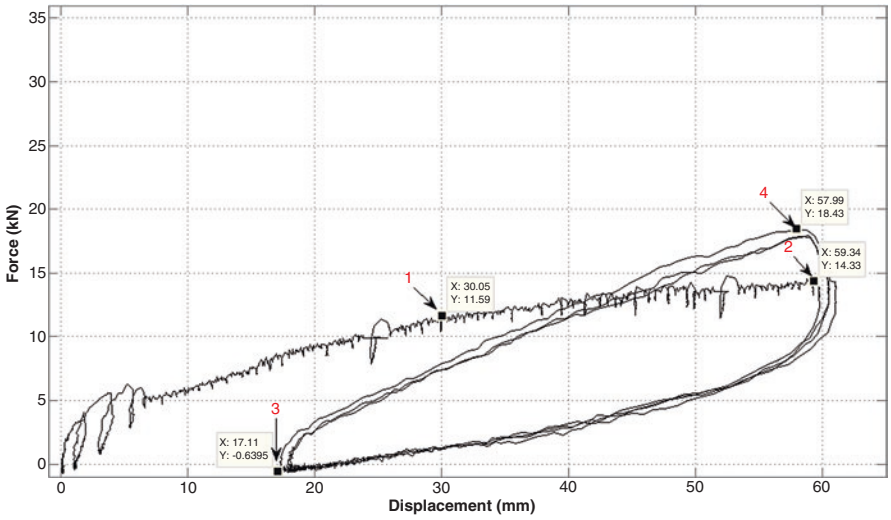

Fig. 12.10 Test 1. Force/displacement relationship of first-tested wall. The points represent: *1*, the transition between the second and third *straight line* with constant stiffness, in a tri-linear scheme; *2*, the load reversal at the end of the first cycle; and *3*, the load reversal at the beginning of the second cycle, the maximum force obtained in the test

The force displacement curve during the third specimen test is shown in Fig. 12.20.

When the control point displacement is 20 mm, the wall behavior was flexural. Cracks were visible on the surface at each horizontal joint, with the crack at mid-height being the widest cracks.

Until 30 mm of displacement is applied at the control point, the wall shows a constantly increasing stiffness due to the lack of defects in the constraints and because the gaps between the components were almost closed during the first test without finish surface.

Between 30 and 40 mm, as shown in Fig. 12.21, the stiffness decreases, probably due to damage of the plastic net, and the crack at mid-height opened up wider.

Added to such incremental damage is also the confinement effect of the wooden boards. In fact the bottom constraint realized to remove the sliding seen in the second test is saggy due to the intrinsic deformability of wood under large displacements.

As mentioned previously, the displacement field is influenced by different constraints between frame and wall.

In Fig. 12.21, the same, particular kinematic noticed in the first test can be observed again, which causes a wider joint opening at the left side of the wall where a greater rotation is permitted. Note that the residual displacement at zero load is essentially the same in tests 1 and 3 or rather, in those cases where the wall can exhibit a flexural mechanism to oppose the out-of-plane forces. It should be noted that the subsequent load cycles show decreasing force values and a progressive stiff-

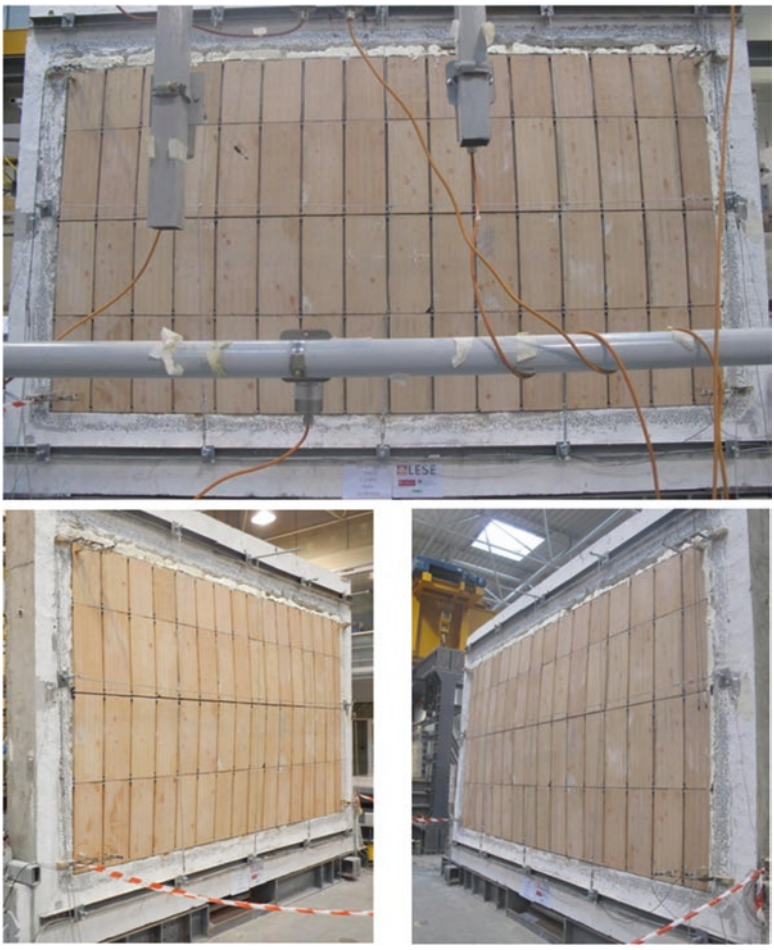

Fig. 12.11 Deformation of the infill at 30 mm displacement of control point 8 during test 1

ness decay. It is probable that this kind of behavior is due to the constraints' efficacy, which provides the wall the capacity to undergo reversible displacements without a non-linear mechanism such as sliding.

12.6.2 Effect of Temperature on Plastic Behavior

In order to study the mechanical behavior of recycled plastic joints and strips under different temperatures, some tests were conducted in a specialized and certified laboratory in Rome. It is known that the plastic strips act as a confinement net, resisting the out-of-plane overturning. It is clear that the variation of external

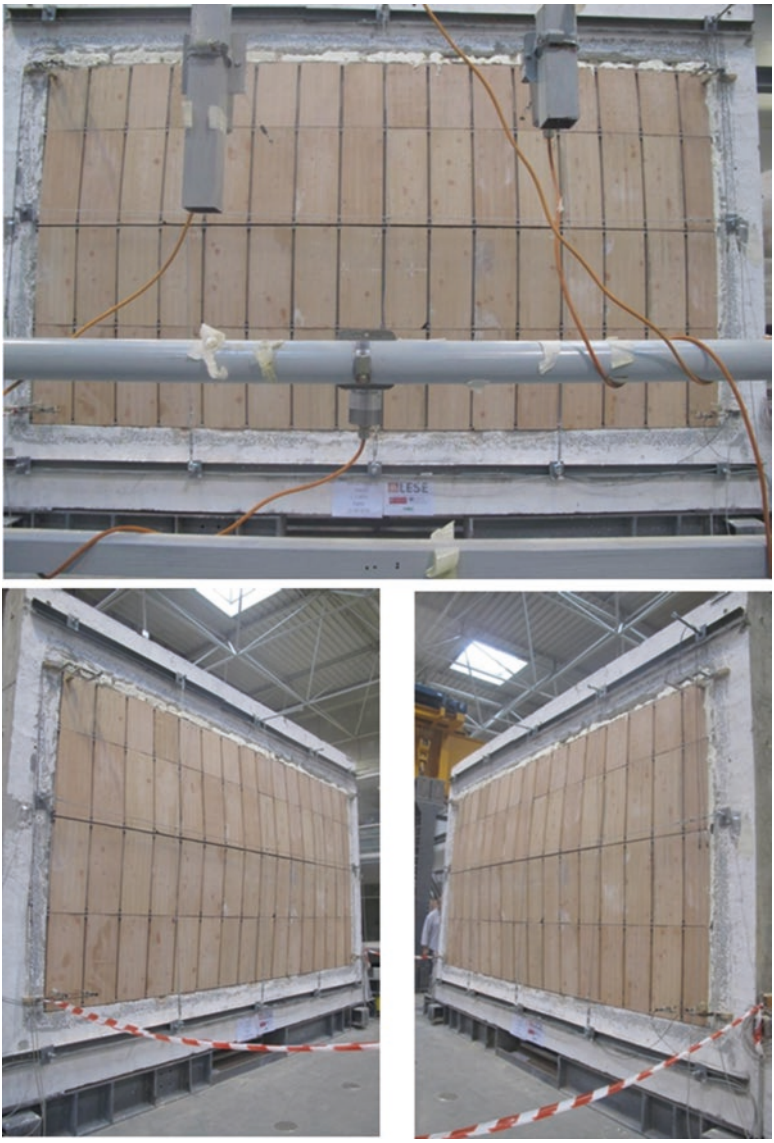

Fig. 12.12 Deformation of the infill at 60 mm displacement of control point 8 during test 1

temperature, due to a fire or seasonal thermal excursions for example, can modify the performance of the wall, decreasing the stiffness and resistance and causing instability. The in-plane mechanism is not affected. Therefore, only tensile strength tests on the plastic strips were performed in different temperature conditions as listed in Table 12.2. Table 12.3 shows the results in terms of ultimate force and displacement obtained in the tests shown in Figs. 12.22, 12.23 and 12.24.

Fig. 12.13 Test 1, point 3. Residual deformation of the infill at zero pressure in the airbags

The results gave important information on the design values of the parameters. The following deformations at F_{max} of specimen 1 in temperature condition 1 were observed: (a) a variation of +5% for specimen 2 in condition 2, (b) a variation of −13% for specimen 3 in condition 2, and (c) a variation of +43% for specimen 4 in condition 3. These results can be summarized as:

1. normal conditions: the design values should be an average of the experimental values observed on specimens 2 and 3 in condition 2;
2. exceptional conditions: the design values should be equal to the experimental values observed on specimen 4 in condition 3.

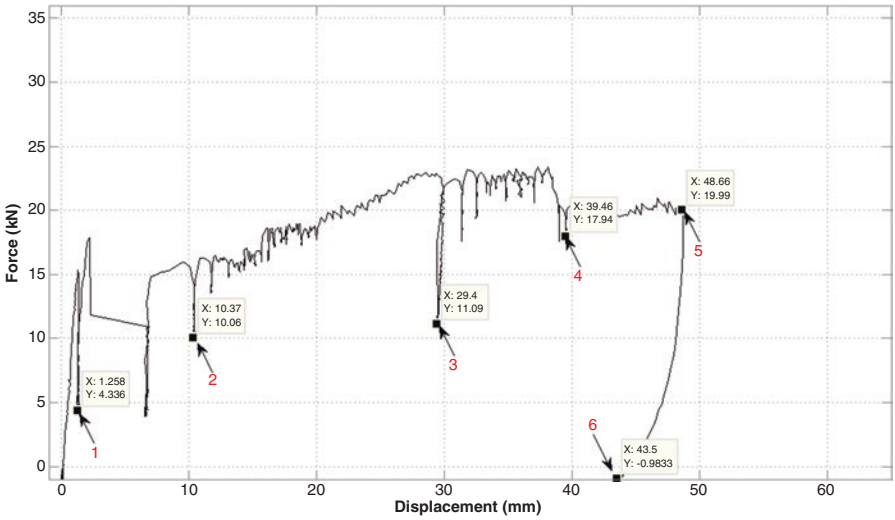

Fig. 12.14 Test 2. Force/displacement relationship of the second tested wall. The points represents: *1*, *2* and *3*. The considerable sliding at the bottom of the infill; *4*, the extension of sliding along the vertical contact surface column/infill; *5*, displacement beyond which the infill can go out from the frame suddenly

Fig. 12.15 Test 2, Deformation of the infill at ~2 mm displacement of control point 8

Fig. 12.16 Test 2, point 2. Deformation of the infill at ~10 mm of displacement of control point 8

Fig. 12.17 Test 2, point 3. Deformation of the infill at ~30 mm of displacement of control point 8

Fig. 12.18 Test 2, point 4. Deformation of the infill at ~40 mm of displacement of control point 8

Fig. 12.19 Test 2, point 5. Deformation of the infill at ~50 mm of displacement of control point 8

If, in some exceptional cases, the design strength values are not sufficient to meet deformation limitations, alternative solutions can be used, for example by using fireproof plaster.

12.7 Acoustic and Thermal Aspects

The European Directive 2002/91/EC requires that member states use energy in a rational manner through energy savings (heat loss reduction in cold periods) and development of renewable sources, all taking into account the thermal comfort of the occupants when designing heating, cooling and ventilation systems. The main

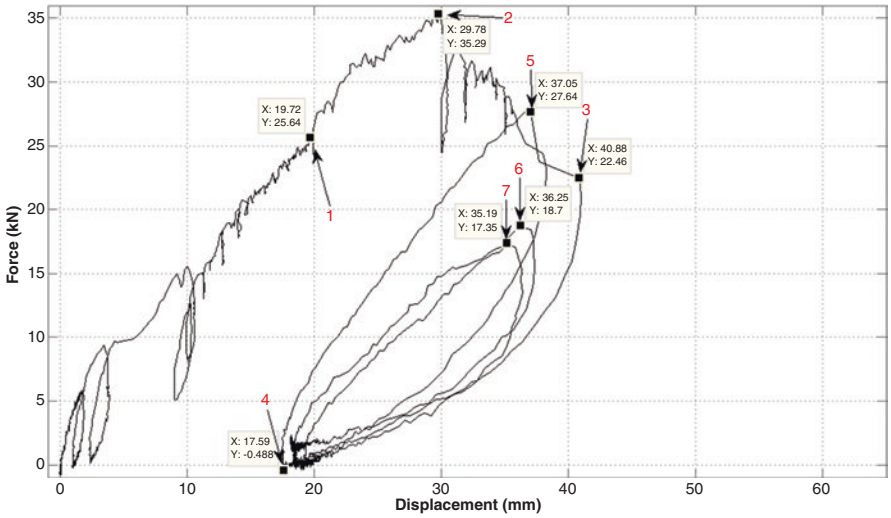

Fig. 12.20 Test 3. Force/displacement relationship of third tested wall

calculations to assess the energy efficiency of the buildings are performed in both steady-state and dynamic-stabilized conditions. The energy performance index (EPI) in kWh/m^2 per year (or kW/m^3 per year for non-residential functions) and the thermal transmittance limits are used in the first case. The EPI takes into account the ratio between the energy needed to keep a room at a temperature of 18 °C and its gross floor area or volume. Moreover, the equation to calculate the thermal steady transmittance is provided by UNI EN ISO 6946. For monolayer walls, it is as follows:

$$U = \frac{1}{\frac{1}{\alpha_i} + \frac{s}{\lambda} + \frac{1}{\alpha_e}} \tag{12.1}$$

where U is in [Kcal/hm^2°C or W/m^{2}K]; α_i is internal adduction coefficient, which represents the amount of heat transferred from internal air for unit area of wall and degree of temperature difference (Kcal/m^2 h°C); α_e is the external adduction coefficient, which represents the amount of heat transferred from external air for unit area of wall and degree of temperature difference (Kcal/m^2 h°C); s is the wall thickness; and λ is the material conductivity (Kcal/h m °C), with s/λ being the inverse of the wall conductance.

For multilayer walls, it is needed to add the laminar resistances and the layer resistances, in series:

$$R = \frac{1}{K} = \frac{1}{\alpha_i} + \sum_i \frac{s_i}{\lambda_i} + \frac{1}{\alpha_e} \tag{12.2}$$

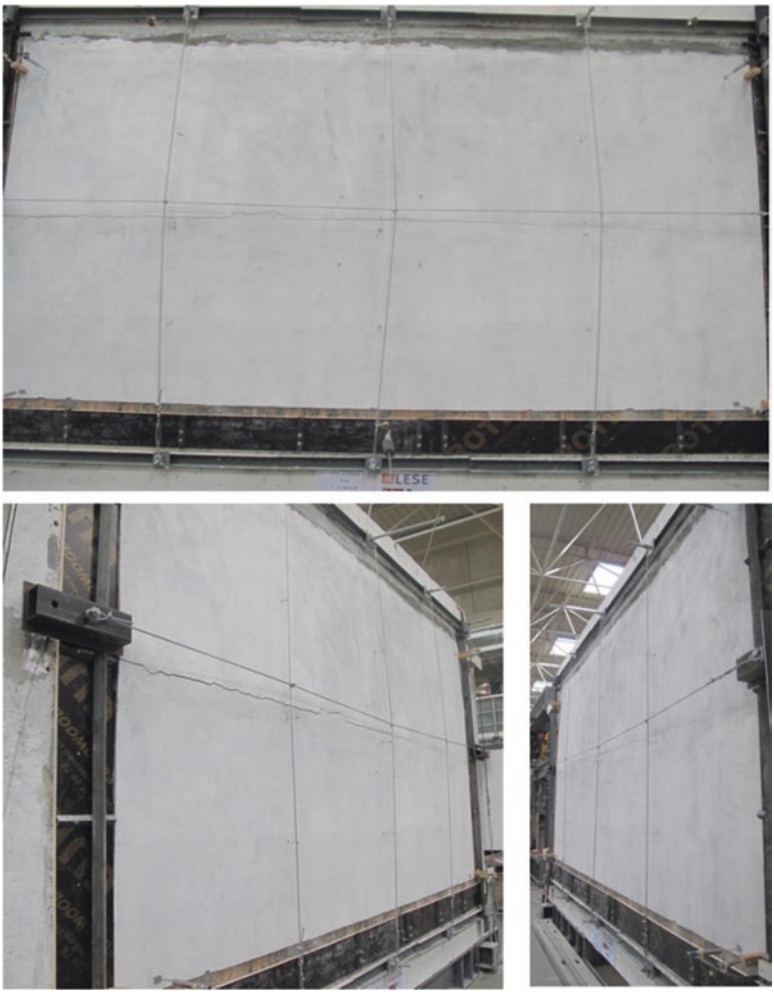

Fig. 12.21 Test 3, deformation of the infill at ~40 mm of displacement of control point 8

Table 12.2 Tensile strength tests of plastic strips

Number of specimens	Condition	Operating method
1	1	+20°
2	2	Thermal load cycles between −20° and +20° for 1 week
1	3	+50° for 12 h

Table 12.3 Results of tensile strength tests

N°	Test type	Yield stress (N/mm^2)	Failure stress (N/mm^2)	Def. at F_{max} %	Failure def. %
1	+20°	15.3	16.8	2.34	2.39
2	Thermal load cycles	13.9	16.6	2.45	2.49
3	Thermal load cycles	14.0	15.7	2.04	2.24
4	+50°	13.4	16.1	3.35	3.48

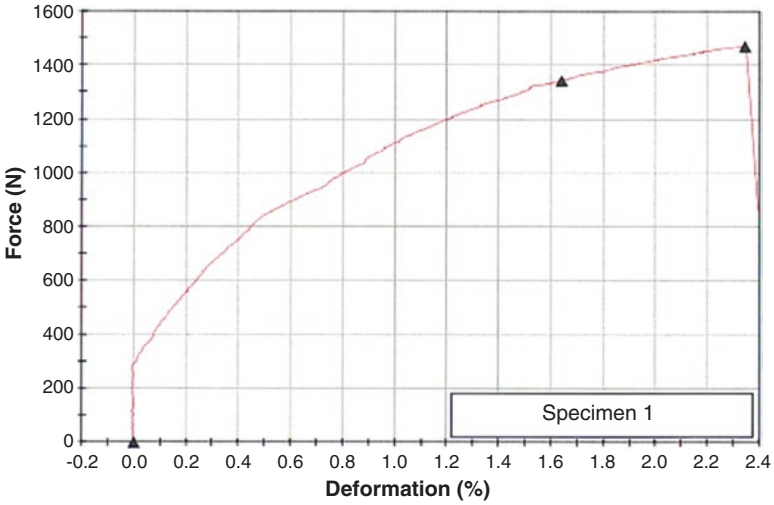

Fig. 12.22 Tensile strength test of specimen 1 in condition 1

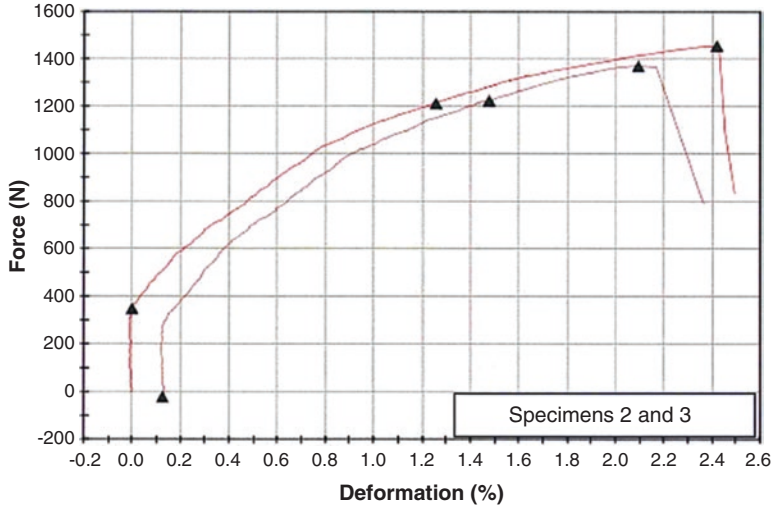

Fig. 12.23 Tensile strength test of specimens 2 and 3 in condition 2

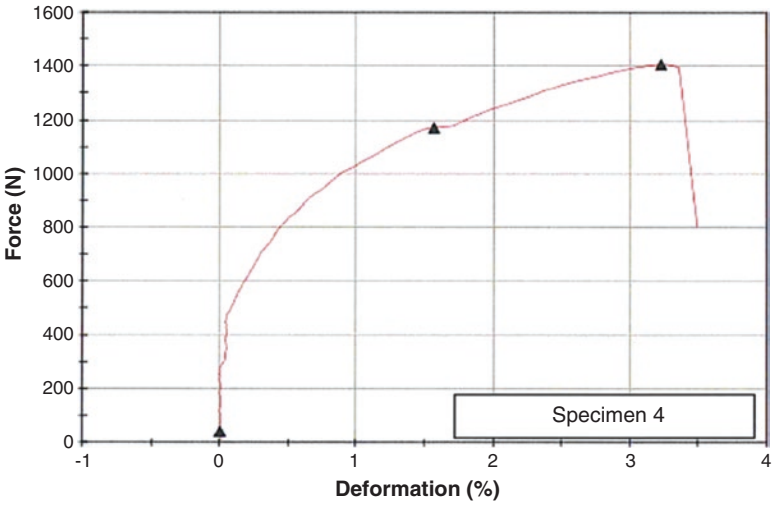

Fig. 12.24 Tensile strength test of specimen 4 in condition 3

where R is in [hm^2°C/Kcal] or [m^{2}K/W]. Thermal conductivity, which appears in the above equations, and frontal mass are the other aspects to assess.

In the second case, during the cooling period, periodic thermal transmittance, softening factor, thermal wave shift factor and the internal surface thermal capacity have to be evaluated, mainly to reduce the sunlight heat input using screening devices for the openings. One of the following requirements has to be satisfied to ensure the verification of the walls: the surface mass of vertical walls has to be greater than 230 kg/m^2, while the periodic thermal transmittance should be less than 0.10 W/m^2 K and less than 0.18 W/m^2 K for horizontal and inclined opaque walls. Thermal inertia is the essential aspect to be considered because it represents the ability of the wall to reduce the effect of dynamic stresses on heat load of internal rooms; this way, a higher softening factor and thermal wave phase shift are provided. First of all, the dynamic thermal transmittance is computed. According to the UNI EN ISO 6946, it is defined as the ratio between thermal flow on the internal side of the wall and temperature on its external side, with internal temperature assumed constant [W/m^{2}K]:

$$U_{dyn} = -\left(\frac{\hat{\Phi}_i}{\hat{\theta}_e}\right)_{\vartheta_i = 0} = -\frac{1}{Z_{12}} \tag{12.3}$$

The thermal flow is, in turn, computed as follows:

$$\Phi = U \cdot \left(\theta_{ave} - \theta_{int}\right) + \mu h_i \cdot \left(\theta_{max} - \theta_{ave}\right) \cdot \cos\left(\omega t + \varphi\right) \tag{12.4}$$

where U is the dynamic thermal transmittance of the structure (W/m^2 K); θ_{ave} is the average external temperature (°C); θ_{int} is the internal temperature (°C); μ is the softening factor, i.e., the temperature variation at a certain depth of the wall compared with the external temperature variation; h_i is the internal adduction coefficient; θ_{max} is the maximum internal temperature (°C); ω is the thermal diffusivity λ/(cρ) (m^2/s); and φ is the time shift. Once the quantities above are evaluated, the thermal wave shift and the softening factor can be calculated. The first one is measured in hours [h] and computed as follows:

$$\Delta t_{12} = \frac{T}{2\pi} \arg\left(Y_{12} \right) \tag{12.5}$$

where arg is the argument of the function, evaluated between -2π and 0 (interval of time that passes from the maximum of temperature variation to the maximum of heat flow variation) and T is the period of sinusoidal variation. The softening factor is, instead, the ratio between the thermal periodic transmittance (Y_{12}) and thermal transmittance (U).

$$\mu = \frac{U_{dyn}}{U} = \frac{\left| Y_{12} \right|}{U} \tag{12.6}$$

If the value of this factor is equal to 1, the wall has no heat storage capacity. Another important aspect to take into account when designing the stratigraphy of infills is the position of the insulation panel with respect to the clay blocks, as shown in Fig. 12.25. In fact, it is clear that the thermal performance of single-and-double layer infills are strongly influenced by its position inside the wall. From the acoustic point of view, the reference is the Italian law n. 447 of October 26, 1995 that provides "*Fundamental principles governing the protection of external and living environments from noise pollution*." One important decree used to determine the acoustic requirements of the buildings is the DPCM from December 15, 1997. Here, the descriptor to assess the apparent sound reduction of vertical infills, R'_w, can be estimated. It is possible to measure it once the construction is complete. Alternatively, tests in laboratories could be performed, or mathematical algorithms can be used, to evaluate the descriptor, R_w. The technical code UNI EN 12354 and technical report TR UNI 11175 are used to design passive requirements of buildings. The last one proposes a simplified calculation method according to technology widespread in Italy to evaluate the R_w index, but it is not sufficiently reliable, especially for the assessment of infills made with clay blocks. The minimum value that both internal partitions and floors have to ensure varies as a function of the intended use of the rooms. In residences, walls and floors that separate different units must have values equal to or greater than 50 dB. To avoid the decrease of acoustic insulation, particular attention has to be paid to the choice of material and to the state of the partition; cracks or discontinuities, bricks with large hole ratios or the presence of glass surfaces might worsen its performance.

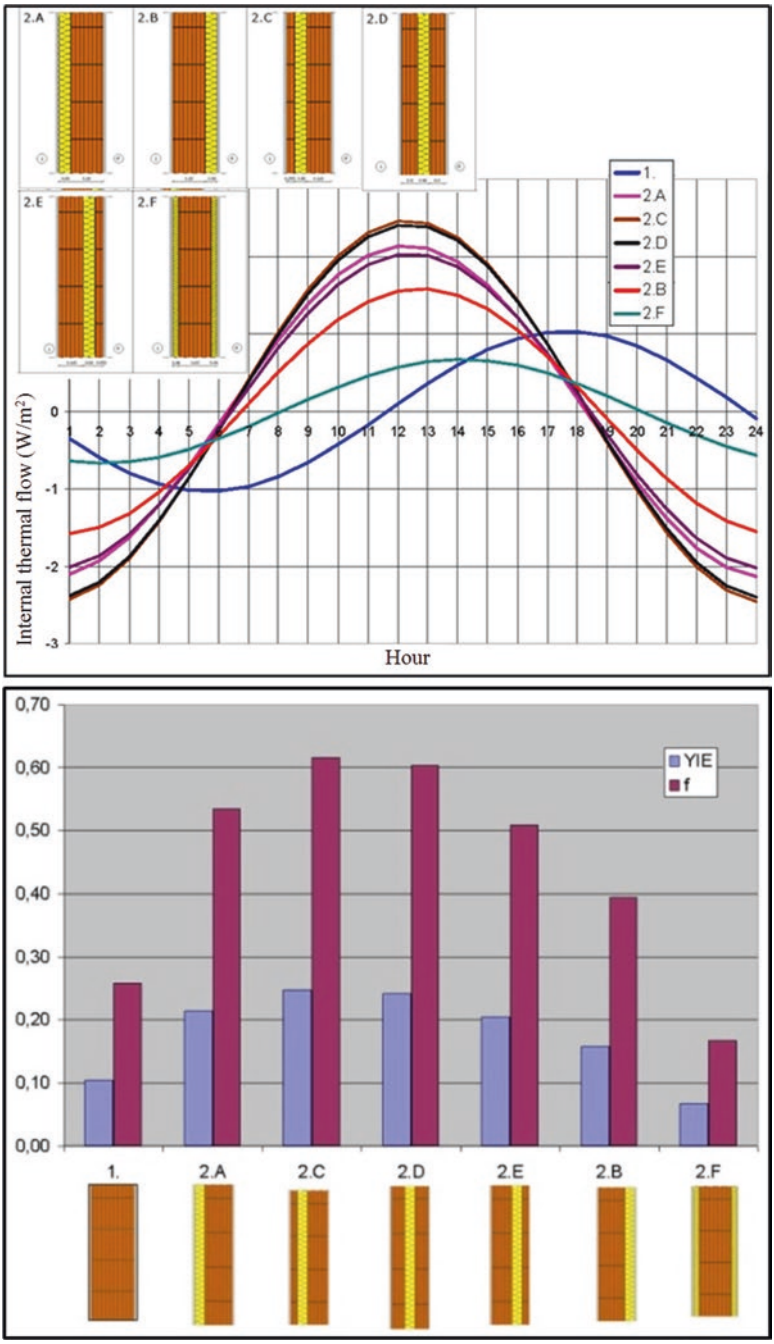

Fig. 12.25 Thermal performance of infills. At the top, the thermal wave shift during the 24 h. At the bottom, the periodic thermal transmittance Y_{IE} and the softening factor f

In these diagrams are represented the thermal wave shift, the periodic thermal transmittance and the softening factor, three important parameters that can help in chosing the best solution for the assigned environmental condition.

As a general principle, the best performance in terms of thermal wave shift can be obtained using the wall with high weight, in other words, with high thermal inertia. The best results in terms of the two last parameters are related to the double-layer infills where the isolation panel is disposed toward the outer side (solution 2.c in Fig. 12.25).

12.8 Proposals for Stratigraphy

To make the innovative solution flexible and adaptable to different needs, four different stratigraphies are proposed hereby and shown in Table 12.4. The choice of materials and thicknesses are dictated by the above-mentioned thermo-acoustic requirements (Fig. 12.26).

In Table 12.5, the parameters used to describe the performance of the different proposed stratigraphies are shown; each of them fulfills the mandatory requirements of the codes, allowing the designer to meet the needs of the customer, also consider-

Table 12.4 The different proposed stratigraphies (thickness in parenthesis)

	b_1 (340)	b_2 (326)	b_3 (340)
1	Lime and gypsum plaster (20)	Fermacell panel (13)	Lime and gypsum plaster (20)
2	Hollow flat blocks (100)	Hollow flat blocks (100)	Hollow flat block (100)
3	FiberTherm panel (100)	FiberTherm panel (100)	EPS panel (100)
4	Kraft paper (0.025)	Kraft paper (0.025)	Kraft paper (0.025)
5	Hollow flat blocks (100)	Hollow flat blocks (100)	Hollow flat blocks (100)
6	Lime and cement plaster (20)	Fermacell panel (13)	Lime and cement plaster (20)

Fig. 12.26 Section view of the different proposed stratigraphies

Table 12.5 Thermo-acoustic efficiency parameters of the above considered stratigraphies

	Thermal transm. [W/m² K]	Frontal mass [kg/m²]	Periodic thermal transm. [W/m² K]	Soft. Factor [adim]	Thermal wave shift [hours]	Int. surface thermal capacity [kJ/m² K]	R_w [dB]
b_1	0.29	212.1	0.10	0.35	11.43	57.1	46.82
b_2	0.29	158.0	0.10	0.37	11.5	43.1	45.12
b_3	0.19	145.6	0.10	0.56	7.56	44.3	46.37

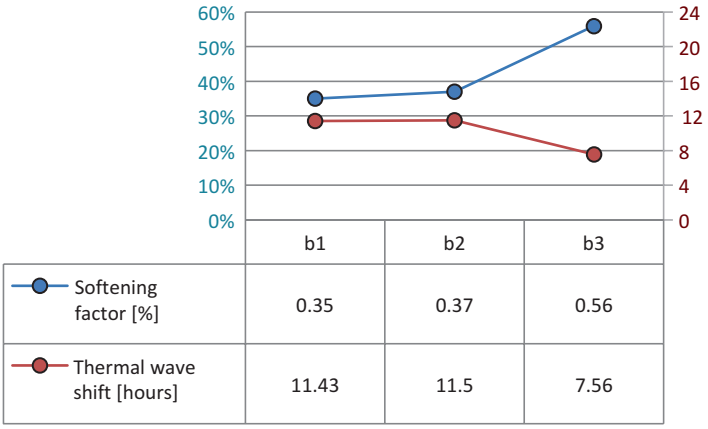

Fig. 12.27 Thermal efficiency comparison among different proposed stratigraphies

Table 12.6 Classification of thermal performance

Thermal wave shift [hours]	Soft. factor [adim]	Classification of performances –
$S > 12$	$f < 0.15$	Excellent
$12 \geq S > 10$	$0.15 \leq f < 0.30$	Good
$10 \geq S > 8$	$0.30 \leq f < 0.40$	Average
$8 \geq S > 6$	$0.40 \leq f < 0.60$	Sufficient
$6 \geq S$	$0.60 \leq f$	Middling

ing the place where the technology is employed. The comparison shown in Fig. 12.27 is particularly effective in identifying the best solution. This diagram shows the performances of the solutions shown in Fig. 12.26. High values of thermal wave shift mean that the infill has good thermal inertia, i.e., the infill changes its temperature slowly during 24 h. This means keeping cool the interior habitat in the summer. In order to the assign values assumed for these parameters, a classification such as that of Table 12.6 can be defined.

When the values of the parameters are not in the interval given to the same line, for the purpose of classification, priority is given to the thermal wave shift parameter.

12.9 Comparison with Traditional Infills

The advantages of the proposed technology are listed below.

1. Exceptional capacity under seismic events, (capacity to sustain interstory drift over 10% of floor height) thanks to the in-plan deformability achieved by means of the sliding joints;
2. Lower manufacturing time and cost, thanks to the dry installation;
3. Reversibility of the assembly process, so that the wall can be easily dismantled and reassembled in another place, limiting demolitions only to surface finishes;
4. Eco-environmental sustainability because the plastic is recycled. At the end of their life cycle, joints and bands can be used again for the production of new buildings; also, the bricks remain intact after disassembly and can be reused;
5. Excellent thermal performance, particularly during summertime in places where the irradiance $I > 290$ W/m^2, thanks to ventilation ducts that allow a natural, vertical air flow;
6. Less thermal bridges due to the absence of mortar joints;
7. Better structural behavior due to the absence of interactions with infills;
8. Rationalization of ducts and fixtures, so that channeling takes place in a clean manner inside the holes of the bricks, arranged vertically, thus avoiding the traces that often damage the integrity of the panels;
9. Considerable savings thanks to the reduced weight applied to the structural elements of the building including foundations (lower dead and inertia loads).

Moreover, the new technology differs from the traditional ones also in design considerations. Traditional systems are conceived as having a high mass (both in terms of thermal performances and from the structural point of view), strength and stiffness that significantly affect the overall behavior of the structural system under seismic shaking, modifying its natural oscillation period. Conversely, this innovative system aims at being lighter and more flexible, decreasing the inertial seismic forces applied to the centroid of the non-structural element, computed as follows:

$$F_a = \frac{S_a \cdot W_a}{q_a} \tag{12.7}$$

where F_a = horizontal seismic force applied to the centroid of the non-structural element in the most unfavorable direction; W_a = element weight; S_a = spectral acceleration, in terms of g; and q_a = behavior factor of the element.

In Italy, where structures are mainly built as reinforced concrete frames, infill panels with solid bricks were used until the 1960s. Subsequently, solid bricks have been replaced with clay blocks placed in monolayer walls or in a double layer with hollow space in between. Joints are made with either mortar or light mortar and horizontal joints have thicknesses varying from 5 to 15 mm. In Table 12.7, traditional stratigraphies are shown. In Table 12.8 and Figs. 12.28, 12.29, the comparison (using the main thermo-acoustic parameters provided by codes) among the

Table 12.7 Traditional stratigraphies (thickness in parenthesis)

	a (350)	c (310)
1	Lime and gypsum plaster (15)	Concrete (60)
2	Porotherm brick (250)	EPS panel (60)
3	XPS panel (70)	EPS panel + graphite (130)
4	Plastic plaster (15)	Concrete (60)

Table 12.8 Thermo-acoustic comparison among the traditional and innovative typologies

	Thermal transmittance [W/m^2 K]	Frontal mass [kg/m^2]	Periodic thermal transmittance [W/m^2 K]	Softening factor [adim]	Thermal wave shift [hours]	Int. surface thermal capacity [kJ/m^2 K]	R_w [dB]
a	0.31	267.1	0.04	0.14	11.56	46.4	44.3
b_1	0.29	212.1	0.10	0.35	11.43	57.1	46.8
b_2	0.29	158.0	0.10	0.37	11.5	43.1	45.1
b_3	0.19	145.6	0.10	0.56	7.56	44.3	46.3
c	0.17	298.6	0.07	0.41	9.28	80.6	47.4

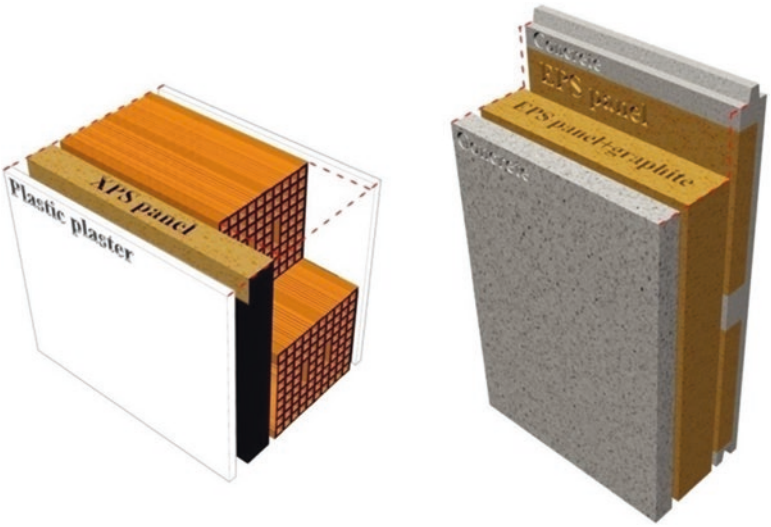

Fig. 12.28 Section view of the different traditional stratigraphies

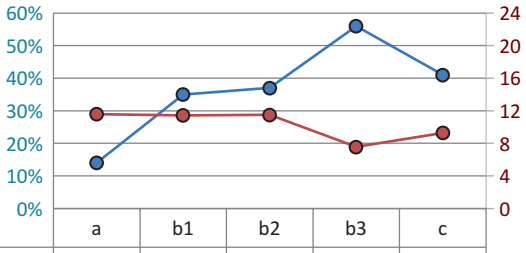

	a	b1	b2	b3	c
Softening factor [%]	0.14	0.35	0.37	0.56	0.41
Thermal wave shift [hours]	11.56	11.43	11.5	7.56	9.28

Fig. 12.29 Thermal efficiency comparison among considered typologies

stratigraphies proposed above and the widespread infill panel typology used in Italy is very effective to highlight advantages provided by the innovative solutions.

The comparison shown above relates to the calculation in dynamic stabilized conditions (summer season). In this case, the thermal inertia of the walls is the main aspect to be considered. The softening factor and thermal wave shift are physical quantities that well represent the performance of the walls in these conditions; low values of the first parameter match better solutions, while the opposite is true for the second one.

12.10 Results and Conclusions

Previous experimental tests (Vailati et al. 2014, 2015) have shown that the in-plane displacement safely sustained by the proposed infill technology is about double, the limit value imposed by the Italian code NTC-08. Furthermore, the displacement capacity in the out-of-plane test is higher than all other conventional systems and equal to 150 mm before collapse for upper constraint failure. In the second part of the tests, better performance of the infill panels was observed in terms of maximum resistance, due to, (a) better confinement effects from the frame and (b) better transmission of tangential forces provided by anchorages and polyurethane foam.

The effect of surface finish was studied and gave important insight into the behavior of the wall in ordinary conditions. In particular, it was observed that, in case of good constraints, the walls exhibit high performance for both resistance and deformation capacity up to a displacement of about 60 mm. When the perimeter constraints are not optimal, the wall still had exceptional performance in terms of deformation capacity but showed larger residual deformation.

The innovative system of dry infill panels also gives an important contribution in terms of energy dissipation, and future studies will allow this technology to advance.

Comparison with traditional infills shows that the proposed technology has much better performance. Traditional infills fail under a much lower acceleration than the infill walls proposed here.

As regards the effects of temperature on the plastic parts, the tests showed that two conditions must be considered in relation to the condition where the wall will work. In particular conditions and in the presence of fire, it is possible to resort to a particular solution of surface finish, such as fireproof plaster or panels.

The acoustic and thermal performance of the proposed infills are also found to be much better than those of traditional infills. The proposed infill with an EPS panel (Sintered Expanded Polystyrene) gives the higher value in terms of the softening factor, while the thermal wave shift is comparable to all others. Note that the periodic thermal transmittance is under the limit established by the rules for cases where the frontal mass is less than 230 kg/m^2.

In the final analysis, it can be stated that the proposed innovative system represents an effective solution for buildings following modern design concepts, investing lower financial resources and reducing the environmental impact.

Acknowledgments The authors thank the "Probe!" company of Rome for providing the specimens wall and dott. eng. André Furtado for the support and his experience during the execution of the tests. Moreover, the authors would like to wholeheartedly thank professors António Arêde and Humberto Varum of the University of Porto, Portugal, for allowing the use of the Laboratory of the Faculty of Engineering, where tests have been performed.

References

Kibert CJ (2013) Sustainable constructions, green building design and delivery. Wiley, Hoboken

Vailati M, Monti G (2014) Recycled-plastic joints for earthquake resistant infill panels. In: Proceedings of the 2nd European conference on earthquake engineering and seismology, Istanbul

Vailati M, Monti G (2016) Earthquake-resistant and thermo-insulating infill panel with recycled-plastic joints. In: D'Amico S (ed) Earthquakes and their impact on society. Springer Natural Hazard, DOI 10.1007/978-3-319-21753-6_16. Springer, Cham, pp 417–432

Vailati M, Caluisi A, Monti G (2014) Environmentally friendly joints for seismic resistant infill panels. In: Proceedings of the AICAP-2014. Structures in the Urban Environment, Bergamo

Vailati M, Monti G, Di Gangi G (2015) Multi-performance innovative infill panels. In: Proceedings of the 2nd international symposium on advances in civil and infrastructure engineering. Vietrisul mare, Salerno, 2015

Part II
Structural Dynamics of Special Bridges

Chapter 13
Full-Scale Measurement and Analysis of Wind-Induced Vibrations of a Longs-Span Suspension Bridge in Complex Terrain

Aksel Fenerci and Ole Øiseth

Abstract Long-term monitoring data of bridge deck accelerations and wind velocities from the Hardanger Bridge were used here to investigate the relationship between the wind characteristics and the bridge response. The bridge, as well as the extensive monitoring system installed on it, is introduced. The wind velocities and bridge deck accelerations were recorded on several locations along the bridge span using 20 accelerometers and 9 anemometers. The lateral, vertical and torsional accelerations of the bridge deck are presented in the form of buffeting curves. Response surface methodology (RSM) was employed to elaborate on the significant variability observed in response components. Using wind field statistics as predictor variables in the analyses, the variability in response was attributed to the variability in the wind field. The effect of wind-related variables on the response and their interactions are presented using surface plots.

Keywords Suspension bridge • Bridge monitoring • Wind characteristics • Response surface methodology

13.1 Introduction

The coastal highway, E39, lies on the west coast of Norway between the cities of Kristiansand and Trondheim. The highway is of great importance to Norway, since the majority of Norway's export is generated by the industry established along the route. As a consequence of the unique and challenging topography of the Norwegian fjords, currently 8 ferries operate along the highway. Elimination of the ferry connections is greatly desired due to possible economic benefits. For this reason, the

A. Fenerci (✉) • O. Øiseth
Department of Structural Engineering, Norwegian University of Science and Technology, Trondheim, Norway
e-mail: aksel.fenerci@ntnu.no

R. Rupakhety, S. Ólafsson (eds.), *Earthquake Engineering and Structural Dynamics in Memory of Ragnar Sigbjörnsson*, Geotechnical, Geological and Earthquake Engineering 44, https://doi.org/10.1007/978-3-319-62099-2_13

Norwegian Public Roads Administration (NPRA) is currently investigating the feasibility of replacing the ferry connections with road transportation, which requires crossing of fjords up to 4 km wide where the seabed is often too deep. This presents many technological challenges to the bridge engineers, one of which being the wind-resistant design of such slender and wind-prone structures.

Reliable design of long-span suspension bridges requires accurate prediction of wind-induced response, which hinges on the description of the gust loading. The stochastic theory for buffeting was introduced to bridge engineering by Davenport (1962) for the first time, and it has been used and improved extensively ever since. In the frequency domain, the wind loading is usually described in terms of a cross-spectral density matrix of turbulence (Simiu and Scanlan 1996; Solari and Piccardo 2001), which contains the spatial and temporal properties of the turbulent wind field. In the current literature, both theoretical and empirical models for wind turbulence spectra exist (Kaimal et al. 1972; von Karman 1948; Larsen and Larose 2015; Xu and Zhu 2005). The models require basic wind statistics such as turbulence intensities or integral length scales as input parameters. In complex terrain, the wind field is expected to be variable due to complex upwind conditions. This variability is often overlooked in response prediction and design, which might cause safety concerns under strong wind loading. To that extent, the variability in the wind-induced vibration of the Hardanger Bridge, as well as its relationship with the wind field statistics, is studied here using long-term monitoring data. The bridge dynamic response and wind field statistics are presented for a 3-year measurement period. Attributing the variability in response to the variable wind field, the wind-related parameters influencing the response are identified using response surface methodology. The effects of the significant parameters are then presented in the form of scatter and surface plots.

13.2 Monitoring the Hardanger Bridge

The Hardanger Bridge (Fig. 13.1) is currently the longest suspension bridge (main span is 1310 m) in Norway. The bridge spans the Hardangerfjord in Hordaland county in Norway and reduces the travel time between Bergen and Oslo. The cross-section of the bridge deck is shown in Fig. 13.2. It is a streamlined box girder, 18.5 m wide and 3.2 m high. Underneath the deck, vortex mitigation devices were installed. The local topography of the bridge site is also shown in Fig. 13.2. The bridge is located at a narrow strait, and it is surrounded by high mountains from the north and the south.

The accelerations and wind velocities on several locations at the Hardanger Bridge have been monitored since 2013. An extensive, state-of-the art measurement system was designed and installed on the bridge soon after the construction had finished. The monitoring system consists of 20 accelerometers and 9 anemometers in total. The sensor layout is shown in Fig. 13.2. The anemometers are attached to the hangers of the bridge at a height of 8 m above the girder. The accelerometers are

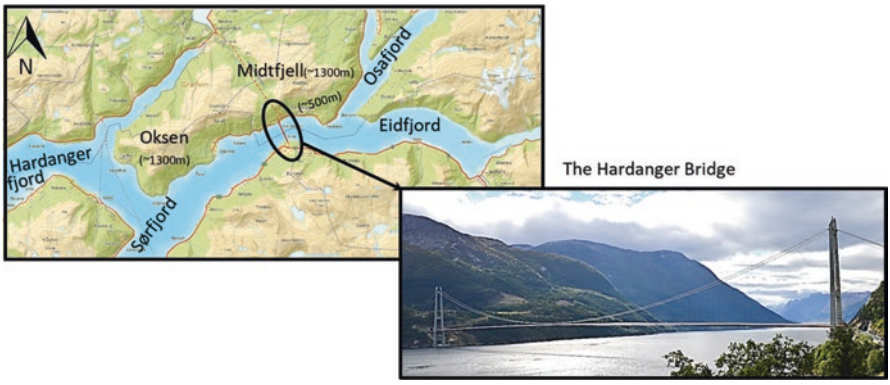

Fig. 13.1 The Hardanger Bridge

located inside the box girder and installed as pairs, one on each side of the girder. The data are initially logged locally by 10 data-logger units distributed inside the deck. Then, by means of wireless sensors, the data from different sensors are collected in a common logger unit, and from there, it is transferred to the servers at the Norwegian University of Science and Technology. The data presented here were recorded in a discontinuous manner between December 2013 and March 2016. The measurement system was triggered and recorded data for 30 m when a wind speed of 15 m/s was exceeded in any of the wind sensors. The system was also triggered manually in a random manner to include recordings with lower wind speeds.

13.3 Wind-Induced Vibrations of the Deck

The acceleration response of the Hardanger Bridge was measured using 20 accelerometers installed inside the bridge deck (Fig. 13.2). The accelerations of the deck were sampled with 200 Hz in three orthogonal directions, which were aligned with the bridge longitudinal, vertical and transverse axes. The data were then down sampled to 20 Hz to reduce the computational burden, assuming that the higher frequency response is irrelevant to the current study. Furthermore, to remove the contribution from vibrations induced by traffic and other sources, a low-pass filter was applied to the acceleration data with a cut-off frequency of 1 Hz (Brownjohn et al. 1994, 2010). The data from the accelerometer pair at the midspan were used to study the acceleration response of the bridge deck. The lateral and vertical acceleration responses were calculated by taking the average of the signals from two sensors, whereas the torsional acceleration response was calculated by dividing the average of the vertical acceleration signals from the two sensors by the width of the bridge deck. Sample time series and spectral densities of turbulence components are given in Figs. 13.3 and 13.4, respectively. The spectral densities were estimated using the Welch spectral estimation method with 8 segments and a 50% overlap.

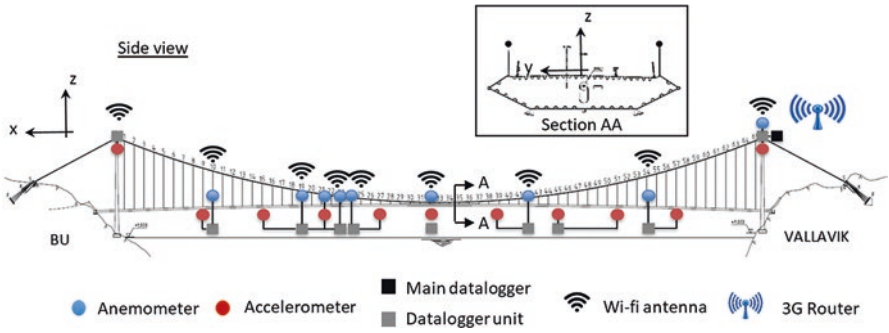

Fig. 13.2 The monitoring system

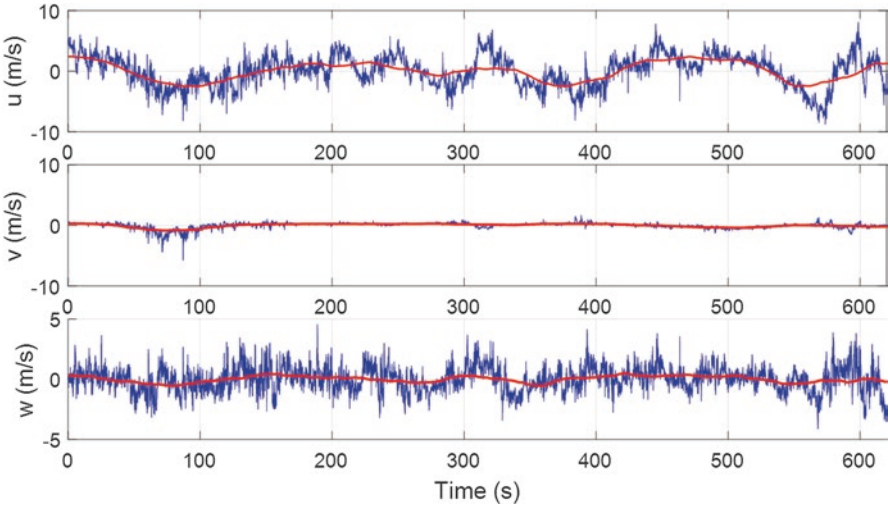

Fig. 13.3 Sample 10-min recordings of turbulence components recorded on 10/01/2015 at 15.20: (**a**) along-wind, (**b**) cross-wind and (**c**) vertical turbulence

Similarly, the time series and spectral density estimates of the lateral, vertical and torsional response components are presented in Figs. 13.5 and 13.6 using the same 10-min recording and data from the accelerometer pair at the midspan. It is seen that the lateral and the torsional responses were dominated by the fundamental modes, whereas multiple modes contributed to the vertical response, which is commonly observed in the case of the Hardanger Bridge. The acceleration measurements on the Hardanger Bridge were previously used by Øiseth et al. (2015) to estimate the natural vibration frequencies and corresponding modal damping ratios of the bridge in an operational modal analysis (OMA) framework. The study showed that the first symmetric horizontal and vertical natural frequencies of the bridge were 0.05 Hz and 0.14 Hz respectively, while the first symmetric vertical natural frequency was found to be at 0.37 Hz.

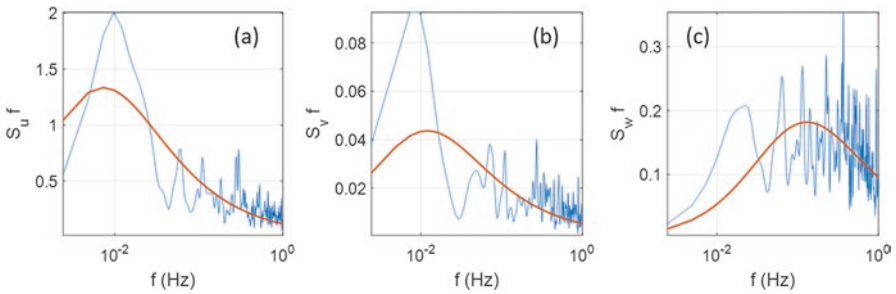

Fig. 13.4 Spectral density of turbulence components from time-series recorded on 10/01/2015 at 15:20 (the smooth line was obtained by a parametric least squares fit to the measured data): (**a**) along-wind, (**b**) cross-wind and (**c**) vertical turbulence

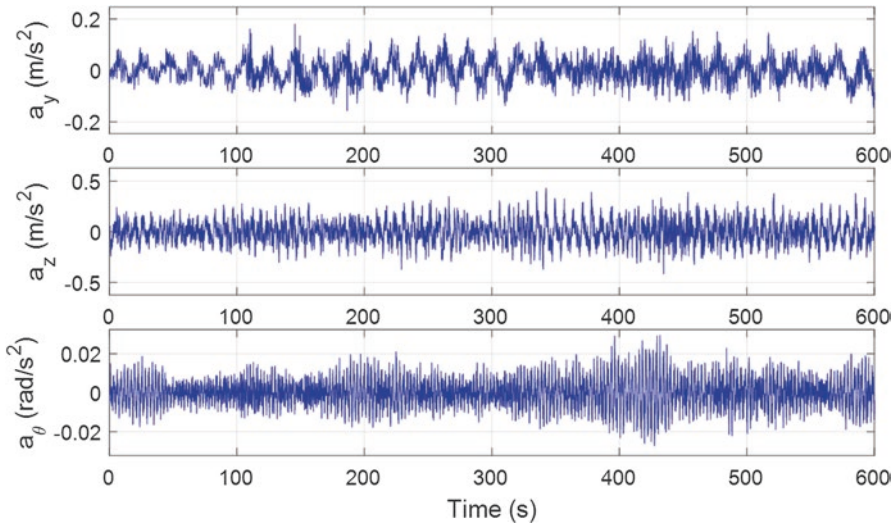

Fig. 13.5 Sample 10-min time series of acceleration components recorded on 10/01/2015 at 15:20: (**a**) lateral, (**b**) vertical and (**c**) torsional response

The root mean square (RMS) acceleration responses in three orthogonal axes were then calculated for 10-min intervals to be compatible with the wind records by taking the standard deviations of the zero-mean acceleration signals. The transient part of the signals mainly induced by the overflowing traffic is removed by the low-pass filter, to a reasonable extent. The lateral, vertical and torsional RMS acceleration responses are presented in Fig. 13.7 against the mean wind speed averaged over the same 10-min interval as used in the wind characteristics calculations. In the figure, σ_y, σ_z and σ_θ denote the lateral, vertical and torsional RMS responses respectively, and I_u and I_w are the along-wind and vertical turbulence intensities. The plots are also color-coded according to the wind directions, namely the easterly and westerly winds. For all response components, a great deal of variability is observed in

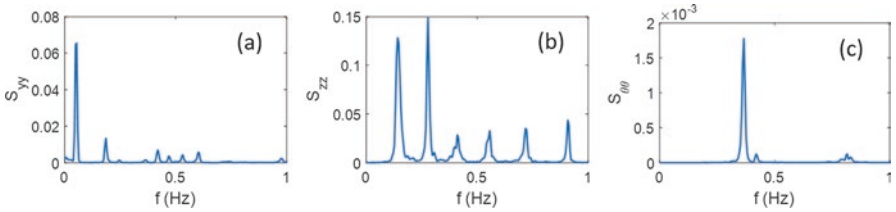

Fig. 13.6 Acceleration spectral density from time-series recorded on 10/01/2015 at 15.20: (**a**) lateral, (**b**) vertical and (**c**) torsional response

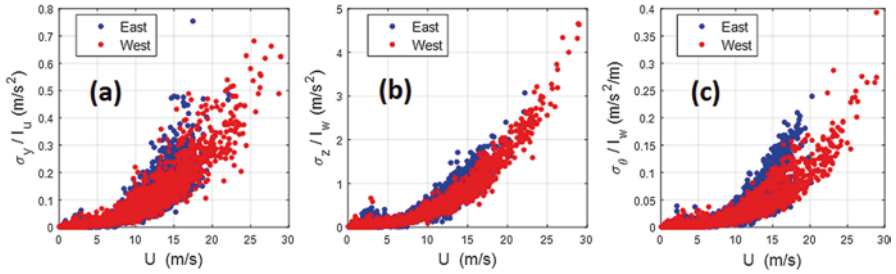

Fig. 13.7 RMS acceleration vs. mean wind speed normalized with turbulence intensity: (**a**) lateral, (**b**) vertical, and (**c**) torsional responses

the response. In general, the largest lateral and vertical responses were measured when the wind speed and the turbulence intensity were relatively high. However, the response process is seemingly rather complex to be explained by only considering the mean wind speed and a single turbulence component. The lateral response component, for instance, shows large scatter for all turbulence intensity ranges, and the scatter apparently increases with the increasing mean wind speed. The vertical response perhaps shows the most orderly behaviour among the three components. It is possible to attribute part of the variability to the vertical turbulence intensity. The torsional response, on the other hand, showed peculiar behaviour, especially for the wind speeds between 10 and 20 m/s. This velocity range accommodates severe variability in response as can be seen in Fig. 13.7. This can be partially attributed to the wind direction. Figure 13.7 shows that the torsional response demonstrates two distinct patterns for the winds from the easterly and westerly directions. The above findings reflect the complexity of the response processes, where the sources of the variability remain to be investigated. Here, the focus will be given to the effect of certain wind field parameters. Some of the other factors contributing to the variability can be listed, such as the temperature changes, upwind terrain roughness, presence of traffic, cable-vibrations, non-stationarity of the wind records, etc.

13.4 Wind Field Characteristics

13.4.1 Mean Wind Speed and Turbulence Intensity

The mean wind speed was calculated using the data from the wind sensor at the midspan of the bridge for all 10-min recordings. A threshold value of 3 m/s was used to filter the recordings, meaning that the recordings with mean speeds smaller than the threshold speed were discarded. A wind rose diagram of the mean wind speed is shown in Fig. 13.8a. In the figure, the 0° direction shows the bridge longitudinal axis where the north is also indicated. Strong winds, mainly perpendicular to the bridge axis, are observed. The wind field is bounded by the mountains from the north and the south. Easterly winds up to 18 m/s and westerly winds up to 30 m/s were measured.

The turbulence intensity for the along-wind (u), cross-wind (v) and vertical (w) turbulence components can be written as (Simiu and Scanlan, 1996):

$$I_u = \frac{\sigma_u}{U}, I_v = \frac{\sigma_v}{U}, I_w = \frac{\sigma_w}{U} \tag{13.1}$$

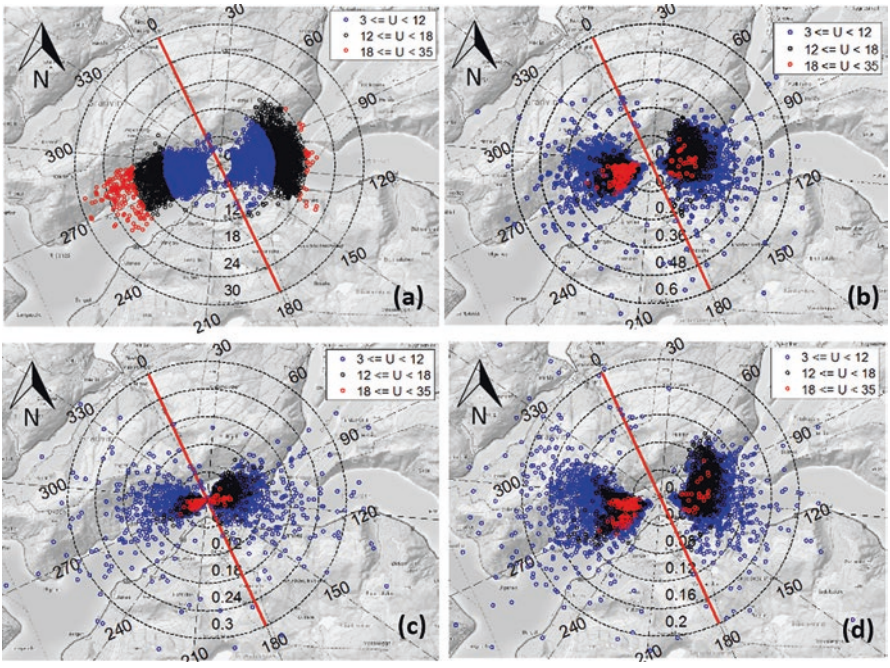

Fig. 13.8 Wind Rose plots: (**a**) 10-min mean wind velocity (m/s), (**b**) along-wind turbulence intensity, (**c**) cross-wind turbulence intensity and (**d**) vertical turbulence intensity

where $\sigma_{u,v,w}$ denote, the standard deviation of turbulence components. The turbulence intensities were calculated for all recordings using the same threshold wind speed value of 3 m/s. Wind roses of the along-wind, cross-wind and vertical turbulence intensities are shown in Fig. 13.8 b–d. The results exhibit considerable variability, even for the strong winds. For wind speeds above 12 m/s, the along-wind turbulence intensity varies between 10–30%, where the turbulence intensity of other components varies between 0–15%.

13.4.2 Integral Length Scale

The integral length scales of turbulence provide information on the spectral content of the turbulence components. Although distinct nine-length scales are possible to define in practice, only the length scales of the u and w components in the along-wind direction will be considered here. Assuming that Taylor's hypothesis of frozen turbulence is valid, the length scales can be written as (Simiu and Scanlan 1996):

$$L_i = \frac{U}{\sigma_i^2}\int_0^\infty R_{ii}(\tau)\,d\tau, \quad i = u, w \tag{13.2}$$

where $R_{ii}(x)$ is the time auto-covariance function of turbulence.

The length scales were calculated for all recordings and are presented in Fig. 13.9 in the form of wind roses. The results show vast variability for westerly winds, where the influence of the topography can be more profoundly observed for the easterly winds. The winds travelling along the fjord had higher length scales. The winds from the 60°–90° region, on the other, had lower length scales due to the roughness change in the upwind terrain. In general, the longitudinal length scale was approximately 2–2.5 times the vertical length scale.

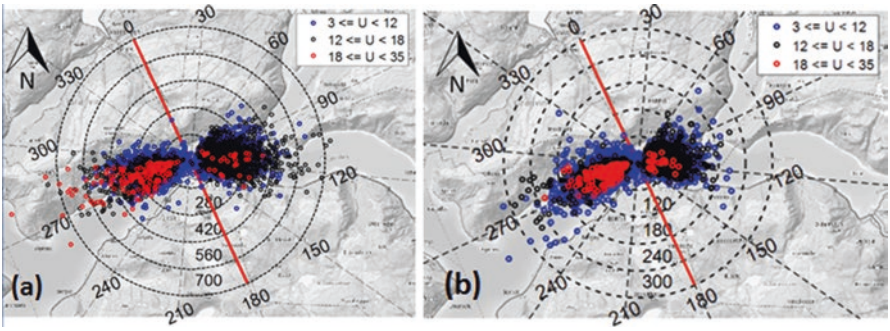

Fig. 13.9 Wind Rose plots of length scales in meters: (**a**) u component and (**b**) w component

13.5 Response Surface Analysis

The response curves given in Fig. 13.7 showed great variability in the wind-induced response of the Hardanger Bridge deck. The sources of this variability should be investigated further, since reliable design of future bridges, as well as reliability assessment of existing bridges, is only possible with accurate estimation of the true response. For this purpose, a statistical analysis was carried out using response surface methodology (RSM, Myers et al. 2009) to investigate the relationship between wind-related parameters and the dynamic response. The following parameters were selected to be included in the analyses:

- the mean wind speed (U, averaged over 10 min)
- the wind yaw angle (α_{yaw})
- the standard deviations of the turbulence components (σ_u, σ_v, σ_w)
- the covariance of the u and w components of turbulence (σ_{uw})
- the along-wind turbulence length scale (L_u)
- the vertical length scale (L_w)
- the vertical angle of attack (β)
- the standard deviation of the mean wind speed values measured at eight locations along the bridge (σ_{ms})

It was aimed to represent the inhomogeneity of the wind field with the last parameter in the above list. It should also be noted that the wind yaw angle (α_{yaw}) was used instead of the wind direction to represent the wind directionality effects. This was due to the fact that the relationship between the wind direction and response, which is shown in Fig. 13.10, is not suitable to be represented by a quadratic surface. Although the effect of topography cannot be represented by just using the yaw angle, its effect is already incorporated in the other parameters, such as turbulence intensities and length scales.

$$y = \beta_0 + \sum_{i=1}^{n}\left(\beta_i x_i + \sum_{j=i+1}^{n}\beta_{ij}x_i x_j + \beta_{ii}x_i^2\right) \tag{13.3}$$

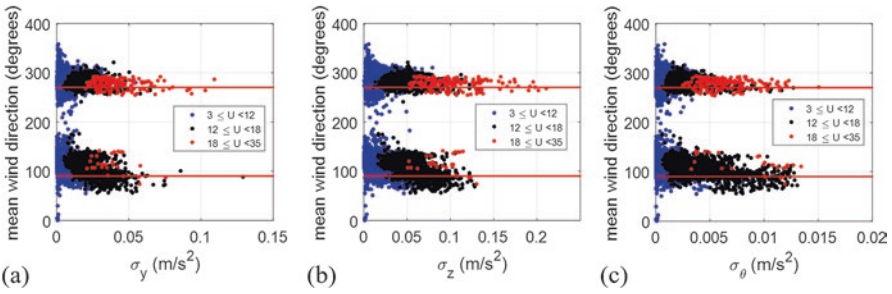

Fig 13.10 Mean wind direction vs. dynamic response: (**a**) lateral, (**b**) vertical and (**c**) torsional response

Where n is the number of predictor variables and β represents the coefficients to be determined by a least-squares fit to the measured response. The insignificant terms were removed from the analysis using hypothesis tests with a 95% significance level. The evolution of the R-squared statistic with the introduction of each variable is shown in Fig. 13.11. The resulting R-squared values were 0.95, 0.89 and 0.81 for the vertical, lateral and torsional acceleration responses, respectively, which indicate a strong correlation between the wind-related parameters and the response components. Moreover, the response surfaces were used to predict the response using the field measurements of the wind parameters. The results are shown in Fig. 13.12. It appears that most of the scatter results from the variability of the wind field parameters.

Fitted response surfaces also allow a more elaborate investigation of the influence of each parameter on the response, as well as the interaction of parameters. Some of the profound interactions affecting the bridge dynamic response are presented in Fig. 13.13 in the form of three-dimensional surface plots. From the figure, it is observed that vertical turbulence and mean wind speed had a profound effect on all the response components. For the vertical and lateral responses, the along-wind turbulence was also found to be important. It is also observed that the cross-wind

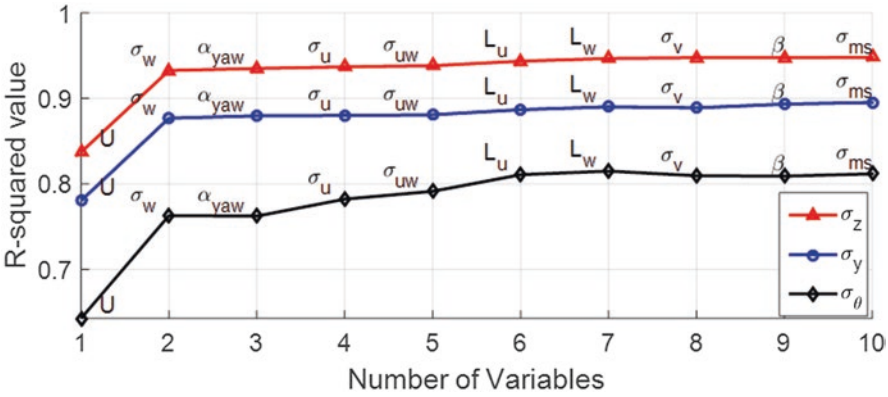

Fig 13.11 Evolution of the R-squared statistic

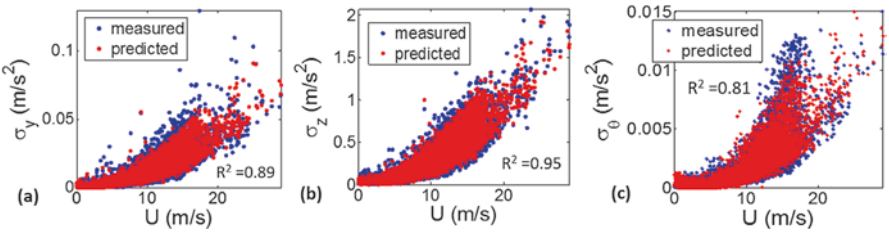

Fig. 13.12 Measured vs. predicted RMS responses using the response surface models: (**a**) vertical response, (**b**) lateral response and (**c**) torsional response

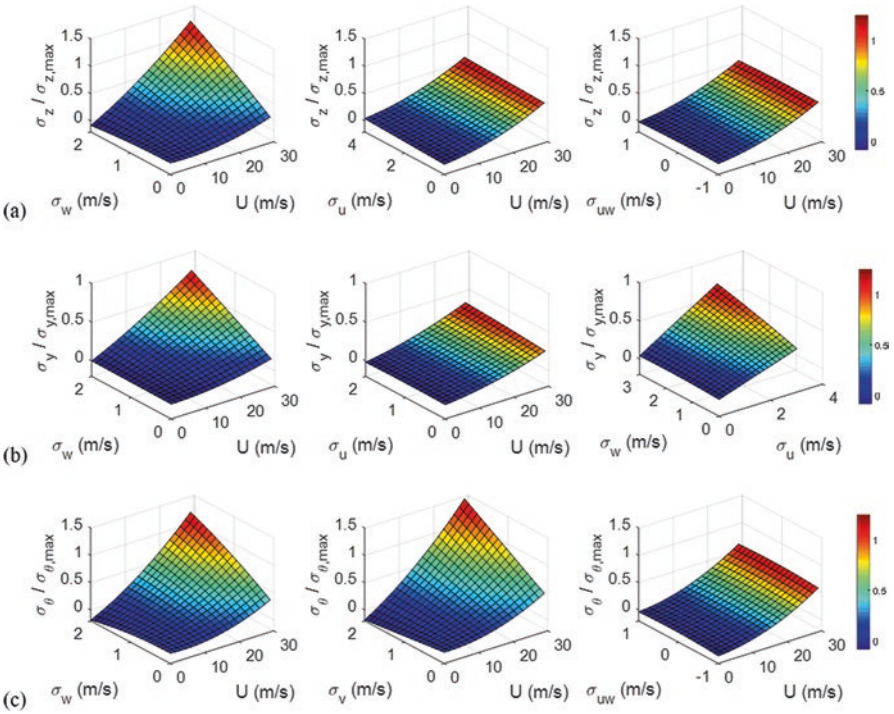

Fig. 13.13 Interaction effects of the turbulence components on the dynamic response: (**a**) vertical response, (**b**) lateral response and (**c**) torsional response

turbulence term had a significant effect on the torsional response. Apparently, larger, cross-wind turbulence caused larger torsional response, which wasn't expected.

13.6 Conclusion

Full-scale measurement results from a long-span suspension bridge located in Norwegian fjords are used to study its wind-induced vibrations and their relation to the wind characteristics at the site. The wind measurements revealed significant variability in mean wind speed, turbulence intensities and length scales. The mean wind speed and vertical turbulence intensities intensity are found to be the two most important wind-related variables influencing the dynamic response of the Hardanger Bridge. The along-wind turbulence is found to be significant only for the lateral response, whereas the cross-wind turbulence influenced the torsional response. The scatter in the response curves was too large to be represented by the mean wind speed alone. Response surface analyses considering wind-related parameters as predictor variables showed that the scatter in the response can be attributed to the variable wind field. The considerable uncertainty present in the wind field statistics is

found to be important for the case of the Hardanger Bridge. Design methods accounting for this variability are essential when designing long-span bridges in such complex and mountainous terrain. The findings are deemed important and applicable in future long and super-long span bridge projects. Further investigations on the terrain effects on wind and response characteristics are ongoing. The valuable database formed during the extensive measurement campaign is expanding, since the monitoring system is still operational. The data will also provide an opportunity for research on system identification studies, investigation of possible interaction of modal properties of the structure with the wind field and structural health monitoring studies.

Acknowledgements The research described in this paper was financially supported by the Norwegian Public Roads Administration.

References

Brownjohn JMW, Bocciolone M, Curami A, Falco M, Zasso A (1994) Humber bridge full-scale measurement campaigns 1990–1991. J Wind Eng Ind Aerodyn 52(1):185–218

Brownjohn JMW, Magalhaes F, Caetano E, Cunha A (2010) Ambient vibration re-testing and operational modal analysis of the Humber Bridge. Eng Struct 32(8):2003–2018

Davenport AG (1962) Buffeting of a suspension bridge by storm winds. J Struct Div 88(3):233–268

Kaimal JCJ, Wyngaard JCJ, Izumi Y, Coté OR, Cote OR (1972) Spectral characteristics of surface-layer turbulence. Q J R Meteorol Soc 98(417):563–589

Larsen A, Larose GL (2015) Dynamic wind effects on suspension and cable-stayed bridges. J Sound Vib, Academic 334(1):2–28

Myers RH, Montgomery DC, Anderson-Cook C (2009) Response surface methodology: process and product optimization using designed experiments. Wiley series in probability and statistics, (June 2015), 704

Øiseth O, Rönnquist A, Kvåle KA, Sigbjörnsson R (2015) Monitoring wind velocities and dynamic response of the hardanger bridge. Conf Proc Soc Exp Mech Ser 77:117–125

Simiu E, Scanlan RH (1996) Winds effects on structures: fundamentals and applications to design. Wiley, New York

Solari G, Piccardo G (2001) Probabilistic 3-D turbulence modeling for gust buffeting of structures. Probab Eng Mech 16(1):73–86

von Karman T (1948) Progress in the statistical theory of turbulence. Proc Natl Acad Sci U S A 34(11):530–539

Xu YL, Zhu LD (2005) Buffeting response of long-span cable-supported bridges under skew winds. Part 2: Case study. J Sound Vib 281(3–5):675–697

Chapter 14
Simulation and Monitoring of Floating Bridge Behaviour

K.A. Kvåle, Ole Øiseth, A. Rönnquist, and S. Remseth

Abstract Firstly, this paper presents a review of the main steps for simulating floating bridge behaviour. Both time-domain and frequency-domain approaches are presented. An exemplified model setup and simulation results from the selected case study are presented. Secondly, data obtained from extensive structural and environmental monitoring of the studied bridge are presented. Data analyses attempting to visualize the correlations between excitation sources and response quantities are discussed. Finally, an operational modal analysis is carried out, to attempt to identify the modal parameters from response measurements only.

Keywords Stochastic dynamic behaviour • Stochastic dynamics • Pontoon bridge • Simulation • Monitoring

14.1 Introduction

The new Coastal Highway Route E39 along the western coast of Norway requires several fjord crossings between 2000 and 5500 m of length. The Norwegian Public Roads Administration is funding an extensive research program, including several studies by PhD students and postdocs at the Norwegian University of Science and Technology, to support safe design of the new fjord crossings.

The late Professor Ragnar Sigbjörnsson had a major role in defining this research program both related to required theoretical development, numerical models, full scale measurements and statistical approaches to arrive at recommended performance-based design.

Various types of bridges, including suspension bridges, floating bridges, suspension bridges with floating towers and submerged floating tunnels are considered for

K.A. Kvåle • O. Øiseth • A. Rönnquist • S. Remseth (✉)
Department of Structural Engineering, Faculty of Engineering, NTNU, Norwegian University of Science and Technology, Trondheim, Norway
e-mail: svein.remseth@ntnu.no

R. Rupakhety, S. Ólafsson (eds.), *Earthquake Engineering and Structural Dynamics in Memory of Ragnar Sigbjörnsson*, Geotechnical, Geological and Earthquake Engineering 44, https://doi.org/10.1007/978-3-319-62099-2_14

the different fjord crossings along the Coastal Highway Route E39. This paper will mainly address floating bridges.

The history of floating bridges may be traced back as far as 2000 BCE (Watanabe and Utsunomiya, 2003), but it is only during the last decades that they have been developed with enough sophistication to operate as critical road links in modern infrastructure networks. Currently, there are only about twenty long floating bridges in the world, and thus, the available information on these structures is very scarce. This is especially true of construction records, environmental conditions, durability, operations and performance. The major trends in the development of floating bridges and other large floating structures are found in Wang and Wang (2014).

Important contributions to the field of floating bridge simulation were made by the research group of Hartz (Hartz 1981; Hartz and Georgiadis 1982; Hartz and Mukherji 1977) in connection with research on the Hood Canal Bridge (Borgman 1967) and at NTNU/SINTEF by the research group of Holand and Langen (Clough et al. 1977; Holand and Langen (1972), (1981). Further developments and exemplifications were made by, e.g., Sigbjörnsson (1979), Langen and Sigbjörnsson (1980), Leira and Langen (1985), and Remseth et al. (1999), in close cooperation with Statens vegvesen. Since the pioneering contributions from the 70s and early 80s mentioned above, few case studies on the use of the methodology have been conducted. The design of both the Mega-Float and the Yumemai Bridge in Japan (Kumamoto and Maruyama 1999; Watanabe et al. 2000) were important drivers in this regard. Morris, Szabo, Yang, and Isaacson (2004) performed a frequency-domain analysis of the William R. Bennett Floating Bridge in British Columbia. Other relevant, scientific contributions of recent years are (Fu et al. 2007; Gao et al. 2011, 2013; Isaacson and Nwogu 1987; Sannasiraj et al. 1995, 2001; Seif and Inoue 1998). A case study investigating the stochastic dynamic behaviour of the Bergsøysund Bridge was presented by Kvåle et al. (2016). That article presents a comprehensive numerical model setup for the Bergsøysund Bridge, investigates response effects due to changes in the modelled sea state and remarks how the bridge shape in combination with relatively low wave severity results in close-to uncorrelated wave action on the discrete pontoons within the range of expected loading situations.

There are many types of floating bridges, with designs made to adapt to the topographical structure of the land and the nature of the waters to cross. Currently, there exist only three, long-span floating bridges exposed to tough sea water conditions for automobile traffic in the world, namely:

- the Hood Canal Bridge in the State of Washington, USA: a 2398 m long pontoon bridge with a 1988 m long anchored floating portion, the longest floating bridge in the world located in a saltwater tidal basin, and the third longest floating bridge overall.
- the Nordhordland Bridge (1994) in Norway: a 1614 m long combined pontoon and cable-stayed bridge with a 1246 m long floating portion, the longest floating bridge in the world without anchorage.

Fig. 14.1 The Bergsøysund Bridge (Photograph by NTNU/K.A. Kvåle)

- the Bergsøysund Bridge (1992) in Norway: a 931 m long pontoon bridge, the second longest floating bridge in the world without anchorage, the first floating bridge built without side-anchorage.

14.1.1 Case Study: The Bergsøysund Bridge

The last of the mentioned bridges is selected as a representative case study. The Bergsøysund Bridge is a 931 m long, arch-shaped pontoon bridge, that runs between the islands of Aspøya and Bergsøya on the northwestern coast of Norway. The bridge is shown in Fig. 14.1. The location of the bridge and the geography surrounding it is depicted in the map shown in Fig. 14.2. The bridge consists of a steel truss resting on 7 discretely distributed pontoons and is supported vertically and horizontally by neoprene bearings at the abutments. Axial steel rods, one at each support, absorb all axial forces.

14.2 Theoretical Outline

Naess and Moan (2012) give an overview of the relevant theory on stochastic modelling of floating structures, but the important details are repeated below.

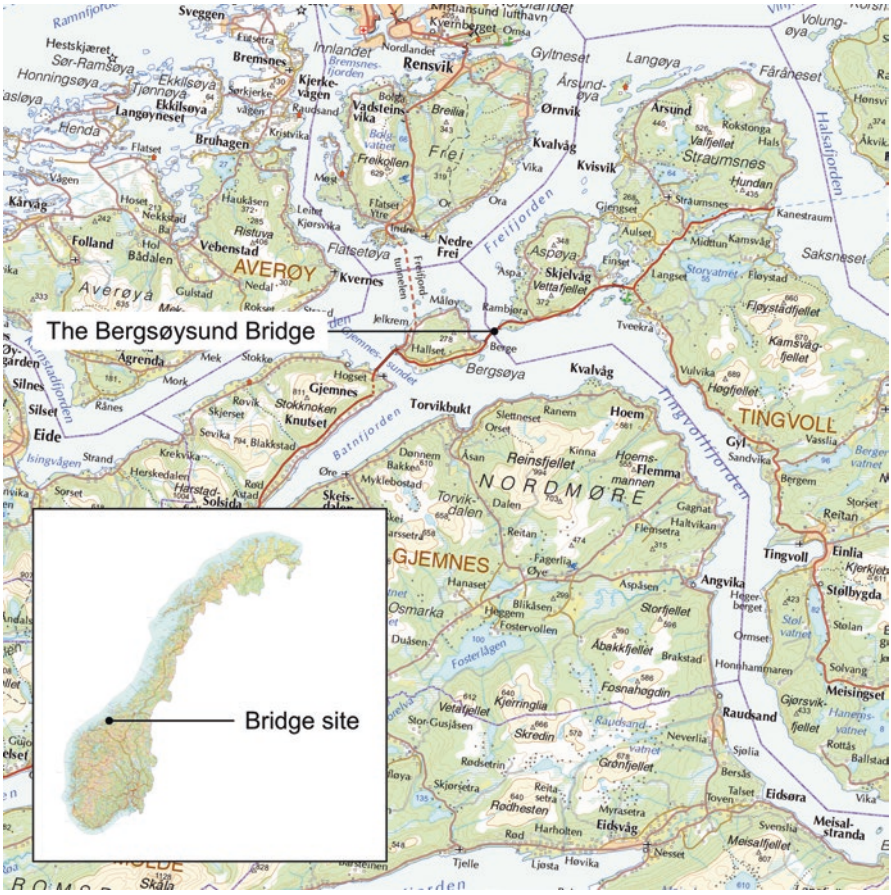

Fig. 14.2 Map sections showing the location of the Bergsøysund Bridge. Map sections: © Kartverket (Reprinted from Kvåle and Øiseth (2017), with permission from Elsevier)

14.2.1 Equations of Motion

The equations of motion describing the linear behaviour of floating bridges can, in principle, be represented within the framework of the finite element method as follows:

$$[M_s]\{\ddot{u}\}+[C_s]\{\dot{u}\}+[K_s]\{u\}=\{p_h(t)\} \tag{14.1}$$

Here, $[M_s]$, $[C_s]$ and $[K_s]$ are the system matrices describing the structural properties of the bridge, respectively, mass, damping and stiffness. $\{u\}$ is the structural response, and the vector $\{p_h(t)\}$ represents the sum of both wave excitation and hydroelastic interaction, referred to as total hydrodynamic action, given as a function of time t.

14.2.1.1 Fluid-Structure Interaction

The total hydrodynamic action process describes both the fluid-structure interaction and the wave excitation. The hydrodynamic transfer functions and the fluid-structure interaction are both commonly established either by potential theory and panel methods or by means of experiments in basins. The first of the two approaches is described below.

It is assumed that water can be modelled as incompressible, non-viscous and irrotational. Within the framework of the potential theory, a potential, $\Phi(\{r\},t)$, as a function of location, $\{r\}$, and time, t, can be used to describe the fluid velocity vector as follows:

$$\{V\} = \begin{Bmatrix} u(\{r\},t) \\ v(\{r\},t) \\ w(\{r\},t) \end{Bmatrix} \tag{14.2}$$

By assuming small-amplitude water waves, referred to as Airy waves, the velocity is obtained as follows:

$$\{V\} = \{\nabla\}\Phi = \frac{\partial \Phi}{\partial x}\hat{i} + \frac{\partial \Phi}{\partial y}\hat{j} + \frac{\partial \Phi}{\partial z}\hat{\mathrm{k}} \tag{14.3}$$

where, Φ is the velocity potential and $\{\nabla\}$ the del operator. Irrotationality implies that the vorticity vector is zero everywhere in the fluid, i.e.:

$$\{\vec{\omega}\} = \{\nabla\} \times \Phi = \{0\} \tag{14.4}$$

Under the assumption of incompressibility, the following holds:

$$\{\nabla\}\{\mathrm{V}\} = 0 \tag{14.5}$$

Then, the velocity potential satisfies the Laplace equation:

$$\{\nabla\}\{\mathrm{V}\} = \{\nabla\}^2 \Phi = \frac{\partial^2 \Phi}{\partial x^2} + \frac{\partial^2 \Phi}{\partial y^2} + \frac{\partial^2 \Phi}{\partial z^2} = 0 \tag{14.6}$$

By applying appropriate boundary conditions, the Laplace equation is solved for the velocity potential, such that fluid motion, pressure and hydrodynamic forces can be derived. The total hydrodynamic action, $\{p_h(t)\}$, induced by a monochromatic small-amplitude wave, proportional to $e^{i\omega t}$, is expressed as follows:

$$\left\{p_h(t)\right\} = \left\{P(\omega)\right\} e^{i\omega t} - \left[M_h(\omega)\right]\left\{\ddot{u}(t)\right\} - \left[C_h(\omega)\right]\left\{\dot{u}(t)\right\} - \left[\mathrm{K}_h\right]\left\{\boldsymbol{u}(t)\right\} \tag{14.7}$$

Here, $[M_h(\omega)]$, $[C_h(\omega)]$ and $[K_h]$ are the added hydrodynamic mass, added hydrodynamic damping, and hydrodynamic stiffness originating from the self-exciting forces; ω is the circular frequency; and $\{P(\omega)\}e^{i\omega t}$ is the wave excitation. In general, all quantities in the above equation are both complex-valued and frequency-dependent. By virtue of the principle of superposition, this can be generalized to represent an irregular stochastic sea state.

The excitation forces acting on a submerged body, arising from a monochromatic small-amplitude wave, is related to the wave elevation as follows:

$$\left\{dZ_p(\omega,\theta)\right\} = \left\{Q_q(\omega,\theta)\right\} dZ_\eta(\omega,\theta) \tag{14.8}$$

where the vector $\{Z_p(\omega,\theta)\}$ denotes the spectral process of the wave excitation; $Z_\eta(\omega,\theta)$ denotes the spectral process of the wave elevation; and $\{Q_q(\omega,\theta)\}$ is the directional wave excitation hydrodynamic transfer function related to the body with index q, yielding forces in six degrees of freedom from a single point wave elevation.

14.2.2 Modelling Random Seas and Corresponding Wave Excitation

For engineering purposes, wind generated water waves can be modelled using locally homogeneous random fields. Faltinsen (1993) and Hauser et al. (2005) give thorough reviews of the relevant theory for the stochastic modelling of irregular sea surfaces, but the most important aspects are repeated below.

The sea surface elevation, η, is a scalar quantity modelled as a function of location in space, $\{r\}$, and time, t, and can be expressed mathematically by the following Riemann-Stieltjes integral:

$$\eta\left(\{r\},t\right) = \int e^{i\{\kappa\}\{r\} - i\omega t} dZ_\eta\left(\{\kappa\},\omega\right) \tag{14.9}$$

where Z_η is the spectral process corresponding to the sea surface elevation and $\{\kappa\}$ is the wave number vector, defined as follows:

$$\left\{\kappa\right\} = \begin{Bmatrix}\kappa_x\\ \kappa_y\end{Bmatrix} = \kappa\begin{Bmatrix}\cos\theta\\ sin\theta\end{Bmatrix} \tag{14.10}$$

and κ is the wave number. For stationary and homogeneous random wave fields, the spectral process is related to the wave spectral density in the following manner:

$$E\left(dZ_{\eta_p}\left(\{\kappa\},\omega\right)dZ_{\eta_q}\left(\{\kappa\},\omega\right)^H\right) = dG_{\eta_p\eta_q}(\{\kappa\},\omega) = S_{\eta_p\eta_q}(\{\kappa\},\omega)d\kappa_x d\kappa_y d\omega \quad (14.11)$$

Here, the indices, p and q, refer to two points in time and space; $G_{\eta_p\eta_q}(\{\kappa\},\omega)$ denotes the spectral distribution and $S_{\eta_p\eta_q}(\{\kappa\},\omega)$ the corresponding three-dimensional cross-spectral density between the wave elevations at points p and q. $E[\cdot]$ is the mathematical expectation operator, and the superscript, H, refers to the transpose and complex conjugate. In the case of small-amplitude waves, the wave number and wave frequency are related through the dispersion relation as follows:

$$\omega^2 = g\kappa \tanh\left(\kappa d\right) \quad (14.12)$$

where g is the gravitational constant, and d is the water depth. For deep water, this reduces to $\kappa=\omega^2/g$. By enforcing the relation between wave number and frequency, the cross-spectral density can be expressed as a function of two variables (two-dimensional spectral density), e.g., the wave frequency, ω, and the wave direction, θ.

Because the random sea is assumed homogeneous, the general, two-dimensional auto-spectral density can be obtained by merging points p and q, as follows:

$$S_\eta\left(\omega,\theta\right) = \mathrm{S}_{\eta_p\eta_p}\left(\omega,\theta\right) = \mathrm{S}_{\eta_q\eta_q}\left(\omega,\theta\right) \quad (14.13)$$

This is commonly referred to as the directional wave spectral density and is traditionally decomposed as follows:

$$\mathrm{S}_\eta\left(\omega,\theta\right) = S_\eta\left(\omega\right)D\left(\omega,\theta\right) \quad (14.14)$$

where $S_\eta(\omega)$ is the one-dimensional wave spectral density and $D(\omega,\theta)$ is the directional distribution, defined such that $\int D(\omega,\theta)d\theta = 1$. The points p and q are separated by the distance $\{\Delta r\}$, and the spectral density between the wave elevations at the two locations is written as follows:

$$\mathrm{S}_{\eta_p\eta_q}\left(\omega\right) = S_\eta\left(\omega\right)\int_{-\pi}^{\pi} D\left(\omega,\theta\right)e^{i\{\kappa\}\{\Delta r\}}d\theta \quad (14.15)$$

The integral term in the equation above expresses the coherency between the wave heights at points p and q. The cross-spectral density matrix originating from the wave excitation between the two points is written as follows:

$$\left[S_{p_p p_q}\left(\omega\right)\right] = \int_\theta \left\{Q_p\left(\omega,\theta\right)\right\}\mathrm{S}_{\eta_p\eta_q}\left(\omega,\theta\right)\left\{Q_q\left(\omega,\theta\right)\right\}^H d\theta \quad (14.16)$$

This 6x6 matrix is then placed in the global matrix, expressing cross-spectral densities between all combinations of locations and force components.

14.2.3 Frequency-Domain Solution Strategy

By insertion of the expression for wave excitation in Eq. 14.7 into Eq. 14.1 and rearranging, the following frequency-domain representation may be obtained:

$$\left(-\omega^2\left[M(\omega)\right]+i\omega\left[C(\omega)\right]+\left[K\right]\right)\left\{dZ_u(\omega)\right\}=\left\{dZ_p(\omega)\right\} \tag{14.17}$$

where the following total system matrices are introduced:

$$\left[M(\omega)\right]=\left[M_s\right]+\left[M_h(\omega)\right] \tag{14.18}$$

$$\left[C(\omega)\right]=\left[C_s\right]+\left[C_h(\omega)\right] \tag{14.19}$$

$$\left[K\right]=\left[K_s\right]+\left[K_h\right] \tag{14.20}$$

and where $\{Z_u(\omega)\}$ and $\{Z_p(\omega)\}$ are the spectral processes related to the displacement, $\{u(t)\}$, and wave excitation, $\{p(t)\}$, respectively. These are related through $\{u(t)\}=\int e^{i\omega t}\{dZ_u(\omega)\}$ and $\{p(t)\}=\int e^{i\omega t}\{dZ_p(\omega)\}$. Equation 14.17 may be rewritten with the frequency domain transfer function and inverted to yield the response, as follows:

$$\left\{dZ_p(\omega)\right\}=\left[H(\omega)\right]^{-1}\left\{dZ_u(\omega)\right\}\Leftrightarrow\left\{dZ_u(\omega)\right\}=\left[H(\omega)\right]\left\{dZ_p(\omega)\right\} \tag{14.21}$$

The cross-spectral densities of the displacement and wave excitation processes can be expressed as follows (Sigbjörnsson 1979):

$$\left[S_u(\omega)\right]d\omega=E\left(\left\{dZ_u(\omega)\right\}\left\{dZ_{\mathrm{u}}(\omega)\right\}^H\right) \tag{14.22}$$

$$\left[S_p(\omega)\right]d\omega=E\left(\left\{dZ_p(\omega)\right\}\left\{dZ_{\mathrm{p}}(\omega)\right\}^H\right) \tag{14.23}$$

By combining Eqs. 14.22 and 14.23 with Eq. 14.21, the following equation, representing the cross-spectral density method, is obtained:

$$\left[S_u(\omega)\right]=\left[H(\omega)\right]\left[S_p(\omega)\right]\left[H(\omega)\right]^H \tag{14.24}$$

This representation captures the probabilistic properties of both the response and wave excitation for zero-mean processes but is, strictly speaking, only valid for linear systems. To deal with nonlinearities, a time-domain solution strategy are normally enforced.

14.2.4 Time-Domain Solution Strategy

It is possible to express a general time domain representation of the hydroelastic system by taking the inverse Fourier transform of Eq. 14.17. That leads to the integro-differential equation given as follows, assuming causality and frequency independent restoring forces:

$$\int_{-\infty}^{\infty}\left[m\left(t-\tau\right)\right]\left\{\ddot{u}\left(\tau\right)\right\}d\tau+\int_{-\infty}^{\infty}\left[c\left(t-\tau\right)\right]\left\{\ddot{u}\left(\tau\right)\right\}d\tau+\left[K\right]=\left\{p\left(t\right)\right\} \tag{14.25}$$

where the time-domain representations of the added hydrodynamic mass and damping are introduced, as follows:

$$\left[m\left(t\right)\right]=\left[M_s\right]+\frac{1}{2\pi}\int_{-\infty}^{\infty}\left[M_h\left(\omega\right)\right]e^{i\omega t}d\omega \tag{14.26}$$

$$\left[c\left(t\right)\right]=\left[C_s\right]+\frac{1}{2\pi}\int_{-\infty}^{\infty}\left[C_h\left(\omega\right)\right]e^{i\omega t}d\omega \tag{14.27}$$

This means that the time-domain solution, valid for a deterministic load history, can be expressed as follows:

$$\left\{u\left(t\right)\right\}=\int_{-\infty}^{\infty}\left[h\left(t-\tau\right)\right]\left\{p\left(t\right)\right\}d\tau \tag{14.28}$$

Here, $[h(t)]$ is the impulse response function of the hydroelastic system, the time-domain equivalent to the frequency domain transfer function. In practice, the solution of the convolution integral above is a computationally demanding task. For non-linear problems, iteration on each time step is required as well, making the simulation very cumbersome. There are various approaches to avoid the direct calculation of the convolution integral, but specifics about these are not presented in this paper. The reader is referred to, e.g., Taghipour et al. (2008a, b) for a review of available methods. The solution outlined by Øiseth et al. (2012) is a simplified procedure to include the motion-dependent, fluid-structure interaction in a traditional FE-beam formulation by augmentation of the number of the degrees of freedom, which depends on the fluid-structure interaction derivatives for each case.

To enable simulation of stochastic problems, the deterministic time-domain solution procedure must be included in a Monte Carlo simulation. This implies that multiple deterministic simulations are run, with deterministic wave excitation history based on sampled data from the wave excitation spectral density. The resulting response histories are transformed to the frequency domain, and averaged.

The solution strategy presented above handles nonlinearities, making it more powerful and versatile than the frequency domain approach. However, the additional computational cost, compared to the simple frequency-domain solution strategy, is tremendous.

14.3 Simulation of the Bergsøysund Bridge

The following is based on the simulation study performed in Kvåle et al. (2016).

14.3.1 Model Set-Up

The problem structure is divided into two sub-structures: (I), an Abaqus finite element (FE) model which includes all structural contributions of the system, $[M_s]$, $[C_s]$ and $[K_s]$, the inertia of the pontoons, denoted $[M_{h0}]$, and the buoyancy, $[K_h]$; and (II), a DNV HydroD WADAM model for each of the pontoons, including the frequency-dependent added damping, $[C_h(\omega)]$, and mass, $[M_h(\omega)]$, from the fluid-structure interaction. Figure 14.3 shows a rendering of the FE model from Abaqus. Figure 14.4 reveals more details regarding the model setup, but the reader is referred to the cited paper for the full description.

Fig. 14.3 Rendering of finite element model from Abaqus (Reprinted from Kvåle et al. (2016), with permission from Elsevier)

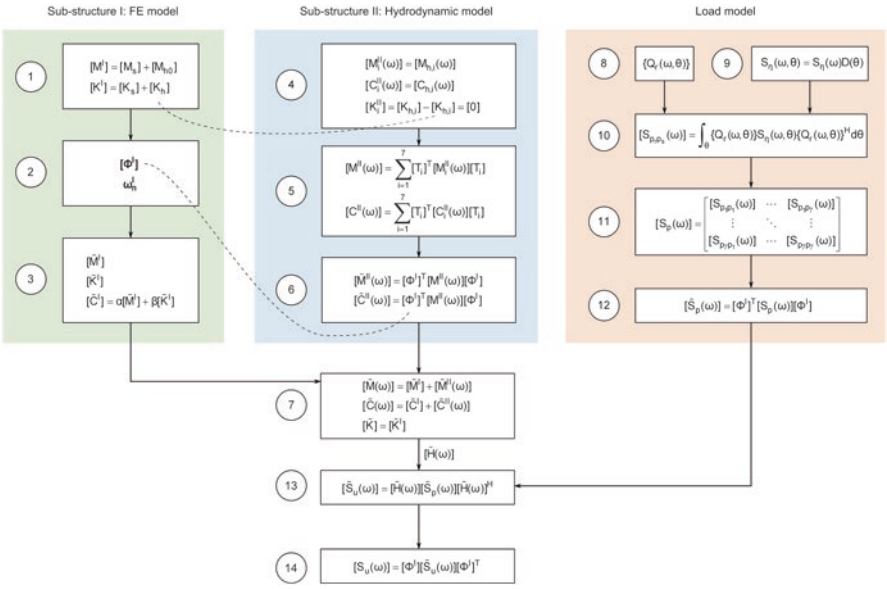

Fig. 14.4 Structure of calculation scheme (Reprinted from Kvåle et al. (2016), with permission from Elsevier)

14.3.2 Load Modelling

As indicated in Sect. 2.2, the wave excitation spectral density is characterized by the one-dimensional wave spectral density and the directional distribution. The one-parameter, Pierson-Moskowitz spectrum and the cos2s-distribution is used in this case study. These are defined as follows:

$$S_\eta(\omega) = \frac{A}{\omega^5} e^{-B/\omega^4} \tag{14.29}$$

$$\mathrm{D}(\theta) = C\cos^{2s}\left(\frac{\theta-\theta_0}{2}\right) \tag{14.30}$$

where $A = \alpha g^2$; $B = 3.11/H_s^2$; $\alpha = 0.0081$; H_s is the significant wave height (SWH), defined as the mean wave height of the highest third of the waves; C is a constant ensuring that the integral of the distribution is unity; s is the spreading parameter, describing the spreading (or inversely, the crest length) of the waves; and θ_0 is the mean wave direction. If not otherwise noted, the following values were used for the characterizing parameters: $H_s = 0.9m$, $s = 3$, and $\theta_0 = 90^\circ$ (i.e., head sea).

14.3.3 Response Prediction

By employing the power spectral density method, the simulated load cross-spectral density matrix is used in conjunction with the frequency domain transfer function to establish the cross-spectral density matrix corresponding to the response. Figure 14.5 shows the resulting spectral densities between the lateral response of pontoons 3, 4 and 5.

14.3.4 Parameter Studies

By altering the parameters characterizing the wave excitation, the effect on the response is visualized. The spreading parameter, s, and the significant wave height, (SWH) H_s, were both varied, in turn, to assess their importance to the response. The resulting effect on the response is shown in Fig. 14.6. The SWH has the largest influence on the response. This is as expected because the SWH is directly related to the energy content in the waves. The figure also reveals that the effect of the spreading parameter is small because a more regular sea (larger s) is likely to reduce

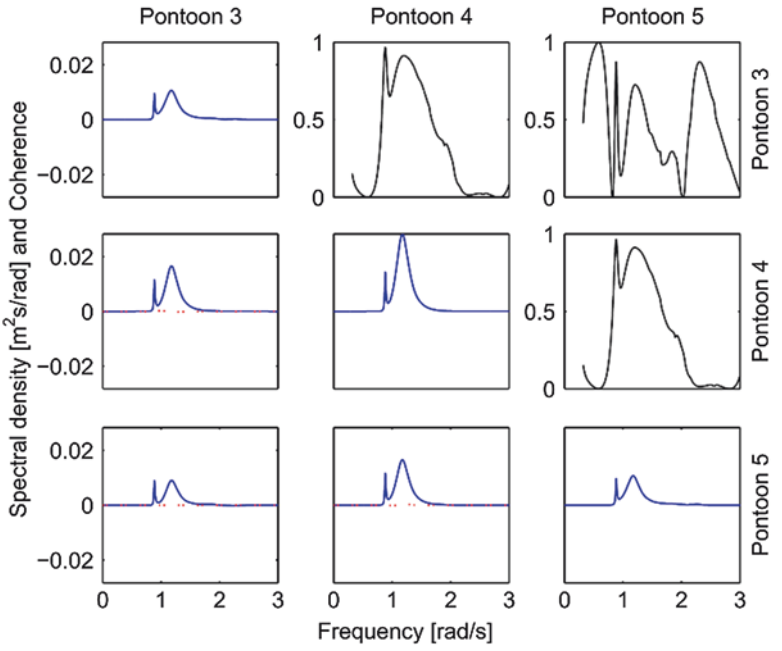

Fig. 14.5 Cross-spectral densities corresponding to lateral response of pontoons 3, 4 and 5. The *black* curves represent the coherency, while the *blue* and *red* curves represent the real and imaginary parts of the spectral densities, respectively (Reprinted from Kvåle et al. 2016a, b, with permission from Elsevier)

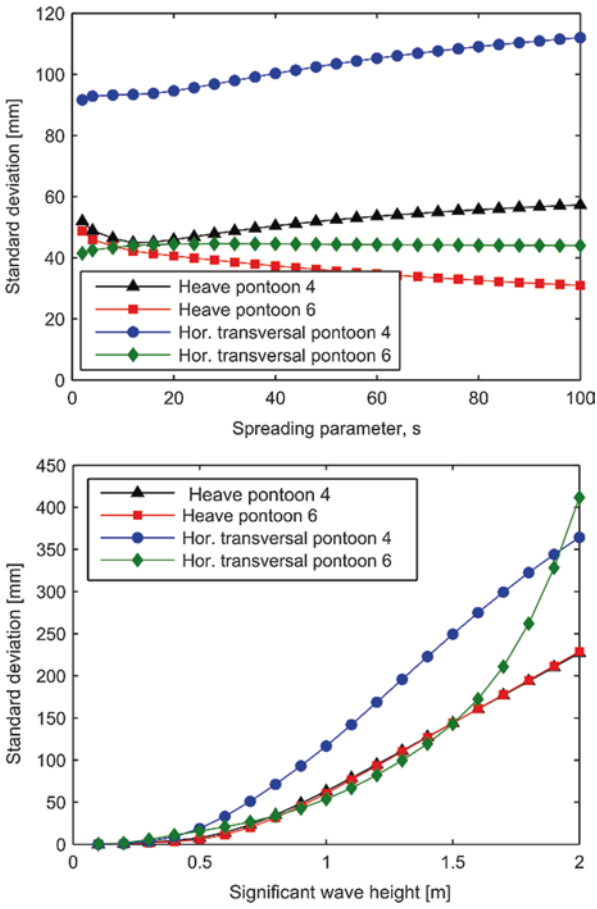

Fig. 14.6 Parameter studies showing effect of the changing sea state on response quantities (Reprinted from Kvåle et al. 2016 with permission from Elsevier)

the response in the anti-symmetric modes, even though it will increase the response in the symmetric modes.

14.3.5 Modal Parameters

Because the added hydrodynamic damping makes the total damping level as high as it does, the damping cannot be neglected when solving the eigenvalue problem. This leads to complex eigenvalues and eigenvectors. Furthermore, the fact that the problem is dependent on frequency makes it non-linear. An iterative algorithm was used to overcome this obstacle. The reader is referred to Kvåle et al. (2016) for the details regarding how to establish the modal parameters from the specified model setup. The natural frequencies and damping ratios resulting from this are presented in Table 14.1.

Table 14.1 Modal parameters for the first 10 modes

Mode	Undamped natural frequency (rad/s)	Damping ratio (%)
1 (Horizonta/l)	0.58	1.63
2 (Vertical)	0.99	12.25
3 (Vertical)	1.03	11.24
4 (Horizontal)	1.05	5.00
5 (Vertical/horizontal)	1.17	7.67
6 (Horizontal/torsional)	1.38	5.91
7 (Vertical)	1.44	3.28
8 (Vertical)	1.87	1.07
9 (Torsional/horizontal)	1.95	3.62
10 (Horizontal/torsional)	2.23	0.43

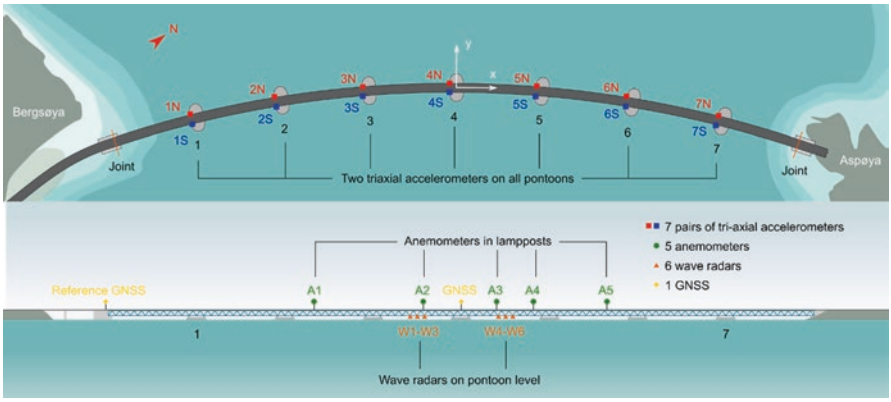

Fig. 14.7 Sensor layout (Reprinted from Kvåle and Øiseth (2017), with permission from Elsevier)

14.4 Structural Monitoring

An extensive monitoring system is currently in operation on the Bergsøysund Bridge. The system is monitoring accelerations, displacements, sea surface elevations and wind velocities. Figure 14.7 depicts the sensor layout, which is supported with details of the sensors found in Table 14.2. Photos of the sensors are found in Fig. 14.8. The monitoring system is thoroughly described, and the recorded data is analysed more in depth, in Kvåle and Øiseth (2017).

In the following, a global analysis of the recordings made between February 2014 and January 2015 are made. The recordings are initiated either manually or due to trigger values being exceeded on certain sensors. All data are interpreted in 10-min long recording segments and are represented by means of statistical quantities. Prior to this, the quality of the data is assessed automatically to avoid false data

Table 14.2 Sensors in the monitoring system

Sensor type	Sensors	Internal sample rate (Hz)
Tri-axial accelerometers (CSI CUSP-3)	1S,1N,…,7S,7N (in total 14)	200
3D sonic anemometer (Gill WindMaster Pro)	A1-A5	32
Wave radar (Miros SM-140 RangeFinder)	W1-W6	50
GNSS displacement sensor (Trimble RTK GNSS)	GNSS (one at mid-span)	20

Fig. 14.8 Sensor photos: (**a**) triaxial accelerometer with closed enclosure, (**b**) accelerometer with open enclosure, (**c**) wave radar, (**d**) anemometer in lamp post, (**e**) GNSS sensor in pole (Reprinted from Kvåle and Øiseth (2017), with permission from Elsevier)

points and is low-pass filtered at 2 Hz (Kvåle and Øiseth 2017). An investigation of the relationship between environmental parameters and bridge response, and how the environmental parameters are interrelated, is needed to describe what parameters are most important to consider for design.

Figure 14.9 shows the mean wind speed and the mean direction of the wind origin of all the recordings. The figure shows that the largest winds are generated along

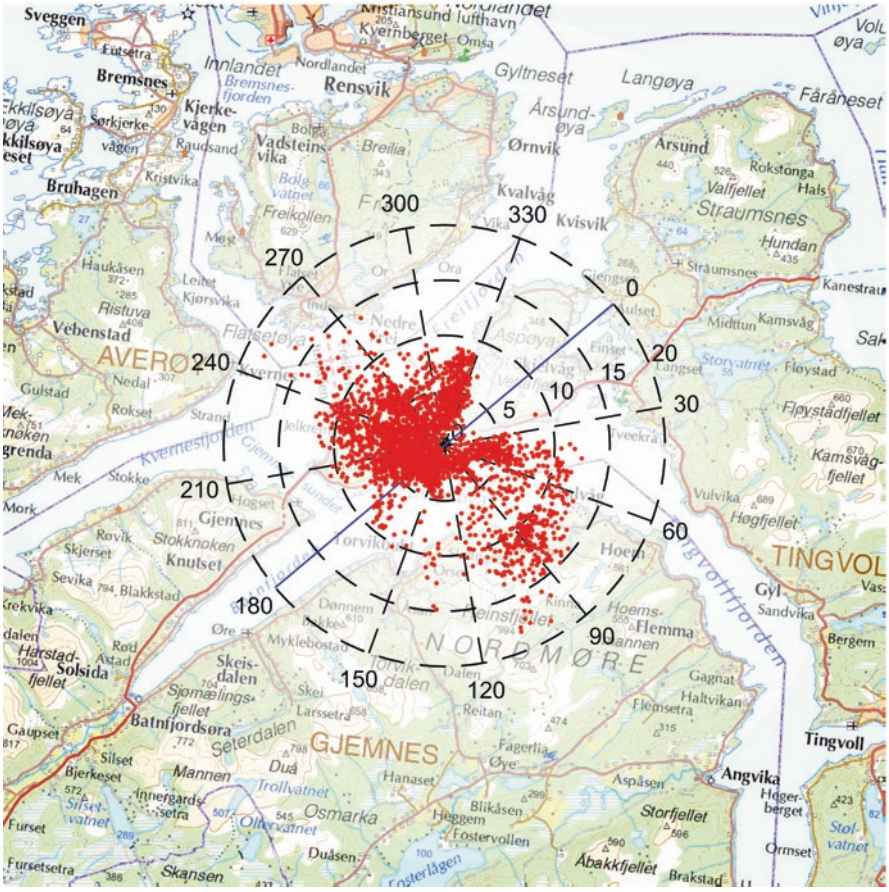

Fig. 14.9 Mean wind speed (radial axis) and mean wind origin direction (circumferential axis). The *blue line* denotes the tangent of the bridge at mid-span (Reprinted from Kvåle and Øiseth (2017), with permission from Elsevier)

the longest straits and how the largest recorded winds are observed from in-land. This is contrary to what is expected but is likely a result of the complex geography. The 372-m tall mountain on Aspøya blocks winds approaching the bridge between 330° and 30°.

The relationship between mean wind speed and SWH, and SWH and heave (vertical) response, is indicated in Fig. 14.10, where the scatter points are divided into groups depending on the origin of the wind. Figure 14.10a shows a high correlation between wind speed and SWH, as expected. Winds approaching the bridge laterally induces more severe seas and, in turn, larger responses (Fig. 14.10b).

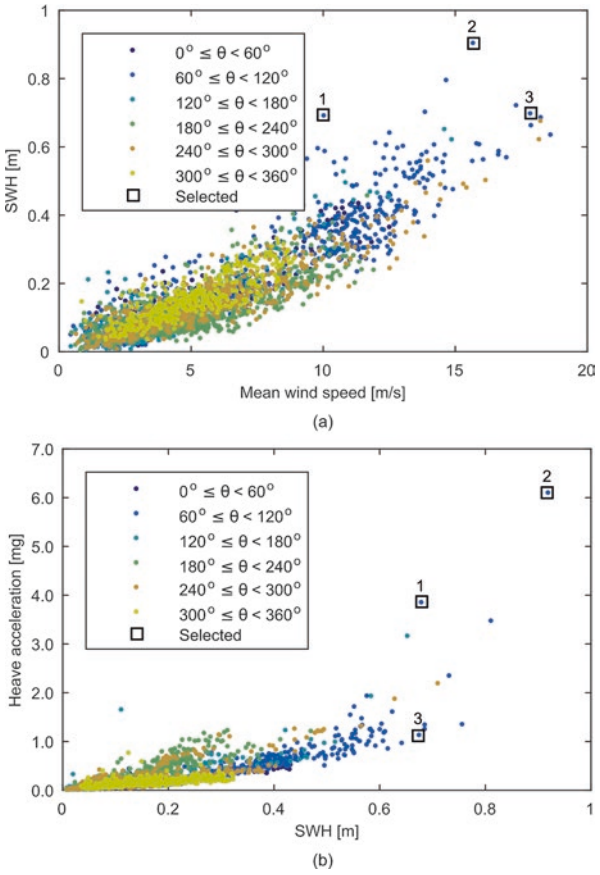

Fig. 14.10 Scatter plots, divided into groups depending on the wind direction, of (**a**) mean wind speed and SWH and (**b**) SWH and standard deviation of heave acceleration of the midmost pontoon (Reprinted from Kvåle and Øiseth (2017), with permission from Elsevier)

14.5 Operational Modal Analysis

By performing modal analysis on the bridge, implying that the modal parameters are estimated from measurements, the structure's dynamic behaviour can be efficiently described. Operational modal analysis (OMA) is the subdiscipline where the dynamic excitation is unknown, i.e., only the response data is used.

The covariance-driven stochastic subspace identification (Cov-SSI) method has proven as one of the most robust methods available for OMA. Kvåle et al. (2015, 2017a, b) perform OMA on the studied bridge, with an emphasis on the Cov-SSI method. To illustrate the application of OMA, and the power of the Cov-SSI method, some results from such an analysis are provided here. Mathematical details about how the method works are considered outside the scope of the current paper, and the reader is, therefore, referred to the cited papers for more details regarding the procedure.

Figure 14.11 shows the mode shapes obtained from Cov-SSI of a selected accelerometer recording compared with the corresponding mode shapes from the numerical prediction, i.e., the ones listed in Table 14.1. Table 14.3 lists the corresponding

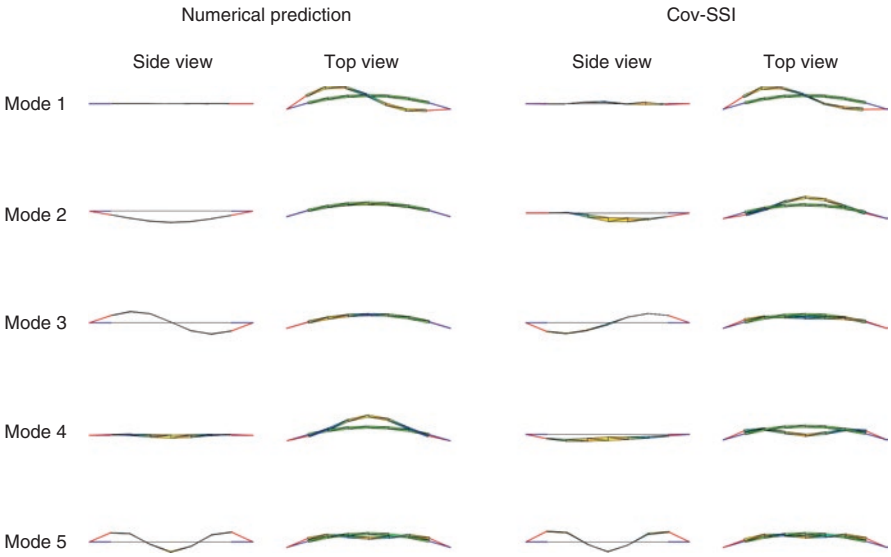

Fig. 14.11 Comparison of mode shapes obtained from numerical prediction and from OMA using the Cov-SSI method

Table 14.3 Identified modal parameters for the first five modes

	Undamped natural frequency (rad/s)		Damping ratio (%)	
Mode	Predicted	OMA	Predicted	OMA
1 (Horizontal)	0.58	0.59	1.63	5.16
2 (Vertical)	0.99	1.08	12.25	4.47
3 (Vertical)	1.03	0.99	11.24	11.62
4 (Horizontal)	1.05	1.02	5.00	2.53
5 (Horizontal/torsional)	1.17	1.22	7.67	4.88

natural frequencies and damping ratios. Even though there are discrepancies, the main character of the dynamic bridge behaviour is captured.

14.6 Summary

Following the planning of the new, ferry-free, Coastal Highway E39 in Norway, the need for extended knowledge about floating bridge behaviour has emerged. The theory required for simulation of floating bridge behaviour has been outlined in the current paper and has been exemplified using a detailed model of the Bergsøysund Bridge, an existing floating, pontoon bridge.

By performing a parametric study, the effects of wave parameters on the response have been investigated. The spreading of the sea affects the resulting response only

to a small extent. The non-linear and complex numerical eigenvalue problem has been solved using an iterative state-space algorithm to predict the modal parameters of the bridge.

Data obtained from a comprehensive monitoring system installed on the same bridge has been interpreted in a statistical and global manner to describe the main aspects of the environmental excitation it is exposed to and its resulting dynamic behaviour. As expected, the wave excitation, described by the significant wave height, is the dominating response-inducing process. Furthermore, the results indicate that the wind and wave directions are not cohering, which is explained by the complex geography surrounding the bridge and the fact that the wave process is a high-inertia process.

An operational modal analysis has been carried out by applying the Cov-SSI method to identify the modal parameters of the structure. For the selected recordings, the resulting modal parameters agree rather well with the predicted ones. However, large variability is observed from recording to recording.

Acknowledgements The research is funded by the Norwegian Public Roads Administration. The authors gratefully acknowledge this. We would also like to thank our dear colleague, the late Prof. Ragnar Sigbjörnsson, for his commitment and inspiration in common scientific endeavours.

References

Borgman LE (1967) Ocean wave simulation for engineering design. DTIC document

Clough D, Sigbjornsson R, Remseth SN (1977) Response of a submerged, buoyant tubular bridge subjected to irregular sea waves. SINTEF Rep., 71 p A77028

Faltinsen O (1993) Sea loads on ships and offshore structures, vol 1. Cambridge University Press, Cambridge/New York

Fu S, Moan T, Chen X, Cui W (2007) Hydroelastic analysis of flexible floating interconnected structures. Ocean Eng 34(11–12):1516–1531. https://doi.org/10.1016/j.oceaneng.2007.01.003

Gao RP, Tay ZY, Wang CM, Koh CG (2011) Hydroelastic response of very large floating structure with a flexible line connection. Ocean Eng 38(17):1957–1966. https://doi.org/10.1016/j.oceaneng.2011.09.021

Gao RP, Wang CM, Koh CG (2013) Reducing hydroelastic response of pontoon-type very large floating structures using flexible connector and gill cells. Eng Struct 52:372–383. https://doi.org/10.1016/j.engstruct.2013.03.002

Hartz BJ (1981) Dynamic response of the Hood Canal Floating Bridge. In: Proceedings of second ASCE/EMD specialty conference on Dynamic Response of Structures, Atlanta

Hartz BJ, Georgiadis C. A finite element program for dynamic response of continuous floating structures in short-crested waves. (1982). Sci. Press. Retrieved from http://www.scopus.com/inward/record.url?eid=2-s2.0-0019936983&partnerID=tZOtx3y1

Hartz BJ, Mukherji B (1977) Dynamic response of a floating bridge to wave forces. In: Proceedings of international conference on Bridging Rion-Antirion. Patras

Hauser D, Kahma K, Krogstad HE (2005) Measuring and analysing the directional spectra of ocean waves. Publications Office of the European Union, Luxembourg

Holand I, Langen I (1972) Salhus floating bridge: theory and hydrodynamic coefficients SINTEF Rep. Progress report

Holand I, Langen I (1981) Dynamic analysis of floating bridges. In: Aune P, Holand I (eds) Norwegian bridge building. Tapir Publishers, Trondheim

Isaacson M, Nwogu OU (1987) Wave loads and motions of long structures in directional seas. J Offshore Mech Arctic Eng 109(2):126–132

Kumamoto N, Maruyama T (1999) Elastic response analysis method for floating bridges in waves Surge (vol 5)

Kvåle KA, Øiseth O (2017) Structural monitoring of an end-supported pontoon bridge. Mar Struct 52:188–207. https://doi.org/10.1016/j.marstruc.2016.12.004

Kvåle KA, Øiseth O, Rønnquist A, Sigbjörnsson R (2015) Modal analysis of a floating bridge without side-mooring. In dynamics of civil structures, vol 2. Springer, pp 127–136 https://doi.org/10.1007/978-3-319-15248-6_14

Kvåle KA, Sigbjörnsson R, Øiseth O (2016) Modelling the stochastic dynamic behaviour of a pontoon bridge: a case study. Comput Struct 165:123–135. https://doi.org/10.1016/j.compstruc.2015.12.009

Kvåle KA, Øiseth O, Rönnquist A (2017a) Operational modal analysis of an end-supported pontoon bridge. Eng Struct 148:410–423, https://dx.doi.org/10.1016/j.engstruct.2017.06.069

Kvåle KA, Øiseth O, Rönnquist A (2017b) Covariance-driven stochastic subspace identification of an End-supported pontoon bridge under varying environmental conditions. In: IMAC-XXXV, Anaheim

Langen I, Sigbjörnsson R (1980) On stochastic dynamics of floating bridges. Eng Struct 2(4):209–216. https://doi.org/http://dx.doi.org/10.1016/0141-0296(80)90002-4

Leira BJ, Langen I (1985) Probabilistic aspects of floating bridge design. In: Proceedings of ICOSSAR, Kobe

Morris E, Szabo V, Yang G, Isaacson M (2004) Frequency domain dynamic analysis of a floating bridge. Coast Struct 2003:1334–1346. https://doi.org/doi:10.1061/40733(147)110

Naess A, Moan T (2012) Stochastic dynamics of marine structures. Cambridge University Press, New York

Øiseth O, Rönnquist A, Sigbjörnsson R (2012) Finite element formulation of the self-excited forces for time-domain assessment of wind-induced dynamic response and flutter stability limit of cable-supported bridges. Finite Elem Anal Des 50:173–183. https://doi.org/10.1016/j.finel.2011.09.008

Remseth S, Leira BJ, Okstad KM, Mathisen KM, Haukås T (1999) Dynamic response and fluid/structure interaction of submerged floating tunnels. Comput Struct 72(4):659–685. https://doi.org/10.1016/S0045-7949(98)00329-0

Sannasiraj SA, Sundar V, Sundaravadivelu R (1995) The hydrodynamic behaviour of long floating structures in directional seas. Appl Ocean Res 17(4):233–243. https://doi.org/10.1016/0141-1187(95)00011-9

Sannasiraj SA, Sundaravadivelu R, Sundar V (2001) Diffraction–radiation of multiple floating structures in directional waves. Ocean Eng 28(2):201–234. https://doi.org/http://dx.doi.org/10.1016/S0029-8018(99)00066-9

Seif MS, Inoue Y (1998) Dynamic analysis of floating bridges. Mar Struct 11(1–2):29–46. https://doi.org/http://dx.doi.org/10.1016/S0951-8339(97)00012-9

Sigbjörnsson R (1979) Stochastic theory of wave loading processes. Eng Struct 1(2):58–64. https://doi.org/http://dx.doi.org/10.1016/0141-0296(79)90014-2

Taghipour R, Perez T, Moan T (2008a) Hybrid frequency–time domain models for dynamic response analysis of marine structures. Ocean Eng 35(7):685–705. https://doi.org/10.1016/j.oceaneng.2007.11.002

Taghipour R, Perez T, Moan T (2008b) Time-Domain hydroelastic analysis of a flexible marine structure using state-space models. J Offshore Mech Arctic Eng 131(1):11603. Retrieved from http://dx.doi.org/10.1115/1.2979800

Wang CM, Wang BT (2014) Large floating structures: technological advances, vol 3. Springer

Watanabe E, Utsunomiya T (2003) Analysis and design of floating bridges. Prog Struct Eng Mater 5(3):127–144. https://doi.org/10.1002/pse.151

Watanabe E, Maruyama T, Tanaka H, Takeda S (2000) Design and construction of a floating swing bridge in Osaka. Mar Struct 13(4–5):437–458. https://doi.org/10.1016/S0951-8339(00)00016-2

Chapter 15
On Stochastic Dynamic Second-Order Response Analysis of Marine Bridges

B.J. Leira

Abstract Floating bridge and submerged floating tunnel concepts have been developed for the purpose of crossing wide straits with a span length of many kilometers. The frequencies of the first dynamic modes of these structures may typically be of the order of 1 min or more. This implies that amplified dynamic response effects need to be assessed both for the wave-frequency and the low-frequency regimes. The low inherent damping levels for the low-frequency response imply that high dynamic amplification may occur. Computational methods for evaluation of the low-frequency hydrodynamic loading and the associated dynamic response are addressed in the present paper, with a focus on developing simplified procedures. These are also compared to more refined calculation methods. A specific case study is considered for the purpose of illustrating the relative effects of the respective dynamic response components. The example structure is a tunnel with a double cross-section which was developed for crossing of the Sognefjord located at the west coast of Norway.

Keywords Stochastic dynamic response • Marine bridges • Second-order loading

15.1 Introduction

Stochastic models have been successfully developed and are being applied for representation of a number of different environmental processes and the corresponding load processes. Particular examples of such models are those which are related to wave, wind and earthquake loading. The two main categories of methods for dynamic response analysis are classified as time-domain versus frequency-domain approaches. The structural response analysis in the time domain is based on a stepwise integration of the dynamic equilibrium equation. In the case of non-linear

B. J. Leira (✉)
NTNU, Department of Marine Technology, Trondheim, Norway
e-mail: bernt.leira@ntnu.no

R. Rupakhety, S. Ólafsson (eds.), *Earthquake Engineering and Structural Dynamics in Memory of Ragnar Sigbjörnsson*, Geotechnical, Geological and Earthquake Engineering 44, https://doi.org/10.1007/978-3-319-62099-2_15

structural behaviour, the incremental form of this equilibrium equation is quite commonly applied. The frequency domain approach is most relevant in connection with linear (or linearized) models of load and structural behavior, and it is generally superior in terms of computation time as well as manual processing time. In the basic work of Sigjørnsson (1979) and Langen and Sigbjørnsson (1980) response calculations for both these two categories of methods are described in relation to floating bridges with continuous pontoons.

Up to now, two floating bridges which are supported by transverse floating pontoons without any anchoring have been built in Norway. The Nordhordaland bridge, which is the longest of these floating bridges, is shown in Fig. 15.1. As part of future plans to cross the widest fjords within the so-called Ferry-free E39 project, submerged floating tunnels are also found to be highly relevant concepts in addition to such floating bridges. These tunnels can be anchored to the seabed, e.g., by means of cables or tethers. Application of surface-piercing pontoons are also being considered, which implies that such anchoring can be avoided. An example of such a submerged tunnel with a double tunnel cross-section is shown in Fig. 15.2.

In the following, focus is on second-order wave loading and the associated dynamic response. Focus is on developing simplified procedures. These are also compared to more refined calculation methods. A brief review of the response analysis for first-order wave loading is first given.

Fig. 15.1 The Norhordaland Bridge with floating pontoons (located at the west coast of Norway)

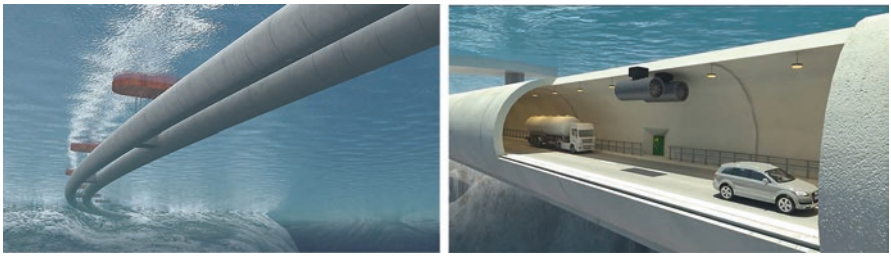

Fig. 15.2 Example of a submerged tunnel concept (Source: Norwegian Public Road Authorities)

15.2 First-Order Wave Loading and Dynamic Response

The dynamic response analysis of continuous floating bridges is outlined in the already cited work of Sigbjörnsson (1979) and Langen and Sigbjörnsson (1980). The analysis of submerged floating tunnels subjected to first-order wave loads is described in Remseth et al. (1999). Linear structural analysis can efficiently be performed in the frequency domain. The matrix which contains the auto- and cross-spectral densities of the response processes is obtained from the corresponding spectral matrix of the nodal forces due to hydrodynamic loading. This is achieved by pre- and post-multiplication with the inverse of the mechanical transfer function matrix for the structure. The spectral matrix of the hydrodynamic loading is, in turn, expressed as the product of a transfer function matrix and the auto-spectral density of the sea-elevation process. Furthermore, the wave elevation and linear structural response are typically represented as stationary Gaussian processes.

It was found that the first-order wave-induced response was strongly dependent on the main wave direction relative to the orientation of the bridge. The wave spreading around the main direction was also observed to have a significant influence (Remseth et al. 1999). If non-linear effects related to the structural behavior need to be considered, a time domain analysis approach will typically be more relevant. The frequency variation of the hydrodynamic loading (including the motion-dependent terms) also needs to be properly accounted for.

15.3 Second-Order Wave-Induced Loading

15.3.1 Basic Formulation

We first consider the slowly varying forces which are acting on the submerged tubes due to second-order effects in the incident waves. We can write the spectral density of the slowly varying force in the lateral (j = 2) and vertical (j = 3) directions as (see

Faltinsen 1990, with the resulting expression also being summarized in the feasibility study of Reinertsen et al. 2012):

$$S_{F_j}(\mu) = \frac{2\cdot\left(\rho A_c L + A_{jj}\right)}{g^2}\cdot\exp\left(-2\frac{\mu^2 d}{g}\right) \cdot\mu^4\cdot\int_0^\infty S(\omega)\cdot S(\omega+\mu)\cdot(\omega+\mu)^2\cdot(2\omega+\mu)^2\cdot\exp\left(-4\frac{\mu\omega d}{g}\right)d\omega \tag{15.1}$$

Here, S(ω) is the sea-elevation auto-spectral density. The explanations of the other quantities are as follows:

ρ = water density
L = considered length of the tunnel
A_c.L = displaced volume of water
Ajj = added mass in direction
g = acceleration of gravity
d = vertical distance between mean free surface and centerline of tunnel.

If we neglect both the hydrodynamic interactions between the tunnels and the free-surface effects, we can approximately write $A_{jj} = 2\rho\pi\cdot L\cdot\left(\frac{D}{2}\right)^2$ with D being the outer diameter of each tunnel.

The low-frequency force spectral density in the longitudinal (j = 1) and vertical (j = 3) directions of the pontoons are expressed as:

$$S_{\bar{F}_j}(\mu) = 8\int_0^\infty S(\omega)\cdot S(\omega+\mu)\left[\bar{F}_j(\omega+0.5\mu)/\zeta_a^2\right]^2 d\omega \tag{15.2}$$

Here, $\bar{F}_j(\omega+0.5\mu)$ is the mean wave force on the pontoon in direction j = 1 and 3 in regular waves with frequency, $(\omega+0.5\mu)$, and wave amplitude, ζ_a. Depending on the frequency content in the wave spectrum, we may approximate $\bar{F}_1(\omega+0.5\mu)$ with the high-frequency asymptotic value. For an accurate quantification of the slowly varying effects in the vertical direction on the pontoons, the factor, $\bar{F}_3(\omega+0.5\mu)$, needs to be calculated by a wave diffraction program such as WAMIT. However, a simplified approach can also be applied during initial studies as discussed below.

15.3.2 Simplified Calculation of Second-Order Loading

In the following, simplified formulations for the second-order loading are given together with numerical calculations. In the feasibility studies for the Sognefjord crossing (Reinertsen et al. 2012; Aas Jakobsen et al. 2012), a typical sea state with a 50 year return period is applied, which has a significant wave height of 2.1 m and a peak period of 5 s. In the following numerical studies, a JONSWAP wave spectral density is applied.

For the tunnels, a rough estimate of the standard deviation of the second-order loading can be obtained as (around) 0.00055kN/m. This implies that the corresponding extreme value (at most) will have a value of around 0.002 kN/m. This is a very small fraction (i.e. 1/400) of the loading due to water current (i.e. which has a magnitude of 0.8 kN/m) which, in turn, only gives rise to very modest load effects. Accordingly, even with a dynamic amplification factor as high as 100 (which corresponds to a modal damping level which is significantly less than a reasonable damping estimate for the present structure), the corresponding slow-drift load effects will not give rise to any significant concern.

For the pontoons, the expression within the integral above as a function of the two frequency arguments is given as:

$$I_P(\mu,\omega) = S(\omega)S(\omega+\mu)\left[\frac{\bar{F}_j(\omega+0.5\mu)}{\zeta_a^2}\right]^2 \tag{15.3}$$

In order to obtain an upper bound for the second order force, we next introduce Maruo's formula (1969), which implies that:

$$I_P(\mu,\omega) = S(\omega)S(\omega+\mu)\left[\frac{0{,}5\rho g\zeta_a^2}{\zeta_a^2}\right]^2 = S(\omega)S(\omega+\mu)\left[0.5\rho g\right]^2 \tag{15.4}$$

for a unit length in the horizontal plane. The resulting expression is, hence, to be multiplied with the square of the extension in the horizontal direction. For the horizontal (i.e. transverse) loading, this is the lateral extension of the pontoon (i.e. with B = 24 m being a typical value). However, a correction factor due to the rounded shape of the end of the pontoon also needs to be applied. (see, e.g., Faltinsen 1990):

For the low-frequency loading in the vertical direction, B is replaced by the longitudinal extension of the pontoon, H (i.e., with H = 80 m being a typical value). For this case, the vertical load level is smaller and the damping level is also likely to be higher.

The integrand, $I_P(\mu,\omega)$, which corresponds to one length unit (and excluding the factor $(0.5\ \rho g)^2$), is shown in Fig. 15.3.

The resulting second-order spectral density for the horizontal force as a function of frequency is calculated (for a representative pontoon width of 24 m), and it is

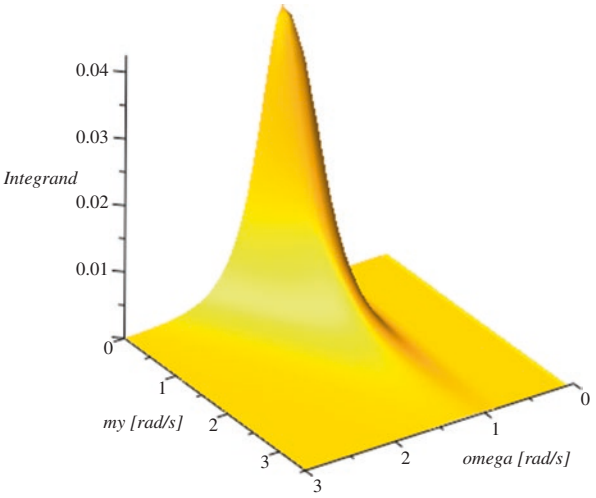

Fig. 15.3 Integrand of expression for slow-drift loading on a pontoon based on the simplified formulation

observed that the peak of the spectral density is at the zero frequency and that it decays relatively rapidly for increasing frequencies.

Based on this figure, the corresponding standard deviation of the loading is roughly estimated as 50 kN. This implies that the corresponding extreme value (at most) will have a value of around 200 kN. This is significantly larger (i.e., by a factor of 10) than the loading due to the water current (i.e. 22 kN). Furthermore, since the dynamic amplification factor for the total response is also expected to be quite significant, corresponding slow-drift load effects must be included. During an initial project phase, such a calculation can be performed by means of a modal response analysis.

15.3.3 Calculation of Second-Order Load by Numerical Panel Method

In the following, the second-order transfer functions in surge and heave for the loading on a generic pontoon are computed by application of the computer program WAMIT. Both a fixed and a completely free pontoon were analysed. The corresponding horizontal and vertical structural responses are subsequently estimated by application of the modal characteristics for the relevant bridge structure.

The geometry of a generic pontoon, which is analysed in WAMIT is shown in Fig. 15.4, including the applied mesh. A convergence study is performed in order to find a mesh size that balances accuracy versus the computational effort. It is found that a mesh size of 0.5 m provides sufficiently accurate results. The computation time is also found to be satisfactory for this mesh size.

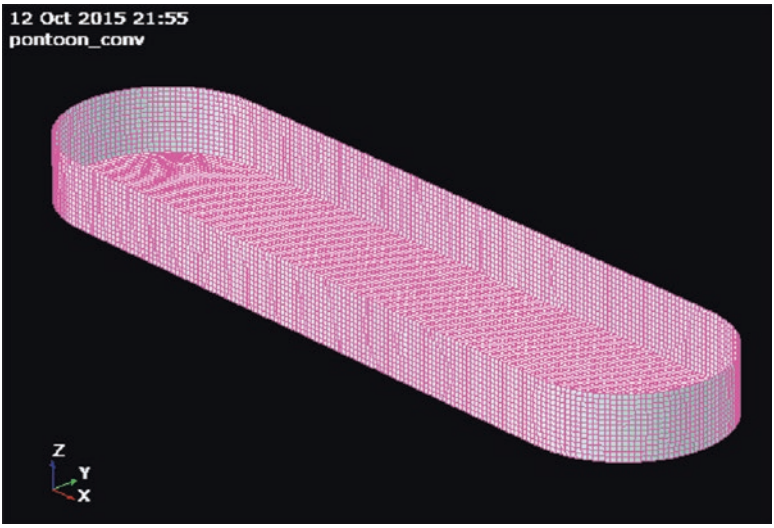

Fig. 15.4 Generic pontoon model (submerged part) for the Sognefjord tunnel bridge

For a low-frequency period of 60 s (which, e.g., corresponds to period combinations of 5 and 5.455 s), the corresponding non-dimensional surge load magnitude is 0.036. It is found that the surge magnitude is rather constant if the (low-frequency) period is kept constant at 60 s.

The magnitude of the heave transfer function, which corresponds to the same period combination (i.e. of 5 and 5.455 s), is found to be around 0.15. However, it is observed that the force magnitude varies more for the heave degree of freedom than for the surge motion even if the (low-frequency) period is kept constant.

It is noted that the dimensionless values above for both the surge and heave degrees of freedom need to be multiplied with the factor $\rho g L$ (where $L = 80$ m is the length of the pontoon) in order to obtain the corresponding physical force magnitude. Accordingly, the magnitude becomes 2.9 ρg for the surge force and 12 ρg for the heave force magnitude.

In reality, the pontoons will not be completely fixed. By assuming that they are completely free to move, the maximum possible effect of flexibility can be quantified. The resulting, dimensionless modulus for this case regarding the second-order transfer functions for the surge and heave force is shown in Fig. 15.5. The new magnitudes, which correspond to a period pair of 5 and 5.455 s, are now 0.045 for the surge force and 0.16 for the heave force, i.e., somewhat larger than for the completely fixed case.

The second-order surge loading for the free versus the fixed pontoon is somewhat increased (i.e., the former is increased by around 25% as compared to the former), while the heave force is only 6% larger.

In Fig. 15.6, the mean drift forces in surge and sway are shown for a free-floating pontoon and a wave angle of 20° relative to the symmetry line of the pontoon as

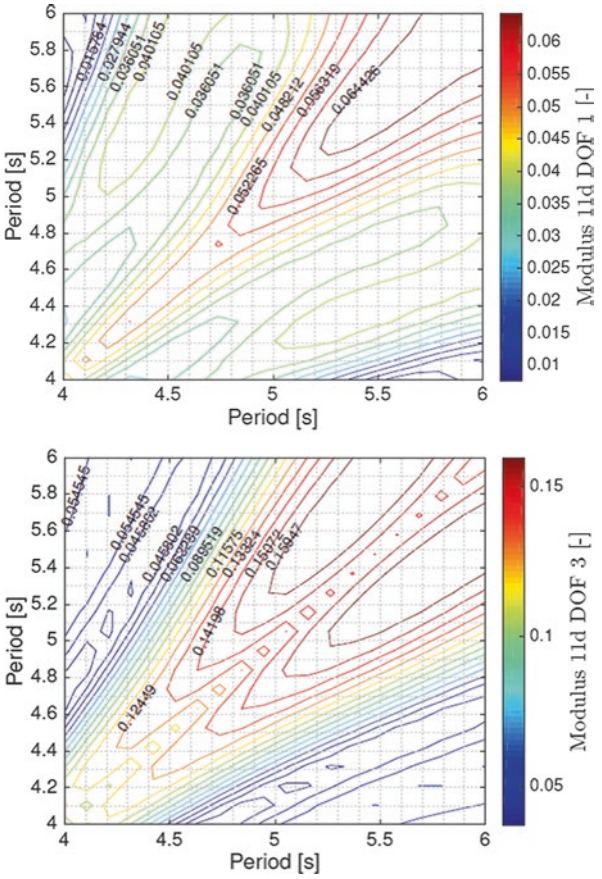

Fig. 15.5 Modulus of transfer function for second-order low-frequency loading on free-floating pontoon (*Left*: Surge. *Right*: Heave)

functions of the wave period. Based on these results, the present load magnitude can be assessed in relation to the upper bound that was applied in conjunction with the simplified calculations according to Eq. (15.4).

It is seen from the figure that the ratio between the load calculated by the refined calculation (i.e., for the free-floating pontoon) and the simplified model (i.e., which was 0.5·24 m ρg if the bow-shape correction is excluded) is around $r_{surge} = (0.065 \cdot 80./12.) = 0.43$ for the surge degree of freedom. This is without inclusion of any bow-shape correction factor. If a relevant bow-shape correction factor of 0.5 is applied, this ratio increases to $0.86 \approx 0.9$ which implies that the simplified calculations will only produce modestly conservative results (i.e. of the order of 10–15%). However, it should be noted that the magnitude of the bow-shape reduction factor will depend somewhat on the wave direction.

The corresponding magnitude for the heave degree of freedom, the mean drift force, is around twice as high as for the surge component. The result for the free-floating pontoon is a little higher than for the fixed pontoon and is, hence, applied here in order to be conservative. For this case, the force ratio is computed as

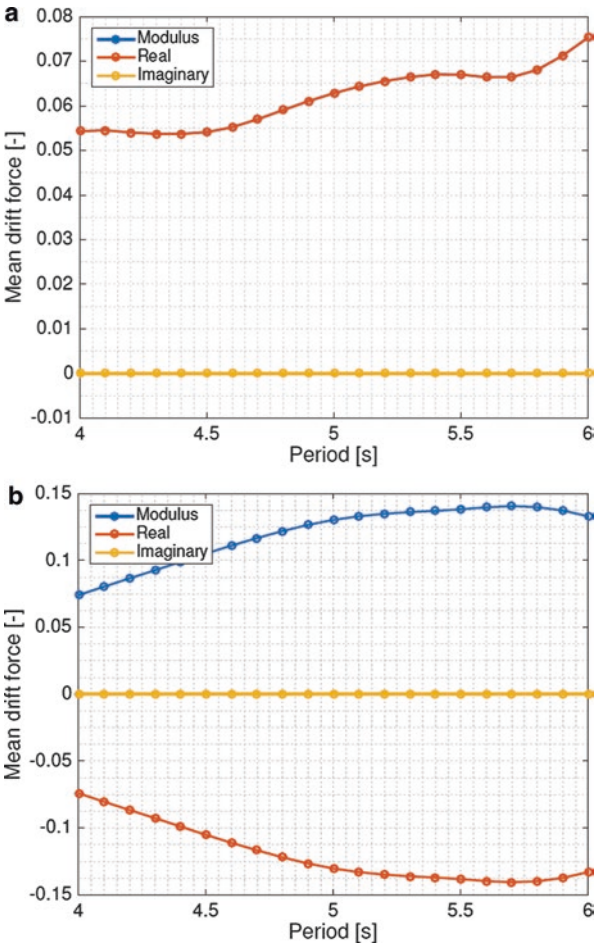

Fig. 15.6 Mean drift force in surge (**a**) and heave (**b**) for a floating pontoon. Wave heading is 20 degrees relative to the longitudinal symmetry line of the pontoon

r_{heave} = (0.138·80./12.) = 0.92 for the heave degree of freedom. Note that, if instead of the pontoon width, the pontoon length is applied in the simplified calculation, the ratio for the heave degree-of-freedom would become r_{heave} = (0.138·80./40.) = 0.28, which is much different than 1.0.

It is believed that the fixed condition will be closer to the real physical condition than the completely free condition (depending somewhat on the stiffness properties of the bridge). An adequately accurate iteration could be performed in the following way: (i) The extreme response displacements for the pontoons along the bridge could be calculated by applying the force magnitudes that correspond to the completely free condition. This amplitude could be compared to the motion amplitude which would result for the freely floating pontoon. (ii) An interpolation of the loading between the fixed and free conditions could subsequently be performed. (iii) A new response analysis would next be carried out with the adjusted (i.e. interpolated)

loading. (iv) The resulting new response amplitude would lead to a new interpolated loading and so on until convergence is achieved.

15.4 Response Analysis Based on Modal Superposition

The spectral density of the modal load in the horizontal direction is obtained by performing a summation across all the N pontoons along the bridge. By assuming that all the pontoons have identical loading in the horizontal direction, the cross-spectral density can be written as:

$$S_{F,Horiz}(\mu) = \sum_{i=1}^{i=N} \left\{ \sum_{j=1}^{j=N} S_{F_{Ai}F_{Aj}}(\mu) \cdot \exp\left[i\{\Delta_{ij}\} \right] \cdot \left[\left(\varphi(x_i) \cdot \varphi(x_j) \right) \right] \right\} \tag{15.5}$$

where the relevant mode shape is given by the mode shape function, φ(x), in the expression above, and the x_i, i = 1..N and x_j, j = 1. N are length coordinates along the bridge (which correspond to the positions of the pontoons); $S_{F_{Ai}F_{Aj}}$ is the (real-valued) cross-spectral density of the load amplitudes at the two pontoons for the case of in-phase loading. If the loads on the two pontoons are identical, we have $F_{Ai} = F_{Aj}$, which implies that $S(F_{Ai}\, F_{Aj}) = S(F_{Ai})$. A phase difference, Δ_{ij}, is included as part of the cross-spectral density due to the relative distance between the pontoons (i.e., in the direction of wave propagation). Note that the imaginary part of the expression in Eq. (15.9) will disappear after performing the double summation due to the hermitean symmetry of the cross spectral density with respect to the sign of the phase difference (i.e., the imaginary part of the terms ij will cancel the imaginary part of the term ji during the summation process).

In general, the spectral density of the second-order modal load will depend on the main direction of the long-crested wave propagation. An upper bound for the modal load is obtained by assuming that the phase angle is such that the load intensity varies along the bridge in perfect phase alignment with the mode shape. This implies that the factor at each pontoon becomes just the squared value of the mode shape. The resulting expression for the upper bound is then obtained as:

$$\begin{aligned} S_{F,Horiz}(\mu) &= \left\{ S_{F_iF_i}(\mu) \cdot \sum_{i=1}^{i=N} \left[\left(\varphi(x_i)^2 \right) \right] \sum_{i=1}^{i=N} \left[\left(\varphi(x_i)^2 \right) \right] \right\} \\ &= S_{F_{Pontoon}}(\mu) \cdot \sum_{i=1}^{i=N} \left[\left(\varphi(x_i)^2 \right) \right] \sum_{i=1}^{i=N} \left[\left(\varphi(x_i)^2 \right) \right] \end{aligned} \tag{15.6}$$

where the first factor is just the auto-spectral density for the horizontal force of a single pontoon.

The maximum displacement and the maximum internal bending moment are next computed by application of modal analysis. The sum in the expression above

is equal to zero for the first horizontal mode for long-crested waves which are propagating at 90° (i.e., transverse) to the bridge secant. This is based on the observation that the first mode consists of two half waves (i.e., which is caused by the bridge having an arch-shape in the horizontal plane). This implies that the mode shape is antimetric. For inclined wave directions, the modal loads for the antimetric mode shapes are non-zero. The modal load will, hence, obtain the maximum value at some inclined propagation angle. This is studied in more detail as part of the case study below.

For a lightly damped structure (i.e. with $\xi_j = 0.015$), we obtain the following expression for the variance of the modal displacement for a particular mode, see, e.g., Lin (1967), Faltinsen (1990):

$$\sigma^2_{Displ,Horiz} = \frac{\pi \cdot S_{F,Horiz}\left(\omega_j\right)}{4\xi_j m_j^2 \omega_j^3} \tag{15.7}$$

where m_j is the modal mass for the relevant horizontal mode shape; ω_j is the corresponding natural frequency (in radians per second); and ξ_j is the modal damping ratio. Similar expressions to Eqs. (15.6) and (15.7) also hold for the vertical displacement corresponding to the vertical mode shapes.

The total response variance (for the horizontal motion) due to secondorder low-frequency loading can subsequently be obtained (by neglecting the cross-terms between the modes) by a direct summation of contributions from all the relevant modes. The expected extreme response value for a given duration can then be obtained by assuming a specific probability distribution for the response peaks.

The first horizontal mode for a curved bridge consists of two half waves (see also the case study below), while the second horizontal mode consists of three half waves. The modal mass and modal stiffness are calculated by a summation of all the different contributions from the bridge tunnels, the transverse connecting members, the vertical columns and the pontoons. Each contribution is multiplied by the square of the mode-shape amplitude at the relevant position of the structural component. For the tunnels, an integration across the length of the bridge is required.

The pontoons will only contribute to the modal stiffness in the vertical direction, but not in the horizontal direction. The reason is that they are treated as rigid bodies and will only resist displacement in the vertical direction due to the corresponding change of buoyancy. In the horizontal direction, there is no such effect and hence no stiffness contribution will arise unless the bridge is equipped with a mooring system.

The modal mass for both of the two, first horizontal modes is herein calculated from the following expression:

$$\begin{aligned}\bar{m}_i = m \int_0^L \left\{\left(\varphi_{i,horizontal}\left(x\right)\right)\right\}^2 dx + \sum_{j=1}^{N} M_j^P \cdot \left\{\left(\varphi_{i,horizontal}\left(x_j\right)\right)\right\}^2 \\ + \sum_{k=1}^{2N} M_k^C \cdot \left\{\left(\varphi_{i,horizontal}\left(x_k\right)\right)\right\}^2\end{aligned} \tag{15.8}$$

where i = 1 for the first mode, and i = 2 for the second mode. The superscript P designates pontoon, while superscript C refers to the vertical columns. The corresponding modal stiffness for the two horizontal modes is, herein, similarly obtained as:

$$\bar{k}_i = EI \int_0^L \left\{ \left(\frac{d^2}{dx^2} \varphi_{i,horizontal} \right) \right\}^2 dx \tag{15.9}$$

where there is no contribution from the pontoons or the columns for this case. It is assumed that the sideways displacement of the columns follow that of the bridge tunnel. For the vertical direction, the contributions from the pontoons need to be included due to the vertical spring effect caused by varying submergence and, accordingly, varying buoyancy.

In the time domain, the second-order transfer function can be applied in order to obtain a time series of the second-order loading. These are expressed in the following form (see Faltinsen 1990):

$$\begin{aligned} F_i^{SV} = \sum_{j=1}^{N} \sum_{k=1}^{N} A_j A_k \Big[& T_{jk}^{ic} \cos\left\{ \left(\omega_k - \omega_j \right) t + \left(\varepsilon_k - \varepsilon_j \right) \right\} \\ & + T_{jk}^{is} \sin\left\{ \left(\omega_k - \omega_j \right) t + \left(\varepsilon_k - \varepsilon_j \right) \right\} \Big] \end{aligned} \tag{15.10}$$

where A_j and A_k are the wave amplitudes which correspond to frequencies, ω_j and ω_k; ε_j and ε_k are the phase angles that correspond to the same frequency components; and T_{jk}^{ic} and T_{jk}^{is} designate the cosine and the sine terms of the second-order transfer function for the two wave components, respectively.

The so-called Newman approximation (which is widely applied) is based on the following simplification of the terms which are located away from the diagonal of the second-order transfer function:

$$T_{jk}^{ic} = T_{kj}^{ic} = 0.5\left(T_{jj}^{ic} + T_{kk}^{ic} \right) \tag{15.11}$$

and

$$T_{jk}^{is} = T_{kj}^{is} = 0 \tag{15.12}$$

A step-wise dynamic response analysis is subsequently performed and the corresponding time series of relevant structural response quantities is obtained.

15.5 Case Study: The Sognefjord Bridge

The span length of the proposed Sognefjord bridge is 3700 m. A finite element beam model of the tunnel bridge is established in the computer program Abaqus, see the left and middle part of Fig. 15.7.

The values of the two, first horizontal modes are 57.6 and 30.4 s, respectively. The two, first horizontal modes have periods of 22.5 and 18.0 s. Modes five to ten have periods in the range from 17.9 to 15.9 s, see Leira (2016). The two, first horizontal mode shapes are illustrated in the right part of Fig. 15.7. The two, first vertical modes have eigenperiods of 57.6 and 30.4 s, respectively, while the two, first vertical modes have periods of 22.5 and 18.0 s. For the first and second sine-shaped horizontal modes, the sum for the modal displacement is evaluated based on the expressions which were presented above (also applying the assumption of a lightly damped response).

The response analysis can also be performed in the time domain by a step-by-step integration. A diagram showing the corresponding variation of the modal load as a function of the main wave direction is shown in Fig. 15.8. The highest response level is observed for a wave direction of 18 degrees.

Response analyses have been performed for the example bridge structure both in the time and frequency domain based on a modal approach. From the simplified analysis, it is estimated that the magnitudes of the displacement and the bending moment due to the horizontal response are around three times as high as the first order wave-induced response that is computed as part of the feasibility study (Reinertsen et al. 2012). For the vertical response, the magnitudes are around twice those for the corresponding wave-induced response, levels. The computed results are based on a total damping value which is 1.5% of the critical damping. The damping level is very important in relation to the response magnitude, as the response amplitude is inversely proportional to the square root of the non-dimensional damping level.

More accurate analyses are performed with respect to the second-order excitation level by application of the computer program WAMIT as outlined above. It is found that the low-frequency response in the horizontal direction is somewhat reduced as compared to the simplified analysis. However, the vertical motion is found to be of the same order of magnitude as that estimated by the simplified

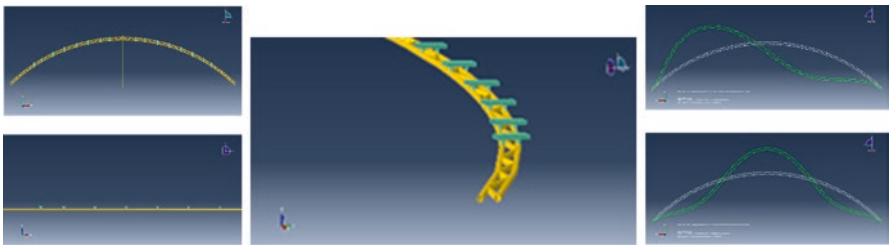

Fig. 15.7 *Left* and *middle part*: General layout of bridge and numerical model. *Right part*: First two horizontal mode shapes

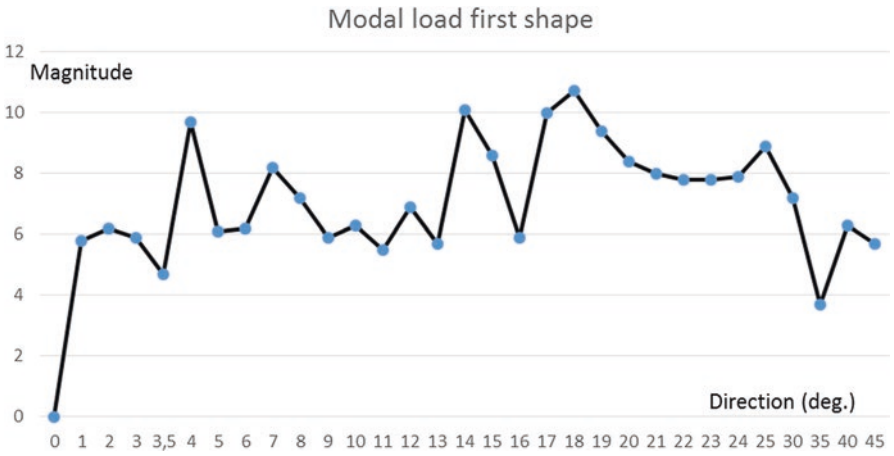

Fig. 15.8 Magnitude of modal load as a function of wave direction for mode shape number 1

Table 15.1 Estimated horizontal and vertical second-order displacements and bending moments for worst direction with long-crested waves

Response component (direction of displacement)	"Refined estimate" Displacement	"Refined estimate" Bending moment
Horizontal (first mode)	0.50 m	3.2 GNm
Vertical	0.55 m	1.55 GNm

approach. A summary of the estimated values of the extreme displacements and bending moments for the horizontal and vertical second-order motions are provided in Table 15.1.

Comparing the magnitudes of the second-order bending moments to those from the first-order analysis, which are reported in (Reinertsen et al. 2012), it is found that the bending moment due to the horizontal motion is around 140% of the first-order, wave-induced bending moment. By including the second mode, this would increase significantly. For the bending moment due to vertical motion, the corresponding value is around 180%, i.e., significantly larger than the first-order, wave-induced response.

The damping will have contributions of both the structural and hydrodynamic type. The latter can further be split into different sources such as linear potential damping, viscous damping and wave-drift damping. Relevant expression, for the wave-drift damping are found in Faltinsen (1990). Additional damping for the submerged bridge can further be achieved by application of, e.g. tuned-mass dampers or sloshing dampers if the dynamic amplification level is found to be too high. It is likely that the damping is higher in the vertical direction than for the horizontal direction, which clearly would reduce the response levels somewhat as compared to the present estimates.

15.6 Conclusions

Simplified formulations for slow-drift excitation of a submerged tunnel bridge concept with pontoons at the sea surface have been summarized. It was found that the results from the simplified calculations were in reasonable agreement with those obtained by more refined methods.

A specific tunnel bridge concept has been considered in more detail, i.e. the one proposed for the Sognefjord crossing. The damping level for the relevant vertical modes could well be higher than for the lowermost horizontal modes due to the corresponding shorter natural periods (which are of the order of 20 s). This has not been taken into account in the present analysis. Furthermore, the effects of wave spreading are presently not accounted for. Accordingly, the low-frequency response level is expected to decrease somewhat as compared to the presently estimated values.

Acknowledgements The support from the Norwegian Road Authorities is greatly acknowledged. Professor Odd Faltinsen is acknowledged for valuable comments and discussions. The work in connection with the numerical bridge model in Abaqus by Master student Senthuran Ravintrakumar is acknowledged. Phd student Jan-Tore H. Horn is acknowledged for the WAMIT analysis and providing the corresponding results.

References

Aas-Jakobsen AS, Johs Holt AS, Cowi AS, NGI AS, Skanska AS (2012) Sognefjorden feasibility study of floating bridge. Document no.: 11258–03

Faltinsen OM (1990) Sea loads on ships and offshore structures. Cambridge University Press, Cambridge

Langen I, Sigbjörnsson R (1980) On stochastic dynamics of floating bridges. Eng Struct 2(4):209–216

Leira BJ (2016) First- and second-order wave-induced dynamic response of submerged floating tunnels. In: Proceedings of the OMAE2016, Busan, Korea

Remseth S, Leira BJ, Okstad KM, Mathisen KM, Haukås T (1999) Dynamic response and fluid/structure interaction of submerged floating tunnels. Comput Struct 72:659–685

Lin YK (1967) Probabilistic theory of structural dynamics. MCGraw-Hill Inc., New York

Maruo H (1969) The drift of a body floating in waves. J Ship Res 4:1–5

Reinertsen AS, Tech Dr, Olav Olsen AS (2012) Feasibility study for crossing Sognefjorden: submerged floating tunnel. Document no.: 11744-ROO-R-001

Sigbjörnsson R (1979) Stochastic theory of wave loading processes. Eng Struct 1(2):58–64

Part III
Seismic Risk Assessment, Communication, Perception, and Management

Chapter 16
New Tools for the Analysis of the Generalized Impact of Earthquake Events

Carlos Sousa Oliveira, Mónica A. Ferreira, F. Mota Sá, and J. Bonacho

Abstract Earthquakes and tsunamis continue to be some of the most disastrous natural events. In this review paper, we present the work developed by the Seismic Risks Group of Instituto Superior Técnico (IST) in the last decade, with emphasis on the performance indicators proposed to deal with the effects of natural disasters. Starting with an appraisal of the world earthquake impacts since 1900, the text summarizes the most relevant impact indicators, namely, SIRIUS and disruption indexes (DI) for the urban and industrial fabrics, which includes cascading effects. Also, the early stage of the analysis of multi-hazard, namely for shaking and tsunami events, is reviewed. Finally, we use these impact indicators in conjunction with performance indicators (RRW – risk reduction worth and RAW – risk achievement worth) to communicate the risk to the population and mitigate the action of future events. Several conclusions can be taken from the work developed. The most important is that earthquake impacts cannot be measured only by human losses and losses to property, but indirect and cascading effects also play a huge role in the global impact, especially in moderate to large events.

Keywords Earthquake impacts • Cascading effects • SIRIUS • Disruption Index • Performance indicators

16.1 Introduction

Earthquakes and tsunamis continue to be some of the most disastrous natural events. Historical data shows that their rates of occurrences are very variable from region to region, depending on where you are on the surface of earth, as well as very variable temporally, but nevertheless, cause great impact on the population, with loss of lives, economic losses, social and psychological distress, etc. It is very difficult to

C.S. Oliveira (✉) • M.A. Ferreira • F. Mota Sá • J. Bonacho
Instituto Superior Técnico (IST) and CERIS, Universidade de Lisboa, Lisbon, Portugal
e-mail: csoliv@civil.ist.utl.pt

R. Rupakhety, S. Ólafsson (eds.), *Earthquake Engineering and Structural Dynamics in Memory of Ragnar Sigbjörnsson*, Geotechnical, Geological and Earthquake Engineering 44, https://doi.org/10.1007/978-3-319-62099-2_16

measure the impact of such events and to compare situations because impacted zones have different cultural, economic and other civilizational characteristics. In general terms, the objectives of the scientific communities and entities responsible for mitigating risks in the areas of higher impact is to anticipate the effects of future events, develop policies and implement actions to reduce vulnerabilities of the existing stock of housing and infra-structures, and to build back better either the damaged stock or the new construction. Worldwide, many advancements have been achieved, especially after the occurrence of a big event which, as a whole, brings a lot of the knowledge. However, in many instances, earthquakes and tsunamis keep creating great impacts which are not acceptable to our modern societies of the twenty-first century. Why is this contradiction still so strong? With other types of natural catastrophes: floods, tornados, hurricanes, volcanic eruptions, landslides, heat waves, etc., science, technology and entities responsible for implementing the accumulated knowledge have made more advancements in reducing some of the impacts on the communities.

To mitigate the impact of an adverse event, it is first and foremost important to understand and quantify the expected impact, not only in the scientific context, but also in a more holistic perspective which can be shared by various stakeholders that are responsible for risk mitigation. Development of such an understanding and indicators for holistic quantification of impacts of earthquakes and tsunamis has been actively pursued by the Seismic Risks Group of Instituto Superior Técnico (IST) in the last decade. This chapter presents an overview of these efforts and highlights some of the most important achievements. Additional details for interested readers are provided in the numerous references listed at the end of the chapter.

16.2 Some Numbers on Impacts

Earthquakes and tsunamis keep on being the natural events with higher impacts, even though they are not the most frequent. Figure 16.1 shows that meteorological and hydrological events are the more common events according to statistics of the last 35 years, as reported by insurance companies. It is important to note that, while the number of disastrous geophysical events has remained more or less steady, the frequency of other events has increased over time, especially the meteorological events.

To provide a scenario of the latest condition, we present the following quote from an insurance company.

> After three years of relatively low nat cat losses, the figures for 2016 are back in the mid-range, where they are expected to be. A number of devastating earthquakes and powerful storms made 2016 the costliest twelve months for natural catastrophe losses in the last four years. Losses totalled US$ 175bn, more than two thirds above the previous year and nearly as high as in 2012 (US$ 180bn). Uninsured losses remained substantial at 70%. Insured losses came to US$ 50bn. (Source: http://www.munichreamerica.com)

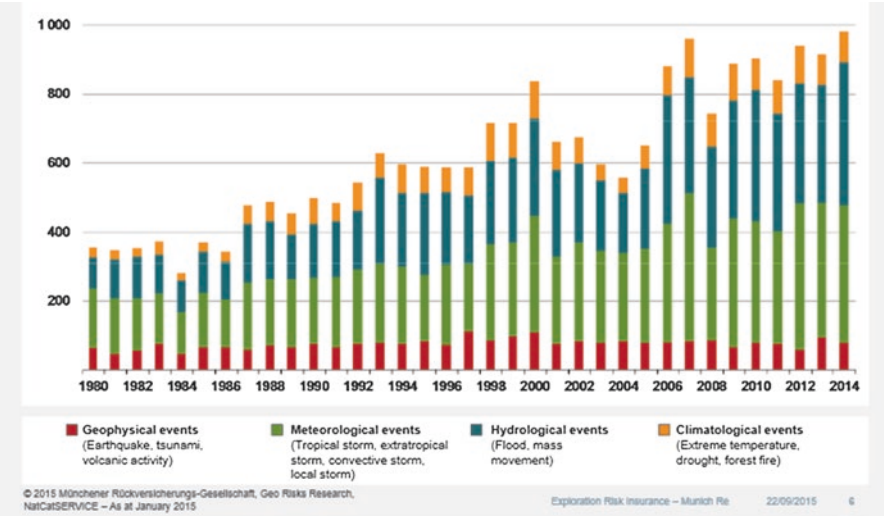

Fig. 16.1 Number of natural events worldwide (1980-2014) causing important economic losses. (Source: http://www.munichreamerica.com)

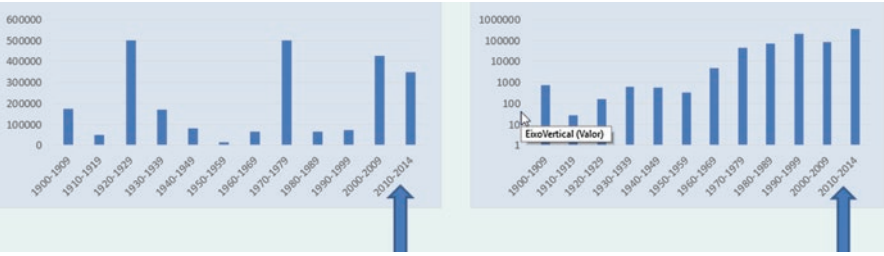

Fig. 16.2 Evolution of losses since 1900: (**a**) lives lost/decade, (**b**) economic losses normalized to 1997 values, in 10^6 $US dollars/decade (Updated from Oliveira et al. 2014)

Looking only at geophysical events (earthquakes and tsunamis), the first impact indicator is the size of population affected and economic losses. In Fig. 16.2, we present the statistics of human and economic losses since 1900. From the geographical distribution of losses, we can observe that, in most cases, a large number of human losses has occurred in less developed countries. The case of Tohoku earthquake and tsunami (2011) in Japan was an exception to this assertion. On the contrary, the economic losses come essentially from the more developed economies. In the twentieth century and the first 15 years of the twenty-first century, the total number of victims per decade shows a tendency of clustering around a few large events: Kanto series in 1923 in Japan, Tangshan in 1976 in China and the ones in the first years of the twenty-first century. The overall average has remained almost constant, and if we consider data per world population, some non-significant decrease has taken place. As far as economic losses, we keep seeing an increasing trend

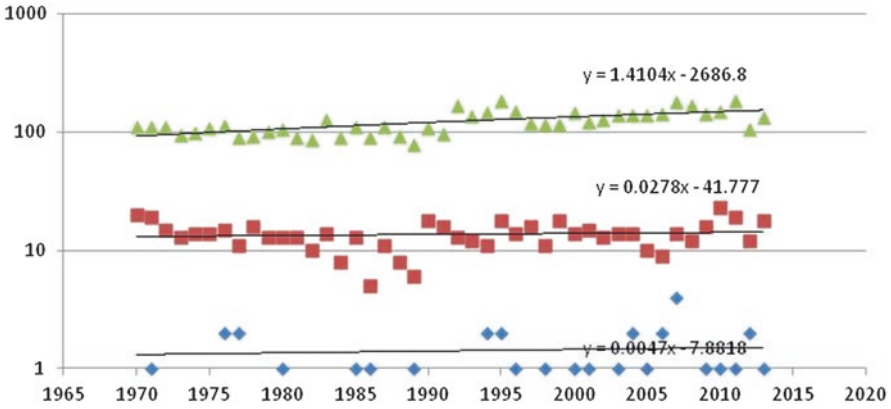

Fig. 16.3 Annual number of earthquakes in the last 43 years in the World by classes of magnitude, 6 < M < 6.9, 7 < M < 7.9, 8 < M. (USGS, 2012, EMSC, 2014) (From Oliveira et al. 2014). Regression equations are valid only for the period under analysis

(ordinates are in a log scale). There are many factors contributing to this increase, namely, new urbanizations leading to higher exposure, higher prevalence of insurance leading to more accurate loss estimates in recent times and the presence of more costly and hazardous industries and facilities.

Oliveira et al. (2014) present a tentative, first correlation of human casualties with earthquake magnitude, and it is very clear that no correlation exists in the last 15 years, even though some trends are present. If we look at the annual number of earthquakes in the last 43 years in the world by classes of magnitude (Fig. 16.3), it is apparent that the frequency of earthquakes has not increased significantly. This pattern is present in the last 2 years. We can say that even small events of magnitude 5.5–6.5, if located nearby populated areas, can cause a large impact, as has happened in the last 20 years in Italy where a series of these type of earthquakes have taken place (Umbria-Marche 1997, L'Aquila 2009, Emilia-Romana 2012 and Amatrice-Norcia 2016).

In Europe, the spatial distribution of different types of natural disasters is very variable. Earthquakes happen in the southern part, whereas hydrological (floods essentially) events are more frequent in the northern parts. Looking to the risk perception in the EU (Fig. 16.4), we understand that earthquakes are only in the 4th place, with floods in the 1st place followed by storms and forest fires. There does not seem to be much concern about tsunamis, which are, nevertheless, very relevant in countries such as Portugal and Spain.

It is very interesting to observe that the economic losses can be split into direct and indirect losses, indirect losses being due to loss of functions or interruption of activities. According to Daniell et al. (2012), there is an interval of ±10 times the mean value between direct and indirect losses due to natural disasters since mid-nineties. So, we cannot neglect this reality (Fig. 16.5).

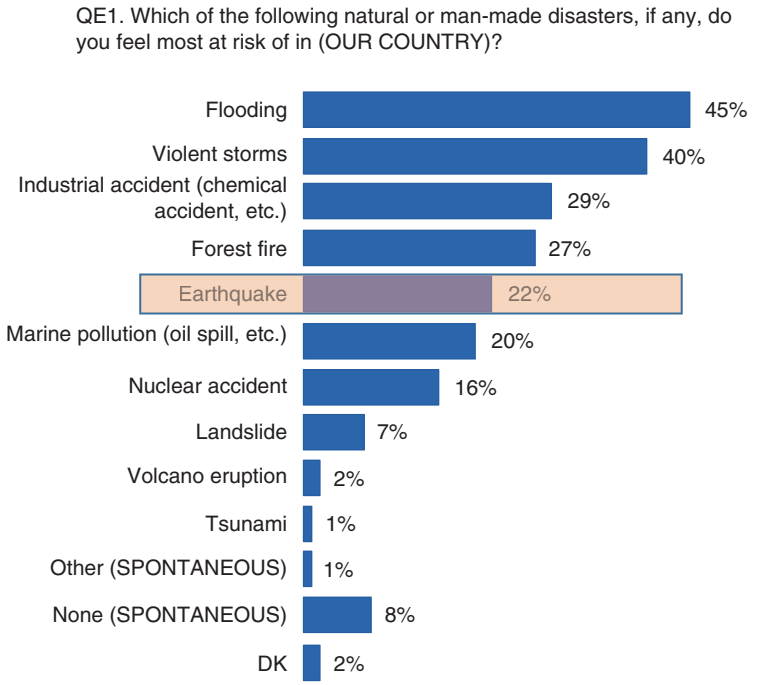

Fig. 16.4 Risk Perception in the EU: "Flooding and storms are the disasters that EU27 residents fear the most" (Special Eurobarometer, European Commission 2009)

Non-structural damage is another topic of great interest, especially for small to moderate earthquakes because they can cause large impacts in population evacuation (in conjunction with Early Warning) and injures. The KnowRISK (2016) EU Project aims at defining the rules for better behaviour of the population to be prepared for non-structural damage and better communication practices.

After some years visiting real earthquake scenarios around the world (Ferreira 2012), it became clear, as nowadays is well known, that earthquake impacts cannot be measured only by human losses and losses to property, but that indirect and propagation effects, many of them due to equipment damage (transformers, piping, life-lines, etc.) or non-structural components, acting as catalysts (amplifiers), play a huge role in the global impact.

16.3 Evolution of Seismic Scenario Simulators

Predicting what may happen during future events in order to be prepared and understand which policies are best to follow, seismic scenario simulators were developed since the early 2000s by different schools of thought. Table 16.1 presents a synopsis of the most renowned ones, adapted from Silva et al. (2013).

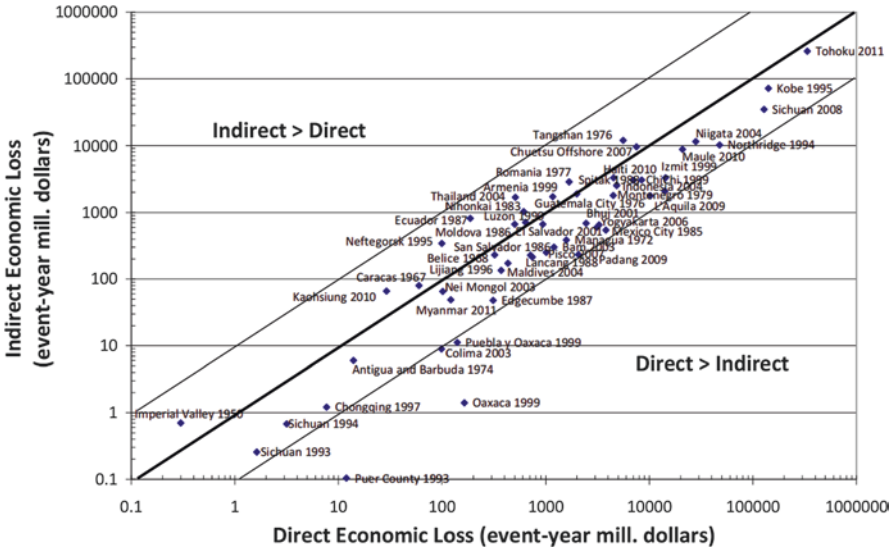

Fig. 16.5 Direct vs. indirect economic losses from selected events in event-year million $US within the CATDAT Damaging Earthquakes Database (Daniell et al. 2012)

Other earthquake scenario simulators not referred in Table 16.1 were also developed, some for rapid evaluation of impacts after the occurrence of an event. ShakeOut and ShakeMaps are available to estimate ground motion. PAGER (Jaiswal and Wald 2012), a USGS tool that estimates human and economic impact of earthquake occurrences anywhere around the world, is another example.

Most of these simulators have, as output (objectives), the population affected and the inflicted damage (Fig. 16.6). They are composed of several modules, aggregated into two groups as shown in the figure, with seismic source definition, the propagation of waves, site effects in one group and with building stock, networks and critical infrastructures in the other group. Some of the simulators look more to the geophysical process, whereas others look more to the building stock and their typologies, inventories, vulnerabilities and fragilities.

Based on the general outline of Fig. 16.6, QuakeIST (Mota de Sá et al. 2016) was developed. The special feature of this development is that it models the propagation effects of damages between different physical elements, considering the subsequent loss of function which has a cascading consequence on various sectors of a society, leading to disruption.

16.4 Impact Indicators

There are several levels of impact indicators as referred to in Sendai (2015) framework (Point 18). Most of them are of the first order, meaning that they only refer to a single variable as shown in Sect. 2, above.

Table 16.1 Synopsis of seismic risk software packages

Software	Institution	Programming language	Applicability	Availability	Graphical user interface	Type of calculators
ELENA	NORSAR	MATLAB/C	User-defined	OS	Yes	SCN/SDA/PEB
EQRM	GA	Python	User-defined	OS	No	SCN/SDA/PEB
ELER	KOERI	MATLAB	User-defined	SA	Yes	SCN/SDA
QLARM	WAPMERR	Java	World	SC	Yes	SCN/SDA
CEDIM	CEDIM	Visual Basic	User-defined	SC	Yes	SCN/SDA/CPB
CAPRA	World Bank	Visual Basic	Central America	SC	Yes	SCN/PEB
RiskScape	GNS	Java	New Zealand	SA	Yes	SCN/SDA
LNECLoss	LNEC	Fortran	Portugal	SC	No	SCN/SDA
MAEviz	MAE Center	Java	User-defined	OS	Yes	SCN/SDA/CPB
OpenRisk	SPA Risk	Java	USA	SA	Yes	CPB/BCR
OpenQuake	GEV1	Phyton	World	OS	Yes	SCN/SDA/PEB /CPB/BCR

Adapted from Silva et al. (2013)
OS open-source (code on a public repository), *SA* standard application (available under request), *SC* source code (available under request)
SCN scenario risk, *DAS* scenario damage assessment, *PEB* probabilistic event-based risk, *CPB* classical PSHA-based risk, *BCR* benefit-cost ratio

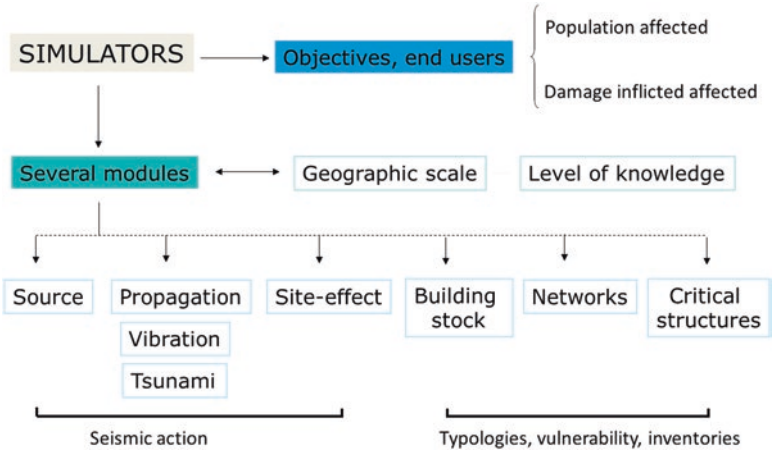

Fig. 16.6 Schematic structure of earthquake scenario simulators (From Oliveira et al. 2014)

We will be presenting the concepts of SIRIUS, urban and industrial DIs for shaking scenarios and how to incorporate them to include multi-hazard scenarios.

16.4.1 SIRIUS

The concept of SIRIUS is one of the second level of importance, because it deals simultaneously with two variables that conveniently and simply translate earthquake risk (eri), one referring the vulnerability of the existing housing and the other reflecting the human concentration.

In this framework, rrd represents the risk due to buildings vulnerability as the major variable responsible for destruction. Risk due to human concentration, as a proxy (indirect indicator) of physical, functional and social vulnerability to major disruptive events, is represented by rhc. Earthquake risk is then a function of these two major variables:

$$\mathrm{eri} = \mathrm{f}\left(\mathrm{rrd},\mathrm{rhc}\right)$$

It is organized into several categories which define the level of impact for that event. Those two variables were calibrated to feed the SIRIUS scale, as shown in Fig. 16.7 (Mota de Sá et al. 2013). This impact indicator is of great interest in selecting the areas of higher problems in urban areas.

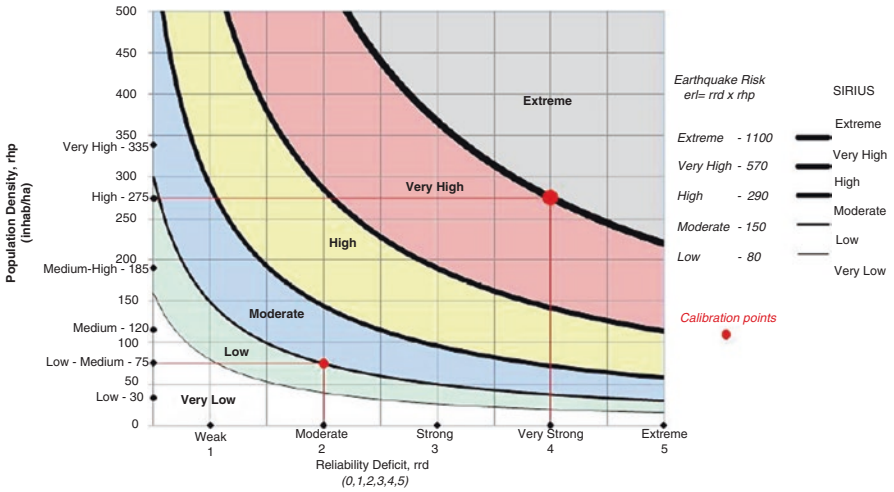

Fig. 16.7 The SIRIUS scale (From Mota de Sá et al. 2013)

16.4.2 Earthquake Simulations Including Cascading Failures (DI)

Sophisticated predictions of the seismic response of buildings and facilities can be simulated nowadays and be used in loss analysis, where the losses are calculated using measures such as repair cost, repair duration and loss of life. One limitation with this type of analysis is that it does not account for the susceptibility of infrastructure systems to decreasing their reliability, which frequently leads to cascade failures. Although such quantitative analyses can be highly robust, they require significant levels of information and can only be applied in a small number of situations, usually in the assessment of a small number of elements.

In this context, the disruption index (DI) (Oliveira et al. 2012, Ferreira 2012, Ferreira et al. 2013) can be used to estimate the potential impacts from earthquakes or other hazardous events, integrating physical, human, social, environmental and economic damage. The analysis proceeds by determining how the top failures can be caused by individual or combined lower-level failures or events. It is a useful tool to evaluate the costs and benefits of risk reduction measures, as well as preparedness and response. It is also desirable for other purposes, such as risk financing.

The disruption index is derived from established and classified functions using dimensions of fundamental human needs: environment, housing, food, healthcare, education and employment. Each dimension contains the functions (service components) that impact welfare and urban life aspects like water, sanitation, telecommunications, electricity, transportation networks and existence of debris. Figure 16.8 illustrates the relationship between these data elements.

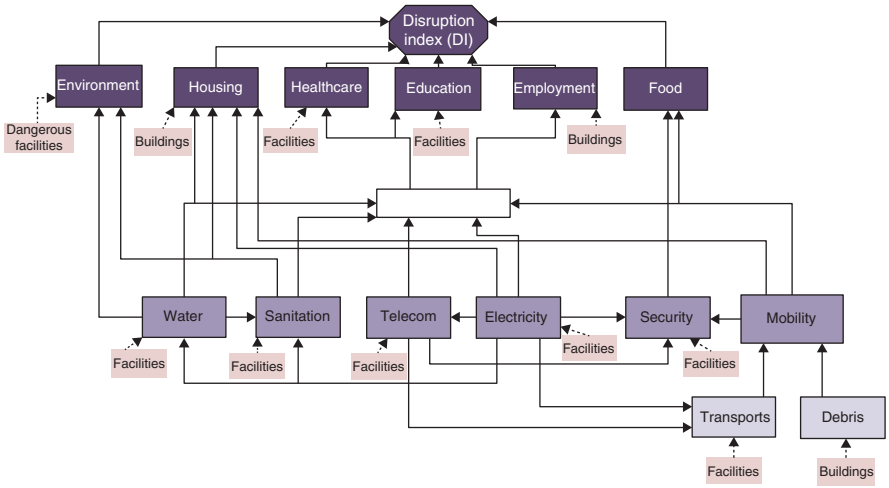

Fig. 16.8 Graph representation of vital or urban functions and their dependencies and incidences (From Oliveira et al. 2014)

During and after an earthquake, several services are unavailable to end users, thereby causing service disruption, and consequently, the failure of main urban functions such as:

- Disruption of water service for drinking/domestic use and for irrigation purposes, hampering agriculture,
- Disruption of electricity, impacting security and the provision of health and other essential services,
- Health problems (degrading health conditions) due to the lack of accessibility to health services providers,
- Hindered access to and from homes to jobs, markets and other communities,
- Disruption of communication within and between communities, impacting security, for example,
- Increased prices of commodities and transportation,
- Disruption of communal functions (social, economic and religious) and so on.

To solve this problem, we proposed to assemble the so-called social impact indicators and create a graph as described in Fig. 16.8.

The main goal of the DI is to understand the relationship between buildings, facilities, utilities, networks and their interdependencies. The destruction or degradation of which, or unavailability for a long period of time, would have an impact on dimensions of *human needs*, like environment, housing, health, education, employment and food. It quantifies the state of disorder induced by the disruption of urban structure and functions.

If we talk about complex industrial systems, we can think of another disruption index, called IDI (Industrial Disruption Index), whose graph is presented in Fig. 16.9. Here we can understand that the concept is similar to the urban DI with

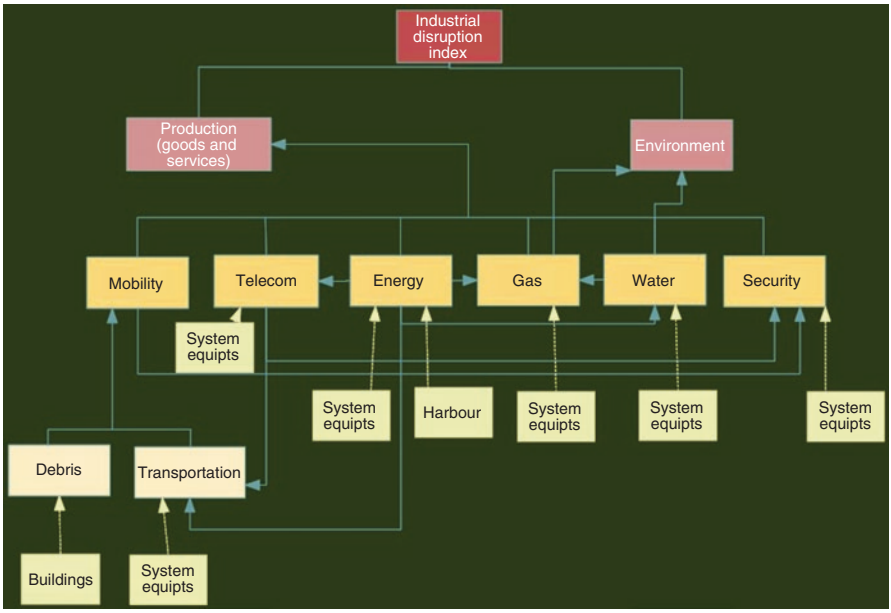

Fig. 16.9 Graph representation of vital functions of an industrial system and their dependencies and incidences (Oliveira et al. 2015; Ferreira et al. 2017)

the difference being that the system is feed with other dimensions such as mobility, telecom, energy, gas, water and security. These are computed with the vulnerability functions of equipment systems that are affected by shaking. Interaction or cascade effects are contemplated in this formulation.

The graph in Fig. 16.10 is transduced into an adjacency matrix where we can see the interactions among systems. An algorithm is used to compute the DI based on this adjacency matrix where the state of the system is 0 or 1, depending on if there is dependency or not. Future developments will introduce a more complex system where values between 0 and 1 can be assigned. QuakeIST is able to consider the DI algorithm (Mota de Sá et al. 2016).

16.4.3 Examples of DI Applications

DI applications to the urban environment were made during the UPStrat-MAFA (2015) EU Project in several locations, namely: Mount Etna in Italy (Meroni et al. 2016), L'Aquila 2009 and Emilia-Romana 2012 Earthquakes in Italy (Ferreira et al. 2014), Algarve in Portugal (Ferreira et al. 2016) and Faial in the Azores (Ferreira 2012 and Oliveira et al. 2012). Other applications include those to the Molise 2002 (Italy) and Port-au-Prince 2010 (Haiti) earthquakes (Ferreira 2012). Apart from earthquakes, the DI has potential applications for other natural disasters. An

		1	2	3	4	5	6	7	8	9	10	11	16	17	18	19	20	21	22	23
Industrial system functional dependencies		DI	Production	Environment	Mobility	Telecom	Energy	Gas	Water	Security	Transportation	Debris	Electric facilities & components	Gas facilities & components	Water facilities & components	Telecom facilities & components	Transportation facilities & components	Harbour facilities	Security facilities & components	Building stock
		Functional disruption											Physical direct damages							
1	DI	1	1	1																
2	Production		-		1	1	1	1	1	1										
3	Environment			-				1	1											
4	Mobility				-						1	1								
5	Telecom					-	1									1				
6	Energy						-						1					1		
7	Gas						1	-	1					1						
8	Water						1		-						1					
9	Security				1	1	1			-									1	
10	Transportation					1	1				-						1			
11	Debris											-								1

Fig. 16.10 The adjacency matrix corresponding to the graph of Fig. 16.9

example of such applications concerns the tropical storm, Washi, that occurred in 2011 in the Philippines (Ferreira 2012).

The final result is presented in a DI scale (Fig. 16.11) with five classes described by descriptors. The application to Algarve, south Portugal is presented in Fig. 16.12, where we can see the influence of the different dimensions of human needs. Starting with an intensity map, we see the propagation effects taking place as long as the various interdependences occur. Figure 16.13 shows the evolution of recovery over time, in the short term and long term.

For the IDI, we have worked during the REAKT (2011) EU Project to develop a model for the Industrial Complex of Sines (Oliveira et al. 2015; Ferreira et al. 2017). Figure 16.14 shows only the effect of an event like the 1755 earthquake on the water and gas networks, and Fig. 16.15 shows the corresponding IDI.

16.4.4 Multi-hazard Influence: Shaking Plus Tsunami

Another topic of great interest is the analysis of multi-hazard impacts. Offshore earthquakes can generate large tsunamis that aggravate or can be worse than the effects of ground shaking alone. Yet, the analysis of tsunamis without consideration of shaking is also not realistic. A clear example of a multi-hazard influence goes

Impact level	Description of the impact level
V	From a serious disruption at the physical and functional levels to the paralysis of the entire system: buildings, population, infrastructure, health, mobility, administrative and political structures, among others. Lack of conditions to exercise the functions and activities of daily life. High costs for recovery.
IV	Partial paralysis of main buildings, housing, administrative and political systems. The region affected by the disaster presents moderate damage and a small percentage of totally collapsed buildings. Victims and injuries and a considerable number of homeless are present because their houses have been damaged, which, although not collapsed, are damaged severely enough to lose their function as housing. Normal daily activities are disrupted; school activities are suspended; economic activities are at a stand-still.
III	Part of the population may lose their property and need to be permanently relocated, which means strong disturbances in everyday life. This level is characterized by significant dysfunction in terms of equipment, critical infrastructures and losses of some assets and certain damage involving the conduct of professional activities for some time. The most affected areas show significant problems in mobility due to the existence of debris or damage to the road network. There may be some significant problems providing food and water, which must be remedied by civil protection agencies.
II	The region affected by the disaster results in a few homeless (approximately 5%) due to the occurrence of some damage to buildings affecting the habitability of a given geographical area. Some people may experience problems with access to water, electricity and/or gas. Some cases require temporary relocation.
I	The region affected by the disaster continues with its normal functions. No injured, killed or displaced people are registered. Some light damage may occur (non-structural damage) that can be repaired in a short time, and a temporary service interruption sometimes exists. The political process begins with an awareness that the problem exists, and some investments in strengthening policy and risk mitigation are/should be made.

Fig. 16.11 Disruption index (DI) scale (From Oliveira et al. 2014)

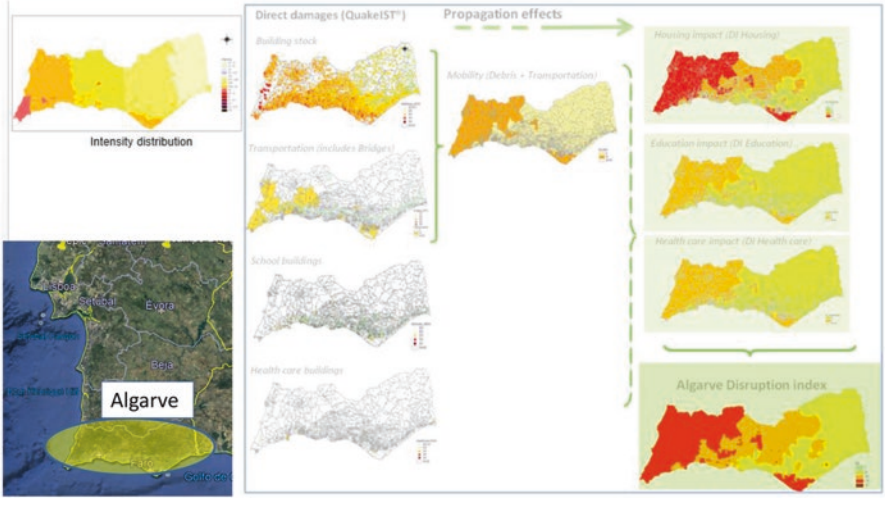

Fig. 16.12 Disruption index: earthquake impact based on the systemic analysis of the urban components: Algarve, south Portugal subjected to 1755 intensity distribution (From Oliveira et al. 2014)

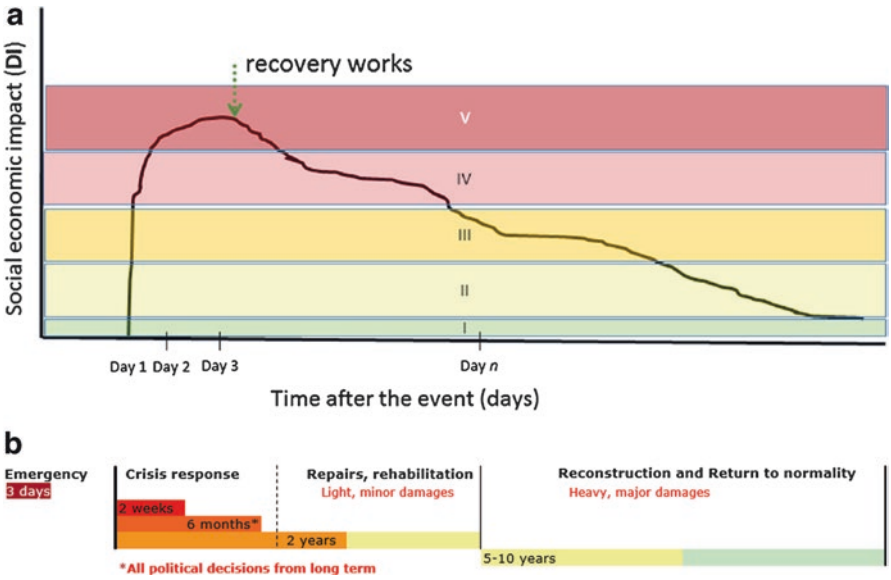

Fig. 16.13 Time evolution: (**a**) DI in short term, (**b**) Recovery in long term (adapted from Oliveira et al. 2014)

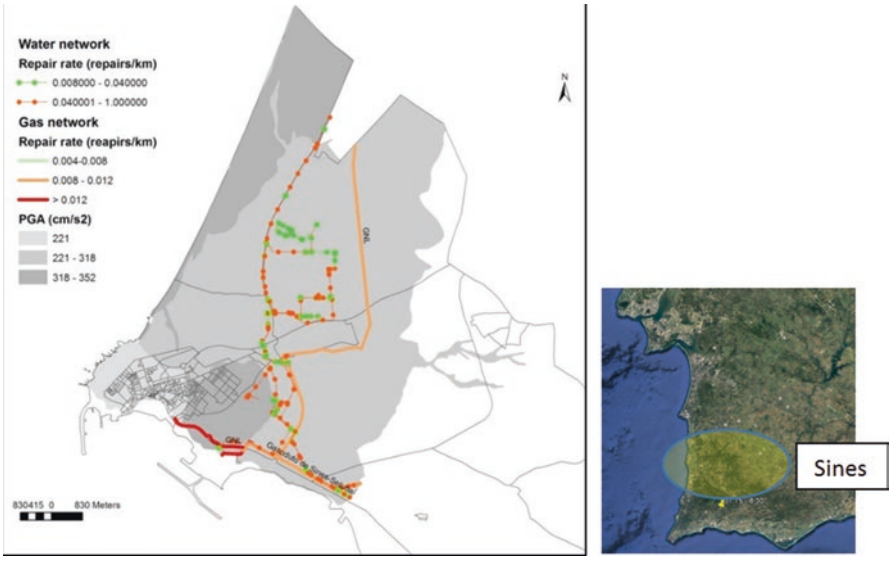

Fig. 16.14 Repair rates for gas and water networks under 1755 scenario applied to the Industrial Complex of Sines, REAKT (2011) EU Project

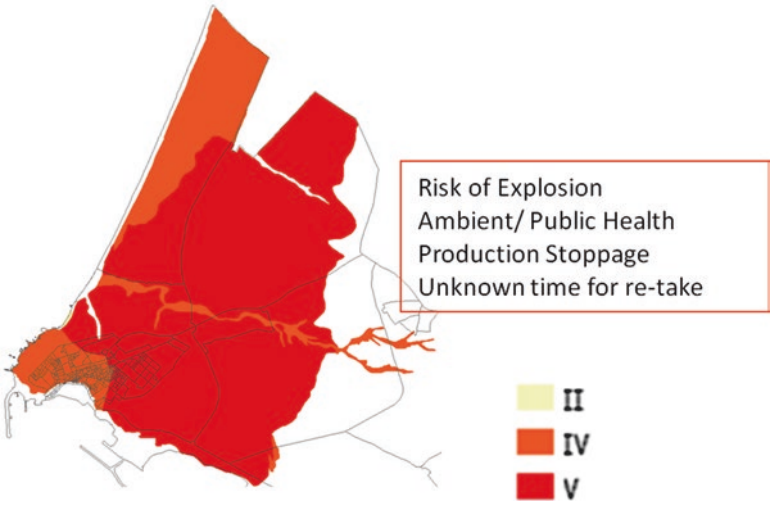

Fig. 16.15 IDI for Sines complex

back to earlier times, such as the 1755 Lisbon event which was impacted by 3 actions: ground shaking, tsunami and urban fire (Oliveira 2012).

Multi-hazard influences can be modelled with the principles of DI through graph theory. Here, we present a simple solution with an aggravation function where the damage state, D_S, is a function of both the damage state caused by shaking only and by tsunami only (Fig. 16.16). To analyze damage due to a tsunami wave, we need to obtain vulnerability curves of the stock of buildings. In future developments, we will consider the interaction of both the shaking and the tsunami, meaning that the damage of a damaged structure is also depending on the level of damage of shaking. These developments require a calibration with real situations.

Figure 16.17 presents an example application in the city of Setúbal, where we plot separately the damage caused by ground shaking alone, shaking due to tsunami only and the aggregation of effects made according to Fig. 16.16. More details of this application are available in Bonacho and Oliveira (2016) and are the subject of a publication in preparation.

16.5 System Performance Indicators/Measures and Disaster Mitigation Strategies

Once the needs for recovery are known, with the complete list of works to be made, it is necessary to have a model that helps the authorities/associations/financial institutions, etc., set priorities and timings for the resources that are available. A few research groups have been dealing with this subject with some promising results.

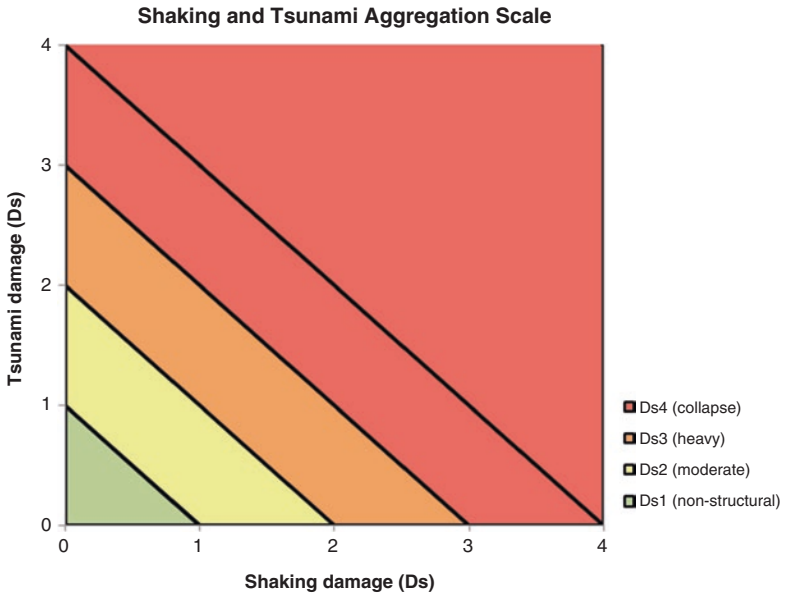

Fig. 16.16 Aggravation due to shaking and tsunami

One of them at the University of Udine, Italy in collaboration with UNESCO and other international organizations, has developed the product VISUS (sprint.uniud.pt) (Grimaz et al. 2016) which permits the implementation of a pragmatic technical triage for planning purposes, and it is adaptable to different local contexts and needs. VISUS was first developed to assess schools in a seismic scenario, but it has evolved into a holistic and multi-hazard approach which includes flooding and fire. It requires the definition of a rational and effective strategy for risk reduction based on the level of risk, criticalities, countermeasures and financial commitment. Other proposals (Ferreira et al. 2016) used concepts developed in the nuclear industry (RRW, RAW, Vesley et al. 1983) to perform prioritization of resources based on the criteria of Phillips and Bana e Costa (2007).

We have developed this last idea, illustrated in Table 16.2, making use of urban DI (for more detail see Ferreira et al. 2016). In fact, the central reasoning underlying the definition of the disruption index is the identification and evaluation of the impacts on a target community, considering the physical elements that most contribute to a severe disruption. The following system-performing indicators/measures were considered: population at stake of some kind of impact, RRW – risk reduction worth and RAW – risk achievement worth.

The population at stake constitutes the first performance indicator developed (Meroni et al. 2016). It considers the number of people within each DI level (DI = I, II,…), informing the percent of population affected by a given dysfunction.

RRW and RAW are well known by risk analysts, and so, abundant bibliography exists about them (Vesely et al. 1983). Risk importance measures (or system per-

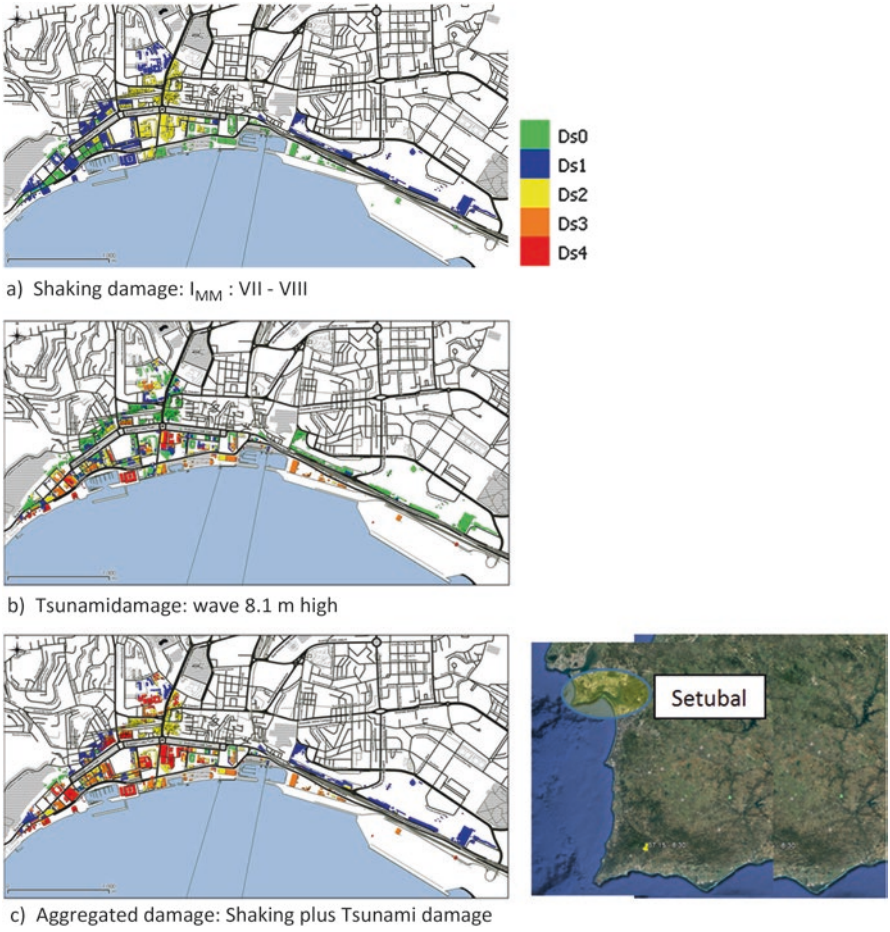

Fig. 16.17 Superposition of shaking with tsunami (data from QuakeIST, Mota de Sá et al. 2016; Bonacho 2016). Water elevation by Santos and Koshimura (2013). Height of wave by adding maximum high tide values

forming indicators) are defined to evaluate the importance of a feature in further reducing the risk and its importance. RRW indicates the potential of subsystem i (column on the left) to reduce the actual risk, whereas RAW indicates the actual potential of subsystem i to aggravate the actual risk.

For example, as seen in Table 16.2 for the entire region of Algarve, $RAW_i = 1.23$ implies that if subsystem i (housing) persists to degrade until some plausible maximum value of the vulnerability that leads to losses or dysfunction in subsystem i to its plausible maximum, while leaving all of the other subsystems performing in their actual state, then the chances of reaching the actual levels of risk will be raised 1.23 times. This value was obtained after running Monte Carlo simulations on vulnerability functions of the various systems (human needs).

Table 16.2 Risk achievement worth (RAW) for Algarve (From Ferreira et al. 2016)

	I	II	III	IV	V
DI		**0.83**	**1.23**	**1.06**	
Environment		1.00			
Housing		0.83	1.23	1.06	
Security		1.00			
Healthcare		0.97	1.05		
Education			0.97	1.06	
Mobility		0.97	1.06		
Building stock	0.59	1.02	1.23	1.06	
Schools	1.00	1.00			
Healthcare fac.	1	1	1		
Electricity		1.00			
Telecom	1				

It is interesting to note, in the illustration presented as well in other examples not referred here, that the results are essentially controlled by the human need, housing, and only the size of DI equal III degree shows appreciable change of the impacted area.

Another note of importance is that cascading effects can induce high dysfunction in the targeted zones, and, in many cases, even dysfunctions in apparently small objects (nodes/sub-systems) can cause important impairments in economy, business, urban life and in the reliability of critical assets.

In practical terms, available funds are always limited to some upper maximum amount, and consequently, portfolio management can come into play. The best portfolio of possible intervention strategies is the one that, with our restricted funds, leads us to the maximum global benefit (the sum of benefits/risk reduction reached by each individual strategy). According to Philips and Bana e Costa (2007), the best portfolio can be reached by ordering the possible strategies i (programs or policies) by decreasing the importance of their value for money (Ratio = $RRW_i/Cost_i$: *Benefit/Cost*) and then retaining the so ordered policies until the budget is reached.

To sum up, the use of the disruption index can be a great opportunity to find policies and alternatives to risk reduction. Of course, its usefulness is not restricted to the above example, and many other cases can be pursued using DI with other risk importance measures (Vesely et al. 1983).

16.6 Final Words

From what was presented in the first part of this chapter, earthquakes and tsunamis continue to have a major impact on millions of people every year, and therefore, earthquake risk management measures need to be implemented with urgency. Failure to enforce and implement appropriate measures could increase the impact of earthquake events and undermine the resilience of a system. To promote a risk management approach in dealing with earthquakes, including prevention, mitigation and recovery is fundamental, as well as to support all initiatives for continuous communication to raise awareness and reinforce preparedness.

The new approaches to seismic risk reduction brought new insight and new open paths in seismic prevention strategies. They also brought new insights in to the so-called holistic approaches (Carreño et al. 2012), until now mainly addressed with resource to traditional multi-criteria decision tools, where fundamental mathematic restrictions imply severe difficulties in leading with non-independent / interdependent impacts.

The different indicators (SIRIUS, DI) provide useful information in risk perception and risk communication, as well as in developing strategies to reduce the consequences of earthquakes and increase the benefits of a decision. These concepts offer a comprehensive description of real, observed scenarios and help:

- to identify critical services or elements in the urban or industrial system,
- to rank the order of priority of services or elements for continuous operations or rapid recovery, and
- to identify internal and external impacts of disruptions.

This approach can also be extended to other natural and man-made disasters and may be used as a tool for optimization of resources of system components.

16.6.1 Future Work

Future work includes the development of other indicators, such as an urban score, a school score and a hospital score, or, at a different level considered as subsystems in this methodology, an education score, a health-system score, a life-line score, a sustainability score, etc.

As an example, the school score can be defined as follows:

(i) degree of inflicted damage,
(ii) concentration of students at the time of event,
(iii) proximity of other schools which perform the same functionalities requiring both mobility as well as the possibility of taking part in the immediate recovery.

Future work in the theme of ranking the type of interventions to reduce the risk should include an analysis of the most critical typologies and not reduce vulnerability in an equal way.

We have presented the SIRIUS and DI concepts (both applied to urban and industrial complexes) as well as an example of how to deal with multi-hazard phenomenon using the tsunami action. New developments should include an analysis of how uncertainties can be dealt with within these concepts, consolidate the IDI and extend the multi-hazard idea to other areas/topics, not only to earthquake/tsunami disasters, but also to floods, hurricanes, etc. Using these concepts, together with cost-benefit and multi-criteria analyses, will make risk mitigation more effective. Communicating the risk is another topic of great importance that needs to be properly addressed as illustrated in the KnowRISK (2016) EU Project.

Acknowledgements A very special word to late Professor Ragnar Sigbjörnsson for all support and encouragement to our work and for the friendship with the first author for a number of years.

Special thanks to Professor Rajesh Rupakhety for the strong support of the ideas presented in this review paper and for the detailed review of the manuscript.

FCT Ph.D. grant SFRH/BD/71198/2010 (Francisco Mota de Sá)

EU—Civil Protection Financial Instrument in the framework of the European Project "Urban disaster Prevention Strategies using MAcroseismic Fields and FAult Sources" (UPStrat-MAFA-Num.230301/2011/613486/SUB/A5), DG ECHO Unit A5.

EU—Civil Protection Financial Instrument in the framework of the European Project. (KnowRISK project (2016) (Know your city, Reduce seISmic risK through non-structural elements). Co-financed by the EC DG-ECHO Agreement No.-ECHO/SUB/2015/718655/PREV28. (https://knowriskproject.com).

Instituto de Engenharia de Estruturas, Território e Construção (ICIST), and CeRIS, Research Units of Instituto Superior Técnico.

References

Bonacho J (2016) Modelo de simulador de efeitos de risco sísmico em meio urbano, integrado num sistema de informação geográfica, como instrumento de apoio ao planeamento de emergência em protecção civil e informação pública, Trabalho de Projecto – Licenciatura em Engenharia da Proteção Civil, ISEC Lisboa (in portuguese)

Bonacho J, Oliveira CS (2016) Multi-hazard analysis of earthquake shaking and tsunami impact. ICUR, International Conference on Urban Risks, Lisbon (Portugal), 30 June to 2 July

Carreño ML, Cardona OD, Barbat AH (2012) New methodology for urban seismic risk assessment from a holistic perspective. *Bull Earthq Eng* 10:547–565

Daniell JE et al. (2012). The world economic impact of historical earthquakes. In: Proceedings of the 15th world conference on earthquake engineering, Lisbon, Portugal

Ferreira MA (2012) Risco sísmico em sistemas urbanos. Ph.D. Dissertation. Instituto Superior Técnico, Universidade Técnica de Lisboa (in portuguese)

Ferreira MA, Oliveira CS, Mota de Sá F (2013) The new seismic ghost cities. In: Proceedings of the, seminar 50 years of Skopje Earthquake, Skopje, Macedonia

Ferreira MA, Mota de Sá F, Oliveira CS (2014) Disruption Index, DI: an approach for assessing seismic risk in urban systems (theoretical aspects). *Bull Earthq Eng* 12:1431–1458. doi:10.1007/s10518-013-9578-5

Ferreira MA, Mota de Sá F, Oliveira CS (2016) The Disruption Index (DI) as a tool to measure disaster mitigation strategies. *Bull Earthq Eng* 14(7):1957–1967

Ferreira MA, Oliveira CS, Mota de Sá F (2017) Industrial disruption index: the new indicator of interdependence and impacts, Paper 4093. In: Proceedings of the 16 world conference on earthquake, Santiago, Chile

Grimaz S, Torres J, Malisan P (2016) VISUS: a methodology for the assessment of safety of learning facilities and for the transfer of scientific knowledge through the capacity building of surveyors. Abstract, 35th General Assembly of ESC, #694. (Accessed: sprint.uniud.it)

Jaiswal KS, Wald DJ (2012) Improving PAGER's real-time earthquake casualty and loss estimation toolkit: a challenge. In: Proceedings of the 15 world conference on earthquake engineering, Lisbon, Portugal

KnowRISK (2016) EU Project - Know your city, Reduce seISmic risK through non-structural elements. Co-financed by the EC DG-ECHO Agreement No.-ECHO/SUB/2015/718655/PREV28. (https://knowriskproject.com)

Meroni et al (2016) The role of urban system dysfunction in the assessment of seismic risk in the Mt. Etna area (Italy). *Bull Earthq Eng* 14(7):1979–2008

Mota de Sá F, Oliveira CS, Ferreira MA (2013) SIRIUS, Seismic risk indicator in urban space. *Earthquake Spectra* 29(2):573–595

Mota de Sá F, Ferreira MA, Oliveira CS (2016) QuakeIST® earthquake scenario simulator using interdependences. *Bull Earthq Eng* 14(7):2047–2068

Oliveira CS (2012) Lessons from the review of the 1755 Lisbon Earthquake, based on the Historical Observations of Different Physical Phenomena. Journal SUR – Sustainable Urban Regeneration, 10:38-45, The University of Tokyo

Oliveira CS, Ferreira MA, Mota de Sá F (2012) The concept of a disruption index: application to the overall impact of the July 9, 1998 Faial earthquake (Azores islands). *Bull Earthq Eng* 10(1):7–25. doi:10.1007/s10518-011-9333-8

Oliveira CS, Ferreira MA, Mota de Sá F (2014) Earthquake risk reduction: from scenario simulators including systemic interdependency to impact indicators. In: Perspectives on European earthquake engineering and seismology, Geotechnical, Geological and Earthquake Engineering Book series #34, Vol 1, Chapter 9. Springer, pp 309–330

Oliveira CS, Mota de Sá F, Lopes M, Ferreira MA, Pais I (2015) Early warning systems: feasibility and end-users' point of view. *Pure Appl Geophys* 172:2353. doi:10.1007/s00024-014-0999-0

Phillips LD, Bana e Costa CA (2007) Transparent prioritisation, budgeting and resource allocation with multi-criteria decision analysis and decision conferencing. *Ann Oper Res* 154(1):51–68

REAKT (2011) EU project – strategies and tools for real time earthquake risK reduction. FP7-ENV-2011. (http://www.reaktproject.eu/)

Santos A, Koshimura S (2013) Tsunami hazards at Setubal urban area considering the 1755 Lisbon Tsunami, ISBN: 978-972-99436-6-9, pp 935-941

Sendai (2015) Framework for disaster risk reduction 2015-2030. UNISDR, United Nations. (http://www.preventionweb.net/files/43291_sendaiframeworkfordrren.pdf)

Silva V, Crowley H, Pagani M, Monelli D, Pinho R (2013) Development of the OpenQuake engine, the Global Earthquake Model's open-source software for seismic risk assessment. *Nat Hazards*. doi:10.1007/s11069-013-0618-x

UPStrat-MAFA (2015) EU Project - Urban disaster Prevention Strategies using MAcroseismic Fields and FAult Sources, (UPStrat-MAFA-Num.230301/2011/613486/SUB/A5), DG ECHO Unit A5

Vesely WE, Davis TC, Denning RS, Saltos N (1983) Measures of risk importance and their applications. Division of Risk Analysis, Office of Nuclear Regulatory Research, U.S. Nuclear Regulatory Commission, Washington, DC

Chapter 17
Urban Disaster Prevention Strategies in the UPStrat-MAFA Project: From Risk Analysis to Communication

Gemma Musacchio, Monica A. Ferreira, Fabrizio Meroni, Rajesh Rupakhety, Carlos Sousa Oliveira, and Gaetano Zonno

Abstract The UPStrat-MAFA (Urban Disaster Prevention Strategies using Macroseismic Fields and FAult Sources) project, funded by the European Commission, had a multi-disciplinary approach to disaster prevention that encompassed strategies based on the analysis of the level of risk and information. Use of macroseismic intensity data and its probabilistic treatment was one of the successful innovations of the project. The method allowed incorporation of knowledge of seismic source, faults and their properties to estimate hazard and provide valuable insights on the level of expected shaking during future earthquakes. A holistic approach to risk assessment was one of the most relevant contributions of this project. It was implemented with a new concept of global damage (the disruption index, DI) that provides a systemic way to measure earthquake impact on urban areas and helps in prevention strategies, as well as in decision-making for emergency planning and post-disaster activities. The project strongly relied on prevention strategies based on education and communication of risk. Analysis on the levels of education was performed and weaknesses identified. Various educational tools were prepared: video games for children and audio-video products for the general public. The results and achievements of the project were widely distributed to both the general public and experts.

G. Musacchio (✉) • F. Meroni • G. Zonno
Istituto Nazionale di Geofisica e Vulcanologia, Italy
e-mail: gemma.musacchio@ingv.it; fabrizio.meroni@ingv.it; gaetano.zonno@ingv.it

M.A. Ferreira • C.S. Oliveira
Instituto Superior Tecnico, Lisbon, Portugal
e-mail: monica.ferreira@ist.utl.pt; csoliv@civil.ist.utl.pt

R. Rupakhety
Faculty of Civil and Environmental Engineering, Earthquake Engineering Research Centre, University of Iceland, Selfoss, Iceland
e-mail: rajesh@hi.is

R. Rupakhety, S. Ólafsson (eds.), *Earthquake Engineering and Structural Dynamics in Memory of Ragnar Sigbjörnsson*, Geotechnical, Geological and Earthquake Engineering 44, https://doi.org/10.1007/978-3-319-62099-2_17

Keywords Seismic hazard and risk • Disruption index • Disaster risk reduction • Risk communication

17.1 Introduction

Prevention is acknowledged as being the most efficient strategy towards disaster risk reduction. Nonetheless, the level of prevention is often constrained by a lack of efficient risk management. When a hazard turns into a disaster, it often exposes weaknesses in disaster risk management and overall preparedness. Although hazard assessment and risk analysis are crucial in implementing prevention strategies through decision and policy makers' involvement, their efficacy can be enhanced efficiently through long-term and widespread education. This was the approach of the UPStrat-MAFA (Urban Disaster Prevention Strategies using Macroseismic Fields and FAult Sources) project, intended to develop innovative methods in seismic hazard assessment, risk analysis and their integration with risk communication and education. It is a multi-dimensional approach that encompasses strategies for prevention of urban disasters. The project was co-financed by the European Union Civil Protection Instrument.

The methods and tools developed in this project were based on seismically active case-study areas in Europe, namely Italy (Mt. Etna, Campi Flegrei), Portugal (Lisbon, Algarve and Azores Islands), Iceland (South Iceland Seismic Zone and Reykjanes Peninsula), and Spain (Alicante-Murcia region). These tools and methodologies include new and innovative concepts and models of ground motion modelling and seismic hazard assessment, holistic quantification of seismic risk in terms of the new idea of disruption index, formulation of disaster prevention strategies supported by adequate long-term actions with emphasis on education and awareness, and other products such as educational video games and audio-visual materials, which were found to support a bottom-up strategy towards disaster mitigation (see, for example, Sigbjörnsson et al. 2016). This chapter describes the tasks and achievements of the project and highlights the innovation in the three, inter-connected fields of hazard assessment, risk analysis and disaster prevention strategies based on education and awareness.

17.2 The Study Areas

Mt. Etna volcano is located along the eastern coast of Sicily, Italy, in a complex geodynamic region dominated by convergence between Africa and Europe (Branca et al. 2011). Apart from the regional high-magnitude seismicity, this zone is locally characterised by creeping and seismogenic faults, which contribute to seismic hazard that might have often been overlooked (Azzaro et al. 2012). Frequent

earthquakes with low to moderate energy release (Ml <5) occur in the area. Despite their small size, such earthquakes can be very dangerous because they occur frequently and can induce cumulative damage in weak structures. In addition, these earthquakes are very shallow (hypocentral depth of only a few kilometres) and can produce ground-shaking effects similar to larger earthquakes occurring deeper in the crust. This hazardous scenario, combined with vulnerable residential buildings and public infrastructure, imposes significant seismic risk to the communities living in this area.

Campi Flegrei is a volcano in southern Italy, which lies northwest of the city of Naples. The structure of the volcano is large, with a 12 km × 15 km caldera, and more than 300,000 people live in areas potentially influenced by it. Together with the present inactive state of the volcano, the predominantly explosive nature of its eruptions put this highly populated region at the highest volcanic risk level worldwide. Since the 1950s, the Campi Flegrei volcano has been in a state of unrest, which is characterised by periods of upraise of the caldera floor (bradyseism) and related seismic swarms. The latest crisis occurred in 1983, when about 40,000 people were evacuated from the town of Pozzuoli. Over the last 10 years, there were several minor uplift phases and seismic swarms and a general intensification of the fumarole outflow. These observations have raised many concerns, indicating the need for a reappraisal of the volcanic activity in the area. Among the people living in the Phlegrean Field area, a paradoxical hazard perception exists among lay people, who are more aware and concerned of the volcanic hazard related to the Vesuvius volcano (Carlino et al. 2008; Ricci et al. 2013) or the seismic hazard related to the general tectonic setting of the area, than the hazard due to one of the most dangerous calderas in the world, in which they are living.

The seismic risk in Portugal derives partly from offshore sources that can cause large events, such as the catastrophic 1755 Great Lisbon earthquake, which generated a tsunami that caused damage over a very wide area in Portugal (especially in the city of Lisbon) and western Spain. The Great Lisbon earthquake of 1755 was the most powerful and destructive one that has ever occurred in Portugal and Europe so far. Although the Portuguese people have heard about this event at least once in their lifetime, they do not have a clear idea of the likelihood of potential future events that can have disastrous effects in their or their children's lives. This can be explained in part due to the fact that large earthquakes are not frequent in Portugal, and, as the memories of a historic disaster fades away, people become more complacent and less concerned about potential risks.

Located on the Mid-Atlantic Ridge, which is a slow-spreading boundary between the Eurasian and the American tectonic plates, the seismicity and volcanic activity in Iceland relate to the interactions between the plate-tectonic settings and a mantle hot spot. In Iceland, inhabitants are acquainted with the widespread geothermal energy that has strongly influenced settlement since its early development. There have been many strong earthquakes in the south Iceland lowland in the recent years, and people living in hazardous areas are, in general, aware of the risks due to natural disasters such as earthquakes and volcanoes. In general, Icelanders are familiar with existing evacuation plans (for example, during volcanic eruptions) and participate in

evacuation exercises (Bernhardsdóttir et al. 2016). During the June 2000 and May 2008 earthquakes in south Iceland, residential buildings and other structures suffered some damage. Fortunately, complete collapse of buildings or human casualty did not occur. This is, in part, due to the high seismic performance of Icelandic buildings, which are inherently strong against lateral shaking as they are also designed to withstand very strong wind action (see, for example, Rupakhety et al. 2016). Despite this, earthquakes pose a risk to people living in the South Iceland Seismic Zone and the Tjörnes Fracture Zone (see, for example, D'Amico et al. 2016a, b) due to, for example, disruption of daily activities, financial loss due to structural and non-structural damage, and risk of injury or death due to movement of building contents during ground movement.

The Alicante-Murcia region is located in the south-eastern area of the Iberian Peninsula, and it includes several Neogene-Quaternary basins in the Betic Cordillera. Among these there are the Vega Baja in the Alicante Province and the Lorca Basin in the Murcia province. Moderate earthquakes, most of which have a shallow focus, occur in the Vega Baja and Lorca Basin. Although the historical seismicity recorded in the Spanish earthquake catalogue reveals the occurrence of very destructive earthquakes with maximum EMS98 intensities reaching IX-X and X, the strongest instrumental events reach magnitudes slightly over 5.0. In the Vega Baja, the strongest event occurred on 21 March 1829, and it was known as the Torrevieja earthquake. It was the main shock in a seismic sequence of at least 42 events that occurred from 1828 to 1830, with EMS98 intensities reaching IX-X. EMS98 intensities VIII were also reported in the region in 1048, 1482 and 1673 in Orihuela, and in 1919 in Jacarilla. On 11 May 2011, two damaging earthquakes (Mw4.5, Mw5.2) killed nine people, injured more than 300 and produced significant building damage in the city of Lorca. According to the Spanish earthquake record, in the Lorca Basin and surrounding regions, significant damaging events have also occurred in historic times, such as those in 1674 (Lorca), 1855 (Alhama de Murcia), 1911 (Lorquí) and 1948 (Cehegín). The most recent activity before the 2011 Lorca earthquakes was events of around magnitude Mw5.0 in 1999, 2002 and 2005, which produced slight damage in several localities of the Murcia region.

17.3 Hazard Assessment

Probabilistic seismic hazard assessment (PSHA) results are generally expressed in terms of some ground motion (or structural response) intensity parameters corresponding to a certain probability of exceedance in a reference mean return period. The most commonly used intensity parameters are peak ground acceleration (PGA) or response spectral acceleration (RSA), which are both derived from instrumentally recorded ground motion data. Before the use of instrumental data, earthquake effects were quantified by some sort of descriptive scale, which could be thought of as a ranking. Macroseismic intensities belong to this class of intensity measure. Because macroseismic data are available for a much longer time and are more

abundant than instrumental data, their use in understanding seismic hazard has been gaining interest for some time. Albarello and Mucciarelli (2002) present a very detailed mathematical treatment of semi-qualitative macroseismic data and demonstrate quantitative hazard estimates based on them. Based on the probabilistic procedure developed by Albarello and Mucciarelli (2002), D'Amico and Albarello (2008) present a computer program called SASHA (Site Approach to Seismic Hazard Assessment) to probabilistically estimate seismic hazard in terms of macroseismic intensity. This method lies on documented effects of past earthquakes at a site of interest but can also incorporate knowledge of seismic source data. In this sense, the approach allows full exploitation of macroseismic information and combines them with knowledge of seismic sources in a framework of formal and coherent treatment of intensity data, taking into account the inherent uncertainties as well as the bounded, ordinal nature of intensity scales. The UPStrat-MAFA project is the first application of this method in many different case study areas with different tectonic environments. In this project, macroseismic data were combined with knowledge of faults and their properties to estimate seismic hazard.

As a first step, this method builds up a local seismic history of intensity at a site. These intensities can either be documented observations at the site or inferred from epicentral intensities, which are often more readily available. Statistical methods are used to infer the completeness, as well as representativeness, of the constructed history (see, for example, Albarello et al. 2001). Hazard estimates are based on this seismic history and rely on estimating a recurrence rate for different intensity thresholds (see, D'Amico and Albarello 2008 for further details).

The SASHA algorithm and the computer code were significantly improved during the UPStrat-MAFA project. The most important change was required to accommodate procedures to the construction of a seismic history at a site by converting epicentral intensities to intensities at the site through either empirical ground motion prediction equations (GMPEs) or from physically constrained stochastic simulations of ground motion using seismological knowledge of past earthquakes. This requirement led to other innovative studies in the project, such as statistical treatment of spatial decay and distribution of macroseismic intensity data. Although GMPEs for instrumental intensity parameters are abundant in the literature, this project developed powerful mathematical models to represent spatial attenuation of macroseismic intensity.

In this regard, the macroseismic fields were modelled using statistical data depth functions (Agostinelli and Rotondi 2016). The challenging task of stochastic attenuation of ordinally scaled, discrete intensity measures was handled. This study allowed us to idnentify the most central pattern of the isoseismic contours of a set of spatially discrete, macroseismic observations. This study led to a proper mathematical framework for modelling attenuation of macroseismic intensity, thereby calibrating GMPEs based on them. The outline of such a framework and the resulting GMPEs applicable to the four study areas of the project are reported in Rotondi et al. (2016). The probabilistic model of macroseismic attenuation results in probability distribution of the intensity at a site for a given epicentral intensity.

Apart from relying on epicentral intensity and attenuation models, stochastic methods of ground motion simulation based on physical properties of the earthquake source, the propagation path and the properties of the site were also undertaken to compile a seismic history at a site. In this approach, seismological information from past earthquakes was used to simulate ground motion time series, from which instrumental intensities were estimated, and then empirically converted to macroseismic intensities. Langer et al. (2016) present such an application for the case study area of Mt. Etna. Recorded data from weak motions were used to calibrate important source and path parameters that were then used to simulate ground motion for typical earthquake scenarios. The simulated intensity measures are compared against observed intensity data from past earthquakes. One such example is shown in Fig. 17.1, below. Similar studies were also conducted in the Campi Flegrei area in Italy (see Galluzo et al. 2016). For the case study in Portugal, source and high-frequency decay parameters in the Azores region were calibrated by Carvalho et al. (2016). Local site effects in altering ground motion intensity were also thoroughly studied in some areas. Path and local elastic site amplification effects on the Mt. Etna, Italy and Vega Baja, Spain are presented in Scarfì et al. (2016).

The attenuation models, the site response models and the observed macroseismic intensities facilitated creation of site seismic histories, which were then used in PSHA using the SASHA code. Azzaro et al. (2016) present seismic hazard maps for the Mt. Etna region in Italy based on both isotropic and anisotropic attenuation of

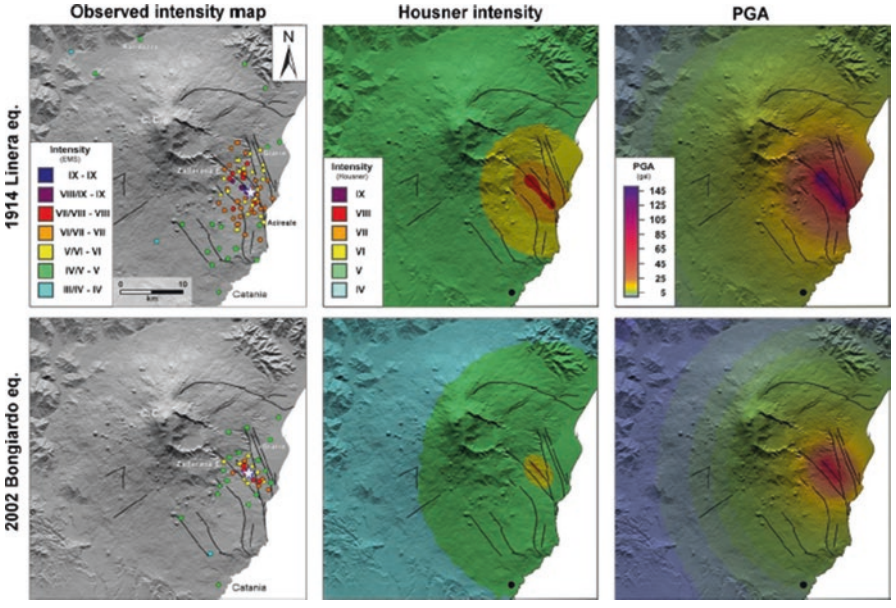

Fig. 17.1 Distribution of observed intensity from two shallow volcano-tectonic earthquakes in the Mt. Etna region compared with the instrumental intensities computed from simulated ground motion (from Langer et al. 2016)

macroseismic intensities. Their results indicate that EMS (European macroseismic scale) intensities of as high as VIII can be expected in the region with a probability of exceedance of 10% in 10 years, and an intensity of IX may be expected in some parts of the area for a 10% probability of exceedance in 30 years. The usefulness of the approach developed in this project is even more relevant for the case study area of southeast Spain, where earthquake databases are mainly comprised of macroseismic intensities from felt effects. Jiménez et al. (2016) present the application of the SASHA methodology to estimate probabilistic seismic hazard in SE Spain. Their results indicate that the computed hazard for a 10% and 2% probability of exceedance in 50 years are comparable to maximum observed intensities in the historical record, and that highest hazard is expected in the Vega Baja area. In the Lorca region, the estimated hazard values corresponding to a 2% exceedance probability in 50 years were found to be closer to observed intensities. Jiménez et al. (2016) also provide valuable insight on the differences between PSHA results obtained from the SASHA method and standard PSHA methods, which place more emphasis on source modelling, and discuss the advantages of the former. The application of SASHA methodology to seismic hazard assessment in mainland Portugal is described in Carvalho and Albarello (2016). Their results provide deep insight into the potential earthquakes contributing most to the seismic hazard in mainland Portugal. Apart from the effect of the 1755 Great Lisbon earthquake, thought to be contributing most in 475 and 975 mean return period hazard over most of the central and southern Portugal (see Sousa and Campos Costa 2009), Carvalho and Albarello (2016) conclude that smaller, nearby earthquakes might be relevant as well. Their results were consistent with what has been understood since the introduction of the first Portuguese seismic design code in 1983; two scenarios are relevant, the first one being large offshore earthquakes and the other one being close-by, moderate magnitude earthquakes.

Similar PSHA was conducted in Iceland using the macroseismic attenuation models developed in the UPStrat-MAFA project. The main results of the analysis are presented in D'Amico et al. (2016a). The resulting hazard maps were found to be qualitatively different from previous hazard maps, expressed in terms of PGA with a 10% probability of exceedance in 50 years, for example, Solnes et al. (2004) and the SHARE (Stucchi et al. 2013) hazard maps. Using a semi-qualitative comparison method based on the procedure described in Mucciarelli et al. (2008), it was found that the results obtained with the SASHA code are substantially different in most parts of Iceland. The hazard estimated using the SASHA method and that reported in the SHARE hazard map were in good agreement in the area around Selfoss, but the latter predicted a relatively higher hazard in Reykjavik, Akureyri, and Höfn. D'Amico emphasizes that use of macroseismic intensities as a measure of hazard can be tricky in a country like Iceland, where building tradition has strongly evolved with time, and because macroseismic intensities are somewhat affected by building vulnerability, the problem of non-stationarity arises. For example, historical earthquakes were more damaging in Iceland than more recent earthquakes of similar size (see, for example, Sigbjörnsson and Rupakhety 2014). In such a situation, macroseismic intensities are time dependent and this non-stationarity needs to be properly modelled.

17.4 Risk and Disruption Analysis

Development of disaster prevention strategies based on the level of risk was the project's main objective. Analysis of seismic risk involved (i) estimation of seismic hazard, as discussed in the previous section; (ii) evaluation and improvement of vulnerabilities of physical elements such as buildings, lifeline systems, with special emphasis on strategic structures such as schools, hospitals, etc.; (iii) convolution of hazard with exposure and vulnerability to the estimated risk. The project went one step further in developing and testing an innovative idea where risk is expressed in terms of overall disruption of physical infrastructure, the services they provide and their effects on society. Such an overall disruption index would invariably need to take into account the interdependencies of different elements of an infrastructure and propagation of damaging effects between different elements. This led to the idea of adisruption index (Ferreira 2012; Ferreira et al. 2014, 2016; Oliveira et al. 2012), a new concept of global damage providing a systemic way to measure earthquake impact on urban areas and helping in prevention strategies, as well as in decisions for emergency planning and the post-event phases.

Quantification of disruption in this manner is very useful for planning disaster prevention strategies based on different levels of risk. In regards to estimating vulnerabilities of different physical components, detailed studies were conducted in the study areas, and the main results are reported in Sousa and Campos Costa (2016), and Rupakhety et al. (2016).

Risk calculation, including the interactions between different elements of the infrastructure, was implemented in a GIS compatible computer program called the QuakeIST® seismic scenario simulator (Mota de Sá et al. 2016). QuakeIST® runs under ArcGIS, ArcView or other open source GIS and is used for estimating potential losses and propagation effects from earthquakes. This platform was used for estimation of disruption index (DI) in the Mt. Etna area in Italy, and the Azores Islands, Lisbon and Algarve in Portugal, and the Lorca region in Spain. In this paper we discuss the DI application to the Mt. Etna and Algarve regions, while we present risk education and information strategies that were used in all the test areas.

17.4.1 Mt. Etna Pilot Area: 1914 Earthquake Scenario (M_w 5.3)

The lower eastern flank of the volcano faces significant seismic risk. It is a dense urban area with 28 municipalities with a total population of about 400,000 inhabitants and contains much critical infrastructure and many lifelines.

The DI for this case study area is estimated for the seismic scenario equivalent to the May 8, 1914, Mt. Etna Earthquake. The damage data used includes residential buildings, hospitals, schools, police stations, lifeline services (electricity, water, gas, wastewater) and roads. The data about buildings were extracted from the 1991 and 2001 Italian National Institute of Statistics (ISTAT) census. The data are grouped

according to the census sections, and the vulnerability indices were evaluated using the approach proposed by Lagomarsino and Giovinazzi (2006). The ISTAT data on residential buildings allows for the definition of the frequencies of groups of homogenous structures with respect to a number of typological parameters: vertical structures, age of construction, number of storeys, state of maintenance and state of aggregation with adjacent buildings. This information was applied at the levels of municipal territories and supplemented with a large quantity of data collected by the local civil defense protection as part of the Lavori Socialmente Utili (Cherubini et al. 1999) project. Regarding the lifelines, electricity main lines were considered. High voltage power lines and their related pylons were mapped into the geographic information system, together with the positions of high and low voltage substations. A dense network of roads connects the villages, and the Messina-Catania main road runs along the coast on the eastern flank of the Mt. Etna volcano. These roads were included in risk analysis. Locations and vulnerabilities of bridges were also considered. Further details on the vulnerability and computed risk can be found in D'Amico et al. (2016b).

The final level of DI was based on the propagation effects of the earthquake impact that are produced by functional disruption (i.e., of human needs), as established using the DI rules (see Ferreira et al. 2016). A typical example of the evolution of disruption from damage to different physical elements is in Fig. 17.2. More detailed results are presented in Meroni et al. (2016). The results provide a holistic picture of earthquake effects and are, therefore, very useful for earthquake preparedness planning and for developing strategies to minimize seismic risk.

17.4.2 Algarve Pilot Area: 1755 Earthquake Scenario (M8.7)

The Algarve region was selected to demonstrate the application of DI in estimating earthquake impact. In this application, detailed information on the geological surface layers, building inventory and population was used. Local site effects were included in hazard assessment, and building stock vulnerability was defined for 55 different classes of structures (Ferreira et al. 2016). A vulnerability index was assigned to each building typology using the approach of the EMS-98 scale to calculate expected damage in buildings. The calculations of DI were performed using the QuakeIST® software. The first level of analysis of the QuakeIST® software is based on obtaining intensity (or PGA) distributions (Fig. 17.3) and estimating spatial distribution of the losses (building and lifeline damage) throughout the region of interest. The second level of analysis is intended to propagate effects and earthquake impacts using the DI formulation (Figs. 17.4 and 17.5). The scenario hazard taken for this application corresponds to the strongest earthquake that hit the region in 1755 (Modified Mercalli Intensity IX-X).

It is important to notice that, despite high exposure and vulnerability of building and facilities to earthquakes, the propagation effects and the number of chain disruptions must be underlined in risk scenarios studies. According to Figs. 17.4 and

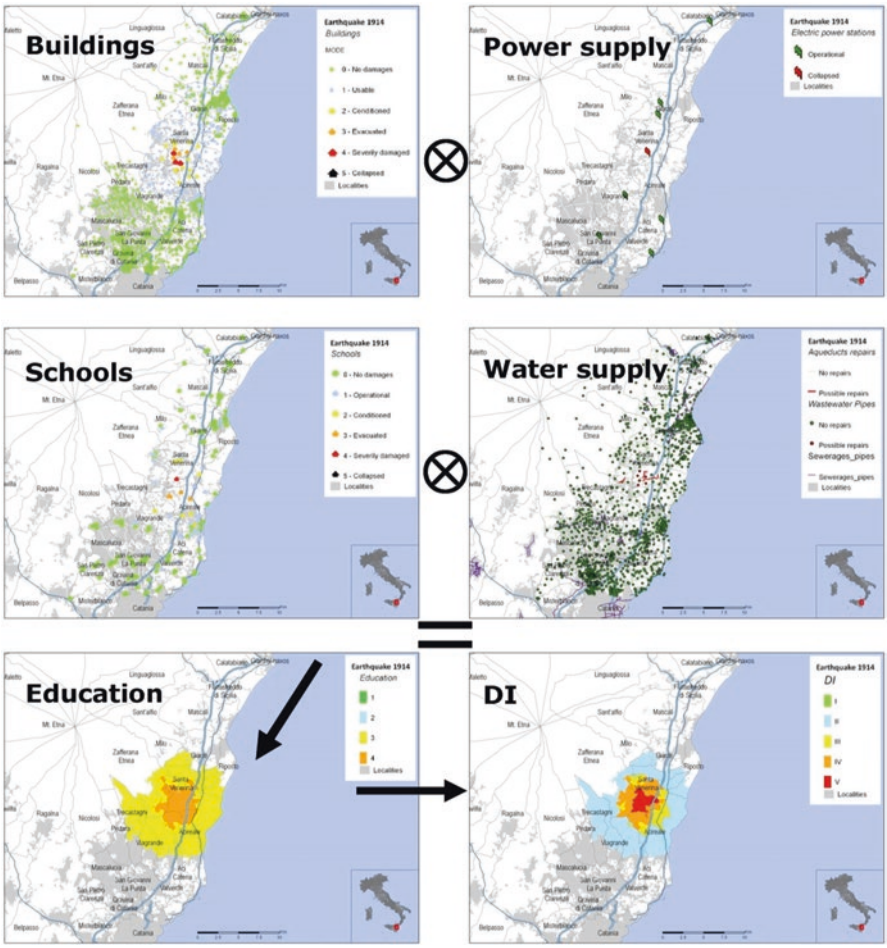

Fig. 17.2 Scenario of the 1914/05/08 earthquake and the evolution of disruption index evaluation for Mt. Etna area. The physical elements considered here are buildings, power supply, schools and water supply, and the expected functional disruption in education (the *bottom left*), as well as the overall DI (*bottom right*)

17.5, the 1755 earthquake scenario (not including the possible tsunami) has high potential to cause disruption on infrastructure and production capacity in the entire Algarve region and, consequently, on the national level.

Evaluation of risk and inferring consequent urban disruption allows formulation of proper strategies to manage and reduce risk. This holistic approach also allows identification of weak links that contribute most to the disruption of an urban system, thereby allowing for optimal and efficient mitigation. It also allows for the definition of priorities and actions to reduce vulnerability of these weak links so that the overall disruption can be reduced. In addition to this information, *risk importance measures* (from the risk analysis field) are defined to evaluate the importance that a

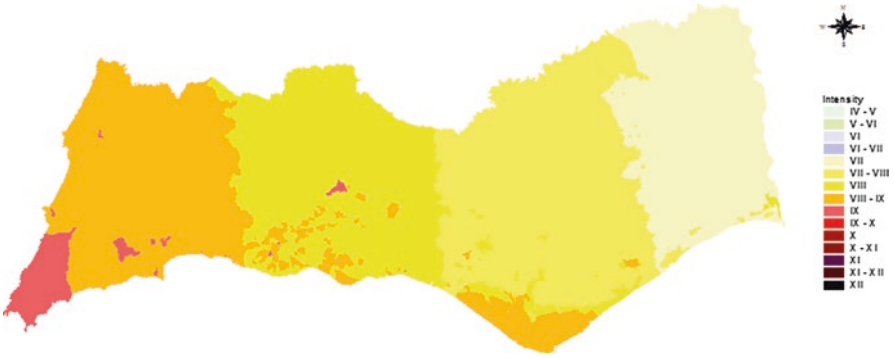

Fig. 17.3 MMI distribution in the Algarve region corresponding to the 1755 earthquake scenario

feature can play in further reducing the risk. One proposed *risk importance measure*, called the risk reduction worth (RRW), is useful for prioritising feature improvements that can be most beneficial in reducing the overall risk. The other important measure, called the risk achievement worth (RAW), is useful for prioritising the most important features in reliability assurance and maintenance activities (Ferreira et al. 2016, Mota de Sá et al. 2016).

17.5 Risk Education Strategies

Portugal, Iceland and Italy are regions where seismic hazard resides in both historical and personal memories. Earthquakes implant their consequences into the roots of societal groups and yield different answers to disaster prevention strongly depending, among other things, on cultural and economic factors (Jóhannesdóttir and Gísladóttir 2010). Furthermore, education and information are fundamental in raising awareness of need of the prevention and allowing choices to be made to reduce risk due to natural disasters and improve resilience of communities (Muttarak and Lutz 2014; La Longa et al. 2012).

The great potential of education as a disaster prevention strategy is in stark contrast to the apparent lack of preparedness in school curricula worldwide (Komac et al. 2013). Bearing this in mind, the UPStrat-MAFA project relied on strategies that started from the assessment of information accessibility at school and within selected vulnerable groups (i.e. hospitals) (Bernharðsdóttir et al. 2016), including the analysis of compulsory school curricula (Musacchio et al. 2015a) and developed different ways to address the population for the dissemination of information in each of the participating countries (Musacchio et al. 2015a, b). The idea is to turn risk management from a bet to a choice.

Risk education is a long-term process that passes from knowledge, through understanding, to choices and actions that place preparedness and prevention over

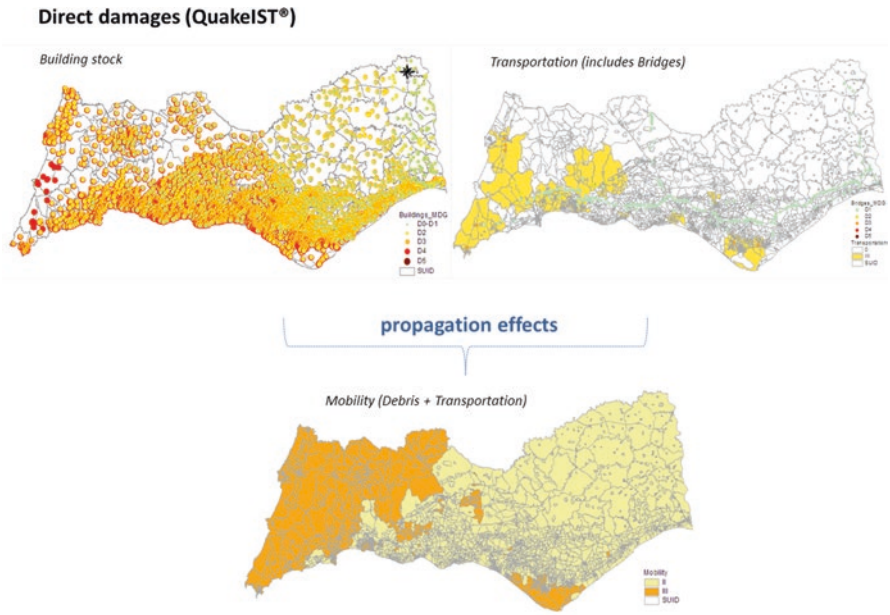

Mobility	
mpact level	**Impact descriptor.** Measures the constraint due to the accumulation of debris or renovation work. Involves the choice of alternative paths, with higher waiting times and travel routes and at a higher cost.
IV	Mobility severely reduced at local and regional level. Geological factors are associated (landslides, rock falls, etc).
III	Local perturbation on mobility linked with landslide or major damages. Used only by recovery teams. Disruptions to commuting trips, work and nonwork trips.
II	Works or some debris causes disruption. Obstacles to customer access.
I	Normal operation or small perturbations with no adverse effects.

Fig. 17.4 Impact on mobility, function of assessment of physical damages to building stocks and bridges. According to DI methodology, the impact on mobility is equal to II and III

recovery. We could argue that strategies for prevention that encompass child and adult education represent a bottom-up approach to building a more resilient society. Clear, transparent and reliable information plays a crucial role in building trust in scientific institutions. That, in regards to risk reduction, is a ground level approach having great potential for effectiveness (Musacchio et al. 2015a).

The condition of education in state plans is a mirror of what any society considers to be valuable for its growth. Analysis of compulsory school education in Italy, Portugal and Iceland reveals a crucial weakness in the age at which seismic hazard

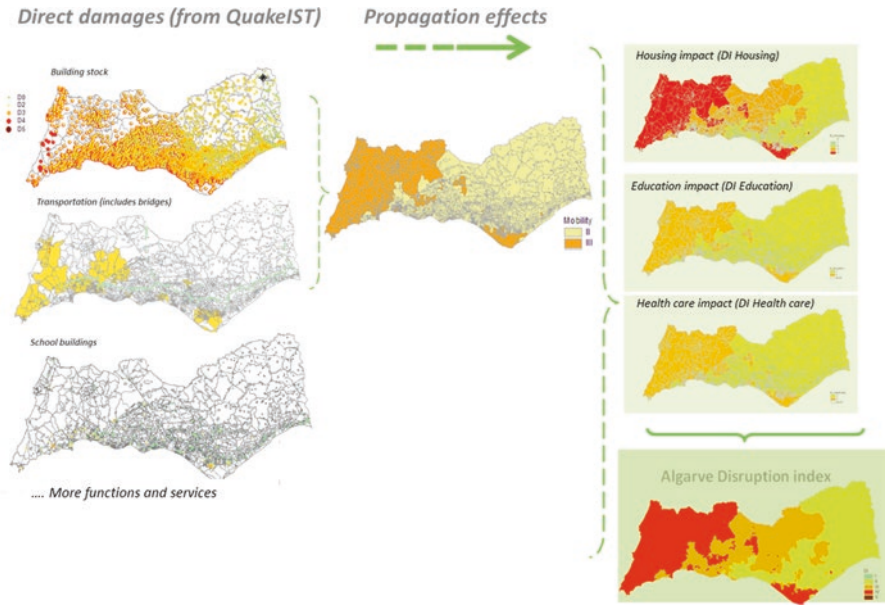

Fig. 17.5 Estimation of disruption index (DI) for the Algarve region. Direct damages to the physical elements are shown in the *left* panel. Incorporation of interaction (propagation) effects results in impact in different sectors as shown in the three *top* diagrams on the right panel. The overall disruption index is shown in the *bottom right*

and risk are addressed. It is not addressed early enough and lacks in-depth information, suitable textbooks and in-depth studies.

Early age education is considered to be a great opportunity to trigger the non-cognitive side of awareness and to imprint mind behaviours that will be recalled in a dangerous situation. On the other hand, an in-depth understanding of the subject is lost by not teaching seismology related topics within the latter years of compulsory education. Textbook analysis confirmed that a major concern is the many mistakes that can lead misconceptions being passed on to students (Musacchio et al. 2015a; Oldershaw 2004; King 2010, Benton et al. 2012, Komac et al. 2013).

School education needs to be more efficient regarding seismic and volcanic hazards. Above all, we found a compelling argument for lowering the age at which hazard education should start to raise interest in the subject and to transfer knowledge on safety measures. Moving from this evidence, we have taken actions for earthquake hazard education, which encompasses various tools that are attractive for children. Hands-on and learn-by-playing approaches are among the best choices to raise the interests of children (Piangiamore et al. 2015). The development of the Treme-Treme videogame (Musacchio et al. 2015a) was thought to be an attractive learning tool to capture attention of digital native generations. The game (Fig. 17.5) focuses on do's and don'ts for earthquake shaking and allows children to think about what might be useful in the case of an evacuation.

Fig. 17.6 Videos screenshots. *Left to right*: "Campi Flegrei", tourists at the Solfatara muds; "Mount Etna", steep slope landscape related to the Timpe fault system; "Before it's too late", street interviews; "Hveragerði... in compliance with nature", a child describing his experience of the 2008 earthquake

Besides schooling, risk education of the general public was addressed using audio-visual products (Fig. 17.6). They were strongly linked to the social, historical and cultural background of each country. Five videos were produced to raise awareness of seismic hazards in Lisbon, The south Iceland lowland, Naples, and Catania, which are all prone to earthquake disasters.

"Voices of earthquake preparedness" is a 29-min-long video that outlines the preparedness and security measures addressing earthquakes in Portugal, Iceland and Italy. The video contains voices of experts who describe earthquakes, referring to the scientific aspects, as well as personal views and experiences of disruptive earthquakes.

"Campi Flegrei" (10-min long) and "Mount Etna" (13-min long) are videos that highlight how the beauty of landscape and the richness of soil can overwhelm the awareness of natural hazards in Italy. In Pozzuoli (Naples), the video shows how only when people living in the calderas experienced the bradyseisms did they become aware of the hazard they were living with.

"Before it's too late" is a 16-min-long video that focuses on memories, experiences and the cultural views of people. Street interviews in the city of Lisbon were used to explore laypeople's concerns, and experts' suggestions are used to disseminate prevention.

"Hveragerði... in compliance with nature" is a 14-min-long video that explains how the inhabitants in this seismically active place have learnt how to live with earthquakes. The effects of the 2008 earthquake that hit the town of Hveragerði are shown, with an emphasis on the damages due to building contents and lack of preparedness.

Once scientific achievements are pursued and communication tools are set up, they need to undergo dissemination that has to be adjusted to different types of publics, namely, peer experts and laymen. The UPStrat-MAFA project placed a strong emphasis on dissemination, providing participation in and promotion of a wide range of events (Table 17.1). Of particular importance are the many scientific papers published in a special issue of the bulletin of earthquake engineering (Sigbjörnsson et al. 2016).

The tools developed for the dissemination of the scientific results were leaflets, newsletters, a layman's report and a multimedia platform (Musacchio et al. 2015b). They were all made available on the Internet and were freely downloadable. The

Table 17.1 Dissemination channels grouped according to the type of audience

Research	Layman	Schools
6/2/2012: Kick-off meeting, Brussels http://ec.europa.eu/echo/en/funding-evaluations/financing-civil-protection-europe/selected-projects/urban-prevention-strategies		2012- on: Contribution to the permanent exhibition in the city of Heveragerdi, Iceland
19–20/8/2012: ESC- European Seismological Commission 33rd General Assembly, Moscow, Russia,		
10 September 2012 – Meeting FNEP, Milano, Italy		
24–28/9/2012: 15th WCEE World Conference on Earthquake Engineering, Lisbon, Portugal	24–28 /9/ 2012: 15th WCEE World Conference on Earthquake Engineering, Lisbon, Portugal	
21–22/3/2013 SYNER-G Systemic Seismic Vulnerability and Risk Analysis for Buildings, Lifeline Networks and Infrastructures Safety Gain, Workshop, Milano, Italy		6–10 /5/ 2013: ScienzAperta, Catania, Italy
16–18 4/2013: Final Workshop of the European Dr. House project, Alessandria, Italy	6–10 /5/ 2013: ScienzAperta, Catania, Italy	12–13 /5/2013: Pre-alpine Geophysical Observatory open doors, Varese, Italy
17–19/6/2013: ICEGE - International Conference on Earthquake Geotechnical Engineering, Istanbul	12–13 /5/2013: Pre-alpine Geophysical Observatory open doors, Varese, Italy	14–16 /5/ 2014: ScienzAperta, Milano, Italy
23–26/7/2013: UPStrat-MAFA 3rd General meeting, Selfoss, Iceland	23–26 /7/2013: UPStrat-MAFA 3rd General meeting, Selfoss, Iceland	30 May – 21/6/ 2013: International Earthquake Engineering and Engineering Seismology graduate summer course, Selfoss, Iceland
11–15/8/2013: StatSei-8 - 8th International Workshop on Statistical Seismology, Beijing		
11–14/12/2013: UPStrat-MAFA 4th General Meeting, Catania, Italy	11–14/12/ 2013: UPStrat-MAFA 4th General Meeting, Catania, Italy	20/11/ 2013: Treme-Treme test, Escola Básica com Jardim de Infância de Setúbal, Setúbal, Portugal

(continued)

Table 17.1 (continued)

Research	Layman	Schools
14/7/2014: Meeting with a Korean Delegation, Milano, Italy	8/7/2014: Pre-alpine Geophysical Observatory open doors, Varese, Italy	21/3/ 2014: Treme-Treme test, Colégio Amor de Deus, Cascais, Portugal
24–29/8/ 2014: 2ECEES, Istanbul, Turkey		
15–19/9/2014: IAEG XII Congress, Torino, Italy		8 /6/2014: Pre-alpine Geophysical Observatory open doors, Varese, Italy
6–7/11/2014: Videojogos2014 (Conference of Science and Art of Video Games), Barcelos, Portugal		
26–28/11/2014: JPEE Congress, Lisbon, Portugal		

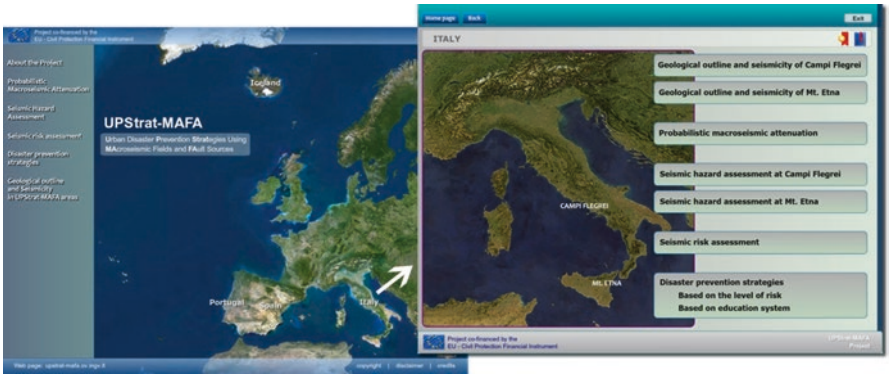

Fig. 17.7 Home page of the multimedia platform (*left*) and a page of the project results relating to Italy (*right*)

multimedia platform (Fig. 17.7) has also allowed us to walk through the doorway of households and schools to reach a wider audience. This platform contains information on four major topics: (1) probabilistic macroseismic attenuation, (2) seismic hazard assessment, (3) seismic risk assessment and (4) disaster prevention strategies. The platform includes interactive contents, videos, images and hyperlinks to raise knowledge in an accessible way. The user can take notes and screenshots and save them to a file. A whole section is devoted to the knowledge of the territory, describing the geologic and seismological settings as the ground level motivation to implement strategies towards natural disaster prevention. The multi-level contents of the platform highlight where the seismicity occurs and its different characteristics in each region, providing details on the most recent damaging earthquakes. The users can find information on the three strategies used for seismic hazard computation: deterministic, statistical and the hybrid approach.

A special section of the platform is devoted to prevention strategies based on the level of risk. For example, the Algarve region in south Portugal is a densely populated area where tourism can triple the population. Here, maps of the disruption index allow stakeholders to visualize those facilities that are most prone to suffering damage. It is also shown how a disruption index scenario for Mt. Etna highlights, for example, how contaminated drinking water might pose a serious health threat for the local population. The worse impact scenario concerns housing and emphasizes the need for semi-permanent housing. Significant displacements of residents might affect traffic patterns, and change school locations, business and commerce. Therefore, the results provide a host of useful information for local government officials, which they can use for disaster preparedness and policy recommendations to raise earthquake resilience.

17.6 Conclusions

Disaster prevention strategies need to take into account the level of risk and implement efficient management planning, but they must take into account that risk is a holistic issue. The Upstrat-MAFA project addressed a wide spectrum of factors related to volcanic and seismic hazard risk and its mitigation in Italy, Portugal, Iceland and Spain. Several innovative developments were achieved in the project. Use of macroseismic intensity data to define seismic hazard and its coherent probabilistic treatment was one of the successful innovations of the project. This led to the development of ground shaking intensity models in the study areas that were subsequently used in hazard assessment. The resulting hazard maps provided valuable insight on the level of expected shaking during future earthquakes, helped identify the relevant hazardous scenarios and highlighted the conformity and differences in the results compared to those based on conventional hazard estimates using instrumental intensities. This project also provided a platform to research and reviewed the exposure and vulnerability of different physical elements of urban infrastructure. Based on existing reports, as well as additional analytical modelling, as in the case of Portugal, vulnerabilities of different elements were identified and documented. Incorporation of hazard, exposure and vulnerability allowed for the estimation of seismic risk expressed in terms of expected damage.

One of the most important contributions of this project is the innovative approach of using a holistic definition of risk. Whereas expected damage to different elements can be individually estimated based on the expected hazard and their vulnerability, the overall impact on society is a very complex interaction of these damages and the loss of functions they induce. In this sense, damages to various physical elements result in loss of various functions, which cascades and propagates into different sectors of societal needs, creating a complex scenario of the disruption of society. The concept of the disruption index (DI) developed in this project is an innovative tool that considers such interactions, and cascading effects, models risk in a holistic way and evaluates the overall disruption by integrating the damages and loss of functions

of different physical elements. This tool was successfully implemented in the case study areas, and the results indicated that it could be very useful to understand and communicate the overall impact of natural disasters. Furthermore, since the overall disruption is derived as an integration of disruption of different services, which are a result of damage to different physical elements, the DI allows analysts to identify weak links in the infrastructure and take necessary steps to strengthen, retrofit or provide back up for the most critical physical elements. In this sense, it is useful for planners and policy makers to understand the most optimal and efficient intervention strategies for disaster risk reduction.

This project placed a strong emphasis on education and communication of risk. Levels of education regarding seismic hazard and risk in the study areas were studied in detail and several weaknesses were identified. The idea of a bottom-up education strategy was tested and applied, and various educational tools, from video games aimed at children to educational videos aimed at adults, were produced and disseminated. The results and achievements of the project were widely distributed, directed towards both the lay population and experts such as seismologists, engineers, planners, policy makers, risk communication experts, social scientists etc. The project was a very successful collaboration of a multi-disciplinary team of experts and resulted not only scientific advancements in the areas of seismic risk and hazard, but also very useful tools and strategies, both for the lay population and local governments for understanding, communicating and reducing risk due to seismic and volcanic hazards in the study areas. The methods and tools developed in this project are based on sound research and validation and can be useful for other areas as well.

Acknowledgements The Urban disaster Prevention Strategies using MAcroseismic Fields and FAult Sources -UPStrat-MAFA project was co-financed by the EU - Civil Protection Financial Instrument with the Grant Agreement N. 23031/2011/613486/SUB/A5. It was a project that involved six different European research centers and universites with the Istituto Nazionale di Geofisica e Vulcanologia (Italy) acting as the coordinator. The partners were Instituto Superior Tecnico (Lisbon, Portugal), Istituto di Matematica Applicata e Tecnologie Informatiche, Consiglio Nazionale delle Ricerche (Milan, Italy), Laboratorio Nacional de Engenharia Civil (Lisbon, Portugal), Agencia Estatal Consejo Superior de Investigaciones Cientificas (Spain) and Earthquake Engineering Research Centre (Selfoss, Iceland). We are thankful to Professor Ragnar Sigbjörnsson, who coordinated the Earthquake Engineering Research Centre partnership, for his enthusiasm, commitment and dedication that were crucial for the success of the project.

References

Agostinelli C, Rotondi R (2016) Analysis of macroseismic fields using statistical data depth functions: considerations leading to attenuation probabilistic modelling

Albarello D, Mucciarelli M (2002) Seismic hazard estimates using ill-defined macroseismic data at site

Albarello D, Camassi R, Rebez A (2001) Detection of space and time heterogeneity in the completeness of a seismic catalog by a statistical approach: an application to the Italian area. Bull Seismol Soc Am 91:1694–1703

Azzaro R, D'Amico S, Peruzza L, Tuvè T (2012) Earthquakes and faults at Mt. Etna: problems and perspectives for a time-dependent probabilistic seismic hazard assessment in a volcanic region. Boll Geofis Teor Appl 53:75–88

Azzaro R, D'Amico S, Tuvè T (2016) Seismic hazard assessment in the volcanic region of Mt. Etna (Italy): a probabilistic approach based on macroseismic data applied to volcano-tectonic seismicity. Bull Earthq Eng 14(7):1813–1825

Benton MJ, Remmert S, Edward J, Drewitt A, Viega P (2012) The Bristol Dinosaur Project. Proc Geol Assoc 123:210–225

Bernharðsdóttir AE, Musacchio G, Ferreira MA, Falsaperla S (2016) Informal education for disaster risk reduction. Bull Earthq Eng. doi:10.1007/s10518-015-9771-9

Branca S, Coltelli M, Groppelli G, Lentini F (2011) Geological map of Etna volcano, 1:50,000 scale. Ital J Geosci 130(3):265–291

Carlino S, Somma R, Mayberry G (2008) Volcanic risk perception of young people in the urban areas of Vesuvius: comparisons with other volcanic areas and implications for emergency management. J Volcanol Geotherm Res 172:229–243

Carvalho A, Albarello D (2016) Application of SASHA to seismic hazard assessment for Portugal mainland. Bull Earthq Eng 14:1827–1847

Carvalho A, Reis C, Vales D (2016) Source and high-frequency decay parameters for the Azores region for stochastic finite-fault ground motion simulations. Bull Earthq Eng 14:1885–1902

Cherubini A, Corazza L, Di Pasquale G, Dolce M, Martinelli A, Petrini V (1999) Risultati del progetto LSU-1. In: Censimento di vulnerabilità degli edifici pubblici, strategici e speciali nelle regioni Abruzzo, Basilicata, Calabria, Campania, Molise, Puglia e Sicilia. Graphic Press s.r.l., L'Aquila, Italy. Italy. Bull Seismol Soc Am 98:2652–2664

D'Amico V, Albarello D (2008) SASHA: a computer program to assess seismic hazard from intensity data. Seismol Res Lett 79:663–671

D'Amico V, Albarello D, Sigbjörnsson R, Rupakhety R (2016a) Seismic hazard assessment for Iceland in terms of macroseismic intensity using a site approach. Bull Earthq Eng 14(7):1797–1811

D'Amico S, Meroni F, Sousa ML, Zonno G (2016b) Building vulnerability and seismic risk analysis in the urban area of Mt. Etna volcano (Italy). Bull Earthq Eng 14:2031–2045

Ferreira MA (2012) Risco sísmico em sistemas urbanos. Ph.D Thesis, Instituto Superior Técnico, Universidade Técnica de Lisboa, 295 pp (in portuguese)

Ferreira MA, Mota de Sá F, Oliveira CS (2014) Disruption Index, DI: an approach for assessing seismic risk in urban systems (theoretical aspects). Bull Earthq Eng. doi:10.1007/s10518-013-9578-5

Ferreira MA, Mota de Sá F, Oliveira CS (2016) The Disruption Index (DI) as a tool to measure disaster mitigation strategies. Bull Earthq Eng 14(7):1957–1977. doi:10.1007/s10518-015-9808-0

Galluzzo D, Bianco F, Rocca ML, Zonno G (2016) Ground motion observations and simulation for local earthquakes in the Campi Flegrei volcanic area. Bull Earthq Eng 14:1903–1916

Jiménez M-J, Albarello D, García-Fernández M (2016) Probabilistic seismic hazard assessment in SE-Spain based on macroseismic site histories. Bull Earthq Eng 14:1849–1867

Jóhannesdóttir G, Gísladóttir G (2010) People living under threat of volcanic hazard in southern Iceland: vulnerability and risk perception. Nat Hazards Earth Syst Sci 10:407–420

King C (2010) An analysis of misconceptions in science textbooks: earth science in England and Wales. Int J of Sc Ed, 31. ISSN: 1464–5289

Komac B, Zorn M, Cigli R (2013) European education on natural disasters – a textbook study. Nat Hazards Earth Sys Sci Discuss 1:2255–2279

La Longa F, Camassi R, Crescimbene M (2012) Educational strategies to reduce risk: a choice of responsibility. Ann Geophys 55(3):445–451

Lagomarsino S, Giovinazzi S (2006) Macroseismic and mechanical models for the vulnerability and damage assessment of current buildings. Bull Earthq Eng 4:415–443

Langer H, Tusa G, Scarfi L, Azzaro R (2016) Ground-motion scenarios on Mt. Etna inferred from empirical relations and synthetic simulations

Meroni F, Zonno G, Azzaro R, D'Amico S, Tuvè T, Oliveira CS, Ferreira MA, Mota de Sá F, Brambilla C, Rotondi R, Varini E (2016) The role of the urban system dysfunction in the assessment of seismic risk in the Mt. Etna Area (Italy) 14(7):1979–2008

Mota de Sá F, Ferreira MA, Oliveira CS (2016) QuakeIST® earthquake scenario simulator using interdependencies. Bull Earthq Eng 14(7):2047–2067. doi:10.1007/s10518-016-9884-9

Mucciarelli M, Albarello D, D'Amico V (2008) Comparison of probabilistic seismic hazard estimates. In: Musacchio G, Solarino S, Eva E and Piangiamore G.L. (2016) Students, earthquakes, media: does a seismic crisis make a difference? Annals of Geophysics, 59, Fast Track 5, 2016; DOI: 10.4401/ag-7239

Musacchio G, Falsaperla S, Bernharðsdóttir AE, Ferreira MA, Sousa ML, Carvalho A, Zonno G (2015a) Education: can a bottom-up strategy help for earthquake disaster prevention? Bull Earthq Eng. doi:10.1007/s10518-015-9779-1

Musacchio G, Falsaperla S, Sansivero F, Ferreira MA, Oliveira CS, Nave R, Zonno G (2015b) Dissemination strategies to instil a culture of safety on earthquake hazard and risk. Bull Earthq Eng. doi:10.1007/s10518-015-9782-6

Muttarak R, Lutz W (2014) Is education a key to reducing vulnerability to natural disasters and hence unavoidable climate change? Ecol Soc 19(1):42. http://dx.doi.org/10.5751/ES-06476-190142

Oldershaw C (2004) Strengthening teaching and learning of geological changes in key stage 3 science, National Strategies, DfES reference 0496–2004 G, 108pp

Oliveira CS, Ferreira MA, Mota de Sá F (2012) The concept of a disruption index: application to the overall impact of the July 9, 1998 Faial earthquake (Azores islands). Bull Earthq Eng 10:7–25. doi:10.1007/s10518-011-9333-8

Piangiamore GL, Musacchio G, Pino NA (2015) Natural hazards revealed to children: the other side of prevention. In: Peppoloni S, Di Capua G (eds) Geoethics: the role and responsibility of geoscientists. Geological Society, Special Publications, London, p 419. http://dx.doi.org/10.1144/SP419.12

Ricci T, Nave R, Barberi F (2013) Vesuvio civil protection exercise MESIMEX: survey on volcanic risk perception. Ann Geophys 56:S0452

Rotondi R, Varini E, Brambilla C (2016) Proabilistic modelling and macroseismic attenuation and forecase of damage scenarios. Bull Earthq Eng 14:1777–1796

Rupakhety R, Sigbjörnsson R, Ólafsson S (2016) Damage to residential buildings in Hveragerði during the 2008 Ölfus Earthquake: simulated and surveyed results. Bull Earthq Eng 14:1945–1955. doi:10.1007/s10518-015-9783-5

Scarfi L, Langer H, Garcia-Fernandez M, Jimenez MJ (2016) Path effects and local elastic site amplification: two case studies on Mt Etna (Italy) and Vega Baja (SE Spain). Bull Earthq Eng 14:2117. doi:10.1007/s10518-016-9883-x

Sigbjörnsson R, Rupakhety R (2014) A saga of the 1896 South Iceland earthquake sequence: magnitudes, macroseismic effects and damage. Bull Earthq Eng 12:171–184

Sigbjörnsson R, Zonno G, Oliveira CS (2016) Foreword to the special issue: the European project UPStrat-MAFA. Bull Earthq Eng 14(7):1773–1776

Solnes J, Sigbjörnsson R, Eliasson J (2004) Probabilistic seismic hazard mapping of Iceland. In: Proceedings of the 13th World conference on earthquake engineering, Vancouver, B.C., Canada, August 1–6, 2004, Paper No. 2237

Sousa ML, Campos Costa A (2009) Ground motion scenarios consistent with probabilistic seismic hazard disaggregation analysis. Application Mainland Portugal Bull Earthq Eng 7:127–147

Sousa ML, Campos Costa A (2016) Evolution of earthquake losses in Portuguese residential building stock. Bull Earthq Eng 14:2009–2029

Stucchi M, Rovida A, Go'mez Capera AA, Alexandre P, Camelbeeck T, Demircioglu MB, Gasperini P, Kouskouna V, Musson RMW, Radulian M, Sesetyan K, Vilanova S, Baumont D, Bungum H, Fa hD, Lenhardt W, Makropoulos K, Martinez Solares JM, Scotti O, Živcic M, Albini P, Batllo J, Papaioannou C, Tatevossian R, Locati M, Meletti C, Viganò D, Giardini D (2013) The SHARE European earthquake catalogue (SHEEC) 1000–1899. J Seismol 17:523–544

Chapter 18
Is Perception of Earthquake Effects Gender Dependent?

Ragnar Sigbjörnsson, Sólveig Ragnarsdóttir, and Rajesh Rupakhety

Abstract This paper addresses the question of whether or not the perception of earthquake effects is gender dependent. The case considered is the south Iceland earthquakes of June 2000. This includes two moderate-sized, shallow, strike-slip earthquakes with high peak ground acceleration in the epicentral area. After the earthquakes, a survey on earthquake intensities was carried out by the Earthquake Engineering Research Centre of the University of Iceland. The survey also included questions addressing safety issues and demographic information. The data dealt with herein cover 249 respondents in the epicentral area. In the analysis presented herein, emphasis is placed on the following questions: Did you manage to seek shelter inside a house during the earthquake? Did you manage to keep your balance? How long did it take you to recover? The main finding is that the data indicate a tendency towards gender-dependent perception of earthquake effects, which in some cases appears to be statistically significant. In particular, the time taken to recover seems to be very different between male and female respondents. The results also indicate that female respondents are biased towards higher estimation of felt earthquake intensity, while the opposite is true for male respondents.

Keywords South Iceland earthquakes • Macroseismic intensity • Earthquake perception • Residential safety

R. Sigbjörnsson • R. Rupakhety (✉)
Earthquake Engineering Research Center, University of Iceland,
Austurvegur 2a, 800, Selfoss, Iceland
e-mail: rajesh@hi.is

S. Ragnarsdóttir
Icelandic Transport Authority (ICETRA), Reykjavík, Iceland
e-mail: solveig.ragnarsdottir@icetra.is

R. Rupakhety, S. Ólafsson (eds.), *Earthquake Engineering and Structural Dynamics in Memory of Ragnar Sigbjörnsson*, Geotechnical, Geological and Earthquake Engineering 44, https://doi.org/10.1007/978-3-319-62099-2_18

18.1 Introduction

Human perception of earthquake effects is an important field of research of practical application in devising preventive measures, risk mitigation, decision-making, and risk management. In the present study, the term "earthquake risk perception" refers to the judgement of laypersons on felt effects caused by seismic actions. This issue is addressed in more detail by Slovic et al. (1982), Slovic (1987), and Slovic et al. (2004). Observations on seismic risk perception can provide useful information about potential measures of coping with earthquake-induced effects and their consequences (see, for instance, Lindell and Perry 2000). Studies have revealed that perceptions of earthquake risk may be influenced by earlier personal experience, and, furthermore, systematic investigations have shown variation in human perception during seismic sequences (Cucci and Tertulliani 2007). In addition, gender dependence in risk perception has been found in several studies (Fothergill 1996; Gustafson 1998; Greenberg and Schneider 1995). In fact, Kung and Chen (2012) state in their investigation on earthquake risk; "[g]ender is one of the most important demographic variables for research of risk perception." These findings underline the importance of further study into the gender dependence of earthquake risk perception for various seismic regions covering different cultural and societal environments.

The human perception of earthquakes, from the seismological point of view, is closely connected to the development and application of macroseismic intensity scales used to assess and quantify earthquake effects (see, for instance, Wood and Neuman 1931; Grünthal 1998; Musson 2000, 2006). How the macroscopic intensities are related to ground-motion intensity measures are discussed, for example, in Sigbjörnsson et al. (2007).

This study analyses human perception of risk during two moderate-sized earthquakes in Iceland, an island in the North Atlantic Ocean inhabited with people, largely originating from Scandinavia and characterised by high standard of living. The built environment is dominated by earthquake-resistant buildings and modern infrastructure systems. In most cases, the building stock can be described as low-rise, especially in earthquake-prone regions.

Iceland is seismically active, with a history of damaging earthquakes that goes far back in time. Even though earthquakes have caused widespread damage through the centuries, the number of fatalities due to earthquakes is small, only roughly one hundred persons during the last millennium. The seismic activity in Iceland is attributed to the boundaries of diverging tectonic plates, the North American Plate and the Eurasian Plate. Shift in this boundary results in two major transform faults, or fracture zones, in Iceland, one in the south, the South Iceland Seismic Zone, and other in the north, commonly called the Tjornes Fracture Zone. All major damaging earthquakes in Iceland have originated within these two zones. Outside these two major earthquake areas, there is significant seismic activity that is most commonly related to the spreading zones and to volcanoes.

In the south Iceland lowland, the historic earthquakes of 1896, along with the destructive 1912 earthquake, are the most noteworthy, instrumentally recorded

events. A detailed description of the damaging effects of the 1896 earthquakes (see, for example, Sigbjörnsson and Rupakhety 2014) adds to the value of the recordings. A damaging, south Iceland earthquake sequence, comparable to the 1896 earthquakes, occurred in June 2000. The sequence began at 15:41 on 17 June 2000, with a moment magnitude of 6.5, whose epicentre was just north of the rural village of Hella. It was followed by major seismic activity throughout the entire South Iceland Seismic Zone and the Reykjanes Peninsula. The second earthquake in the sequence, which exceeded magnitude 6, occurred on 21 June at 00:52. The moment magnitude was assessed to be 6.4 and the epicentre was approximately 17 km west of the epicentre of the first event.

The June 2000 earthquake induced widespread damage (Sigbjörnsson and Ólafsson 2004). However, major damage was mostly limited to the epicentral region of the two biggest events. The elliptically shaped damage areas around the main causative faults stretch out towards the north and south from the epicentres. It should be noted that the borderlines of these areas are less than 20 km from the causative faults. A significant proportion of the damage in the first earthquake occurred in the rural village of Hella, situated no more than 5 km from the southern end of the causative fault. The latter earthquake also caused a great deal of damage to buildings in the epicentral area, but this was mostly confined to individual farms, groups of summer cottages, and utility and communication systems. Considerable damage was caused to equipment, household articles, and objects inside buildings, both in individual dwellings and on company premises. It is worth noting that very heavy objects moved out of place, slid or toppled, indicating that horizontal, as well as vertical, acceleration was considerable, a finding which is fully supported by accelerometric recordings from the Icelandic Strong Motion Network. Details and individual recordings are available on-line (Ambraseys et al. 2004; to obtain data, see, http://www.ISESD.hi.is).

No serious accidents occurred during the earthquakes, but many things indicate that good fortune had a great deal to do with this (Ákason et al. 2006a, b). In this context, it is worth pointing out that the first earthquake occurred on Iceland's National Day, 17 June, when many people were gathering outdoors or in well-built assembly houses. There were, however, several physical injuries, which were all classified as medically minor. Based on historical experience, the 21 June event was expected and people had prepared for it, for instance, by fixing or removing indoor objects that could fall or topple and cause danger to occupants.

The objective of this study is to address the question of whether or not perceived earthquake effects are gender dependent. Furthermore, we aim to study whether or not such dependence might influence macroseismic intensities obtained by public surveys (Sigbjörnsson and Ragnarsdóttir 2008). This is based on survey data collected after the June 2000 earthquakes. In the following, the sample, research area, and main results are outlined.

18.2 Methodology, Research Area, and Sample

The elements of the model applied in earthquake effects analysis are summarised in Fig. 18.1 in a simplified way indicating three basic variable groups. These distinct variable groups are:

A. Seismic variables containing information on the earthquake and the propagation of seismic waves from the source to the site. Here, the basic variables are earthquake intensity quantified using the Modified Mercalli Intensity, MMI (see, for instance, Wood and Neuman 1931), the peak ground acceleration quantified as a fraction of g (g being the acceleration of gravity), and distance from source to site given by the shortest distance to the causative fault (rather than the epicentral distance).
B. Built environment variables containing information on building types, building material, building age, and location.
C. Human or individual variables referring to the individual person. In this study, the basic variables in this group are gender, age, and location.

The objective of the modelling process is to relate state variables, termed herein the derivative variables, to the basic variables through quantitative models to enhance the understanding of the underlying processes.

The application of the MMI scale was an attempt to preserve continuity with earlier studies and a recognition of the fact that the bulk of intensity data collected in Iceland so far are according to the MMI scale. However, the survey also included information relevant to the European Macroscopic Scale, or EMS (Grünthal 1998; Musson 2000). The numerical values of these two scales in the study area did not seem to be much different.

The research area is defined by a borderline at a 20 km distance from the causative fault of each event. Within this area, the mean value of the resultant peak ground acceleration is 0.59 g, with a standard deviation of 0.28 g, minimum value of 0.21 g, and maximum value of 1 g. The obtained earthquake intensity, applying the Modified Mercalli Intensity scale, is in the range IV to X, reflecting great variability, as do the strong-motion recordings. The earthquake intensity is a holistic

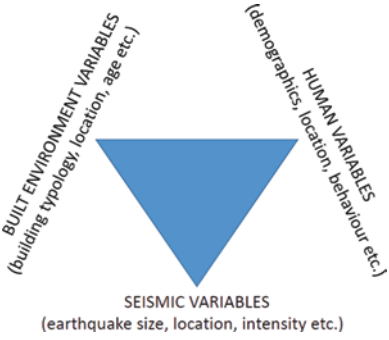

Fig. 18.1 Elements of the earthquake effect analysis represented as a triangle indicating the three basic variable groups

Table 18.1 Characteristic values for the age of respondents in the 2002 survey

	All	Male	Female
Number of respondents	249	122	127
Mean age (year)	54.3	57. 5	51.2
Median age (year)	52	56	48
Standard deviation (year)	14.5	13.7	14.6
Maximum age (year)	87	87	82
Minimum age (year)	23	30	23

measure of the earthquake's action and perceived effects. In an earlier study, it was found that the earthquake intensity measure (MMI) correlates better with rotation-invariant, strong-motion amplitudes than with the amplitudes of individual acceleration components. Such quantities are, e.g., the resultant acceleration and the first invariant of the Arias intensity tensor (Sigbjörnsson et al. 2007). The problem regarding the invariance of the earthquake response spectrum and strong-motion duration is dealt with in detail by Rupakhety and Sigbjörnsson (2013, 2014).

The sample of informants was derived from a random sample of 168 residential buildings augmented by houses hosting strong-motion stations. In all cases, the dwellings are low-rise, single-family houses located in rural areas. The construction materials are cast-in-situ concrete, timber, and masonry constructed with pumice blocks. The sample of houses was also selected to ensure that it would reflect fundamental geographical and structural qualities with regard to the nature of the building stock in the area. These included:

1. geographical distribution
2. age distribution
3. distribution of building types and building material

The foundation conditions are judged rock or firm soil in most cases. The basic information on the informants is summarised in Table 18.1. In all cases, emphasis was placed on respondents that were inside their houses during the earthquakes.

18.3 Survey

A questionnaire was used with an emphasis on the perceived earthquake intensity, location (i.e. the distance to causative faults), respondents' sex and age, as well as where they were when the earthquakes struck. In addition, the analysis addresses explicitly the following safety related questions:

1. Did you manage to seek shelter inside a house during the earthquake?
2. Did you manage to keep your balance?
3. How long did it take you to recover?

The questionnaire was administrated via telephone by reading the questions for the individuals in the preselected sample. The earthquake intensity was treated uniformly by applying the MMI scale, which was read for the respondents. The survey was carried out 2 year after the earthquakes.

18.4 Results

In the official guidelines issued in Iceland regarding how to act during an earthquake, it is recommended that people inside a house seek shelter by "moving to a safe place" indoors. In view of this recommendation, it is interesting to look at the responses to the question:

Did you manage to seek shelter inside a house during the earthquake?

The options given in the questionnaire were the following five activities:

1. I did not think of seeking shelter
2. I assumed there was no danger and therefore I did not seek shelter
3. I sought shelter and I succeeded in seeking shelter
4. I could not move
5. I judged that moving might have caused injuries

The responses to this question are summarized in Fig. 18.2. It can be observed that the most frequent male responses was not to think of seeking shelter, while the females responded predominantly by seeking shelter. A two-sample t-test was performed to whether the male and female responses are statistically significant. This resulted in a t-statistic of 2.41 with a p-value of 0.02, which means that the difference in male and the female responses is statistically significant at a 2% confidence level. It is also noteworthy that a similar proportion of males and females could not move during the earthquakes. The reason is, at least partly, due to the high acceleration and violent movements in some of the buildings close to the causative faults.

Another safety related issue is how people manage to keep their balance during earthquakes and whether or not they fall because of the shaking. An uncontrolled and unexpected fall is a potential threat that may cause injuries, which we have examples of from the 17 June 2000 earthquake. The ability of respondents to maintain balance during the earthquakes was assessed by the following question.

Did you manage to keep your balance?

The options given in the questionnaire to answer this question were:

1. I kept my balance
2. I was close to falling
3. I kept my balance by leaning on something
4. I fell
5. I was sitting but fell when I tried to stand up
6. I was sitting and did not try to stand up

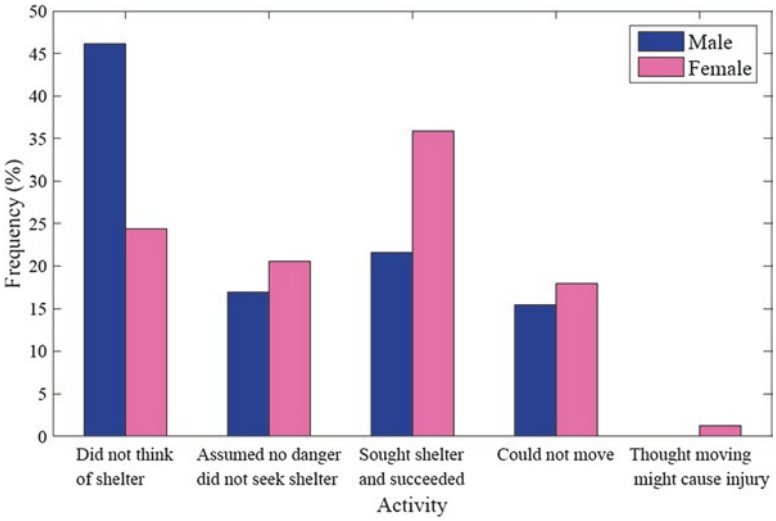

Fig. 18.2 Response to the question: Did you manage to seek shelter inside a house during the earthquake? Total number of respondents is 143; number of males is 65 and number of females is 78

A summary of the responses to this question is presented in Fig. 18.3. It seems that the female respondents admit to falling or having difficulty keeping their balance more often than the males. The t-statistic in this case was 0.24 with a p-value of 0.81. This indicates that the difference in overall responses of the males and females is more likely due to random chance than being statistically significant.

It is generally recognised that an earthquake is a threatening event that often has significant psychological stress-related effects and traumatic injuries that may take time to heal. Reflecting on this, the following question was incorporated in the questionnaire.

How long did it take you to recover?

The options given defined the following simplified time or recovery scale:

1. I was not scared and I did not need any time for recovery
2. I recovered early on
3. It was considerable time to recover
4. I have not fully recovered, which implies at least a 2-year period after the earthquake struck

A summary of the responses to this question are presented in Fig. 18.4. The results show that females admit more frequently than the male respondents that they have not fully recovered 2 years after the earthquakes. It is also observed that about 1/3 of the females had not recovered when the survey was carried out. The t-statistic in this case was found to be 2.3 with a p-value of 0.001. Since the number of responding samples for each of the four possible answers is larger than five for both males and females, a chi-squared test of independence was also performed with the null hypothesis that

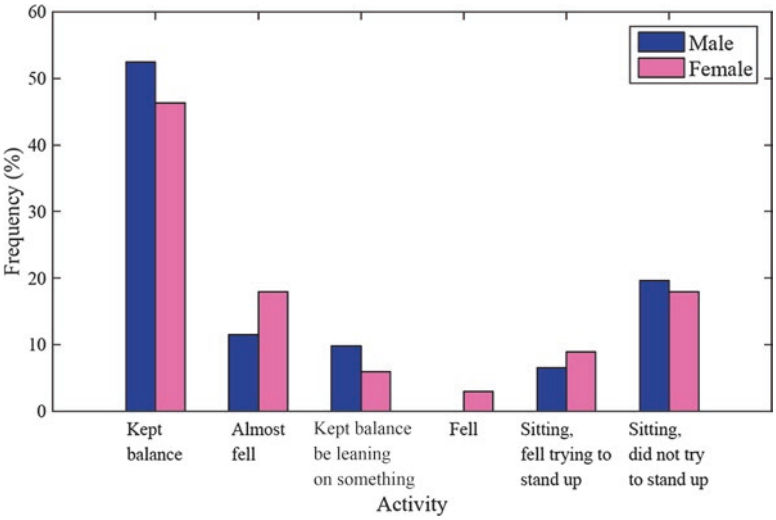

Fig. 18.3 Response to the question: How did you manage to keep your balance? Total number of respondents is 128; number of males is 61 and number of females is 67

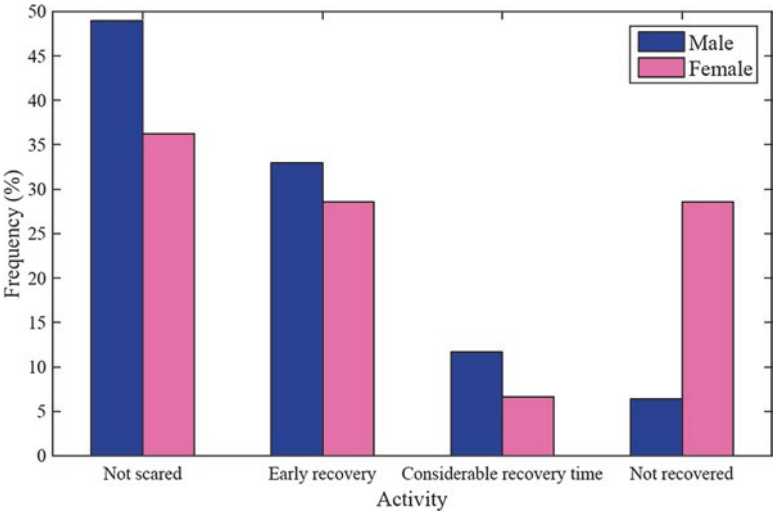

Fig. 18.4 Response to the question: How long did it take you to recover? Total number of respondent is 185, number of male is 94 and number of female is 91

recovery time is independent of gender. The χ^2 statistic was 16.5. With a degree of freedom equal to three, its probability of being exceeded (p-value) is equal to 0.001, which implies that the difference in recovery time between males and females is more likely to be statistically significant than being due to random chance.

Further analysis of the data reveals a weak but significant correlation between recovery time and earthquake intensity as indicated in Fig. 18.5. The overall correlation is about 0.33, slightly higher for the male respondents and somewhat lower for the females. Furthermore, there is a weak, positive association between recovery time and age, which implies that older people need a longer time to recover than younger ones. The correlation is about 0.25 and statistically significant at a 5% confidence level. In this context, it should be stressed that the respondents participating in the survey were all adults (see Table 18.1). Furthermore, it is worth pointing out that psychological questions were addressed in another survey (Bödvarsdottir and Elklit 2004), leading to comparable results.

The results presented above suggest that there might be some gender-dependent perception of earthquake effects. Therefore, it was decided to investigate whether or not the assessed earthquake intensities depend on the gender of the respondents.

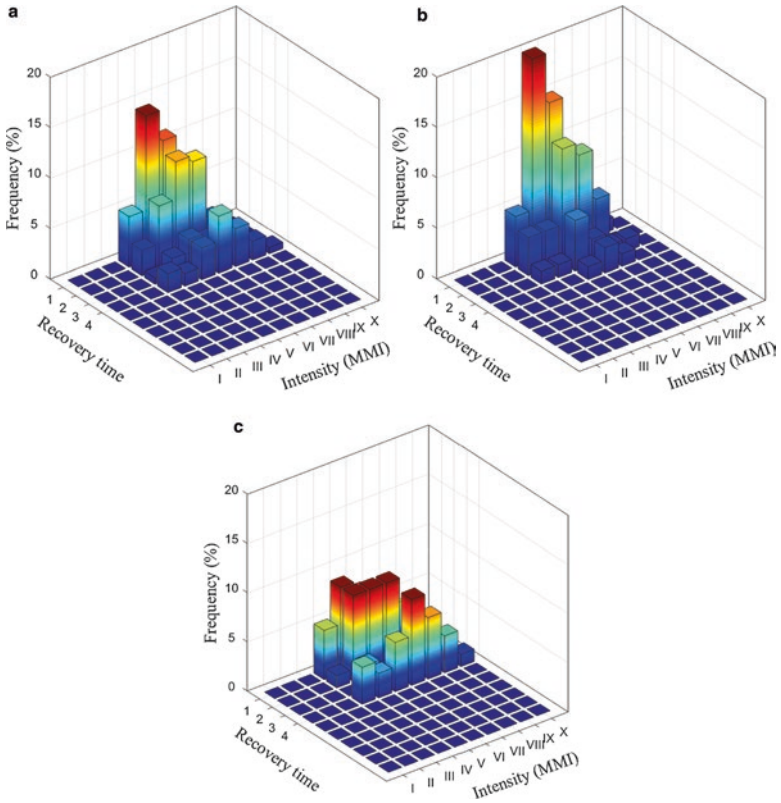

Fig. 18.5 Frequency distribution of recovery time and earthquake intensity. (**a**) All respondents: Correlation between recovery time and earthquake intensity is Pearson's r equal to 0.3273 ($p < 0.0001$). (**b**) Male respondents: Correlation between recovery time and earthquake intensity is Pearson's r equal to as 0.3421 ($p = 0.0018$). (**c**) Female respondents: Correlation between recovery time and earthquake intensity is Pearson's r equal to 0.2972 ($p = 0.0070$). Total number of respondent is 162, number of males is 81, and number of females is 81

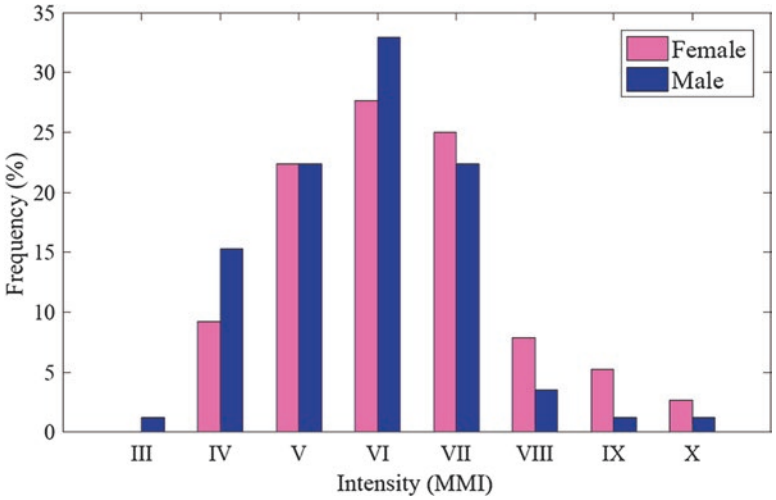

Fig. 18.6 Histogram of perceived earthquake intensities by males and females. Total number of respondents is 161, number of males is 85, and number of females is 76. Mean intensity values reported by males and females are 5.81 and 6.26, respectively

The results of the analysis are displayed in Fig. 18.6. It can be seen that the frequency of intensities above seven (MMI $\geq$ VII) are assessed more often by females tend than those by males, while the opposite is true for smaller intensities. On average, the mean intensity assessed by females is slightly greater than the mean intensity assessed by males. A two-sample t-test was performed to test the statistical significance of the difference between the MMI reported by males and females. The null hypothesis was that males and females access the same intensity. The t-statistic was found to be 2.14 with a p-value of 0.03, which means that the difference is statistically significant at a 3% confidence level.

The presented data indicate a tendency towards gender-dependent earthquake perception, which, in some cases, appears to be statistically significant. This applies, in particular, to the question of what to do during an earthquake and the time needed to recover psychologically after the earthquake. Finally, the earthquake intensities, expressed by the MMI scale, are found to be gender-dependent. The female respondents were found to be biased towards higher intensities while the male respondents were found to be biased towards lower intensities. This observation is more applicable at areas close to the earthquake epicentre, where the intensities are larger, in this case, MMI VII or higher. It is not clear whether or not the male-assessed earthquake intensities are more correct or more realistic than the female assessed ones. In this context, it is, however, worthwhile to point out that it is a known tendency of males, being traditionally the physically stronger gender, to downplay, in hindsight, the strength of threatening events or frightening forces. This male characteristic could, hypothetically, lead to an underestimation of earthquake intensities in a survey of the type dealt with herein. The results are based on limited data and are far from being universal for different socioeconomic and seismic environments.

Nevertheless, we believe they are relevant and need to be tested with further research after major earthquakes worldwide. Gender issues in this context are important not only due to potential bias in estimation of felt earthquake intensities, but also in emergency management and planning. If males indeed tend to downplay the adverse experiences, and under-estimate time to recovery, and because most people involved in emergency management and disaster recovery planning are men, bias towards perceived effects and risk could potentially affect decision making.

Acknowledgments The present work was supported by grants from the University of Iceland Research Fund and RANNIS, the Icelandic Centre for Research. Furthermore, we thank the people participating in the survey for their important contribution as well as the staff at the Earthquake Engineering Research Centre for administrating the survey. We appreciate contribution of Dr. Stephen Platt who reviewed this work and provided valuable comments and suggestions for improvement.

References

Ákason JB, Ólafsson S, Sigbjörnsson R (2006a) Phases of earthquake experience: a case study of the June 2000 South Iceland earthquakes. Risk Anal 26(5):1235–1246

Ákason JB, Ólafsson S, Sigbjörnsson R (2006b) Perception and observation of residential safety during earthquake exposure: a case study. Saf Sci 44:919–933

Ambraseys N, Smit P, Douglas J, Margaris B, Sigbjörnsson R, Ólafsson S, Suhadolc P, Costa G (2004) Internet-site for European strong-motion data. Boll Geofis Teor Appl 45(3):113–129

Bödvarsdottir I, Elklit A (2004) Psychological reactions in Icelandic earthquake survivors. Scand J Psychol 45:3–13

Cucci L, Tertulliani A (2007) Variation of human perceptiveness of earthquakes during seismic sequences. J Seismol 11:205–219

Fothergill A (1996) Gender, risk, and disaster. Int J Mass Emerg Disasters 14(1):33–56

Greenberg MR, Schneider DF (1995) Gender differences in risk perception: effects differ in stressed vs. non-stressed environments. Risk Anal 15(4):503–511

Grünthal G (1998) European macroseismic scale. European Seismological Commission, Luxemborg. (The English version)

Gustafson PE (1998) Gender differences in risk perception: theoretical and methodological perspectives. Risk Anal 18(6):805–811

Kung Y-W, Chen S-H (2012) Perception of earthquake risk in Taiwan: effects of gender and past earthquake experience. Risk Anal 32(9):1535–1546

Lindell MK, Perry RW (2000) Household adjustment to earthquake hazard: a review of research. Environ Behav 32(4):461–501

Musson RMW (2000) Intensity-based seismic risk assessment. Soil Dyn Earthq Eng 20(5–8):353–360

Musson RMW (2006) On the perceptibility of earthquakes. J Seismol 10:157–162

Rupakhety R, Sigbjörnsson R (2013) Rotation-invariant measures of earthquake response spectra. Bull Earthq Eng 11(6):1885–1893

Rupakhety R, Sigbjörnsson R (2014) Rotation-invariant mean duration of strong ground motion. Bull Earthq Eng 12(2):573–584

Sigbjörnsson R, Ólafsson S (2004) On the South Iceland earthquakes in June 2000; Strong-motion effects and damage. Boll Geofis Teor Appl 45:131–152

Sigbjörnsson R, Ragnarsdóttir S (2008) Gender dependent perception of earthquake effects. In: The 14th world conference on earthquake engineering, October 12–17, 2008, Beijing, China

Sigbjörnsson R, Rupakhety R (2014) A saga of the 1896 South Iceland earthquake sequence: magnitudes, macroseismic effects and damage. Bull Earthq Eng 12(1):171–184
Sigbjörnsson R, Ólafsson S, Snæbjörnsson JT (2007) Macroseismic effects related to strong ground motion: a study of the South Iceland earthquakes in June 2000. Bull Earthq Eng 5:591–608
Slovic P (1987) Perception of risk. Science 236:280–285
Slovic P, Fischhoff B, Lichtenstein S (1982) Why study risk perception? Risk Anal 2(2):83–93
Slovic P, Finucane ML, Peters E, MacGregor DG (2004) Risk as analysis and risk as feelings: some thoughts about affect, reason, risk, and rationality. Risk Anal 24(2):311–322
Wood HO, Neuman F (1931) Modified Mercalli intensity scale. Bull Seismol Soc Am 21(4):277–283

Chapter 19
Factors Affecting the Speed and Quality of Post-Disaster Recovery and Resilience

Stephen Platt

Abstract This chapter pulls together insights about post-disaster resilience and recovery from a comparison of 10 recent earthquake disasters. Recovery is a complex process that starts immediately after a disaster. In simple terms, it involves a return to normality. But recovery is not only about speed; the quality of reconstruction and the idea of building back better are also important.

To better understand which factors may affect the speed of recovery, data from the 10 earthquake events are analysed in terms of 3 exogenous factors that are given, and 5 sets of endogenous factors that are within the control of decision-makers and planners – authority, decision-making, planning, finance and science.

The somewhat surprising finding is that there appears to be little relation between speed of recovery and the exogenous factors of size of impact, population demographics and economic factors. However, there is a clear relationship between the standard of post-disaster management decision-making and both the speed ($R^2 = 0.56$) and quality of recovery ($R^2 = 0.90$). The relationship between post-disaster decision-making and the quality of recovery in terms of whether crucial aspects of the society and economy are built back better is striking.

Keywords Disaster recovery • Resilience • Earthquakes • Recovery speed • Build back better

19.1 Introduction

This chapter pulls together insights about post-disaster resilience and recovery from a comparison of 10 recent earthquake disasters. It is aimed at people in earthquake engineering who may have focused on understanding hazards or mitigating their impact but who would like to know more about long-term recovery after a disaster.

S. Platt (✉)
Cambridge Architectural Research, Cambridge, UK
e-mail: steve.platt@carltd.com

R. Rupakhety, S. Ólafsson (eds.), *Earthquake Engineering and Structural Dynamics in Memory of Ragnar Sigbjörnsson*, Geotechnical, Geological and Earthquake Engineering 44, https://doi.org/10.1007/978-3-319-62099-2_19

The chapter analyses the effect of 8 factors on both the speed and quality of recovery.

19.1.1 Resilience

The word resilience derives from the Latin word *resiliens*, meaning to rebound. In engineering, resilience is defined as a measure of how easily a material returns to its original shape after elastic deformation (Hollnagel et al. 2006; Oxford Dictionary of Construction, Surveying and Civil Engineering 2013). In ecology, Holling (1973) defined resilience as the capacity to absorb shock and linked resilience to the idea of systemic stability. The concept of resilience has been used extensively in disaster research (Tierney 1997; Comfort 1999; Petak 2002; Bruneau et al. 2003). Zolli and Healy (2012, p 7; Aldrich 2012) define resilience as "the critical ability to anticipate change, heal when damaged, to reorganize … to maintain core purpose, even under radically changed circumstances". Resilience encompasses a society's level of preparedness to confront or deal with a disaster and its ability to recover quickly and successfully (Alexander 2013a). The UNISDR (2004, p 16), in their global review of disaster reduction initiatives, define resilience as "the capacity of a system, community or society exposed to hazards to resist, absorb, accommodate to and recover from the effects of a hazard in a timely and efficient manner, including through the preservation and restoration of its essential basic structures and functions". Bruneau et al. (2003) define seismic resilience as the ability of a system to reduce the chances of a shock, to absorb such a shock if it occurs, and to recover quickly after a shock. They argue that a resilient system is one that shows reduced failure probabilities, reduced consequences from failures, in terms of lives lost, damage, and negative economic and social consequences, and reduced time to recovery (restoration of a specific system or set of systems to their normal level of functional performance).

19.1.2 Recovery

Recovery is a complex process that starts immediately after a disaster. Recovery is defined in this chapter as "the act or process of returning to a normal state after a period of difficulty" (Merriam-Webster). Most (lay) people think about disaster recovery as a return to normality, although this raises the question of what is normal. The normal may not be a return to the status before the event; in fact, this may be undesirable. Quarantelli (1999) suggests that the word recovery implies an attempt to bring the post-disaster situation to some level of acceptability. Bruneau et al. (2003) include restoration of the system to its normal level of performance in their definition of recovery. This conception of recovery as a return to normality is the one used in this chapter. But recovery is not only about speed; the quality of reconstruction and the idea of building back better are also important.

To try to better understand which factors may affect the speed of recovery, data from the 10 earthquake events are analysed in terms of exogenous factors, i.e., those factors that are given and are outside the control of decision-makers and planners, and endogenous factors, i.e., those factors that are amenable to decision-making. The following are the factors considered in this chapter.

19.2 Methodology

Exogenous Factors

1. **Size** of the disaster: people displaced, deaths, economic loss
2. **Demography**: age profile of population, birth rate
3. **Economy**: regional and national annual growth in GDP

Endogenous Factors

1. **Authority,** leadership and governance
2. **Decision-making** and window of opportunity
3. **Planning**: repair or rebuild; master planning urban environment
4. **Finance**: resourcing recovery and reconstruction
5. **Science** and engineering: informing decision-making with evidence

The author has studied recovery in 10 places affected by earthquakes (See Table 19.1). This chapter analyses these case studies in terms of the 8 exogenous and endogenous factors listed above. Although the disasters are all earthquake-related, many of the insights would apply to recovery after other types of natural disaster, including tropical cyclones, floods, and volcanic eruptions.

19.2.1 Data Collection

Five types of data collection methods were used in a complementary way to provide both quantifiable and qualitative data and to improve the reliability of the evidence (See Fig. 19.1). The methodology of measuring recovery and resilience is reported in more detail in Platt (2016).

Remote Sensing Manual and semi-automatic analysis of satellite imagery was used to provide accurately quantifiable measures of recovery of relatively small sample areas in Pakistan, Thailand, China, and Turkey. Twelve indices of recovery were identified, covering transport, housing, shelter, services, environment, and livelihoods (Platt et al. 2016). However, the satellite imagery analysis was partial. The

Table 19.1 Data from 10 major earthquakes

Country	Name	Year	Date	Mw	Displaced	Deaths	Loss US$ bn	Size
USA	Northridge	1994	Jan-17	6.7	125,000	61	44	0.1
Iran	Bam	2003	Dec-26	6.6	75,000	26,271	1.5	82
Thailand	Indian Ocean	2004	Dec-26	9.2	1,690,000	276,025	14	3979
Pakistan	Kashmir	2005	Oct-08	7.6	3,500,000	100,000	2.3	1313
China	Wenchuan	2008	May-12	8.0	1,940,000	90,000	75	1393
Italy	L'Aquila	2009	Apr-06	5.8	67,000	309	16	0.7
Chile	Maule	2010	Feb-27	8.8	800,000	550	30	45
New Zealand	Christchurch	2011	Feb-22	6.3	25,000	185	16	39
Japan	Tohoku	2011	Mar-11	9.0	130,927	18,499	235	5502
Turkey	Van	2011	Oct-23	7.1	50,000	604	1	0.4

This table provides a comparison of the scale of the disaster in different countries. Size is measured by the formula: Size = deaths * (economic loss/GDP) (Dacy and Kunreuther 1969; Padli et al. 2010; Suppasri et al. 2016)

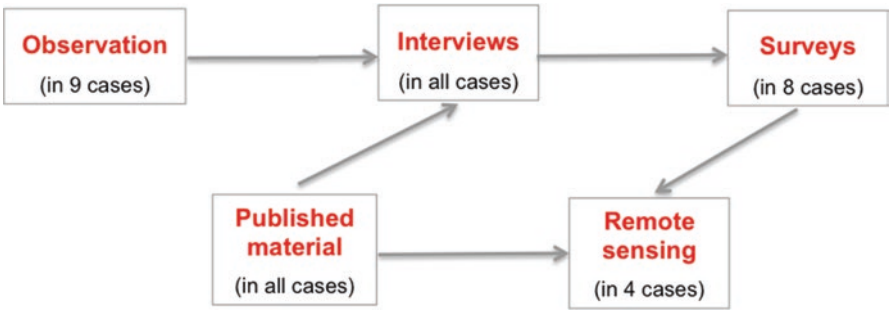

Fig. 19.1 Data collection methodology

analysis covered only part of the affected area for specific snapshots over the first 2 years of recovery.

Interviews Semi-structured interviews and focus groups were conducted with decision-makers, planners, stakeholders, and residents. Typically, 30 key informants were interviewed in each location and about half of them attended a focus group

workshop to explore issues in greater detail. Their perceptions and opinions formed the basis of the meta decision analysis reported below. No specialised software was used, but interview quotes were coded into a thematic framework using a standard ethnographic procedure (See Appendix A).

Surveys Household surveys of a small sample of residents were used in 6 of the 10 disaster locations (Chile, Japan, New Zealand, Pakistan, Thailand, and Turkey) to collect data about the timing and quality of recovery, plus many other qualitative aspects of the process (See Appendix B). Household surveys of 50 households chosen randomly were used to collect data about the timing of recovery. People were asked by what percentage different aspects of society (access, debris clearance, environmental recovery, schooling, healthcare, mains water, and livelihoods) had recovered at given intervals after the disaster. Other resilience factors, such as governance, leadership, planning, science, and construction, were derived, in part, from published sources and in part from the interviews.

Analysis of Published Material As much use as possible was made of reports, statistical data, and documents produced by government departments and international agencies. This helped provide baseline data on population, housing, and economic activities and was used to validate the extent and timing of various aspects of recovery, for example school and health provision. There was, however, limited data about rehousing, business continuity, funding recovery, and regional GDP. Published sources also provided data about the impact of the disaster in terms of deaths, displaced persons and economic loss, and pre-disaster resilience attributes, for example demography, economic production, and socio-economic factors such as equity and education. It would have been most helpful to have obtained published data about the timing of recovery, for example about population movements, housing and the local economy, but it was extremely difficult to get any useful information.

19.2.2 Measuring the Speed and Quality of Recovery

Speed of recovery was measured using key informant interviews in every case, as well as satellite imagery analysis in Pakistan, Thailand, Turkey, Italy, China, and New Zealand. The timings reported by key informants were compared to that from remote sensing and were found to correlate closely (Platt et al. 2016).

Five indicators were used to calculate a single measure of the speed of recovery, a return to normality, based on the time taken to return and comply with all the conditions listed in Table 19.2. Recovery quality was assessed using data from interviews, field observations, and published material. Five indicators were used (see Table 19.3) to calculate a measure of quality of recovery based on the concept of building back better (Kim and Olshansky 2015). Each indicator was assessed on a 5-point scale in terms of whether the recovered state was worse, the same, or better than the pre-disaster state, and the scores were summed to give a single measure of the quality of recovery in each country. This was a similar approach to that adopted by Burton (2012 p 3) in research that aimed at measuring the multi-dimensional nature of disas-

Table 19.2 Indicators of speed and quality of recovery

Speed indicators		Quality indicators	
Access	Fully restored		Scale 1–5
Temporary housing	Completely cleared	Safety	
Permanent housing	≥90% displaced rehoused	Amenity	
Schooling	≥90% children in school	Ecology	
Livelihoods	≥90% back in work	Housing	
Power	Fully restored	Local economy	
Time taken for all above conditions to be met		Recovery quality = sum of indicator scores	

Reduced set of indicators devised by the author to measure speed and quality of recover

ter resilience; "what set of indicators provide the best comparative assessment of disaster resilience and to what extent do these predict disaster recovery".

19.3 Exogenous Factors

19.3.1 Size of the Disaster

There is evidence from historic disasters of a directly proportional relationship between the number of fatalities and the years it takes to recover (Kates and Pijawka 1977). Figure 19.2 plots their data, separating pre and post twentieth-century disasters to reflect the enormous strides in pre-disaster mitigation and preparedness and in post-disaster health care and disease control. The graphs show a strong correlation between the number of fatalities and the time to recover ($R^2 = 0.83$ and 0.91).

For the 10 case study events analysed here, there is an obvious relationship between the magnitude of the event and its impact as indicated by the trend lines for deaths and economic loss in Fig. 19.3. However, the relationship is not that strong (R^2 ranges from 0.22 to 0.33). Other factors, including the economic wealth of the country, the condition of its building stock, and the level of preparedness, affect how robust a place is in terms of its capacity to resist an earthquake. Four disasters had significantly high deaths tolls: Indian Ocean Tsunami 2004, Wenchuan Earthquake 2008, Kashmir Earthquake 2005, and the Bam Earthquake 2003. In three of these disasters, the main cause was poor building construction. Three disasters had significantly high economic losses: Tohoku 2011, Wenchuan 2008, and Northridge 1994.

The question is, does this mean recovery is slower after larger events with bigger impacts? Kates and Pijawka (1977) argued that, for historic earthquakes, the speed of recovery was principally related to the magnitude of the damage (Fig. 19.2). This makes intuitive sense, but does the relationship still hold for current disasters? Surprisingly, there is little evidence from these 10 events that the speed of recovery is related to the magnitude of the event or the size of its impact (see Fig. 19.4, left

Table 19.3 Assessment of speed and quality of recovery

	USA	Iran	Thailand	Pakistan	China	Italy	Chile	NZ	Japan	Turkey
	Northridge	Bam	Indian Ocean	Kashmir	Wenchuan	L'Aquila	Maule	Christ-church	Tohoku	Van
	1994	2003	2004	2005	2008	2009	2010	2011	2011	2011
Speed (years to recover)										
Access restored	<1	1	1	1	<1	<1	<1	<1	<1	<1
Temp housing cleared	<1	4	2	4	<1	>7	2	<1	5	<1
Rehousing	2	8	2	10	2	>7	4	5	9	2
Schooling	<1	2	<1	2	<1	<1	<1	<1	<1	<1
Restore livelihoods	1	20	3	4	1	>7	2	1	5	5
Speed (years to restore to normality)	2	25	5	15	5	20	5	10	12	5
Quality (score 1–5)										
Safety	4	3	3	1	4	4	4	5	5	4
Amenity	3	1	2	2	1	1	4	2	2	2
Ecology	3	2	2	2	1	3	4	4	4	2
Housing	3	2	2	1	2	1	5	3	2	3
Local economy	3	1	4	2	5	1	4	3	2	3
Quality (% of possible maximum score)	64%	36%	52%	32%	52%	40%	84%	68%	60%	56%

This table synthesises a great deal of research. The measure of **speed** of recovery is based on field observation, key informant surveys and published data, together with satellite imagery analysis in a small subset of cases (Pakistan, Thailand, Turkey, China, Italy and New Zealand). The detailed data of speed of recovery in months for 12–13 indicators has been reduced to 5 indicators and is given in years

The assessment of **quality** is also based on field study, key informant interviews and published information. The scoring, however, is subjective and was done by the author. A 5-point scale was used to assess whether the recovered state was much worse, worse, the same, better or much better than the pre-disaster state. The scores were summed and normalised to percentages to give a single measure of the quality of recovery in each country

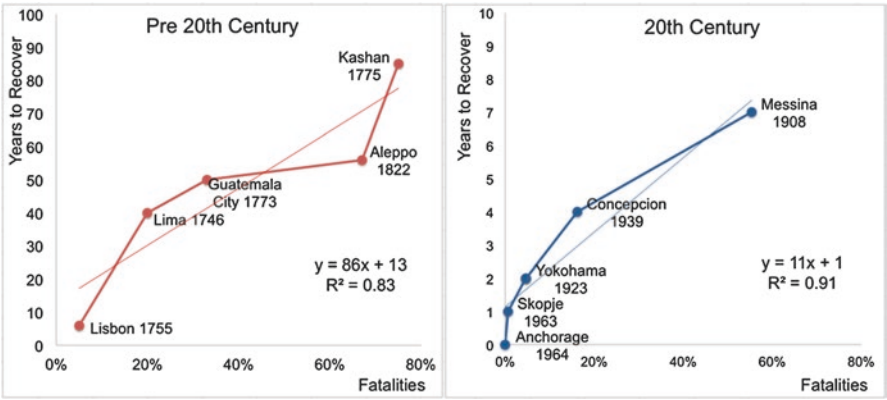

Fig. 19.2 Fatalities and speed of recovery after historic disasters (Source: Kates and Pijawka 1977). Note the vertical scale of the Pre twentieth century is 10 times larger than that of the twentieth century data

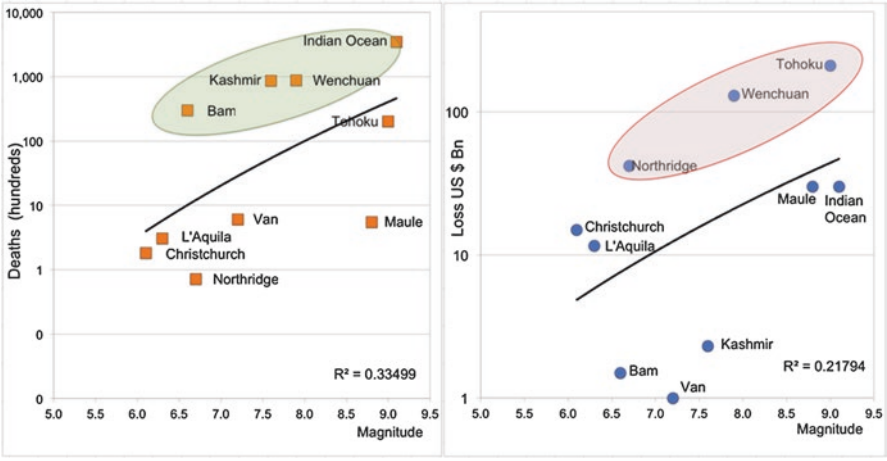

Fig. 19.3 Impact of events in terms of deaths and economic loss (axes logarithmic)

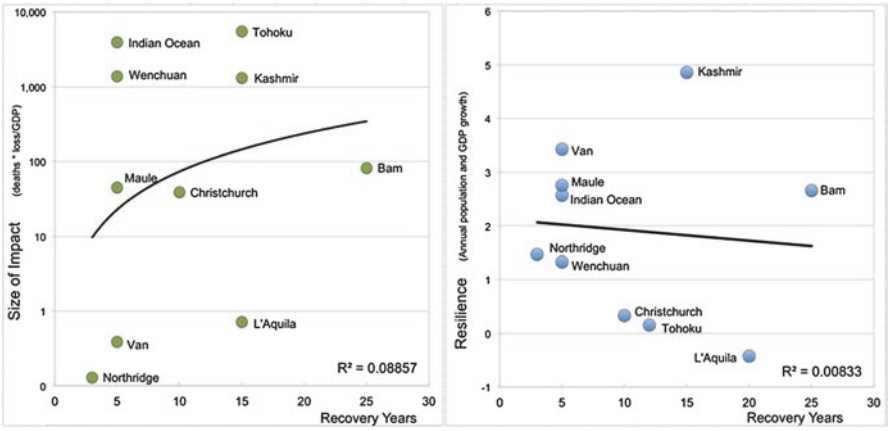

Fig. 19.4 Effect of exogenous factors on the speed of recovery
Size of impact is measured by the formula: Size = deaths * (loss / GDP). (Dacy and Kunreuther 1969; Padli et al. 2010; Suppasri et al. 2016. Resilience is measured by the formula: Resilience = Annual Population Growth 2010–2015 * Annual GDP Growth 2010–2015 * GINI Index of Equality 2015 (Sources: see Table 19.3)

hand graph). Therefore, other factors must account for the wide variation in recovery times. Kates (1977) acknowledged that other factors, including the prevailing pre-disaster economic and demographic trends, the resources available for recovery, and the quality of leadership, planning, and organization, are also important and stated that exceptional performance could reduce recovery time by as much as half. This chapter, therefore, seeks to measure the effect of these other factors mentioned by Kates on both the timing and quality of recovery.

19.3.2 Demography and 3 Economy

Two other exogenous variables to be considered are demography and economy. It might be expected that a country with a dynamic population, i.e. a high population growth rate, would recover quicker. It might also be expected that a wealthier country with a buoyant economy would have more resources to aid recovery. Finally, a country with a more equitable division of wealth might also be expected to recover more quickly since a large proportion of the funds for recovery come from individual families and local communities. The 10 countries have widely differing demographic and economic profiles, and differing levels of equality. Are these differences reflected in recovery rates? Table 19.4 presents the data to test this.

There is, however, no relationship between the speed of recovery and any of the demographic and economic indicators (See Table 19.5).

It is possible that the exogenous variables interact to produce a combined effect. To test this, the three indicators of average annual population growth, annual GDP growth, and the GINI equality index can be combined into a single measure of societal resilience, where

Table 19.4 Speed of recovery against population growth, economic growth, and equality

Name	Year	Av Annual Pop. Growth 2010–15	Av Annual GDP Growth 2010–15	Equality (GINI Index) 2015	Resilience	Return to 'normality' years
Northridge, USA	1994	0.9	4	0.41	1.5	2
Bam, Iran	2003	1.0	7	0.38	2.7	25
Indian Ocean	2004	1.1	6	0.39	2.6	5
Kashmir, Pakistan	2005	1.8	9	0.3	4.9	15
Wenchuan, China	2008	0.4	9	0.37	1.3	5
L'Aquila, Italy	2009	0.2	−6	0.35	−0.4	20
Maule, Chile	2010	0.9	6	0.51	2.8	5
Christchurch, NZ	2011	1.0	1	0.33	0.3	10
Tohoku, Japan	2011	−0.1	−5	0.32	0.2	12
Van, Turkey	2011	1.1	8	0.39	3.4	5

Sources: Population growth rate: United Nations, Department of Economic and Social Affairs, Population Division, GDP growth: World Bank http://data.worldbank.org/indicator/NY.GDP.MKTP.KD.ZG,GINI Index http://data.worldbank.org/indicator/SI.POV.GINI

Table 19.5 Effect of exogenous factors on the speed of recovery

Exogenous factor	R2
Deaths + missing	0.046
Economic loss US$bn	0.042
Loss/GDP	0.001
Total national population (year of disaster)	0.083
Population growth (av. annual)	0.002
Total national GDP (year of disaster	0.086
GDP growth (av. annual)	0.093
Regional GDP (year of disaster)	0.179
GINI equality index	0.196

$$R = P^{*}E^{*}G$$

(R = resilience; P = population growth; E = economic GDP growth; G = GINI index)

Figure 19.4 shows, surprisingly, that there appears to be no relation between speed of recovery and either size of impact of the disaster or the combined resilience index of demographic and economic factors.

19.4 Endogenous Factors

The following five sets of endogenous factors are considered:

- Authority, leadership and governance
- Decision-making and window of opportunity
- Planning: repair or rebuild, master planning urban environment
- Finance: resourcing recovery and reconstruction
- Science and engineering: informing decision-making

19.4.1 Authority, Leadership and Governance

Governance is defined in this chapter as the extent to which control and decisions about recovery are top-down and centralised or bottom-up and delegated to regional and local authorities with a degree of community consultation and involvement. In 5 of the 10 countries (China, Iran, Pakistan, Thailand and Turkey), there is a top-down governance structure. There are, however, differences of detail.

In Pakistan, governance is conducted through military institutions and government departments. Turkey also has a centralised top-down structure with little tradition of community involvement. Van is far to the east, away from the centres of power in Ankara and Istanbul, and local involvement of stakeholders was hampered by political tensions of the Kurdish separatist movement. Decisions about reconstruction were taken by AFAD, the Prime Minister's Office for Disaster Management, and Toki, the Government Housing Agency. Interviews with personnel in AFAD revealed that geologists made planning decisions in Van on the basis of distance from a known fault and whether the land was government-owned; there was no public consultation (Platt and Durmaz 2016). Iran, Thailand and China have similar top-down governance structures.

In Italy, decision-making was initially top-down, but after the first phase, there was a lack of coordination between regional, provincial, and municipal authorities. The many people who spoke at the forum organised by the OECD (OECD 2012) and Groningen University (Brezzi and McCann 2012) on recovery in L'Aquila, attended by the author of this chapter, related how the national, regional, provincial, and municipal authorities had failed to cooperate effectively, with each accusing the other of being the cause of delay. This judgement is supported by Alexander (2010) and Daziel (2012). Nor was there any genuine community involvement and consultation, even with local architects, engineers, or academics. Leadership after the L'Aquila earthquake might be characterised by chaos and failure of government.

In contrast, governance in the USA, Japan, New Zealand, and Chile, was more balanced with delegation of authority to regional and local government, and with stakeholder involvement and community consultation. In Chile, the government appointed a national coordinator to develop a reconstruction plan. The plan was based on the premise that "the State is unable to reconstruct everything or even

Fig. 19.5 Architect Carolina Arriagada at weekly briefing to a residents association and resulting master plan for Tubul, Chile. KEY: *1* health centre; *2* school; *3* police; *4* fire brigade; *5* wetland park; *6* housing (266); *7* main street; *8* waterfront; *9* info centre; *10* park; *11* cycleway; *12* port infrastructure; *13* new road; *14* evacuation assembly

control the process of recovery centrally from Santiago. With the support of the state, it is the responsibility of each region, town council and community to develop its own plans" (MINVU 2010 p. 108; English translation MINVU 2013 p. 2). This meant that authority was delegated to the regional government.

The distinctive aspect about recovery in Chile, however, was the quality of the participation process that involved the community in decision-making and kept them informed about progress (See Fig. 19.5). The architects who were master planning recovery in the 18 coastal settlements visited their areas at least once a week, briefing residents groups and business people, and walking the streets to monitor progress and meet residents. Maps, sketches, and plans were used throughout this process to communicate ideas and get feedback. The main objective was to get business up and running again. So restaurants and fish processing plants operated in temporary structures while permanent accommodation was planned and built.

Similarly in Japan after the Tohoku disaster in 2011, the central government took control providing the resources and setting the agenda, and the regional and municipal authorities interpreted this policy and implemented plans. There is also a legal obligation in Japan to consult members of the community. But there are cultural differences between Chile and Japan that impacted the speed and quality of recovery. The political structure in Japan is more strongly centralised and the national government maintains a closer oversight over the prefectures, cities, and other local government institutions, so there is much less delegation of decision-making (Sorensen 2004). Public consultation in Japan was, therefore, more formalised, less inclusive and gave priority to a smaller section of opinion.

In New Zealand, the Canterbury Earthquake Authority (CERA) and Christchurch City Council (2011) made efforts to involve citizens in the debate about the future of the city. CERA conducted community workshops and public consultation on the

Recovery Strategy for Greater Christchurch (CERA 2011). The City Council planning department's focus was on replanning the central business district, and it ran the Share an Idea campaign that involved residents through an interactive website and an exhibition attended by over 10,000 people (Carlton 2013). However, despite these initiatives, more power lay with the Minister for Canterbury Earthquake Recovery and CERA than with the city council or local citizens and stakeholders.

There were considerable differences in which authority was responsible for recovery decision-making, i.e., whether existing ministries and local government are in charge or a special, dedicated organisation is in control. Typically, the creation of a dedicated body needs special legislation. In 6 of the 10 case studies (China, Iran, New Zealand, Pakistan, Thailand and Turkey), authority was vested in a special body.

The Government of Pakistan established the Earthquake Reconstruction and Rehabilitation Authority (ERRA) on October 24, 2005, 2 weeks after the disaster, to control all aspects of relief and recovery and to "convert adversity into opportunity" by "building back better" (GFDRR 2014, p. 4). In coordinating the various organisations involved, ERRA adopted the UN cluster approach that grouped humanitarian organisations into specific areas of responsibility, for example health and water/sanitation (United Nations 2005). The early performance of clusters in Pakistan was uneven; responsibilities were not clearly defined, and some clusters struggled until government departments were involved, but it provided a framework for coordination in a chaotic operational environment (Hidalgo and Lopez-Claros 2007).

In New Zealand, the local authorities, Christchurch City Council, and Waimakakiri District Council were initially in charge after the September 2010 earthquake. This changed after the second, more devastating earthquake the following February 2011. Two weeks after the February quake, the Government passed the Canterbury Earthquake Recovery Act 2011 granting extraordinary powers to the Canterbury Earthquake Recovery Authority (CERA) as a department of government. Instead of working to strengthen the city council, CERA took over its core recovery functions and the city council was, initially, side-lined. However, despite the tensions, CERA and the municipal authorities cooperated and power gradually reverted to the city council. In January 2015, CERA was downgraded from a department to an agency within the Department of the Prime Minister.

After the disaster in Tohoku in 2011, the Japanese government immediately sought to broaden the recovery strategy by setting up an advisory council. Within 2 months the council issued seven principles for the reconstruction framework, that became the basis for the government guidelines that were decided on by the National Policy Unit 3 months after the disaster (Government of Japan 2012). The new governmental Reconstruction Agency, reporting to the Cabinet, was established in February 2012. Its aim was to plan and coordinate all national reconstruction policies and measures and to support the efforts of afflicted local governments by serving as a one-stop shop. The role of the central government was, therefore, to provide guidelines for reconstruction and support in terms of finance, human resources, and know-how, but the main administrative actors were the municipalities.

In Chile, the central government recognised it would be unable to reconstruct everything or even control the process, and national coordination was limited to

defining the scale of the problem and allocating resources. Planning and implementation were the responsibility of the regional government and specialist teams of experts. What distinguished recovery in Chile was the community consultation and the desire from the bottom up to rebuild as quickly as possible, but also to build back better (Platt and So 2016).

19.4.2 Decision-Making and the Window of Opportunity

Societal resilience, the level of preparedness and rapid and successful recovery depend, to a large extent, on good decisions (Coles and Zhuang 2011).

If official agencies do not act quickly, many victims will begin to rebuild where and how they choose. Although speed is necessary, it is also vital to take the time to plan post-disaster reconstruction. Planning can create opportunities to improve land use and infrastructure, enhance safety, promote good design, involve citizens in decision-making, and find cost-effective solutions. If planning takes too long, though, it will be ineffective. Alexander (2013b) cautions that reconstruction that occurs very rapidly should be treated with suspicion, for it implies that there has been a failure to consult adequately with interested parties. Time is not limitless, however. The worst cases, he suggests, are either those in which planners ride roughshod over local interests or those in which a conflict of interest leads to stalemate. Many of these problems can be mitigated by pre-disaster planning that sets out general principles and policies that can be updated after the disaster.

Reactive policies are understandable in the context of the urgent policy needs in post-disaster situations (Ingram et al. 2006). Relief has to be rapid and short-term recovery efforts must aim to minimise the time needed to rehouse people safely and to re-establish livelihoods. During this transitional phase it is critical that communities are informed about longer-term plans in order to reduce anxiety and frustration. Long-term recovery policies require comprehensive, site-based assessments of risk and vulnerability and effective consultation with stakeholders. Long-term, multisector strategic planning can facilitate the sustainable management of resources, supply livelihood support, strengthen infrastructure, improve urban planning and design, extend insurance, and enhance disaster preparedness at the national, regional, and community level.

The window of opportunity for effecting radical change and for accomplishing post-disaster improvements is narrow, in many cases lasting for just 18–36 months after a disaster (Birkmann et al. 2010). Although there is little research on this topic, Comerio (1998) suggests that basic functions should be restored within 2 years to ensure successful recovery. This window of opportunity varies from one country to another, not so much because it is an inherent quality of disaster recovery, but rather because it is a product of a particular country's political climate. Having to deal with a crisis moves issues higher up a government's policy agenda (Kingdon 1995, 2010). In time, other pressing problems divert attention.

Turkey and Japan represent extremes in this regard. In Turkey, following the Van earthquake in October 2011, the window of opportunity was extremely limited in duration and extent. Post-disaster planning by the Disaster and Emergency Management Presidency (AFAD) and the various government ministries adhered to strict protocols with well-defined criteria, and there were a small number of decision-makers and little stakeholder or community involvement. The window of opportunity to do things better may have been open for 6 months at most.

In Japan, following the Tohoku earthquake in March 2011, there was, by contrast, a massive, concerted effort by many sections of society to come to terms with the issues and to devise safer solutions. Despite the efforts of the national government to speed up the process by providing resources and imposing deadlines, the effect was to delay reconstruction. The window of opportunity was still, to an extent, open 5 years after the event.

In Chile, meanwhile, following the Maule earthquake in February 2010, the window of opportunity was open for about 18–24 months, during which architects seconded from the University of Bío Bío by the regional government worked on master plans for the disaster-affected coastal communities, and planners from the Ministry of Transport in Santiago devised a new master plan for Concepción, the capital of the Bío Bío Region (Platt 2012a). Subsequently, the planners who had been seconded to special teams went back to their old jobs, and the government's priorities shifted with the change of government from Sebastián Piñera's centre-right Alliance for Chile to former President Michelle Bachelet's centre-left New Majority party in December 2013 (Meyer 2014).

Figure 19.6 shows the results of an attempt to estimate this window of opportunity for 12 countries (in terms of recovery and the number of months after the event). The estimates are based on fieldwork interviews in 10 of the 12 countries and an intense search of published sources. None of the papers and reports specifies this time period, but, in most cases, inferences can be drawn from how long policy committees consulted and when final plans were published.

19.4.3 Planning: Repair or Rebuild; Master Planning Urban Environment

Reconstruction after an earthquake is a complex process entailing economic, political, and social issues as well as geotechnical considerations. Public awareness of the risk is high, and the issue is accorded high priority on political agendas (Scholl 1986). It is, therefore, an opportunity to change how things are done – to build back better (Gunewadena and Schuller 2008). Opportunities exist in the aftermath of earthquakes to enhance hazard mitigation (Birkmann et al. 2010). However, experience shows that current hazard response and mitigation practices often sustain communities as they are and merely perpetuate the disaster-damage cycle rather than address the root causes of the problems (Graham 1999). There is a natural tendency

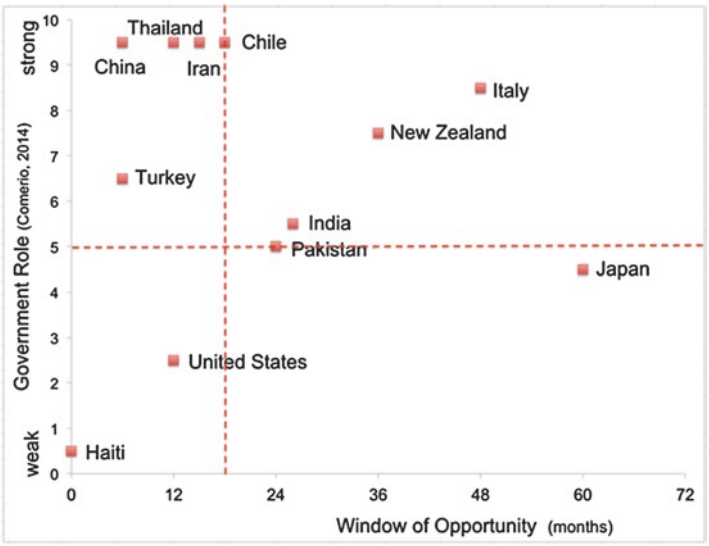

Fig. 19.6 The window of opportunity
Sources: various reports and papers were used to estimate these times, but the following represent the main sources: Chile: Platt (2012a); Sandoval and Gonzalez (2015); China: Huang et al. (2014); Haiti: Fan (2013); India: Thiruppugazh (2001); Iran: Omidvar et al. (2010); Italy: OECD (2013); Japan: Matanle (2011); New Zealand: Toomey (2015); Pakistan: Kirk (2008); Thailand: Srivichai et al. (2007); Turkey: Turan (2012); United States: Wu and Lindell (2004)

among survivors to want to restore their lives and communities to normal as quickly as possible (Scholl 1986), putting pressure on the authorities and inhibiting mitigation strategies and long-term planning. Nevertheless, most communities do become safer and less vulnerable to earthquakes as a result of post-disaster reconstruction (Haas et al. 1977; Rubin et al. 1985).

19.4.3.1 Speed or Safety

Decisions about whether the emphasis should be on rapid reconstruction or on increased safety and building back better are, perhaps, the most critical of post disaster meta-decisions (Kim and Olshansky 2015). The key question facing the authorities is whether they should aim to reinstate livelihoods and rebuild homes as quickly as possible or whether the crisis is an opportunity to change – to increase safety, to strengthen the economy, and to improve the urban environment. Speed of reconstruction was exceptionally fast in two of the studied countries, China and Turkey, where a large proportion of displaced families were rehoused within 2 years and infrastructure and livelihoods were restored (Miao 2010; Dunford and Li 2011).

In Italy, after the L'Aquila earthquake in 2009, the main issue was the slow recovery of the local economy. Most of the historic buildings were safeguarded with

an exoskeleton of scaffolding; however, it may take years to repair them (See Fig. 19.5). Meanwhile, much of the city centre of L'Aquila was closed. Although the main priorities of residents were repair and reconstruction of their homes, reconstruction of the historic centre and re-establishing employment (OECD 2012), rebuilding was on the outskirts of the town (Alexander 2010; EEFIT 2013). In 2016, the centre of L'Aquila was still partially closed and the university, the main economic driver in the region, was operating in temporary rented accommodation. Instead of repairing existing homes, the government built 12,000 new homes in 19 new settlements 15 kilometres from the old city centre (Alexander 2010). Although these were built within 8 months of the disaster, they were built without consulting local opinion and are not where people want to live.

In Chile, there was pressure from the residents to rebuild homes, restore facilities and get the economy moving, but there was also a desire on the part of the authorities to develop new urban plans that would improve these communities and make them safer. Master planning of the 18 coastal settlements affected by the disaster was completed within 10 months by a team of architects and planners seconded from the University of Bío Bío. The aim of these master plans was to restart business, rehouse residents, and to improve safety. This involved relocating critical facilities, a setback for buildings of 50–80 metres from the beach, and constructing new sea defences, including tree planting and a promenade forming a sea wall. The teams also produced designs for tsunami-resistant housing (Platt 2012a).

In Japan, after the 2011 Tohoku earthquake, the government's top priorities were also economic revival and safety. In contrast to Chile, however, these two aims seemed to be at odds and were causing delay. The safety imperative in Japan meant that ways of life and people's relationship to the sea had to change, and this was painful and caused dissent. Up to 9 m high tsunami protection levees were built, homes were moved to higher ground along the fiord-like Rias Coast, and on the Sendai Plain, where there are no natural hills, housing was concentrated on raised platforms. By law, the authorities had to consult people, and it is in the nature of Japanese society to try to reach consensus rationally (Heath 1995; Kopp 2012). This takes time, which undermined the possibility of recovery in places that were already in economic and demographic decline.

In Turkey, the imperative was speed, particularly to rehouse people in permanent housing. Transitional container shelters were provided within 3 months and 35 camps comprising 30,000 containers and 175,000 inhabitants were established in Van and Erçis (Basbuğ Erkan et al. 2015). The containers were smaller than those provided in Japan and housed bigger families, but people didn't have to stay in them nearly as long as people did in Japan. The author visited Van 10 months after the earthquake, while temporary camps were in operation. The author visited again 18 months after the disaster and the camps were nearly all empty. Within 15 months, the Ministry for Housing Development (TOKI) had built 10,000 dwellings in Van, and 5000 in Erçis (Fig. 19.7). This rate of reconstruction is unprecedented (Platt and So 2016).

Fig. 19.7 New TOKI housing (photo by author) taken on landing at the airport in Van 10 months after the disaster

19.4.3.2 Construction: Repair or Rebuild

Unless the decision is to relocate the whole city or settlement, people need to decide whether to repair or rebuild after a disaster. Two case study countries – Iran and China – opted for complete rebuilding. The remaining countries opted for a mixed strategy.

In New Zealand, there was a feeling amongst engineers that some decisions to demolish were unjustified and that demolition was driven by the high level of insurance penetration and by a conservative approach to safety (Lynch 2012). The engineers the author interviewed at Canterbury University in Christchurch and GNS Science in Wellington confirmed this. One of the key issues was that few cities hit by recent earthquakes had suffered such a high intensity of aftershocks, and this had influenced decisions about reinsuring buildings in Christchurch (Merkin 2012; Watson 2012).

The main policy outlined in the Christchurch City Council's Central City Plan was for a more compact, low-rise, greener city centre, in which building heights would be strictly controlled (Christchurch City Council 2011). City centre businesses were relocated to the periphery. The City Council was also engaged in a debate about saving historic buildings, the most heated concerned the Anglican Cathedral (Interviews; Burdon 2015). Christchurch was unusual for the quality of its Gothic Revival public buildings and the city's Victorian and Edwardian character (Lochhead 2012). A serious architectural loss was the collapse of the Canterbury Provincial Council Chamber (1865), a remarkable colonial example of High Victorian Gothic by the local architect, Benjamin Mountfort (New Zealand Historic Places Trust 2012). This example from New Zealand, an advanced country that values its historic buildings, illustrates the importance of decisions about repair or demolition and how, unless these issues have been debated and decided in advance,

there is a risk that irreplaceable cultural heritage will be lost for lack of adequate protection during the period of aftershocks.

Emergency legislation removed all statutory protection for heritage buildings and over 150 listed heritage buildings were demolished in Christchurch. In contrast in L'Aquila, over 3000 medieval buildings were damaged, many as badly as those in Christchurch, but were subsequently supported with scaffolding (Comune di L'Aquila 2011). Over half of the city centre of Christchurch was demolished; many historic buildings were lost, and extensive areas of residential land were taken out of use. There is clearly a tension between a desire to conserve the familiar and repair damage, usually the preferred option of residents, and the ambition to make safer and build back better, often led by government. Balancing these competing goals is one of the main aims of meta decision-making.

In Pakistan, after the earthquake in 2005, the federal government directed the Housing Ministry to upgrade building codes to match international standards and in March 2006, the Ministry, in collaboration with National Engineering Services Pakistan Limited (NESPAK), drafted new building codes. But in the years following the release of the codes, there was evidence that few people had the followed recommended construction practice. The high cost of standard building materials, especially steel and cement, the lack of understanding about sound concrete construction, and the lack of adequate site supervision meant that reconstruction was not as safe as supposed.

19.4.3.3 Master Planning

An aspect of the wider question about speed and safety is whether homes and activities should be reconstructed in the same place or relocated to safer areas. Relocation is generally considered as a last resort because of land ownership issues and public opposition (González 2012). Although the policy decision to relocate is taken at high levels, detailed implementation involves local land-use planning decisions about which built-up land should be abandoned and new green-field or agricultural land be taken into use.

In Christchurch, in neighbourhoods bordering the lower River Avon and along the River Waimakariri in Kaiapoi to the north, there was widespread liquefaction (Quigley et al. 2012; Ballegooya et al. 2014). The water table raised nearer the surface and the crustal thickness was reduced and less able to support the weight of built structures. Severe widespread liquefaction affected many of the Christchurch suburbs, especially Avonside, Avondale, and Bexley, and its central business district. This meant a loss of large areas of the city. Approximately 20,000 houses were seriously affected by liquefaction, out of which between 6000–7500 were damaged beyond economic repair and were abandoned (Cubrinovski et al. 2012). Buried pipe networks suffered extensive damage and the wastewater system was particularly affected resulting in loss of service to large areas (MacAskill 2016). Extensive areas along the lower River Avon and around the estuary and coastal zones, and in the town of Kaiapoi, were deemed as unsuitable for rebuilding, and the government

bought the affected properties and cleared the land. Complete neighbourhoods and some communities were displaced (Swaffield 2013).

In Pakistan, after the 2005 earthquake, the plan was to relocate the city of Balakot, which had been almost completely destroyed, to a safer location 23 kilometres south towards Mansehra (Ismail 2012). Yet when the author visited the town 9 months after the disaster, new inhabitants had already migrated to the site of the original town because of its strategically important location and had set up businesses and were building homes. For various reasons, including costs, land ownership, poor governance, and corruption, plans for the new town were not realised (Asad 2014). Owners of the land that was designated for the new city refusing to leave their land and a failure to involve the local community in the plans were other reasons for the failure of the project (Shafique and Warren 2015).

19.4.4 Finance: Resourcing Recovery and Reconstruction

Financing recovery is about providing the resources for business continuity and reconstruction. This involves decisions about whether businesses should fend for themselves or receive support, whether individual households or the state should rebuild homes, and whether government should try to control resource allocation and prices or leave demand and supply to market forces. In part, these decisions depend on sovereign wealth and insurance penetration.

All the countries studied, with the possible exception of Iran, prioritised business continuity, and some gave significant amounts of assistance to help business continue. In Chile, Japan, and New Zealand the local government financed the construction of temporary shops and restaurants, and these became local tourist attractions (see Fig. 19.8).

Insurance penetration ranged from near 100% in New Zealand to virtually zero in Pakistan. Chile was somewhere between these extremes. Nevertheless, insurance played a role in Chile in facilitating recovery and reconstruction (Franco and Siembieda 2010), even though insurance penetration was low (30% of the residen-

Fig. 19.8 Temporary shops and restaurants: Dichato Chile, Kesennuma Japan, Christchurch New Zealand

tial properties in the capital Santiago and 10% elsewhere, and about 60% for commercial and industrial properties throughout the country).

In New Zealand, less than 0.5% of all damaged dwellings were uninsured and most non-residential buildings in the CBD were fully insured. The government insurance scheme will pay losses of more than NZ$7 billion and private insurers will pay upwards of a further NZ$10 billion towards the cost of rebuilding Christchurch. The government expected to spend an additional $8.5 billion. One of the more difficult issues was that authorities were keen to have buildings seismically strengthened, but there was a question about who paid for the enhanced performance.

In terms of housing, most reconstruction in China was done by the state and a proportion of new homes were also built by the state in Japan, Turkey, and Italy (OECD 2012). In contrast, in Pakistan, to ensure that homes were rebuilt the way people wanted, the policy was for people to self-build on the same plot with government advice about safer construction and grants for reconstruction (Bajwa 2007). It was hoped that this approach would more adequately match people's needs, but the financial assistance was insufficient; the technical advice was unclear, and people lacked understanding of safe construction practice.

Various authors have pointed out the problem of what has come to be known as welfare dependence. Sandoval and Voss (2016) describe how this was a problem after the volcanic eruption in Chaitén, Chile, in May 2008. They describe how a lack of control over the benefits may have produced a welfare dependency in which people were reliant on government benefits for more than 2 years. The author of this paper observed a similar phenomenon in Thailand after the Indian Ocean tsunami of 2008. Survivors in Ban Nam Khem, the town studied by the author, received aid for over 2 years. The unprecedented level of international aid and compensation resulted in fishermen receiving two or three boats and families being given two houses. This excess attracted migrants and produced an unhelpful indolence amongst some. Similar patterns were reported in Indonesia and India (Régnier et al. 2008).

19.4.5 Science and Engineering: Informing Decision-Making

There have been major advances in our scientific understanding of natural hazards, in quantifying vulnerability, exposure and risk, and in engineering solutions to mitigate damage. This knowledge, particularly its application in building codes and enforcement, has dramatically reduced the casualty rates in developed countries. Better disaster preparedness, early warnings and evacuation, immediate response, and international relief have also had a positive impact. Fatalities, however, in very large disasters, such as Tohoku 2011, and in less developed countries, such as Haiti, Pakistan, and Nepal, are still unacceptably large. Damage and economic losses are also huge and can impose severe strains even on developed economies like Japan. Nevertheless, the widening application of scientific knowledge and engineering expertise means that things are steadily improving.

New Zealand was perhaps the most impressive of the case studies in terms of the engineering and science that went into understanding the earthquakes and resultant damage and the development of clear guidance. In particular, a simple system of zoning land was devised according to the future risk of liquefaction and the type of foundation required. For example, Tonkin & Taylor, a firm of consulting engineers collated all the survey data, insurance claims, and other information into a GIS that it made available to all the players (Platt 2012b).

Worldwide, there has been less progress in terms of understanding recovery and providing the information decision-makers need to manage reconstruction. One area in which the author has personal experience is in the use of remote sensing to monitor recovery (Van Westen 2000; Brown et al. 2010, 2011; Blaschke 2010; Bello and Aina 2014). There have been big strides recently in the use of data collected from satellite and airborne sensors to map hazards, assess post-earthquake damage, manage humanitarian and financial assistance, and plan and monitor long-term recovery. The most useful application in the disaster management field is to estimate the vulnerability of buildings to earthquake and tsunami risk (Geiß and Taubenbšck 2013; Geiß et al. 2014, Mück et al. 2013; Wurm et al. 2015). However, the take up of this technology by disaster management practitioners and planners is disappointing.

19.4.5.1 Two Types of Information Needs

The Nobel prize-winning economist Kahneman (2012) suggested that we have two ways of thinking. Fast thinking involves intuition and instinctive behaviour while slow thinking demands deliberation and rational analysis. The people charged with disaster management have to make choices fast, using experience, instinct, and following established protocols. They find it difficult to think about using the kind of information research scientists are able to provide. Moats et al. (2008) describe how, after major disasters, leaders are required to make high-consequence decisions with incomplete or inaccurate information, ill-defined goals, the pressures of time, and a constantly changing situation by drawing on their training and experience. They posit scenario planning as a way that managers can understand better their environments so as to avoid disastrous events and to put in place efficient and effective plans for coping if disaster should strike. Bradfield et al. (2005) say public policy makers are increasingly using scenarios to involve multiple agencies and stakeholders in policy decisions, enabling joined-up analysis and creating an accommodation platform to assist policy implementation.

As part of the EU project Framework to integrate Space-based and in-situ sENSing for dynamicvUlnerability and recovery Monitoring (SENSUM), the author devised a scenario planning game to better understand the information needs of disaster management decision-makers (See Fig. 19.9; Platt et al. 2014). The game aimed to explore how information is needed at different stages in the recovery process and to address the question of why the take-up of new data technology, specifically remote sensing based maps, is slower than one might have expected. In the

Fig. 19.9 Disaster recovery scenario planning game with disaster managers and reconstruction planners in Kyrgyzstan/Tajikistan (*left*) and Turkey (*right*)

disaster management field, this approach has been applied in ShakeOut preparedness exercises and drills (William Spangle Associates 1994; Wein and Rose 2011) and civil defence exercises (Bradfield et al. 2005). Of particular interest, Chermack (2004) analyses decision failure by isolating three key issues that affect dynamic decision-making in situations similar to those found in disaster management: bounded rationality, exogenous variables, and friction.

Although the scenario planning game worked remarkably well, disaster managers in both countries had difficulty in transferring information needs into requests for data products. At the time, we put this down to the pace of the disaster event forcing decision makers to follow standard protocols. We assumed that, with more familiarity with GIS and remote sensing, information products would be more widely adopted. However, Kahneman's thesis of thinking fast, thinking slow suggests that the problem is more fundamental. The need to respond quickly means that disaster managers use intuitive, System 1 thinking almost exclusively and may not be able to use the kind of information scientists are able to provide currently.

19.4.5.2 Two Types of People Needed for Disaster Management and Recovery Planning

This analysis suggests that governments need to authorise two teams to respond to disasters: one, the usual civil defence team managing relief and immediate recovery who are good at System 1 thinking, and the other, who are good at both System 1 and System 2 thinking, planning long-term physical, social, and economic recovery. The second team might have a few key people from civil defence who would provide liaison but would be led by and comprise people seconded on merit for 18 months to 2 years from academia, industry, and the civil service.

19.5 Disaster Management and the Speed and Quality of Recovery

The preceding 5 endogenous factors can be used to construct an index of post-disaster management and recovery planning where each factor is scored between 0 and 4 on a 5-point subjective scale. It should be stressed that, although the data used to construct this index is based on careful study of the available evidence, the assessments are subjective and based on the considered opinion of the author alone (see Table 19.6).

Figure 19.10 shows that there is a clear relationship between the standard of post disaster management decision-making (as assessed by the author) and both the speed ($R^2 = 0.56$) and quality of recovery ($R^2 = 0.90$). The relationship between post-disaster decision-making and the quality of recovery in terms of whether crucial aspects of the society and economy improve, i.e., are built back better is striking, although perhaps unsurprising.

19.6 Discussion

Disaster resilience is widely assumed to be determined by how well a society resists the impact of a disaster event and by how quickly it recovers. But speed is not everything and that, as well as returning to normality building back better is also important in assessing recovery since it increases resilience to future disasters.

Table 19.6 Disaster management indicators and the speed and quality of recovery

Name	Governance	Decision-making	Build back better	Finance	Science information	Normalised	Speed	Quality (%)
Northridge, USA	3	3	2	2	3	65	3	64
Bam, Iran	1	1	1	1	2	30	25	36
Indian Ocean	1	2	1	3	2	45	5	52
Kashmir, Pakistan	2	1	1	1	1	30	15	32
Wenchuan, China	2	2	2	2	3	55	5	52
L'Aquila, Italy	1	0	1	1	2	25	20	40
Maule, Chile	4	3	3	3	2	75	5	84
Christchurch, NZ	2	2	2	3	4	70	10	68
Tohoku, Japan	2	2	2	3	3	60	12	60
Van, Turkey	2	3	2	2	1	50	5	56

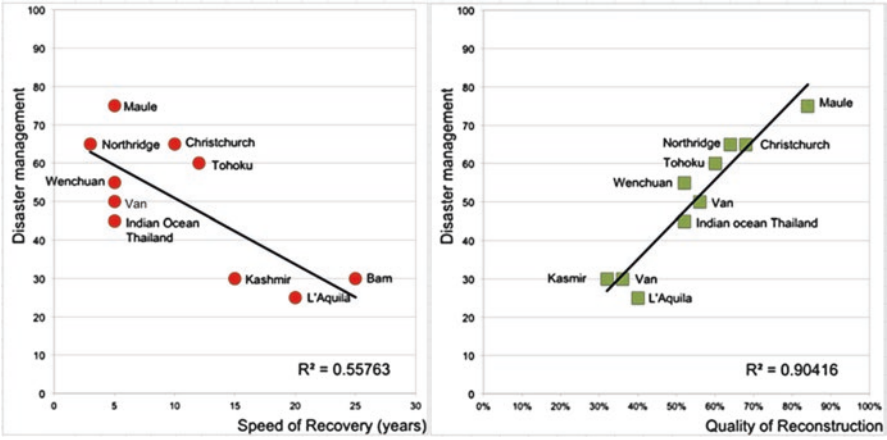

Fig. 19.10 Disaster management and the speed and quality of recovery
Note the data plotted is an assessment of disaster management and the speed and quality of recovery for specific earthquakes, for example L'Aquila 2009, rather than an assessment of disaster management in general for all events in that country

It has been widely assumed by many people, including the author of this paper, that both exogenous and endogenous factors play a part in determining the speed and quality of recovery (for example Rubin and Barbee 1985). The finding that none of the exogenous factors considered in this analysis has an effect on the speed of recovery sounds counter-intuitive. Common sense suggests that Japan is taking longer to recover than Turkey or the USA because the events were quite different in size of impact. One might assume that Pakistan is taking longer to recover than China because its economy is much weaker.

A possible explanation for this lack of relationship is that there are interactions between population and economic variables. The analysis, therefore, combined measures of population growth, GDP growth, and the GINI index of equality to derive a simple index of societal resilience. This single index of societal resilience also had little effect. We know, however, that societal resilience is much more complex than population and economic dynamics. Various authors have argued that social capital is important in building community resilience (for example Cutter et al. 2010; Aldrich 2012), and others have talked about the adaptive capacity of families, communties, and societies to respond to crises (for example Dovers and Handmer 1992; Kleina et al. 2003). This is a rich area for further research, not least to determine to what extent social capital and adaptive capacity are exogenous and, therefore, fixed, and to what extent they can be encouraged and developed in advance of disasters.

Before concluding, it is important to question the reliability and replicability of the method of analysis adopted here. The author has studied recovery after more than a dozen disasters, 10 of which are reported here. This has afforded him a broad understanding of the issues involved in post-disaster recovery. However, the data

used in the analysis is, in part, subjective. Although the assessments are based on evidence from field studies, remote sensing analysis, interviews, and published data, there is the possibility of subjective bias.

There is also a danger of treating variables as independent when they are possibly inter-related. This is especially true of the relationship between the assessment of post-disaster management and the quality of outcomes. Post-disaster management was assessed in terms of the five exogenous factors: governance, decision-making, build back better, finance, and science and information. Conceptually, these are different from changes in the quality of housing, amenity, etc. The author was aware of this risk and made efforts to differentiate the assessments. Nevertheless, there is a possibility that an assessment of governance and policies of building back better, for example, are confounded with the quality of recovery. In other words, one is judging the standard of disaster management by the quality of recovery outcomes.

19.6.1 Next Steps

The factors affecting the speed and quality of recovery would seem to be a promising area for further research. The reliability findings from this limited study of ten cases would be improved with events from more countries. It would also be useful to study other earthquakes in the same countries to see if the variation in speed and quality varied as much within the same country as it does between countries.

In terms of exogenous and endogenous factors, it would be interesting to see if the frequency of earthquakes within a country has any effect. One might expect that in countries where earthquakes are frequent, national and local government and businesses and households would be better prepared, more resilient, and recover faster than in places where earthquakes occur infrequently.

19.7 Conclusion

Disaster recovery is a huge subject for investigation. It applies to all sectors of society: housing, transport, infrastructure, industry, environment, etc. and covers many aspects of human behaviour, from individual wellbeing to the macroeconomy of whole regions. Our understanding of the issues ranges from the scientific to the intuitive and initiatives taken encompass professionally engineered solutions and spontaneous community action.

Governments seem unable to learn lessons from previous disasters in other countries. In part, this is because of the relative infrequency of major disasters and a lack of direct experience amongst the key players. But it is also a product of the extreme time pressure on decision-makers from the public and press to be seen to be doing

something. It is perhaps not surprising then that progress in understanding and managing recovery has been relatively slow.

This chapter has explored to what extent pre-existing resilience (exogenous factors) and post-event response (endogenous factors) determine the speed and quality of disaster recovery. Careful analysis of the evidence from ten recent earthquake related disasters tentatively suggests that exogenous factors – the magnitude of the event, population dynamics, the wealth of the nation, and the state of the economy – play a smaller role in determining outcomes than has hitherto been supposed. Endogenous variables, i.e., the decisions, policies, and choices governments and societies make, seem to have a greater effect on recovery outcomes than has perhaps been supposed.

The critical factors in determining speed and quality of recovery would seem, therefore, to be within the control of government decision-makers, recovery planners and local communities. The evidence suggests that the quality of decision-making determines the difference between the post-disaster performance of different countries rather than the size of the impact of disaster or pre-existing demographic and economic conditions. If substantiated by other research, this would be a significant breakthrough in our understanding of resilience and post-disaster recovery.

In conclusion, the key issues for governments and decision makers in hazard prone countries are:

19.7.1 Authority

Governments need to decide who is in charge of recovery and prepare the necessary legislation to assign this responsibility. They need to ensure that they form the most competent teams of people to manage the process of recovery (i.e. people good at System 2, long-term strategic thinking). As far as possible, they need to involve local residents and business people in decision-making.

19.7.2 Decision-Making

National, regional, and local governments need to improve their preparedness in terms of rehearsing critical decisions before an event.

19.7.3 Build Back Better

Every effort needs to be made to find ways of building back better both in terms of building structures, but also urban planning and economic development.

19.7.4 Finance

Governments need to know where the money is coming from to finance reconstruction and to develop procedures for getting this money to the grass roots as quickly as possible.

19.7.5 Science and Engineering

Decisions about reconstruction need to apply science to inform decision-making and engineering and construction know-how to build back better.

Above all, the people charged with managing recovery need to learn lessons from previous disasters, both in the same country and in other places. This is not happening nearly enough at the moment. Nevertheless, the idea that exogenous variables are more significant than endogenous is literally empowering. It means that recovery outcomes after major disasters are in our own hands and we can decide how to recover quicker and build back better.

Appendices

Appendix A. Interview Questions

Personal: You and your Involvement with a Particular Earthquake

1. What is your role or experience in disasters?
2. What relations do you have with local or central government?
3. What event do you have experience of? How big an event? Casualties, fatalities?

The Event: Impact of the Earthquake – Preparedness Phase

4. Amount of damage – residential, commercial, infrastructure?
5. How well prepared were you physically, economically and in terms of organisation?
6. In what way was the economy affected?
7. How has society or social organization been affected?

Meta Decisions: Strategic Decisions Made at High Level by Central Government

8. Who was in charge – the existing authorities or a special dedicated body?
9. Was new legislation passed or were new authorities created?
10. Was the emphasis on speed or on community involvement and building back better?
11. Was the aim to reinstate what had been lost or was it an opportunity to change?
12. How far was the Government involved in recovery?
13. What proportion of resources went on relief and what on long-term recovery?

Operational Emergency Management Decisions – Relief and Response Phase

14. How did central, regional and local government respond?
15. Who coordinated relief and made operational decisions?
16. Could information be provided quickly enough to influence decision-making?
17. How many people were displaced and how many needed temporary shelter?
18. Where were transitional shelters located? Did this affect permanent housing?
19. Who provided temporary units, of what size, material etc.?
20. What essential public services were disrupted?
21. What proportion of people were insured?
22. How badly were water, sanitation and food supplies affected?
23. Which access roads were blocked and needed clearing?
24. Where were public services located? Health, schools etc.?

Planning Decisions – Recovery and Reconstruction Phase

25. Who was in charge of recovery and reconstruction?
26. Has the urban planning process changed to manage post-earthquake recovery?
27. How is policy developed and by whom?
28. Who does land use, transport or economic development planning?
29. Was there an urban or regional plan? Was there an economic development plan?
30. What other organisations were involved? Scientific institutes, universities?
31. What scientific, land use or census information was used?
32. How is policy and action coordinated between national regional and local authorities?
33. Is recovery and reconstruction monitored?
34. How is information used to guide the planning process?
35. What stage is recovery at? How long do you think it will take?
36. What is the impact of demographic change and migration?
37. How were people helped or compensated? Insurance? Government assistance?

38. How resilient is the community and to what extent can family networks drive recovery
39. How were displaced people rehoused? Who decided about resettlement?
40. How is housing need or demand assessed?
41. How is speedy recovery balanced against deliberation?
42. What cultural issues are involved in recovery and reconstruction?
43. Are local residents involved in decision-making, for example where to rebuild?
44. Is anyone working on plans to improve the city? What new projects are planned?

Long-Terms Decisions – Future Mitigation

45. In what ways is the country/city better prepared for another disaster?
46. Have any previous built up areas been defined as too hazardous to rebuild?
47. Has critcial infrastructure and essential services been relocated?
48. Have building design codes changed?
49. How effective is inspection to ensure buildings are repaired properly?
50. Were lessons learnt and has the public perception of risk been improved?

Appendix B. Disaster Recovery Survey

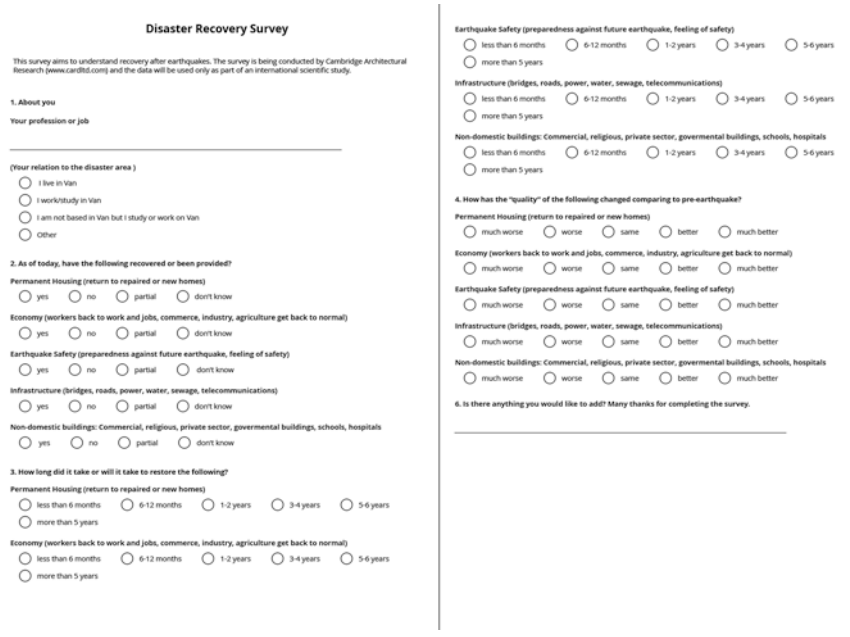

Disaster Recovery Survey

This survey aims to understand recovery after earthquakes. The survey is being conducted by Cambridge Architectural Research (www.cardltd.com) and the data will be used only as part of an international scientific study.

1. About you

Your profession or job

_____

(Your relation to the disaster area)

- ◯ I live in Van
- ◯ I work/study in Van
- ◯ I am not based in Van but I study or work on Van
- ◯ Other

2. As of today, have the following recovered or been provided?

Permanent Housing (return to repaired or new homes)

◯ yes ◯ no ◯ partial ◯ don't know

Economy (workers back to work and jobs, commerce, industry, agriculture get back to normal)

◯ yes ◯ no ◯ partial ◯ don't know

Earthquake Safety (preparedness against future earthquake, feeling of safety)

◯ yes ◯ no ◯ partial ◯ don't know

Infrastructure (bridges, roads, power, water, sewage, telecommunications)

◯ yes ◯ no ◯ partial ◯ don't know

Non-domestic buildings: Commercial, religious, private sector, govermental buildings, schools, hospitals

◯ yes ◯ no ◯ partial ◯ don't know

3. How long did it take or will it take to restore the following?

Permanent Housing (return to repaired or new homes)

◯ less than 6 months ◯ 6-12 months ◯ 1-2 years ◯ 3-4 years ◯ 5-6 years
◯ more than 5 years

Economy (workers back to work and jobs, commerce, industry, agriculture get back to normal)

◯ less than 6 months ◯ 6-12 months ◯ 1-2 years ◯ 3-4 years ◯ 5-6 years
◯ more than 5 years

Earthquake Safety (preparedness against future earthquake, feeling of safety)

◯ less than 6 months ◯ 6-12 months ◯ 1-2 years ◯ 3-4 years ◯ 5-6 years
◯ more than 5 years

Infrastructure (bridges, roads, power, water, sewage, telecommunications)

◯ less than 6 months ◯ 6-12 months ◯ 1-2 years ◯ 3-4 years ◯ 5-6 years
◯ more than 5 years

Non-domestic buildings: Commercial, religious, private sector, govermental buildings, schools, hospitals

◯ less than 6 months ◯ 6-12 months ◯ 1-2 years ◯ 3-4 years ◯ 5-6 years
◯ more than 5 years

4. How has the "quality" of the following changed comparing to pre-earthquake?

Permanent Housing (return to repaired or new homes)

◯ much worse ◯ worse ◯ same ◯ better ◯ much better

Economy (workers back to work and jobs, commerce, industry, agriculture get back to normal)

◯ much worse ◯ worse ◯ same ◯ better ◯ much better

Earthquake Safety (preparedness against future earthquake, feeling of safety)

◯ much worse ◯ worse ◯ same ◯ better ◯ much better

Infrastructure (bridges, roads, power, water, sewage, telecommunications)

◯ much worse ◯ worse ◯ same ◯ better ◯ much better

Non-domestic buildings: Commercial, religious, private sector, govermental buildings, schools, hospitals

◯ much worse ◯ worse ◯ same ◯ better ◯ much better

6. Is there anything you would like to add? Many thanks for completing the survey.

_____

References

Aldrich D (2012) Building resilience: social capital in post-disaster recovery. University of Chicago Press, Chicago

Aldrich D, Meyer A (2015) Social capital and community resilience. Am Behav Sci 59(2):254–269

Alexander D (2010) The L'Aquila earthquake of 6 April 2009 and Italian government policy on disaster response. J Nat Resour Policy Res 2(4):325–342

Alexander D (2013a) Resilience and disaster risk reduction: an etymological journey. Nat Hazards Earth Syst Sci 13:2707–2716

Alexander D (2013b) Planning for post-disaster reconstruction. http://www.grif.umontreal.ca/pages/papers2004/Paper%20-%20Alexander%20D.pdf. Last Accessed 26 Oct 2016

Asad A (2014) Disaster, development, good governance and the time frame nexus: a case study of Balakot, Hazara, Pakistan. J Humanit Soc Sci 22(3):53

Bajwa E (2007) Urban development: a strategy for reconstruction, rehabilitation and development of earthquake affected urban areas. Government of Pakistan

Ballegooya S, Malana P, Lacrossea V, Jackam M, Cubrinovski M, Bray J, O'Rourke T, Crawford S, Cowane H (2014) Assessment of liquefaction-induced land damage for residential Christchurch. Aust Geomech 30(1):31–56

Basbuğ Erkan B, Karanci N, Sibel Kalaycıoğlu S, Özden T, Çalışkan I, Gamze Özakşehir G (2015) From emergency response to recovery: multiple impacts and lessons learned from 2011 Van earthquakes. Earthqauke Spectra 31(1):527–540

Bello O, Aina Y (2014) Satellite remote sensing as a tool in disaster management and sustainable development: towards a synergistic approach. Procedia Soc Behav Sci 120:365–373

Birkmann J, Buckle P, Jaeger J, Pelling M, Setiadi N, Garschagen M, Fernando N, Kropp J (2010) Extreme events and disasters: a window of opportunity for change? Analysis of organizational, institutional and political changes, formal and informal responses after mega-disasters. Nat Hazards 55:637–655

Blaschke T (2010) Object based image analysis for remote sensing. ISPRS J Photogramm Remote Sens 65:2–16

Bradfield RW, Burt G, Cairns G, Van Der Heijden K (2005) Futures 37:795–812

Brezzi M McCann P (2012) Abruzzo 2030: on the Wings of L"Aquila. Issue paper, Forum – 17 MARCH 2012 Laboratori Nazionali del Gran Sasso, L'Aquila. Groningen University

Brown D, Platt S, Bevington J (2010) Disaster Recovery indicators: guidelines for monitoring and evaluation. CURBE, Cambridge University Centre for Risk in the Built Environment. University of Cambridge

Brown D, Platt S, Bevington J, Saito K, Adams B, Chenvidyakarn T, Spence R, Chuenpagdee R, Khan A (2011) Monitoring and evaluating post-disaster recovery using high-resolution satellite imagery – towards standardised indicators for post-disaster recovery. Martin Centre, Cambridge

Bruneau M, Chang S, Eguchi R, Lee G, O'Rourke T, Reinhorn A, Shinozuka M, Tierney K, Wallace W, von Winterfelt D (2003) A framework to quantitatively assess and enhance the seismic resilience of communities. Earthq Spectra 19(4):733–752

Burdon P (2015) Cathedral demolition simply not an option. The Press. http://www.stuff.co.nz/the-press/opinion/67547535/cathedral-demolition-simply-not-an-option. Accessed 20 Sept 2016

Burton C (2012) The development of metrics for community resileince to natural disasters. PhD Thesis. University of South Carolina

Carlton S (2013) Share an idea, spare a thought: community consultation in Christchurch's time-bound post-earthquake rebuild. J Hum Rights Commonwealth 2:4–13. sas-space.sas.ac.uk/5219/1/1714-2293-1-SM.pdf

CERA (2011) Draft recovery strategy for greater Christchurch Canterbury Earthquake recovery authority. September

Chermack T (2004) Improving decision-making with scenario planning. Futures 36:295–30911

Christchurch City Council (2011) Central City plan. Draft central city recovery plan for ministerial approval. Christchurch City Council, Christchurch
Coles J, Zhuang J (2011) Decisions in disaster recovery operations: a game theoretic perspective on organization cooperation. J Homeland Sec Emerg Manage 8(1):1547–7355
Comerio M (1998) Disaster hits home: new policy for urban housing recovery. University of California Press, Berkeley
Comfort L (1999) Shared risk: complex seismic response. Pergamon, New York
Cubrinovski M, Henderson D, Bradley B (2012) Liquefaction impacts in residential areas in the 2010–2011 Christchurch earthquakes. Tohoku Special Conference Paper 183. http://ir.canterbury.ac.nz/handle/10092/6712
Cutter S, Burton C, Emrich C (2010) Disaster resilience indicators for benchmarking baseline conditions. J Homeland Sec Emerg Manag 7:1–22. doi:10.2202/1547-7355.1732
Dacy D, Kunreuther H (1969) The economics of natural disasters: implications for Federal Policy. The Free Press, New York
Daziel P (2012) Quake lessons shared in L'Aquila. The Press. Christchurch New Zealand. 9 April. http://www.stuff.co.nz/the-press/opinion/perspective/6711790/Quake-lessons-shared-in-L-Aquila. Accessed 20 Sept 2016
Dovers S, Handmer J (1992) Uncertainty, sustainability and change. Glob Environ Chang 2(4):262–276
Dunford M, Li L (2011) Earthquake reconstruction in Wenchuan: assessing the state overall plan and addressing the 'forgotten phase'. Appl Geogr 31:998–1009
EEFIT (2013) Return mission to the L'Aquila earthquake. A joint evening meeting EEFIT/SECED/ISTRUCTE. Institution of Structural Engineers. 25 March 2013
Fan L (2013) Disaster as Opportunity? Building Back Better in Aceh, Myanmar and Haiti. ODI - Overseas Development Institute
Franco G, Siembieda W (2010) Chile's 2010 M8.8 earthquake and tsunami: initial observations on resilience. J Disaster Res 5(5):577–590
Geiß C, Taubenbšck H (2013) Remote sensing contributing to assess earthquake risk - from a literature review towards a road map. Nat Hazards 68(1):7–48
Geiß C, Taubenbšck H, Post J, Tisch A, Tyagunov S, Lakes T (2014) Assessment of buildings' seismic vulnerability from space. Earthq Spectra 30(4):1553–1583
GFDRR (2014) Pakistan Earthquake 2005: the case of centralized recovery planning and decentralized implementation. Country Case Study Series Disaster Recovery Framework Guide May 2014. https://www.gfdrr.org/sites/gfdrr/files/documents/docs/Pakistan_April%202014.pdf. Accessed 20 Sept 2016
González MC (2012) Planning back better, urgent and important. Paper presented to the 45th annual Salzburg Congress on Urban Planning and Development, Salzburg, Austria, 9–12 May 2012. https://www.researchgate.net/profile/Claudia_Gonzalez-Muzzio/publications. Last Accessed on 26 Oct 2016
Government of Japan (2012). Road to recovery. Reconstruction Agency, Prime Minister's Office. http://www.kantei.go.jp/foreign/incident/road_to_recovery.html. Accessed 5 Sept 2013
Graham A (1999) Sustainability and community resilience: the holy grail of hazards planning? Environ Hazards 1(1):13–25
Gunewadena N, Schuller M (2008) Capitalizing on catastrophe. Altamira Press, Lanham
Haas J, Kates R, Bowden M (eds) (1977) Reconstruction following disaster. MIT Press, Cambridge, MA
Heath R (1995) The Kobe earthquake: some realities of strategic management of crises and disasters. Disaster Prev Manag 4(5):11–24
Hidalgo S, Lopez-Claros A, (2007) Humanitarian response index 2007: measuring commitment to best practice. Development Assistance Research Associates (DARA)
Holling C (1973) Resiliency and stability of ecological systems. Annu Rev Ecol Syst 4:1–24
Hollnagel E, Woods D, Leveson N (eds) (2006) Resilience engineering: concepts and precepts. Ashgate, Aldershot

Huang Y, Zhou L, Wei K (2014) 5.12 Wenchuan earthquake recovery government policies and non- governmental organizations' participation. Asia Pacific J Soc Work Dev 21(2):77–91
Ingram J, Franco G, Rumbaitis-del Rio C, Khazai B (2006) Post-disaster recovery dilemmas: challenges in balancing short-term and long-term needs for vulnerability reduction. Environ Sci Pol 9(7–8):607–613
Ismail M (2012) Bridging the GAP from destruction to rehabilitation for Balakot Town, Pakistan. J Seismol Earthq Eng 14(1):69
Kahneman D (2012) Thinking, fast and slow. Macmillan, New York
Kates, R (1977) Major insights: a summary and recommendations, in reconstruction following disaster, edited by J. Eugene Haas, Robert W. Kates, and Martyn J Bowden. Cambridge, MA: MIT Press
Kates R, Pijawka D (1977) From rubble to monument: the pace of recovery. In: Haas JE, Kates RW, Bowden MJ (eds) Reconstruction following disaster. MIT Press, Cambridge, MA, pp 1–23
Kim K, Olshansky R (2015) The theory and practice of building back better. J Am Plan Assoc 80(4):289–292
Kingdon JW (1995) Agendas, alternatives and public policies, 2nd edn. HarperCollins, New York
Kingdon JW (2010) Agendas, alternatives, and public policies, Updated edn. HarperCollins College Publishers, New York
Kirk J (2008) Building back better: post-earthquake responses and educational challenges in Pakistan. http://unesco.org.pk/eedrmu/erp/publications/Building%20back%20better.pdf (last accessed on 26 October 2016)
Kleina R, Nicholls R, Thomalla F (2003) Resilience to natural hazards: how useful is this concept? Environ Hazards 5:35–45
Kopp R (2012) The decision making process in Japan. Japan Close-Up Magazine. April 2 http://www.japanintercultural.com/en/news/default.aspx?newsID=154 Accessed 13 July 2016
Comune di L'Aquila (2011) Il piano di ricostruzione dei centri storici di L'Aquila e frazioni: Linee di indirizzo strategico. Parts 1–4 Dicembre
Lochhead I (2012) An endangered city: Christchurch New Zealand and the earthquakes of 2010 and 2011 Society of Architectural Historians of Great Britain Newsletter No. 105 Winter/Spring 2012
Lynch D (2012) Quake destruction avoidable. New Civil Engineer p 6
MacAskill K (2016) Post-disaster reconstruction of civil infrastructure networks. Unpublished PhD manuscript, University of Cambridge
Matanle P (2011) The great East Japan earthquake, tsunami, and nuclear meltdown: towards the (re) construction of a safe, sustainable, and compassionate society in Japan's shrinking regions. Int J Justice Sustain 16(9). http://www.tandfonline.com/doi/abs/10.1080/13549839.2011.607160
Merkin R (2012) The Christchurch earthquakes insurance and reinsurance issues. Canterbury Law Review [Vol 18, 2012]
Meyer P (2014) Chile: political and economic conditions and U.S. Relations. 10 January. Congressional Research Service, Washington, DC
Miao, H (2010) Wenchuan earthquake 2008: recovery and reconstruction in Sichuam Province. Recovery Status Report 04. United Nations International Strategy for Disaster Reduction (UNISDR) https://www.unisdr.org/we/inform/publications/16777
MINVU (2010) Plan de Reconstrucci— Chile Unido Reconstruye Mejor. Ministerio de Vivienda y Urbanismo, Gobierno de Chile 3era Edición Octubre 2010
MINVU (2013) MINVU reconstruction plan: a united chile rebuilds better. Government of Chile
Moats J, Chermack T, Dooley L (2008) Using scenarios to develop crisis managers: applications of scenario planning and scenario-based training. Adv Dev Hum Resour 10:397. originally published online 3
Mück M, Taubenböck H, Post J, Wegscheider S, Strunz G, Sumaryono IF (2013) Assessing building vulnerability to earthquake and tsunami hazard using remotely sensed data. Nat Hazards 68(1):97–114

New Zealand Historic Places Trust (2012) Pouhere Taonga report for the Canterbury earthquakes royal commission – Heritage Buildings, Earthquake strengthening and damage, The Canterbury Earthquakes September 2010–January 2012 Final 8 March

Oakland CA, Shafique K, Warren C (2015) Significance of community participation in success of post natural disaster reconstruction project – evidence from developing country. In: Paper ID: 533. 5th International Conference on Building Resilience. Newcastle, Australia 15–17th July

OECD (2012) Building resilient regions after a natural disaster ÒAbruzzo 2030: On the wings of L'AquilaÓ. Issue paper Forum – 17 MARCH 2012 Laboratori Nazionali del Gran Sasso, L'Aquila. https://www.oecd.org/gov/regional-policy/49866886.pdf. Accessed 20 Sept 2016

Omidvar B, Zafari H, Derakhshan S (2010) Reconstruction management policies in residential and commercial sectors after the 2003 bam earthquake in Iran. Nat Hazards 54:289–306, https://link.springer.com/article/10.1007/s11069-009-9468-y

Oxford Dictionary of Construction, Surveying and Civil Engineering (2013) Oxford University Press. www.oxfordreference.com/view/10.1093/acref/9780199534463.001.0001/acref-9780199534463-e-5743?rskey=f8DtdK&result=5739

Padli J, Habibullah M, Baharom A (2010) Economic impact of natural disasters' fatalities. Int J Soc Econ 37(6):429–441

Petak W (2002) Earthquake resilience through mitigation: a system approach. In: Paper presented at the international institute for applied systems analysis, Laxenburg, Austria

Platt S (2012a) Reconstruction in Chile post 2010 earthquake. CAR, Cambridge

Platt S (2012b) Reconstruction in New Zealand post 2010–11 Christchurch earthquakes. CAR, Cambridge

Platt S (2016) Meta decision making and the speed and quality of disaster resilience and recovery. In: Trell E-M, van Hoven B, Restemeyer B, Bakema M (eds) Governing for resilience in vulnerable places. Ashgate Publishing, Farnham

Platt S, Durmaz B (2016) Disaster management decision making in Turkey: case studies of van and İzmir. IJDRR Int J Disaster Risk Reduct 17:220–237

Platt S, So E (2016) Speed or deliberation – a comparison of post disaster recovery in Japan, Turkey and Chile. Disasters (Online; forthcoming in print)

Platt S, So E, Bevington J, Verrucci E, So E, Pittore M (2014) Thinking fast, thinking slow: bridging the gap between research and practice in disaster recovery. In: Second European conference on earthquake engineering and seismology, Istanbul, Aug 25–29

Platt S, Brown D, Hughes M (2016) Measuring resilience and recovery. Int J Disaster Risk Reduct 19:447–460

Quarantelli E (1999) The disaster recovery process – what we know and do not know from research. Preliminary Paper #286. University of Delaware Disaster Research Center

Quigley M, Bastin S, Bradley B (2012) Recurrent liquefaction in Christchurch, New Zealand, during the Canterbury earthquake sequence. Geology 41(4):419–422

Régnier R, Neri B, Scuteri S, Miniati S (2008) From emergency relief to livelihood recovery: lessons learned from post-tsunami experiences in Indonesia and India. Disaster Prev Manage Int J 17(3):410–430

Rubin C, Barbee D (1985) Disaster recovery and hazard mitigation: bridging the intergovernmental gap. Public Administration Review Vol. 45, Special Issue: Emergency management: a challenge for public administration (Jan., 1985), pp. 57–63

Rubin CB, Saperstein MD, Barbee DG (eds.) (1985) Community recovery from a major natural disaster. FMHI Publications. Paper 87. http://scholarcommons.usf.edu/cgi/viewcontent.cgi?article=1086&context=fmhi_pub. Last Accessed 27 Oct 2016

Sandoval V, Gonzalez-Muzzio C (2015) Examining disaster capitalism: post-disaster actions in Chile. 7th i-Rec Conference 2015: Reconstruction and Recovery in Urban Contexts. http://www.grif.umontreal.ca/i-Rec2015/RT6_31_Sandoval_Examining%20Disaster%20Capitalism.pdf

Sandoval V, Voss M (2016) Disaster governance and vulnerability: the case of Chile. Polit Gov 4(4):107–116
Scholl R (1986) Reducing earthquake hazards: Lessons learned from earthquakes. Earthquake Engineering Research Institute
Shafique K, Warren C (2015) Significance of community participation in success of post natural disaster reconstruction project – evidence from developing country. Paper ID: 533. 5th International Conference on Building Resilience. Newcastle, Australia 15-17th July
Sorensen A (2004) The making of urban Japan: cities and planning from Edo to the twenty- first centuries, Nissan institute Routledge Japanese studies series. Routledge, New York, 400 pp
Srivichai M, Supharatid S, Imamura F (2007) Recovery process in Thailand after the 2004 Indian Ocean Tsunami. J Nat Dis Sci 29(1):3–12, https://www.jstage.jst.go.jp/article/jnds/29/1/29_1_3/_article
Suppasri A, Latcharote P, Imamura F (2016) Lessons from the 2011 Tohoku tsunami and tsunami mitigation in Japan
Swaffield S (2013) Place, culture and landscape after the Christchurch Earthquake. Space place and culture. www.futureleaders.com.au
Thiruppugazh (2001) What has changed after Gujarat earthquake 2001? Gujarat State Disaster Management Authority [Online]. http://www.jst.go.jp/astf/document/43abst.pdf
Tierney K (1997) Impacts of recent disasters on businesses: the 1993 Midwest Floods and the 1994 Northridge Earthquake. In: Jones B (ed) Economic consequences of earthquakes: preparing for the unexpected. National Center for Earthquake Engineering Research, University at Buffalo
Toomey E (2015) The Recovery Phase in Post-Earthquake Christchurch, New Zealand. University of Canterbury. 3rd United Nations World Conference on Disaster Risk Reduction. http://www.wcdrr.org/wcdrr-data/uploads/339/1-4_The%20Recovery%20Phase%20in%20Post-Earthquake%20Christchurch%20New%20Zealand%20(Toomey).pdf
Turan M (2012) Lessons learnt from Van and Erciş earthquakes 2011, Turkey: an evaluation of disaster management. Int J Bus Soc Sci 3(22) (Special Issue—November). http://ijbssnet.com/journals/Vol_3_No_22_Special_Issue_November_2012/5.pdf (last accessed on 27 October 2016)
UNISDR (2004) Living with risk: a global review of disaster reduction initiatives. http://www.unisdr.org/files/657_lwr1.pdf. Accessed 3 June 2016
United Nations (2005) What are clusters? https://business.un.org/en/documents/249. Accessed 23 May 2015
Van Westen C (2000) The modelling of landslide hazards using GIS. Surv Geophys 21(2–3):241–255
Watson W (2012) New Zealand re/insurance industry feels aftershocks of quakes. 6 February. http://blog.willis.com/2012/02/new-zealand-reinsurance-industry-feels-aftershocks-of-quakes/. Accessed 20 Sept 2016
Wein A, Rose A (2011) Economic resilience lessons from the ShakeOut earthquake scenario. Earthq Spectra 22:559–573
William Spangle and Associates (1994) Earthquake recovery exercise for local governments. Spangle Associates, Portola Valley
Wu JY, Lindell MK (2004) Housing reconstruction after two major earthquakes: the 1994 Northridge earthquake in the United States and the 1999 Chi-Chi earthquake in Taiwan. Disasters 28(1):63–81
Wurm M, Schmitt A, Taubenböck H (2015): Building types classification using shape-based features and linear discriminant functions. Accepted in JSTARS. pp.12
Zolli A, Healy A (2012) Resilience: why things bounce back. Free Press, New York